

## EDITORIAL

### National Conference “Sofia Electrochemical Days 2012” (SED2012)

The current issue of the Bulgarian Chemical Communications consist of the papers, presented as lectures and poster at the national conference “Sofia Electrochemical Days” (SED 2012), having international participants present, and held in Sofia in 10 – 13 December 2012.

Following the last three successful conference meetings, Sofia Electrochemical Days has establishing itself as an important national forum for exchanging information on the latest scientific and technical developments in the field of electrochemical science and technology. Sofia Electrochemical Days 2012 (SED2012) brought together both young and experienced Bulgarian and international scientists, engineers, university researchers along with industry and government employees to share results and ideas trough oral presentations, poster and educational sessions, and discussion.

Sofia Electrochemical Days 2012 noted 45 years from the founding of the Academician Evgeni Budevski Institute of Electrochemistry and Energy Systems and 90 years from the birth of the founder of the Bulgarian Electrochemical School Acad. Evgeni Budevski.

SED2012 was co-organized by the Academician Evgeni Budevski Institute of Electrochemistry and

Energy Systems - BAS, the Rostislav Kaishew Institute of Physical Chemistry - BAS and the University of Chemical Technology and Metallurgy. The conference was supported by the Bulgarian Electrochemical Society, the Bulgarian section of the International Society of Electrochemistry, the Bulgarian Hydrogen Society, and the Joint Innovation Centre of the Bulgarian Academy of Sciences.

We would like to thank the SED 2012 participants for their contribution to the conference success as well as for the warm and collaborative atmosphere they created. We express our sincere gratitude to the SED Organizing Committee, as well as to the authors for their incentive presentations, to the referees for their efforts in reviewing the submitted manuscripts and the Editorial Board of the Bulgarian Chemical Communications for the publications in this issue.

*Guest Editors:*

*Antonia Stoyanova*

*Reneta Boukoureshylieva*

*Academician Evgeni Budevski Institute of  
Electrochemistry and Energy Systems-  
Bulgarian Academy of Sciences*



## Half a century of excellence

Founded in 1967 as the Central Laboratory of Electrochemical Power Sources (CLEPS), the Academician Evgeni Budevski Institute of Electrochemistry and Energy Systems (IEES) maintains the traditions of the Bulgarian Physical Chemistry School of Stranski and Kaishev, advancing electrochemical research. For five decades already, IEES successfully applies fundamental electrochemical research in the development of novel electrochemical power sources, provides international expertise in the field of energy systems, and trains highly qualified researchers and scientists.

Ever since the first years of its existence, the Institute solves practical problems of the Bulgarian battery industry:

- separators of unwoven fabrics and the first plastic case for lead-acid batteries, introduced in the Targovishte battery plant, a number of technological enhancements for the Bulgarian and international lead-acid batteries production;
- primary zinc-air batteries, successfully introduced in the Samokov plant, provide power for an electrical vehicle developed by CLEPS six months earlier than General Motors. They power the communication of the First Bulgarian Himalayan Expedition and have been exported continually in Poland and Germany;
- primary lithium batteries, ranking Bulgaria among the first ten countries in the world to adopt this advanced production.

The successful application of zinc-air batteries for electrically driven vehicles continues with the next generation of mechanically rechargeable zinc-air batteries. A world record is achieved in cooperation with a German innovation enterprise in 1997 during a competition in Salt Lake City (USA).

The expertise attained in the field of batteries is efficiently directed towards novel and prospective rechargeable systems. The Institute is an internationally recognized research center for its experience in the development of innovative ideas and technologies.

IEES enters the 21st century with a new priority – green energy and hydrogen energetics. Extensive research is carried out at present on the production, conversion and storage of hydrogen (fuel cells, electrolyzers, metal hydrides).

Recently developed tools for e-science implementation enhance the possibilities for international cooperation and dissemination of the avant-garde electrochemical testing and diagnostic methods developed at the Institute.

IEES has a long-term tradition in intensive international collaboration with other scientific structures and firms. In the last ten years the Institute has over 250 scientific and business partners from 32 countries. More than 20 joint investigations are contracted yearly with other national and international institutions.

IEES started its participation in European Programs in 1994. 14 successful projects have been implemented up to now, five of which in the Seventh Framework Program.

Since 2003 IEES is a European Centre of Excellence in “Portable and Emergency Energy Sources”. The institute is a host organization of national and international scientific structures and forums: European Internet Center for Impedance Spectroscopy, publishing a free access electronic peer reviewed journal; Bulgarian Electrochemical Society; Bulgarian section of the International Electrochemical Society; LABAT international conference on lead-acid batteries, Sofia Electrochemical Days – a national forum with international participation; Technical Committee TK64 for standardization in the field of Power Sources.

Today the Institute's staff comprises 90 employees. The academic staff consists of 7 full professors, 5 professors emeritus, 5 honorable professors, 11 associate professors, 30 assistants. The auxiliary scientific staff includes 18 specialists with Master's or Bachelor's degrees. An international consulting board elected by the Scientific Board of the Institute aids by elaboration of the scientific strategy of IEES.

IEES publicity relies on world renowned scientists: Acad. Detchko Pavlov, Acad. Alexander Popov, Prof. Zdravko Stoynov, Prof. Vesselin Bostanov, Prof. Iovka Dragieva, Prof. Raicho Raicheff, Assoc. Prof. Anastasia Kaisheva, Assoc. Prof. Prokopi Andreev, Assoc. Prof. Geno Papazov, Assoc. Prof. Temelaki Rogachev.

I would like to congratulate the people who have been in IEES since the establishment of CLEPS and who are still actively devoted to the prosperity of the Institute: Detchko Pavlov, Zdravko Stoynov, Alexander Popov, Katia Veleva, Geno Papazov, Petar Getmanov, Bogdana Parusheva, Margarita Georgieva.

*Prof. Daria Vladikova,  
Director*

*Academician Evgeni Budevski Institute of  
Electrochemistry and Energy Systems-  
Bulgarian Academy of Science*



## Academician Evgeni Budevski – scientist and mentor



1922 – 2008

Acad. Evgeni Budevski is a founder and the first Director of the Institute of Electrochemistry and Energy Systems (former Central Laboratory of Electrochemical Power Sources).

However, before the establishment of CLEPS, he was already world renowned with his famous dislocation-free single crystal.

The story starts in 1932 when Stranski and Kaischew published their theory of 2-Dimensional growth of “ideal” single crystals. For more than 30 years Acad. Kaischew pushed his assistants to prove his theory experimentally. In 1958 the turn came for the young Evgeni Budevski. He gathered a small interdisciplinary team and finally overcoming numerous obstacles the “perfect” crystal was created at last.

The year was 1965. The theory was proven; the atomically flat single crystal surface became the ideal object for fundamental studies – nucleation and growth, double layer structure, adsorption of inorganic and organic species

But that is not all.... The dislocations problem was of decisive importance in many other fields – Metallurgy, Semiconductor Electronics and Materials Science. Only two years later and after Budevski’s lectures in 15 American universities, the leading Company Texas Instruments modified our method and started to produce dislocation-free silicon single crystals. Thus the highway for microelectronics development was open.

At that time, the Bulgarian government decided to establish the Central Laboratory for Electrochemical Power Sources. The idea of Acad. Pavlov to merge Budevski’s intelligence with the large domestic battery industry was fruitful and strategically sustainable. In just a few years, CLEPS created several innovations adopted in industrial production and soon became highly recognized all over the world.

Being an excellent scientist, Evgeni Budevski was also a careful director. He paid a lot of attention to select gifted young chemists, physicists, engineers and more experienced specialists. He was our mentor – with his university lectures, during everyday research work and in leisure – skiing, camping, sailing and traveling. With his intelligence, experience, and remarkable personality he was the living standard for us. In our eyes Budevski has grown as the perfect international scientist – with hundreds of personal relations worldwide, participating and organizing dozens of international meetings, he was elected as Vice-President of the International Society of Electrochemistry.

Today, celebrating the 45th anniversary of IEES (CLEPS), we are admiring the 90th anniversary of Budevski’s birth, remembering with deep gratitude Evgeni Budevski – our teacher, mentor and friend – as we thank destiny for the chance to know the remarkable scientist, manager, and human being Evgeni Budevski.

*Prof. Zdravko Stoynov*

*Academician Evgeni Budevski Institute of  
Electrochemistry and Energy Systems-  
Bulgarian Academy of Science*



## Characterization of humidity sensors with Ce-modified silica films prepared via sol-gel method

Z.P.Nenova<sup>1\*</sup>, S.V.Kozhukharov<sup>2</sup>, T.G.Nenov<sup>1</sup>, N.D.Nedev<sup>1</sup>, M.S.Machkova<sup>2</sup>

<sup>1</sup> Technical University of Gabrovo, 4 H.Dimitar Str., 5300 Gabrovo (Bulgaria)

<sup>2</sup> University of Chemical Technology and Metallurgy, 8 Kliment Ohridski Blvd., 1756 Sofia (Bulgaria)

Received January 21, 2013; Revised May 21, 2013

Silica films modified by Ce-compounds have been deposited on corundum substrates with silver-palladium electrodes. The depositions have been performed through dip-coating procedure of the substrates into sol-gel systems composed by tetraethyl orthosilicate (TEOS) and cerous nitrate ( $\text{Ce}(\text{NO}_3)_3$ ) as Si and Ce providers, respectively. After posterior sintering of the obtained sensors at 400°C and 800°C, their electrical properties have been characterized by means of precision impedance analyzer, in a humidity conditioning chamber. The respective superficial films have been observed by scanning electron microscopy (SEM). As a result, the relation between the surface morphology and electrical characteristics, as well as the properties of the investigated samples and their performance as humidity sensing elements have been determined.

**Key words:** humidity sensors, sol-gel method, silica, cerium-dopant, impedance spectroscopy

### INTRODUCTION

Humidity sensors are widely used in industry, agriculture, medicine, for storage and transportation of various products and raw materials, pieces of art, etc. Various types of humidity sensors are known. Ceramic and film elements based on metal oxide materials, such as:  $\text{Al}_2\text{O}_3$ ,  $\text{TiO}_2$ ,  $\text{SiO}_2$ ,  $\text{SnO}_2$ , and  $\text{ZnO}$  also belong to this group. They possess numerous advantages, as a comparatively easy manner of manufacturing, stability in aggressive media, relatively low cost, etc. [1, 2].

One of the directions in the preparation of thin film humidity sensing elements based on oxide materials is by a sol-gel method [3, 4]. This method makes possible the synthesis of nanostructured ceramic films. The specific features of nanostructured materials should lead to humidity sensing elements with improved parameters and characteristics.

Humidity sensing elements based on  $\text{SiO}_2$  are less studied. Their application to the preparation of humidity sensing elements with nanostructure is promising, since it enables their integration with other elements in the semi-conductor technology. Previous studies [5-7] have investigated  $\text{SiO}_2$ -based sensor elements obtained by the sol-gel method, using tetraethyl orthosilicate (TEOS) as a precursor. The influence of humidity on sol-gel derived  $\text{SiO}_2$ -based films, doped with  $\text{Fe}_2\text{O}_3$  has also been

studied [8, 9]. Cerium as an additive ingredient for metal oxide humidity sensors excels other frequently used dopants, because it corresponds to the environmental regulations which impose severe restrictions on the use of heavy metals [10, 11].

This paper proposes thin film humidity sensing elements based on silica films, doped with Ce-compound and prepared by a sol-gel method. The characteristics and parameters of the sensing elements obtained at different sintering temperatures have been investigated. Their impedance characteristics and equivalent electric circuits have also been determined.

### EXPERIMENTAL

#### *Sol-gel procedure*

The initial sol was composed of 60 ml of TEOS, „Alfa Aesar“- Karlsruhe (Germany), and 40 ml of n-Butanol (n-BuOH), preliminary heated up to 70°C in a covered beaker. The hydrolysis-polymerization process was induced by the addition of 2 ml of saturated solution (at room temperature) of  $\text{Ce}(\text{NO}_3)_3$  „Alfa Aesar“- Karlsruhe (Germany) in concentrated  $\text{HNO}_3$ . The sol-gel process was performed at 70°C for 1 hour, on magnetic stirrer. Finally, it was cooled at room temperature for 20 min. The sol-gel system obtained in this way was left for one day at 5°C, in a covered vessel, in order to avoid any evaporation of its ingredients, during the polymerization process.

\* To whom all correspondence should be sent:  
E-mail: z\_nenova@yahoo.com

### Film deposition

The film was deposited by a dip-coating procedure by triple dipping of alumina substrates with Ag-Pd electrodes. The sizes of the substrates are 18x10x0.5mm, identical to those, used in previous investigations [12, 13]. The procedure was performed by subsequent dipping of the substrates in the solution for 30 minutes at 70°C, and drying at the same temperature. Finally, the samples were sintered for 30 min, either at 400°C, or at 800°C. The samples are marked as: S\_400 or S\_800, respectively. Photograph of a sample, prepared as a humidity sensor, is shown in Fig.1.

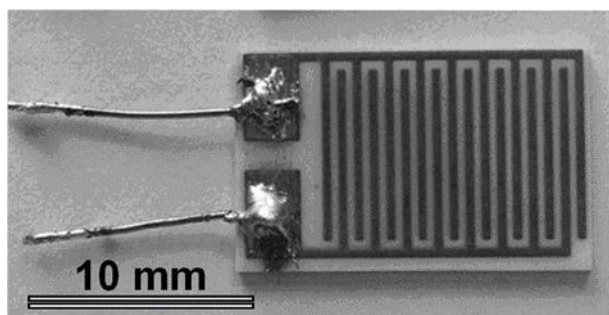


Fig. 1. Photograph of an investigated sample

### Measurements

- *Surface morphology observations:* They were performed by scanning electron microscopy (SEM), in order to determine the morphological features of the respective surface films. They were taken by scanning electron microscope TESCAN, SEM/FIB LYRA I XMU.

- *Electrical characteristics and parameters:* The measurement of the impedance of the obtained samples was taken by Precision Impedance Analyzer 6505P, produced by Wayne Kerr Electronics Ltd, at 500 mV of the excitation signal. The influence of frequency was investigated in the range from 20Hz to 1MHz. The investigated samples were placed inside a humidity generator VAPORTRON H-100BL, produced by BUCK RESEARCH INSTRUMENTS L.L.C., which provides conditioning of accurately controlled humidity with maximal deviation of up to  $\pm 1.5\%$  of relative humidity (RH). The range of relative humidity used is from 30 to 93%.

## RESULTS AND DISCUSSION

### Scanning electron microscopy

Fig.2 presents low magnification SEM-images of the surface of prepared samples S\_400 and S\_800, sintered at 400°C or 800°C, respectively. These images show that the sintering temperature

affects the size of the deposited aggregates of primary crystals and the areas between them. The size of these aggregates and areas between them increases with the rise of sintering temperature.

Quartz, tridymite and cristobalite are the three basic crystalline phases of pure SiO<sub>2</sub>. According to [14], the phase transition of silica from quartz to tridymite takes place at 870°C, whereas transformation to cristobalite proceeds at a temperature of 1470°C. Both sintering temperatures used for the present research are lower than these temperatures. Consequently, there are no phase transitions of these types.

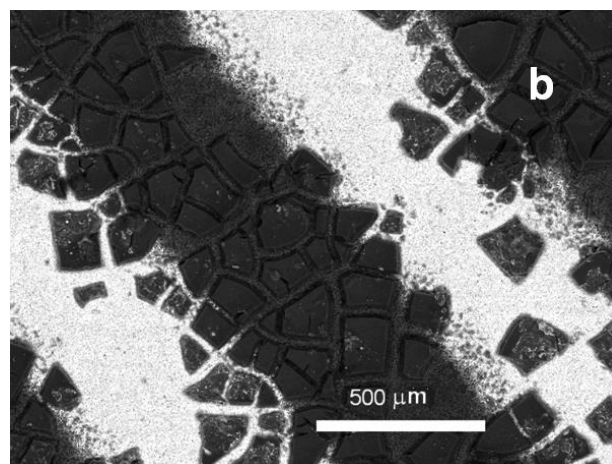
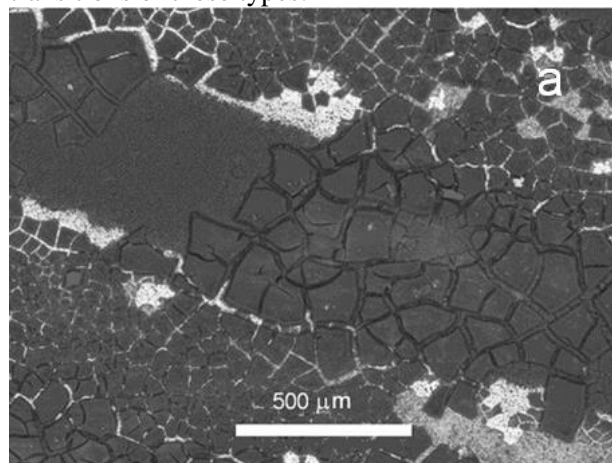


Fig.2. SEM – images of samples: (a) S\_400; (b) S\_800

### Electrical measurements

#### RH-impedance characteristics

The most widely used measure for humidity determination is relative humidity (RH). It can be defined as the percentage ratio of the measured partial pressure of water vapours to the saturated water vapours for given temperature [2]. The performance of the obtained humidity sensors was determined by impedance measurements at various humidity levels and at 25°C. Fig.3 presents the characteristics of samples S\_400 and S\_800 at

different frequencies in the range from 20Hz to 1MHz and at a temperature of 25°C, where  $z$  is the impedance and RH is the relative humidity.

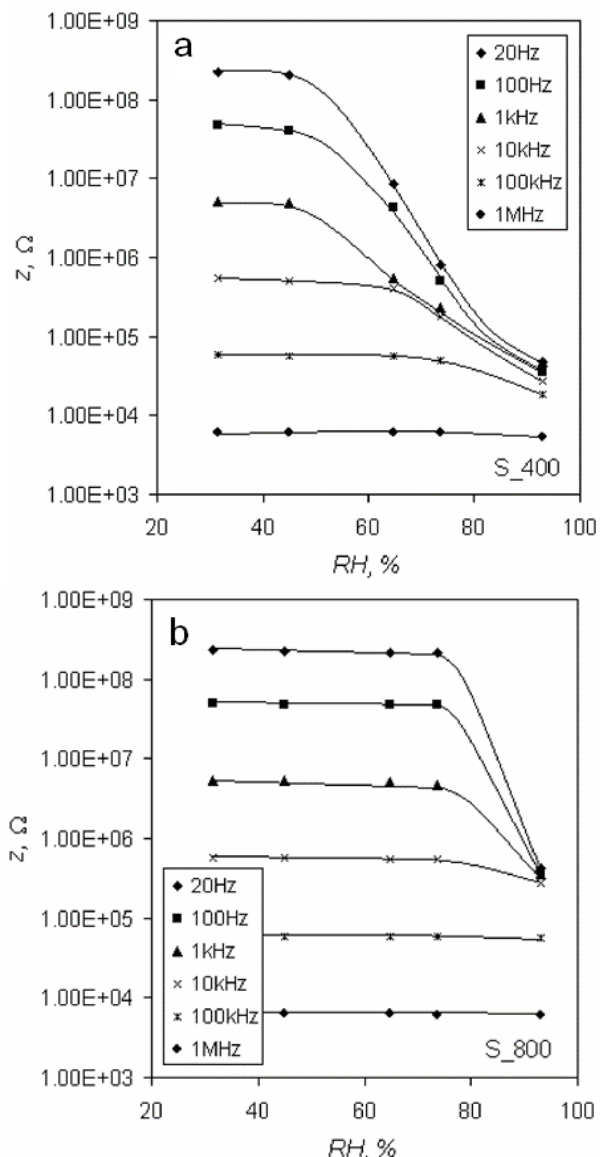


**Fig. 3.** Characteristics of samples: (a) S\_400 and (b) S\_800 at a temperature of 25°C

The figures are similar for both samples – when frequency increases, electric resistance decreases but at the same time, to our regret, sensitivity to humidity also decreases for both samples.

Sample S\_400, sintered at a temperature of 400°C, exhibits higher sensitivity of impedance to relative humidity in the range of 40-93 %RH. The maximal sensitivity value is 7.0 MΩ/%RH, 1.4 MΩ/%RH and 166.5 kΩ/%RH for 20Hz, 100Hz and 1kHz, respectively. Sample S\_800 has exhibited practically a constant value of the impedance for the 30-75%RH range, while at RH higher than 75%, its impedance abruptly drops, accompanied by enhancing its sensitivity, reaching

10.8 MΩ/%RH, 2.4 MΩ/%RH and 222.9kΩ/%RH for 20Hz, 100Hz and 1kHz, respectively. Thus, its characteristics are of switching type.

The impedance of the samples decreases with an increase in the relative humidity due to the chemical and physical adsorption and condensation of water in the areas between the deposited aggregates. In the initial stage of adsorption there is chemical adsorption of water molecules on the surface of crystals [2]. The active role in this process belongs to metallic atoms. They interact with the water molecules to form hydroxyl groups M-OH. In this way, the surface of crystals is covered by a monolayer of water molecules.

After the formation of the first chemically adsorbed layer, there is a second stage of physical adsorption of water molecules on it. During this stage, physical adsorption of water molecules proceeds on the formed layer [2]. The physically adsorbed layer is more weakly bonded to the surface of crystals, only by intermolecular interactions. The process of condensation of water vapour depends on the size and distribution of the areas between the deposited aggregates in the thin film. The filling of areas of smaller size starts at lower humidity, while the filling of areas of larger size happens at higher humidity levels.

Based on the topographies of the samples from the SEM images in Fig.2 and the investigations on their electrical properties (Fig.3), it can be concluded that an increase in the sintering temperature causes enlargement of the size of the areas between the deposited aggregates, lowers the sensitivity of the elements at lower humidity, and vice versa. This correlation of the size of areas between deposited aggregates with the sensitivities corresponds to the water vapour adsorption mechanism described above.

#### Impedance spectra

The frequency characteristics  $z(f)$  and  $\theta(f)$  of the samples have also been studied, where  $z$  is the impedance, and  $\theta$  is the angle, which change with the change in frequency. Based on these characteristics, the Nyquist plots of reactive resistances on active resistances for samples S\_400 and S\_800 at various RH and a temperature of 25°C have been obtained. Impedance spectra and equivalent electric circuits for the sensor elements are shown in Fig.4 and Fig.5.

In the absence of humidity, these plots are close to a straight line which corresponds to Nyquist plots of the initial films [15]. At lower levels of humidity (in the case of 30% - Fig.4a and Fig.5a)

Nyquist plots are arcs from semicircles of very large radii, and their equivalent circuit consists of a resistance  $R_1$  and capacitance  $C_1$  connected in parallel.

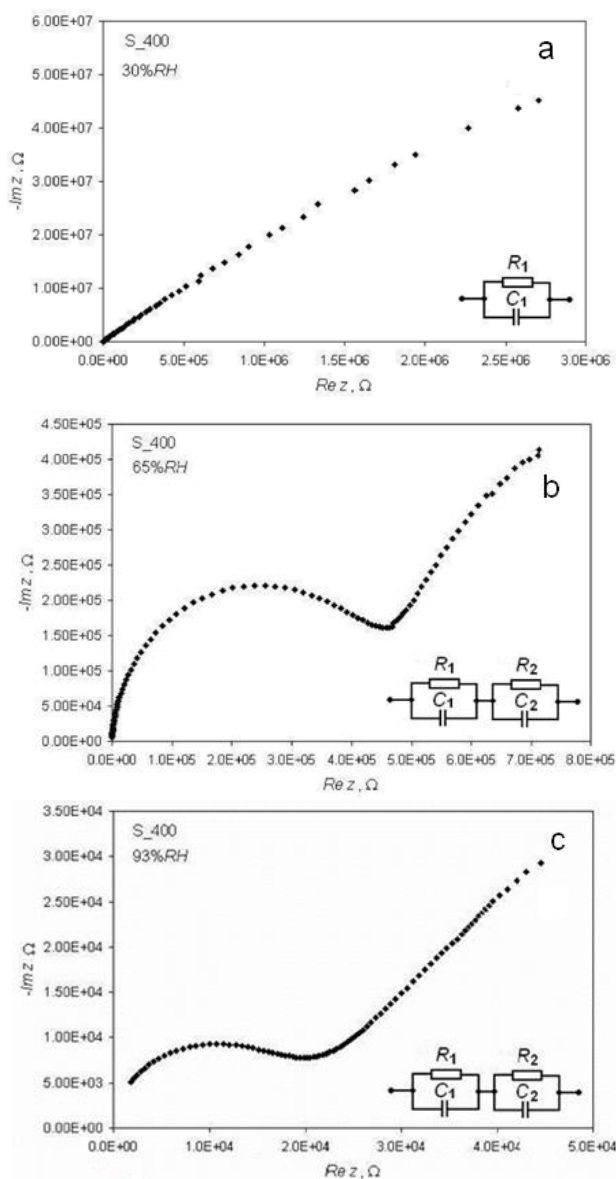


**Fig.4.** Nyquist plots and equivalent electric circuits for sample S\_400 at a temperature of 25°C and at relative humidity of: (a) 30%; (b) 65 % and (c) 93%

This type of impedance spectra can be explained by the prevailing type of electron conduction through the base material and the adsorbed water in the stage of chemical adsorption [15]. With an increasing RH (Fig.5b – 65%RH for S\_800) the chemisorption enhancement and leakage current increment lead to growing the curvature of the arc and it gradually approximates a complete semicircle. For sample S\_400 this transition occurs at humidity lower than 65%. Simultaneously, a decrement in the sample impedance is observed

related to the enhancement of this conduction. For sample S\_400 at 65%RH (Fig.4b), the equivalent circuit is composed of two groups of resistance and capacitance with parallel connection. The second group of  $R_2C_2$  is explained by the appearance of ionic type of conduction, as a consequence of the presence of physical adsorption as well. Therefore, the entire conduction mechanism is a combined action of both electron conduction and ionic conduction [15, 16]. In the Nyquist plots this is shown with the initiation of a second semicircle with a very large radius. For sample S\_800 this type of equivalent circuit and conduction is observed at higher level of humidity of 93% (Fig.5c) where the electron conduction still remains significant.

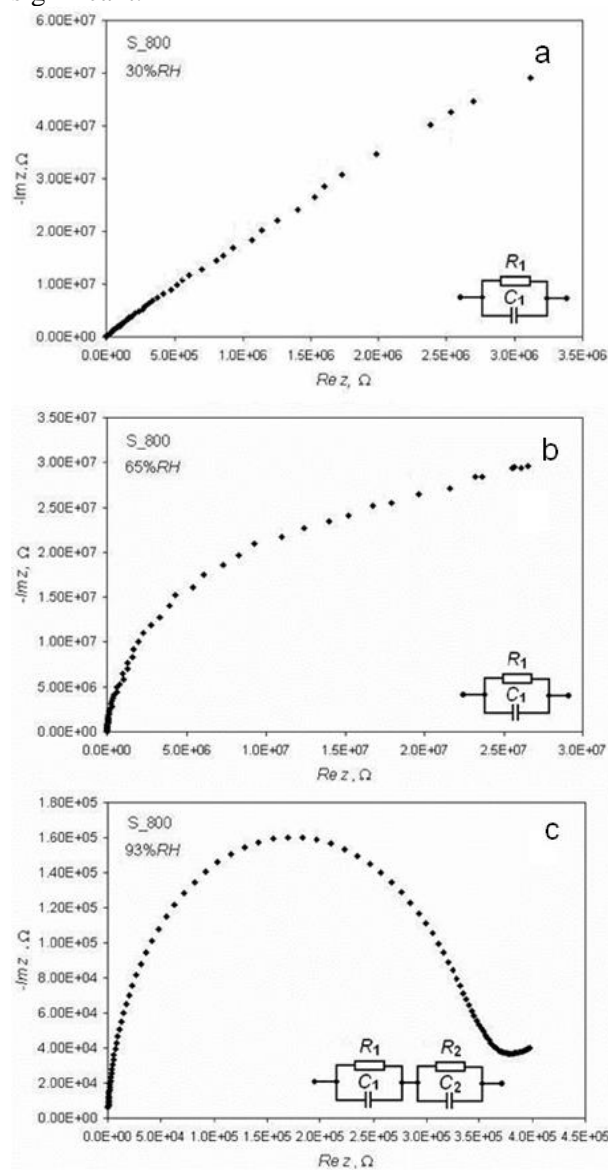


**Fig.5.** Nyquist plots and equivalent electric circuits for sample S\_800 at a temperature of 25°C and at relative humidity of: (a) 30%; (b) 65 % and (c) 93%

For sample S-400 at higher level of relative humidity of 93% (Fig.4c) the ionic conduction is higher compared to electron conduction, which is illustrated by extending the predominance of the second semicircle which turns into a nearly straight line. The appearance of ionic conduction results in sharp decrease in sample impedance. For sample S\_400 this happens at lower levels of humidity (at humidity levels below 65%RH – Fig.4b). This correlates also with the lower impedances of this sample at lower levels of humidity (Fig.3). On the basis of the impedance characteristics and spectra, it can be concluded that the samples sintered at 400°C, possess better sensing properties to humidity, compared to those sintered at 800°C. Therefore, it can be concluded that samples S\_400 can be used as humidity sensing elements within the range from 45 to 93%RH, and samples S\_800 can be used as trigger switching elements for humidity sensing.

### CONCLUSION

Humidity sensing elements have been obtained by deposition of SiO<sub>2</sub> films with the addition of Ce-compound by a sol-gel method. Among the samples investigated in the present work, increasing the sintering temperature from 400°C to 800°C increases the size of the deposited aggregates of primary crystals and the areas between them, leading to changes in the samples' electrical characteristics and parameters. Regarding the application of the obtained samples as humidity sensing elements, the best humidity sensing properties belong to the samples treated for 30 minutes in solution with Ce(NO<sub>3</sub>)<sub>3</sub> and sintered at 400°C. The samples, sintered at 800°C, can be used as trigger switching elements for humidity sensing.

**Acknowledgements:** This work was supported by the National Scientific Research Fund of Bulgaria under Contract № DO 02-148/2008.

### REFERENCES

1. Z. Chen, C. Lu, *Sensor Lett.*, **3**, 274 (2005).
2. T. Nenov, S. Yordanov, *Ceramic Sensors: Technology and Applications*, TECHNOMIC Publ. Co., Inc. Lancaster - Basel - 1996.
3. C. J. Brinker, G. W. Scherer, *Sol-Gel Science: The Physical and Chemistry of Sol Gel Processing*, Acad. Press. San Diego-New York-Boston, 1990.
4. E. Traversa, *Sensors and Actuators, B* **23**, 135 (1995).
5. P. Innocenzi, A. Martucci, M. Guglielmi, A. Bearzotti, E. Traversa, *Sensors and Actuators, B* **76**, 299 (2001).
6. C-T. Wang, C.-L. Wu, I-C. Chen, Yi-H. Huang, *Sensors and Actuators, B* **107**, 402 (2005).
7. J. Tua, N. Li, W. Geng, R. Wang, X. Lai, Y. Cao, T. Zhang, X. Li, S. Qiu, *Sensors and Actuators, B* **166**, 758 (2012).
8. R. Tongpool, S. Jindasuwan, *Sensors and Actuators, B* **106**, 523 (2005).
9. Q. Qi, T. Zhang, X. Zheng, L.Wan, *Sensors and Actuators, B* **135**, 255 (2008).
10. EU Directive 2002/95/EC “Restriction of Hazardous Substances in Electrical and Electronic Equipment” (RoHS directive 2002) ([www.broadcom.com/docs/](http://www.broadcom.com/docs/); [www.chem.agilent.com/](http://www.chem.agilent.com/))
11. U.S. Department of Health and Human Services, Public Health Service, Agency for Toxic Substances and Disease Registry, (2008) Toxicological profile for Chromium. ([www.atsdr.cdc.gov/toxprofiles/tp7.pdf](http://www.atsdr.cdc.gov/toxprofiles/tp7.pdf))
12. S. Kozhukharov, T. Nenov, Z. Nenova, M. Machkova, Impact of Dopants on the Characteristics of Thin-Film Humidity Sensor Elements, Proc. Sensor + Test Conf., 7 - 9. 6. 2011, Nürnberg, (Germany).
13. S. Kozhukharov, Z. Nenova, T. Nenov, S. Ivanov, *Ann. Proc., “Angel Kanchev” University of Rousse* (Bulgaria), **49**, 33 (2010).
14. D. L. Lakshtanov, S. V. Sinogeikin, J. D. Bass. *Phys. Chem. Minerals*, **34**, 11 (2007).
15. Y. Zhang, Y. Chen, Y. Zhang, X. Cheng, C. Feng, L. Chen, J. Zhou, S. Ruan, *Sensors and Actuators, B* **174**, 485 (2012).
16. E. C. Dickey, O. K. Varghese, K. G. Ong, D. W. Gong, M. Paulose C. A. Grimes, *Sensors*, **2**, 91 (2002).

## ОХАРАКТЕРИЗИРАНЕ НА СЕНЗОРИ ЗА ВЛАЖНОСТ С Се-ЛЕГИРАНИ СИЛИЦИЕВО-ДИОКСИДНИ СЛОЕВЕ, ИЗГОТВЕНИ ПО ЗОЛ-ГЕЛ МЕТОД

З. П. Ненова<sup>1</sup>, С. В. Кожухаров<sup>2</sup>, Т. Г. Ненов<sup>1</sup>, Н. Д. Недев<sup>1</sup>, М. С. Мачкова<sup>2</sup>

<sup>1</sup> Технически университет – Габрово, ул. "Хаджи Димитър" 4, 5300 Габрово (България)

<sup>2</sup> Химикотехнологичен и металургичен университет, бул. "Климент Охридски" 8, 1756 София (България)

Постъпила на 21 януари 2013 г.; Коригирана на 21 май, 2013 г.

(Резюме)

Получени са тънки слоеве от силициев диоксид, легиран с Се, върху подложки от двуалуминиев триоксид с предварително нанесени сребърно-паладиеви електроди. Отлагането на слоевете е извършено чрез метода на потапяне на подложките в зол-гел система от тетраетил ортосиликат (TEOS) и цериев нитрат ( $\text{Ce}(\text{NO}_3)_3$ ). След последващо синтероване на получените образци при 400°C и 800°C, са изследвани техните електрическите свойства с помощта на прецизен импедансен анализатор като те са поставяни в калибрираща камера за влажност. Получените слоеве са наблюдавани чрез сканиращ електронен микроскоп (SEM). Като резултат е определена връзката между структурната морфология и електрическите характеристики на изследваните образци, както и техните свойства и възможности за използване като чувствителни елементи за влажност.

## Classification and functional characterization of the basic types of photovoltaic elements

V. Bozhilov\*, S. Kozhukharov, E. Bubev, M. Machkova, V. Kozhukharov

University of Chemical Technology and Metallurgy, 8 Kliment Ohridski Blvd., 1756 Sofia, (Bulgaria)

Received February 6, 2013; Revised April 10, 2013

Nowadays, the continuous rise of the Human population emerges diversification of the energetic sources, for reliable energy supply. Furthermore, the sustainable development of the modern communities relies to environmentally friendly energy production equipment. The apparent energy demand arisen during the last decades has promoted remarkable scientific efforts for elaboration of entire new generations of photovoltaic elements (cells). In that means, the present brief literature review is attempt to classify the basic types photovoltaic elements

**Key words:** Photovoltaics, Silicon Solar Cells (SSC), Copper Indium Gallium Selenide Cells (CIGS), Cadmium Telluride Solar Cells (CTSC); Dye Sensitized Solar Cells (DSSC), Organic Solar Cells (OSC).

### INTRODUCTION

Each system, composed by electron conductors (electrodes), separated by ion conductor (electrolyte) can be considered as “electrochemical system” [1]. The basic processes that proceed inside the electrochemical systems are: electrochemical oxidation/reduction reactions on the electrode surfaces (that proceed by participation of electrons) and ionic transport between the electrodes, through the electrolyte. In order to work, all electrochemical systems require external electric chain for delivery of electrons for the respective electrochemical reactions. Additionally, all electrochemical systems could be divided into two general groups: (i) – electrochemical sources of electricity (they convert the chemical energy of spontaneous electrochemical reactions to 120 electric power) and (ii) – electrolyzers, and Galvanic baths (for conversion of electrical power to promote desirable electrochemical reactions). To the former kind of electrochemical systems belong all batteries from the most classical as the elements of Danielli [2], Weston [3], Volta, [4], through the widely used lead-acid accumulators (batteries) of Gaston Planté [5] to the nowadays elaborating lithium-ion batteries [6-10], and various kinds of fuel cells [11–16].

Alternative approach for elaboration of new generations of sources of energy is based on the employment of the solar energy for excitation of electrochemical reactions or metal/semiconductor's charge transfers on the interface between the

electrolyte and the electrodes. By that manner, the thermodynamic demand for excitation of an electrochemical reaction or alternatively electron-hole charge transition can be satisfied by involution of light energy via illumination. The response for the necessity for development of systems for elaboration of light induced energy sources is the solar cells, or otherwise called “photovoltaics”. The recent interest to these elements (devices) is predicted from their potential application as sensors for the industrial automation, as well [17].

In that means, the purpose of the present brief review is description and classification of the recently developed generations of photo-electrochemical cells.

### CLASSIFICATION OF THE BASIC TYPES OF PHOTOVOLTAICS

As a result of the literature review, it was established that there is a large variety of photovoltaic elements (cells), but all they belong to five general groups: Silicon Solar Cells (SSC), Copper Indium Gallium Selenide Cells (CIGS); Cadmium Telluride solar cells (CTSC), Dye Sensitized Solar Cells (DSSC), and Organic Solar Cells (OSC). All of them are based either on conductor/semiconductor junction, or photo-activated electrochemical reactions. In the former case, the light energy promotes electron-hole transitions through the metal/semiconductor interface, whereas in the latter case, photoactivated oxidation/reduction reactions proceed on the interface between electrolyte and electrode. Bube [18] summarizes 6 kinds of semiconductor junctions, according to the interface between the

\* To whom all correspondence should be sent:  
E-mail: valentin\_kitov@abv.bg

respective semiconductors. Completely all electrochemical devices are based on oxidation/reduction reactions on the electrode/electrolyte interface, combined by ion transport across the electrolyte.

### Silicon Solar Cells (SSC)

It is the most widely spread kind of solar cells, owing their origin since 1953 [19]. Cross-sectional schematic view of such kind of photovoltaic element is depicted in Fig. 1 [20].

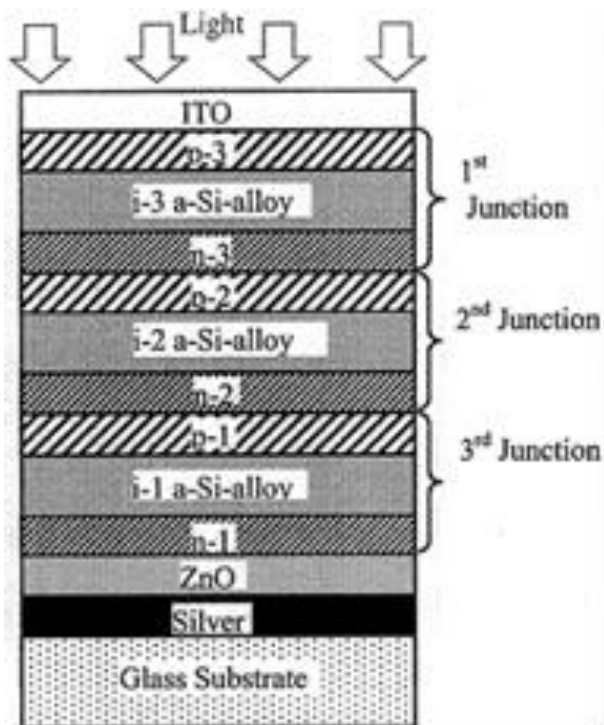


Fig. 1. Schematic cross-section of multilayered triple conjunction Si-solar cell [20].

### Copper Indium Gallium Selenide solar cells (CIGS)

During the recent decades, large variety of semiconductor non-electrochemical photovoltaic elements (cells) have (has) been elaborated as an alternative to the silicon ones. Among the most favorite pretenders are the chalcopyrite CIGS and the kesterite  $\text{Cu}_2\text{ZnSn}(\text{S},\text{Se})_4$  types of semiconductive materials, as is mentioned elsewhere [21, 22]. As all the rest types of photovoltaics, these cells are with multilayer structure, as well. Example for this kind of solar elements is depicted in Fig. 2.

In the construction, shown in Fig. 2, the p-n transition proceeds on the  $\text{Cu}(\text{InGa})\text{Se}_2 - \text{CdS}$ . This transition is excited by ZnO photoactive layer. The Indium Tin Oxide and the metallic molybdenum perform the function of electric

contact layers for connection with the external electrical chain.

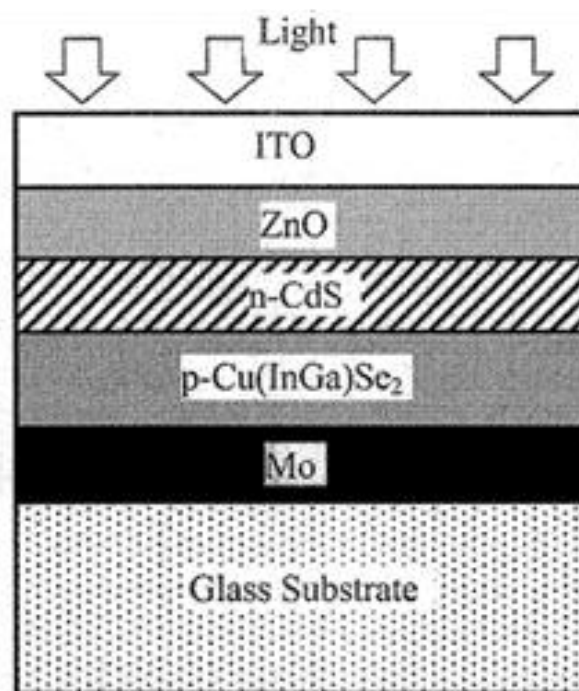


Fig. 2. Schematic illustration of CIGS –photovoltaic [20].

### Cadmium Telluride solar cells (CTSC)

Besides CIGS, cadmium telluride also can be employed as adsorptive material. Nevertheless, Cd is considered to be highly toxic metal. Its use is limited by severe environmental restrictions [23].

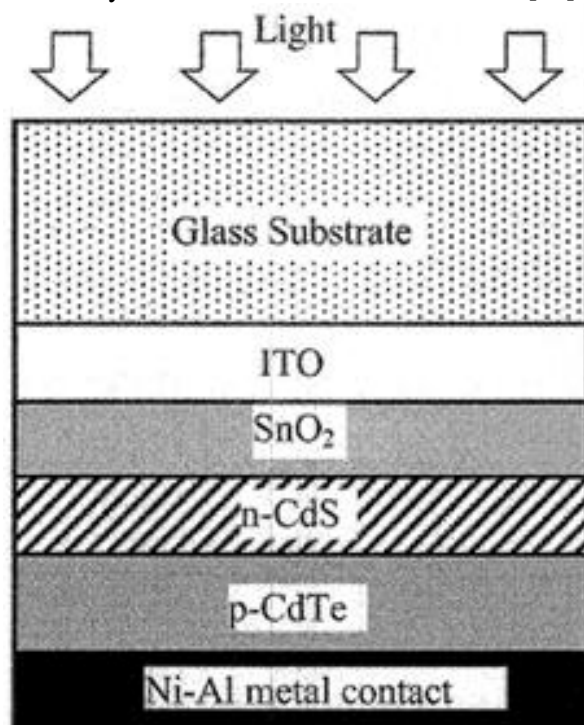


Fig. 3. Cross-section of CdTe –solar cell [20].

The organic chemical synthesis provides a great variety of organic conductive materials as an alternative to the application of heavy and toxic metals. In that means, various materials as organic dyes for Dye Sensitized Solar Cells, and even entirely organic solar cells are object of intensive research activities.

#### Dye Sensitized Solar Cells

These elements are based on photoactivated (activated) electrochemical processes, unlike all the rest photovoltaics. The interest to these elements (cells) has been raised remarkably, after the publications of O'Regan and Grätzel [24]. Its construction is depicted in Fig. 4.

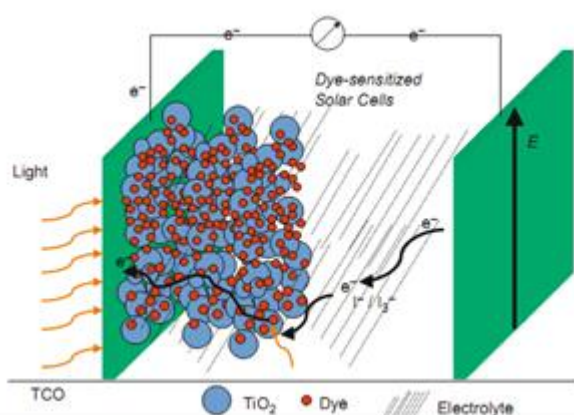


Fig. 4. Scheme of Dye Sensitized Solar cell [25]

The principle of function of these cells is based on reversible electrochemical oxidation of iodine ions ( $I_3^- \rightarrow I^-$ ) from (in) the electrolyte and their diffusion through the electrolyte. This process proceeds being promoted by photoactivation by dye sensitized mesoporous titania [24 – 27]. This oxide is considered to be non-toxic and biocompatible and even appropriate for fabrication of implants [28 – 30], or drug delivers [31 – 33]. At last, this oxide is described as a versatile material for large variety of applications [34].

According to Stacow et al. [35], the photosensitizers are substances, generally with organic origin, able to transmit the light energy, absorbed by them, to neighboring molecules. Nevertheless,  $TiO_2$  decomposes many organic substances when is illuminated by UV light. This fact means that titania is able to deactivate the photosensitizer by its decomposition. In addition, the presence of a liquid phase together with the photosensitizer decreases the life time of these elements. Furthermore, the simultaneous presence of oxidized and reduced iodine ions in the bulk of the electrolyte results in the recombination of the former by their “quenching” by the reduced form.

As a result, difficulties related to the reaching of high efficiency exist.

Among the most durable and reliable photosensitizers are the tetrapyrrole derivatives, such as: porphyrines, chlorines, phthalocyanines and naphthalocyanines. These compounds enable formation of metal complexes, where the metallic moiety could predetermine the optical properties of the respective metal-organic complex [36]. The properties of the respective metal-organic photosensitizer could be rather easily modified by involvement of different metal ions. Another advantage of these substances is their tremendous thermal and chemical durability, resulting in their compatibility to  $TiO_2$ -composed solids. Additionally, in the same book, these compounds are described as generally non-toxic and environmentally friendly substances. Indeed, the most famous presenters of these classes of compounds are the chlorophyll [37] in the algae and plants and the haemoglobin in the human and animal’s blood [38]. Generally, the tetrapyrrole-based dyes have various applications, for instance: photodynamic therapy of cancer diseases, bleaching of textile and paper, purification of air, or water disinfection, as is mentioned elsewhere [39].

Various approaches for improvement of the Dye Sensitized Solar Cells are available. The chemical modification of  $TiO_2$ , as DSSC layer enables covalent binding with the organic photosensitizers, in order to obtain a robust hybrid material (formed by covalent bonded dye sensitizer on chemically modified  $TiO_2$  with maximal porosity and specific surface area). Its activity could be supplementary enhanced by its modification with by involvement of transition metal ions, [40 - 43], noble metals [44, 45], or by other supplements [46 - 48] prior to dye deposition.

Other approach for optimization of the DSSC elements (cells) is the substitution of the liquid electrolyte by solid state ones [49, 50]. However, the solid state electrolytes supply unsatisfying contact, as is established by Gong et al. [51]. In the same article, they propose application of quasi-solid (gel) electrolyte, remarking its advantages as: (i) relatively high ambient ionic conductivity ( $6-8 \text{ mS}\cdot\text{cm}^{-1}$ ), (ii) intimate interfacial contact with  $TiO_2$ , and (iii) remarkable electrolyte stability. At the initial step, the solvent with a low viscosity penetrates the  $TiO_2$ . The gels are considered as “quasi-solid” state, because they are composed by equally distributed liquid in the bulk of a solid matrix [52].

In quasi-solid electrolytes, framework materials play an important role for providing of a liquid channel for the  $I_3^-/I^-$  diffusion [53]. Examples for such “quasi-solid” electrolytes by involvement of nanoparticles [54 - 57], or organic gelator [58 - 63] could be found in the literature. In [51] is mentioned that an alternative direction for optimization of the DSSC-elements (cells) is the substitution of the iodine compounds by other electrochemical mediators (electrolytes). Different works are dedicated in this field [64 - 66].

Alternative direction for enhancing of DSSC efficiency is via employment of carbon nanotubes [67, 68]. They can be produced extremely easy by simple spray pyrolysis of saccharose [69, 70].

Besides implementation of organic dyes, fabrication of almost entire organic solar cells is available, as well.

#### Organic solar cells

The organic chemical synthesis provides a great variety of compounds composed by only several elements: C, H, N, S, and O. In that means, the Organic Solar Cells could be fabricated without of any heavy metal (such as Cd), and rather less amounts of semiconductors or novel elements. Other advantage of OSC is that their industrial fabrication could proceed at moderate temperatures, without of remarkable energetic expense.

The functional principle of a typical organic solar cell is described to be opposite to this of the light emitting diodes [71]. When light is absorbed an electron is promoted from the highest occupied molecular orbital (HOMO) to the lowest unoccupied molecular orbital (LUMO) forming an exciton (see Fig. 5). In a PV device, this process is followed by exciton dissociation. The electron reaches one electrode while the hole must reach the other electrode.

Sn-oxides could be SnO or SnO<sub>2</sub>, according to the oxidation state of tin, whereas the most typical

oxidation state of Indium is +3. In that means, the difference the doping of Sn(IV)-oxide by In(III) promotes depletion of electrons (vacancies), while the In(III) added Sn(II)-oxide should possess excess of electrons. When the element in Fig. 5-b is illuminated, the organic substance becomes electric conductor, and the more active metals from the counter-electrode render their electrons to compensate the electron vacancies in the  $In_xSn_{1-x}O_4^{\delta+}$ .

The conductivity of the organic substances could appear only when they possess a “conjugated” structure. This class of organic substances has cyclic structures with subsequent repetition of double bonds. They enable the presence of delocalized  $\pi$ -molecule orbitals enabling transmission of electrons through the entire organic molecules [72]. All organic substances with: (i) aromatic structures, (such as benzene, naphthalene, the anthraquinones, phenantrenes); (ii) pyrrole (iii) aniline derivatives, etc. possess electric conductivity. Among the most appropriated organic conductors are the mentioned in the previous section porphyrines and phtalocyanines.

Regardless the apparent similarity between the Dye Sensitized Solar Cells and the Organic Solar Cells, the latter (e.g. OSC) are not electrochemical devices, because any ionic transport is not involved in their function. Consequently, the Organic Solar Cells do not relay to the definition for an “electrochemical device” [1].

Nowadays, there are various approaches for optimization of the organic solar cells in both directions of increasing of their efficiency, and extending of their durability [73]. One of the basic trends in the elaboration of new OSC is the employment of junctions of more than one polymer.

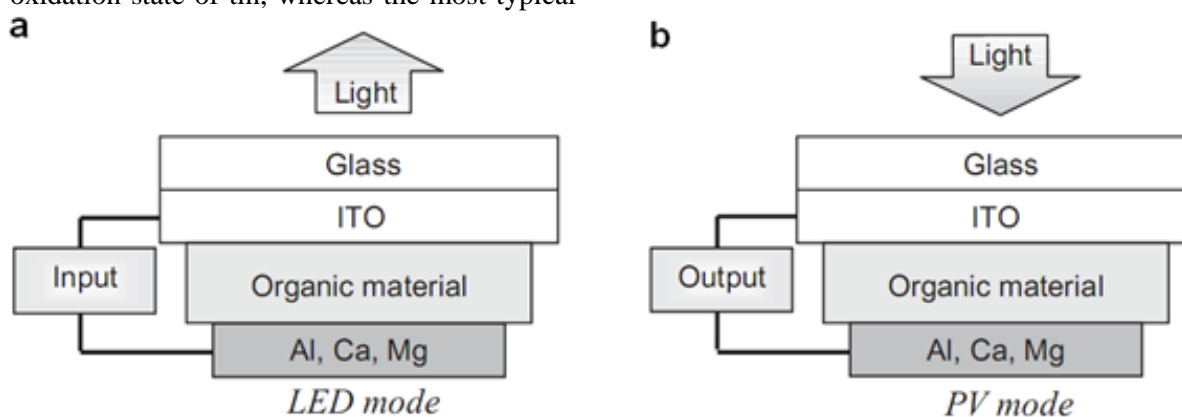


Fig. 5. Illustrations of light emitting diode (a) and organic photovoltaic element (b) [71], ITO - Indium Tin Oxide

Here should be mentioned that when elements as O, S, or N are included in the organic compound, it could reveal semiconductors properties. The reason for these properties is the aptitude of these elements to change their oxidation state (for example N(III) → N(V); S(II) → S(VI), etc.). In that means various polymers of organic substitution derivatives are investigated [74 – 80]. Involvement of carbon nano-particles is also described in the literature [73, 81]. Besides, there are technologies for their easy production [69, 70].

The main disadvantages of the organic solar cells are their relatively low efficiency [73], and low durability. The main processes of deterioration of these elements are: water and O<sub>2</sub> uptake that lead to corrosion of the metallic electrodes, decomposition oxidation and hydration of the organic stuff as is describe in detail, elsewhere [82].

### CONCLUSION

As a result of the literature review done, several important conclusions were reached:

The photovoltaics can be divided into five main groups: (i) - Silicon Solar Cells (SSC), (ii) - Copper Indium Gallium Selenide Cells (CIGS), (iii) - Cadmium Telluride solar cells (CTSC); (iv) - Dye Sensitized Solar Cells (DSSC), (v) - Organic Solar Cells (OSC). The former three groups are completely composed by inorganic materials, whereas the latter two contain organic compounds in their structures.

The latter two groups of PV are more perspective for R & D, then the former, because they are relatively newer classes, and do not require toxic or environmentally incompatible elements, such as cadmium.

From all five groups of PV, only DSSC can be considered as photoelectrochemical devices, because of presence of purely electrochemical processes of oxidation/reduction and ion transport between the electrodes.

**Acknowledgements:** The authors appreciate the EC financial support of this work in 7<sup>th</sup> project No 286605, "FABRIGEN".

### REFERENCES

1. R. Petrucci, W. Horwood, General Chemistry. Modern principles and applications, 7<sup>th</sup>. Edition, publ. Prentice Hall Iberia, Madrid (1999) p. 728 – 729.
2. <http://de.wikipedia.org/wiki/Daniell-Element>
3. I. Nenov, "Bases of the Electrochemistry", *Gov. ed. "Technicka"*, Sofia, (1989), pp. 164- 165.
4. <http://www.chemieunterricht.de/dc2/echemie/voltaelt.htm>
5. [http://en.wikipedia.org/wiki/Lead%E2%80%93acid\\_battery](http://en.wikipedia.org/wiki/Lead%E2%80%93acid_battery)
6. C. Julien, Z. Stoynev (ed.), "Materials for Lithium Ion batteries", Kluwer academic publishers, (publ. house) Dordrecht, (The Netherlands) – 2000.
7. H. Vasilchina, A. Aleksandrova, A. Momchilov, B. Banov, A. Barau, M. Zacharesku, "Spherical graphite as anode in high efficient lithium batteries", Proceedings of the international Workshop "Portable and Emergency Energy Sources – from materials to systems", 16 – 22 September 2005 Primorsko (Bulgaria), P. 1-4 – P.4-6.
8. V. Manev, A. Momchilov, K. Tagawa, A. Kozawa, *Prog. Batteries Battery Mat.*, **12**, 157 (1993).
9. N. Ilchev, B. Banov, *J. Power Sour.*, **35**, 175 (1991).
10. V. Manev, I. Naidenov, B. Puresheva, G. Pistoia, *J. Power Sour.*, **57**, 133 (1995).
11. S.M. Hristov, R.I. Boukoureshtlieva, Y.D. Milusheva, *Bul. Chem. Comm.*, **43**, 111 (2011).
12. Z. Stoynev, D. Vladikova, G. Raikova, D. Soysal, Z. Ilhan, S. Ansar, "Impedance Behavior of LSCF/YDC/LSCF Symmetrical Half Cell Prepared by Plasma Spray", *Proceeds. Advances and Inovations in SOFCs*, Katarino, Bulgaria (2009) p. 77.
13. V. Kozhukharov, N. Brashkova, M. Ivanova, J. Carda, M. Machkova, *Bol. Esp. Ceram. Vidrio*, **41**, 471 (2002).
14. E. Budevski, *J. Optoelectronics Adv. Mat.* **5**, 1319 (2003).
15. S. Simeonov, M. Machkova, V. Kozhukharov, J-C. Grenier, *Annual Proceed. "Angel Kanchev" University of Ruse (Bulgaria)* **49**, 8. (2010).
16. S. Simeonov, S. Kozhukharov, M. Machkova, N. Saliyski, V. Kozhukharov, *J. Univ. Chem. Technol. Met.* **47**, 1319 (2012).
17. Z. Nenova, S. Ivanov, T. Nenov, *Sensors in the Industrial automation, "Ex-Express" Ltd. ed. – Gabrovo, (Bulgaria), 2011, pp. 104 – 107.*
18. R. H. Bube, "Photovoltaic materials", *Imperial Press Colledge Press.* (1998), 17 – 24.
19. Chapin DM, Fuller CS, Pearson GL. "A new silicon p–n junction photo cell for converting solar radiation into electrical power". *Journal of Applied Physics*; **25**: 676 (1954)
20. K. L. Chopra, P. D. Paulson, V. Dutta, *Prog. Photovolt. Res. Appl.*, **12**, 69 (2004).
21. D. Fraga, R. Marti, T. Lyubenova, L. Oliveira, A. Rey, S. Kozhukharov, J. Carda, *Proceed. "Angel Kanchev" University of Ruse* **51**, (9.1), (2012), 46 – 49.
22. S. Ahmed, K. B. Reuter, O. Gunawan, L. Guo, L. T. Romankiw, H. Deligianni, *Adv. Energy Mater.* **2**, 253 (2012).
23. EU Directive 2002/95/EC "Restriction of Hazardous Substances in Electrical and Electronic Equipment" (RoHS directive 2002), [www.broadcom.com/docs/www.chem.agilent.com/](http://www.broadcom.com/docs/www.chem.agilent.com/)

24. B. O'Regan, M. Gratzel, *Nature*, **353**, 737 (1991).
25. A. Hagfeldt, U. Cappel, G. Boschloo, L. Sun, L. Kloo, H. Pettersson, E. Gibson, Practical Handbook of Photovoltaics, *Elsevier Ed.* 2012, p. 498.
26. Md. K. Nazeeruddin, E. Baranoff, M. Grätzel, *Solar Energy*, **85**, 1172 (2011).
27. M. Grätzel, A. J. McEvoy, "Principles of Dye Sensitized Nanocrystalline Solar Cells", accessible via: [www.photoelectrochemistry.epfl.ch/EDEY/AJEE.pdf](http://www.photoelectrochemistry.epfl.ch/EDEY/AJEE.pdf)
28. S-H. Lee, H-W. Kim, E-J. Lee, L-H. Li, H-E. Kim, *J. Biomater. Appl.*, **20**, 195 (2006).
29. K. Gotfredsen, A. Wennenberg, C. Johanson, L.T. Skovgaard, E. Hjorting-Hansen, *J. Biomed. Mater. Res.*, **29**, 1223 (1995).
30. A. Kar, K. S. Raja, M. Mishra, *Surf. Coat. Technol.*, **201**, 3723 (2006).
31. Y. Qin, L. Sun, X. Li, Q. Cao, H. Wang, X. Tang, L. Ye, *J. Mater. Chem.*, **21**, 18003 (2011).
32. H. Jiang, T. Wang, L. Wang, C. Sun, T. Jiang, G. Chen, S. Wang, *Micropor. Mesopor. Mater.*, **153**, 124 (2012).
33. H. Peng, S. Feng, X. Zhang, Y. Li, X. Zhang, *Sci. Total Env.*, **438**, 66, (2012).
34. V. Bozhilov, S. Kozhukharov, E. Bubev, M. Machkova, V. Kozhukharov, "Application of TiO<sub>2</sub> and its derivatives for alternative energetic sources", Proceedings of "Angel Kanchev" University of Ruse (Bulgaria), 51, (9.1), (2012), 36 – 40.
35. R. J. Stakow, R. Burstein, UCLA, *Grad. Sci. Jour*, **68** (2002).
36. R. Bonnett, "Chemical aspects of photodynamic therapy", Ed. Gordon & Breach Sci. Publication, (London) – 2000, pp. 142 – 145.
37. D. Schumm, Essentials of biochemistry, 2<sup>nd</sup>. Ed. Little Brown & Co. (Inc.) (Boston OH – USA (1988), 286 – 288.
38. E. Ganchev, T. Nickolov, Biochemistry for medicals and dentists, Kl. Okhridsky ed. (1995), 591 – 596.
39. M. Krysteva, S. Artarsky, S. Kozhukharov, *J. Univ. Chem. Technol.*, **38**, 793 (2003).
40. A. T. Vu, Q. T. Nguyen, T. H. L. Bui, M. C. Tran, T. P. Dang, T. K. H. Tran, *Adv. Nat. Sci.*, doi:10.1088/2043-6254/1/1/015009
41. M. Chong, B. Jin, Christopher P. Saint, *Chem. Eng. Jour.*, **171**, 16 (2011).
42. C. Karanukaran, A. Vijabalan, G. Manikandan, *Res. Chem. Intermed.* DOI 10.1007/s11164-012-0700-0.
43. J. Zhu, F. Chen, J. Zhang, H. Chen, M. Anpo, *J. Photochem. Photobiol.*, **A-180**, 196 (2006).
44. N. Dragan, D. Crisan, M. Crisan, M. Raileanu, A. Braileanu, A. Ianculescu, V. Teodorescu, "Sol-Gel Ag/TiO<sub>2</sub> films from nanopowders – structural study", Proceedings, "4<sup>th</sup>. Balkan Conference on glass science and technology & 16<sup>th</sup> conference on glass and ceramics", 27 September – 01 October, 2011, Varna (Bulgaria), Vol. 2, "Ceramics", 145 - 150.
45. D. Crisan, N. Dragan, M. Crisan, M. Raileanu, A. Braileanu, A. Ianculescu, D. Mardare, D. Luca, A. Nastuta, "Sol-Gel Au/TiO<sub>2</sub> films from nanopowders – structural study", Proceedings, "4<sup>th</sup>. Balkan Conference on glass science and technology & 16<sup>th</sup> conference on glass and ceramics", 27 September – 01 October, 2011, Varna (Bulgaria), Vol. 2, "Ceramics", 138 - 144.
46. S-J. Cho, C-K. Junk, Y-H. Song, J-H. Boo, "Synthesis of N-doped TiO<sub>2</sub> photocatalytic thin films with controlled nitrogen partial pressure and study on their catalytic activity", Proceedings "First international conference on materials for energy" – 4-8 July 2010, Karlsruhe, (Germany), B-1121.
47. M. Crisan, M. Raileanu, A. Braileanu, M. Crisan, N. Dragan, I. Nitoi, A. Ianculescu, "Sol-Gel pure and S-doped TiO<sub>2</sub> with ecological applications", Proceedings, "4<sup>th</sup>. Balkan Conference on glass science and technology & 16<sup>th</sup> conference on glass and ceramics", 27 September – 01 October, 2011, Varna (Bulgaria), Vol. 2, "Ceramics", pp. 151-155.
48. D. Li, H. Haneda, S. Hishita, N. Ohashi, N. K. Labhsetwar, *Jour. Fluor. Chem.*, **126**, 69 (2005).
49. A. Dualeh, R. Humphry-Baker, J. H. Delcamp, M. K. Nazeeruddin, M. Gratzel, *Adv. Energy Mater.* DOI: 10.1002/aenm.201200701
50. H. Sakamoto, S. Igarashi, K. Niime, M. Nagai, *J. Ceram. Soc. Japan*, **120**, 304 (2012).
51. J. Gong, J. Liang, K. Sumathy, *Renewable and Sustainable Energy Reviews* **16**, 5848 (2012).
52. S. Kozhukharov, *J. Univ. Chem. Technol. Met.*, **44**, 143 (2009).
53. F-T. Kong, S-Y. Dai, K-J. Wang, *Adv. OptoElectronics*, ID 75384, (2007), 13 pages.
54. P. Wang, S. Zakeeruddin, P. Comte, I. Exnar, M. Grätzel, *J. Amer. Chem. Soc.*, **125**, 1166 (2003).
55. Z. Lan, J. Wu, J. Lin, M. Huang, *J. Sol-Gel Technol.* **53**, 599 (2010).
56. J. Park, D. Roh, S. Ahn, J. Kim, *J. Nanosci. Nanotechnol.*, **11**, 1718 (2011).
57. H. Usui, H. Matsui, N. Tanabe, and S. Yanagida, *J. Photochem. Photobiol.* **A-164**, 97, (2004).
58. L. Gu o, S.-Y. Dai, K.-J. Wang, X.-Q. Fang, C.-W. Shi, and X. Pan, *Chem. Jour. Chinese Univ.*, **26**, 1934 (2005).
59. V. Jovanovski, E. Stathatos, B. Orel, P. Lianos, *Thin Solid Films*, **511**, 634 (2006).
60. L. Wang, S. Fang, Y. Lin, X. Zhou, and M. Li, *Chem. Commun.*, **45**, 5687 (2005).
61. P. Wang, S. M. Zakeeruddin, I. Exnar, M. Grätzel, *Chem. Commun.*, **8**, 2972 (2002).
62. K. Suzuki, M. Yamaguchi, M. Kumagai, N. Tanabe, and S. Yanagida, *Comptes Rendus Chimie*, **9**, 611 (2006).
63. J. Kang, W. Li, X. Wang, Y. Lin, X. Xi ao, and S. Fang, *Electrochim. Acta*, **48**, 2487 (2003).
64. Gorlov M, Pettersson H, Hagfeldt A, Kloo L., *Inorg. Chem.*, **46**, 3566 (2007).
65. J. Yum, E. Baranoff, F. Kessler, T. Moehl, S. Ahmad, T. Bessho, A. Marchioro, E. Ghadiri, J. Moser, C. Yi, M. Nazeeruddin, M. Grätzel, *Nature Commun.*, **3**, 631 (2012).

66. N. Papageorgiou, Y. Athanassov, M. Armand, P. Bonhote, H. Pettersson, A. Azam, M. Grätzel, *J. Electrochem. Soc.* **143**, 3099 (1996).
67. K. Atiola, A. Kaskela, J. Halme, V. Ruiz, A. Nasibulin, E. Kauppinen, P. D. Lund, *Electrochem. Soc.* **157**, 1831 (2010).
68. G. Hashmi, K. Miettungen, T. Peitola, J. Halme, I. Asghar, K. Aitola, M. Toivola, P. Lund, *Renewable and Sustainable Energy Reviews*, **15**, 3717 (2011).
69. M. Fortunato, M. Rostam-Abadi, K. Suslick, *Chem. Mater.*, **22**, 1610 (2010).
70. Al. Darabont, P. Nemes-Incze, K. Kertész, L. Tapasztó, A. A. Koós, Z. Osváth, Zs. Sárközi, Z. Vértesy, Z. E. Horváth, L. P. Biró, *J. Optoelectronics Adv. Mat.*, **7**, 631 (2005).
71. H. Spanggaard, F. C. Krebs, *Sol. Energy Mater. Sol. Cells*, **83**, 125 (2004).
72. G. Petrov, Organic Chemistry, "Kl. Okhridsky" Acad. Ed. (1996), p. 227.
73. W. Cai, X. Gong, Y. Cao, *Sol. Energy Mater. Sol. Cells*, **94**, 114 (2010).
74. N. Blouin, A. Michaud, M. Leclerc, *Adv. Mater.*, **19**, 2295 (2007).
75. F. Banishoeib, A. Henckens, S. Fourier, G. Vanhooyland, M. Breselge, J. Manca, T. J. Cleij, L. Lutsen, D. Vanderzande, L. H. Nguyen, H. Neugebauer, N. S. Sariciftci, *Thin Solid Films*, **516**, 3978 (2008).
76. H. Hoppe, N. S. Sariciftci, *Adv. Polym. Sci.*, **214**, 1 (2008).
77. F. Banishoeib, P. Adriaensens, S. Berson, S. Guillerez, O. Douheret, J. Manca, S. Fourier, T. J. Cleij, L. Lutsen, D. Vanderzande, *Sol. Energy Mater. Sol. Cells*, **91**, 1026 (2007).
78. C. J. Brabec, J. R. Durrant, *M.R.S. Bull.*, **33**, 670 (2008).
79. B. C. Thompson, J. M. Frechet, *Angew. Chem. Int. Ed.*, **47**, 58 (2008).
80. C.Y. Yu, C.P. Chen, S.H. Chan, G.W. Hwang, C. Ting, *Chem. Mater.* **21**, 3262 (2009).
81. J. K. Lee, W. L. Ma, C. J. Brabec, J. Yuen, J. S. Moon, J. Y. Kim, K. Lee, G. C. Bazan, A. J. Heeger, *J. Am. Chem. Soc.*, **130**, 3619 (2008).
82. M. Jørgensen, K. Norrman, F. C. Krebs, *Sol. Energy Mater. Sol. Cells*, **92**, 686 (2008).

## КЛАСИФИКАЦИЯ И ФУНКЦИОНАЛНА ХАРАКТЕРИСТИКА НА ОСНОВНИТЕ ВИДОВЕ ФОТОВОЛТАИЧНИ ЕЛЕМЕНТИ

В. Божилов\*, С. Кожухаров, Е. Бубев, М. Мачкова, В. Кожухаров

Химикотехнологичен и Металургичен университет, бул. Климент Охридски 8, 1756 София, България

Постъпила на 6 февруари, 2013 г.; Коригирана на 10 април, 2013 г.

(Резюме)

В днешно време, поради непрекъснатото увеличаване на населението възниква диверсификация на енергийните източници. Освен това, устойчивото развитие на съвременното общество се променя към производство на екологично чиста енергия. Високото потребление на енергия през последните десетилетия е насърчило забележително научните изследвания за разработване на цели нови поколения фотоволтаични елементи (клетки). В този смисъл ще бъде представен кратък литературен обзор на основните видове фотоволтаични елементи.

## Influence of the deposition conditions on the properties of D16 AM clad alloy, dip-coated in Ce-containing baths

D. S. Rodríguez<sup>1</sup>, S. Kozhukharov<sup>2\*</sup>, M. Machkova<sup>2</sup>, V. Kozhukharov<sup>2</sup>

<sup>1</sup>University of Vigo, Lagoas, Marcosende 36310 (Spain)

<sup>2</sup>University of Chemical Technology and Metallurgy, 8 “Kl. Okhridsky” blvd., Sofia 1756 (Bulgaria)

Received January 31, 2013; Revised April 11, 2013

The aim of the present research work is to elucidate the influence of various conditions on the spontaneous deposition of cerium conversion layers from solutions of diammonium pentanitrocerate  $(NH_4)_2Ce(NO_3)_5$  on D16 AM clad alloy, via dip-coating, and to perform posterior comparative analysis on both the performance and features of the obtained coatings. Their characterizations are done by means of durability tests in a model corrosive medium, composed by 3.5% NaCl solution, combined by regular electrochemical measurements, and subsequent morphological characterizations. The former were executed by Electrochemical Impedance spectroscopy (EIS) coupled by Linear Sweep Voltammetry (LSV), whereas the latter were performed by Scanning Electron Microscopy (SEM), combined by Energy Dispersive X-ray Analysis (EDX). As a result, the optimal conditions for deposition of cerium conversion layers via dip-coatings are determined.

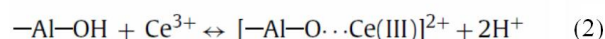
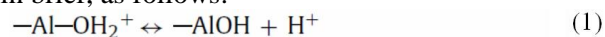
**Key words:** Aluminium alloy, corrosion, EIS, LSV, SEM, EDS

### INTRODUCTION

The metal alloys encounter extreme importance for all kinds of aircraft, automobile, railway, pipeline and marine transport. Nevertheless, they always possess considerable aptitude to suffer corrosion. On the other hand, the recent environmental restrictions [1 - 4], emerge the application of environmentally friendly compounds for coating depositions. In that means, intensive research activities for application of Ce-compounds as corrosion inhibitors or coating ingredients on steels [5 - 9], aluminium [10 - 15] or magnesium [16, 17] alloys have been undertaken. The real coating systems are multilayered, and each layer has its own function, contributing to the entire coating system [18 - 20].

In that means, the Cerium Conversion Coatings (CeCC) can serve as an excellent base for primer and finishing layers, providing better adherence of the upper layers, and active corrosion protection via “self healing” effect [21, 22]. Arenas describes the conversion coatings as products of chemical or electrochemical process, consisted on formation of a metallic oxide, with different properties, being substitute of the native superficial oxide layer of the respective substrate [22]. Undoubtedly, the features and performance of the CeCC are predetermined by

the metallic surface prior to deposition, as well as the deposition conditions. Conde et al. [23] remark that the obtaining of desirable covering layer passes through chemisorption processes on the superficial oxide layer of the aluminum that could be described in brief, as follows:



According to them, this chemisorption process passes via formation of intermediated complexes on the metallic surface, such as:  $Al-O-Ce-(OH)_2^{2+}$ . This intermediate process is crucial for the formation of adherent protective film instead of colloidal precipitates and sediments in the solution.

Taking into account that the superficial oxide layer of the aluminum consists simultaneously on:  $Al_2O_3$ ,  $Al(OH)_3$  and  $AlO(OH)$  phases [24], it could be assumed that the composition of the oxide layer has extreme importance for the formation of well defined adherent protective layer, instead of precipitates and sediments. The oxide layer as structure and composition depends so on the preliminary treatment applied, so on the pH of the medium during the deposition.

Besides the metallic superficial composition and roughness, the Al-oxide layer composition, the bulk and localized solution pH, concentrations of reactants, products and additives, reaction time and

\* To whom all correspondence should be sent:

E-mail: stephko1980@abv.bg

temperature, are some of the more important parameters that must be controlled [21].

The aim of the present research activities is to follow the correlations between several important parameters of CeCC deposition and combinations of them on the features of the respective coatings, and their performance in a model corrosive medium

## EXPERIMENTAL

### *Metallic substrates*

Clad alloy D16 AM, classified by GOST 172342-99 [25] delivered by Klöckner Metalsnab (Bulgaria) was used as a substrate material. According to the standard, this aluminium alloy contains: Cu, 3.8 – 4.9 %<sub>wt</sub>; Mg, 1.2 – 1.8%<sub>wt</sub>; Fe 0.5%<sub>wt</sub>, Si 0.5 %<sub>wt</sub>, Mn 0.3 – 0.9 %<sub>wt</sub>, Zn 0.25 %<sub>wt</sub>, Ti – up to 0.15%<sub>wt</sub>, Cr – up to 0.10%<sub>wt</sub> as alloying elements. Five coupons with equal sizes of 40x40x4 mm have passed different treatments and subsequent depositions.

### *Preliminary treatments*

All the substrates have passed preliminary superficial treatment, either by only mechanical, or combined with alkaline etching and acidic activation, according to the following procedures:

- *Mechanical grinding*: All of the samples underwent mechanical treatment. It was performed by subsequent grinding with: 250, 500, 800 and 1000 grit SiC emery papers, followed by cleaning with tap – and distilled water.

- *Alkaline etching*: The chemical treatment was executed by etching in 50 g/l. NaOH aqueous solution for 2 minutes at 55 °C. Afterwards, the plates passed vigorous cleaning by tap and distilled water. Finally, the samples have passed acidic activation in HNO<sub>3</sub>: H<sub>2</sub>O (1:1) for 10 minutes at ambient temperature. After each stage of preliminary treatment, the plates passed vigorous cleaning by tap and distilled water.

### *Deposition conditions*

The deposition procedures were performed by dip-coating for 2 hours into the respective coating solutions at 55 °C in thermostat. All of the coating solutions contained (NH<sub>4</sub>)<sub>2</sub>Ce(NO<sub>3</sub>)<sub>5</sub>, NaCl, H<sub>2</sub>O<sub>2</sub> in distilled water. For the purpose of the investigation, the respective ingredients had different concentrations. Only the NaCl was always added to be 35 g. per liter of the coating solution. The compositions of the solutions and the preliminary treatments are ordered in Table 1. Taking into account the extreme importance of pH of the coating solution, it was maintained by Lourier buffer [26]. It was prepared by mixing of two initial

solutions in appropriated relation. Solution 1 was obtained by dilution of 8.5 ml of 36% HCl, up-to 1000 ml. Solution 2 was prepared by dissolving of 7.5 g. glycine and 5.85 g. NaCl in 1000ml. of distilled water. The final buffer solution was obtained by addition of 600 ml of solution 2 to 400 ml. of solution 1, in measuring flask.

### *Measurements and characterization*

*Electrochemical measurements* - A three-electrode electrochemical flat cells with 100 ml. of 3.5%wt. NaCl solution were used for all electrochemical measurements. Circular section (area equal to 2 cm<sup>2</sup>) from each sample surface was selected as a working electrode (WE). The counter electrode (CE) was a platinum net with two orders of magnitude larger area than that of the working electrode in order to avoid the influence of its surface capacitance on the experimental results. All WE-potential values were measured versus a commercial Ag/AgCl – 3M KCl, referent electrode, model 0726100, produced by Metrohm, with potential  $E(\text{Ag}^+/\text{AgCl}) = 0.2224 \text{ V}$ . The polarization and impedance measurements were carried out by means of a potentiostat/galvanostat AUTOLAB PG 30/2 of ECOCHEMIE, Netherlands, supported by a frequency response analyzer FRA-2. In order to avoid the influence of the external static electric fields, the electrochemical cell was inserted in a Faraday cage.

- *Electrochemical impedance spectroscopy*: Frequency range: between 10<sup>4</sup> and 10<sup>-2</sup> Hz, distributed in 7 steps per decade, at signal amplitude: 10 mV vs. OCP.

- *Cathodic polarization curves* - in range: from (OCP -500 mV), to (OCP + 10mV) with potential sweep range: 1mV/s.

- *Anodic polarization curves* - in range: from (OCP -10 mV), to (OCP + 500mV) with potential sweep range: 1mV/s.

- *Surface observation* – The observations via SEM were executed only on the best samples (e.g: these specimens, that showed the highest barrier abilities) using Scanning Electron Microscopy (SEM), (TESCAN, SEM/FIB LYRA I XMU). The SEM observations were combined by Energy Dispersion X-Ray Spectroscopy (EDS), performed by E, (Quantax 200 of BRUKER detector), connected to the SEM-device.

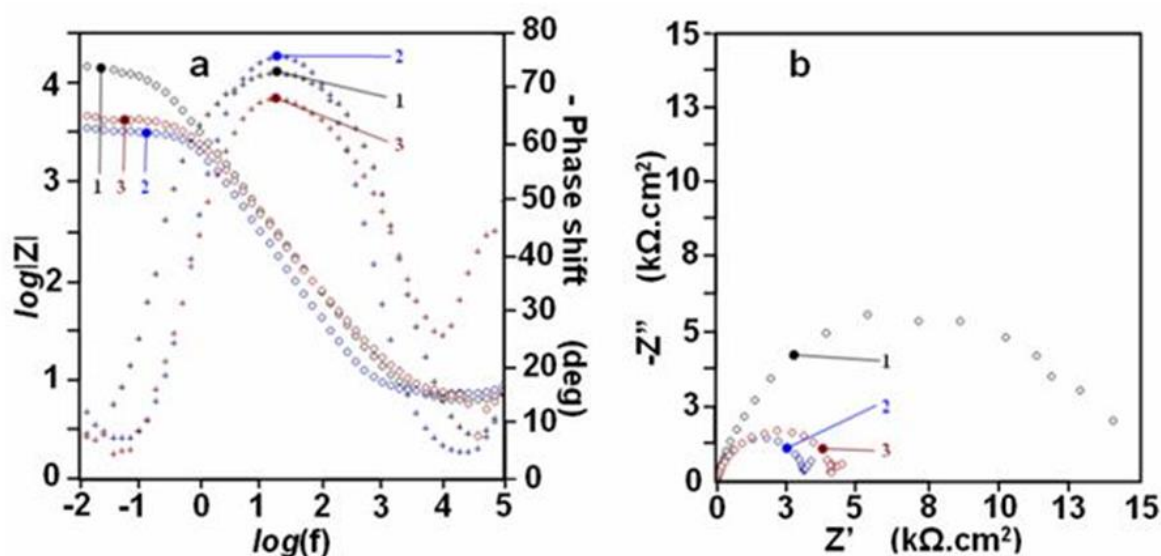
## RESULTS AND DISCUSSION

### *Comparison of the impedance spectra*

Fig. 1 represents three impedance spectra in Bode (a) and Nyquist (b) plots of the first three samples, coated either in solutions with different

**Table 1.** CeCC coatings and conditions of their preparations

Sample	Basic compound	Concentration (M)	pH	Presence of buffer	Quantity of H <sub>2</sub> O <sub>2</sub> (ml / l)	Preliminary treatment
P1	(NH <sub>4</sub> ) <sub>2</sub> Ce(NO <sub>3</sub> ) <sub>5</sub>	0.10	2.00	+	25	Only mechanical
P2	(NH <sub>4</sub> ) <sub>2</sub> Ce(NO <sub>3</sub> ) <sub>5</sub>	0.10	2.00	+	25	Mechanical and alkaline
P3	(NH <sub>4</sub> ) <sub>2</sub> Ce(NO <sub>3</sub> ) <sub>5</sub>	0.05	2.00	-	25	Mechanical and alkaline
P4	(NH <sub>4</sub> ) <sub>2</sub> Ce(NO <sub>3</sub> ) <sub>5</sub>	0.05	2.61	-	25	Mechanical and alkaline
P5	(NH <sub>4</sub> ) <sub>2</sub> Ce(NO <sub>3</sub> ) <sub>5</sub>	0.10	2.00	+	50	Only mechanical

**Fig. 1.** Bode (a) and Nyquist (b) plots of the EI-spectra of three samples of Group 6. 1 – sample P1; 2 – sample P2; 3 – sample P3

concentrations of (NH<sub>4</sub>)<sub>2</sub>Ce(NO<sub>3</sub>)<sub>5</sub>, or after different preliminary treatments.

It is obvious that the first sample P1 remarkably excels the other two. The real part  $Z'$  of its Nyquist plot reaches 15 k $\Omega$ .cm<sup>2</sup> (curve 1), while the rest two stay between 3 and 5 k $\Omega$ .cm<sup>2</sup> (curves 2 and 3). The first one (P1) is prepared by higher content of cerous ammonium nitrate, as the second one (P2), but its substrate was prepared by only mechanical grinding in contrast to specimens P2 and P3.

This fact means that the alkaline preliminary treatment procedure possesses generally detrimental character. Although this approach is widely used for pretreatment of Al-alloys, it obviously modifies the metallic surface composition. In alkaline media, the Cu-containing Al alloys suffer preferential dissolution of the Al matrix surrounding the Cu-intermetallics. That is the reason for undermining and removal of the Cu-containing particles and the resulting superficial copper depletion. Furthermore, its impact is much

more remarkable than the concentration of the basic substance in the coating solution. This fact is also obvious, because the difference between the samples prepared by 0.1 or 0.05 M of (NH<sub>4</sub>)<sub>2</sub>Ce(NO<sub>3</sub>)<sub>5</sub> (curves 2 and 3) is negligible, compared to the difference of the preliminary treatment approaches (curves 1 and 2).

Regardless the weak difference between the samples coated by 0.05 and 0.1 M Ce-salt solutions, the one with lower Ce-content seems to possess better barrier properties (curves 2 and 3 in Fig. 1). Obviously, the presence of buffer compensates the double Ce-addition, by hindering of its deposition. Probably, it does not allow the local pH increment necessary for CeCC deposition, by formation of Ce(OH)<sub>3</sub>/Ce(OH)<sub>4</sub> species. Besides, in the case of double addition of the Ce-compound (sample P2), the relation of the addition of H<sub>2</sub>O<sub>2</sub> to the basic Ce-substance decreases. In other words, the coating solution for P2 contained 25 ml/l of H<sub>2</sub>O<sub>2</sub> for 0.1 M (NH<sub>4</sub>)<sub>2</sub>Ce(NO<sub>3</sub>)<sub>5</sub>, and this relation was twice higher

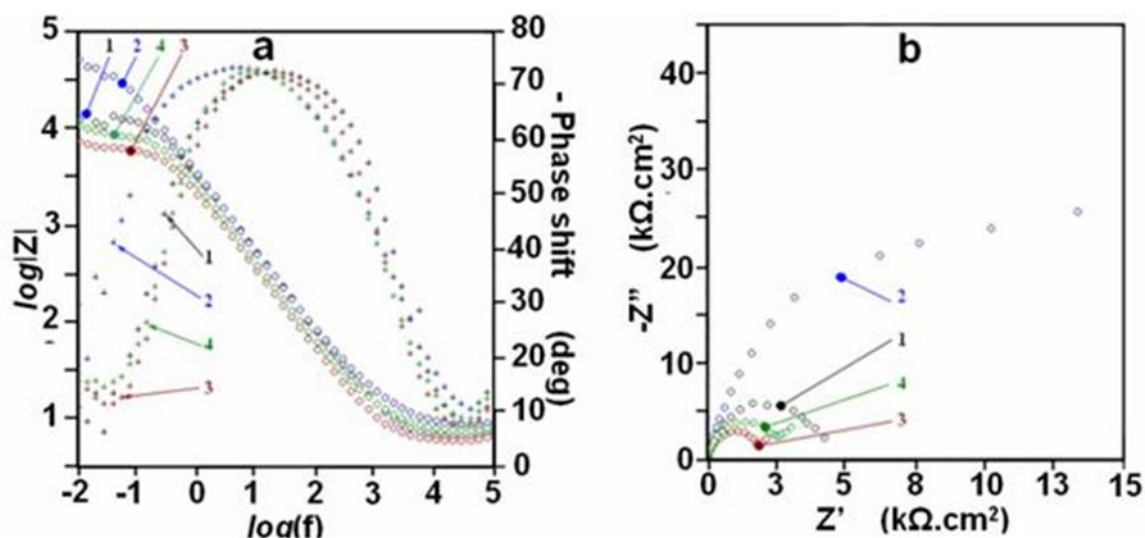


**Fig. 2.** Bode (a) and Nyquist (b) plots of the EI-spectra of CeCC coatings deposited after mechanical pretreatment and different H<sub>2</sub>O<sub>2</sub> additions: 1 – sample P1, after 48 hours of exposition; 2 – sample P5 after 48 hours of exposition; 3 – sample P1 after 168 hours of exposition; 4 - sample P5 after 168 hours of exposition

for sample P3 ( prepared with 25 ml/l. H<sub>2</sub>O<sub>2</sub> but only 0.05 M. Ce-salt). That was the reason to compare the barrier ability and durability of two samples with equal addition of 0.1 M Ce-salt, and different additions of H<sub>2</sub>O<sub>2</sub>. The additions of the peroxide were 25 and 50 ml/l, for P1 and P5, respectively.

Experiments on samples with only 0.01 M content were performed, as well. All of the samples revealed completely unsatisfying results, regardless the preliminary treatment approach, oxidant additions, duration and temperature of coating deposition, applied on the respective substrate. This fact was the reason to terminate any further measurements on samples coated by this concentration of the Ce-compound.

Figure 2 contains impedance spectra, recorded for both mechanically pre-treated samples P1 and P5, after 48 and 168 hours of exposition to 3.5% NaCl corrosive medium.

The spectra after 24 h of exposure had not clear shapes because the data points were strongly dissipated. This fact imposed evaluation of the sample barrier abilities by the spectra acquired after 48 hours (curves 1, and 2). The  $\log|Z| = f(\log(f))$  curve of the Bode plot for the sample with 50 ml / l of H<sub>2</sub>O<sub>2</sub>, at 0.01 Hz is by almost entire order of magnitude higher than this of the sample with only 25 ml/l of the oxidizer. The respective Nyquist plots reveal even higher difference. The analysis via “find circle” function, reveals that the total resistance  $R_{total} = R_p + R_{coat}$  possess 15 kΩ.cm<sup>2</sup>, compared to 50 kΩ.cm<sup>2</sup>. On the basis of all these observations, it could be concluded, that the optimal ratio between the oxidizer and the basic

ingredient is about 500 ml. of 30% H<sub>2</sub>O<sub>2</sub>, for each mol of (NH<sub>4</sub>)<sub>2</sub>Ce(NO<sub>3</sub>)<sub>5</sub>. This optimal ratio is correct only for the investigated system (i.e: between 0.05 and 0.1 mol of the Ce-salt, or P3, and P5, respectively). This ratio allows obtaining the highest barrier ability for the investigated system.

Nevertheless, it could be also concluded, comparing the curves 3 and 4 that they almost overlap. These curves were recorded after 168 hours of exposition of samples P1, and P5 to the corrosive medium. Regardless the fact that the P5 slightly excels P1, after one week of exposition the former one has obviously lost its barrier ability, (curves 2 and 4). The clear difference between the spectra recorded after 48 and 168 hours of exposition to the corrosive medium for the sample P5, reveal its low durability in these conditions.

Influence of pH of the coating solution was also followed. The pH value was maintained to be 2.00 by correction via dropping of HCl : H<sub>2</sub>O (1 : 3). However, the sample P3 (prepared by mechanical and alkaline treatment of the substrate, and coating by 25 ml/l. H<sub>2</sub>O<sub>2</sub> and 0.05 M. Ce-salt, with corrected pH = 2.00) was repeated by another sample P4, but with its own pH = 2.61.

The comparison between the spectra of samples P3 and P4 reveals that the specimen, coated by the bath with pH = 2.61 has much better barrier ability, than this one, with the pH = 2.00 corrected by acid addition. The  $\log|Z|$  value at 0.01 Hz, for P4 excels by 1.5 orders of magnitude this one of P3. Additional difference between the respective Bode plots is that the curve  $\varphi = f(\log(f))$  possesses two, clearly distinguishable maxima. This fact undoubtedly evinces the presence of two superficial

layers. It could be supposed that during the deposition of the Ce-conversion coating, additional oxide layer grows, due to the acidic nature of the coating solution. These conditions cause supplemental growth of Al-oxide layer on the sample P3, as well. However, because of absence of uniform film of CeCC, in the case of P3, its  $\varphi = f(\log(f))$  curve has only one maximum at the middle frequencies. It is originated from the Al-oxide layer appeared in the conditions, described above.

After 168 hours of exposition, the spectra remain their shapes. This fact is indication for the relatively good durability of both coatings. The Nyquist plots of P4 show that the real part (i.e:  $Z'$ ) of the semi-circles decrease from relatively 55  $k\Omega.cm^2$ , detected at 48 hours of exposition to 20

$k\Omega.cm^2$ , after one week of exposure (Compare Fig. 3 (a, b) and (c, d)).

#### Linear polarization curves

When the cathodic curves acquired after 24 h. are compared, it becomes obvious that the buffer stabilizes the deposition process. The specimens P3, and P4, prepared without buffer reveal deviation from the rest. However, the lowest cathodic current density belongs to P4, whereas the highest one relays to P3. As a result, current density of the coating deposited at pH = 2.61, without buffer is about entire order of magnitude lower than the buffer assisted coatings. Reciprocally, the other coating deposited without buffer at pH = 2.00 possesses the highest current density.

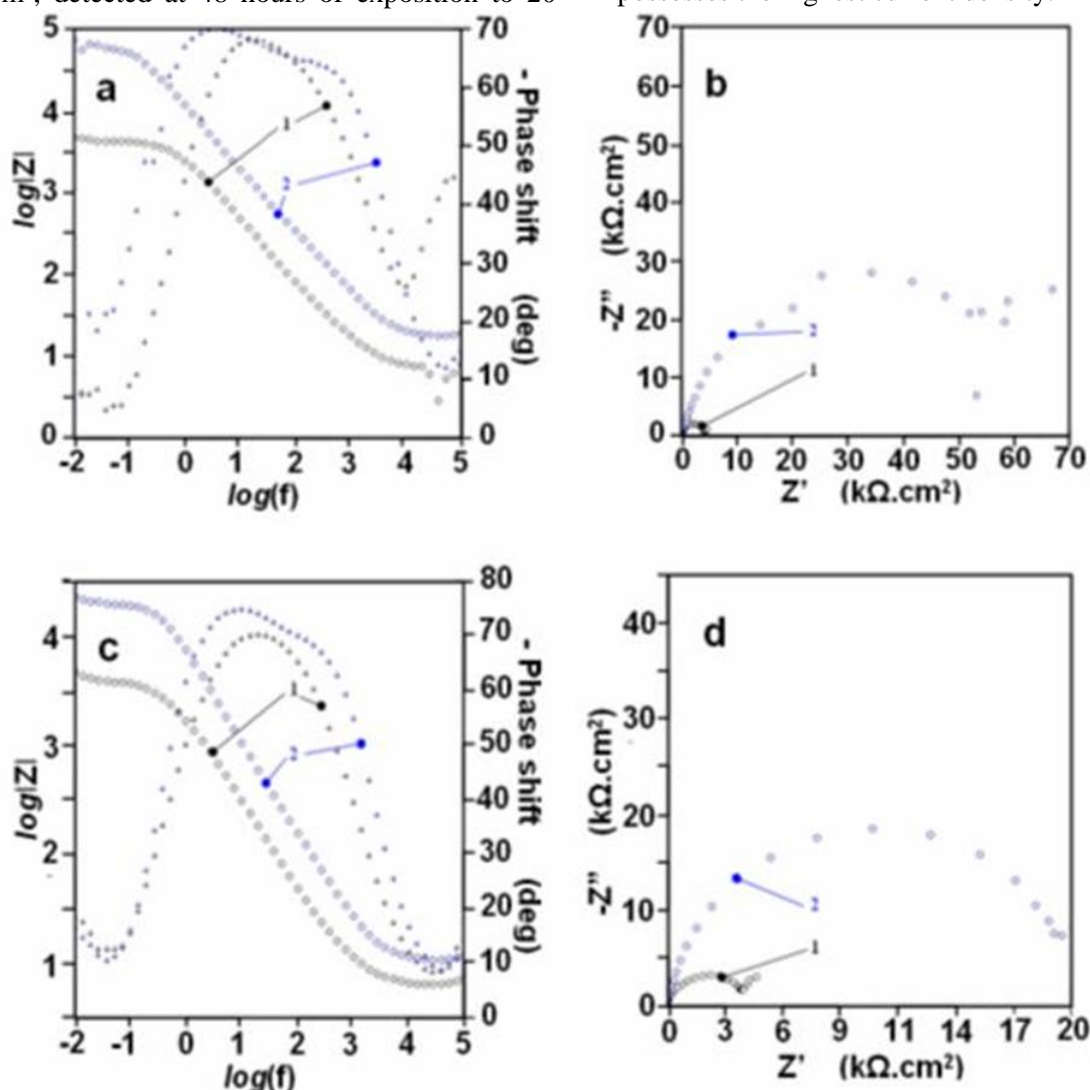


**Fig. 3.** Electrochemical Impedance Spectra recorded after 48 (a) and 168 (b) hours of exposure of two samples with different pH of the coating solutions. 1 – specimen P3; 2 – specimen P4.

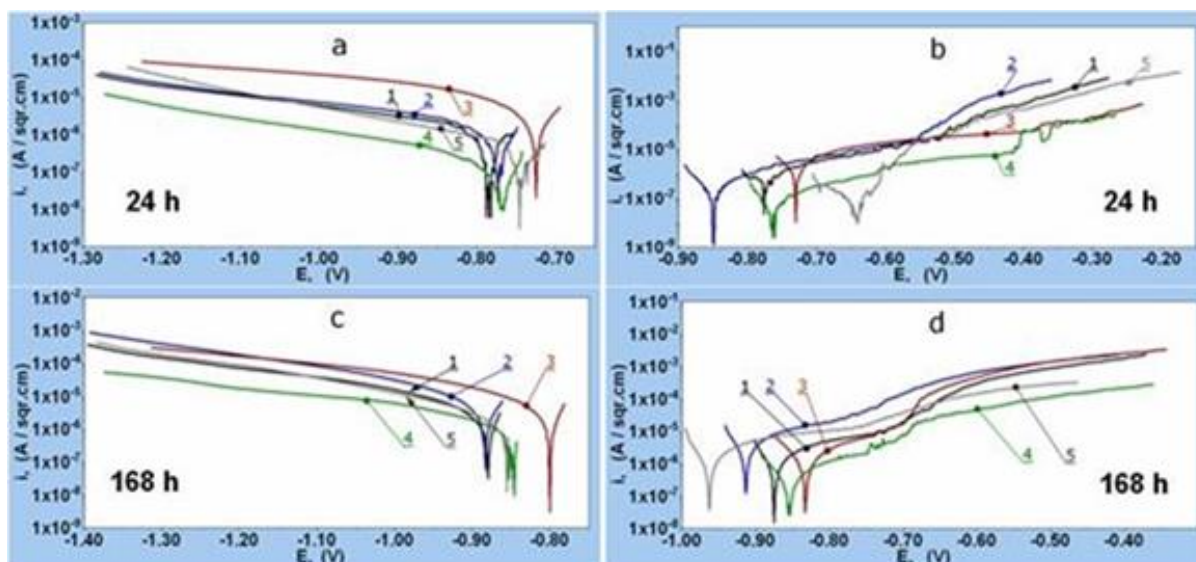


**Fig. 4.** LSV-curves of the samples acquired after 24 (a) and 168 (b) hours of exposition to 3.5% NaCl model corrosive medium. 1 – sample PI; 2 – sample P2, 3 – sample P3, 4 – sample P4, 5 – sample P5,

The respective anodic curves confirm the statements done for the cathodic ones. The lowest current density belongs to P4. In addition, the largest passivity region (between -760 and -410 mV) is attributed to this sample. The length of this region is described in [27] as a measure for “strength against pitting nucleation”. This measure, together with the lower corrosion current densities in both the cathodic and anodic polarization curves indicate that the barrier ability of sample P4 excels these of all the rest specimens in this study. Obviously, the relatively higher pH value (pH = 2.61) prevents severe attack to the oxide layer on the matrix, observed at pH = 2.00.

After 168 hours, the current densities of the respective cathodic and anodic curves for P4 still remain with up to about an order of magnitude lower than the rest, although the remarkable shortening of the passivity region of its anodic curve. Both these facts indicate that after 168 hours of exposition, the specimen prepared at higher pH is relatively more durable than the rest samples, regardless the loss of its strength against pitting nucleation.

#### *Morphological characterization of the samples*

The different behavior of the samples in corrosive medium reflect their individual structures, as consequence of the conditions applied for the deposition of the respective coatings. On the other hand, the structures of these coatings could be assessed by their superficial morphologies. For these reasons, SEM – observations were executed for description of the topographies of the coating surfaces. The respective SEM – images are shown in Fig. 5.

The SEM images reveal that the samples possess completely different morphologies. Even the preliminary treatments of the substrates result in the mechanism of coating deposition (compare positions (a) and (b)). The former has equally distributed morphology, while the latter reveals additional layer of deposits. The ratio between the Ce-salt, and the oxidant renders its influence, as well. The additional deposits observable for the sample P2 are presented neither for sample P3, nor for P4 (see positions (c) and (d)). This fact means that because of the lower content of oxidant, compared to the Ce-salt in the case of sample P2, there is not enough intensive precipitation of Ce-oxides/hydroxides.

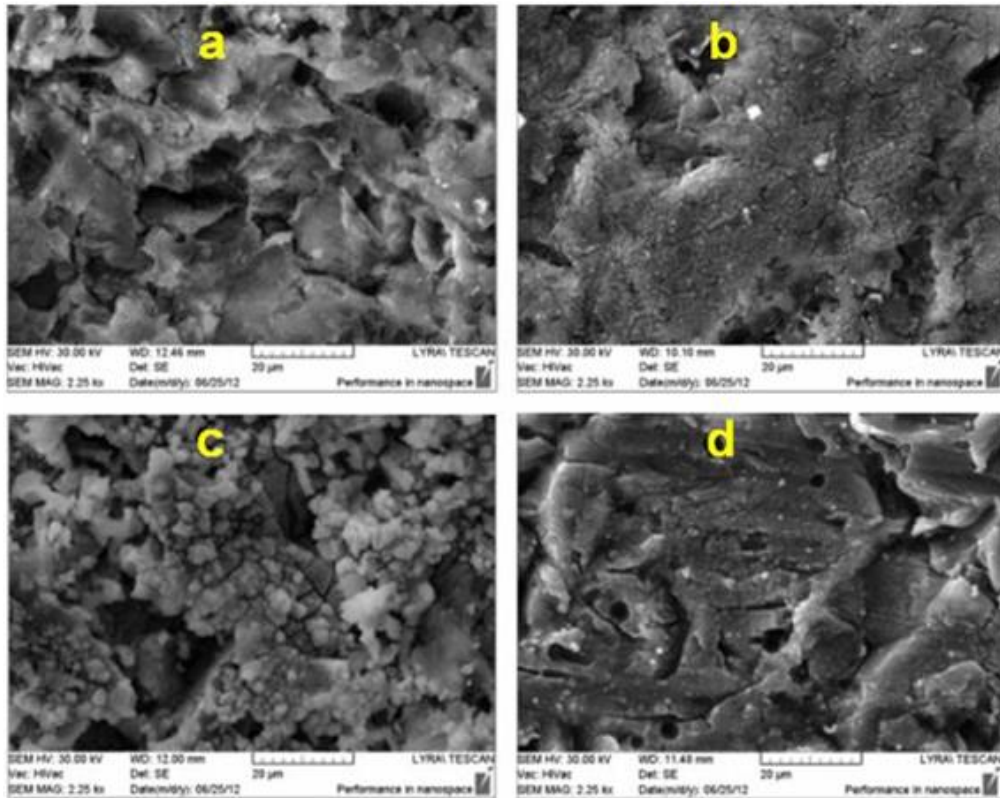


**Fig. 5.** SEM topological images of the investigated samples: a – specimen P1; b – specimen P2; c – specimen P3; d – specimen P4

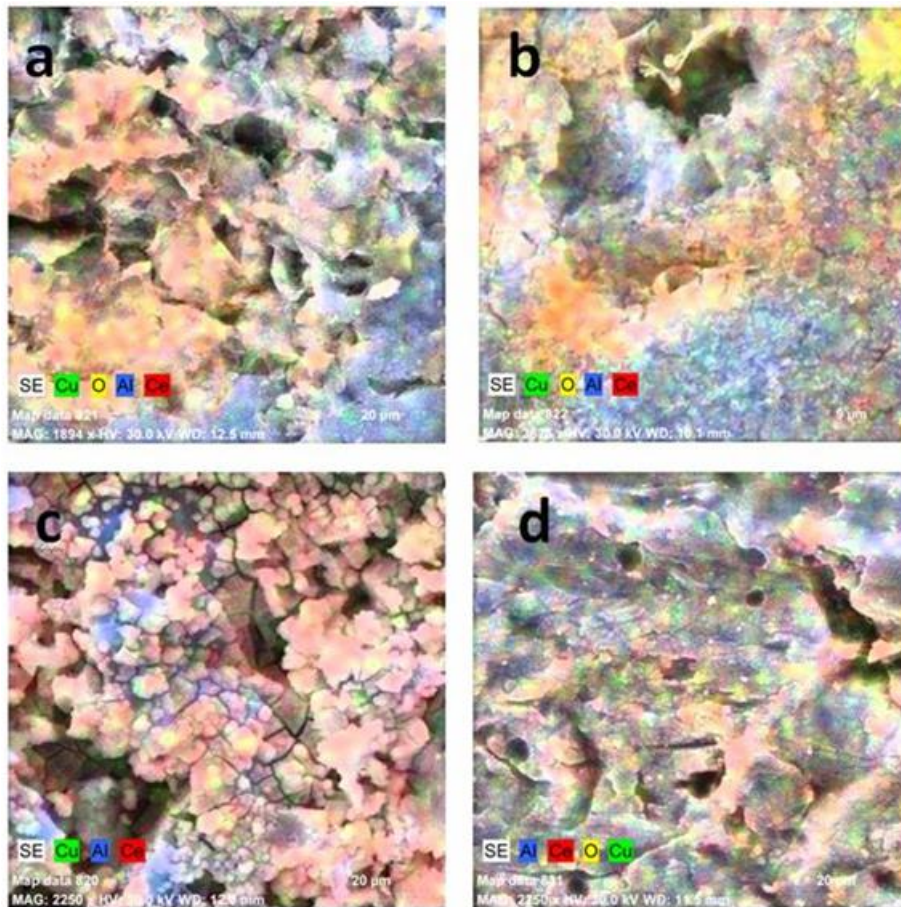


**Fig. 6.** EDS topological images of the investigated samples: a – specimen P1; b – specimen P2; c – specimen P3; d – specimen P4

As consequence, the coating deposition passes accompanied by corrosion process. That is the reason for the coverage of the Ce-coating by corrosion products, such as  $\text{Al}(\text{OH})_3$ . The comparison between samples P3 and P4 (positions (c) and (d)) shows that the pH has strong influence during the deposition process. The unique difference between the samples is that the former coating was deposited at  $\text{pH} = 2.00$ , while the latter is done at  $\text{pH} = 2.61$ . The corresponding coatings possess entirely different morphology.

The EDS map analysis confirms the conclusions done for the SEM observations. The superficial sediments that cover the coating of P2 (see position (b), Fig. 6) are almost entirely composed by Al - compounds.

## CONCLUSION

New electrolyte was elaborated, for deposition of Cerium based conversion coatings (CeCC) for protection of D16-AM alloy against corrosion. The cerium salt - Diammonium pentanitrocerate was used, in which, contrary to all rest electrolytes used up to nowadays, the Cerium is represented in the anionic moiety.

During its development, the influence of various conditions was elucidated, related to the preliminary treatment, the composition of the electrolyte, and the deposition regime.

It is demonstrated that the preliminary treatment has remarkable importance for the features of the coatings. Two basic approaches were employed for preliminary treatment of the D16-AM substrates: only mechanical grinding, or in combination with alkaline etching, and acidic activation. It is established that the coatings deposited after only mechanical treatment results in uniform films.

It is ascertained that the best Cerium Conversion Coatings are obtained by the following electrolyte composition: concentration of the Ce-salt 0.05 up to 0.1 M; molar ratio between the peroxide and the Ce-salt, from 4 to 8; pH about 2.6; and NaCl content – 35g/l.

It was observed that during the CeCC deposition, pH of the coating solution rises, resulting in undesirable precipitation of Ce-oxides/hydroxides. The maintenance of the electrolyte pH, in narrow optimal interval and to avoid the precipitation of the Ce-salt, the conversion bath was buffered by buffer of Lourier, based on amino-acid. Nevertheless, the addition of

buffer should be compensated by higher Ce-content.

By SEM-EDS observations was evinced that even insignificant change of whatever parameter of the deposition process results in completely different superficial morphology of the coating.

By application of two, electrochemical methods independent between themselves: Linear Voltammetry and Electrochemical Impedance Spectroscopy, the barrier ability and the durability were investigated. As a result, it was established that the best specimen possesses the highest value for the total resistance  $R_{\text{total}} = 5 \times 10^4 \Omega \cdot \text{cm}^2$  which is a measure for the barrier properties of the coating.

After 168 hours of exposition, the CeCC deposited at higher pH on mechanically grinded substrate is relatively more durable than the rest samples, regardless the loss of its strength against pitting nucleation.

**Acknowledgements:** *The authors gratefully acknowledge the financial support of project BG 051PO001-3.3.06-0038. Dr. Gustavo Pelaez is acknowledged for the opportunity for the international collaboration activities.*

## REFERENCES

1. EU Directive 2002/95/EC “Restriction of Hazardous Substances in Electrical and Electronic Equipment” (RoHS directive 2002), [www.broadcom.com/docs/](http://www.broadcom.com/docs/) a [www.chem.agilent.com/](http://www.chem.agilent.com/)
2. Directive 2004/107/EC of the European Parliament and of the Council of 15 December 2004 relating to arsenic, cadmium, mercury, nickel and polycyclic aromatic hydrocarbons in ambient air. Official Journal of the European Communities L 23, 26.1.2005, p. 3–16, Special edition in Bulgarian: Chapter 15 Volume 13 P. 124 – 137
3. U.S. Department of Health and Human Services, Public Health Service, Agency for Toxic Substances and Disease Registry (2008) Toxicological profile for Chromium. [www.atsdr.cdc.gov/toxprofiles/tp7.pdf](http://www.atsdr.cdc.gov/toxprofiles/tp7.pdf)
4. U.S. Environmental Protection Agency Washington, DC, August (1998) Toxicological review of hexavalent chromium. Accessible via: <http://www.epa.gov/iris/toxreviews/0144tr.pdf>
5. D. Nikolova, E. Stoyanova, D. Stoychev, P. Stefanov, I. Avramova, *Surf. Coat. Technol.*, **202**, 1876 (2008).
6. E. Stoyanova, D. Guergova, D. Stoychev, I. Avramova, P. Stefanov, *Electrochim. Acta*, **55**, 1725 (2010).
7. E. Stoyanova, D. Nikolova, D. Stoychev, P. Stefanov, Ts. Marinova, *Corros. Sci.*, **48**, 4037 (2006).

8. D. Nikolova, E. Stoyanova, D. Stoychev, P. Stefanov, Ts. Marinova, *Surf. Coat. Technol.*, **201**, 1556 (2006).
9. I. Avramova, P. Stefanov, D. Nicolova, D. Stoychev, Ts. Marinova, *Composites Sci. Technol.*, **65**, 1663 (2005).
10. S. Kozhukharov, V. Kozhukharov, M. Schem, T. Schmidt, M. Wittmar, M. Veith, Electrochemical properties of Sol-Gel Oxi-silane coatings for corrosion protection of aluminium alloys, Proceed 4th Balkan Conference on Glass and Ceramics 29 sept. – 02 Oct. 2008, pp. 166 – 171; ISBN 978-954-629—038-0
11. S. Kozhukharov, V. Kozhukharov, M. Wittmar, M. Schem, M. Aslan, H. Caparrotti, M. Veith, *Prog. Org. Coat.*, **71**, 198 (2011).
12. S. Kozhukharov, V. Kozhukharov, M. Schem, M. Wittmar, M. Veith, *Prog. Org. Coat.*, **73**, 96 (2012).
13. A. A. Salve, S. Kozhukharov, J. E. Pernas, E. Matter, M. Machkova, *J. Univ. Chem. Technol. Met.*, **47**, 319 (2012).
14. E. A. Matter, S. Kozhukharov, M. Machkova, V. Kozhukharov, *Mater. Corros.*, DOI: 10.1002/maco.201106349
15. E. A. Matter, S. Kozhukharov, M. Machkova, V. Kozhukharov, *Corros. Sci.* **62**, 22 (2012).
16. A. L. Rudd, C. B. Breslin, F. Mansfeld, *Corros. Sci.*, **42**, 275 (2000).
17. S. C. Linz, S. K. Fang, *J. Electrochem. Soc.*, **B54-B59**, 152 (2005).
18. D. Balgude, A. Sabnis, *J. Sol-Gel Sci. Technol.* DOI 10.1007/s10971-012-2838-z
19. S. A. Kulinich, A. S. Akhtar, *Russian J. Non-Ferrous Metals*, **53**, 176 (2012).
20. G. Tsaneva, V. Kozhukharov, S. Kozhukharov, M. Ivanova, J. Gerwann, M. Schem, T. Schmidt, *J. Univ. Chem. Technol. Met.*, **43**, 231 (2008).
21. T. O’Keefe, P. Yu, S. Hayes, A. Williams, M. O’Keefe, Fundamental Evaluation of the Deposition of Cerium Oxide For Conversion Coating Applications, Proceeds., 2003 Tri-Service Corrosion Conference, Las Vegas, 17 – 21 Nov. (2003), Nevada – USA.
22. M. A. Arenas, J. J. de Damborenea, *Rev. Metal, Extr. Vol.* 433 (2005). (Spanish).
23. A. Conde, M.A. Arenas, A. de Frutos, J. de Damborenea, *Electrochim. Acta*, **53**, 7760 (2008).
24. A. Aballe, M. Bethencourt, F.J. Botana, M. Marcos, *J. Alloys Comp.*, **323-324**, 855 (2001).
25. [http://www.splav.kharkov.com/en/e\\_mat\\_start.php?name\\_id=1438](http://www.splav.kharkov.com/en/e_mat_start.php?name_id=1438)
26. Y. Y. Lourier “Manual on Analytical Chemistry” Gov. Ed. “Chemistry” (Moscow) (1967), 305 – 307.
27. M. Bethencourt, F.J. Botana, M.J. Cano, M. Marcos, J.M. Sánchez-Amaya, L. González-Rovira, *Corros. Sci.* **51**, 518 (2009).

## ВЛИЯНИЕ НА УСЛОВИЯТА НА ОТЛАГАНЕ НА ПОКРИТИЯ ОТ Се-КОНВЕРСИОННИ БАНИ ВЪРХУ СВОЙСТВАТА НА ПЛАКИРАНА СПЛАВ Д16 АМ

Д. С. Родригез<sup>1</sup>, С. Кожухаров<sup>2\*</sup>, М. Мачкова<sup>2</sup>, В. Кожухаров<sup>2</sup>

<sup>1</sup>Университет Виго, Лагоас, Марконсенде 36310 (Испания)

<sup>2</sup>Химикотехнологичен и Металургичен Университет, бул. “Климент Охридски”, София П.К 1756 (България)

Постъпила на 31 януари юли, 2013 г.; Коригирана на 4 април, 2013 г.

(Резюме)

Целта на Настоящата работа е да се оцени влиянието на различни условия върху спонтанното отлагане на цериеви конверсионни слоеве из разтвори на диамониев пентанитроцерат  $(NH_4)_2Ce(NO_3)_5$  върху плакирана сплав Д16 АМ, покрита чрез потапяне в цериеви конверсионни вани, и да се проведе последващ анализ върху поведението и характеристиките на получените покрития. Техните охарактеризирания са проведени чрез тестове за устойчивост спрямо моделна корозионна среда, съставена от 3,5% разтвор на NaCl, съчетани с периодични електрохимични измервания и последващи морфологични охарактеризирания. Първият вид измервания бяха проведени чрез Електрохимична Импедансна Спектроскопия (ЕИС), съчетана с линейна волтамперометрия с линейна разгъвка на потенциала (ЛВА), а вторите бяха проведени чрез Сканираща Електронна Микроскопия (СЕМ), съчетана с Енергийно Разпределителен Рентгенов Анализ (ЕРРА). Като резултат, бяха определени оптималните условия за отлагане на цериеви конверсионни слоеве.

## Electrodeposition of cerium conversion coatings for corrosion protection of D16 AM clad alloy

J. A. P. Ayuso<sup>1</sup>, S. Kozhukharov<sup>2\*</sup>, M. Machkova<sup>2</sup>, V. Kozhukharov<sup>2</sup>

<sup>1</sup>University of Vigo, Lagoas, Marcosende 36310 (Spain)

<sup>2</sup>University of Chemical Technology and Metallurgy, 8 “Kl. Okhridsky” Blvd., Sofia 1756 (Bulgaria)

Received January 31, 2013; Revised May 21, 2013

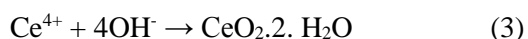
The present research work is investigation on the probabilities for application of a new cerium compound, for cathodic electrodeposition of Cerium based conversion coatings (CeCC) for protection of D16 AM alloy against corrosion. For the purpose of the present study, diammonium pentanitrocerate ((NH<sub>4</sub>)<sub>2</sub>Ce(NO<sub>3</sub>)<sub>5</sub>) was used, where the cerium is represented in the anionic moiety, instead of the electrolytes used up to nowadays. The barrier abilities against corrosion of all coatings were evaluated by two electrochemical methods – Linear Sweep Voltammetry (LSV), and Electrochemical Impedance Spectroscopy (EIS). Additionally, selected specimens underwent morphological characterization by Scanning Electron Microscopy (SEM) combined with Energy Dispersive X-ray spectroscopy (EDX). As a result, the influences of the concentrations of the basic substance and the deposition activator, as well as the density of the applied electric current were elucidated.

**Key words:** corrosion protection, Cerium Conversion Coatings, LSV, EIS, SEM, AFM

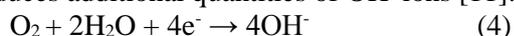
### INTRODUCTION

The aluminium alloys, especially, AA2024 and AA7075 are objects of special attention, due to their remarkable mechanical strength [1], predetermining their tremendous importance so for the commercial [2], so for military [3 - 6] aircraft, and recently, for the automotive [7, 8] industries. For industrial applications, the alloys are usually coated prior to their use as components for various transport vehicles and equipment. In the aircraft industry, it is commonly accepted to apply multilayered, multifunctional coatings [9].

The Cerium Conversion Coatings (CeCC) are generally composed by cerium oxides and hydroxides, originated from the conversion of the respective water-soluble cerium salts, according to the following reactions [10]:



The dissolved oxygen in the solution also could participate in reactions, and being reduced, it produces additional quantities of OH<sup>-</sup> ions [11]:



All these reactions lead to formation of insoluble

products of Cerium oxides or/and hydroxides. Here should be mentioned that according to the conditions, these products could form either precipitates (undesirable product), or layer deposition (the aimed product).

The aim of the present research work is to elucidate the influence of the addition of H<sub>2</sub>O<sub>2</sub> and the current applied as enhancers of the deposition process, by evaluation of the features and performance of the respective CeCC in 3.5% NaCl model corrosive medium.

### EXPERIMENTAL

The basic material was D16 AM clad alloy, with analogical composition to AA2024. For confirmation of its content, Inductively Coupled Plasma Optical Emission Spectroscopy (ICP-OES) was performed in the Central Laboratory of Scientific Research “Geohimia”, to “Ivan Rilsky” University of Mining and Geology. The composition determined is represented in Table 1.

Prior to CeCC deposition, the D16 AM substrates with 60x60x4 mm of size dimensions were submitted to: mechanical grinding with emery papers, up to 1200 grit, cleaning in acetone for 10 min at room temperature, and at last, alkaline etching in NaOH solution (50 g/l) at 55 °C for 5 minutes. Finally, the specimens underwent activation in diluted HNO<sub>3</sub> (1:1) for 5 minutes, at ambient temperature.

\* To whom all correspondence should be sent:  
E-mail: stephko1980@abv.bg

**Table 1.** Composition of the investigated alloy according to ICP – OES analysis

Element	Al	Cu	Fe	Mg	Mn	Ni	Si
Concentration (wt.%)	Residual	3.716	0.404	1.259	0.537	0.055	< 0.01

The basic substance was 0.05M (NH<sub>4</sub>)<sub>2</sub>Ce(NO<sub>3</sub>)<sub>5</sub> in the conversion bath solution, and presence of 10, 25, 50 or 100ml/l. of 30% H<sub>2</sub>O<sub>2</sub>. The depositions were performed at Galvani-static regime for 5 minutes either at -2 or at -5 mA/cm<sup>2</sup>. In order to compare the barrier abilities of the coatings, obtained after different additions of H<sub>2</sub>O<sub>2</sub>, electrochemical measurements were performed after 24 hours of exposition to 3.5% NaCl model corrosive medium.

The electrochemical procedures were performed by PG-stat, “Autolab”- 30, coupled by Frequency Response Analyzer FRA – 2.

The depositions and electrochemical characterizations were performed in flat cells with Ag/AgCl electrode and a platinum net as a counter electrode, and 100 ml of volume. In order to avoid the influence of the edge-effects on the measurements, the areas for deposition were larger than these for testing. Thus, the depositions were performed on circuit areas with diameter equal to 39 mm, whereas the tests were executed on areas with 15 mm. of diameter. The depositions and the tests were performed in the cells shown in Figure 1.

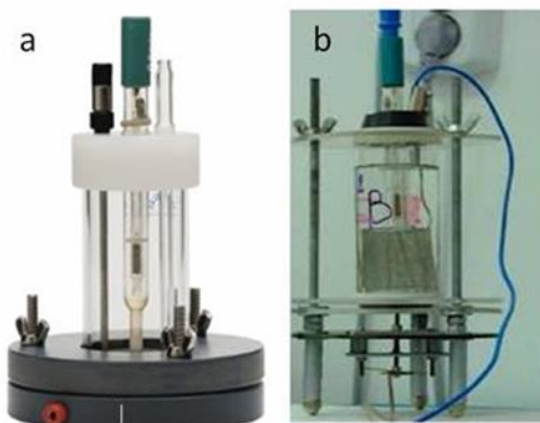


**Fig. 1.** Photographs of deposition (a), and test (b) cells

After 24 hours of exposition to 3.5% w/w. NaCl solutions, the respective impedance spectra were acquired at frequency range from 10<sup>4</sup> to 10<sup>-2</sup> Hz, distributed in 7 frequencies per decade, with signal amplitude of 10 mV vs. OCP. At last, individual cathodic and anodic polarization curves were recorded in a larger potential interval (OCP ± 500 mV), at 1 mV/s potential sweep range. The anodic curves were recorded after restoration of the OCP, deviated by the respective cathodic ones. By maintenance of this sequence, no disgrace of the

experimental data as a consequence of any electrode polarization could be admitted.

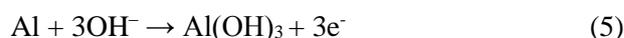
## RESULTS AND DISCUSSION

### *Chrono-potentiometric curves*

During the deposition, the equipment was continuously measuring the potentials versus the Ag/AgCl reference electrode and their evolutions within the deposition process. The obtained potential/time diagrams are shown in Fig. 2.

There, after the initial immediate fall of the potential down to almost -1.65 V, the potential reverses its values reaching about -1.30 to -1.32 V. The initial potential drop is related to the current spent for hydrogen evolution on the metallic surface. This process appears due to both of the reducing role of the cathodic current, and the generally acidic character of the deposition solution.

The subsequent reversion of the potential is probably related to removal of the H<sub>2</sub> – gaseous bubbles from the metallic surface. Probably the reason for this removal and the reversion of the potential is the so called “cathodic dissolution of the aluminium” [12-15]. The peculiarities of the corrosion damage to cathodically polarized aluminum in aqueous solutions of different composition cannot be explained by the electrochemical process in which only the anodes should be dissolved [12, 13]. The most probable reaction is a chemical attack by hydroxyl ions (product of reactions (2) and (4)) on the aluminium cathode [13]. This process proceeds according to the following reactions [14, 15]:



The most extended continuation of the potential reversing is observable for the samples prepared with 100 and 50 ml/l H<sub>2</sub>O<sub>2</sub> (175 seconds for curve 1, and 125 seconds for curve 2). The curves 3 and 4 of the samples with more uniform, dense and homogeneous Ce-coatings achieve a minimum after 10 - 15 seconds.

After reaching maxima the potentials start to reverse gradually again for all curves. This phenomenon is related either to gradual growth of uniform coatings (curves 3 and 4), or to occupation of the metallic surface by cerium containing agglomerates.

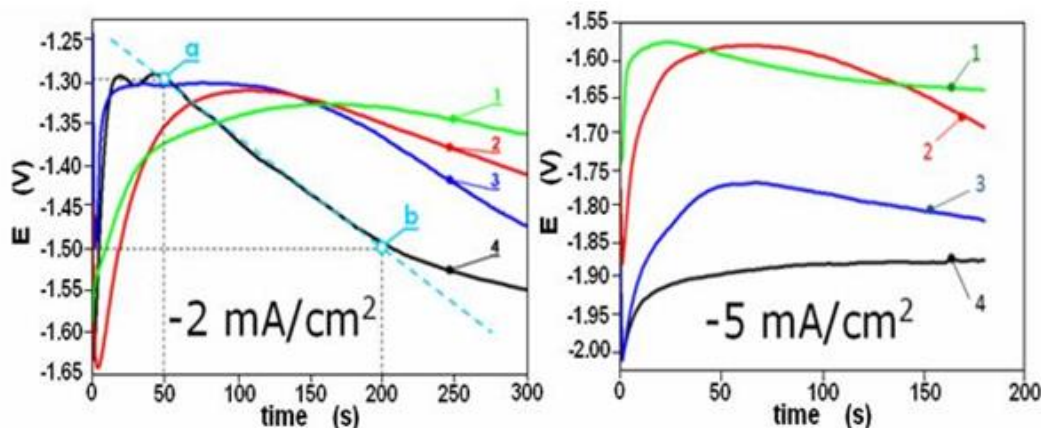


**Fig. 2.** Chronopotentiometric curves obtained during the Galvani-static depositions of CeCC coatings after different additions of H<sub>2</sub>O<sub>2</sub> to the coating solutions: 1 – 100ml/l H<sub>2</sub>O<sub>2</sub>; 2 - 50 – 10ml/l H<sub>2</sub>O<sub>2</sub>; 3 – 25ml/l H<sub>2</sub>O<sub>2</sub>; 4 - 10ml/l H<sub>2</sub>O<sub>2</sub>.

For the best coating, obtained by addition of only 10 ml/l. H<sub>2</sub>O<sub>2</sub>, this gradual drop of potential continued from the 50<sup>th</sup> (point (a)) to 200<sup>th</sup> (point (b)) second after the beginning of the deposition. During this time, the potential drops with 200 mV. Taking into account that the deposition is performed in Galvani-static regime (i.e: -2 mA/cm<sup>2</sup>) and, applying the law of Ohm, it could be calculated that the resistance of the deposited film increases with 100 Ω.cm<sup>2</sup>/s. In other words, for the entire period of film growth (between points (a) and (b)) the total resistance of the best film (curve 1) raises up to 15 k Ω.cm<sup>2</sup>). As a general conclusion, it looks that the increase of the H<sub>2</sub>O<sub>2</sub> content in the deposition solutions probably favors the cathodic dissolution of the underlying aluminum, hindering the formation of uniform and homogeneous CeCC coatings.

The curves, obtained during the electrodeposition at -5 mA/cm<sup>2</sup> do not possess the slope related to film growth. Consequently, at this current density, any uniform and homogeneous coating layer does not form (Fig. 2). It either favors the hydrogen evolution process, or promotes the mentioned above cathodic Al-dissolution. In both cases, the acquired coatings possess elevated porosity, or lower homogeneity.

#### EIS – examination

After the depositions, the obtained samples were exposed to 3.5 %NaCl model corrosive media. Their barrier abilities were examined by means of electrochemical measurements (EIS, and LSV). Unexpectedly, the addition of oxidant has not presented its contribution in the impedance spectra. In Fig. 3 (a, b), all of the spectra of the coatings obtained at -2mA/cm<sup>2</sup> possess almost the same shapes, regardless the significant difference of the

H<sub>2</sub>O<sub>2</sub> additions to the solution of the conversion bath.

For the EIS – spectra of the samples with films deposited at -5 mA/cm<sup>2</sup>, also cannot be seen any significant difference among the shapes in Bode plots. However, when the Nyquist plots of Fig. 3 (b, d) are compared, clear Warburg diffusion elements are observable in the latter position (e. g: at -5 mA/cm<sup>2</sup>). This fact evinces that the higher deposition currents applied result in formation of rather less uniform deposits. Indeed, the visual inspections of the samples revealed rough and grain-formed (agglomerated) precipitates, when the higher current was applied. The unsatisfying homogeneity of the coatings favors the access of corrosive species to the metallic surface, resulting in appearance of the Warburg diffusion impedance.

#### LSV – measurements

The linear voltammograms reveal more distinguishable features of the respective specimens, than the EIS spectra. Fig. 4 represents cathodic (a, c) and anodic (b, d) polarization curves of specimens coated after different H<sub>2</sub>O<sub>2</sub> additions, and current densities, recorded after 24 hours of exposition to the model corrosive medium. Fig. 4, (a, b) reveals that for the coatings deposited at -2 mA/cm<sup>2</sup>, the increase of the H<sub>2</sub>O<sub>2</sub> content deteriorates the barrier ability of the resulting coatings. Thus, the coatings prepared at lower content of the oxidant (10 and 25 ml. 30% H<sub>2</sub>O<sub>2</sub> per liter of coating solution), resemble lower current densities, compared to the other two (50 and 100 ml. 30% H<sub>2</sub>O<sub>2</sub> per liter of coating solution). The anodic curve of the sample, prepared at 50 ml./l. H<sub>2</sub>O<sub>2</sub>, does not possess any passivity region. Both curves of the sample with 100 ml. H<sub>2</sub>O<sub>2</sub> addition stay at lower current

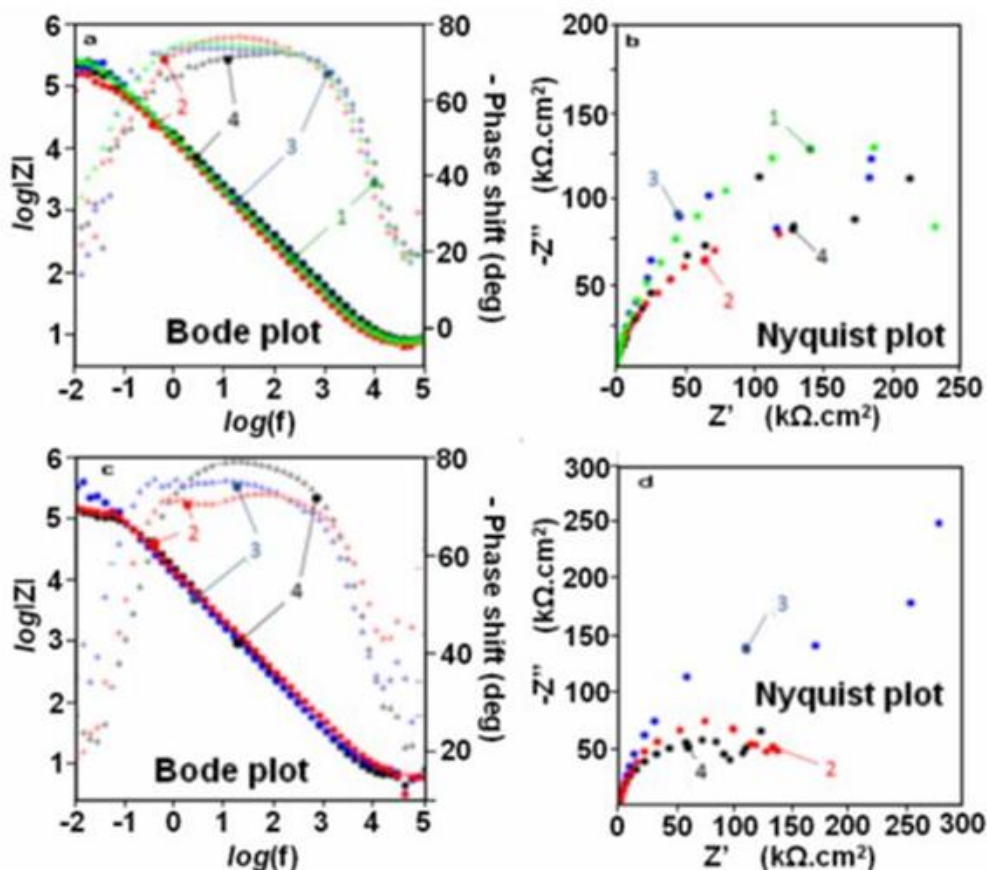


**Fig. 3.** Electrochemical impedance spectra, acquired after 24 hours of exposition to the model corrosive medium of four specimens coated after different  $H_2O_2$  additions. a, c – Bode plots; b, d – Nyquist plots: 1 – 100ml/l addition of  $H_2O_2$ ; 2 – 50 – 10ml/l addition of  $H_2O_2$ ; 3 – 25ml/l addition of  $H_2O_2$ ; 4 – 10ml/l addition of  $H_2O_2$

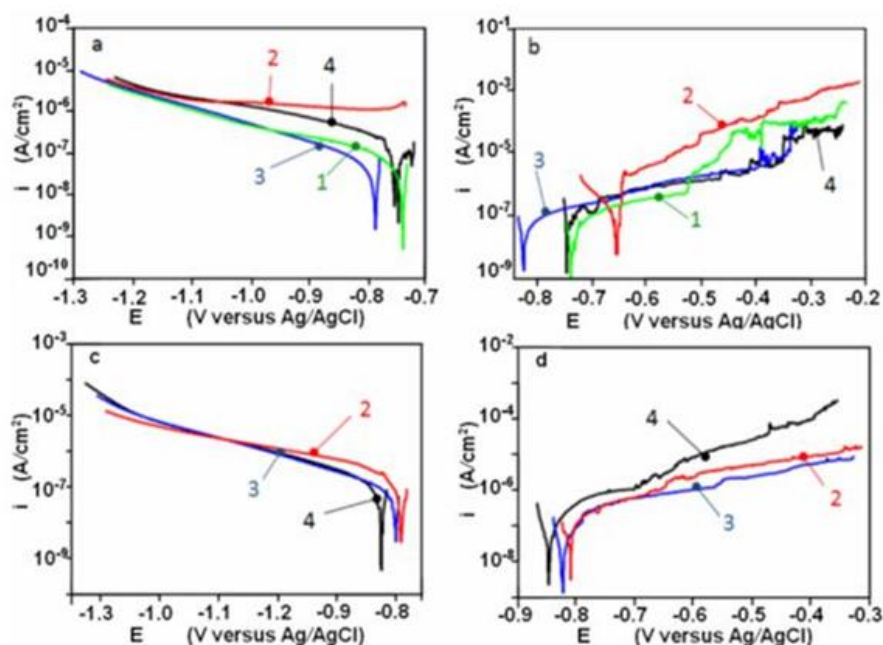


**Fig. 4.** Cathodic (a, c) and anodic (b, d) polarization curves recorded after 24 hours of exposition to the model corrosive medium of specimens coated at  $-2mA/cm^2$  (a,b) and  $-5mA/cm^2$  (c, d) after different  $H_2O_2$  additions. 1 – 100ml/l addition of  $H_2O_2$ ; 2 – 50ml/l addition of  $H_2O_2$ ; 3 – 25ml/l addition of  $H_2O_2$ ; 4 – 10ml/l addition of  $H_2O_2$

densities, than these of the sample coated after 50 ml.  $H_2O_2$  addition. Nevertheless, the respective anodic curve (of the sample with 100 ml.  $H_2O_2$ ) has shorter region of passivity (from -750 to -550 mV) than the curves of the samples with lower  $H_2O_2$  additions. According Bethencourt and co. [16], the shorter passivity regions indicate lower strength against pitting nucleation.

Between the samples, prepared at lower  $H_2O_2$  content, the cathodic curve of the sample prepared after 25 ml / l.  $H_2O_2$  addition, stays at lower current densities, than this of the sample with 10 ml. However, the respective anodic curves stay at the same current densities, revealing very similar barrier ability. Furthermore, the curve of the sample with 10 ml. oxidant addition have relatively larger passivity region. From these relatively equivocal features of the polarization curves, could be concluded that the optimal addition of peroxide should be in the range of 10 and 25 ml. 30%  $H_2O_2$  for liter of conversion bath.

Fig. 4 (c, d) reveals that at  $-5mA/cm^2$ , the voltammograms of the samples with different  $H_2O_2$  additions are less distinguishable, compared to those, deposited at lower current densities. This phenomenon could be explained, having in mind that the deposition current plays a role of reducer. As a result, at higher current densities ( $-5mA/cm^2$ ), the influence of the  $H_2O_2$  as oxidant is less notable.

The supply of charged particles towards the specimen (by the electric current) leads to deactivation of the peroxide by obtaining of  $OH^-$  ions (equation 2) and acceleration of oxygen reduction (equation 4). Both these processes result in alkalisation of the medium near the substrate surface and acceleration of Ce-precipitation (equation 3).

However, the obtained  $Ce(OH)_3/Ce(OH)_4$  precipitates do not form a coating layer, but rather conjunction of clusters.

#### *Superficial morphological observations*

Following the literature [10], the increase of the oxidant content should accelerate the coating deposition. Consequently, it is expectable to improve the density and barrier ability of the coating after increase of  $H_2O_2$  addition. Nevertheless, it was observed that the elevated content of peroxide has detrimental effect on the homogeneity and uniformity of the obtained coatings. As could be seen in Fig. 5, all the samples prepared with elevated additions of  $H_2O_2$  have not uniform coatings, but rather they are covered by rough aggregates. Furthermore, these aggregates did not possess almost any adherence to the metallic substrates, so that metallic shining under the Ce-deposits was clearly observable, as a result of partial removal of the Ce-containing aggregates.

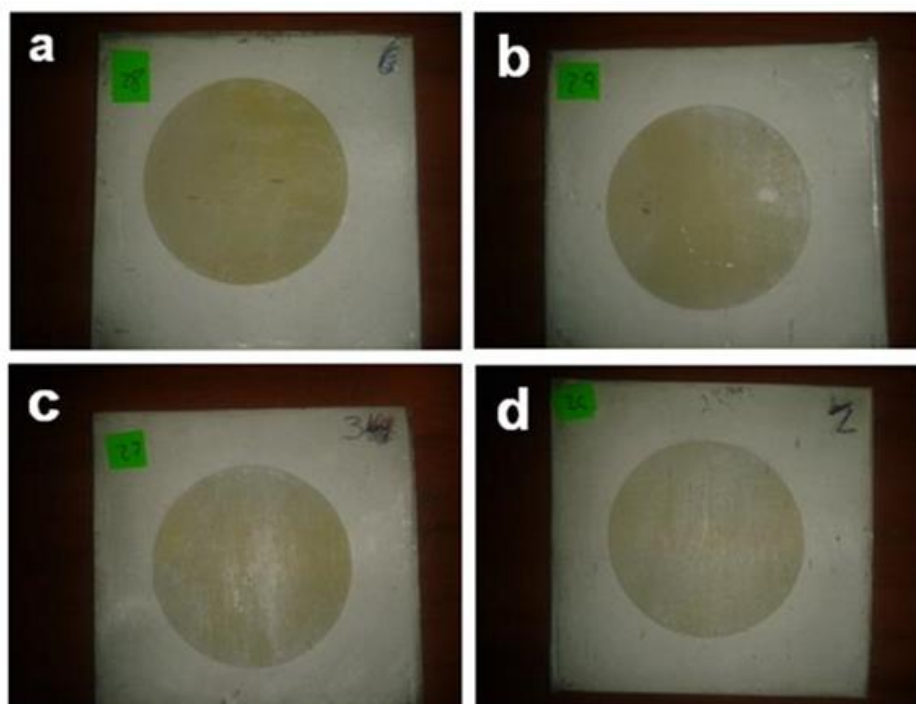


**Fig. 5.** Photographs of four samples with coatings, deposited after different additions of oxidant: a – 10ml/l addition of  $H_2O_2$ ; b - 25ml/l addition of  $H_2O_2$ ; b - 50ml/l addition of  $H_2O_2$ ; d - 100ml/l addition of  $H_2O_2$ ;

The CeCCs, deposited at  $-5\text{mA}/\text{cm}^2$  generally reveal inferior features than those with CeCC electrodeposited at  $-2\text{mA}/\text{cm}^2$ .

In order to observe the morphology of the coating, Scanning Electronic Microscopy (SEM), combined by energy dispersion X-ray analysis were applied on the best samples before and after 168 hours of exposition to naturally aerated 3.5% NaCl model corrosive medium. These coatings possess peculiar features. Larger oval hills are clearly distinguishable on the surfaces. Probably these sides are locations of preferential deposition of the layer, as was observed in previous works [17-21]. Consequently, these oval hills are formed as consequence of preferential deposition on intermetallics.

- *EDX analysis* – In order to clarify the real composition of the samples, and the distribution of the elements on their surfaces, EDX – map analyses were executed during the SEM observations. The next figure represents the elemental distributions of the most important chemical elements: Al, Ce, Cu, and oxygen. These elements were selected because the aluminium could be presented not only from the metallic substrate, but also to compose corrosion

products, in form of  $\text{Al}(\text{OH})_3$ , etc. The cerium was selected because this element together with the oxygen is the basic components of the coating. The copper was also selected to be monitored, because it should reveal whether the S-phases are preferable locations of deposition, and is there a copper re-deposition as evidence of corrosion during the deposition. Fig. 6 shows EDX –map data and SEM image of CeCC, obtained by deposition for 5 min. from 0.05 M  $(\text{NH}_4)_2\text{Ce}(\text{NO}_3)_5$  with 10ml/l addition of 30%  $\text{H}_2\text{O}_2$ .

The Al-distribution map in Fig. 6 reveals that there is aluminum deposited on the coating. It is undoubtedly originated from corrosion products formed during the deposition. The EDX-map of cerium shows that the sides of preferable deposits coincide with the highest abundance of cerium. Nevertheless, there is uniform distribution of this element on the rest part of the coated surface. The copper is also equally distributed on the metallic surface. This fact is consequence and indication of copper re-distribution. This process passes because of the cathodic Al-dissolution of the metallic matrix.

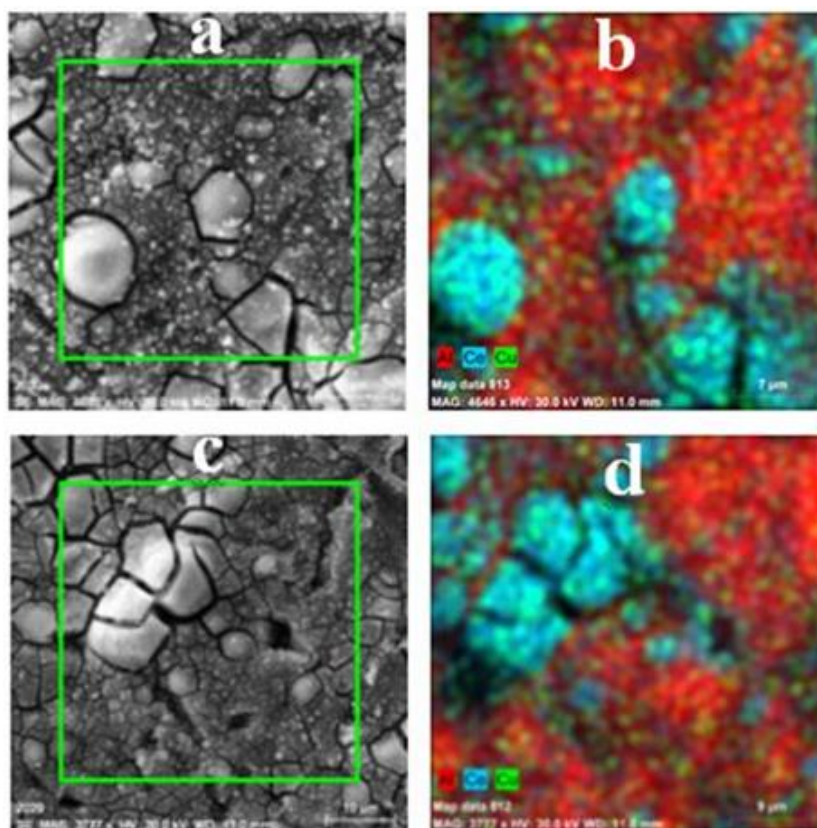


**Fig. 6.** SEM images (a, c), and EDX map data (b, d) of sample after prepared by deposition for 5 min. from 0.05 M  $(\text{NH}_4)_2\text{Ce}(\text{NO}_3)_5$  with 10ml/l addition of  $\text{H}_2\text{O}_2$

## CONCLUSION

As a result of the investigations performed, the following conclusions are done:

Diammonium pentanitrocerate was used as provider of Ce-ions during the coating deposition. In this substance, the Ce is presented in the anionic compositional part in difference of the widely used  $\text{CeCl}_3$ , or  $\text{Ce}(\text{NO}_3)_3$ .

It is found that at different concentrations of  $(\text{NH}_4)_2\text{Ce}(\text{NO}_3)_5$  in range 0.01 to 0.1 moles per liter, the optimal concentration is about 0.05 M  $(\text{NH}_4)_2\text{Ce}(\text{NO}_3)_5$ .

It is determined that the optimal content of peroxide is in the range of 10 and 25 ml/l. of 30%  $\text{H}_2\text{O}_2$  for the investigated system.

It is established that the best CeCC were electrodeposited at  $i = -2\text{mA}/\text{cm}^2$  current density and 5 minutes.

It was determined by SEM observations that the morphology of the coating does not repeat those of the metallic substrate, showing complete coverage by the coating.

The Cerium conversion coatings elaborated in the present research work could serve as a basis for future coating systems.

**Acknowledgements:** The authors gratefully acknowledge the financial support of project BG 051PO001-3.3.06-0038. Dr. Gustavo Pelaez is acknowledged for the opportunity for the international collaboration activities.

## REFERENCES

1. E.A. Starke and J. T. Staley, *Prog. Aerospace Sci.* **32**, 131 (1996).
2. AIRBUS A380, *Airplane characteristics*, Issue 30.03.05 (2005), [www.content.airbusworld.com/SITES/Technical.../A\\_C\\_A380.pdf](http://www.content.airbusworld.com/SITES/Technical.../A_C_A380.pdf)
3. M. J. O'Keefe, S. Geng, S. Joshi, *Metalfinishing* (2007) 25 – 28
4. S. Geng, S. Joshi, W. Pinc, W.G. Fahrenholtz, (1)M.J. O'Keefe, T.J. O'Keefe, and P. Yu "Influence of processing parameters on cerium based conversion coatings" Proceed "TRI – Service – 2007" - corrosion conference: Accessible via: <https://www.corrdefense.org/Technical%20Papers/Influence%20of%20Processing%20Parameters%20on%20Cerium%20Based%20Conversion%20Coatings.pdf>
5. B. Hindin "Corrosion protection of aluminium alloys by corrosion prevention compounds as measured by electrochemical techniques" accessible via: <https://www.corrdefense.org/Academia%20Government%20and%20Industry/XVIII%20-%20HINDIN%20-%20Corrosion%20Protection%20of%20Aluminum%20Alloys%20by.pdf>
6. P. Ostash, I. M. Andreiko, Yu. V. Holovatyuk, O. I. Semenets, *Mater. Sci.* **44**, 672 (2008).
7. J.A. Rodríguez-Martínez, A. Rusinek, A. Arias, Thermo-Viscoplastic behaviour of AA2024 aluminium sheets subjected to low velocity perforation at different temperatures, accessible via: [http://e-archivo.uc3m.es/bitstream/10016/11941/1/rodriguez\\_thermo\\_TWS\\_2011\\_ps.pdf](http://e-archivo.uc3m.es/bitstream/10016/11941/1/rodriguez_thermo_TWS_2011_ps.pdf)
8. Y. Komatsu, New Pretreatment and Painting Technology for All Aluminum Automotive Body, paper no. 910787, SAE Technical Paper Series-International Congress/AIRP Meeting (Warrendale, PA: SAE International, 1991).
9. G. Tsaneva, V. Kozhukharov, S. Kozhukharova, M. Ivanova, J. Gerwann, M. Schem, T. Schmidt, *J. Univ. Chem. Technol. Met.*, **43**, 231 (2008).
10. M. J. O'Keefe, S. Geng, S. Joshi, *Metalfinishing*, 25 (2007).
11. K. A. Yasakau, M. L. Zheludkevich, S. V. Lamaka, M. G. S. Ferreira, *J. Phys. Chem.*, **B- 110**, 5515 (2006).
12. M. D. Tkalenko, *Protection of Metals*, **37(4)**, 301, (2001).
13. T. Picard, G. Cathalifaud-Feuillade, M. Mazet, C. Vandesteendam, *J. Environ. Monit.* **2(1)**, 77 (2000).
14. M. Mokaddem, P. Volovitch, F. Rechou, R. Oltra, K. Ogle, *Electrochim. Acta*, **55**, 3779 (2010).
15. S. K. Ogle, M. Serdechnova, M. Mokaddem, P. Volovitch, *Electrochim. Acta*, **56**, 1711 (2011).
16. M. Bethencourt, F.J. Botana, M.J. Cano, M. Marcos, J.M. Sánchez-Amaya, L. González-Rovira, *Corros. Sci.* **51**, 518 (2009).
17. J. E. Pernas, S. Kozhukharov, A. A. Salve, E. A. Matter, M. Machkova, *J. Univ. Chem. Technol. Met.*, **47**, 311 (2012).
18. E. A. Matter, S. Kozhukharov, M. Machkova, V. Kozhukharov, *Mater. Corros.*, DOI: 10.1002/maco.201106349
19. E. A. Matter, S. Kozhukharov, M. Machkova, V. Kozhukharov, *Corros. Sci.* **62**, 22 (2012).
20. E. Matter, S. Kozhukharov, M. Machkova, SEM and EDS determination of the impact of inhibitor containing corrosive media over the AA2024 superficial morphology, Ann. Proc. of "Angel Kanchev" – University of Rousse (Bulgaria), **50**, 60, (2011). Accessible via: <http://conf.uni-rouse.bg/bg/docs/cp11/9.1/9.1-10.pdf>
21. M. Machkova, E.A. Matter, S. Kozhukharov, V. Kozhukharov, *Corros. Sci.*, **69**, 396 (2013).

## ЕЛЕКТРОХИМИЧНО ОТЛАГАНЕ НА ЦЕРИЕВИ КОНВЕРСИОННИ ПОКРИТИЯ ЗА КОРОЗИОННА ЗАЩИТА НА ПЛАКИРАНА СПЛАВ Д16 АМ

Х. А. П. Айюсо<sup>1</sup>, С. Кожухаров<sup>2\*</sup>, М. Мачкова<sup>2</sup>, В. Кожухаров<sup>2</sup>

<sup>1</sup>Университет Виго, Лагоас Марконсенде 36310 (Испания)

<sup>2</sup>Химикотехнологичен и Металургичен Университет, бул. "Климент Охридски" № 8 София 1756 (Б)

Постъпила на 31 януари, 2013 г.; Коригирана на 21 май, 2013 г.

(Резюме)

Настоящата работа представя изследване върху възможностите за използване на ново цериево съединение за катодно електрохимично отлагане на цериево-основани конверсионни покрития (ЦКП) за защита на плакирана сплав Д16 АМ против корозия. За целите на настоящето изследване беше използван диамониев пентанитроцерат  $((\text{NH}_4)_2\text{Ce}(\text{NO}_3)_5)$ , при който церият е представен в анионната съставна част на съединението, за разлика от електролитите, използвани до сега. Бариерната способност против корозионна атака на всички изследвани образци в настоящата работа беше оценена по два различни електрохимични метода: Волтаперометрия с Литнейна Разгъвка на Потенциала (ВЛРП) и Електрохимична Импедансна Спектроскопия (СЕМ). В допълнение, избрани образци преминаха морфологично описание чрез Сканираща Електронна Микроскопия (СЕМ), съчетана с Енергийно Разпределителна Рентгенова Спектроскопия (ЕРРС). Като резултат, беше оценено въздействието на концентрациите на основното вещество и активатора за отлагане, както и плътността на приложения ток.

## Influence of hydroxyethylated-2-butyne-1,4-diol on copper electrodeposition from sulphate electrolytes containing large amounts of zinc

G. A. Hodjaoglu\*, I. S. Ivanov

<sup>1</sup> Institute of Physical Chemistry, Bulgarian Academy of Sciences, Acad. G. Bonchev Str., bl.11, 1113 Sofia, Bulgaria

Received February 5, 2013; Revised June 15, 2013

The influence of an organic additive hydroxyethylated-2-butyne-1, 4-diol (Ferasine) on the electroextraction of copper from sulphate electrolytes was studied through of potentiodynamic and galvanostatic methods. It was found that Ferasine decreases the cathodic currents reached at different vertex potentials and quantities of deposited copper which shows that it inhibits the cathodic reaction of copper deposition. The influence of Ferasine is stronger expressed in electrolytes containing 130 g/L H<sub>2</sub>SO<sub>4</sub> than in neutral electrolytes. The inhibiting effect of additive increases with increase in cathodic potential. Dense and smooth copper coatings on Cu cathodes with current efficiency higher than 90% are deposited when Cu<sup>2+</sup> concentration is higher than 5 g/L and current densities are in the range 0.5 ÷ 2 A/dm<sup>2</sup>. More fine-grained coatings are obtained in the presence of H<sub>2</sub>SO<sub>4</sub> and hydroxyethylated-2-butyne-1, 4-diol (Ferasine). Non-adherent, dark-red Cu slime is obtained when the concentration of Cu<sup>2+</sup> - ions is lower than 5 g/L. Ferasine changes the preferred crystallographic orientation (hkl) of Cu coatings from (220) to (111) only during deposition in electrolytes containing H<sub>2</sub>SO<sub>4</sub>. In the absence of acid the preferred orientation, both in the absence or presence of Ferasine remains (111).

**Key words:** copper; cyclic voltammograms; deposition; electroextraction; zinc.

### INTRODUCTION

The main part of the wastes containing Zn or Cu is generated from hydrometallurgy, metal galvanizing, plating industry and smelting processes. For example, the waste product known as “blue powder” that results by condensing furnace gases during the thermometallurgical processing of non-ferrous ores contains: Zn (25-41 wt.%), Pb (20-25 wt.%), Fe (3-5 wt.%), Cu (0.5-1 wt.%), etc. [1, 2]. The purification of the electrolytes for Zn electrowinning by cementation is another process that produces wastes containing large amount of different metals such as: copper cake, containing 36-54 wt.% Cu and 5-10 wt.% Zn; copper-cadmium cake, containing 10 wt.% Cu, 30 wt.% Zn, 12 wt.% Cd; collective cake, containing 5.8 wt.% Cu, 35.9 wt.% Zn, 7.2 wt.% Cd; cobalt-nickel cake, containing 25 wt.% Cu, 20 wt.% Zn and 3 wt.% Cd. [3]. Cementates obtained during the hydrometallurgical zinc winning process, where the sulphate leach liquor is treated with arsenic trioxide and zinc powder for the removal of Cu, Ni, Co, Cd and other impurities contain: Cu (28.6 wt.%), Zn (22.4 wt.%) and Cd (6.7 wt.%) [4]. Flue dusts at a secondary copper smelter treated in the electrowinning zinc plant contain: Zn (40-65 wt.%) and Cu (1-6%). [5]. These industrial wastes are a

source of different valuable metals like copper, zinc, cadmium, etc.

There are numerous investigation concerning the influence of organic additives on the process of Cu electrodeposition in sulphate electrolytes, containing only Cu<sup>2+</sup> ions but their influence on the Cu electroextraction from electrolytes, containing large amounts of Zn<sup>2+</sup> is not studied.

Muresan et al. [1, 2]. studied the effect of horse-chestnut extract (HCE) and IT-85, representing a mixture of triethyl-benzyl-ammonium chloride (TEBA) and hydroxyethylated-2-butyne-1, 4-diol (Ferasine) upon the morphology and structure of Cu deposits, as well as upon the cathodic polarization and compared to the effect exerted by thiourea and animal glue. Varvara et al. [6-9] studied the influence of TEBA, Ferasine and IT-85 on the kinetics of Cu electrodeposition from such electrolytes and on the morphology and structure of Cu deposits. Maher Alodan and William Smyrl [10] established that at concentrations of thiourea >1 mM strong effects on copper in solutions of sulfuric acid is observed. Moo Seong Kang et al. [11] observed that even in the presence of very low concentrations of thiourea in sulphate electrolyte extremely smooth and bright copper deposits. M. Quinet, et al. [12] investigated the effects of thiourea and saccharin, on copper electrodeposition from acid sulphate solutions using different

\* To whom all correspondence should be sent:  
E-mail: gyunver@ipc.bas.bg

electrochemical methods: cyclic voltammetry, chronoamperometry, and electrochemical quartz crystal microbalance as well as using different observation techniques: scanning electron microscopy (SEM) and atomic force microscopy (AFM). A. L. Portela et al. studied copper electrodeposition on platinum electrodes from slightly acidic solutions of copper sulphate containing nicotinic acid (NA) [13]. Run-lan YU et al. [14] studied the inhibition behavior of some new mixed additives such as gelatin + hexadecylpyridinium bromide (HDPBr), gelatin + polyethylene glycol(PEG), gelatin + polyacrylamide (PAM), gelatin + PEG + cetyl-tri-methyl ammonium bromide (CTABr) and gelatin + PAM + CTABr using cyclic voltammetry as well as cathodic polarization in order to improve the quality of cathodic copper [14]. DC and pulse plating of copper in acidic sulphate solutions containing benzotriazole (BTA) has been studied by N. Tantavichet and M. Pritzker [15]. Using electrochemical and spectroelectrochemical techniques B. Bozzini et al. investigate the effects of PEG during Cu electrodeposition from an acidic sulphate solution [16]. B. Bozzini et al. report in situ visible electroreflectance measurements carried out during potentiostatic electrodeposition of Cu from acidic sulphate solutions in the absence and presence of PEG [17]. The behaviour of 3-diethylamino-7-(4-dimethylaminophenylazo)-5-phenylphenazinium chloride (Janus Green B, JGB) during Cu electrodeposition from an acidic sulphate solution was studied by B. Bozzini et al. [18]. The effect of a new ionic liquid additive 1-butyl-3-methylimidazolium hydrogen sulfate-[BMIM]HSO<sub>4</sub> on the kinetics of copper electro-deposition from acidic sulfate solution was investigated by cyclic voltammetry, polarization and electrochemical impedance measurements and compared with those exerted by the conventional additive, thiourea (Q.B. Zhang et al. [19]. Copper electrodeposition on to a platinum substrate from an acid sulphate plating bath was investigated with and without the additive benzotriazole (BTAH) by A. C. M. de Moraes et al. [20]. Copper electrodeposition in the presence of various types of aromatic and aliphatic amines was studied by H.H. Abdel-Rahman et al. [21]. M. Gu and Q. Zhong investigated copper electrodeposition and nucleation on a glassy carbon electrode from acid sulfate electrolytes in the presence of 3-mercapto-1-propanesulfonate sodium salt (MPS) and its combinations with chloride ions (Cl) or/and polyethylene glycol (PEG) by utilizing cyclic voltammetry (CV), chronoamperometry (CA) and

scanning electron microscopy (SEM) [22]. To improve the quality requirements for copper deposits, the influence of some inhibition agents added to the acidic copper bath has been studied by C. C. Vaduva et al. [23].

The aim of this paper is to study the influence of hydroxyethylated-butyne-2-diol-1,4 (Ferasine) and some experimental conditions on the process of Cu electroextraction from sulphuric acid electrolytes containing large concentrations of Zn<sup>2+</sup> - ions. This study is an attempt, using electrolytes modelling wastes produced in zinc hydrometallurgy, to obtain conditions for separately electrowinning of these metals.

## EXPERIMENTAL

The experiments were carried out in a thermostated (37 ± 1°C), three-electrode glass cell without stirring of the electrolyte. The cathode (2.0 cm<sup>2</sup>) and both anodes (4.0 cm<sup>2</sup> total area) were Pt plates. The reference electrode was a mercury/mercurous sulphate electrode in 0.5 M H<sub>2</sub>SO<sub>4</sub> (SSE), its potential vs. NHE being +0.720 V. The studies were carried out using a cyclic potentiodynamic technique. Potential scanning at a rate of 30 mV/sec in the potential range from +1.000 to -1.800 V vs SSE was performed by means of a computerized PAR 263A potentiostat / galvanostat using Soft Corr II software. Amount of deposited metals was obtained by integration of the respective anodic peaks on cyclic voltammograms (CVAGs).

Galvanostatic deposition was carried out on copper cathodes (4.0 cm<sup>2</sup>) at current densities in the range 0.5 ÷ 2 A/dm<sup>2</sup> using two Pb-Ag (1%) anodes. Pt and Cu electrodes were degreased in ultrasound bath and than only Cu cathode was etched in HNO<sub>3</sub> (1:1).

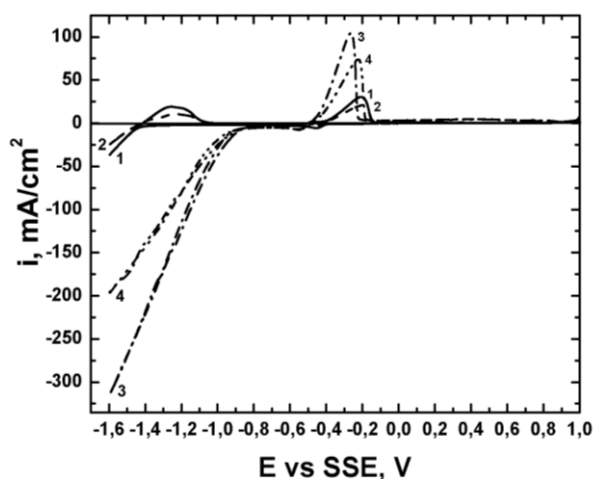
Cu<sup>2+</sup> ions (1, 5 or 10 g/L) were added to the base electrolytes: BE-1, containing 220 g/L ZnSO<sub>4</sub>·7H<sub>2</sub>O (50 g/L Zn<sup>2+</sup>) and BE-2, containing 220 g/L ZnSO<sub>4</sub>·7H<sub>2</sub>O (50 g/L Zn<sup>2+</sup>) and 130 g/L H<sub>2</sub>SO<sub>4</sub>. The organic additive in both electrolytes was 30% solution of hydroxyethylated-butyne-2-diol-1,4 (Ferasine).

X-ray powder diffraction patterns for phase identification of copper cathode and deposits were recorded in the angle interval 20-110θ (2θ) on a Philips PW 1050 diffractometer, equipped with Cu Kα tube and scintillation detector. The surface morphology of the deposits was examined and EDX Analysis was made by scanning electron microscopy (SEM) using a JEOL JSM 6390 microscope.

## RESULTS AND DISCUSSION

### Potentiodynamic studies

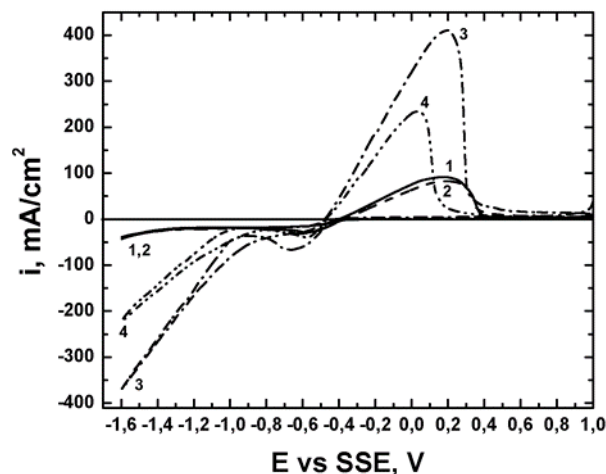
Figure 1 shows CVAGs obtained in electrolytes, containing 1 g/l  $\text{Cu}^{2+}$  and 50 g/l  $\text{Zn}^{2+}$  without Ferasine (curve 1), and with 1 ml/l Ferasine (curve 2) and 1 g/l  $\text{Cu}^{2+}$ , 50 g/l  $\text{Zn}^{2+}$  and 130 g/l  $\text{H}_2\text{SO}_4$  without Ferasine (curve 3) and with 1 ml/l Ferasine (curve 4). The scan direction is changed at cathodic potential (vertex potential) -1.6 V.



**Fig. 1.** Cyclic voltammograms obtained on Pt cathode in electrolytes, containing: 1)  $\text{Cu}^{2+}$  - 1 g/L and  $\text{Zn}^{2+}$  - 50 g/L, 2)  $\text{Cu}^{2+}$  - 1 g/L,  $\text{Zn}^{2+}$  - 50 g/L and Ferasine 1 mL/L, 3)  $\text{Cu}^{2+}$  - 1 g/L,  $\text{Zn}^{2+}$  - 50 g/L and  $\text{H}_2\text{SO}_4$  - 130 g/L, 4)  $\text{Cu}^{2+}$  - 1 g/L,  $\text{Zn}^{2+}$  - 50 g/L,  $\text{H}_2\text{SO}_4$  - 130 g/L and Ferasine 1 mL/L.  $E_{\text{vertex}} = -1.6$  V vs SSE.

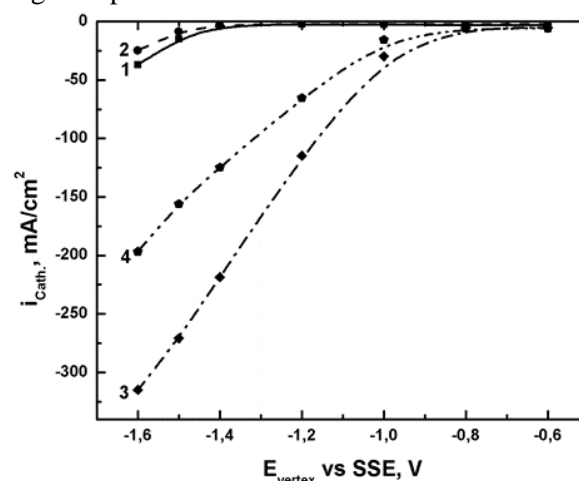
It is observed that at potentials between -0.4 V and -0.2 V anodic peaks, obviously due to the Cu dissolution, appear. It is seen that only on the curves obtained in electrolytes without  $\text{H}_2\text{SO}_4$  (curves 1 and 2) more negative (at -1.250 V) anodic peaks, due to the Zn dissolution, appear. The anodic peaks obtained in the electrolytes containing Ferasine (curves 2 and 4) are lower than those obtained in electrolytes without additive (curves 1 and 3) which means that Ferasine inhibit the metal deposition.

Figure 2 shows CVAGs obtained in electrolytes, containing 10 g/L  $\text{Cu}^{2+}$  and 50 g/L  $\text{Zn}^{2+}$  (curve 1), 10 g/L  $\text{Cu}^{2+}$ , 50 g/L  $\text{Zn}^{2+}$  and 1 mL/L Ferasine (curve 2), 10 g/L  $\text{Cu}^{2+}$ , 50 g/L  $\text{Zn}^{2+}$  and 130 g/L  $\text{H}_2\text{SO}_4$  (curve 3) and 10 g/L  $\text{Cu}^{2+}$ , 50 g/L  $\text{Zn}^{2+}$ , 130 g/L  $\text{H}_2\text{SO}_4$  and 1 mL/L Ferasine (curve 4). The scan direction is changed at cathodic potential (vertex potential) -1.6 V. The cyclic voltammograms are similar to those obtained in the case with the lower  $\text{Cu}^{2+}$  concentration (1 g/L). In this case (10 g/L) at all (even at more negative than -1.6 V) vertex potentials only Cu deposition takes place.



**Fig. 2.** Cyclic voltammograms obtained on Pt cathode in electrolytes, containing: 1)  $\text{Cu}^{2+}$  - 10 g/L and  $\text{Zn}^{2+}$  - 50 g/L, 2)  $\text{Cu}^{2+}$  - 10 g/L,  $\text{Zn}^{2+}$  - 50 g/L and Ferasine 1 mL/L, 3)  $\text{Cu}^{2+}$  - 10 g/L,  $\text{Zn}^{2+}$  - 50 g/L and  $\text{H}_2\text{SO}_4$  - 130 g/L, 4)  $\text{Cu}^{2+}$  - 10 g/L,  $\text{Zn}^{2+}$  - 50 g/L,  $\text{H}_2\text{SO}_4$  - 130 g/L and Ferasine 1 mL/L.  $E_{\text{vertex}} = -1.6$  V vs SSE.

The influence of Ferasine on the cathodic currents reached at different vertex potentials and on the amount of deposited Cu during scanning to different vertex potentials is shown in Figures 3, 4, 5 and 6. It is seen that Ferasine decreases significantly the current values and the amounts of deposited Cu or Zn only in electrolytes containing  $\text{H}_2\text{SO}_4$ . The polarizing effect of additive is more strongly expressed at more negative vertex potentials which, perhaps, is due to the increased Ferasine adsorption on the cathodic surface at more negative potentials.



**Fig. 3.** Current densities reached at different vertex potentials on Pt cathode in electrolytes, containing: 1)  $\text{Cu}^{2+}$  - 1 g/L and  $\text{Zn}^{2+}$  - 50 g/L, 2)  $\text{Cu}^{2+}$  - 1 g/L,  $\text{Zn}^{2+}$  - 50 g/L and Ferasine 1 mL/L, 3)  $\text{Cu}^{2+}$  - 1 g/L,  $\text{Zn}^{2+}$  - 50 g/L and  $\text{H}_2\text{SO}_4$  - 130 g/L, 4)  $\text{Cu}^{2+}$  - 1 g/L,  $\text{Zn}^{2+}$  - 50 g/L,  $\text{H}_2\text{SO}_4$  - 130 g/L and Ferasine - 1 mL/L.

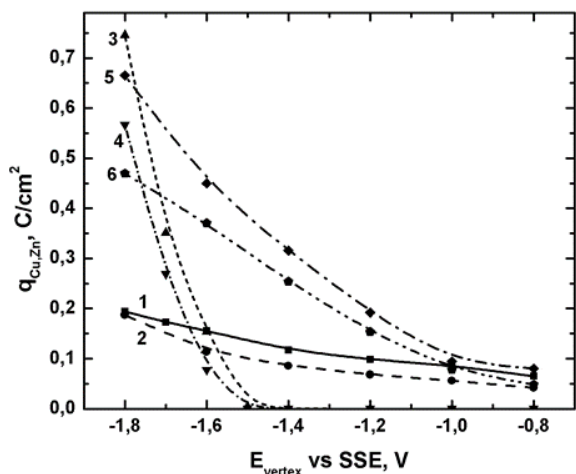


**Fig. 4.** Amounts of copper or zinc deposited during scanning to different vertex potentials in electrolytes, containing: 1)  $\text{Cu}^{2+}$  - 1 g/L and  $\text{Zn}^{2+}$  - 50 g/L 2)  $\text{Cu}^{2+}$  - 1 g/L,  $\text{Zn}^{2+}$  - 50 g/L and Ferasine 1 mL/L, 3)  $\text{Cu}^{2+}$  - 1 g/L and  $\text{Zn}^{2+}$  - 50 g/L - Zinc, 4)  $\text{Cu}^{2+}$  - 1 g/L,  $\text{Zn}^{2+}$  - 50 g/L and Ferasine 1 mL/L 5)  $\text{Cu}^{2+}$  - 1 g/L,  $\text{Zn}^{2+}$  - 50 g/L and  $\text{H}_2\text{SO}_4$  - 130 g/L - Copper, 6)  $\text{Cu}^{2+}$  - 1 g/L,  $\text{Zn}^{2+}$  - 50 g/L,  $\text{H}_2\text{SO}_4$  - 130 g/L and Ferasine 1 mL/L.

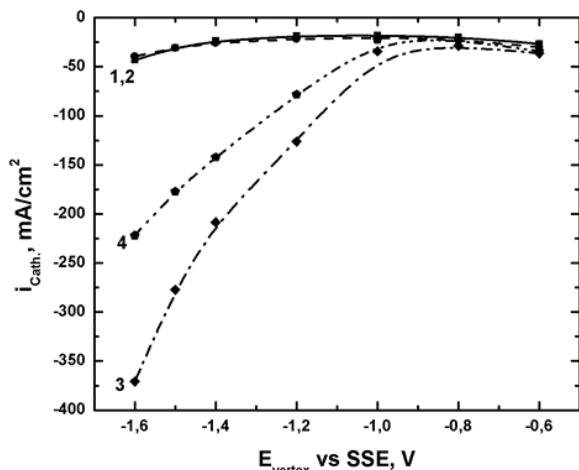


**Fig. 5.** Current densities reached at different vertex potentials on Pt cathode in electrolytes, containing: 1)  $\text{Cu}^{2+}$  - 10 g/L and  $\text{Zn}^{2+}$  - 50 g/L, 2)  $\text{Cu}^{2+}$  - 10 g/L,  $\text{Zn}^{2+}$  - 50 g/L and Ferasine 1 mL/L, 3)  $\text{Cu}^{2+}$  - 10 g/L,  $\text{Zn}^{2+}$  - 50 g/L and  $\text{H}_2\text{SO}_4$  - 130 g/L, 4)  $\text{Cu}^{2+}$  - 10 g/L,  $\text{Zn}^{2+}$  - 50 g/L,  $\text{H}_2\text{SO}_4$  - 130 g/L and Ferasine - 1 mL/L.

#### Galvanostatic studies

The effect of Ferasine on the preferred crystallographic orientations, surface morphology and composition of galvanostatically deposited coatings on Cu substrates was also studied. In all cases only copper is detected by EDX Analysis.

Ferasine changes preferred crystallographic orientations (hkl) of Cu coatings from (220) to (111) during deposition in electrolytes containing  $\text{H}_2\text{SO}_4$  (Figures 7 and 8). In the case of deposition from electrolytes without acid proffered orientation is (111) both in the presence or absence of Ferasine.

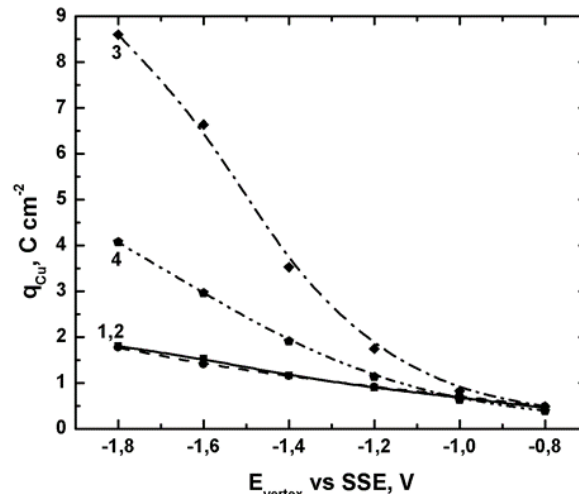


**Fig. 6.** Deposited copper versus vertex potentials obtained on Pt cathode in electrolytes, containing: 1)  $\text{Cu}^{2+}$  - 10 g/L and  $\text{Zn}^{2+}$  - 50 g/L, 2)  $\text{Cu}^{2+}$  - 10 g/L,  $\text{Zn}^{2+}$  - 50 g/L and Ferasine 1 mL/L, 3)  $\text{Cu}^{2+}$  - 10 g/L,  $\text{Zn}^{2+}$  - 50 g/L and  $\text{H}_2\text{SO}_4$  - 130 g/L, 4)  $\text{Cu}^{2+}$  - 10 g/L,  $\text{Zn}^{2+}$  - 50 g/L,  $\text{H}_2\text{SO}_4$  - 130 g/L and Ferasine - 1 mL/L.

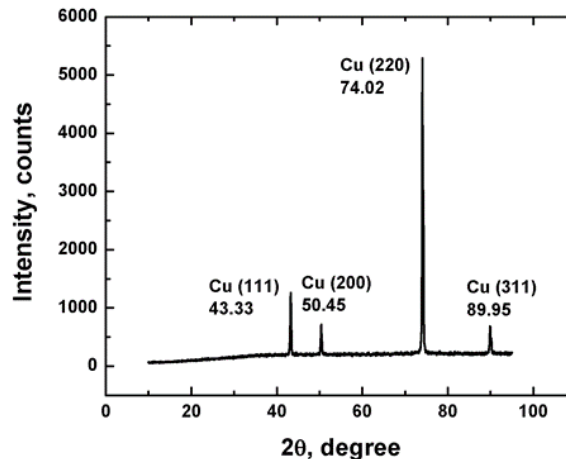


**Fig. 7.** Preferred crystallographic orientations (hkl) of Cu deposited from electrolyte containing:  $\text{Cu}^{2+}$  - 10 g/L,  $\text{Zn}^{2+}$  - 50 g/L and  $\text{H}_2\text{SO}_4$  - 130 g/L.

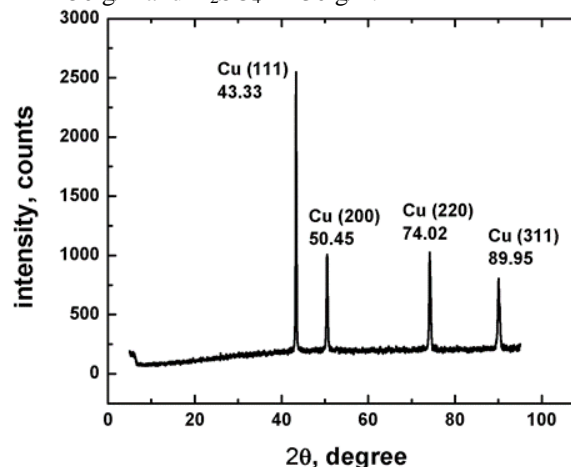


**Fig. 8.** Preferred crystallographic orientations (hkl) of Cu deposited from electrolyte containing:  $\text{Cu}^{2+}$  - 10 g/L,  $\text{Zn}^{2+}$  - 50 g/L,  $\text{H}_2\text{SO}_4$  - 130 g/L and Ferasine - 1 mL/L.

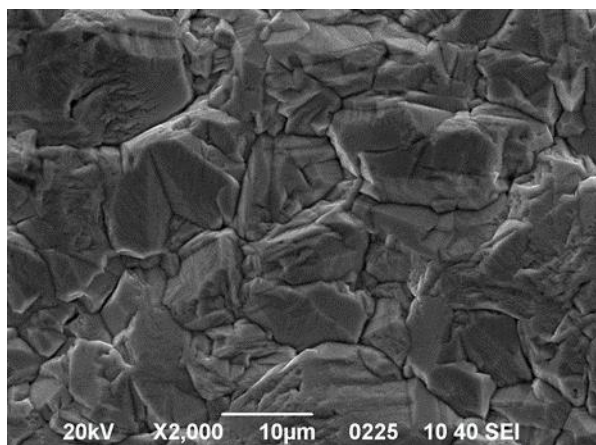


**Fig. 9.** SEM micrograph of Cu coating obtained after 30 min. deposition at 1 A/dm<sup>2</sup> in an electrolyte, containing 10 g/L Cu<sup>2+</sup>, 50 g/L Zn<sup>2+</sup> and 130 g/L H<sub>2</sub>SO<sub>4</sub>. Magnification x 1000.

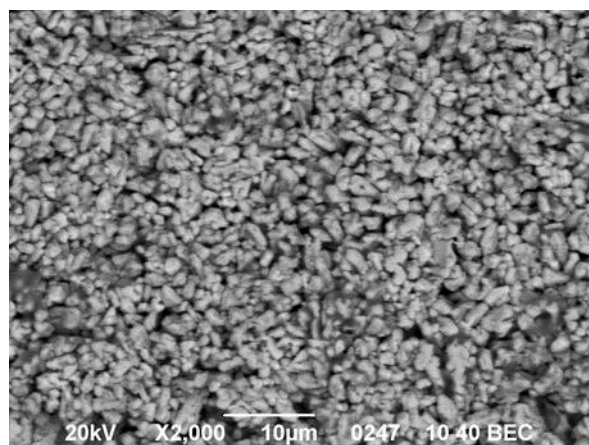


**Fig. 10.** SEM micrograph of Cu coating obtained after 30 min. deposition at 1 A/dm<sup>2</sup> in an electrolyte, containing 50 g/L Zn<sup>2+</sup>, 10 g/L Cu<sup>2+</sup>, 130 g/L H<sub>2</sub>SO<sub>4</sub> and 5 mL/L Ferasine. Magnification x 1000.

**Table 1.** Grain size (µm) of Cu coatings obtained in different electrolytes

Electrolyte	Grain size (µm)
10 g/L Cu <sup>2+</sup> + Zn <sup>2+</sup> 50 g/L	25-30
10 g/L Cu <sup>2+</sup> + 50 g/L Zn <sup>2+</sup> + 1 mL/L Ferasine	15-18
10 g/L Cu <sup>2+</sup> + 50 g/L Zn <sup>2+</sup> + 130 g/L H <sub>2</sub> SO <sub>4</sub>	12-18
10 g/L Cu <sup>2+</sup> + 50 g/L Zn <sup>2+</sup> + 130 g/L H <sub>2</sub> SO <sub>4</sub> + 1 mL/L Ferasine	10-12
10 g/L Cu <sup>2+</sup> + 50 g/L Zn <sup>2+</sup> + 130 g/L H <sub>2</sub> SO <sub>4</sub> + 5 mL/L Ferasine	< 3
20 g/L Cu <sup>2+</sup> + 50 g/L Zn <sup>2+</sup> + 130 g/L H <sub>2</sub> SO <sub>4</sub> + 5 mL/L Ferasine	9-12
20 g/L Cu <sup>2+</sup> + 100 g/L Zn <sup>2+</sup> + 130 g/L H <sub>2</sub> SO <sub>4</sub> + 5 mL/L Ferasine	15-20
5 g/L Cu <sup>2+</sup> + 50 g/L Zn <sup>2+</sup> + 130 g/L H <sub>2</sub> SO <sub>4</sub> + 5 mL/L Ferasine	< 6
1.25 g/L Cu <sup>2+</sup> + 14 g/L Zn <sup>2+</sup> + 16.5 g/L H <sub>2</sub> SO <sub>4</sub> + 0.6 mL/L Ferasine	< 1-2

Figure 9 shows SEM micrograph of Cu coatings obtained after 30 min. deposition at 1 A/dm<sup>2</sup> in an electrolyte, containing 10 g/L Cu<sup>2+</sup>, 50 g/L Zn<sup>2+</sup> and 130 g/L H<sub>2</sub>SO<sub>4</sub>. The addition of Ferasine (5 mL/L) – Figure 10, leads to more fine-grained surface morphology of the coatings. In all cases the coatings are light-red, smooth and bright.

It has been established that dense and smooth Cu coatings are deposited when the Cu<sup>2+</sup> concentration is higher than 5 g/L and the current density is in the range of 0.5 ÷ 2 A/dm<sup>2</sup>. At 1 A/dm<sup>2</sup> the deposition potential is -0.500 ÷ -0.600 V. In all cases the current efficiency of Cu deposition is higher than 90%. Non-adherent, dark-red Cu slime is obtained when the concentration of Cu<sup>2+</sup>-ions is lower than 5 g/L. In the case of low Cu<sup>2+</sup> concentration the deposition potential is more negative (between -1.000 and -1.100 V) due to the concentration polarization. In this case the current efficiency is less than 75% because of increased hydrogen evolution.

The grain size of all coatings is presented in Table 1. It is observed that in all cases the coatings deposited in electrolytes containing Ferasine are more fine-grained.

## CONCLUSION

1. Organic additive Ferasine decreases the cathodic currents reached at different vertex potentials and quantities of deposited copper which shows that it inhibits the cathodic reaction of copper deposition. The influence of Ferasine is stronger expressed in electrolytes containing 130 g/L H<sub>2</sub>SO<sub>4</sub>. The inhibiting effect of additive increases with increase in cathodic potential.

2. Dense and smooth copper coatings on Cu cathode with current efficiency higher than 90% are deposited when Cu<sup>2+</sup> concentration is higher than 5 g/L and current densities are in the range 0.5 ÷ 2 A/dm<sup>2</sup>. More fine-grained coatings are obtained in the presence of H<sub>2</sub>SO<sub>4</sub> and organic additive hydroxyethylated-2-butyne-1,4-diol (Ferasine). Non-adherent, dark-red Cu slime is obtained when the concentration of Cu<sup>2+</sup> - ions is lower than 5 g/L.

3. Ferasine changes the preferred crystallographic orientation (hkl) of Cu coating from (220) to (111) during deposition in electrolytes containing H<sub>2</sub>SO<sub>4</sub>. In the absence of acid the preferred crystallographic orientation both in the absence or presence of Ferasine.

**Acknowledgements:** The authors are grateful to Tz. Tzacheva for the assistance in SEM observations and G. Avdeev, PhD for fruitful discussions of x-ray analyses.

The authors gratefully acknowledge the financial support of Project BG 051PO001-3.3.06-0038.

#### REFERENCES

1. L. Muresan, A. Nicoara, S. Varvara, G. Maurin, *J. Appl. Electrochem.*, **29**, 719 (1999).
2. L. Muresan, S. Varvara, G. Maurin, S. Dorneanu, *Hydrometallurgy* **54**, 161 (2000).
3. V.D. Karoleva, Metallurgy of heavy non-ferrous metals, Part II, c/o Jusautor, Sofia (in Bulgarian). (1986).
4. D. Melzner, J. Tilkowski, A. Mohrmann, W. Poppe, W. Halwachs, K. Schogerl, *Hydrometallurgy* **13**, 105 (1984).
5. R. Kammel, M. Goktepe, H. Oelmann, *Hydrometallurgy* **19**, 11 (1987).
6. S. Varvara, L. Muresan, A. Nicoara, G. Maurin, I.C. Popescu, *Materials Chemistry and Physics* **72**, 332 (2001).
7. S. Varvara, L. Muresan, I. C. Popescu, G. Maurin, *J. Appl. Electrochem.*, **33**, 685 (2003).
8. S. Varvara, L. Muresan, I.C. Popescu, G. Maurin, *Hydrometallurgy* **75**, 147 (2004).
9. S. Varvara, L. Muresan, I.C. Popescu, G. Maurin, *J. Appl. Electrochem.* **35**, 69 (2005).
10. M. Alodan, W. Smyrl, *Electrochim. Acta*, **44**, 299 (1998).
11. M. S. Kang, S.-K. Kim, K. Kim, J. J. Kim, *Thin Solid Films* 516 3761 (2008).
12. M. Quinet, F. Lallemand, L. Ricq, J.-Y. Hihn, P. Delobelle, C. Arnould, Z. Mekhalif, *Electrochim. Acta* **54**, 1529 (2009).
13. I.A.L. Portela, G.I. Lacconi, M.L. Teijelo, *J. Electroanal. Chem.* **495**, 169 (2001).
14. R. Yu, Q. Liu, G. Qiu, Zh. Fang, J. Tan, P. Yang, *Transactions of Nonferrous Metals Society of China* 1280-1284 (2008).
15. N. Tantavichet, M. Pritzker *Journal of Applied Electrochemistry* **36**, 49 (2006).
16. B. Bozzini, C. Mele, L.D'Urzo, G. Giovannelli, S. Natali, *Journal of Applied Electrochemistry*, **36**, 789 (2006).
17. B. Bozzini, C. Mele, L.D'Urzo, *Journal of Applied Electrochemistry*, **36**, 87 (2006).
18. B. Bozzini, C. Mele, L. D'Urzo, V. Romanello, *Journal of Applied Electrochemistry*, **36**, 973 (2006).
19. Q.B. Zhang, Y.X. Hua, Y.T. Wang, H.J. Lu, X.Y. Zhang, *Hydrometallurgy* **98**, 291 (2009).
20. A.C.M. de Moraes, J.L.P. Siqueira, L.L. Barbosa, I.A. Carlos, *J Appl Electrochem.*, **39**, 369 (2009).
21. H.H. Abdel-Rahman, A.M. Ahmed, A.A. Harfoush, A.H.E. Moustafa, *Hydrometallurgy* **104**, 169 (2010).
22. M. Gu, Q. Zhong, *J Appl Electrochem.* **41**, 765 (2011).
23. C. C. Vaduva, N. Vaszilcsin, A. Kellenberger, M. Medeleanu, *J Appl Electrochem.* **42**, 217 (2012).

## ВЛИЯНИЕ НА ХИДРОКСИЕТИЛИРАНИЯ-2-БУТИН-1,4-ДИОЛ ВЪРХУ ЕЛЕКТРООТЛАГАНЕТО НА МЕД ОТ СУЛФАТНИ ЕЛЕКТРОЛИТИ СЪДЪРЖАЩИ ГОЛЕМИ КОЛИЧЕСТВА ЦИНК

Г. А. Ходжаоглу, Ив. С. Иванов

Институт по физикохимия "Акад. Р. Кашиев", Българска Академия на Науките,  
ул. "Акад. Г. Бончев", блок 11, София 1113

Постъпила на 5 февруари, 2013 г.; Коригирана на 15 юни, 2013 г.

(Резюме)

Посредством потенциодинамични и галваностатични методи беше изследвано влиянието на органичната добавка хидроксиетилиран-2-бутин-1,4-диол (ферасин) върху електроекстракцията на мед от сулфатни електролити съдържащи големи количества  $Zn^{2+}$  - йони. беше установено, че ферасинът намалява количеството на медта отложена по време на сканирането до различни потенциали, което показва, че той инхибира катодната реакция на отлагането й. Влиянието на ферасина е по-силно изразено в електролити съдържащи  $H_2SO_4$ . Инхибиращото действие нараства с повишаването на катодния потенциал. Плътни и гладки медни покрития върху медния катод, с добив по ток по-висок от 90%, се отлагат, когато концентрацията на  $Cu^{2+}$  е по-висока от 5 г/л и плътностите на тока са в интервала  $0.5 \div 2$  А/дм<sup>2</sup>. По-дребнозърнести покрития се получават в присъствие на  $H_2SO_4$  и на органичната добавка ферасин. Тъмночервен Си шлам се получава, когато концентрацията на  $Cu^{2+}$  е по-ниска от 5 г/л. Ферасинът променя преимуществената ориентация на медното покритие от (220) на (111) само при отлагане в електролити съдържащи  $H_2SO_4$ . В отсъствие на киселина преимуществената ориентация, както в отсъствие, така и в присъствие на ферасин остава (111).

## AC-anodized and Ni-pigmented aluminum for selective solar absorption

P. L. Stefchev<sup>1</sup>, R. P. Kirilov<sup>1</sup>, Ch. A. Girginov<sup>2\*</sup>, E. H. Klein<sup>2</sup>

<sup>1</sup>Laboratory for Solar Energy and New Energy Sources, 1784 Sofia

<sup>2</sup>University of Chemical Technology and Metallurgy, 1756 Sofia

Received February 7, 2013; Revised March 12, 2013

A phosphoric acid solution (0.5 and 1.0 M) modified with addition of  $\text{FeSO}_4 \cdot 7\text{H}_2\text{O}$  has been used to form porous  $\text{Al}_2\text{O}_3$ -films on technical purity aluminum via AC-polarization. By combining the anodizing conditions (voltage and time) porous aluminum matrices with different thickness have been formed. The nickel electrodeposition has been carried out in a  $\text{NiSO}_4$  (pH 4.0) solution at different voltages and durations. Spectral characteristics of the colored electrodes have been recorded in the UV-VIS-NIR (200-2500 nm) and IR (2.5–20  $\mu\text{m}$ ) regions. It has been found, that during absorbance in the solar spectrum, the thickness has no significant influence due to the small values of reflected light. The emission capability in the infrared region, however, depends strongly on the layer thickness. The tests carried out show that the obtained coatings exhibit high absorption in terms of solar light and relatively low emission in the infrared. These technical features present them as very promising for use in low and medium temperature solar collectors.

**Key words:** alumina films, AC anodization, nickel electrodeposition, selective solar absorbance.

### INTRODUCTION

In the late 19th century, at the very beginning of anodic oxidation studies, alternating current (AC) has been used to grow alumina coatings. The advantage of this regime over direct current polarization has been accounted for the use of two identical electrodes and much simpler technological equipment. AC-anodizing has been still abandoned because of the severe condition to ensure equal surface and composition of the electrodes, as well as a superior quality of contacts.

Nowadays, the series production of some aluminum-based parts, for instance panels for solar absorption, seems to provoke the revival of the AC-technology. Moreover, the anodic oxidation of aluminum alloys with a relatively high content of alloying elements has been found [1-4] to proceed more easily in AC than in DC mode.

The aim of the present paper was to investigate the possibilities to obtain efficient selective coatings on the base of alumina matrices grown by AC-anodization and filled by electrochemical deposition of nickel. From technological point of view, it was expedient to grow the porous matrices in phosphoric acid solutions over aluminum of technical purity. The alumina structures formed in phosphoric acid are known [5] to have comparatively larger pore diameters; the anodization in some modified electrolytes has been

found [6] to lead to formation of thicker films at equal other conditions.

The incorporation of metals into the porous alumina films is normally carried out through their AC polarization in aqueous solutions of metal containing salts. Alongside with their decorative and anti-corrosion properties, porous matrices with incorporated metal particles exhibit selective absorption of solar light. Nickel is one of the mostly used metals for this purpose [7-15]. By varying the conditions of matrix growth and of nickel deposition, coatings with good selective absorption can be obtained. In general, the efficiency of a selective coating is determined [16-19] by high absorption within the solar spectrum (0.2 - 2.5  $\mu\text{m}$ ) and low emission in the far infrared region (2.5 - 25  $\mu\text{m}$ ).

### EXPERIMENTAL

The working electrodes were cut from technical purity aluminum sheets (99.5% Al). The pretreatment of the electrodes was carried out at room temperature according to the following procedure: (i) degreasing with acetone, (ii) etching in sodium hydroxide (10%), (iii) neutralizing in nitric acid (30%) and (iv) washing with distilled water. The exposed working area of the samples was 60 x 25 mm.

Anodizing was carried out in 0.5 M and 1.0 M aqueous solutions of phosphoric acid, modified by the addition of 5 g  $\text{dm}^{-3}$   $\text{FeSO}_4 \cdot 7\text{H}_2\text{O}$ , as suggested

\* To whom all correspondence should be sent:  
E-mail: christian.girginov@gmail.com

in [6]. The porous matrices were simultaneously formed on both electrodes under AC-polarization (50 Hz) at 20 °C. The process was carried out at two formation voltages (18 V and 50 V) for two different durations (15 min and 30 min). Through variation of anodizing voltage and time, porous alumina matrices with different thickness were formed. The time dependence of the current density was registered with a Mastech MS 8050 multimeter through a PC-based data acquisition system.

The electrodeposition of nickel was carried out by AC-polarization (50 Hz), at two polarization voltages (14 V and 50 V) for different coloring durations (2 - 8 min). The coloring electrolyte consists of 70 g dm<sup>-3</sup> NiSO<sub>4</sub>·6H<sub>2</sub>O, 30 g dm<sup>-3</sup> MgSO<sub>4</sub>·5H<sub>2</sub>O and 15 g dm<sup>-3</sup> H<sub>3</sub>BO<sub>3</sub> (pH = 4.0). After coloring the samples were "sealed", by immersing them in boiling water for 2 minutes.

The spectral characteristics of the colored specimens were recorded in the UV-VIS-NIR region (200 - 2500 nm) by reflectance spectra at normal incidence using a Shimadzu UV-3100 with BaSO<sub>4</sub> sphere. Reflectance in the IR region (2.5 - 20 μm) was registered with a FTIR spectrophotometer equipped with mirror reflectance accessory.

## RESULTS AND DISCUSSION

### *Formation of porous anodic oxides and nickel electrodeposition*

The AC-anodizing kinetics in the modified phosphoric acid electrolytes followed the well-known current density vs. time dependence observed during potentiostatic DC-anodization in phosphoric acid. Initially, the formation of a compact barrier layer of aluminum oxide takes place, followed by partial dissolution of the compact layer by the acidic electrolyte and nucleation of pores. Finally, a balance between oxide formation and dissolution at the pore bases is reached, thus imposing steady current density conditions.

The incorporation of nickel into the alumina matrices obtained under various conditions in the phosphoric acid solutions led to the coloration of the coatings in beige, brown, or black shades. The choice of the appropriate conditions both for matrix growth and nickel deposition permitted to produce highly reproducible black-colored coatings.

### *Spectral characteristics*

The reflectance spectra of colored anodic films were recorded at normal incidence of the light in two different wavelength ranges.

### UV-VIS-NIR range from 200 to 2500 nm

Reflectance spectra of two samples (Nr. 2 and Nr. 6) obtained through anodization and coloration at boundary conditions are shown in Fig. 1.

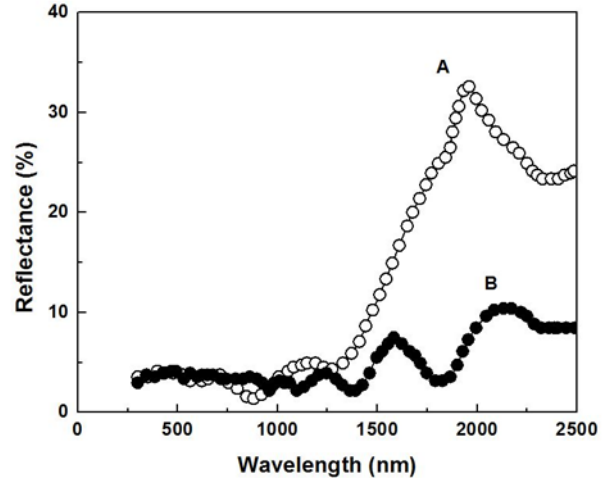


**Fig. 1.** UV-VIS-NIR reflectance spectra of two samples: (A) Sample Nr.2, anodized in 1 M H<sub>3</sub>PO<sub>4</sub> (30 min, at 50 V), colored for 8 min at 50 V; (B) Sample Nr. 6, anodized in 0.5 M H<sub>3</sub>PO<sub>4</sub> (15 min, at 18 V), colored for 2 min at 14 V.

The solar absorption coefficient ( $\alpha_s$ ) was calculated in accordance with the European Standard EN 410 (1998) using the formula:

$$\alpha_s = 1 - \rho_s = 1 - \frac{\sum_{i=1}^n S_i \rho(\lambda) \Delta\lambda}{\sum_{i=1}^n S_i \Delta\lambda} \quad (1)$$

$\Delta\lambda = 300 - 2500 \text{ nm}.$

Here,  $S_i$  is the spectral distribution of solar energy,  $\rho(\lambda)$  is the spectral reflectance coefficient and  $\Delta\lambda$  the wavelength range. The results obtained for the solar absorption coefficient  $\alpha_s$  of different samples are summarized in Table 1.

### IR range from 2.5 to 20 μm

Reflectance spectra of the same samples (Nr.2 and Nr.6) in the wavelength range from 2.5 to 20 μm are presented in Fig. 2.

The heat emission coefficient ( $\varepsilon_t$ ) was calculated in accordance with the European Standard EN 673 (1997) from the data on surface reflection and on heat emissivity of a black body at 373 K by using the formula:

$$\varepsilon_t = 1 - R_n = 1 - \frac{1}{30} \sum_{i=1}^{i=30} R_i(\lambda_i) \quad (2)$$

Here,  $R_n$  is the average value of standard reflectance and  $R_i(\lambda_i)$  - the reflectance at  $\lambda_i$ . The values of the heat emission coefficient  $\varepsilon_t$  of the samples at 100 °C ( $\varepsilon_{100}$ ) are summarized in Table 1

in dependence of the anodizing and coloring conditions.

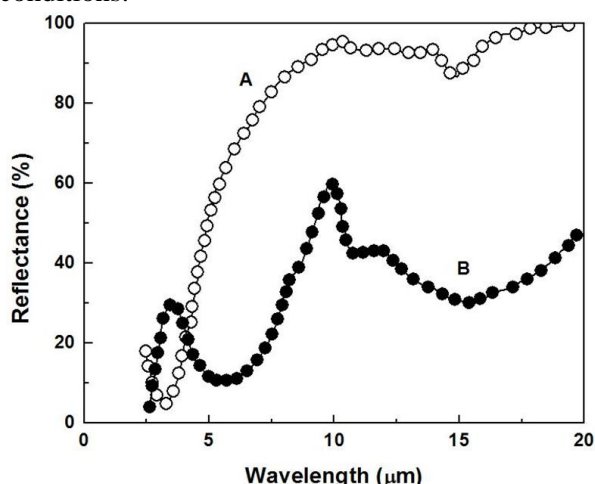


**Fig. 2.** IR reflectance spectra of two samples: (A) Sample Nr.2, anodized in 1 M H<sub>3</sub>PO<sub>4</sub> (30 min at 50 V), colored for 8 min at 50 V; (B) Sample Nr.6, anodized in 0.5 M H<sub>3</sub>PO<sub>4</sub> (15 min at 18 V), colored for 2 min at 14 V.

**Table 1.** Light absorbance and heat emission of samples obtained at different conditions

Sample Nr.	AC-anodization		Nickel deposition		H <sub>3</sub> PO <sub>4</sub> [mol.dm <sup>-3</sup> ]	$\alpha_s$ %	$\epsilon_{100}$ %
	U [V]	t [min]	U [V]	t [min]			
1	18	15	0	0	1.0	14.5	8.5
2	50	30	50	8.0	1.0	96.4	68.4
3	50	30	50	2.0	1.0	80.5	48.0
4	18	15	14	2.0	1.0	85.6	21.0
5	18	15	14	2.5	1.0	92.0	24.0
6	18	15	14	2.0	0.5	95.7	16.6
7	18	15	14	2.5	0.5	93.6	25.8

Both the conditions of matrix growth and of nickel deposition proved strongly to affect the optical properties of the coatings. The nano porous structure of the anodic films caused interference interactions in the whole wavelength range of investigation, judging by the waves observed in the reflectance spectra. The interference upon absorption in the solar spectrum range (Fig. 1) had no negative consequences because of the low intensity of the reflected light. The emission capability in the infrared region, however, strongly depended on the thickness of the layer. Relatively thick interference layers caused a noticeable increase of the heat emission in the IR range, as seen from the data for samples Nr.2 and Nr.6. The solar absorption coefficients of both samples are over 90 %, but the thicker sample (Nr.2), anodized for 30 min at 50 V, had a high heat emission coefficient,  $\epsilon_{100} = 68.4$  %, while the thinner sample (Nr.6), anodized for 15 min at 18 V, had a coefficient  $\epsilon_{100} = 16.6$  %.

It can be summarized that the deposition of nickel particles into a dielectric alumina matrix provides high light absorption in the solar spectrum range (over 90 %). With sufficiently thin matrices, the heat emission in the IR range can be reduced below 20 %. Hence, the requirements for an efficient selective coating are fulfilled.

#### Solar absorption calculation test

It was of interest to determine the absorptive capacity of the produced coatings in terms of solar radiation in the wavelength range from 300 nm to 2400 nm. For the purpose, the spectral data obtained for sample Nr.6 in Table 1 were used with ASTM G173-03 reference spectra derived from SMARTS v. 2.9.2 (AM1.5) spectral radiation from the solar disk plus sky diffuse light and diffuse light reflected from the ground on a south facing surface tilted 37 deg from the horizontal position [20]. In the chosen wavelength range, a solar spectral absorbance of 960.5 W m<sup>-2</sup> was calculated. The highest possible absorbance being 1000.9 W m<sup>-2</sup>, a solar absorption coefficient of the selective coating amounting to 96.0 % was calculated. Using the same procedure, a solar absorption of 94.2 % was calculated for a commercially available selective coating on copper base.

#### Stagnation temperature natural test

The stagnation temperature ( $T_p$ ) is defined as the maximum temperature achieved by a solar collector under specific conditions. This temperature is reached when the total heat losses in the collector exactly balance the energy absorbed by it. High stagnation temperatures are a reliable indication that the solar collector would have superior performance in cold environment even at high temperatures of the heated fluid. Under stagnation conditions, no heat is delivered to the load and a solar collector dissipates all the absorbed energy. In terms of Duffie *et al.* [21] it means

$$U_L (T_p - T_a) = \tau \alpha G, \quad (3)$$

where ( $\tau$ ) is the transmittance of the glazing, ( $\alpha$ ) is the absorbance of the absorber plate, ( $U_L$ ) is the total collector heat loss coefficient, ( $T_p$ ) is the temperature of the solar collector absorber plate, ( $T_a$ ) is the surrounding air temperature and ( $G$ ) is the solar radiation in the plane of the solar collector. Using this expression, the temperature of the absorber during stagnation ( $T_p$ ) has been estimated.

From the point of view of the absorber coating, the temperature of the absorber ( $T_p$ ) depends on the

absorbance of the absorber plate,  $\alpha_s$ , and on  $\varepsilon$ , the heat emission of the absorber coating in the infrared region, which is a part of  $U_L$ . The higher the ratio  $\alpha/\varepsilon$ , the better is the collector performance. This ratio was used to compare different absorber coatings. A simple side by side test for stagnation temperatures was carried out to practically compare the optical properties of sample Nr.6 with the commercial selective coating on copper base. Samples with small film resistance temperature detectors (RTD's) sealed on their back sides were placed side by side in a well insulated wooden box. The transparent cover was common for both samples. The *natural stagnation temperature test* was carried out with two types of covers:

(i) with a single cover of a standard 4 mm float glass (Fig. 3, curves A);

(ii) with a cover of double glazed stack with low coating on the inner glass, commonly used in today's fenestration units (Fig. 3, curves B).

As seen in Fig. 3 sample Nr. 6 proved to behave as well or even better than the commercial specimen, showing higher stagnation temperatures.

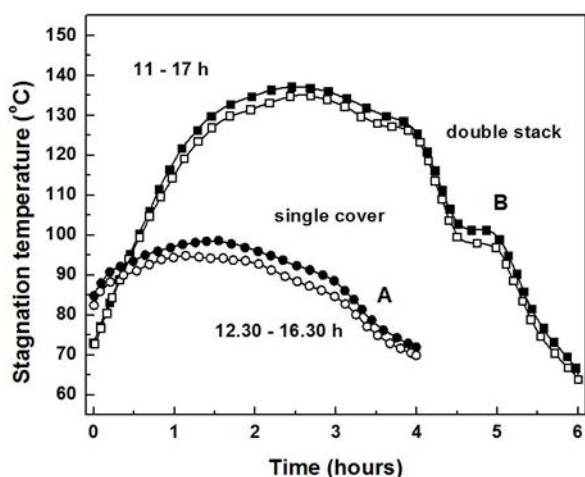


**Fig. 3.** Stagnation temperature vs. time: (A) single cover; (B) double glazed stack. The filled symbols denote sample Nr. 6, while the empty ones - coating on a copper base.

### CONCLUSION

Phosphoric acid solutions modified with addition of ferrous ions proved to be suitable for the formation of porous alumina matrices on technical purity aluminum under AC-polarization conditions. The careful choice of polarization conditions enabled the obtainment of reproducible black-colored coatings through electrochemical deposition of nickel into the pores of the matrix.

Optimal results for the absorbance ( $\alpha_s$ ) of the coatings within the UV-VIS-NIR range (200 - 2500

nm), as well as for their emission ( $\varepsilon_{100}$ ) within the IR range (2.5 nm – 20  $\mu$ m) are reached for samples with low thickness of the absorbing interference layer. The high selectivity of the low thickness coatings is testified by the measured high absorbance of solar light and low heat emission in the IR range.

A side by side natural test for stagnation temperatures ascertained the superiority of the developed selective coating over a commercial coating on copper base. Spectral characteristics and test measurements of the developed coating indicate its suitability for low and medium temperature solar collectors. The main positive features of the coating are associated with low production costs and good radiation parameters at commonly used temperatures: a solar absorption coefficient of 94 - 96 % and a heat emission coefficient of 14 - 18 %.

**Acknowledgements:** The authors are grateful to the National Science Fund of Bulgaria for financial support of the contract DDVU 02/103-2010 "Nanoporous anodic oxides as a new generation of optically active and catalytic materials (NOXOAC)"

### REFERENCES

1. J. M. Kape, *Trans. Institute Metal Finishing*, **63**, 90 (1983).
2. S. John, V. Balasubramanian, B. A. Sheno, *Met. Finishing*, **82**, 33 (1984).
3. S. A. Harris, *Trans. Institute Metal Finishing*, **65**, 155 (1987).
4. J. M. Kape, *Trans. Institute Metal Finishing*, **66**, 41 (1988).
5. A. Wazwaz, J. Salmi, R. Bes, *Energ. Convers. Manage.*, **51**, 1679 (2010).
6. Chr. Girginov, I. Kanazirski, A. Zahariev, P. Stefchev, *J. Univ. Chem. Tech. Met.*, **47**, 187 (2012).
7. H. Masuda, K. Yada, A. Osaka, *Jap. J. Appl. Phys.*, **37**, L1340 (1998).
8. D. R. Gabe, *Trans. Institute Metal Finishing*, **65**, 152 (1987).
9. A. Andersson, O. Hunderi, C. G. Granqvist, *J. Appl. Phys.*, **51**, 752 (1980).
10. S. N. Kumar, L. K. Malhotra, K. L. Chopra, *Solar Energy Materials*, **3**, 519 (1980).
11. S. N. Kumar, L. K. Malhotra, K. L. Chopra, *Solar Energy Materials*, **7**, 439 (1983).
12. T. Bostrom, E. Wackelgard, G. Westin, *Solar Energy*, **74**, 497 (2003).
13. M. Zemanova, M. Chovancova, Z. Galikova, P. Krivosik, *Renew. Energ.*, **33**, 2303 (2008).
14. M. Zemanova, M. Chovancova, P. Krivošik, *Chem. Pap.*, **63**, 62 (2009).

15. M. Zemanova, M. Gal, E. Usak, J. Jurisova, *J. Appl. Electrochem.*, **40**, 981 (2010).
16. G. L. Hornyak, C. R. Martin, *Thin Solid Films*, **303**, 84 (1997).
17. T. Moller, D. Honicke, *Solar Energy Mater.*, **54**, 397 (1998).
18. T. Tesfamichael, A. Roos, *Solar Energy Mater.*, **54**, 213 (1998).
19. Lingchuan Li, *Solar Energy Materials & Solar Cells*, **64**, 279 (2000).
20. Reference Solar Spectral Irradiance: ASTM G-173 <http://rredc.nrel.gov/solar/spectra/am1.5/ASTMG173/ASTMG173.html>
21. Duffie, J. A. and W. A. Beckman, "Solar Engineering of Thermal Processes", 2nd Edn., John Wiley and Sons Inc., 1991.

## СЕЛЕКТИВНИ ПОКРИТИЯ НА ОСНОВА НА ПРОМЕНЛИВОТОКОВО АНОДИРАН И ОЦВЕТЕН С Ni АЛУМИНИЙ

П. Л. Стефчев<sup>1</sup>, Р. П. Кирилов<sup>1</sup>, К. А. Гиргинов<sup>2\*</sup>, Е. Х. Клайн<sup>2</sup>

<sup>1</sup>Лаборатория слънчева енергия и нови енергийни източници - БАН, 1784 София, България

<sup>2</sup>Химикотехнологичен и Металургичен Университет, 1756 София, България

Постъпила на 7 февруари, 2013 г.; Коригирана на 12 март, 2013 г.

(Резюме)

Използван е разтвор на  $\text{H}_3\text{PO}_4$  (0.5 и 1.0 М) модифициран с добавка на  $\text{FeSO}_4 \cdot 7\text{H}_2\text{O}$  ( $5 \text{ g dm}^{-3}$ ) за формиране на порести  $\text{Al}_2\text{O}_3$ -филми върху технически алуминий в условия на АС-поляризация (50 Hz). Чрез комбиниране на условията на анодиране (напрежение и време) са формирани порести алуминиеви матрици с различна дебелина. Електроотлагането на никел е извършено от разтвор на  $\text{NiSO}_4$  (рН 4.0) също при АС-поляризация с различно напрежение и продължителност. Снети са спектралните характеристики на оцветените образци в UV-VIS-NIR (200-2500 nm) и IR (2.5–20  $\mu\text{m}$ ) области. Намерено е, че при абсорбцията на слънчевия спектър дебелината на филмите не оказва съществено влияние, поради малките стойности на отразената светлина. Емисионната способност в инфрачервената област обаче зависи силно от дебелината на слоя. Проведените тестове показват, че получаваните покрития имат висока абсорбционна способност по отношение на слънчевата светлина и сравнително слабо излъчване в инфрачервената област. Тези техни характеристики ги представят като много подходящи за използването им в ниско и средно температурни слънчеви колектори.

## Electrolytic coloring of porous aluminum oxide films in CoSO<sub>4</sub> solution

Ch. A. Girginov<sup>1\*</sup>, I. A. Kanazirski<sup>2</sup>, V. G. Ilcheva<sup>1</sup>

<sup>1</sup>University of Chemical Technology and Metallurgy, 1756 Sofia, Bulgaria

<sup>2</sup>University of Mining and Geology "St. Ivan Rilski" 1700 Sofia, Bulgaria

Received February 9, 2013; Revised April 10, 2013

Anodic oxide matrices have been formed in a 15 % H<sub>2</sub>SO<sub>4</sub> solution on three types of aluminum electrodes: Al (99.5%) and two alloys (8006 and 8011). The obtained Al<sub>2</sub>O<sub>3</sub>-films (thickness 20 μm, porosity 0.15) have been colored in a CoSO<sub>4</sub> solution using AC-polarization with different duration (2-15 min) and at frequencies in the range (20-100 Hz). A comparative study has been conducted on the spectral characteristics (in the UV-VIS-NIR region) of the colored films with two different surface pretreatments: electropolished and chemically mat. It has been found, that in all cases the increase of coloring time (the quantity of cobalt incorporated in the pores respectively) leads to an increased absorbance capability of the coatings. The optimal process frequency is determined to be 60 Hz. Furthermore, the pretreatment of the metal surface has no significant influence on the quantity of cobalt incorporated in the Al<sub>2</sub>O<sub>3</sub>-matrices. The obtained results show that the colored in CoSO<sub>4</sub> porous anodic films on aluminum and its alloys exhibit good absorbance characteristics in the visible, as well as in the UV and NIR regions. This makes them suitable to serve as decorative (black) coatings and also have a potential application as solar collector elements.

**Key words:** alumina films, cobalt electrodeposition, aluminum alloys, spectral characteristics.

### INTRODUCTION

In the pores of anodic oxide films on aluminum various metals can be electrochemically incorporated. This is done by AC polarization [1] in different aqueous solutions of salts of these metals. The most common application of the porous Al<sub>2</sub>O<sub>3</sub> colored in electrolytes containing metal ions is to form decorative and corrosion resistant coatings on aluminum and its alloys. The colored porous alumina films have found increasing implementation as light-absorbing coatings to produce conversion layers as part of solar collectors. Recently there has been a profound interest in Al<sub>2</sub>O<sub>3</sub> matrices incorporated with cobalt [2-5]. This interest is motivated by the attractive magnetic properties [4] these systems exhibit. The colored with cobalt Al<sub>2</sub>O<sub>3</sub> films also demonstrate good color decorative properties [6]. Through incorporation of cobalt it is possible to successfully prepare black films [7] for short times (5 min) of electrolytic coloring. A strict pre-treatment procedure of the aluminum surfaces and control of the coloring conditions of the porous arrays is required in order to obtain high quality and reproducible functional layers [8]. It is a matter of interest to investigate the light reflectance of anodic Al<sub>2</sub>O<sub>3</sub> colored in cobalt-containing solutions

depending on the forming conditions, the type of the aluminum alloy and the metal surface pretreatment. The determination of the amount of cobalt incorporated within the pores is of practical interest as well.

### EXPERIMENTAL

The electrodes (8 cm<sup>2</sup>) were cut from aluminum sheets (99.5%) and two aluminum alloys: 8006 (97.90% Al, 0.25% Si, 1.44% Fe, 0.37% Mn) and 8011 (98.55% Al, 0.66% Si, 0.70% Fe, 0.06% Mn). They were put through a standard pretreatment procedure: annealing, degreasing, electropolishing, rinsing and finally drying. Some of the specimens were mat in an aqueous solution (2% NaOH and 3% NaNO<sub>3</sub>). The film formation was carried out in 15 % H<sub>2</sub>SO<sub>4</sub> at constant current density (15 mA cm<sup>-2</sup>), for 45 min, at 20°C. The formed under these conditions anodic films have a thickness of 20 μm [9] and porosity of about 0.15 [10]. A two-electrode cell with a platinum mesh serving as counter electrode was used for anodization. The cobalt deposition was carried out by AC (sinusoidal) polarization in an electrolyte consisting of: CoSO<sub>4</sub> (10 g dm<sup>-3</sup>), (NH<sub>4</sub>)<sub>2</sub>SO<sub>4</sub> (30 g dm<sup>-3</sup>) and H<sub>3</sub>BO<sub>3</sub> (50 g dm<sup>-3</sup>) at 20°C. A custom AC galvanostat was used as a power source for delivering and keeping a constant current density of 3.75 mA cm<sup>-2</sup>, in the frequency range 20 - 100 Hz. Graphite rods were used as counter electrodes. The light reflectance

\* To whom all correspondence should be sent:  
E-mail: christian.girginov@gmail.com

spectra ( $R$ ) in the UV-VIS-NIR region (200-2500 nm) have been measured using a Shimadzu UV-3100 spectrophotometer with  $\text{BaSO}_4$  sphere. The amount of cobalt deposited within the pores was estimated by means of ICP-OES (Prodigy, Teledyne Leeman Labs). For this purpose the coloured films were dissolved in a mixture of concentrated nitric acid and water (1:1), at  $20^\circ\text{C}$  for 3-4 min.

## RESULTS AND DISCUSSION

### 1. Spectral characteristics

#### 1.1. Effect of AC polarization frequency on the light absorbance

The influence of the AC polarization frequency on the light absorbance of the colored porous matrices in the UV-VIS-NIR wavelength range (200-2500 nm) has been investigated. The colored oxide films are in the light grey, grey, black hue. It is of practical interest to determine the light absorbance and color characteristics of the obtained functional coatings, depending on the AC polarization frequency. For this purpose the characteristics of the films obtained during the longest (15 minutes) coloring have been plotted. The spectral characteristics were determined as a function of wavelength for five AC frequencies (20-100 Hz). Fig. 1 presents results obtained for polished and mat aluminum (99.5%) samples colored at three frequencies.

The results show that with increasing frequency the absorbance capacity of the films decreases. For the experiments an operating frequency of 60 Hz was chosen, which is relatively close to the industrial power frequency (50 Hz).

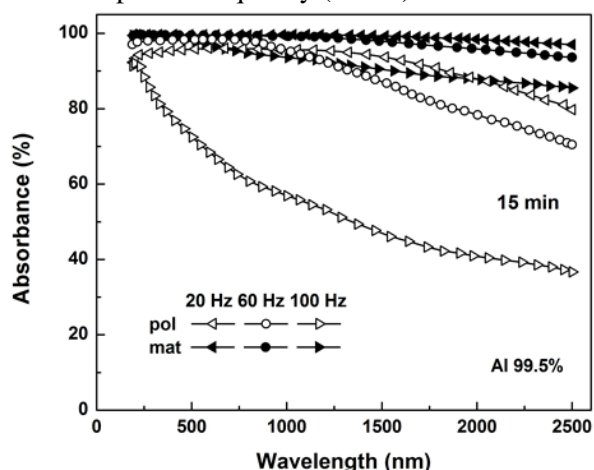


**Fig. 1.** UV-VIS-NIR absorbance spectra of samples colored in  $\text{CoSO}_4$  for 15 min at three frequencies. The empty symbols denote electropolished, while the filled ones – mat samples.

#### 1.2. Effect of coloring time on the light absorbance

The  $\text{Al}_2\text{O}_3$ -matrices (thickness 20  $\mu\text{m}$ , porosity 0.15), formed in  $\text{H}_2\text{SO}_4$  and electrochemically colored in a  $\text{CoSO}_4$  solution demonstrate good light absorption properties in the wavelengths range 200-2500 nm. The formed and colored under these conditions oxide matrices are promising functional layers with possible application in solar selective absorbers. Moreover, their color characteristics present them as very good decorative coatings. The increase of coloring time leads to higher spectral absorbance (Fig. 2), and to an increase of the color intensity, respectively.

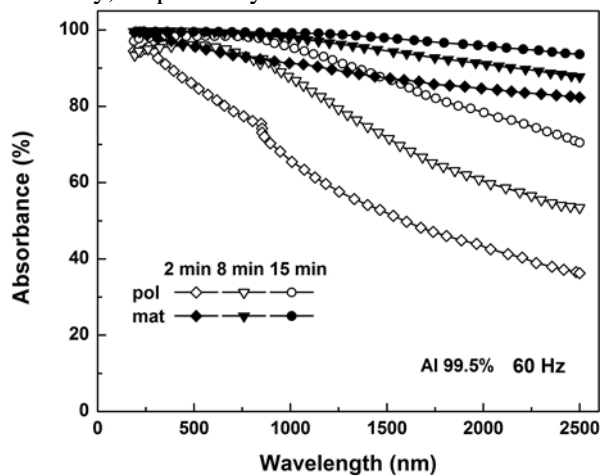


**Fig. 2.** Absorbance spectra of samples, colored with different duration, here also the empty symbols denote polished, and filled ones – mat electrodes

#### 1.3. Effect of surface pretreatment on the light characteristics

The influence of the aluminum surface pretreatment on the light reflectance has been studied. In all cases, the preliminary matting of the aluminum surface leads to an increase of the light absorbance, which is clearly evident from the data presented in Fig. 1 and Fig. 2.

#### 1.4. Effect of alloy type on spectral characteristics

It was of practical interest to study the influence of the aluminum sample type. Comparative studies of three types of aluminum samples (99.5%) and two aluminum alloys: 8006 and 8011 have been conducted. The results (Fig. 3) show that in all cases, Al (99.5%) exhibits higher reflectance than the aluminum alloys. This result indicates that the presence of alloying elements increases the light absorbance capacity of the colored anodic films.

## 2. Amount of cobalt deposited into the pores

### 2.1. Effect of AC polarization duration

The amount of cobalt incorporated within the pores was determined by the ICP-OES method. This amount per unit area as a function of coloring time has been estimated (Fig. 4), it can be seen that it is proportional to the coloring time.

This result is logical and similar dependencies have been obtained by other authors for different metals [10] incorporated within the pore volume.

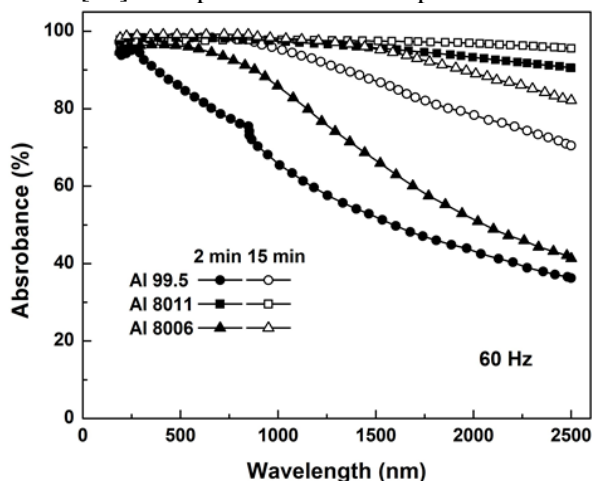


Fig. 3. Reflectance spectra of three types of aluminum samples at two coloring durations (2 and 15 minutes).

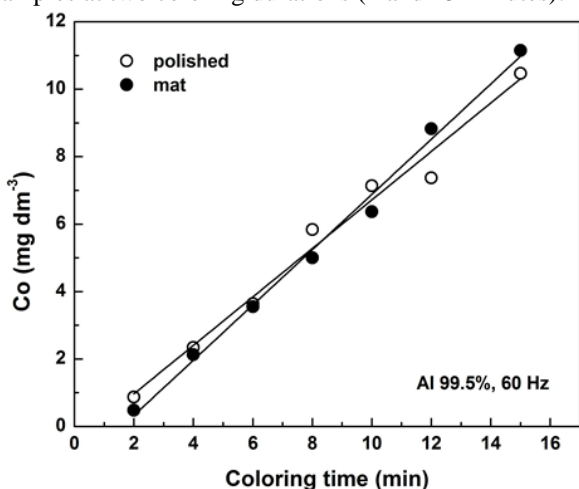


Fig. 4. Cobalt amount deposited in matrices with different coloring duration. Empty symbols are for polished electrodes, and filled ones – mat samples.

### 2.2. Effect of AC polarization frequency

The amount of cobalt incorporated into the porous matrices has been assessed according to the AC-polarization frequency. It turns out that this quantity is significantly affected by the frequency of the coloring current. An example of this influence for films formed on aluminum (99.5%) is presented in Fig. 5.

The data presented in Fig. 5 demonstrate a linear  $m_{\text{Co}}(f)$ -dependence. Furthermore the surface pretreatment (polishing, matting) has no significant influence.

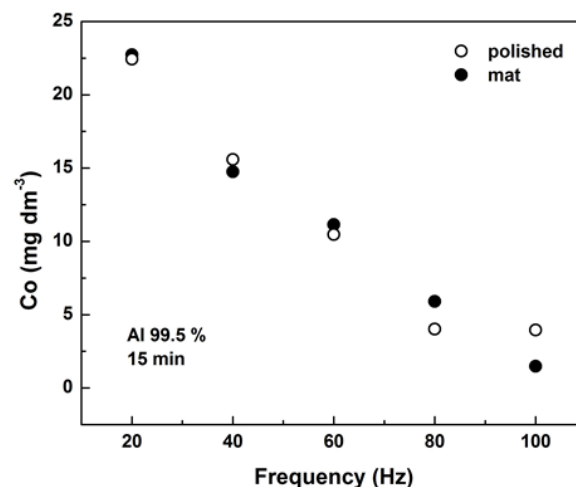


Fig. 5. Amount of Co deposited in matrices (15 minutes) vs. coloring current frequencies. The empty symbols denote polished, and filled ones – mat electrodes.

### 2.3. Effect of alloy type

The actual application of colored oxide films involves the use of different types of technical purity aluminum and aluminum alloys. In this respect investigating the influence of the type of anodized aluminum on the amount of deposited cobalt may be crucial for the application of these coatings. For this purpose three different types of aluminum have been used in the study: 99.5% Al sheets and two (8006 and 8011) aluminum alloys (Fig. 6).

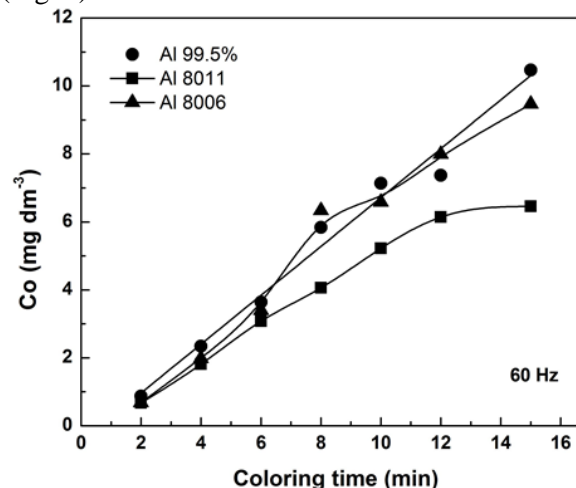


Fig. 6. Cobalt amount deposited in matrices of three types aluminum samples, colored at 60 Hz.

The obtained results show a linear increase of the amount of incorporated cobalt with coloring time. For the 8011 alloy there is a tendency for a

slower growth of incorporated cobalt. This may be due to the presence of more alloying elements in larger quantities than Al 99.5%. In general, the spectral characteristics of colored samples demonstrate high light absorbance capacity.

### 3. Absorbance of the colored coatings

As it has already been mentioned, the colored porous matrices could find application as decorative coatings and selective solar absorbers. In this sense it was of interest to determine the absorbance values ( $A$ ) of the colored coatings in two spectral regions:

i) visible range (380 - 740 nm)

ii) far infrared-visible-near UV (200 – 2500 nm).

It is necessary to take on account the incident solar energy on the ground [11]. For this purpose, data about the spectral dispersion of the solar energy (AM2) that is characteristic for present geographic location are used. The solar absorbance ( $A$ ) is defined as a fraction of the radiation, incident on the surface of the material that is absorbed. It is a function of both the intensity of solar radiation  $I_{\text{sol}}(\lambda)$ , and the total reflectance of the sample  $R(\lambda)$ , and is given by [12]:

$$A = \frac{\int_{\lambda_1}^{\lambda_2} I_{\text{sol}}(\lambda)[1-R(\lambda)]d\lambda}{\int_{\lambda_1}^{\lambda_2} I_{\text{sol}}(\lambda)d\lambda}$$

The integration is done numerically using *Gauss* quadrature method with 32 points. The values of the integral absorbance ( $A$ ) within these two spectral regions for some of the samples are given in Table 1.

**Table 1.** Absorbance of the colored coatings

Samples	Aluminum	Frequency (Hz)	Absorbance (380-740 nm) (%)	Absorbance (200-2500 nm) (%)
1	99.5%	20	95.45	93.81
2	99.5%	60	95.33	92.95
3	8006	20	94.37	93.59
4	8006	60	93.84	91.49
5	8011	20	91.95	89.97
6	8011	60	92.83	91.22

The obtained results indicate, that the colored in CoSO<sub>4</sub> solution porous Al<sub>2</sub>O<sub>3</sub>-matrices exhibit high light absorbance in the visible, as well as in the far infrared-visible-near UV regions. This makes them suitable as decorative (black coatings) and perspective for application as a part of solar energy collectors.

## CONCLUSION

The Al<sub>2</sub>O<sub>3</sub>-matrices (thickness 20 μm, porosity 0.15), formed in H<sub>2</sub>SO<sub>4</sub> and electrochemically colored in a CoSO<sub>4</sub> solution demonstrate good light selective properties in the wavelengths range 200-2500 nm. The most intense coloring at equal other conditions is achieved in AC (sinusoidal) polarization at a frequency of 60 Hz. In all cases with increasing coloring duration the obtained coatings increase their spectral absorbance. It is found that the amount of cobalt deposited per electrode area is proportional to the coloring time. The surface treatment (polishing, matting) influences the characteristics of the colored porous Al<sub>2</sub>O<sub>3</sub>-films. The mat surface provides greater light absorbance. The formed and colored in CoSO<sub>4</sub> solution oxide matrices are promising functional layers with possible application as light-absorbing coatings in solar collectors.

**Acknowledgements:** National Science Fund of Bulgaria, Contract No. DDVU 02/103-2010 “Nanoporous anodic oxides as a new generation of optically active and catalytic materials (NOXOAC)” for financial support.

## REFERENCES

1. The Surface Treatment and Finishing of Aluminum and its Alloys, Sixth Edition (2001), Vol. 1-2, Redwood Books, Trowbridge, Wilts BA 148 RB, UK.
2. H. R. Khan, O. Loebich, G. Rauscher, *Thin Solid Films*, **275**, 207 (1996).
3. Jianchun Bao, Zheng Xu, Jianming Hong, Xiang Ma, Zuhong Lu, *Scripta Materialia*, **50**, 19 (2004).
4. Abdolali Ramazani, Mohammad Almasi Kashi, Ghafour Seyedi, *Journal of Magnetism and Magnetic Materials*, **324**, 1826 (2012).
5. A. Foyet, A. Hauser, W. Schäfer, *Materials Science and Engineering*, **C 27**, 100 (2007).
6. Ch. Girginov, I. Kanazirski, Ts. Dimitrov, *Proceedings of Ruse University*, **51**, book 9. 1, 57 (2012).
7. Y. Akihito, H. Taichi, I. Mitsunobu, T. Hiroaki, I. Seishiro, *J. Japan Society Colour Materials*, **78**, 2 (2005).
8. Ghafar Ali, Maqsood Ahmad, Javed Iqbal Akhter, Muhammad Maqbool, Sung Oh Cho, *Micron*, **41**, 560 (2010).
9. G. Patermarakis, P. Lenas, Ch. Karavassilis, G. Papayiannis, *Electrochim. Acta*, **36**, 709 (1991).
10. Chr. Girginov, I. Kanazirski, A. Zahariev, P. Stefechev, *J. Univ. Chem. Tech. Met.*, **47**, 193 (2012).
11. A. Andersson, O.Hunderi, C.G.Granqvist, *J. Appl. Phys.*, **51**, 752 (1980).
12. S.N. Kumar, L.K. Malhotra, K.L. Chopra, *Solar Energy Materials*, **7**, 439 (1983).

## ЕЛЕКТРОХИМИЧНО ОЦВЕТЯВАНЕ НА ПОРЕСТИ ОКСИДНИ ФИЛМИ ВЪРХУ АЛУМИНИЙ В РАЗТВОРИ НА CoSO<sub>4</sub>

К. А. Гиргинов<sup>1</sup>, И. А. Каназирски<sup>2</sup>, В. Г. Илчева<sup>1</sup>

<sup>1</sup>Химикотехнологичен и Металургичен Университет, 1756 София, България

<sup>2</sup>Минно-геоложки Университет "Св. Иван Рилски", 1700 София, България

Постъпила на 9 февруари, 2013 г.; Коригирана на 10 април, 2013 г.

(Резюме)

В разтвор на H<sub>2</sub>SO<sub>4</sub> (15 %) са формирани анодни оксидни матрици върху три вида алуминиеви образци: Al (99.5%) и две сплави (8006 и 8011). Получените Al<sub>2</sub>O<sub>3</sub>-филми (дебелина 20 μm, порестост 0.15) са оцветявани в разтвор на CoSO<sub>4</sub> при променливо-токова поляризация с различна продължителност (2-15 мин) и при различна честота (20 - 100 Hz). Проведено е сравнително изследване на спектралните характеристики (в UV-VIS-NIR област) на оцветените филми върху електроди с две различни предварителни обработки на повърхността: електрополирани и химично матирани. Установено е, че във всички случаи с увеличаване на продължителността на оцветяване (респективно на внедреното количество кобалт в порите) абсорбционната способност на покритията нараства. Оптималната честота на процеса на електрохимично оцветяване е 60 Hz. Предварителната обработка не оказва значимо влияние върху количеството метал отложен в Al<sub>2</sub>O<sub>3</sub>-матрица. Получените резултати показват, че оцветените в CoSO<sub>4</sub> порести анодни филми върху алуминий и негови сплави проявяват добри абсорбционни характеристики както във видимата, така и в UV-VIS-NIR области. Това ги прави подходящи като декоративни (черни покрития) и с перспектива за приложения като елементи в слънчевите колектори.

## Electrodeposition and structure of Co coatings (CoCu, NiCo and CoNiCu) in potentiostatic and pulse potential modes

K. N. Ignatova<sup>1\*</sup>, Y. S. Marcheva<sup>2</sup>

<sup>1</sup> University of Chemical Technology and Metallurgy – Sofia, Sofia 1000, Bulgaria

<sup>2</sup> Technical University- Sofia, Sofia 1000, Bulgaria

Received April 18, 2013; Revised May 24, 2013

The kinetics of the individual deposition of Cu, Co and Ni as well as the alloy deposition of CoCu, NiCo and NiCoCu in the slightly acidic citrate electrolyte (pH= 5,5) was investigated. Data about the alloy deposition in pulse potentiostatic mode at different pulse frequencies was received also. The morphology and the elemental composition of the coatings (using SEM and EDSA analysis) at stationary and pulse mode were compared. At potentiostatic conditions the produced coatings have average grain size of 250 to 500 nm and Co content up to 85 wt.%. Using the pulse mode of deposition decreases the grain size and the Co content was up to 76 wt.% for the three alloys. Applying the pulse frequencies up to 500 Hz for CoCu alloy lowers the grain size under 100nm (60-70 wt.% Co). At the same conditions the coatings of CoNi and CoNiCu have rounded grains with average grain size about 200-300 nm. The X-ray analysis show that the binary alloys CoCu and NiCo are two-phased, composed from Co, Cu (in CoCu) and Ni and Co (in NiCo) with face centred cubic lattice (f.c.c.). Only in the ternary alloy coating of Co-Ni-Cu, a presence of cobalt-containing phase with hexagonal crystal lattice (h.p.c.) was ascertained also together with the cubic phases.

**Key words:** constant and pulse potential modes, nano-structured alloys, morphology, phase composition.

### INTRODUCTION

Due to their high hardness, wear resistance, endurance and corrosion resistance, the cobalt alloys are widely used in medicine, in nuclear-power systems, chemical- and oil industry etc. The particular interest towards nano-sized Co alloys is due to their increasing application in magnetosensor technologies and magnetoelectronics where miniaturization of items is the underlying purpose [1-6].

Presence of Cu in Co crystallinities makes the spectra of electrical resistance of the deposits wider and as result widening of their magnetic properties [4]. Recently, electrodeposits of Co and CoCu alloys have attracted intensive interest because of their wide use as magnetic materials in electronic devices for data saving, as electrical resistance devices and in semiconductor technologies but the electrocrystallization of CoCu alloy has been considered little so far [11]. Low amounts of Ni in CoCu alloy system can improve the properties of the thin films and can favour the segregations of small ferromagnetic particles and increase the magnetoresistance of the ternary CoNiCu coatings; decreases the stress in the copper/ ferromagnetic interface and can improve the corrosion resistance of the deposits [6]. The possibility for deposition of

CoNiCu alloy coatings is proposed as alternative to Cu-Co -Ni/Cu multilayer preparation [12].

Recently, pulse electrodeposition has received considerable attention for synthesis of nanocrystalline and amorphous alloy coatings [7]. The advantage of the pulse over stationary electrodeposition is that the properties of the deposit could be improved by control of pulse parameters, which gives a possibility for producing of nanostructured coatings [8]. Pulse electrodeposition can be used as a means for producing the coatings with properties unachievable by stationary deposition. Plating at extremely high amplitude polarization gives conditions for non-equilibrium growth of the coating, which may results in changes of the alloy phase composition and formation of unusual (anomal) metastable structures [8-10].

The electrodeposition of Co and Co-Cu coatings was studied using sulphate [8, 11, 12], citrate [13-15] and sulfamate [16] baths. Several authors studied the pulse plating of CoCu alloys [10]. The CoNi coatings were deposited mainly from sulphate [17] and citrate [6, 18, 19] electrolytes.

The growing interest in using citrate electrolyte in recent years was determined because of its ability to serve as buffer, to form complexes, and to add coating lustre, thus avoiding the need of introduction of special organic additives in the

\* To whom all correspondence should be sent:  
E-mail: katya59ignatova@gmail.com

electrolyte [18]. The difficulties in using citrate electrolytes come from its stability, which depend strongly on pH.

The magnetic properties of electrodeposited Co films can be correlated with their structure and plating conditions [7]. The electroplating parameters effect on the structure and growth modes of Co, CoCu [12] and CoNi [2, 4, 5] that is why a great interest exists to investigate the relation between the plate parameters, coatings structure and coating properties [11, 14, 21-24]. Anomalous galvanostatic deposition in gluconate bath of CoNi [20] and potentiostatic deposition of CoNi and CoNiCu [14] in citrate bath were performed. It was established formation of CoNi solid solution with hexagonal close packed lattice (hcp) [5] and solid solution of NiCoCu with face centred cubic lattice (fcc) [14].

In our previous study [25] some preliminary results concerning the possibility for codeposition of CoNi and CoNiCu alloy coatings in slightly acid citrate electrolyte were presented.

The present paper resumes the conditions of electrodeposition of the CoCu, CoNi and CoNiCu coatings and the effect of the mode of deposition (potentiostatic and pulse potentiostatic modes) on the structure (morphology, elemental and phase composition) of the alloy coatings.

## EXPERIMENTAL

The experimental setup consisted of a three-electrode cell (total volume 150 dm<sup>3</sup>) with disk-shaped cathode (surface area 1cm<sup>2</sup>) from pure electrolytic copper and Pt plate anode. The surface area ratio anode: cathode was 30:1. The reference electrode was saturated calomel electrode (SCE). The experiments were conducted at room temperature (20°C ±1). Before the experiment the cathode surface was etched in acid etching solution and washed with distilled water. The anode was cleaned in hot 1n HNO<sub>3</sub> and washed with distilled water.

The experiments were conducted in slightly acid citrate baths with composition as follows: 0.025M Cu (as CuSO<sub>4</sub> 5H<sub>2</sub>O); 0.32M Co (as CoSO<sub>4</sub> 7H<sub>2</sub>O); 0,38M Ni (as NiSO<sub>4</sub> H<sub>2</sub>O); 0.2M Na<sub>3</sub> citrate (Na<sub>3</sub>C<sub>6</sub>H<sub>5</sub>O<sub>7</sub>); pH = 5,3-5,5. The pH was adjusted using NaOH and H<sub>2</sub>SO<sub>4</sub> and measured using pH-meter.

The kinetics of deposition was studied using a method of potentiodynamic polarization curves (potential sweep rate 30 mVs<sup>-1</sup>) using a potentiostatic Wenking. The pulse electrodeposition of the coatings was carried out using pulse potential

with rectangular shape, generated by pulse generator, connected to the input of a specially designed potentiostat, connected to the three-electrode cell. The average values of the polarization,  $\overline{\Delta E}$ , (calculated as a difference between the potential at the current and the equilibrium potential) and the average current,  $I_{av}$ , were measured using digital voltmeter with high input resistance and milliammeter. The amplitude values of the polarization,  $\Delta E_p$ , were controlled using an oscilloscope.

The relation between the average ( $\overline{\Delta E}$ ) and amplitude ( $\Delta E_p$ ) polarization values at potentiostatic rectangular pulse conditions is:

$$\overline{\Delta E} = \theta \cdot \Delta E_p, \text{ where } \theta = \frac{\tau_p}{\tau_p + \tau_z}, \tau_p - \text{ pulse time,}$$

and  $\tau_z$  – time between the pulses. At each pulse frequency ( $f = \frac{1}{T}, Hz, T = \tau_p + \tau_z$ ), and  $\theta = 0,5$  the

relations  $\overline{\Delta E} - I_{av}$  and  $\Delta E_p - I_{av}$  were calculated. Data about the average polarization ( $\overline{\Delta E}$ ) and the amplitude values of the polarization ( $\Delta E_p$ ) as a function of applied pulse frequencies for the same value of the average current density were compared.

The morphology and the elemental composition (in wt %) of the coatings were determined using scanning electron microscope (SEM) with Energy Dispersive Spectral Analysis (EDSA) - equipment of Oxford Instruments JSM-6390 – Jeol.

The phase and crystal structure of the coatings were investigated using automatic Philips PW 1050 X-Ray diffractometer, equipped with secondary graphite monochromator for Cu K $\alpha$  radiation, and scintillation counter. The diffractograms were recorded in 2 $\theta$  range from 10° to 100° with a step length 0.04° and a counting time of 1s per step.

## RESULTS AND DISCUSSION

### *Individual deposition of Cu, Ni and Co at potentiostatic mode.*

The dependences of the individual deposition of Cu (curve 2), Ni (curve 3) and Co (curve 4) onto Cu surface (S= 1cm<sup>2</sup>), compared to the polarization dependence in background electrolyte (0,2m Na<sub>3</sub>citrat, curve 1), are presented in Fig.1.

The polarization curve, received in the background electrolyte shows wide polarization up to potential -1,4V; the following current growing is due to the hydrogen evolution on the electrode. When 0,025m Cu was introduced in the electrolyte the increasing of the current begins at potential -

0,96V and the polarization curve has two steps. The processes in the bath for Cu deposition include two stages of electrons transfer, the second one is the real copper deposition (at -1,35 V). Between the two, a chemical stage exists, related to the reaction of disproportionation of the copper. This mechanism was proved in Cu deposition from ammonium-nitrate electrolyte [26], as well as in other Cu electrolytes [27].

The polarization curves for individual electrodeposition of Ni and of Co have only one plateau of the limiting current, related to the reduction of the metallic ions. The voltammograms at different potential sweep rate [25] have shown that in both cases a part of the polarization has a diffusion reason, but in the Ni electrolyte the activation part is prevailed.

The electrodeposition of Ni begins at potential -1,1V and of Co at -1,2V (Fig.1).

In the studied electrolyte the continuity of the electrodeposition of the metals under applying of sufficiently high cathodic potential is Ni – Co – Cu (Fig.1).

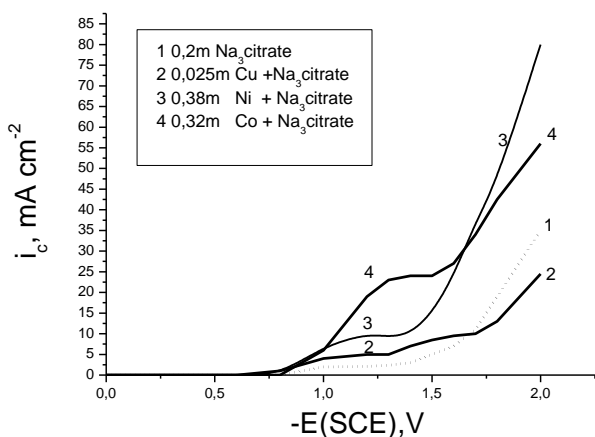


**Fig.1** Polarization curves in background electrolyte (0,2m Na<sub>3</sub>citrat, pH=5,5) – (1); of individual deposition of Cu (2), Ni (3) and Co (4) in electrolytes with content: 0,025M Cu(1); 0,38M Ni(2) and 0,32M Co(3) all with 0,2M Na<sub>3</sub>citrat;  $v = 30 \text{ mV}\cdot\text{s}^{-1}$ .

#### Electrodeposition of CuCo, NiCo CoNiCu alloys at potentiostatic mode

Fig.2 represents voltammograms (potential sweep rate  $30 \text{ mV}\cdot\text{s}^{-1}$ ) of deposition of Co-Cu (2), Co-Ni (3) and Co-Ni-Cu (4) alloys. With the aim of comparison, the dependence in the background electrolyte is shown as a curve 1.

The lowest values of the limiting current were established for the electrolyte, containing simultaneously Co and Cu (2). In all studied electrolytes for alloy deposition, the range of potentials was overlapped with this one for the pure

metal deposition. The alloy coatings of Co-Cu, Co-Ni and Co-Ni-Cu with high quality in the studied electrolyte can be deposited in the range of potentials respectively -1,13V ÷ -1,3V (SCE); -1,2V ÷ -1,4V (SCE) and -1,25V ÷ -1,35V (SCE).

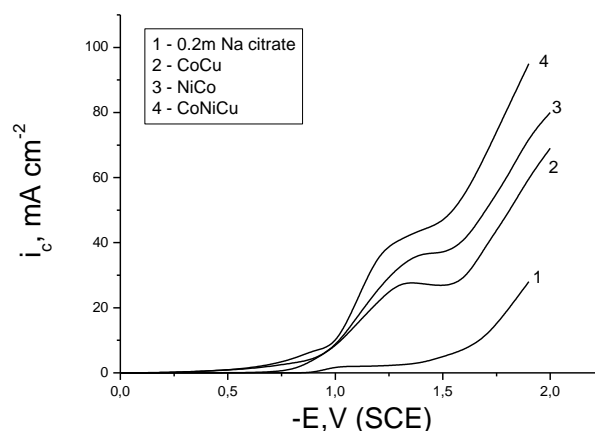


**Fig. 2.** Polarization curves in background electrolyte (0,2M Na<sub>3</sub>citrat, pH=5,5) – (1) and in electrolytes for deposition of CoCu (2); NiCo (3) and NiCoCu (4). Content of electrolytes: 0,025M Cu(2,4); 0,38M Ni(3) and 0,32M Co(2-4) all with 0,2M Na<sub>3</sub>Citrat;  $v = 30 \text{ mV}\cdot\text{s}^{-1}$ .

#### Pulse deposition

In the values of the average and amplitude polarization the ohmic drop in the solution (between Lugin capillary and working electrode), as well as polarization, used for Double Electrode Layer (DEL) charging are included. While the first goes to negligible values as the polarization increase, the second one is significant and is about 1/3 of the total polarization, especially at frequencies over 1 000 Hz. At these frequencies the pulse time is of the same order as the time for DEL charging ( $\tau_p \ll 0,5 \text{ ms}$ ), that is why an assumption exists that at frequencies over 1 000Hz the plating is no effective. Nevertheless, frequencies of 5 000Hz and even 10 000Hz were applied with the aim the change in the structure of the Co alloys at these unusual conditions to be established.

Data about the average polarization ( $\overline{\Delta E}$ ) and the amplitude values of the polarization ( $\Delta E_p$ ) as a function of applied pulse frequencies (from 100 Hz to 2500 Hz at  $\theta = 0,5$ ), are shown in fig. 3. Data was read in the three electrolytes for deposition of CoNiCu (curves 1,1\*), CoNi (curves 2,2\*), CoCu (curves 3,3\*) for the same value of the average current density ( $30 \text{ mAcm}^{-2}$ ). The same dependence was established at each value of the cathodic current density, higher than the showed. On the same figure the value of the polarization at

the same current density in the stationary conditions is given.

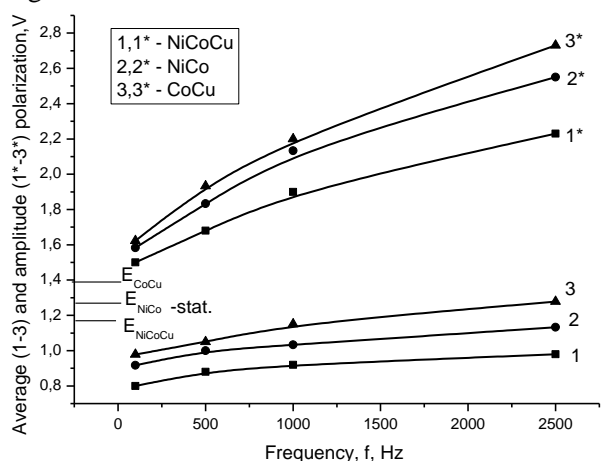


**Fig. 3.** Current densities reached at different vertex potentials on Pt cathode in electrolytes, containing: 1)  $\text{Cu}^{2+}$  - 1 g/L and  $\text{Zn}^{2+}$  - 50 g/L, 2)  $\text{Cu}^{2+}$  - 1 g/L,  $\text{Zn}^{2+}$  - 50 g/L and Ferasine 1 mL/L, 3)  $\text{Cu}^{2+}$  - 1 g/L,  $\text{Zn}^{2+}$  - 50 g/L and  $\text{H}_2\text{SO}_4$  - 130 g/L, 4)  $\text{Cu}^{2+}$  - 1 g/L,  $\text{Zn}^{2+}$  - 50 g/L,  $\text{H}_2\text{SO}_4$  - 130 g/L and Ferasine - 1 mL/L.

With the raise of pulse frequency from 100Hz to 2500 Hz the measured average polarization in the three electrolytes (Fig.3, curves 1-3) is lower than this one in stationary condition, which may be explain with a possible decreasing of the diffusion limitations as a result of diffusion gradient relax during the time of pauses – effect, more important at low frequencies. At the same time, with the rise of the pulse frequency in the studied range, the amplitude values of the polarization increase almost twice (Fig.3, curves 1\* -3\*). As the polarization may be used as a measure for oversaturation, it is awaited to reach more fine-structured coatings when apply higher frequencies especially in the range 100Hz to 1 000Hz.

At the frequencies over 2 500Hz the tendency towards lower average polarization than this one in stationary condition was kept, but the “useful” part of the measured total polarization (used for the alloy deposition) decrease and the part for DEL charging increase.

*Morphology and elemental composition of CoCu, NiCo and CoNiCu coatings.*

Fig.4-6 show the SEM images of the CoCu (Fig.4), CoNi (Fig.5) and CoNiCu (Fig.6) coatings. The applied potentials, respectively polarizations, correspond to the same value of current density, which however is different for each type of coating ( $28 \text{ mA}\cdot\text{cm}^{-2}$  for CoCu,  $35 \text{ mA}\cdot\text{cm}^{-2}$  for NiCo and

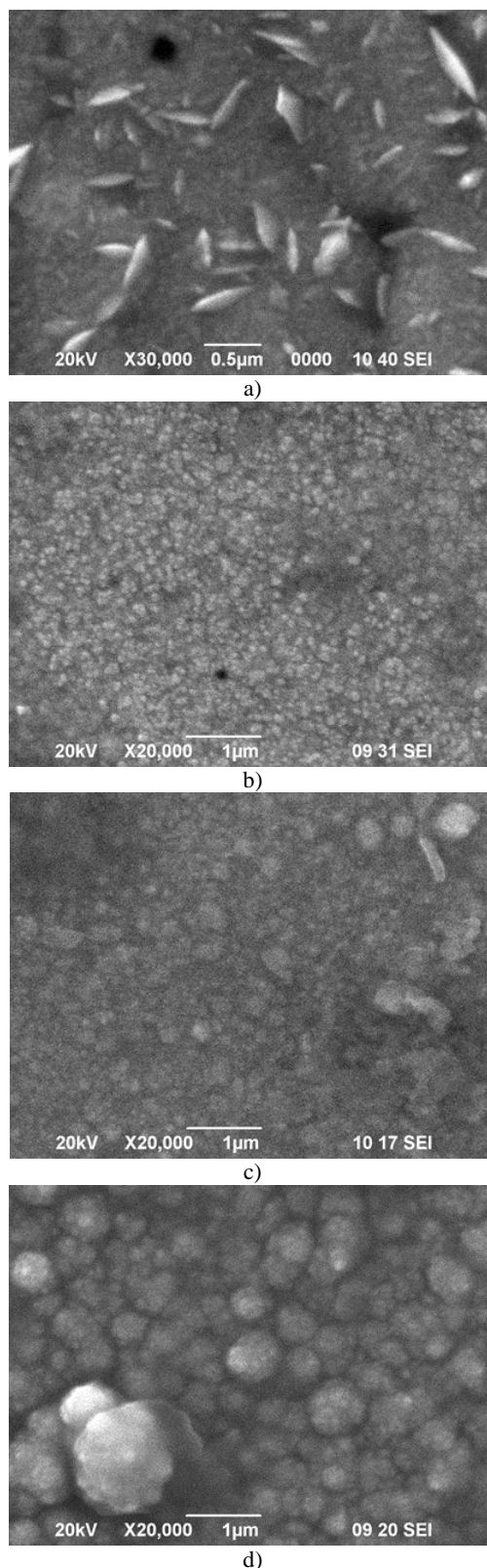


**Fig.4.** SEM images of CoCu coatings, deposited at potentiostatic mode (a) and at pulse frequencies: 500 Hz (b); 1000 Hz (c); 10000 Hz (d) in bath: 0,32M Co, 0,0,25M Cu and 0,2M  $\text{Na}_3\text{citrat}$ . The applied deposition polarization corresponds to the same average current  $I_{av}=28 \text{ mA}$  ( $S=1 \text{ cm}^2$ ) in the polarization curve. Coating composition (in wt.%): (a) 73%Co-27%Cu; (b) 35%Co-75%Cu; (c) 38%Co-55%Cu (7%O); (d) 64%Co-32%Cu (4%O)

45 mA.cm<sup>-2</sup> for CoNiCu). Current density chosen corresponds to the same point of each polarization curve, close to and before the plateau, thus ensuring realization of identical kinetic conditions for the deposition of each alloy. EDSA results for elemental composition (wt. %) of the coatings are given in the text captions.

Co-Cu (Fig.4): The deposited at stationary conditions CoCu coatings are with numerous needle-shaped crystals (Fig.4a) and bigger spherical crystals. Small negative shift of the applied potential makes the coating more fine-crystal with average grain size of about 250-500 nm. The coating composition is ranging within wide limits - from 2% Co to about 82% Co.

Using the pulse mode changes significantly the coating structure (Fig.4,b-d). The structure becomes more homogeneous, with more levelled surface compared to this one in stationary condition. At pulse conditions the structure is levelled and with round to spherical shaped crystals. Applying frequencies up to 500 Hz (Fig.4,b), the coatings are fine-crystal, with nano – measurements (grain size less than 100 nm), with low Co content (35% Co). With the increase of pulse frequency the content of Co in coatings grow up (up to 64%) and the average grain size increases up to 300 nm, in the same time the coatings become smoother (Fig.4,c,d). This result is in good correlation with the pulse mode results which showed, that at frequencies over 1000 Hz the average polarization and the part of amplitude polarization, responsible for the Faraday reaction, are close to these in potentiostatic condition.

Ni-Co (Fig.5): Compared to the coatings obtained in stationary mode (Fig.5,a), the ones obtained in pulse mode (Fig.5, b-d) have low Ni content (up to 12%). Judging on the weight % of oxygen, the presence of oxides was found in the coating at high frequencies. The application of pulse mode in general and the higher frequencies of pulses result in increased share of the more oval crystals compared to the needle-shaped ones, their size decreases reaching 200-400 nm and the surface smoothes as a whole. The increase of frequency of pulses above 1 000 Hz results in obtaining alloys enriched in cobalt (about 90% Co). The blurred SEM images at increased frequencies are explained with obtaining of nano-size structure and smoothing the surface.

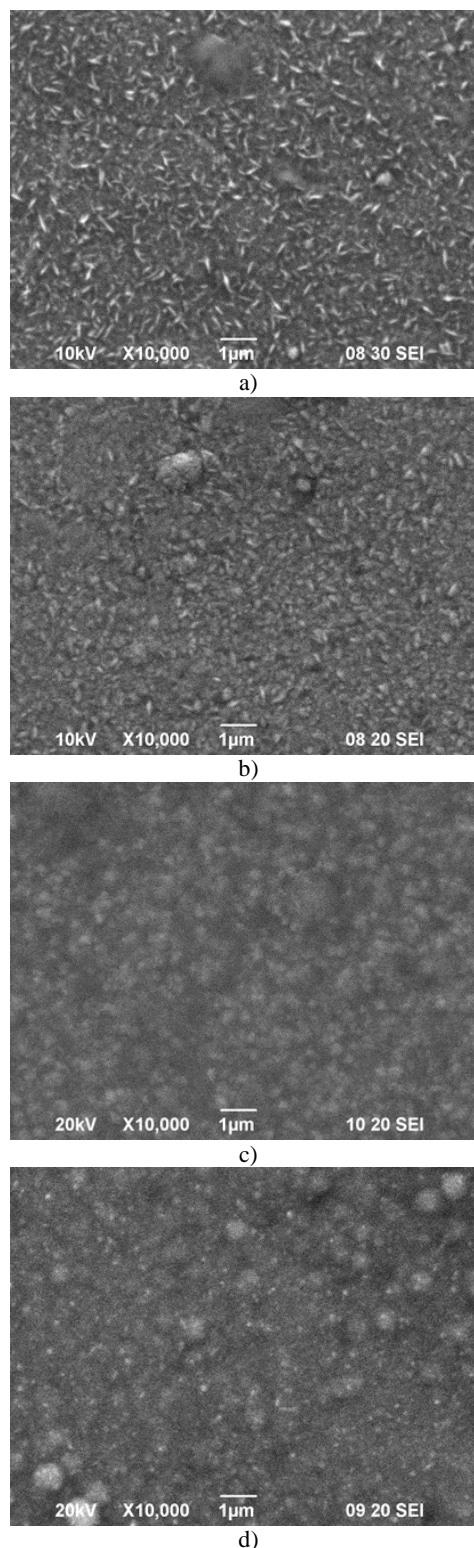


**Fig.5** SEM images and EDSA data of NiCo coatings deposited at stationary mode (a) and at pulse frequencies: (b) 500 Hz; (c) 1000 Hz; (d) 10000 Hz in electrolyte with composition: 0,32M Co, 0,38M Ni and 0,2M Na<sub>3</sub>citrat. The applied deposition polarizations correspond to the average current  $I_{av} = 45$  mA ( $S = 1$  cm<sup>2</sup>) in the polarization curves. Coating composition (in wt.%): (a) 76%Co-21%Ni (3%O); (b) 88%Co -12% Ni (c) 96%Co- 4%Ni, (d) 90%Co-5%Ni (5%O)

CuNiCo (Fig.6): It was found that in the case of deposition of the triple alloy CuNiCo, the coatings obtained at frequency 500 Hz have larger crystals and are more inhomogeneous compared to CoNi coatings (Fig. 5,c and Fig.6,a). The increase of the pulse frequency up to 1000 Hz results in obtaining of rounded, more uniform, and finer crystals of average diameter 400-500 nm (Fig.6, b). Moreover, the percentage of nickel in the alloys increases (up to 27% Ni). The percentage of cobalt, however, does not change significantly and remains about 71-76 %, and the content of copper decreases from 8% to less than 5% at the applied potentials.

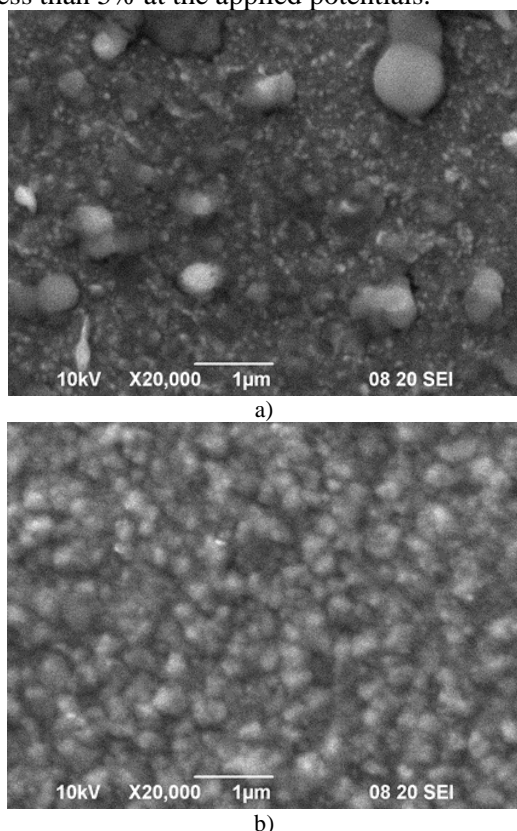


**Fig. 6** SEM images and EDS data of CoNiCu coatings deposited in electrolyte: 0,32M Co, 0,38M Ni, 0,025M Cu and 0,2M Na<sub>3</sub>citrat in pulse mode with pulse frequencies: (a) 500 Hz; (b) 1000 Hz. The applied deposition polarizations correspond to the average current  $I_{av} = 35$  mA ( $S=1\text{cm}^2$ ). Coating composition (in wt.%): (a)76%Co-9%Ni-8%Cu-(7%O); (b)71%Co-21%Ni-(5%Cu)-3%O

*Phase composition of CoCu, NiCo u CoNiCu coatings*

The results from the X-Ray analysis show (Fig.7), that in the studied alloy coatings Cu, Co and Ni crystallize in cubic lattice (f.c.c.). Only in the ternary CoNiCu coating deposited at pulse frequency 1000 Hz (Fig.7, 4), a presence of Co both with face-centred cubic crystal lattice (f.c.c.) and with hexagonal crystal lattice (h.p.c.) was

found. All diffraction images are characterized with relatively wide peaks due to their fine structure reaching nano-sizes. The clear Cu spectrum is due mainly to the fact, that the coatings have small thickness (about 3μm) and are deposited on copper.

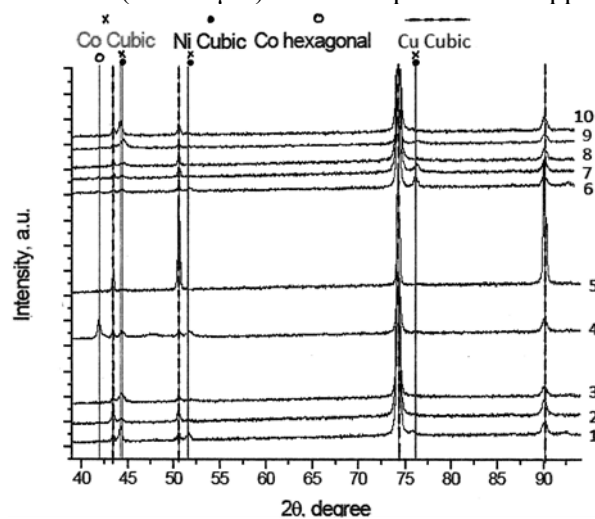


**Fig.7** X-Ray diffractograms of the CoCu coatings(1-3), deposited at pulse condition at frequencies: 500 Hz (1); 5000 Hz (2); 10000 Hz (3); of the CoNiCu coatings at pulse frequencies 1000 Hz (4) and of the CoNi coatings (5-10) deposited in stationary (5) and pulse mode at pulse frequencies: 500 Hz (6); 1 000 Hz (7); 5 000 Hz (8); 10 000 Hz (9,10) in bath with the same composition and at the same polarizations as these in Fig.4-6.

**CONCLUSION**

The conditions for the electrodeposition of CuCo, CoNi and CoNiCu in potentiostatic and pulse potentiostatic modes in citrate solutions were determined. It was found that the applying of pulse potentiostatic mode and higher frequency of pulses significantly smoothes the surface and resulted in finer crystals with rounded shape and average size under 100 nm for CoCu coatings; up to 200-300 nm for CoNi and up to 500 nm for CoNiCu (wt.% Co up to 80%).

**REFERENCES**

1. B. Y. C. Wu, P. J. Ferreira, and C. A. Schuh, *Metallurgical and Materials Transactions A*, **36A**, 1927 (2005)
2. J. Horkans, J. Chia, H. Chang, P. C. Andricacos and E.Chassing, *J. Electrochem. Soc.*, **138**, 441 (1991)
3. A. Bastos, S. Zaefferer, D. Raabe, *Advanced Materials Research*, **15-17**, 274 (2007)
4. A. Bastos, S. Zaefferer, D. Raabe, *J. of Microscopy*, **230**, pt3, 487 (2008)
5. A. Hiroki, I. Masanobu, *Papers of Technical Meeting on Magnetic*, IEE, Japan, **50-63**, 49 (2005)
6. M. Uhlemann, A. Gebert, M. Herrich, A. Krause, L. Shulz, *Electrochim. Acta*, **48**, 3005 (2003)
7. S. Armyanov, *Electrochim. Acta*, **45**, 3323 (2000)

8. Q. Huang, D. Davis, E. J. Podlaha, *J. Appl. Electrochem.*, **36**, 871 (2006)
9. P. Neufeld, A. T. Kuhn, H. A. Skinner, *Inst. Chem. Eng. Symp. Proc.*, **69**, 1 (1983)
10. A. E. Mohamed, S. M. Rashwan, S. M. Abdel-Wahaab, M. M. Kamel, *J. Appl. Electrochem.*, **33**, 1085 (2003)
11. M. Gu, *Electrochimica Acta*, **52**, 4443 (2007)
12. J. J. Kelly, M. Cantoni, D. Landolt, *J. Electrochem. Soc.*, **148**, C620 (2001)
13. G. R. Pattanaik, D. K. Pandya, S. C. Kashyap, *J. Electrochem Soc*, **149**, C363 (2002)
14. C. P. Singh, R. K. Shukla, S. C. Srivastava, *Surface Technology*, **16**, 219 (1982)
15. S. Pané, E. Cómez, E. Vallés, *J. Electroanalytical Chem.*, **596**, 87 (2006)
16. D. Golodnitski, N. V. Gudín, G. A. Volynuk, *J. Electrochem. Soc.*, **147**, 4156 (2000)
17. N. J. Petch, *J. Iron Steel Inst.*, **174**, 25
18. E. Chassaing, *J. Electrochem. Soc.*, **148**, C690 (2001)
19. A. M. El-Sherik, PhD.Thesis, Queen's University, Kingston, Canada, 1993
20. T. A. Green, A. E. Russel, S. Roy, *J. Electrochem. Soc.*, **145**, 875 (1998)
21. T. Ohgai, X. Hoffer, L.G ravier, J.-Ph. Anseremet, *J. Appl. Electrochem.*, **34**, 1007 (2004)
22. S. K. Gupta, M. G. Gartley, *J.CPDS International Centre for Diffraction Data*, 688 (1999)
23. H. J. Blythe, V. M. Fedosyuk, O. I. Kasyutich, *Materials Letters*, **26**, 69 (1996)
24. R. Loloee, P. A. Schroeder, W. P. Pratt Jr., J. Brass, A. Fert, *Physica B: Condensed Matter*, **204**, 274 (1995)
25. K. Ignatova, Y. Marcheva, *Journal of the University of Chemical Technology and Metallurgy*, to be published (vol.2, 2013)
26. L. Petkov, K. Ignatova, *Bulgarian Chemical Communication*, **41**, 39 (2009)
27. D. Grujicic, B. Pestic, *Electrochimica Acta*, **50**, 4426 (2005)

## ЕЛЕКТРООТЛАГАНЕ И СТРУКТУРА НА Co ПОКРИТИЯ (CoCu, NiCo AND CoNiCu) В ПОТЕНЦИОСТАТИЧЕН И ИМПУЛСЕН РЕЖИМ

К. Н. Игнатова<sup>1</sup>, И. С. Марчева<sup>2</sup>

<sup>1</sup> Химикотехнологичен и металургичен университет, София 1000, България

<sup>2</sup> Технически университет, София 1000, България

Постъпила на 18 април, 2013 г.; Коригирана на 24 май, 2013 г.

(Резюме)

Изследвана е кинетиката на самостоятелно отлагане на Cu, Co и Ni както и на отлагането на сплавите CoCu, NiCo и NiCoCu в слабокисел цитратен електролит (pH= 5,5). Получени са и данни за отлагането на сплавите в импулсен потенциостатичен режим при различни честоти на импулсите. Съпоставени са морфологията и елементния състав (чрез SEM и EDSA анализи съответно) на получените в стационарен и в импулсен режим сплавни покрития от всеки вид.

Установено е, че докато отлаганите покрития в стационарен потенциостатичен режим са със среден размер на кристалитите от около 250 до средно 500 nm, а съдържанието на Co е над 85 wt.%, то в импулсен режим се наблюдава намаление на средния размер на кристалитите, а съдържанието на Co е под 76 wt.% за всички сплави. Прилагането на честоти на импулсите до 500 Hz при отлагане на CoCu сплави, води до понижение на размера на кристалитите под 100 nm (при 60-70 wt.% Co). В същите условия покритията от CoNi and CoNiCu се характеризират с окръглена структура на кристалитите, със среден размер около 200-300 nm. Данните от X-Ray анализа показват, че двойните сплави CoCu и NiCo са двуфазни и се състоят от фази на мед, кобалт и никел с кубична стенноцентрирана решетка (f.c.c.). Единствено в тройното покритие Cu-Co-Ni освен кубични фази на трите метала е установено и наличие на Co-съдържаща фаза в хексагонална сингония (h.p.c.).

## Thermogravimetric way to test the oxidation resistance of Pt/C catalysts for fuel cells

S. V. Mentus\*, I. A. Pašti, N. M. Gavrilov

University of Belgrade, Faculty of Physical Chemistry, Studentski trg 12, 11158 Belgrade, Serbia

Received: 01.03.13; Revised 27.04.13

Carbon supported platinum catalysts for fuel cell applications were subjected to linearly programmed heating in air atmosphere under thermogravimetric control. Relative to pure supporting carbon, the carbons composing the Pt/C catalysts were significantly less resistant toward oxidation. Moreover, the Pt/C catalyst samples differed mutually in their oxidation resistances depending on platinum content, carbon texture and presence of additive. Thus, besides of both in-situ and cyclic voltammetric methods, thermogravimetric method was proposed as a fast supplementary way to test the resistance of Pt/C catalyst against oxidation degradation.

**Key words:** carbon oxidation, fuel cell, Pt/C catalysts, thermogravimetry.

### INTRODUCTION

The nanodispersed, carbon supported, Pt catalysts are widely used to catalyse both cathodic and anodic electrode reactions in polymer electrolyte membrane fuel cells (PEMFC). Apart of being current collector, the carbon support prevents the Pt nanoparticles of agglomeration. Under working regime, the cathode catalyst layer is permanently exposed to gaseous oxygen, to provide the electrode potential through the oxygen reduction reaction:



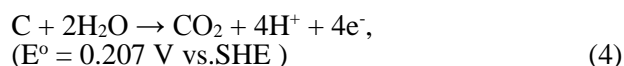
Thus the carbon support undergoes oxidation, and the loss in its mass enables the loss in active surface area of Pt catalyst through agglomeration. Apart of this, positive potential causes slow anodic dissolution of platinum, being an additional reason of catalyst deterioration.

Searching for an acceptable mechanism, the model of carbon oxidation by ozone reported by Donnet [1], was adapted by Kinoshita et al [2], and followed by other authors [3-5], in description of carbon oxidation in fuel cells. According to these reports, CO<sub>2</sub> is formed in two independent and parallel paths:



where oxidation by mediation of surface carbon oxides (CO<sub>surf</sub>) is much slower than the direct oxidation. In fuel cells, the overall reaction (2) may be presented as a part of the following

electrochemical reaction [2]:



Although the potentials of oxygen reduction reaction (1) is typically well above the standard potential of the reaction (4), low kinetic parameters of oxidation make carbon black relatively stable. In addition, the growth of surface oxides (2) may either protect corrosion sites or make a barrier for diffusion of the reactants [2].

The durability of Pt/C composite catalyst manifest itself through the stability of the power of the fuel cell. Usually, it is tested ex-situ, by a persistent cyclic voltammetry and a subsequent observation by electron microscope [6,7]. For example, Wang et al. [6], for a commercial Pt/C catalyst with 20% Pt, provided by Johnson – Matthey, evidenced the decrease of active surface area in function of number of polarization cycles in nitrogen purged perchloric acid solution after 4000 polarization cycles. The TEM pictures taken before and after the cyclo-voltammetric test, unveiled that the agglomeration of Pt particles appeared obviously to be one of the reasons of catalyst collapse. In cyclic voltammetry, the fastest degradation takes place when the potential passes the vertex anodic value, since the concentration of adsorbed oxygen species then passes maximum. This way of testing of catalyst durability is very time consuming. Platinum dissolution and deposition under potentiodynamic condition may cause regrouping of platinum particles resulting in coarsening on account of disappearing of smaller particles. The cyclic voltammetry test does not allow to observe the contribution of carbon oxidation separately from the contribution of

\* To whom all correspondence should be sent:  
E-mail: slavko@ffh.bg.ac.rs

platinum dissolution/deposition, in an overall catalyst degradation. Therefore it would be useful to dispose with the testing procedure which can characterize carbon resistance to oxidation separately from the other factors of catalyst durability.

The present authors applied the thermogravimetric analysis for accurate determination of platinum content in Pt/C catalysts. In these experiments, the catalysts were subjected to a progressively rising temperature in air atmosphere up to complete combustion of carbon, and the residual mass presented the mass of pure platinum [8, 9]. These experiments indicated that the Pt/C catalyst, obtained from various sources, differ in respect of initial temperature of carbon oxidation. Since the thermogravimetric curves reflect also the kinetics of the observed chemical process, we suggest that the thermogravimetric measurements of Pt/C catalysts in air may be used as an efficient method to characterize their durability, supplementary to a usual cyclic voltammetry method.

## EXPERIMENTAL

### *The device*

The device used in the experiments was the thermobalance TA Instruments Model 2960. The air flow rate of  $70 \text{ cm}^3 \text{ s}^{-1}$ , and heating rate of  $10 \text{ }^\circ\text{C min}^{-1}$ , were constant in all experiments.

### *The samples*

A commercial nanodispersed carbon provided by Cabot Corp., trade mark Vulcan XC 72, used as a support of commercial Pt/C catalyst of Johnson Matthey Co., was used in this study as a reference sample. According to the product specifications, its BET specific surface area  $220 \text{ m}^2 \text{ g}^{-1}$ , and according to the TEM picture shown in the reference [10], the mean particle diameter is close to 50 nm.

The second sample was a commercial Pt/C catalyst sample HiSpecTM 4000, provided by Alfa Aesar (with 40 wt% Pt nanoparticles dispersed on Vulcan XC 72). The TEM picture of this sample one may see in the reference [11].

The third, homemade sample Pt/C catalyst sample, contained Vulcan support modified by thin layer of  $\text{Ta}_2\text{O}_5$  in quantity 20%, overlaid by 10% of nanodispersed Pt. The oxide layer was applied first, by drying the suspension of Vulcan in ethanol + tantalum isopropoxide solution, and then Pt nanoparticles were deposited by polyol method [12].

The fourth of investigated samples was a Degussa Pt/C catalyst, trade mark F 105 R/W, with 10% nanodispersed platinum deposited over nanodispersed activated carbon with high surface area of nearly  $1000 \text{ m}^2 \text{ g}^{-1}$ .

## RESULTS AND DISCUSSION

Fig 1, shows the thermogravimetric curves of the three carbon supported platinum catalyst samples described in the experimental section, compared to the thermogravimetric curve of Vulcan XC R2 used as a reference sample. The F105 R/W (Degussa) sample, thanks to a developed surface area of supporting carbon black (CB), contains a lot of adsorbed water, which caused an initial mass drop of almost 15% on heating up to  $100 \text{ }^\circ\text{C}$ . The Vulcan based catalysts do not absorb significant amount of moisture, as visible from a negligible mass change up to at least  $200 \text{ }^\circ\text{C}$ . The main mass drop observed in Fig. 1 is due to the combustion of the carbon material. According to the position of the TG curves along the temperature axis, there is an obvious difference between the observed samples in the resistance toward oxidation. The final residual mass in Fig. 1., manifesting itself as a plateau, corresponded precisely to an actual fraction of non-combustible matter, Pt or  $\text{Pt}+\text{Ta}_2\text{O}_5$ .

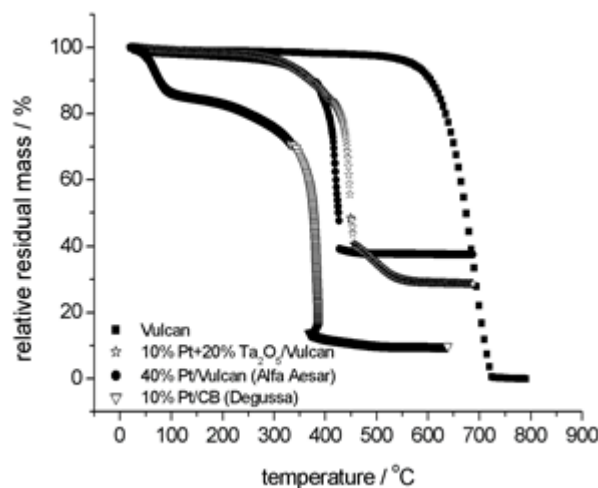


**Fig. 1.** TG curves of Vulcan XC R2, (10% Pt +20%  $\text{Ta}_2\text{O}_5$ )/Vulcan, 40% Pt/Vulcan (HiSpecTM 4000, Alfa Aesar) and 10% Pt/CB (F105 R/W, Degussa) recorded in air stream at a heating rate  $10 \text{ }^\circ\text{C min}^{-1}$ .

For the purpose of more efficient comparison of oxidation resistance of investigated materials, in Fig. 2, the thermogravimetric data from Fig. 1 were expressed in a form of absolute reaction rate in function of temperature. To do this, the fraction reacted ( $\alpha$ ) was calculated:

$$\alpha = (m_i - m_t)/(m_i - m_f) \quad (5)$$

where  $m_i$ ,  $m_t$  and  $m_f$  are initial, actual and final mass, respectively; for a linearly rising temperature  $T$ , time is  $t = T/b$ , where  $b$  is heating rate. In relation to pure Vulcan, for any of the Pt/C samples, the combustion process was shifted markedly toward lower temperatures. The combustion of Pt/C samples was self-accelerated reaction, since, as Fig. 1 shows, for  $\alpha > 0.4$ , overheating happened relative to the programmed temperature rise. The overheating might be prevented by dilution of the sample with inert substance, for instance with corund or silica, however this was not performed in this study. Therefore, only initial parts of the TG curves, where overheating was negligible, were used to compare the observed samples. As already expected from Fig. 1, Fig. 2 confirms clearly that the resistance toward oxidation, in average, decreases in the series 10% Pt/CB (F105 R/W, Degussa) < 40% Pt/Vulcan (HiSpecTM 4000, Alfa Aesar) < (10% Pt +20% Ta<sub>2</sub>O<sub>5</sub>)/Vulcan (homemade) < Vulcan (XC72, Cabot Corp.).

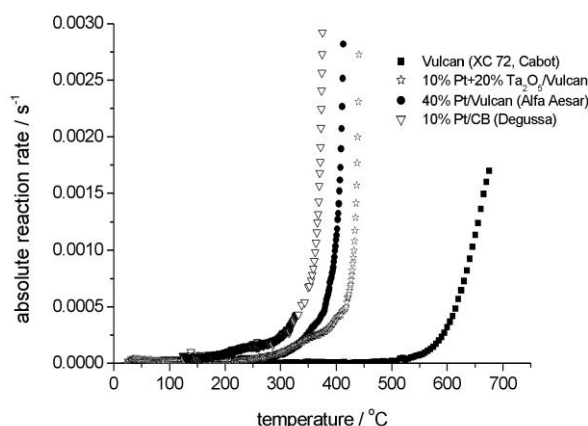


**Fig 2.** Absolute oxidation rates in function of temperature for Vulcan XC R2, (10% Pt +20% Ta<sub>2</sub>O<sub>5</sub>)/Vulcan, 40% Pt/Vulcan (HiSpecTM 4000, Alfa Aesar) and 10%Pt/CB (F105 R/W, Degussa); air atmosphere; heating rate 10 °C min<sup>-1</sup>.

There is the possibility to use thermogravimetric data to express the reactivity in more quantitative manner. Namely, first derivation of  $\alpha$  vs.  $t$  gives the dependence of absolute reaction rate ( $da/dt$ ) on time. Absolute reaction rate as a function of temperature, generally, obeys the equation [13, 14]:

$$\frac{d\alpha}{dt} = Ae^{-\frac{E}{RT}} f(\alpha) \quad (6)$$

Here  $A$  and  $E$  are preexponential factor and activation energy, respectively, and  $f(\alpha)$  is a function, the form of which depends on the nature and morphology of the sample, and involves the

reaction order,  $n$ . The list of available theoretically derived functions for various predicted limiting steps and for particles of variable geometry, one may find in the corresponding literature [13, 14]. The determination of reaction parameters and most suitable function  $f(\alpha)$  is the matter of regression analysis, which may be relatively simple by means of a suitable software, some of which are published elsewhere [15, 16].

The rate of oxidation of pure Vulcan XC 72, may be compared with the literature data for non-catalysed oxidation of various carbon materials. As shown in a recent review published by Neff et al [17] and Stanmore et al. [18], the kinetic of carbon combustion is studied mostly with the aim to remove the soot emitted from diesel engines. The detailed study of carbon oxidation is provided by Marsh et al. [19]. They proposed that the combustion involves free carbon sites, chemisorbed both localised and mobile molecular oxygen, and chemisorbed both localised and mobile atoms of oxygen. Moulijn et al. [20] proposed a relatively simple carbon surface during combustion, involving three types of carbon–oxygen complex, carbonyl, semiquinone and pyrone groups, ordered according the increased stability. According to these authors [21], only less stable fraction of the oxygen-containing surface complexes take part in oxidation reactions. One can expect that for different carbons obtained in a similar way, these with higher specific surface area show higher sensitivity toward oxidation, on account of higher number of reactive surface groups. Accordingly, comparing to the results published by López-Fonseca et al. [22], the initial temperature of combustion of Vulcan XC 72 visible in Fig 1, lies between that of Degussa carbons Flammruss 101 (30 m<sup>2</sup> g<sup>-1</sup>) (combustion started at 600 °C) and Printex XE-2B (1170 m<sup>2</sup> g<sup>-1</sup>) (combustion started at 400 °C). By means of two isoconversional methods, averaged value of activation energy of 150 kJ mol<sup>-1</sup> for Flammruss 101, and 132 kJ mol<sup>-1</sup> for Printex XE-2B was estimated, while the pre-exponential factors amounted to 2.0·10<sup>6</sup> and 2.9·10<sup>6</sup> min<sup>-1</sup>, respectively [22]. Therefore, one may expect intermediate values of these parameters for Vulcan CX 72.

Many literature data evidence that the combustion of carbon may be accelerated by means of various catalysts [17, 23-33]. On the basis of results of TPO experiments, Fe<sub>2</sub>O<sub>3</sub>,  $\gamma$ -Al<sub>2</sub>O<sub>3</sub>, V<sub>2</sub>O<sub>5</sub>, CuO, TiO, as well as Pt/ $\gamma$ -Al<sub>2</sub>O<sub>3</sub>, may accelerate shoot oxidation [17]. This was investigated and evidenced in the reactors where the shoot was mixed

with the catalysts [23-30]. To explain catalytic activity of nanodispersed Pt supported by  $\gamma$ -Al<sub>2</sub>O<sub>3</sub> in the oxidation of coke, oxygen spillover has been postulated by several authors [29, 30]. The same hypothesis has been suggested to explain higher activity of alumina or copper oxide containing low amounts of platinum in shoot combustion [31, 32, 33]. This hypothesis is in agreement with the report that the oxygen ions of alumina are more mobile when located in vicinity of Pt particles [34]. Moreover, platinum is known to enable the exchange gaseous <sup>18</sup>O<sub>2</sub> with the <sup>16</sup>O of the alumina [35]. On this basis, it can be suggested that oxygen is first adsorbed dissociatively on the surface of the noble metal, and then activated oxygen spills over on the supporting surface, where it is able to react with carbon particles at a temperature lower than in the absence of platinum. The experimental arrangement for coke and shoot oxidation in references [23-33], where carbon particles were mechanically mixed with catalyst particles, differ from that used for oxidation of Pt/C catalysts studied here. Namely, in the last case, Pt nanoparticles are applied directly through chemical processes on carbon particles. The suggestion of concentration of adsorbed oxygen on platinum surface [29-35] as a factor of higher corrosion rate of supporting carbon is applicable here, even without any need of oxygen spillover, thanks to a direct contact of platinum and carbon as the reactant.

Between (10% Pt +20% Ta<sub>2</sub>O<sub>5</sub>)/Vulcan (homemade) and 40% Pt/Vulcan (Alfa Aesar) samples, one might reasonably expect higher oxidation resistance of the first one, based on the lower content of platinum. It appears to be actually so at higher  $\alpha$  values (i.e. higher temperatures), as Fig. 2. shows. However, in initial oxidation stages, the oxidation rate is almost identical for both samples, indicating synergistic effect of the Pt/Ta<sub>2</sub>O<sub>5</sub> combination in oxidation catalysis. The disappearance of this effect at higher temperatures may indicate the gradual disappearance of the three/phase boundaries Pt/Ta<sub>2</sub>O<sub>5</sub>/C with the progress of carbon oxidation.

The comparison between two Pt/C catalyst with high and low surface area of supporting carbon (i.e., the Degussa and Alfa Aesar samples), respectively, indicate higher oxidation resistance of Alfa Aesar sample, in spite of its higher platinum content. This emphasizes the importance of surface area effect, connected reasonably with the content of reactive C atoms [19,20].

After the experiments described in this contribution, one may conclude that thermogravimetric analysis under air flow is well capable of detect fine differences in the resistance of different carbon materials and Pt/carbon catalysts towards oxidation. On the basis of similarity of oxidation mechanism of carbons in gaseous and aqueous media [2], the reactivity order of Pt/C catalyst toward oxidation in air established by thermogravimetry, may be expected to reflect the reactivity order in fuel cells, too.

## CONCLUSION

Thermogravimetric analysis under air flow is capable of detect fine differences in the resistance of different carbon materials and Pt/carbon catalysts towards oxidation. Among investigated samples, the resistance toward oxidation, decreases in the series 10% Pt/CB (F105 R/W, Degussa)<40% Pt/Vulcan (HiSpec<sup>TM</sup> 4000, Alfa Aesar) < (10% Pt + 20% Ta<sub>2</sub>O<sub>5</sub>)/Vulcan (homemade) < Vulcan (XC72, Cabot Corp.). Having in mind similar mechanism of oxidation of carbon in gaseous and aqueous media, one may expect similar order of oxidation resistances in electrolyte media of fuel cells, too.

The thermogravimetric experiments confirmed that

- Pt nanoparticles in Pt/C catalyst cause a significant increase of the oxidation rate of supporting carbon;
- the transition metal oxides used as additives to Pt/C catalyst may influence the rate of carbon oxidation, Ta<sub>2</sub>O<sub>5</sub> being the catalyst of oxidation;
- the specific surface area of supporting carbon competes to the platinum content in determination of oxidation resistance of carbon.

**Acknowledgements:** *This work was supported by the Serbian Ministry of Education and Science (Contract III45014). S.V.M. acknowledges the support provided by the Serbian Academy of Sciences and Arts through the project "Electrocatalysis in the contemporary processes of energy conversion".*

## REFERENCES

1. J.-B. Donnet, P. Ehrburger, A. Voet, *Carbon*, **10**, 737 (1972).
2. K. Kinoshita, J. Bett, *Carbon*, **11**, 237 (1973).
3. J. Willsau, J. Heitbaum, *J. Electroanal. Chem.*, **161**, 93 (1984).
4. S. Maass, F. Finsterwalder, G. Frank, R. Hartmann, C. Merten, *J. Power Sources*, **176**, 444 (2008).

5. A. M. Chaparro, N. Mueller, C. Atienza, L. Daza, *J. Electroanal. Chem.*, **591**, 69 (2006).
6. R. Wang, C. Xu, X. Bi, Y. Ding, *Energ. Environ. Sci.*, **5**, 5281 (2012).
7. B. Avasarala, R. Moore, P. Haldar, *Electrochim. Acta*, **55**, 4765 (2010).
8. N. M. Gavrilov, I. A. Pašti, G. Ćirić-Marjanović, V. M. Nikolić, M. P. Marčeta Kaninski, Š. Miljanić, S. V. Mentus, *Int. J. Electrochem. Sci.*, **7**, 6666 (2012).
9. N. Gavrilov, M. Dašić-Tomić, I. Pašti, G. Ćirić-Marjanović, S. Mentus, *Mater. Lett.*, **65**, 962 (2011).
10. F. Si, L. Ma, C. Liu, X. Zhang, W. Xing, *RSC Adv.*, **2**, 401 (2012).
11. J. Parrondo, R. Santhanam, F. Mijangos, B. Rambabu, *Int. J. Electrochem. Sci.*, **5**, 1342 (2010).
12. H.-S. Oh, J.-G. Oh, Y.-G. Hong, H. Kim, *Electrochim. Acta*, **52**, 7278 (2007).
13. H. Tanaka, *Thermochim. Acta*, **267**, 29 (1995).
14. B. Janković, S. Mentus, *Metall. Mater. Trans. A*, **40**, 609 (2009).
15. A. K. Burnham, R. L. Braun, *Energy & Fuels*, **13**, 1 (1999).
16. A. Rotaru, M. Gosa, *J. Therm. Anal. Calorim.*, **97**, 421 (2009).
17. G. Neff, L. Bonaccorsi, A. Donato, C. Milone, M. Grazia Musolino, A. Maria Visco, *Appl. Catal. B*, **11**, 217 (1997).
18. B. R. Stanmore, J. F. Brilhac, P. Gilot, *Carbon*, **39**, 2247 (2001).
19. H. Marsh, K. Kuo, Kinetics and catalysis of carbon gasification. In: H. Marsh, editor, Introduction to carbon science, carbon active sites in the gasification of coal chars. Fuel, London: Butterworths, 1989, p. 107.
20. J. A. Moulijn, F. Kapteijn, *Carbon*, **33**, 1155 (1995).
21. F. Kapteijn, R. Meijer, J.A. Moulijn, D. Cazorla-Amorós, *Carbon*, **32**, 1223 (1994).
22. R. López-Fonseca, I. Landa, M. A. Gutiérrez-Ortiz, J. R. González-Velasco, *J. Therm. Anal. Cal.*, **80**, 65 (2005).
23. J. O. Uchisawa, A. Obuchi, Z. Zhao, S. Kushiyama, *Appl. Catal. B*, **18**, L183 (1998).
24. G. Neri, L. Bonaccorsi, A. Donato, C. Milone, L. M. Grazia Musolino, A. Maria Visco, *Appl. Catal. B*, **11**, 217 (1997).
25. C. Chien, T. Huang, *Ind. Eng. Chem. Res.*, **34**, 1952 (1995).
26. R.J. Farrauto, K.E. Voss, *Appl. Catal. B*, **10**, 29 (1996).
27. H.J. Stein, *Appl. Catal. B*, **10**, 69 (1996).
28. M. Hosoya, M. Shimoda, *Appl. Catal. B*, **10**, 83 (1996).
29. E. Baumgarten, A. Schuck, *Appl. Catal.*, **37**, 247 (1988).
30. J. Parera, E. Traffano, J. Masso, C. Pieck, *Stud. Surf. Sci. Catal.*, **17**, 101 (1983).
31. A. F. Ahlström, C. U. I. Odenbrand, *Appl. Catal.*, **60**, 157 (1990).
32. C. C. Chien, T. J. Huang, *Ind. Eng. Chem. Res.*, **34**, 1952 (1995).
33. R. E. Marinangeli, E. H. Homeier, F. S. Molinaro, *Stud. Surf. Sci. Catal.*, **30**, 457 (1987).
34. V. Ducarme, J.C. Vedrine, *J. Chem. Soc. Faraday Trans. 1*, **74**, 506 (1978).
35. H. Abderrahim, D. Duprez, *Stud. Surf. Sci. Catal.*, **30**, 359 (1987).

## ТЕРМОГРАВИМЕТРИЧЕН МЕТОД ЗА ТЕСТВАНЕ НА УСТОЙЧИВОСТТА НА ОКИСЛЕНИЕ НА Pt/C КАТАЛИЗАТОРИ ЗА ГОРИВНИ КЛЕТКИ

С. В. Ментус\*, И. А. Пашти, Н. М. Гаврилов

Белградски университет, факултет по физикохимия,  
Студентски трг 12, 11158 Белград, Сърбия

Постъпила на 1 март, 2013 г.; преработена на 27 април, 2013 г.

(Резюме)

Платиновни катализатори, отложени върху въглеродни носители за горивни клетки са подложени на линейно програмируемо нагряване във въздушна атмосфера под термогравиметричен контрол. Установено е, че спрямо чистия въглероден носител, катализаторът Pt/C е значително по-устойчив към окисление. Устойчивостта към окисление за различните Pt/C – композиции е различна в зависимост от съдържанието на платина в тях, въглеродната им текстура и наличието на добавки. В работата освен in-situ методът и методът на цикличната волтаметрометрия, е използван термогравиметричният метод като бърз начин за допълнителна проверка на устойчивостта на Pt/C катализатор към окисление.

## Crystallization and dielectric properties of BaTiO<sub>3</sub>-containing invert aluminoborosilicate glass-ceramics

R. Harizanova<sup>1\*</sup>, C. Bocker<sup>2</sup>, G. Avdeev<sup>3</sup>, C. Rüssel<sup>2</sup>, I. Gugov<sup>1</sup>

<sup>1</sup>University of Chemical Technology and Metallurgy, 8 Kl. Ohridski Blvd., 1756 Sofia, Bulgaria,

<sup>2</sup>Otto-Schott-Institut, Jena University, Fraunhoferstr. 6, 07743 Jena, Germany

<sup>3</sup>Institute of Physical Chemistry, Bulgarian Academy of Sciences, Block 11, Acad. G. Bonchev Str., 1113 Sofia, Bulgaria

Received: February 22, 2013; Revised March 13, 2013

The synthesis of invert glasses is possible in the oxide system Na<sub>2</sub>O/TiO<sub>2</sub>/BaO/Al<sub>2</sub>O<sub>3</sub>/B<sub>2</sub>O<sub>3</sub>/SiO<sub>2</sub>/Fe<sub>2</sub>O<sub>3</sub> for glass-former concentrations less than 30 mol%. The prepared glasses are further annealed at different temperatures above the glass transition temperature for different periods of time. This resulted in the simultaneous crystallization of cubic and tetragonal BaTiO<sub>3</sub> as shown by x-ray diffraction. The scanning electron microscopy imaging shows precipitation of globular crystals with sizes varying from some ten nanometers to 1-2 micrometers. The dielectric properties of the glass-ceramic samples are investigated by the method of impedance spectroscopy as a function of frequency. High dielectric constants of the order of 1000 at room temperature and frequency 13 Hz are obtained.

**Key words:** barium titanate, invert glass, crystallization, impedance spectroscopy, dielectric constant.

### INTRODUCTION

Oxide glasses and glass-ceramics, containing less than 50 mol% glass-forming oxides have high tendency to crystallization and are known as invert glasses [1]. These systems, although difficult to obtain as amorphous solid, can be crystallized using an appropriate thermal treatment in order to obtain crystalline phases with distinct physical properties. In an ideal case, the obtained glass-ceramic materials combine advantageous properties of the amorphous and of the crystalline phase. The precipitation of crystalline phases with extremely high melting temperature from such invert glasses allows to decrease the synthesis temperature of the corresponding material and to obtain high volume fraction of the crystals. This technique can also be applied to the preparation of dielectric materials such as barium titanate. Barium titanate, BaTiO<sub>3</sub> is a well-known dielectric which possesses numerous allotropic modifications. In most cases, the tetragonal modification of BaTiO<sub>3</sub> is preferred since it is ferroelectric up to about 120°C and may be utilized for the preparation of capacitors due to its high dielectric constant and as a substitute of the magnetic RAM, e.g. as ferroelectric RAM (FRAM) [2-6]. The cubic modification of BaTiO<sub>3</sub> also possesses high dielectric constant and due to the lack of ferroelectricity has isotropic dielectric properties [2, 5, 6]. So, it can be applied for the preparation of different types of electronic elements, for example as multilayered capacitor for

energy storage [2, 4, 5]. Depending on its optical properties, the cubic modification may be a promising candidate for UV laser preparation for optoelectronic applications [6]. Multiple experimental techniques are used for the preparation of barium titanate as bulk material, [2, 3, 5, 6]. There are also reports dedicated to the preparation of BaTiO<sub>3</sub> in the form of thin films [4, 7].

Some authors report on the addition of 3d-transition metal oxides, for example Fe, to systems in which BaTiO<sub>3</sub> is crystallized [3]. Often, the crystallization of BaTiO<sub>3</sub> with or without the addition of iron oxide is achieved by treatment at high temperatures [3]. Other investigations are devoted to the preparation of barium titanate nanorods with cubic symmetry showing emission in the blue part of the visible spectrum [6] using hydrothermal methods or, however, of the tetragonal modification with potential application in electronics [8]. There are also authors who prefer traditional glass melting techniques to precipitate core-shell nanoparticles composed of barium titanate and magnetite which are promising candidates for application in spintronics [9, 10]. The as obtained modifications of barium titanate exhibit numerous interesting properties, i.e. electric, optical and piezoelectric [6, 8, 11] which promotes the further interest in their investigation.

Another important aspect in the preparation of barium titanate or core/shell particles composed of barium titanate and magnetite is the proper choice of the initial glass composition, so that a tailored

\* To whom all correspondence should be sent:  
E-mail: ruza\_harizanova@yahoo.com

size of the precipitated crystals and large enough volume fraction may be achieved. Studies carried out using the composition 12Na<sub>2</sub>O/12Al<sub>2</sub>O<sub>3</sub>/14B<sub>2</sub>O<sub>3</sub>/37SiO<sub>2</sub>/25Fe<sub>2</sub>O<sub>3</sub> [12] or similar oxide systems [13-19] show that the varied ratio of the alkaline and alkaline earth oxides leads to controlled viscosity of the melt. This allows controlling the crystallite size and volume fraction in the corresponding materials.

This work reports the results from the synthesis of glasses from invert compositions with less than 30 mol % glass-forming oxides in the system (23.1-x)Na<sub>2</sub>O/23.1BaO/23TiO<sub>2</sub>/7.6B<sub>2</sub>O<sub>3</sub>/17.4SiO<sub>2</sub>/5.8Fe<sub>2</sub>O<sub>3</sub>/xAl<sub>2</sub>O<sub>3</sub> and the resulting microstructures. Further, it shows the possibility to crystallize BaTiO<sub>3</sub> with varying particle sizes from glass compositions with different ratios [Na<sub>2</sub>O]/[Al<sub>2</sub>O<sub>3</sub>]. The dielectric constants of the synthesized glass-ceramic materials are determined by impedance spectroscopy.

## EXPERIMENTAL

The ratio [Na<sub>2</sub>O]/[Al<sub>2</sub>O<sub>3</sub>] is varied and a series of compositions with the formula (23.1-x)Na<sub>2</sub>O/23.1BaO/23TiO<sub>2</sub>/7.6B<sub>2</sub>O<sub>3</sub>/17.4SiO<sub>2</sub>/5.8Fe<sub>2</sub>O<sub>3</sub>/xAl<sub>2</sub>O<sub>3</sub> x = 0; 3 in mol% (batch composition) are melted from reagent grade raw materials: Na<sub>2</sub>CO<sub>3</sub>, BaCO<sub>3</sub>, TiO<sub>2</sub>, Al(OH)<sub>3</sub>, B(OH)<sub>3</sub>, SiO<sub>2</sub> and Fe<sub>2</sub>O<sub>3</sub>. All glasses are melted in 60 g batches for 1 h at 1250 °C in air using a Pt crucible in a furnace with SiC heating elements. Then, the melts are quenched (without pressing) on a copper block and, in order to reduce the mechanical stresses in the glass, transferred to a pre-heated C-mould and held for 10-15 min at 450°C in a muffle furnace. Then, the furnace is switched off and the samples are allowed to cool to room temperature.

The phase compositions of the samples from all melted compositions are studied by x-ray diffraction (XRD), *Siemens D5000*, using Cu-K $\alpha$  radiation ( $\lambda = 1.541874$  Å) and Ni-filter. The microstructure and the elemental composition of the prepared glasses and subsequently, of the crystallised ones is further analysed by scanning electron microscopy (SEM), combined with energy-dispersive (EDAX) analysis, (*JSM-7001F*, *JEOL Ltd., Japan*). Imaging of the crystallised samples is performed on both polished and if no good contrast is achieved – on etched surfaces (5 s in 1% HCl solution). The dielectric properties are investigated by impedance spectroscopy at room temperature in the frequency range from 1 Hz to 130 kHz. First the impedance modulus and the phase angle are measured as function of frequency

and then an appropriate equivalent circuit is proposed (impedance meter *Zahner IM6*, *Kronach, Germany*). The capacitance derived from the equivalent circuit is determined at several frequencies and the dielectric constant is calculated.

## RESULTS AND DISCUSSION

All prepared glasses after quenching on a copper plate possess dark brown coloration. There are some parts of the surface which seems to be slightly crystallised. Here, the formation of droplet-shaped light brown regions is observed. The bulk of all samples appears glassy, as seen at a fractured surface and as concluded from XRD patterns and SEM imaging. The XRD patterns of the untreated glass and samples annealed at 550°C for different periods of time are shown for the composition with 20.3 mol% Na<sub>2</sub>O and 3 mol% Al<sub>2</sub>O<sub>3</sub> in Figs. 1 and 2 (samples G1 to G7).

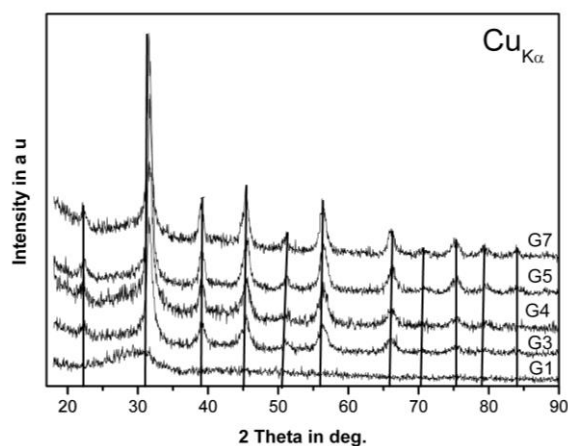


**Fig. 1.** XRD patterns of samples with 5.8 mol% Fe<sub>2</sub>O<sub>3</sub> and 3 mol% Al<sub>2</sub>O<sub>3</sub> – glass as prepared (G1) and crystallization of BaTiO<sub>3</sub> (JCPDS 1-74-1962) after annealing for 30 min (G3), 1 h (G4), 2 h (G5) and 5 h (G7) at 550°C; lines – peaks of BaTiO<sub>3</sub>.

Increasing annealing times lead to peaks of larger intensity and to a larger volume fraction of crystalline phase. The same results are observed earlier for the same system [20] and for similar borosilicate glasses from which BaTiO<sub>3</sub> can also subsequently be crystallized [21]. In the present study and from our previous work [20], we have the idea that with increasing Al<sub>2</sub>O<sub>3</sub> concentration, the crystallization tendency on the surface decreases up to the ratio [Na<sub>2</sub>O]/[Al<sub>2</sub>O<sub>3</sub>] = 12.1/11. For a concentration of 15 mol% Al<sub>2</sub>O<sub>3</sub>, already spontaneous and sporadic crystallisation occurs in the bulk, although in the XRD-pattern no distinct lines are observed. The average size of the crystals

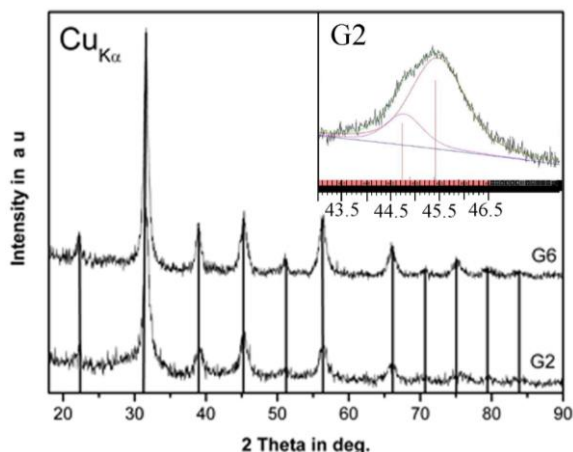


**Fig. 2.** XRD patterns of samples from the system Na<sub>2</sub>O/BaO/TiO<sub>2</sub>/B<sub>2</sub>O<sub>3</sub>/SiO<sub>2</sub>/Fe<sub>2</sub>O<sub>3</sub> with 5.8 mol% Fe<sub>2</sub>O<sub>3</sub> and 3 mol% Al<sub>2</sub>O<sub>3</sub> – crystallization of BaTiO<sub>3</sub> after annealing for 15 min (G2) and 3 h (G6) at 550°C; lines – peaks of BaTiO<sub>3</sub>; inset: magnified peak at 45.3° with peaks of the tetragonal phase fitted.

formed during annealing at 550°C and for equal periods of time show that an increasing ratio sodium oxide/alumina leads to an increase in the average crystallite size – as already reported in [20]. Such a dependency of the size of the formed crystals on the ratio [Na<sub>2</sub>O]/[Al<sub>2</sub>O<sub>3</sub>] is attributed to the increase in the viscosity with decreasing ratio and was already observed in other non-transition metal containing aluminoborosilicate glasses [14-16] or in glasses containing minor quantities of polyvalent elements, e.g. tin or iron [17-19]. However, the same dependency on the viscosity and thus, of the size of the precipitated crystalline phase on the ratio between the alkali and aluminum oxides is also seen for borosilicate glass melts with higher Fe<sub>2</sub>O<sub>3</sub> concentration (between 14 and 25 mol%) [12]. The same situation is observed for the crystallization products in the present study – see Figs. 3 and 4. Here the formed crystals for compositions without Al<sub>2</sub>O<sub>3</sub> are of the order of 1 micrometer while the crystals precipitated under the same annealing schedule but for an alumina concentration of 3 mol% are less than 600 nm. The XRD analyses show that for both compositions always one and the same crystalline phase – cubic BaTiO<sub>3</sub>, JCPDS 1-74-1962, is formed. The same observation was already reported in our earlier works [20, 21]. The Rietveld refinement of the peak at 45.3°, however, shows that the peak may be represented as a combination of two peaks – see the inset in Fig. 2, i.e. in the annealed samples with 3 mol% Al<sub>2</sub>O<sub>3</sub> obviously also the tetragonal modification of barium titanate is present. This type of analysis has already proved to be a trustful way to establish the presence of cubic or/and tetragonal

BaTiO<sub>3</sub> [2, 8]. Usually, the size of the formed particles and the preparation conditions are decisive for the formation of either cubic or tetragonal barium titanate [2, 4-8, 11]. The fit in Fig. 2, however, suggests that here simultaneously cubic and tetragonal BaTiO<sub>3</sub> are present. The simultaneous presence of the tetragonal modification which is ferroelectric but also of the cubic one – paraelectric with isotropic dielectric properties – may have an interesting impact on the dielectric properties of the resulting glass-ceramics. As seen in Figs. 3 and 4, the prepared glass-ceramic materials are characterized by a high degree of crystallization in the bulk and thus, high dielectric constants are expected for them as already observed in the work of other authors concerning barium titanate based glass-ceramics [23].

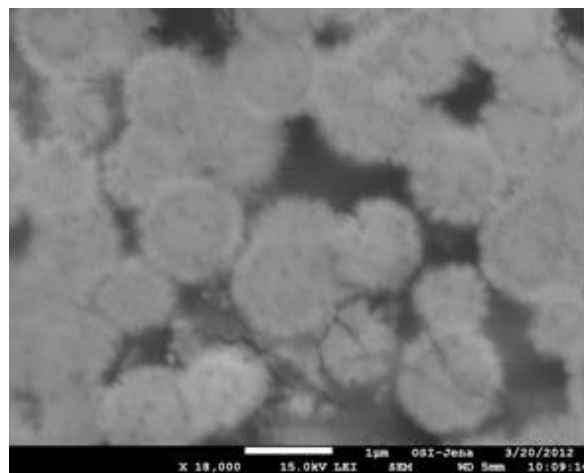


**Fig. 3.** SEM of a polished and C-covered sample with 5.8 mol% Fe<sub>2</sub>O<sub>3</sub> and no Al<sub>2</sub>O<sub>3</sub> – formation of spherical core-shell crystals after annealing for 4 h at 550°C

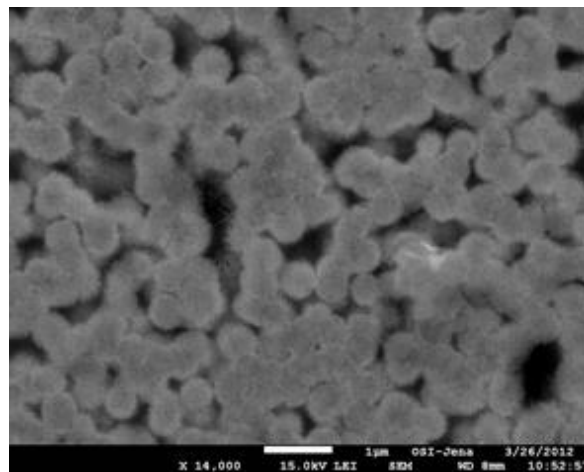


**Fig. 4.** SEM of a C-covered sample with 3 mol% Al<sub>2</sub>O<sub>3</sub> and 5.8 mol% Fe<sub>2</sub>O<sub>3</sub>, annealed for 3 h at 550°C – crystallization of globular BaTiO<sub>3</sub> in the bulk [20].

The tendency of combining different transition metals – here Fe and Ti – is a well-known method for changing the type and the properties of the

resulting crystals and is already observed in other (Ba,Fe,Ti)-containing glass systems [3, 9]. The simultaneous presence of two or more transition metals in the composition of an oxide glass can result in formation of core-shell structures consisting of ferroelectric and ferromagnetic crystals [9]. Such structures may combine the properties of the two phases formed, which results in a multiferroic property and finds novel and interesting practical applications in electronics [9, 10]. Anyway, from the presented XRD data, as seen in Figs. 1 and 2, and as concluded from the elemental EDAX analyses performed on the crystals from Fig. 3, only Ba and Ti are present in the formed crystals, however, Fe is not detected in the crystals. One reason for the total lack of Fe or only undetectable minor Fe concentrations incorporated in the BaTiO<sub>3</sub> crystals might be the relatively low Fe<sub>2</sub>O<sub>3</sub> concentration. This is in contrast to the results reported by other authors, who by sintering routes obtain Fe-doped barium titanate [3] or by applying appropriate annealing programs crystallize core-shell multiferroic particles from a borosilicate amorphous matrix with a comparable iron oxide concentration [9]. It should be noted, that the Fe-doped barium titanate crystals from Ref. [3] change their symmetry from tetragonal into hexagonal due to the incorporation of Fe in the crystals. This effect is disadvantageous because the hexagonal phase exhibits no ferroelectricity and also, possesses worse dielectric parameters, in comparison to the cubic one as reported in [3].

In order to evaluate the dielectric constants of the obtained barium titanate based glass-ceramics, impedance measurements were performed. Samples from both compositions are prepared by roughly polishing two plane parallel surfaces and sputtering gold electrodes at them. Then, two points measurement was done using an impedance analyzer, first measuring the impedance modulus and phase angle as function of frequency. Then, after attributing the electrical behaviour at room temperature to an RC-circuit in parallel, the capacity is measured at a fixed frequency. The results from the performed measurements at a fixed frequency allow, for a known geometry of the samples, to calculate the dielectric constants as a function of the frequency at room temperature. Data for two annealed samples are shown in Fig. 5. It is to be mentioned that the samples show a dependency of the dielectric constant on the frequency typical for all dielectric materials – no matter what the crystalline phase is [22].

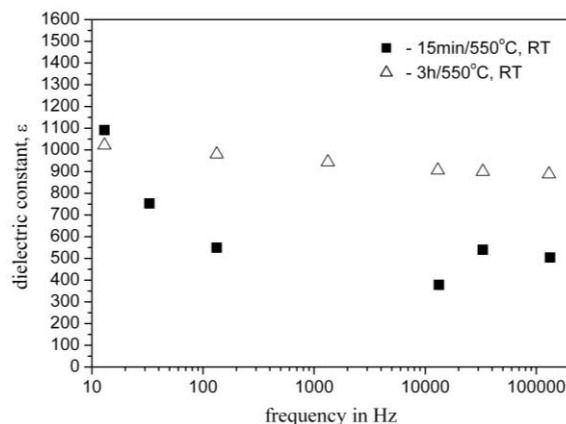


**Fig. 5.** Dielectric constant as function of frequency at room temperature for samples with 20.1 mol% Na<sub>2</sub>O and 3 mol% Al<sub>2</sub>O<sub>3</sub> – annealed for 15 min (G2) and 3 h (G6) at 550°C.

However, in the present case a very high dielectric constant in the whole frequency region is obtained – results comparable to the results reported by other authors in case of purely ferroelectric barium titanate [23]. From Fig. 5 in the present work it becomes clear that a longer annealing time and the same annealing temperature lead to a higher dielectric constant at one and the same frequency. This fact can be explained by the larger degree of crystallization of the sample annealed for 3h compared to that crystallized for 15 min, though both are well-crystallized since in the XRD-patterns almost no glassy halo is seen, cf. Fig.2. The data in Fig. 2 also suggests that the volume fraction and the size of the crystals in the sample annealed for 15 min at 550°C, are smaller with respect to those for the sample crystallized at the same temperature but for 3h. In Fig. 5 it is also shown that the decrease in the dielectric constant with increasing frequency is steeper for the sample crystallized for 15 min. One possible reason could be the higher losses in comparison to those in the sample crystallized for 3h for which the dielectric constant shows only a slight variation with the frequency. The explanation of this phenomenon for the present system is still not clear.

## CONCLUSION

The quenching of melts from the studied compositions results in glass formation in the bulk and slight crystallization at the surface. Annealing of samples from the bulk above T<sub>g</sub> leads to the crystallization of spherical particles of cubic BaTiO<sub>3</sub> for all ratios [Na<sub>2</sub>O]/[Al<sub>2</sub>O<sub>3</sub>]. The Rietveld refinement of the x-ray diffraction data reveals simultaneous crystallization of the tetragonal and the cubic BaTiO<sub>3</sub> phase. No influence of Fe on the crystal phase composition and symmetry is

observed. The dielectric constant, calculated at room temperature, is about 1000 at 13Hz and its decrease with the increasing frequency depends on the annealing time applied.

**Acknowledgements:** This work was financially supported by means of contract № D02-180/14.02.2013, index: P-6-07/13, project: BG051PO001-3.3-05/0001 «Science-business», funded by Operational program «Development of human resources».

#### REFERENCES

1. H.J.L. Trap, J.M. Stevels, *Phys. Chem. Glasses* **4** 193 (1963).
2. J.F. Capsal, E. Dantras, L. Laffont, J. Dandurand, C. Lacabanne, *J. Non-Cryst. Solids* **356** 629 (2010).
3. G.P. Du, Z. J. Hu, Q. F. Han, X. M. Qin, W.J. Shi, *J. Alloys & Compounds* **492** L79 (2010).
4. T.J Jackson, I.P. Jones, *J. Mater. Sci.* **44** 5288 (2009).
5. Z. Libor, S.A. Wilson, Q. Zhang, *J. Mater. Sci.* **46** 5385 (2011).
6. R. Vijayalakshmi, V. Rajendran, *Digest J. Nanomater. Biostructures* **5** 511 (2010).
7. S.F. Mendes, C.M. Costa, C. Caparros, V. Sencadas, S. Lanceros-Mendez, *J. Mater. Sci.* **47** 1378 (2012).
8. U.Joshi, S.Yoon, S. Baik, J.S.Lee, *J. Phys. Chem. B* **110** 12249 (2006).
9. R.P. Maiti, S. Basu, S. Bhattacharya, D. Chakravorty, *J. Non-Cryst. Solids* **355** 2254 (2009).
10. A.K. Zvezdin et al., *Bulletin of Russian Academy of Sciences: Physics* **71** 1561 (2007).
11. S.D. Vacche, F. Oliveira, Y. Leterrier, V. Michaud, D. Damjanovic, J.E. Manson, *J. Mater. Sci.* **47** 4763 (2012), DOI 10.1007/s10853-012-6362-x.
12. C. Worsch, P. Schaaf, R. Harizanova, C. Rüssel, *J. Mater. Sci.* **47** 5886 (2012).
13. W. Vogel in: *Glasschemistry*, 3 Ed. Springer, Berlin-New York-London-Paris-Tokyo-Hong Kong-Barcelona-Budapest, 1992.
14. K. El-Egili, *Phys B* **325** 340 (2003).
15. S. Hornschuh, B. Messerschmidt, T. Possner, U. Possner, C. Rüssel, *J Non-Cryst Solids* **347** 121 (2004).
16. L. Hong, P. Hrma, J.D. Vienna, M. Qian, Y. Su, D.E. Smith, *J Non-Cryst Solids* **331** 202 (2003).
17. D. Benne, C. Rüssel, M. Menzel, K. Becker, *J Non-Cryst Solids* **337** 232 (2004).
18. H. Schirmer, R. Keding, C. Rüssel, *J Non-Cryst Solids* **336** 37 (2004).
19. D. Benne, C. Rüssel, D. Niemer, M. Menzel, K. Becker, *J Non-Cryst Solids* 345-346 203 (2004).
20. R. Harizanova, L. Vladislavova, C. Bocker, C. Rüssel, I. Gugov, *Bul. Chem. Comm.* – accepted 18.02.2013.
21. L. Vladislavova, R. Harizanova, S. Vasilev, I. Gugov, *Advances in Natural Science: Theory and Applications* **1** (2012) 89–94.
22. P. Prapitpongwanich, R. Harizanova, K. Pengpat, C. Russel, *Mater. Lett.* **63** 1027 (2009).
23. M.S. Al-Assiri, M.M. El-Desoky, *J Non-Cryst Solids* **358** 1605 (2012).

## КРИСТАЛИЗАЦИЯ И ДИЕЛЕКТРИЧНИ СВОЙСТВА НА ИНВЕРТНИ АЛУМОБОРОСИЛИКАТНИ СЪТЪКЛОКЕРАМИКИ, СЪДЪРЖАЩИ БАРИЕВ ТИТАНАТ

Р. Харизанова<sup>1\*</sup>, Хр. Бокър<sup>2</sup>, Г. Авдеев<sup>3</sup>, Хр. Рюсел<sup>2</sup>, Ив. Гугов<sup>1</sup>

<sup>1</sup>Химикотехнологичен и Металургичен университет, бул. „Климент Охридски“ №8, 1756 София, България

<sup>2</sup>Ото Шот институт, Университет Йена, ул. „Фраунхофер“ №6, 07743 Йена, Германия

<sup>3</sup>Институт по Физикохимия, БАН, бл. 11, ул. „Акад. Г. Бончев“, 1113 София, България

Постъпила на 22 февруари, 2013 г.; Коригирана на 13 март, 2013 г.

(Резюме)

В системата Na<sub>2</sub>O/TiO<sub>2</sub>/BaO/Al<sub>2</sub>O<sub>3</sub>/B<sub>2</sub>O<sub>3</sub>/SiO<sub>2</sub>/Fe<sub>2</sub>O<sub>3</sub> е възможен синтезът на инвертни стъкла за концентрации на стъклообразователите по-малки от 30 мол%. Получените стъкла са подложени на термично третиране при различни температури над температурата на стъклообразуване за различно време. Резултатът е едновременната кристализация на кубичен и тетрагонален BaTiO<sub>3</sub>, както свидетелстват данните от рентгеновата дифракция. Анализите с помощта на сканираща електронна микроскопия показват образуването на глобуларни кристали с размери, вариращи от няколко десетки нм до 1-2 микрометра. Диелектричните свойства на стъклокерамичните проби са изследвани по метода на импедансната спектроскопия в зависимост от честотата. Определени са високи диелектрични константи от порядъка на 1000 при стайна температура и честота 13 Hz.

## Ionic and electronic conductivity of the surface film on titanium during pulse electrolysis of water

D. Hristova<sup>1\*</sup>, I. G. Betova<sup>2</sup>, Tzv. B. Tzvetkoff<sup>1</sup>

<sup>1</sup>Department of Physical Chemistry, University of Chemical Technology and Metallurgy, 1756 Sofia, Bulgaria

<sup>2</sup>Department of Chemistry, Technical University of Sofia, 1000 Sofia, Bulgaria

Received February 26, 2013; Revised April 12, 2013

The processes of corrosion and degradation of electrode materials are crucial for the efficiency of pulse electrolysis and are expected to depend on the electrical characteristics of the pulse (current/voltage, frequency, duty cycle). The aim of the present paper is to investigate the effect of these characteristics on the electrochemical properties of Ti electrodes. Pulse electrolysis was carried out in 6 M KOH for 24 and 72 h with current amplitude of 65 mA, frequencies of the signal of 0.5-10 kHz and pulse duty cycle between 1 and 99%. The electrochemical properties of the titanium anode and cathode surfaces after operation were characterized by electrochemical impedance spectroscopy in a borate buffer solution (pH 7.4) at the open circuit potential, as well as by linear sweep voltammetry in a similar solution containing an equimolar mixture of  $K_4Fe(CN)_6$  and  $K_3Fe(CN)_6$  as a redox couple to probe the electronic conductivity of the surface films.

**Key words:** pulse electrolysis, titanium, electrochemical impedance spectroscopy, linear sweep voltammetry, electronic and ionic conductivity.

### INTRODUCTION

Pulse electrolysis of water is a highly efficient method of production of hydrogen/oxygen gas mixtures, sometimes called hydroxygen, that are successfully used as additives to hydrocarbon fuels in internal combustion engines [1-4]. The papers on pulse electrolysis of water to obtain hydrogen/oxygen mixtures are somewhat scarce [5-9], focusing on the effect of pulse regime on the overall process efficiency and the combustion properties of the respective gas mixtures. It was also demonstrated that application of short inductive voltage pulses to the cell allows the power of the primary circuit to be reduced, thereby reducing the total power necessary for electrolysis and achieving water splitting with an input voltage as low as 1 V [7,8]. The interpretation of the phenomena associated with hydroxygen production has been recently a cause of controversy, invoking a range of explanations from the formation of new forms of matter [10-12] to that of charged water gas clusters [13]. Regardless of the exact mechanism of the process, it seems well established that in conditions of pulse electrolysis of water, the rate of the process is increased in comparison to the dc regime. This poses more stringent requirements for the electrode materials since the processes of their corrosion and degradation are expected to depend

on the electrical characteristics of the pulse (current/voltage, frequency, duty cycle). In most of the commercial hydroxygen generators described thus far, austenitic stainless steels, as well as pure titanium were employed as both cathode and anode materials [14]. A search of the literature revealed a dearth of studies relevant to characterization and optimization of the electrode material with respect to its corrosion/degradation rates.

The aim of the present paper is to investigate the effect of pulse characteristics (duty cycle and frequency) on the electrochemical properties of commercially pure Ti under pulse electrolysis operating conditions and to correlate these properties with the surface state of the material. The electrochemical properties are characterized using both electrochemical impedance spectroscopy in an inert electrolyte and linear sweep voltammetry in a similar electrolyte containing a redox couple to probe the electronic conductivity of the surface film.

### EXPERIMENTAL METHODS

The laboratory setup to study the effect of electrical characteristics of the pulse consisted of a home-designed high-power pulse generator (60 V/15 A), a dc power supply (BK Precision, 100 V/15 A), a 7-digit multimeter (Tektronix), a digital oscilloscope (Tektronix), and a flow meter (Aalborg, 240 L/h). The setup was originally designed for studies of the hydroxygen generation

\* To whom all correspondence should be sent:  
E-mail: dhristova@hotmail.com

efficiency in larger electrolysis cells using current amplitudes up to 5 A. In the present paper, however, a smaller cell was used since the main goal was to investigate the degradation of the electrode material. Thus pulse electrolysis with current amplitudes of 12–250 mA, pulse frequencies ( $f$ ) of 0.5 to 10 kHz and duty cycles ( $D$ ) between 1 and 99% and a duration of 24 h was performed. The distance between the anode and the cathode in the pulse electrolysis cell was 1 cm.

Investigations were carried out on Grade 2 titanium (99.2%) that served both as an anode and cathode material. Its pretreatment consisted of mechanical abrasion with emery paper up to 2400 grade followed by rinsing with bi-distilled water. 6 M KOH prepared from a p.a. chemical and bi-distilled water was used as electrolyte.

The electrochemical properties of the electrodes after operation were characterized by electrochemical impedance spectroscopy in a borate buffer solution (0.5 M  $\text{H}_3\text{BO}_3$ , 0.05 M  $\text{Na}_2\text{B}_4\text{O}_7 \cdot 10\text{H}_2\text{O}$ , pH 7.4) at the open circuit potential, as well as by linear sweep voltammetry in a similar solution containing 0.5 M  $\text{K}_4\text{Fe}(\text{CN})_6$  and 0.5 M  $\text{K}_3\text{Fe}(\text{CN})_6$  (1:1) as a redox probe of the electronic conductivity of the surface films. Electrochemical measurements were performed with an Autolab PGSTAT30/FRA2 driven by GPES and FRA software (Eco Chemie). The sweep rate in voltammetric measurements was  $1 \text{ mV s}^{-1}$ , whereas the frequency range of the electrochemical impedance measurements was from 0.01 Hz to 50 kHz with an ac signal amplitude of 15 mV (rms). The linearity of the impedance spectra was checked by measuring at signal amplitudes from 5 to 15 mV, whereas their causality – by a Kramers-Kronig transform compatibility test embedded in the measurement software. Fitting of experimental voltammograms and impedance spectra to appropriate functions was performed using Originlab software.

## RESULTS AND DISCUSSION

### *Electronic conductivity of the surface film*

Results of the electrochemical probing of the electronic conductivity of surface films on cathodes and anodes after 24 h of operation with voltammetry in a borate buffer solution (pH 7.3) containing a  $\text{K}_3\text{Fe}(\text{CN})_6/\text{K}_2\text{Fe}(\text{CN})_6$  redox couple are presented in Fig. 1 and Fig. 2, respectively. The curves were fitted to a Butler-Volmer equation describing a first-order electrochemical reaction limited by charge transfer, expressed as follows

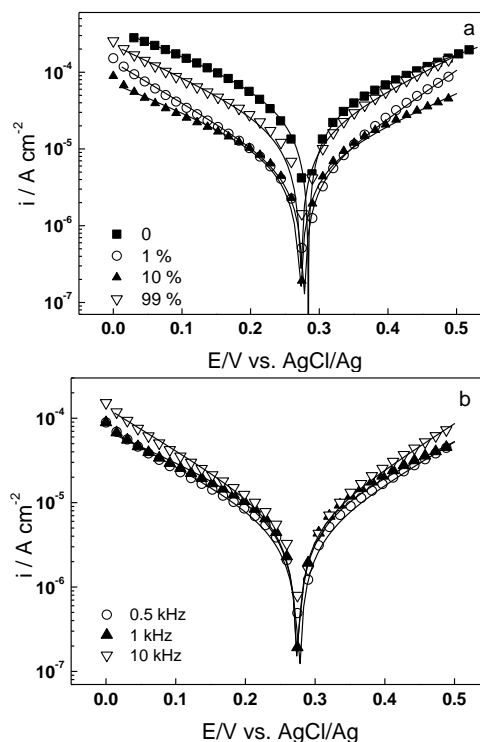


**Fig. 1.** Effect of pulse duty cycle (%) at constant frequency of 1 kHz (a) and frequency at a constant duty cycle of 10% (b) on the voltammetric response of Ti cathodes after 24 h of operation at 65 mA, measured in a borate buffer solution containing an equimolar mixture of  $\text{K}_2\text{Fe}(\text{CN})_6$  and  $\text{K}_3\text{Fe}(\text{CN})_6$ . 0 – fresh sample. Points – experiment, lines – best-fit calculation.

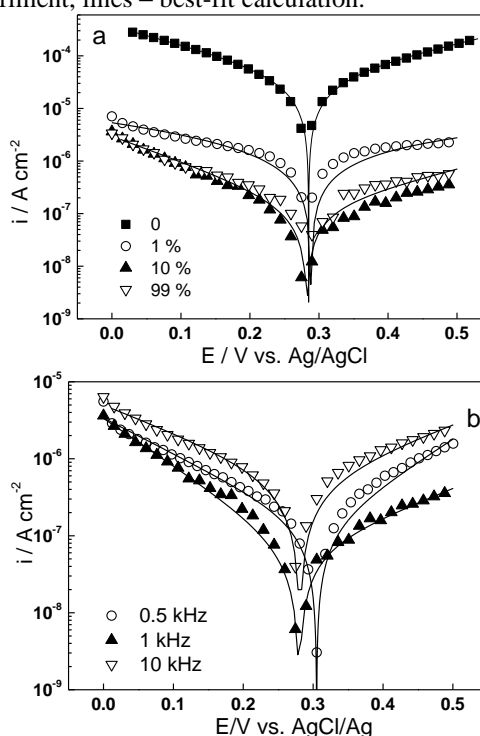


**Fig. 2.** Effect of pulse duty cycle (%) at constant frequency of 1 kHz (a) and frequency at a constant duty cycle of 10% (b) on the voltammetric response of Ti anodes after 24 h of operation at 65 mA, measured in a borate buffer solution containing an equimolar mixture of  $\text{K}_2\text{Fe}(\text{CN})_6$  and  $\text{K}_3\text{Fe}(\text{CN})_6$ . 0 – fresh sample. Points – experiment, lines – best-fit calculation.

$$i = i_0 \left[ \exp(b_a(E - E_{eq})) - \exp(-b_c(E - E_{eq})) \right] \quad (1)$$

where  $i_0$  is the exchange current density of the redox reaction,  $b_a$  and  $b_c$  are the exponential coefficients and  $E_{eq}$  is the equilibrium potential of the redox couple ( $0.30 \pm 0.02$  V vs. AgCl/Ag). The best-fit calculations are shown in Fig. 1 and Fig. 2 with solid lines and demonstrate that this simple model describes adequately the experimental voltammograms.

In general, the electronic conductivity of the surface films formed on both anodes and cathodes, as characterized by the exchange current density, decreases with increasing the duty cycle at a constant frequency of 1 kHz (with the exception of 99% and dc regime) as well as with the increase of the pulse frequency at a duty cycle of 10% (Fig. 3).

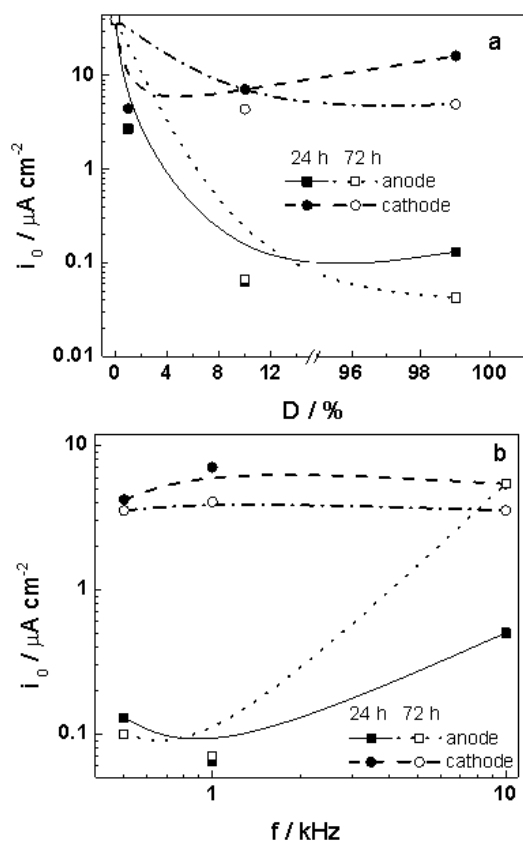


**Fig. 3** A comparison between the exchange current density for Ti anode and cathode surfaces after 24 h and 72 h of operation at 65 mA/40 V for different duty cycles at a constant frequency of 1 kHz (a) and at different frequencies and a duty cycle of 10% (b).

However, this decrease is much more pronounced in the case of films formed on anodes and can be related to the increase of the thickness and/or decrease in the number of defects during the pulse anodic polarization. In that respect, it is worth

mentioning that the exponential coefficient of the oxidative partial reaction ( $b_a$ ) is of the order of  $6 \text{ V}^{-1}$ , whereas that of the reductive partial reaction ( $b_c$ ) is ca.  $10 \text{ V}^{-1}$ , i.e. the transfer coefficient for oxidation is smaller than that for reduction, as expected for an n-type semiconductor layer formed on the Ti surface during operation. The sum of the two exponential coefficients is however less than  $40 \text{ V}^{-1}$  which is expected for one-electron reaction at a bare metal surface. This fact is also in accordance that an oxide film is present on the surface and part of the applied potential is consumed as a potential drop in this oxide.

The superimposed effect of the increase of thickness (which lowers the probability for direct tunneling of carriers) and the decrease of the number of point defects (lowering the probability of resonance tunneling and/or polaron hopping) [15-17] qualitatively explains the influence of duty cycle on exchange current density (Fig. 3a). In the simplest case, when only direct tunneling is involved, the exchange current density should decrease exponentially with film thickness according to the equation

$$i_0 = i_{0,L_0} e^{-\beta(L-L_0)} \quad (2)$$

where  $i_{0,L_0}$  is the exchange current density of the fresh sample (bearing a native oxide with a thickness  $L_0$ ),  $L$  is the thickness of the oxide on an electrode that has been in operation and  $\beta$  is the tunneling constant (of the order of  $10^8 \text{ cm}^{-1}$  [17,18]). The thickness of the native film on Ti being reported as 7.9 nm [19], the values of  $L$  estimated from equation (2) are of the order of 10-12 nm as depending on the duty cycle. These values demonstrate that during operation, film growth plays a minor role and most of the charge passed goes for water splitting.

#### Ionic conductivity of the surface films

Further insight into the influence of operational conditions on the electrochemical properties of the surface films on Ti was sought by registering electrochemical impedance spectra at open-circuit potential in a borate buffer solution (pH 7.3). The effect of the duty cycle at constant frequency of 1 kHz on the spectra is illustrated in Fig. 4 and Fig. 5 for the cathodes and anodes, respectively, after 24 h of service at current amplitude of 65 mA. Qualitatively similar spectra (not shown for the sake of brevity) were obtained as depending on the

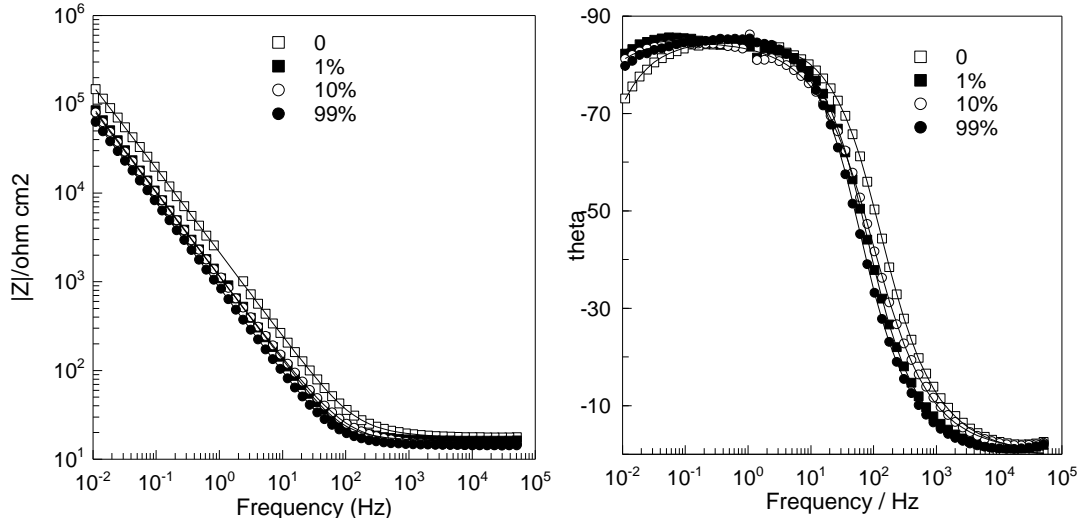


**Fig. 4.** Effect of pulse duty cycle at constant frequency of 1 kHz on the impedance spectra of Ti cathodes after 24 h of operation at 65 mA/40 V. Left- impedance magnitude vs. frequency, right – phase shift vs. frequency, 0 – fresh sample. Points – experiment, lines – best-fit calculation.

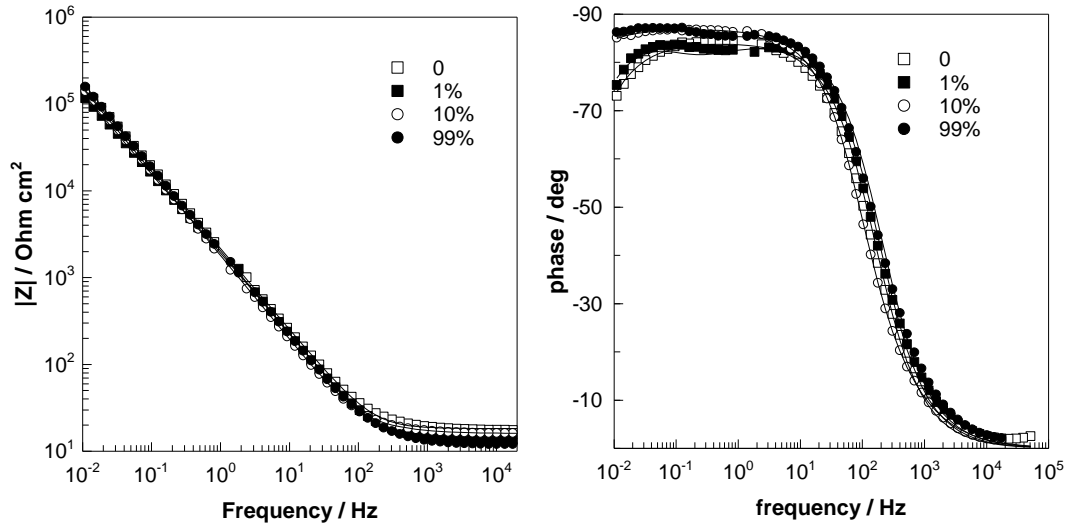


**Fig. 5** Effect of pulse duty cycle at constant frequency of 1 kHz on the impedance spectra of Ti anodes after 24 h of operation at 65 mA/40 V. Left- impedance magnitude vs. frequency, right – phase shift vs. frequency, 0 – fresh sample. Points – experiment, lines – best-fit calculation.

pulse frequency at constant duty cycle. In the phase angle vs. frequency dependences, two overlapped time constants were detected by preliminary deconvolution of the impedance spectra. The higher frequency time constant is tentatively ascribed to the charge transfer processes at the film/solution interface, whereas the time constant at lower frequencies that is characterized by a much larger value of the associated resistance would correspond to the capacitance of the surface film in parallel to the resistance of ionic transport through it.

In order to extract quantitative information concerning the influence of pulse regime on the electrochemical properties of the surface films and their interface with the electrolyte, the impedance spectra were interpreted with the following transfer function

$$Z = R_{el} + \frac{1}{j\omega C_d + R_{ct}^{-1} + \frac{1}{j\omega C_f + R_{ion}^{-1}}} \quad (3)$$

where  $R_{el}$  is the uncompensated electrolyte resistance,  $C_d$  the interfacial double layer capacitance,  $R_{ct}$  – the charge transfer resistance at the film/solution interface,  $C_f$  – the capacitance of the semiconducting surface film and  $R_{ion}$  – the ionic transport resistance through the latter. It is worth mentioning that due to the geometrical and/or energetic non-homogeneity of the surface the capacitance of the double layer was approximated with a constant-phase element (CPE) and the values of the apparent capacitance were extracted from the data using the approach of Brug et al. [14]:

$$Q_{CPE}^{-1} = C_d^{1-\alpha} (R_{el}^{-1} + R_{ct}^{-1})^{\alpha} \quad (4)$$

where  $Q_{CPE}$  and  $\alpha$  are the CPE parameters.

The best-fit calculations according to the above transfer function are presented in Fig. 4 - Fig. 5 with solid lines and demonstrate the adequacy of the model in describing the experimental data. It is worth mentioning that due to the significant overlap

of the two time constants, the values of the charge transfer resistance  $R_{ct}$  were computed with a large error and will not be commented further. Plots of the estimated values of the remaining transfer function parameters ( $C_d$ ,  $R_{ion}$  and  $C_f$ ) as depending on the operational characteristics of the pulse (duty cycle and frequency) for both anodes and cathodes that have been in service for 24 and 72 h at 65 mA are presented in Fig. 6 - Fig. 7.

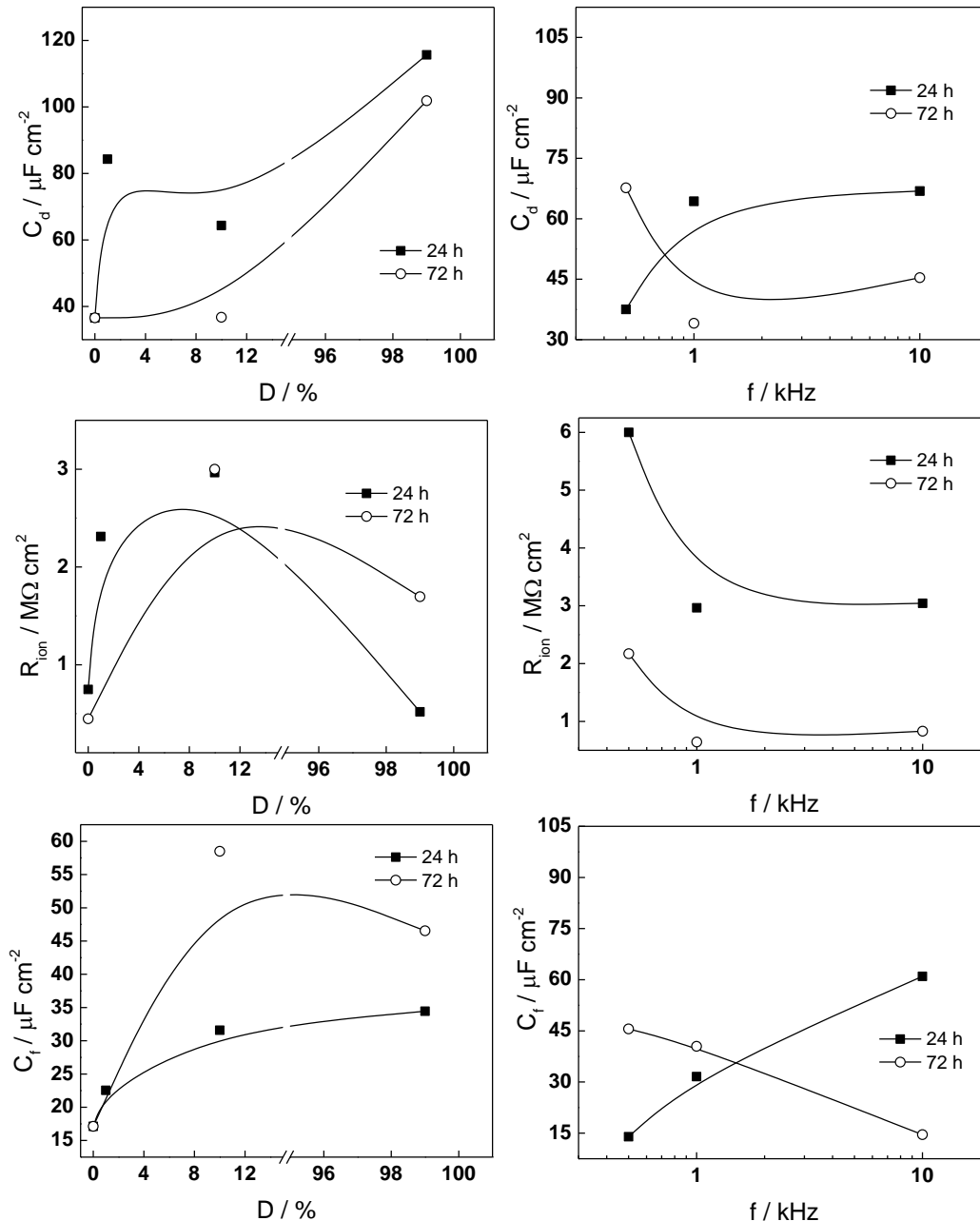


**Fig. 6** A comparison between the double layer capacitance (above), the ionic transport resistance (middle) and the surface film capacitance (below) for Ti cathodes after 24 and 72 h of operation in a pulsed regime for different duty cycles at a constant frequency of 1 kHz (left) and for different frequencies at a duty cycle of 10% (right).

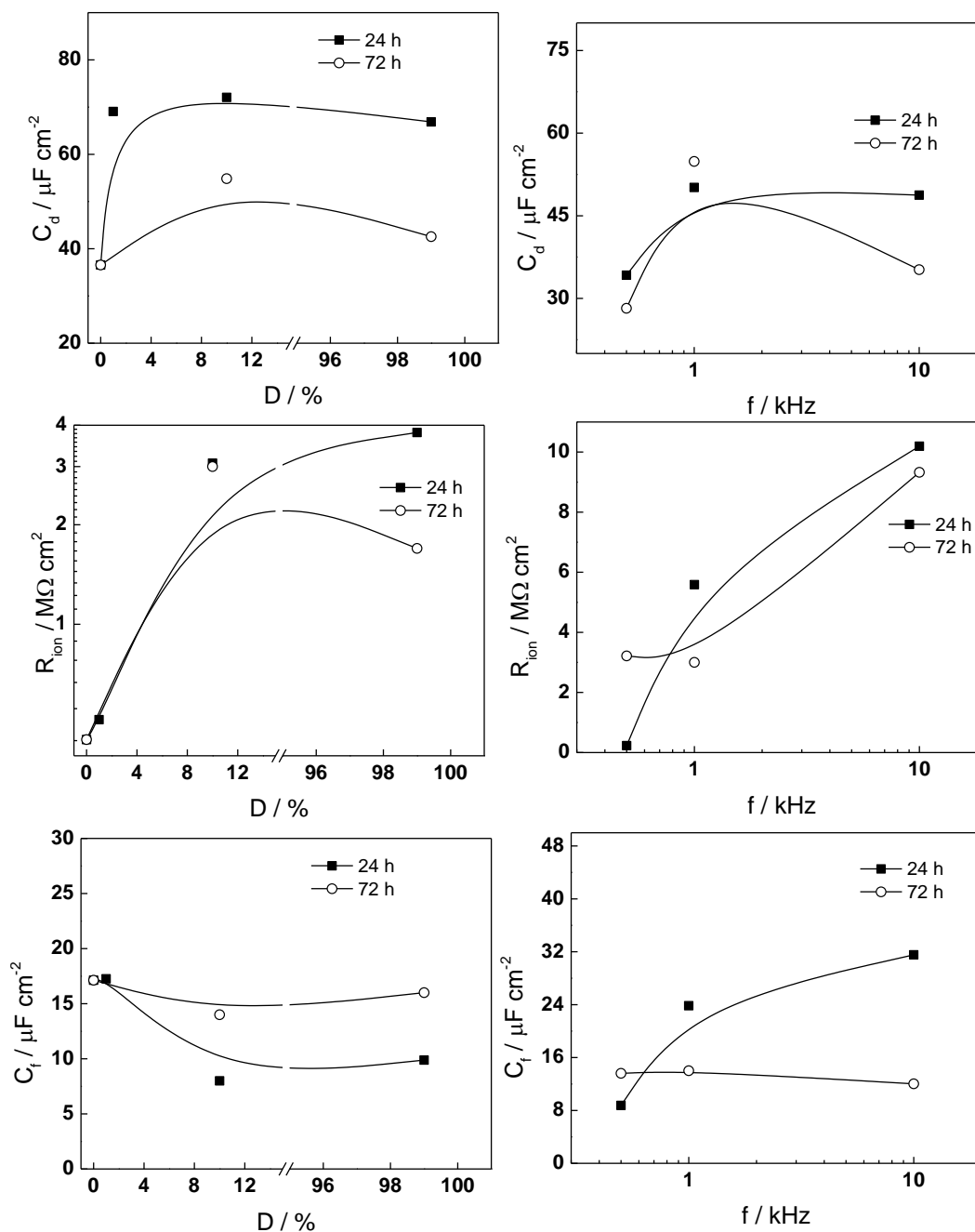


**Fig. 7** A comparison between the double layer capacitance (above), the ionic transport resistance (middle) and the surface film capacitance (below) for Ti anodes after 24 and 72 h of operation in a pulsed regime for different duty cycles at a constant frequency of 1 kHz (left) and for different frequencies at a duty cycle of 10% (right).

The double layer capacitance increases with duty cycle, indicating an increase of the geometric and/or energetic heterogeneity of the surface as a result of pulse electrolysis operation. This increase is much more pronounced for the cathodes in accordance to what we reported in a parallel study of the effect of operational conditions on cathodes made of AISI 316L stainless steel [21].

The ionic conductivity of the oxide, that can be assumed to be inversely proportional to  $R_{ion}$ , decreases significantly for anodes in comparison to

a reference sample that has not been in operation. This trend can once more be correlated to oxide growth on the Ti surface during pulse electrolysis and/or decrease of the number of defects in the oxide. It is to a certain extent corroborated by the decrease of the film capacitance  $C_f$ , although the comparatively small decrease of this parameter indicates that it most probably represents the depletion layer in the semiconducting oxide, rather than being correlated to the whole thickness of the oxide.

If we assume that the oxidation reaction at open circuit is the growth of the oxide at the metal/film interface via inward high-field assisted migration of oxygen by a vacancy mechanism, balanced by chemical film dissolution at the oxide/solution interface, then the following approximate expression can be derived for the ionic transport resistance [22]

$$R_{ion} = \frac{RTa}{4F^2 D_o' (1-\alpha) k_g} k_c e^{L/a} \quad (5)$$

where  $a$  is the half-jump distance for ion transport,  $D_o'$  is the apparent (field-dependent) diffusion coefficient,  $\alpha$  is the part of the applied potential consumed at the film/solution interface,  $k_g$  is the rate constant of generation of oxygen vacancies at the metal/film interface,  $k_c$  – the rate constant of consumption of the vacancies at the film/solution interface and  $L$  is the film thickness. According to this equation, the resistance of ionic transport is an exponential function of film thickness. Since it has been demonstrated above in relation to the effect of film thickness on the exchange current density of the redox reaction that film thickness increases with duty cycle, the exponential increase of  $R_{ion}$  with duty cycle that is detected in Fig. 7 can be understood in terms of equation (4). Of course, to quantify the effect of pulse parameters on film thickness and composition, surface analytical data are needed. In that context, further investigations of the composition of the oxide film with surface analytical techniques are underway in order to establish a quantitative correlation between surface layer composition and electrochemical properties.

## CONCLUSION

The effect of dynamic characteristics of the process on the electrical and electrochemical properties of surface films formed on Grade 2 titanium during pulse electrolysis of alkaline solutions was characterized using voltammetry and electrochemical impedance spectroscopy. A conclusion can be drawn that the combination of electrochemical and surface analytical methods employed is suitable for the characterization of the electrochemical properties of electrode materials for pulse electrolysis of water. The decrease of the electronic conductivity of the anodes as a result of operation can be understood in terms of an increase of film thickness and hence a decrease of the probability of direct tunneling through the oxide as

the rate-controlling step of the redox reaction. The increase of film thickness, however, has been estimated to be relatively small and thus most of the charge passed is consumed for water splitting and formation of hydroxygen gas mixture. The ionic transport through the anodes has been qualitatively in terms of film growth via high-field assisted inward migration of oxygen by a vacancy mechanism. Further investigations using surface analytical techniques to obtain information on the composition and structure of the surface films would enable a quantitative correlation of these characteristics with the electrical and electrochemical properties of the oxides. Such studies are underway and the results will be reported in the near future.

**Acknowledgements:** The financial support by the Bulgarian Science Fund, Ministry of Science, Youth and Education, under contract DDVU-02-99 “Pulse electrolysis as a highly efficient method for generation of hydrogen gas mixtures”(2010-2013) is gratefully acknowledged.

## REFERENCES

1. C. Yilmaz, E. Uludamar, K. Aydin, *Int. J. Hydrogen Energy*, **35**, 11366 (2010).
2. S. Bari, M. Mohammad Esmaeil, *Fuel*, **89**, 378 (2010).
3. S. Wang, C. Ji, J. Zhang, B. Zhang, *Int. J. Hydrogen Energy*, **36**, 11164 (2011).
4. S. Wang, C. Ji, B. Zhang, X. Liu, *Int. J. Hydrogen Energy*, **37**, 13209 (2012).
5. N. Shimizu, S. Hotta, T. Sekiya, O. Oda, *J. Appl. Electrochem.*, **36**, 419 (2006).
6. M. Vanags, J. Kleperis, G. Bajars, A. Lasis, *J. Phys.: Conference Ser.*, **93**, 012025 (2007).
7. M. Vanags, J. Kleperis, G. Bajars, *Int. J. Hydrogen Energy*, **36**, 1316 (2011).
8. M. Vanags, J. Kleperis, G. Bajars, *Latvian J. Phys. Tech. Sci.*, **48**, 34 (2011).
9. S.K. Mazloomi, N. Sulaiman, *Renewable and Sustainable Energy Rev.*, **16**, 4257 (2012).
10. R.M. Santilli, *Int. J. Hydrogen Energy*, **31**, 1113 (2006).
11. J.M. Calo, *Int. J. Hydrogen Energy*, **32**, 1309 (2007).
12. J.V. Kadeisvili, *Int. J. Hydrogen Energy*, **33**, 918 (2008).
13. M. B. King, *Physics Procedia*, **20**, 435 (2011).
14. <http://www.drive60mpg.com/titaniumhho.html>
15. J.W. Schultze, L. Elfental, *J. Electroanal. Chem.*, **204**, 153 (1986).
16. J.W. Schultze, V.A. Macagno, *Electrochim. Acta*, **31**, 355 (1986).
17. M. Kamrunnahar, J.E. Bao, D.D. Macdonald, *Corros. Sci.*, **47**, 3111 (2005)

18. T. P. Moffat, H. Yang, F.-R. F. Fan, A. J. Bard, *J. Electrochem. Soc.*, **139**, 3158 (1992).
19. E. McCafferty, J.P. Wightman, *Appl. Surf. Sci.*, **143**, 92 (1999).
20. G. J. Brug, A.L.G. Van Den Eeden, M. Sluyters-Rehbach, J.H. Sluyters, *J. Electroanal. Chem.*, **176**, 275 (1984).
21. D. Hristova, I. Betova, Tz. Tzvetkoff, *Int.J. Hydrogen Energy* (2013, submitted).
22. M. Bojinov, G. Fabricius, T. Laitinen, K. Mäkelä, T. Saario, G. Sundholm, *Electrochim. Acta*, **46**, 1339 (2001).

## ЙОННА И ЕЛЕКТРОННА ПРОВОДИМОСТ НА ПОВЪРХНОСТНИ ФИЛМИ ВЪРХУ ТИТАН ПО ВРЕМЕ НА ИМПУЛСНА ЕЛЕКТРОЛИЗА НА ВОДА

Д. Ст. Христова<sup>1</sup>, И. Г. Бетова<sup>2</sup>, Цв. Б. Цветков<sup>1</sup>

<sup>1</sup>Център по водородни технологии, Химико-технологичен и металургичен университет, бул. Св. Климент Охридски 8, 1756 София

<sup>2</sup>Технически университет – София, бул. Св. Климент Охридски 8, 1000 София

Постъпила на 26 февруари, 2013 г.; Коригирана на 12 април, 2012 г.

(Резюме)

Процесите на корозия и деградация на електродните материали са от решаващо значение за ефективността на импулсната електролиза и най-вероятно зависят от електричните характеристики на импулса (ток/напрежение, честота, наситеност на импулса). Целта на настоящата работа е да се изследва ефекта на тези характеристики върху електрохимичните свойства на титанови електроди. Импулсната електролиза е проведена в 6 М КОН за 24 и 72 часа с амплитуда на тока 65 mA, честоти на сигнала в интервала 0.5 – 10 kHz и наситеност на импулса между 1 и 99 %. Електрохимичните свойства на повърхностите на титановите аноди и катоди след електролиза са изследвани чрез електрохимична импедансна спектроскопия в разтвор на боратен буфер (pH 7.4) при потенциал на отворена верига, а също така и с линейна волтаметрия в подобен разтвор, съдържащ еквинормална смес от  $K_4Fe(CN)_6$  и  $K_3Fe(CN)_6$  като редокс двойка с цел изследване на електронната проводимост на повърхностните филми.

## Analytical study of the process of sulphuric acid dissolution of Waelz-clinker with Eh - pH diagrams

K. Draganova, Vl. Stefanova, P. Iliev

University of Chemistry Technology and Metallurgy 8 St. Kl. Okhridski Blvd., 1756 Sofia, Bulgaria

Received February 27, 2013; Revised May 15, 2013

A thermodynamical analysis of the sulfuric acid dissolution process into oxidation and reducing conditions of the Waelz-clinker (a waste product of zinc production) was carried out. The analytical study was executed by the help of a professional program HSC Chemistry Ver. 5.11 as the module for the calculation and construction of Eh - pH diagrams. The Fe-Cu-S-H<sub>2</sub>O and Fe-Ag-S-H<sub>2</sub>O systems which describe the dissolution of iron, copper and silver compounds (oxides and sulfides) in a sulfuric acid medium were investigated. The influence of temperature (70 and 80°C) and oxidation potential on the substance composition of the solutions was determined based on the calculated and construction Eh - pH diagrams.

**Key words:** waelz clinker, dissolution, sulfuric acid, sodium sulfite, Eh pH- diagrams.

### INTRODUCTION

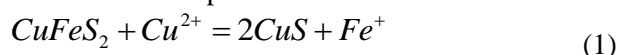
In the process of zinc production in waelz furnaces, a waste called waelz clinker is formed. It contains copper (1.92–2.0 %) and silver (128-146 g/t) in quantities comparable to those in ores which makes it a valuable raw material. The main reason of the lack of a method suitable for recovery of these metals is the high iron (36.87-37.35%) and carbon (13.55%) content in the clinker.

Besides, according to the waste product classifications, it falls within the „hazardous waste” category which requires search for a technology suitable for its treatment.

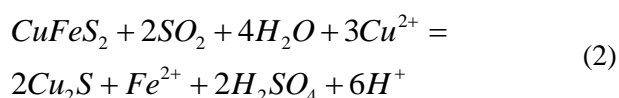
Currently, one of the main methods for clinker processing in Bulgaria is floatation which yields copper concentrate with high carbon content without, however, recovery of the silver.

In the world practice, there are a number of hydrometallurgical methods for recovery of copper and silver from lean raw materials, and quite a few research studies on the application of sulphuric-acid dissolution of copper bearing raw materials using SO<sub>2</sub> or Na<sub>2</sub>SO<sub>3</sub> as reducer were conducted over the recent years. According to a number of authors: C. Sequeira et al. [1], R. Bartlett et al. [2], E. Silvester et al. [3], W. Yuill et al. [4], G. Fuentes et al. [5] the purpose of sulphuric-acid dissolution of sulphide copper-bearing raw materials with sulphur dioxide as reducer is transformation of the more complex copper sulphides such as: chalcopyrite and bornite into the less complex sulphides chalcocite

(Cu<sub>2</sub>S), digenite (Cu<sub>1.8</sub>S) or covellite (CuS). The interaction takes place as follows:

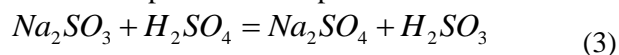


In the presence of reducer, such as sulphur dioxide, the reaction velocity is considerably increased [6]. The process can be described by the following reaction:



According to D. Collier et al. [6] SO<sub>2</sub> and Na<sub>2</sub>SO<sub>3</sub> (sodium sulphite) are the reducers most suitable for chalcopyrite and bornite. The authors explain the higher velocity of dissolution in the presence of SO<sub>2</sub> by dissolution of the hematite and clearing of the reacting surface of the sulphide-bearing minerals. According to Sohn and Wadsworth [7], the presence of SO<sub>2</sub> in the solution creates conditions for selective recovery of copper. At high concentration of Na<sub>2</sub>SO<sub>3</sub>, (for example, 150 g/l) the copper will precipitate in the form of double salt - Cu<sub>2</sub>SO<sub>3</sub>·CuSO<sub>3</sub>·2H<sub>2</sub>O [8].

In the opinion of S. I. Sobol [9], the chemical interactions taking place during dissolution of different metal sulphides with the participation of sulphur dioxide or sodium sulphite are accompanied by separation of elementary sulphur. When sodium sulphite is used, initially the reaction runs with separation of sulphurous acid:

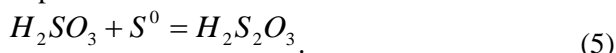


Which, upon heating, can decompose with emission of sulphur dioxide

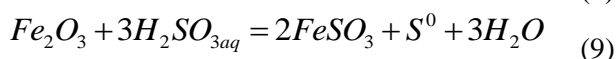
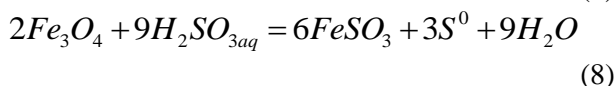
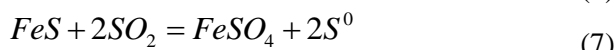
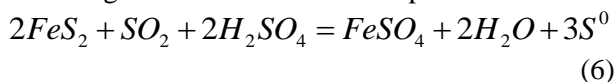
\* To whom all correspondence should be sent:  
E-mail: K333444@abv.bg



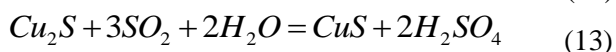
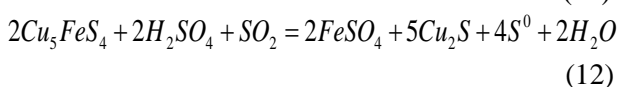
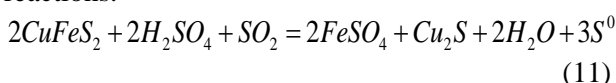
or form thiosulphate upon reaction with free sulphur



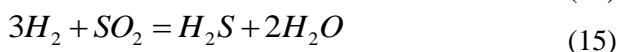
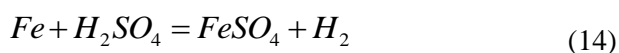
During dissolution of the iron-bearing minerals in the presence of SO<sub>2</sub> (or sulphurous acid) the following chemical reactions take place:



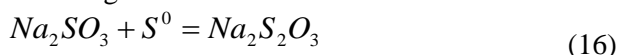
Dissolution of the copper-bearing sulphide phases according to [6] takes place through the reactions:



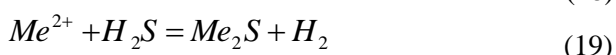
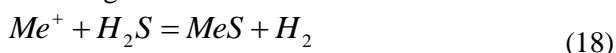
In principle, the reactions of metal sulphide dissolution in the presence of SO<sub>2</sub> do not result in formation of hydrogen sulphide. However, in the presence of a metal phase in the raw material, for example iron, in gaseous hydrogen sulphide is released in the system as a result of the following interactions:



Upon introduction of Na<sub>2</sub>SO<sub>3</sub> in the solution formation of Na<sub>2</sub>S is also possible as a result of the following reactions:



The reaction products (H<sub>2</sub>S and Na<sub>2</sub>S) sulphidize metal ions present in the solution by one of the following reactions:



Where Me<sup>2+</sup> and Me<sup>+</sup> are: Cu<sup>+</sup>, Cu<sup>2+</sup>, Ag<sup>+</sup>, Fe<sup>2+</sup>, etc.

Herein, a thermodynamic analysis of the process of sulphuric-acid dissolution in the reducing medium of waelz clinker is carried out and Eh-pH

diagrams have been built in order to assess the thermodynamic probability of execution of the reactions and stability of the elements in the Fe-Cu-S-H<sub>2</sub>O and Fe-Ag-S-H<sub>2</sub>O systems.

#### Chemical and Mineralogical Composition of Clinker

The chemical composition of waelz clinker is presented in Table 1. It is determined by means of atomic adsorption analysis.

**Table 1.** Chemical composition of the waelz-clinker

Fe, %	Cu, %	Ag g/t	S, %	C, %	Others
36.87	1.92	128	4.33	13.55	~43.23

Beside the elements indicated in the table in the column „others”, the total content of Pb, Zn, Mn, As below 1%, NaO, K<sub>2</sub>O, CaO, MgO, SiO<sub>2</sub>, Al<sub>2</sub>O<sub>3</sub> etc., is indicated.

The mineralogical studies of the clinker carried out show that the main minerals in the clinker are magnetite, hematite, jarosite, siderite, metal iron, pyrite, bornite, chalcocite, arsenic pyrite, pyrrhotite, galenite, sphalerite (10-15 %), oxides; calcium, iron, lead, zinc and copper sulphates and carbonates (5 %), aluminum silicates of potassium, sodium, magnesium, iron, lead and copper (20-25 %) and carbon (15-20 %).

The phase analyses of iron and copper in the clinker show that ~28 % of the iron is in metal phase, ~ 58 % as FeO and the rest is in the form of Fe<sub>2</sub>O<sub>3</sub> and Fe<sub>3</sub>O<sub>4</sub>. The copper is found mainly in a sulphide phase (~ 80 %). The rest of the copper is distributed between the oxide (~ 15 %) and metal (~ 5 %) phases. Silver in the clinker is found mainly in the form of sulphide.

Therefore, the process of dissolution of iron, copper and silver compounds (oxides and sulphides) in a sulphur-acidic medium with the participation of sulphur dioxide or sodium sulphite as reducer can be described by the systems Fe-Cu-S-H<sub>2</sub>O and Fe-Ag-S-H<sub>2</sub>O.

#### Analytical Investigation of the Process of Waelz Clinker Dissolution

The analytical investigation is carried out by means of a professional code HSC Chemistry Ver. 5.11. Two modules are used: Reaction Equation and Eh-pH diagrams.

#### Computation of Gibbs function

On the basis of the literature study carried out as above, the possible reactions in both investigated systems were divided in two main groups: reactions with participation of reducer and reactions with formation of copper and silver sulphides. The

**Table 2.** Computed values of the Gibbs function and equilibrium constant of the possible chemical interactions during reducing dissolution of the clinker

Reactions	T=25°C		T=80°C	
	$\Delta G$ , kJ	LogK	$\Delta G$ , kJ	LogK
<b>A. Reactions with participation of reducer</b>				
$\text{Na}_2\text{SO}_3 + \text{H}_2\text{SO}_4 = \text{Na}_2\text{SO}_4 + \text{H}_2\text{SO}_3(\text{a})$	-111,33	19.51	-115,05	17,02
$\text{Fe} + \text{H}_2\text{SO}_4 = \text{FeSO}_4 + \text{H}_2(\text{g})$	-135.01	23.65	-138,57	20,49
$\text{SO}_2(\text{g}) + 3\text{H}_2(\text{g}) = \text{H}_2\text{S}(\text{g}) + 2\text{H}_2\text{O}$	-207.52	36.37	-191,58	28,34
$2\text{FeS}_2 + \text{SO}_2(\text{g}) + 2\text{H}_2\text{SO}_4 = 2\text{FeSO}_4 + 2\text{H}_2\text{O} + 5\text{S}^0$	-124,07	21.74	-117,27	17,3
$\text{FeS} + 2\text{SO}_2(\text{g}) = \text{FeSO}_4 + 2\text{S}$	-122.74	21.52	-102,36	15,14
$2\text{CuFeS}_2 + 2\text{H}_2\text{SO}_4 + \text{SO}_2(\text{g}) = 2\text{FeSO}_4 + \text{Cu}_2\text{S} + 2\text{H}_2\text{O} + 4\text{S}^0$	-149.69	26,24	-139,52	26,84
$2\text{Cu}_5\text{FeS}_4 + 2\text{H}_2\text{SO}_4 + \text{SO}_2(\text{g}) = 2\text{FeSO}_4 + 5\text{Cu}_2\text{S} + 4\text{S}^0 + 2\text{H}_2\text{O}$	-91,45	16,03	-80,79	11,95
$\text{Cu}_2\text{S} + 3\text{SO}_2(\text{g}) + 2\text{H}_2\text{O} = 2\text{CuS} + 2\text{H}_2\text{SO}_4$	-25.65	4.51	-4,69	-0,69
$\text{Na}_2\text{SO}_3 + \text{S}^0 = \text{Na}_2\text{S}_2\text{O}_3$	-3.61	2.64	-3.306	2.046
$\text{Na}_2\text{S}_2\text{O}_3 = 3/4\text{Na}_2\text{S} + 1/4\text{Na}_2\text{SO}_4 + \text{SO}_2(\text{g})$	138.12	-24.20	126.99	-18.78
<b>B. Reactions of sulfide formation</b>				
$\text{CuFeS}_2 + \text{Cu}^{+2} = 2\text{CuS} + \text{Fe}^{+2}$	-73,53	12.89	-73,36	10,85
$2\text{Cu}^{2+} + \text{H}_2\text{S}(\text{a}) + 4\text{e}^- = \text{Cu}_2\text{S} + \text{H}_2(\text{g})$	-189,72	33.065	-191,44	28.32
$2\text{Ag}^+ + \text{H}_2\text{S}(\text{a}) + 2\text{e}^- = \text{Ag}_2\text{S} + \text{H}_2(\text{g})$	-166,10	29.08	-158,12	23.39

thermodynamic probability for the possible chemical interactions to take place is assessed in a temperature range from 25 to 80 °C at atmospheric pressure. The computed values of the Gibbs function and equilibrium constants are given in Table 2.

The analysis of results obtained shows that the process of clinker dissolution in a sulphuric acid medium in the presence of reducer ( $\text{SO}_2$  or  $\text{Na}_2\text{SO}_3$ ) will take place with formation of elementary sulphur and sulphides.

The reaction of hydrogen sulphide generation from  $\text{SO}_2$  and  $\text{H}_2$  present in the system has the highest value of the Gibbs function ( $\Delta G = -208.99$  kJ). The latter will form upon dissolution of the metal iron. The reactions of sulphidization of the copper ions ( $\Delta G = -189,72$  kJ) and silver ions ( $\Delta G = -166,10$  kJ) present in the solution are also thermodynamically probable.

The low value of the Gibbs function of the reaction with formation of sodium thiosulphate and its decomposition to  $\text{Na}_2\text{S}$  is thermodynamically impossible in the conditions of the investigation. In all interactions with the participation of  $\text{SO}_2$  accompanied by temperature rise the values of  $\Delta G$  and  $\text{LogK}$  negligibly decrease.

#### Computation and building of Eh-pH diagrams

A module of the code HSC Chemistry – Eh-pH Diagrams is used to determine the stability ranges of ionic and nonionic forms of the substances Fe-Cu-S- $\text{H}_2\text{O}$  and Fe-Ag-S- $\text{H}_2\text{O}$  present in the studied systems. In the process of building the diagrams, the molar composition of the solution was taken into consideration. The computations were carried

out for molar concentrations of the elements present expressed as mol/kg $\text{H}_2\text{O}$ : 0.175 Na, 1.727 S, 0.66 Fe, 0.030 Cu and 0.000186 Ag. They correspond to the molar composition obtained upon dissolution of 20 g clinker (Table 1) in 100 ml solution with concentration 150 g/L  $\text{H}_2\text{SO}_4$  and 75 g/L  $\text{Na}_2\text{SO}_3$ . The analysis is carried out with serial multiplication of the diagrams: Na-S- $\text{H}_2\text{O}$ ; Na-S-Fe- $\text{H}_2\text{O}$ , Na-S-Cu- $\text{H}_2\text{O}$ , Na-S-Ag- $\text{H}_2\text{O}$ , Na-S-Fe-Cu- $\text{H}_2\text{O}$  and Na-S-Fe-S- $\text{H}_2\text{O}$ .

The species of ionic and nonionic forms of the substances present in the solution and the Gibbs function used in building of the respective diagrams are presented in Table 3.

Figure 1 presents a diagram of Na-S- $\text{H}_2\text{O}$  at temperature 25 and 80°C.

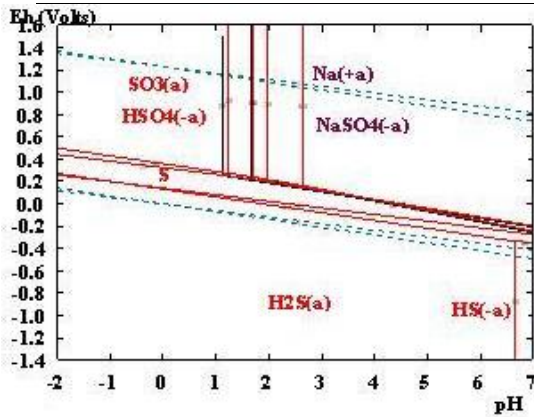
It can be seen that with rising of the temperature to 80°C the stability range of sulphur and of the  $\text{HSO}_4^-$  and  $\text{NaSO}_4^-$  ions negligibly expands in the direction of a higher potential and lower acidity.

Figures 2, 3 and 4 present the triple diagrams Na-S-Fe- $\text{H}_2\text{O}$ , Na-S-Cu- $\text{H}_2\text{O}$  and Na-S-Ag- $\text{H}_2\text{O}$  built for 80°C.

The analysis of the Eh-pH diagrams shows that in a highly acidic medium and low reduction potential, the stable phases are  $\text{FeS}_2$ ,  $\text{CuS}$ ,  $\text{Cu}_2\text{S}$  and  $\text{Ag}_2\text{S}$ . Upon reduction of the solution's acidity the stability of these phases shifts towards lower potentials which, in practice, means establishment of a highly reducing medium. Therefore, upon dissolution of the clinker at low reduction potential, one can expect, besides the  $\text{Fe}^{2+}$  ions, the presence of insoluble  $\text{FeS}_2$  as well.

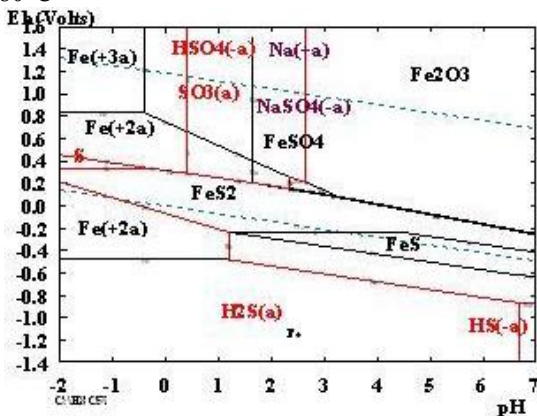
**Table 3.** Types of ionic and nonionic forms in the systems Na-Cu-Fe-S-H<sub>2</sub>O and Na-Ag-Fe-S-H<sub>2</sub>O and free energy of their formation

Species	$\Delta G^0_{298}$ (kJ/mol)	Species	$\Delta G^0_{298}$ (kJ/mol)	Species	$\Delta G^0_{298}$ (kJ/mol)
<b>Copper</b>		<b>Iron</b>		<b>Silver</b>	
Cu	0.000	Fe	0.000	Ag	0.000
Cu <sup>2+</sup>	65.52	Fe <sup>3+</sup>	-10.96	Ag <sup>2+</sup>	268.63
Cu <sup>+</sup>	45.76	Fe <sup>2+</sup>	-91.82	Ag <sup>+</sup>	71.7
CuFeS <sub>2</sub>	-190.53	FeO	-241.79	Ag <sub>2</sub> O	-7.50
Cu <sub>5</sub> FeS <sub>4</sub>	-394.85	Fe <sub>2</sub> O <sub>3</sub>	-725.99	Ag <sub>2</sub> S	-41.79
CuO	-123.00	FeS	-102.04	Ag <sub>2</sub> SO <sub>3</sub>	-396.19
Cu <sub>2</sub> O	-143.65	FeS <sub>2</sub>	-156.66	Ag <sub>2</sub> SO <sub>4</sub>	-600.29
CuS	-56.73	FeSO <sub>4</sub>	-805.69	AgSO <sub>4</sub> <sup>-</sup>	-648.92
Cu <sub>2</sub> S	-87.48				
CuSO <sub>4</sub>	-640.61				
Cu <sub>2</sub> SO <sub>4</sub>	-636.51				
<b>Sulfur</b>		<b>Sodium</b>		<b>Sulfuric acid</b>	
S	0.000	Na	0.000	H <sub>2</sub> SO <sub>4</sub>	
HS <sup>-</sup>	17.93	Na <sup>+</sup>	266.03	H <sub>2</sub> SO <sub>3</sub> (a)	-667.18
H <sub>2</sub> S(a)	-27.09	Na <sub>2</sub> S	-352.53	H <sub>2</sub> S <sub>2</sub> O <sub>3</sub> (a)	-524.29
SO <sub>2</sub> (a)	-297.74	Na <sub>2</sub> SO <sub>3</sub>	-990.26	H <sub>2</sub> S <sub>2</sub> O <sub>4</sub> (a)	-518.24
SO <sub>3</sub> (a)	-505.03	Na <sub>2</sub> SO <sub>4</sub>	-1248.22		-595.17
SO <sub>3</sub> <sup>2-</sup>	-457.41	NaSO <sub>4</sub> <sup>-</sup>	-982.96		
SO <sub>4</sub> <sup>2-</sup>	-712.25				



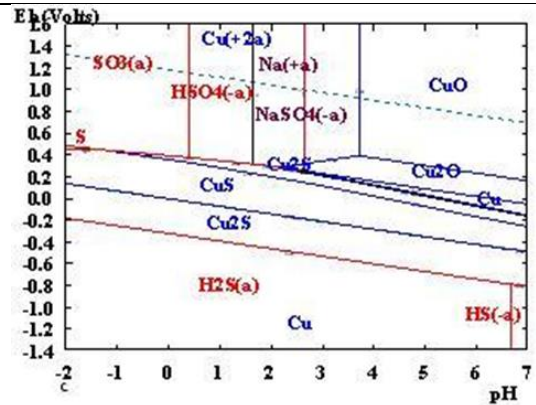
Elements	Molality	Pressure
Na	1.750E-1	1.000E+00
S	1.727E+00	1.000E+00

**Fig. 1.** Eh-pH diagram of the system Na-S-H<sub>2</sub>O at 25 and 80°C



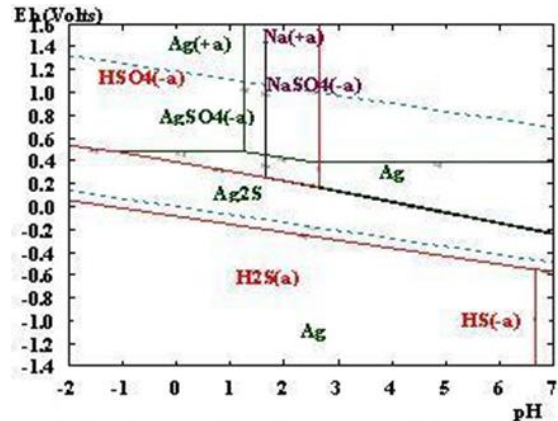
Elements	Molality	Pressure
Na	1.750E-01	1.000E+00
Fe	6.600E-01	1.000E+00
S	1.727E+00	1.000E+00

**Fig. 2.** Eh-pH diagram of the system Na-Fe-S-H<sub>2</sub>O at 80°C



Elements	Molality	Pressure
Na	1.750E-01	1.000E+00
Cu	3.020E-02	1.000E+00
S	1.727E+00	1.000E+00

**Fig. 3.** Eh-pH diagram of the system Na-Cu-S-H<sub>2</sub>O at 80°C



Elements	Molality	Pressure
Na	1.750E-01	1.000E+00
Ag	1.860E-04	1.000E+00
S	1.727E+00	1.000E+00

**Fig. 4.** Eh-pH diagram of the system Na-Ag-S-H<sub>2</sub>O at 80°C

Figures 5 and 6 present Eh-pH summary diagrams of the systems Na-Cu-Fe-S-H<sub>2</sub>O and Na-Ag-Fe-S-H<sub>2</sub>O at a temperature of 80°C.

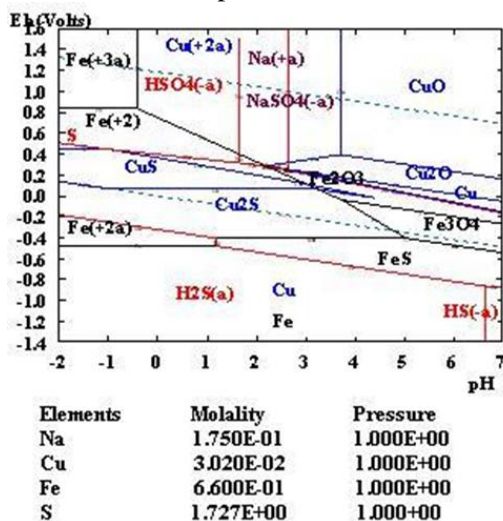


Fig. 5. Eh-pH diagram of the system Na-Cu-Fe-S-H<sub>2</sub>O at 80°C

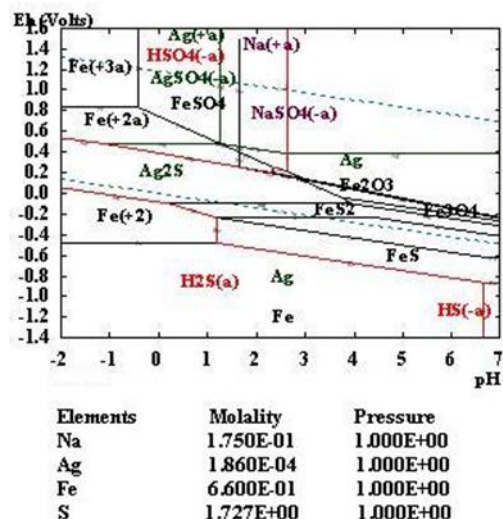


Fig. 6. Eh-pH diagram of the system Na-Ag-Fe-S-H<sub>2</sub>O at 80°C

The diagrams indicate that at initial concentration of H<sub>2</sub>SO<sub>4</sub> – 150 g/l, i.e. high acidity (pH ~ -1.5), the simple sulphides of copper and silver are stable phases in both systems. The electrochemical potentials of the stability range of copper sulphides vary as follows: of CuS from 0.1V to 0.43V, and of Cu<sub>2</sub>S from 0.2V to 0.12V. The stability range of Ag<sub>2</sub>S is at a potential from -0,1V to 0.55V. At the same pH of the solution the stable phase of iron are the ions of Fe<sup>2+</sup> (-0,52÷0.82V).

## CONCLUSION

On the basis of computed values of the Gibbs function, a thermodynamic assessment of the possible chemical interactions taking place during dissolution of the waelz clinker in sulphuric acid in the presence of reducer (Na<sub>2</sub>SO<sub>3</sub>) is made. It is determined the raise of temperature (from 25 to 80°C) has a negligible effect on the investigated reactions.

The analysis of the stability ranges of ionic and nonionic forms in the systems Na-Cu-Fe-S-H<sub>2</sub>O and Na-Ag-Fe-S-H<sub>2</sub>O shows that the process of waelz clinker dissolution in a highly acidic medium (pH ~ -1.5) in the presence of sodium sulphite reducer (0.3 mol/L) will take place with formation of copper and silver sulphides.

## REFERENCES

1. C.Sequeira, D.Santos, Y. Chen, G. Anastassakis, *Hydrometallurgy*, **92** (3–4), 135 (2008).
2. R. Bartlett, *Metall. Trans B: Process Metallurgy*, **23** (3), 241 (1992).
3. E. Silvester, F. Grieser, T. Healy, D. Meisel, J. Sullivan., *Journal of the Chemical, Society Faraday Transactions*, **90** (21), 3301 (1994).
4. W. Yuill, B. Krebs, D. Willson, R. Armstrong, 1989, Redox beneficiation of complex sulfide ores for froth flotation. Canadian US Patent 1258,181, August 8, (1989).
5. G. Fuentes, J. Vinals, O. Herreros., *Hydrometallurgy*, **95** (1–2), 104(2009).
6. D. Collier, R. Ring, B. Wedderburn, K. Ehrig, B. Day, C. Wroblewski, P. Wigley, A. Manis, Redox treatment with acidic leaching to upgrade the chalcopryrite copper-ore concentrate by replacement of iron. PCT 2004106561, December 9, 2004.
7. H. Sohn, M. Wadsworth, *Journal of Metals*, **32** (11), 18(1980).
8. A. Fischmann, D. Dixon, “Upgrading of a chalcopryrite concentrate by reaction with copper(II) and sulfite – Unexpected formation of Chevrel’s salt, Cu<sub>2</sub>SO<sub>3</sub>.CuSO<sub>3</sub>.2H<sub>2</sub>O”, *Min. Eng.*, **23**, 746 (2010).
9. С.И.Соболь, Т.М.Фраш, Сернистый ангидрид в автоклавной технологии переработки сульфидного сырья, *Цветные металлы*, **2**, 14 (1974)

## **АНАЛИТИЧНО ИЗЛЕДВАНЕ НА ПРОЦЕСА НА РАЗТВАРЯНЕ НА ВЕЛЦ-КЛИНКЕР В СЯРНА КИСЕЛИНА С ПОМОЩТА НА Eh – pH ДИАГРАМИ**

К. Драганова, Вл. Стефанова, П. Илиев

*Химико-технологичен и металургичен университет, бул. Св. Климент Охридски 8, 1756 София*

Постъпила на 27. 02. 2013 г., приета за печат на 15. 05. 2013 г.

(Резюме)

Проведен е термодинамичен анализ на процеса на разтваряне на велц-клинкер (отпадъчен продукт от производството на цинк) в сярна киселина. Аналитичното изследване е реализирано с помощта на професионална програма HSC Chemistry вер. 5.11, като модул за изчисляване и построяване на Eh - pH диаграми. Изследвани са системите Fe-Cu-S-H<sub>2</sub>O и Fe-Ag-S-H<sub>2</sub>O, които описват разтварянето на железни, медни и сребърни съединения (оксиди и сулфиди) в сярно-кисела среда. Влиянието на температурата (70 и 80 °C) и окислителния потенциал върху състава на разтворите е определен на основа на изчислените и построени Eh - pH диаграми.

## Anodic oxidation mechanism of aluminum alloys in a sulfate-fluoride electrolyte

Ch.A. Girginov\*, M.S. Bojinov

Department of Physical Chemistry, University of Chemical Technology and Metallurgy, 1756 Sofia, Bulgaria

Received February 28, 2013; Revised March 21, 2013

In recent years, fluoride containing electrolytes are used for the formation of porous structures on valve metals such as Ti, Nb, W, Ta and alloys thereof. The presence of fluoride ions allows the growth of nanoporous/nanotubular templates with well-defined structures. Very recently neutral sulfate-fluoride solutions have been successfully used to form nanoporous films on Al as well. As a continuation of this work, the present study reports on the initial stages of growth of porous anodic films on two Al alloys in fluoride-containing electrolytes by voltammetry and electrochemical impedance spectroscopy. A kinetic model based on the surface charge approach was employed to fit the impedance spectra and to estimate the main transport parameters of the oxide formation and dissolution process as depending on applied potential and alloy type.

**Key words:** aluminium alloy, sulfate-fluoride electrolyte, nanoporous alumina, electrochemical impedance spectroscopy, surface charge approach

### INTRODUCTION

In recent years, there has been a growing interest towards the electrochemical formation of nanoporous and nanotubular structures on a number of valve metals, including Al and its alloys [1-9]. Nanoporous anodic films on aluminum and its alloys allow the incorporation of metallic or oxide nanoparticles within their pores, resulting in the production of new functional nanomaterials. These materials find increasing application as sensors, catalysts, electrodes for fuel cells and batteries with enhanced photo-catalytic and electro catalytic activity.

Neutral fluoride-containing electrolytes are widely used for the formation of porous structures on Ti, Nb, W, Ta, Zr, as well as on Al [10-13]. In that respect, the present paper aims at investigating the initial stages of nanoporous alumina formation in a neutral fluoride-containing electrolyte. First, results from electrochemical measurements (cyclic voltammetry, chronoamperometry and electrochemical impedance spectroscopy) are reported and discussed in view of the parallel processes of alumina formation and dissolution of the substrate through the forming oxide. Second, the surface charge approach proposed earlier by some of us [14] is adapted to the aluminum/oxide/electrolyte system and by fitting EIS data to the transfer function of the model, the main transport parameters of the model are estimated as depending on applied potential and alloy type.

### EXPERIMENTAL

The electrodes (4 cm<sup>2</sup>) were cut from pure aluminum (99.999%) sheets and two aluminum alloys: 8006 (97.90% Al, 0.25% Si, 1.44% Fe, and 0.37% Mn) and 8011 (98.55% Al, 0.66% Si, 0.70% Fe, and 0.06% Mn). The specimens were then degreased and electro polished in a phosphoric-chromic acid electrolyte (210 cm<sup>3</sup> H<sub>2</sub>O, 40 g CrO<sub>3</sub>, 450 g 85 % H<sub>3</sub>PO<sub>4</sub>, 150 g 96 % H<sub>2</sub>SO<sub>4</sub>) at 80°C and by constant anodic current density of 0.2 – 0.3 A cm<sup>-2</sup> for ca. 3 min. Finally, they were rinsed with bi-distilled water and dried at 40°C in air. Prior to the experiments, the electrodes were brightened in an aqueous solution (1.8% CrO<sub>3</sub> and 7% H<sub>3</sub>PO<sub>4</sub>) at 75°C for 3 minutes and rinsed with bi-distilled water.

The electrochemical measurements were carried out at constant temperature (20±1 °C) in a three-electrode cell featuring a Pt-mesh counter electrode, situated symmetrically around the working electrode, and a Ag/AgCl/3M KCl reference electrode. An electrolyte with a composition of 0.5M (NH<sub>4</sub>)<sub>2</sub>SO<sub>4</sub> + 0.075M NH<sub>4</sub>F, prepared from analytical grade chemicals and bi-distilled water, was employed. Electrochemical measurements were carried out with an Autolab PGSTAT 30 with a FRA2 module driven by GPES and FRA software (Eco Chemie, The Netherlands). Current density vs. time dependencies were registered by 1 h of polarization at each applied potential (-1.2 V to 5.0 V). After reaching a constant value of the current density at a given potential, electrochemical impedance spectra were measured in the frequency

\* To whom all correspondence should be sent:  
E-mail: christian.girginov@gmail.com

range (10 mHz to 10 kHz) with an amplitude of 10 mV of the superimposed AC signal (rms). Fitting of the impedance spectra to equivalent circuits has been performed using ZView software (Scribner).

## RESULTS AND DISCUSSION

### Current vs. potential curves

The steady-state current-potential curves for the studied alloy types compared to pure Al (Fig. 1) suggest several process stages:

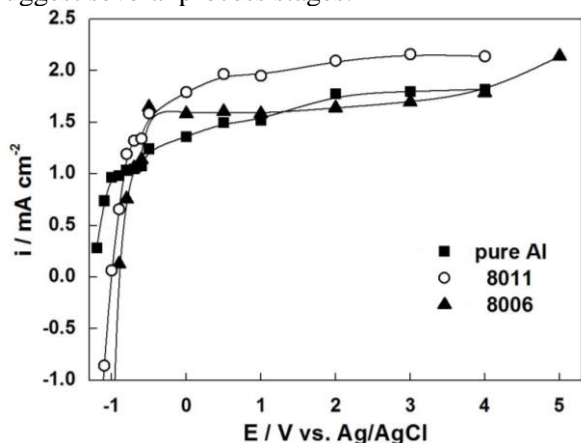


**Fig. 1** Current vs. potential curves for pure Al and the two studied alloys in sulfate-fluoride electrolyte

- i. Quasi-exponential increase of the current (-1.2/-0.9 V) due to dissolution of Al (and other alloying elements) superimposed to hydrogen evolution
- ii. Much slower increase of the current (-1.0/0.0 V) that can be associated with barrier layer formation (passivation)

iii. At ca. 0-0.5 V, a current plateau is reached, indicating that chemical dissolution of the oxide is rate determining. At still higher potentials, there is some indication of current increase, especially for the 8006 alloy.

The obtained results for the three alloy types demonstrate that the current densities vs. potential dependences are qualitatively similar. At the most negative potentials, hydrogen evolution predominates over Al dissolution for both alloys, which can be due to preferential reduction of water on secondary Si, Fe and Mn-containing phases. On the other hand, the higher current density in the passive range registered for 8011 Al alloy was apparently due to the greater amount of the alloying element Si which is actively complexed by fluoride ions.

### Impedance spectra

Impedance spectra have been recorded in the range of potentials -1.2 to 5.0 V. Typical spectra at several potentials as depending on the type of material are shown in Fig. 2-Fig.4.

The spectra consist of three time constants: high-frequency capacitive, intermediate -frequency pseudo-inductive and a further low frequency capacitive. These time constants can be interpreted as a first approximation by taking into account the migration of main current carriers (probably oxygen vacancies) and recombination of oppositely charged current carriers. The capacitive branch detected at lowest frequencies can be interpreted by a thickness modulation at a constant potential

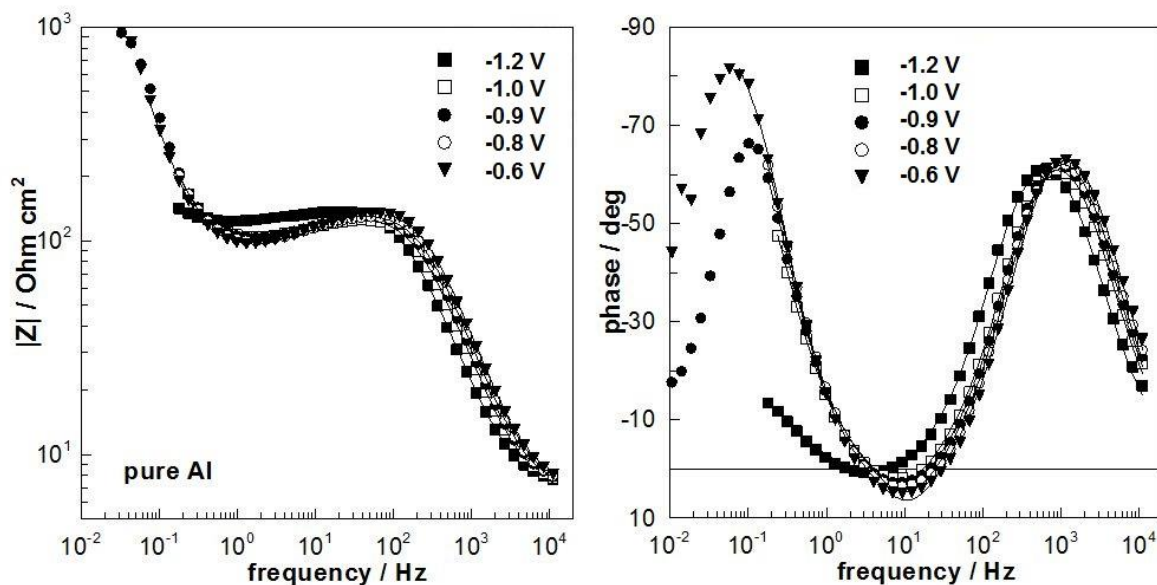


**Fig. 2** Electrochemical impedance spectra of pure Al in the range of potentials -1.2 to -0.6 V. Left-impedance magnitude vs. frequency, right – phase angle vs. frequency. Points – experimental data, solid lines – best-fit calculation.

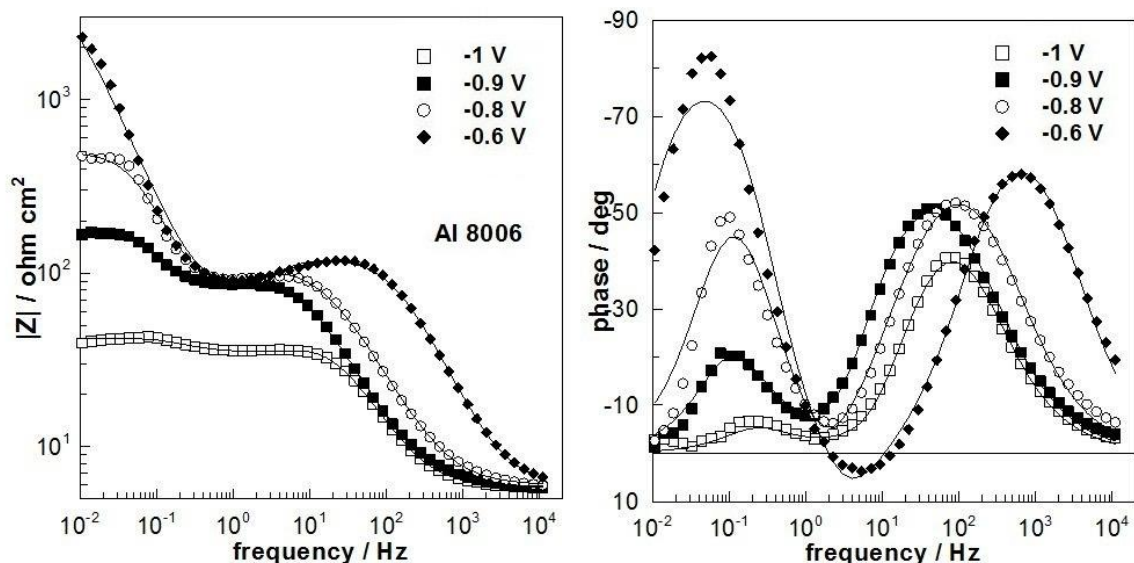


**Fig. 3** Electrochemical impedance spectra of 8006 alloy in the range of potentials -1.2 to -0.6 V. Left-impedance magnitude vs. frequency, right – phase angle vs. frequency. Points – experimental data, solid lines – best-fit calculation.

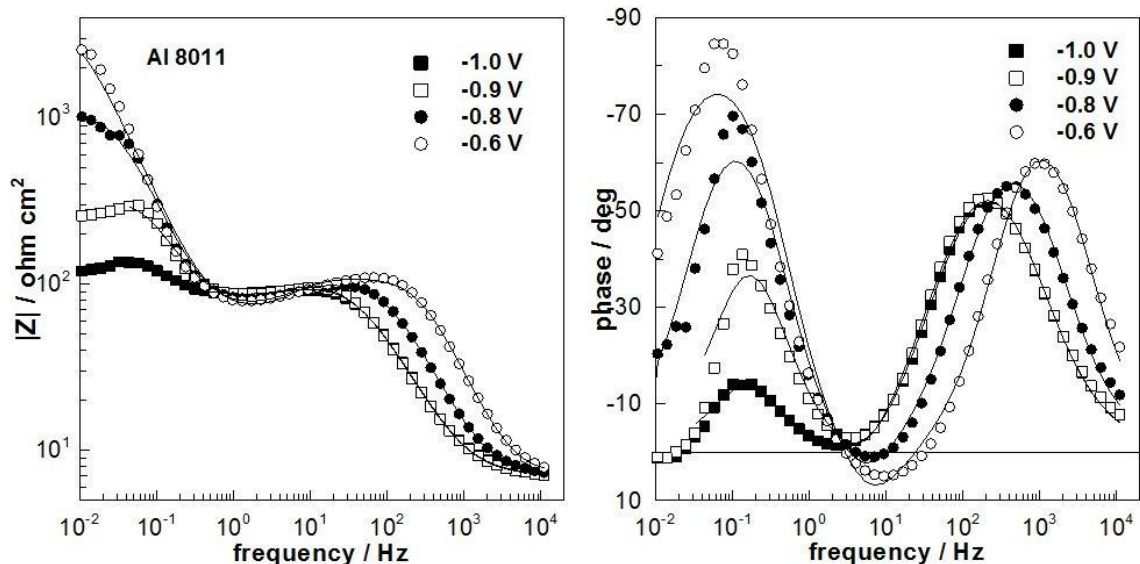


**Fig. 4** Electrochemical impedance spectra of 8011 alloy in the range of potentials -1.2 to -0.6 V. Left-impedance magnitude vs. frequency, right – phase angle vs. frequency. Points – experimental data, solid lines – best-fit calculation.

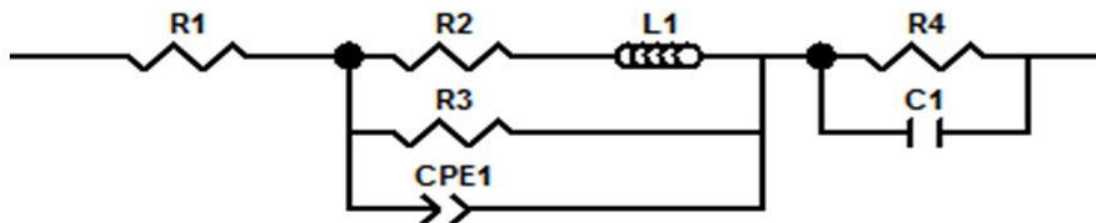


**Fig. 5** Equivalent circuit according to the surface charge approach [14].  $R_1$  – electrolyte resistance,  $R_2$  – surface charge resistance,  $L_1$  – surface charge pseudo-inductance,  $R_3$  – ion migration resistance,  $CPE_1$  – oxide capacitance generalized in the form of a constant phase element,  $R_4$  – charge transfer resistance at the film/solution interface,  $C_1$  – faradaic and/or adsorption pseudo-capacitance.

due to the ac signal or by slow adsorption of some intermediate species of the overall reaction. Thus the obtained spectra can be compared with an appropriate equivalent circuit [14] (Fig. 5). Fits to this equivalent circuit are presented in Fig.2-4 with solid lines and illustrate the ability of this model to reproduce the data for all the studied materials. The parameters of the equivalent circuit for both alloys and pure aluminum are determined for all applied potentials.

At this stage of the investigation, main attention is paid to the parameters associated with film growth. According to the surface charge approach [14], the following dependences of the parameters on the applied potential (E) and current density (i) are predicted:

$$R_3 i = (RT / 2FaE_F) E$$

$$R_2 i = [(1-\alpha) / \alpha] (RT / 2FaE_F) E$$

$$L_1 i^2 = [(1-\alpha) / \alpha] (RT / 2FaSE_F) E$$

where E is the applied potential, a is the half-jump distance (cm), EF - field strength in the oxide (V

cm-1),  $\alpha$  - part of the applied potential consumed at the oxide/solution interface as opposed to film bulk and S - capture cross-section for a point defect (cm<sup>2</sup> C-1). In addition, for a quasi-dielectric oxide (i.e. a total depletion of the film with electronic charge carriers) the high-frequency film capacitance is given by

$$C_b = \epsilon\epsilon_0 E_F / (1-\alpha) E$$

The film capacitance was estimated from the CPE element in Fig.5 by using the formula proposed by Brug et al. [15].

The values of C<sub>b</sub>, R<sub>3</sub>i, R<sub>2</sub>i and L<sub>1</sub>i<sup>2</sup> as depending on the applied potential are presented in Fig. 6.

All the dependences in Fig. 6 are linear in the range of potentials -0.5 to 5.0 V, further supporting the validity of the model. At lower potentials, a more complex interplay between film growth and dissolution is observed for the alloys. From the obtained linear dependences, the main transport parameters of oxide growth are estimated and collected in Table 1 as depending on alloy composition.

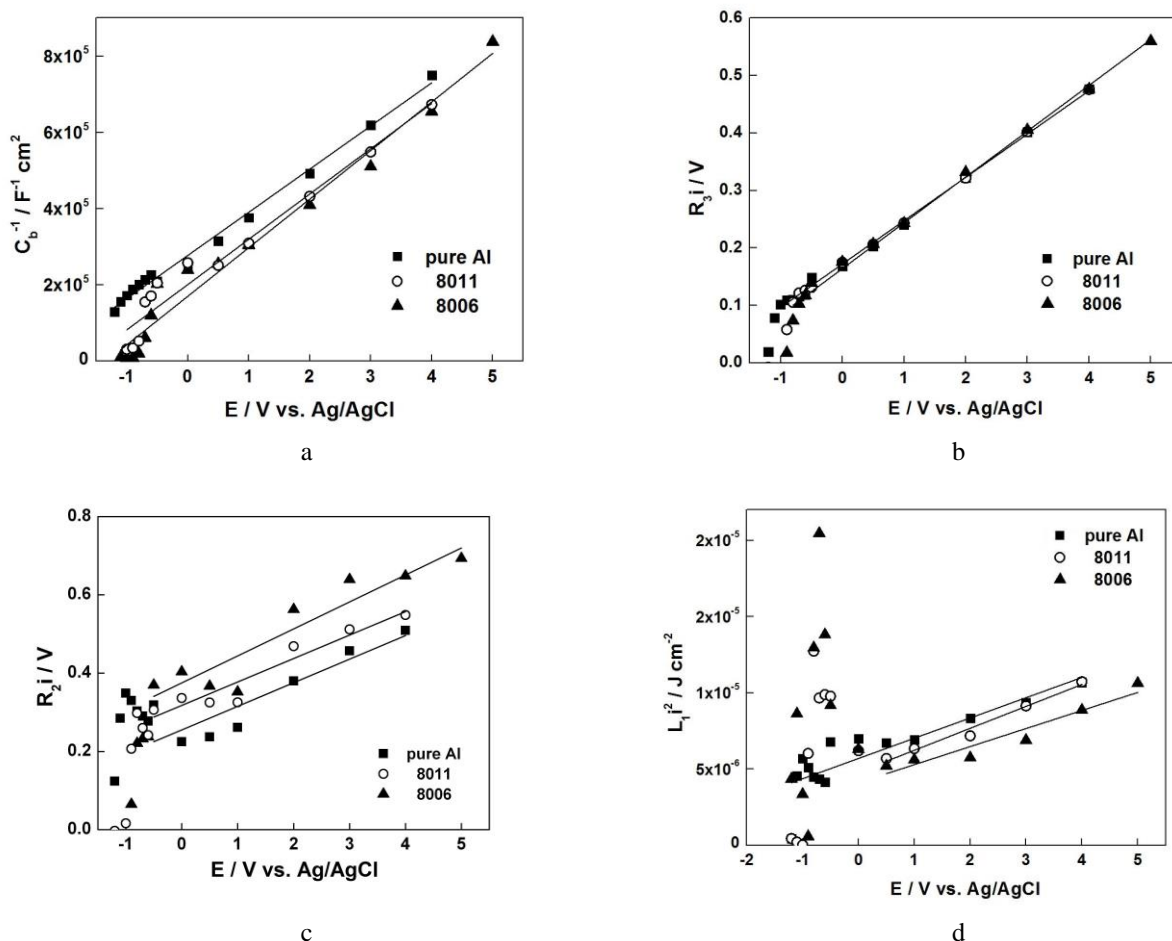


**Fig. 6** Dependences of the equivalent circuit parameters associated with film growth and dissolution on applied potential

**Table 1.** Transport parameters estimated from the fitting of the impedance data to the model equations. A value of 8.9 was adopted for the dielectric constant of the oxide.

Material	$\alpha$	$E_F / \text{MV cm}^{-1}$	$(1-\alpha) E_F^{-1} / \text{nm V}^{-1}$	$a / \text{nm}$	$S / \text{cm}^2 \text{mC}^{-1}$
Pure Al	0.51	5.46	0.90	0.31	58.7
8006	0.44	5.91	0.94	0.27	53.1
8011	0.49	5.07	1.01	0.31	52.4

The values of the parameters are only slightly dependent on alloy composition and exhibit values in agreement with those recently estimated for the anodic oxides on Al in sulfuric acid-oxalic acid mixtures using fitting of EIS data by the surface charge approach [16]. In particular, the anodizing ratio is very close to that usually reported for sulfuric acid anodizing [17]. The main differences between the alloys and pure Al are in the parameter S characterizing to the formation of negative surface charge at the film/solution interface, which in turn is related to dissolution of the alloying elements. In order to correlate this to the properties of the oxide formed on the alloys, additional data on its composition and structure are needed. Such data are being produced and will be reported in the near future.

### CONCLUSIONS

In the present work, an investigation of the initial stages of anodic alumina growth in neutral sulfate-fluoride electrolyte using voltammetry and electrochemical impedance spectroscopy is reported. The following conclusions can be drawn on the basis of the obtained results:

- Voltammetric results indicate that at the most negative potentials, hydrogen evolution predominates over Al dissolution for both alloys, which can be due to preferential reduction of water on secondary Si, Fe and Mn-containing phases. On the other hand, the higher current density in the passive range registered for 8011 Al alloy was apparently due to the greater amount of the alloying element Si which is actively complexed by fluoride ions.
- A kinetic model based on the surface charge approach employed to fit the impedance spectra and to evaluate the dependences of the main parameters of the oxide formation and dissolution on alloy type.
- Fitting of the impedance spectra to the equations of the surface charge approach adapted to the aluminum oxide growth demonstrated that the process of film thickening is assisted by constant field strength, the anodizing ratio being within the range of values typical for porous anodic alumina.
- At lower potentials, a more complex interplay between film growth and dissolution is observed for

the alloys. Additional data on the composition and structure of the surface film as depending on potential and alloy composition are needed in order to establish a quantitative correlation between film nature, its electric and electronic properties.

**Acknowledgement:** The financial support of the National Science Fund, Contract No. DDVU 02/103-2010 “Nanoporous anodic oxides as a new generation of optically active and catalytic materials (NOXOAC)” is gratefully acknowledged.

### REFERENCES

1. D. Gong, C.A. Grimes, O.K. Varghese, Z. Chen, E.C. Dickey, *J. Mater. Res.*, **16**, 3334(2001).
2. M.S. Gudixsen, L.J. Lauhon, J.F. Wang, D.C. Smith, C.M. Lieber, *Nature*, **415**, 617 (2002).
3. K. Lee, U. Goesele, K. Nielsch, *Nature Mater.*, **5**, 741 (2006).
4. J. Macak, K. Sirotna, P. Schmuki, *Electrochim. Acta*, **50**, 3679 (2005).
5. J. Macak, H. Tsuchiya, P. Schmuki, *Angewandte Chemie*, **44**, 2100 (2005).
6. Q. Cai, M. Paulose, O.K. Varghese, C.A. Grimes, *J. Mater. Res.*, **20**, 230 (2005).
7. L. V. Taveira, J. M. Macák, H. Tsuchiya, L. F. P. Dick, P. Schmuki, *J. Electrochem. Soc.* **152** (2005) B405.
8. I. Sieber, P. Schmuki, *J. Electrochem. Soc.* **152**, C639 (2005).
9. A. Ghicov, P. Schmuki, *Chem. Commun.*, 2791 (2009).
10. H. Tsuchiya, S. Berger, J. M. Macak, A. G. Munoz, P. Schmuki, *Electrochem. Commun.*, **9**, 545 (2007).
11. C. Girginov, M. Bojinov, *Bulg. Chem. Comm.*, **42**, 312 (2010).
12. C. Girginov, M. Bojinov, In *Nanoscience and Nanotechnology 11*, E. Balabanova, I. Dragieva, Eds., Heron Press, 2011, 93-96.
13. E. Clark, Y. X. Gan, L. Su, *Nanoscience and Nanotechnology Letters*, **4**, 61 (2012).
14. M.Bojinov, *Electrochim. Acta*, **42**, 3489 (1997).
15. G. J. Brug, A.L.G. Van Den Eeden, M. Sluyters-Rehbach, J.H. Sluyters, *J. Electroanal. Chem.*, **176**, 275 (1984).
16. R. Giovanardi, C. Fontanesi, W.Dallabarba, *Electrochim. Acta*, **56**, 3158 (2011).
17. J. W. Diggle, T.C. Downie, C. W. Goulding, *Chem. Rev.*, **69**, 365 (1969).

## МЕХАНИЗЪМ НА АНОДНО ОКИСЛЕНИЕ НА АЛУМИНИЕВИ СПЛАВИ В СУЛФАТНО-ФЛУОРИДЕН ЕЛЕКТРОЛИТ

К. А. Гиргинов\*, М. С. Божинов

*Катедра Физикохимия, Химикотехнологичен и металургичен университет, 1756 София, България*

Постъпила на 28 февруари, 2013 г.; Коригирана на 21 март, 2012 г.

(Резюме)

През последните години, флуорид-съдържащи електролити се използват за формиране на порести структури върху вентилни метали като Ti, Nb, W, Ta и техни сплави. Наличието на флуоридни йони позволява растежа на нанопорести / нанотубуларни матрици с добре дефинирани структури. Съвсем наскоро са били успешно използвани неутрални сулфатнофлуоридни електролити за формиране на нанопорести филми и върху алуминий. Настоящото изследване е посветено на началните етапи на растеж на порести анодни филми върху две алуминиеви сплави в тези електролити чрез волтамметрия и електрохимична импедансна спектроскопия. Приложен е кинетичен модел, основан на подхода на повърхностните товари, за интерпретация на получените импедансни спектри. Оценени са основните транспортни параметри при процесите на формиране и разтваряне на оксида в зависимост от приложения потенциал и вида на сплавта.

## Anodic oxide films on antimony formed in oxalic acid solutions

E. Lilov, Ch. Girginov, E. Klein\*

University of Chemical Technology and Metallurgy, 8 St. Kl. Okhridski Blvd., 1756 Sofia, Bulgaria

Received February 28, 2013; Revised April 13, 2013

Anodic oxide films on antimony were grown in aqueous solutions of oxalic acid in a large current density and acid concentration range. Under galvanostatic conditions, the common linear increase of the formation voltage with time proved to occur at current densities higher than  $2 \text{ mA cm}^{-2}$  and in electrolytes with oxalic acid concentrations lower than 0.01 M. Under these only conditions the relationship between the ionic current density and the field strength is described by *Güntherschulze* and *Betz* equation.

The electrical breaking down of anodic antimony oxide in the oxalic acid electrolytes was studied. The experimental data obtained for the breakdown voltages are well described by *Burger* and *Wu* equation. The amplitude and the frequency of voltage oscillations during electrical breaking down were found practically not to depend on current density.

The results are compared with those obtained for anodic oxidation of antimony in other aqueous solutions. Under specified conditions, the oxalic acid electrolyte proved to be suitable for the formation of anodic oxide films on antimony.

**Key words:** anodic antimony oxide, galvanostatic anodization, breakdown voltage, oxalic acid

### INTRODUCTION

Apart from the assumed effect of its formation in lead–acid batteries, antimony oxide has found applications as electro catalyst, photoconductor, for thin film capacitors and in preparing electro chromic devices [1]. Barrier-type anodic oxide films on antimony have been grown in a number of aqueous solutions of acids, bases and salts [2-11], as well as in non-aqueous electrolytes [12, 13]. In all cases, however, a strong influence of nature and concentration of the forming electrolyte on the kinetics of anodizing has been established. The anodizing of antimony often exhibits a specific kinetics, such as appearance of induction periods, S-shaped curves and maxima in the kinetic dependencies [3-6, 10]. It was therefore of interest to search for electrolytes ensuring a linear potential growth during galvanostatic anodizing of antimony in a wide range of concentrations and current densities.

In the present study, data for the formation kinetics and the breakdown phenomena of antimony oxide films in aqueous solutions of  $(\text{COOH})_2$  at various current densities were obtained.

### EXPERIMENTAL

Specimens of high purity (99,999%) antimony were cut out of polycrystalline Sb with a working area of  $2.5 \text{ cm}^2$ . The electrodes were mechanically

polished with sandpaper R 4000 ( $d = 5 \text{ }\mu\text{m}$ ). The anodizing was carried out under galvanostatic conditions at a temperature of 293 K. The current densities ( $J$ ) varied from  $2 \text{ mA cm}^{-2}$  to  $20 \text{ mA cm}^{-2}$ . Various  $(\text{COOH})_2$  solutions in the range from 0.01 M to 0.1 M were used as forming electrolytes. The electrolytes were not stirred in order to avoid the influence of hydrodynamic effects.

The formation of the films was carried out in a two-electrode cell with a platinum mesh serving as a counter electrode, using a high voltage generator of constant current (600 V, 0.5 A). Kinetic curves, i.e. dependences of the formation voltage ( $U_f$ ) on time ( $t$ ) were registered with a precision multi meter (Mastech MS 8050) and a PC-based data acquisition system.

### RESULTS AND DISCUSSION

#### *Kinetics of galvanostatic anodization*

The formation of barrier anodic films on valve metals at galvanostatic and isothermal conditions is known to be associated with a linear increase of the formation voltage ( $U_f$ ) with time ( $t$ ), or respectively with the density of electric charge passed ( $Q$ ). It turned out that the concentration of the oxalic acid and the current density used had a strong influence on the kinetics of the process. Examples of kinetic  $U_f(t)$ -curves (respectively  $U_f(Q)$ -dependencies) obtained in solutions with different concentrations at a constant current density of  $2 \text{ mA cm}^{-2}$  are presented in Fig.1.

\* To whom all correspondence should be sent:  
E-mail: klnrdwr@yahoo.com

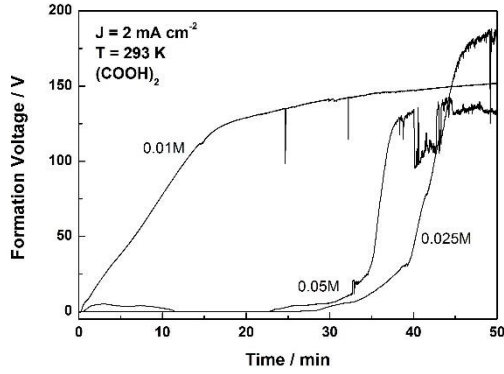


**Fig. 1.** Kinetic curves of galvanostatic anodization of antimony in oxalic acid solutions with different concentrations

The kinetic curves proved to have different shapes depending on the concentration of the oxalic acid. As it was shown earlier [14], a linear relationship between formation voltage ( $U_f$ ) and time ( $t$ ) was observed only at the lowest concentration (0.01 M). That is why the corresponding electrolyte was chosen for subsequent experiments.

It was of interest to trace the influence of current density ( $J$ ) on the anodization kinetics. Figure 2 presents kinetic curves obtained at different current densities. The slopes ( $\partial U_f / \partial Q$ ) of these curves are also calculated.

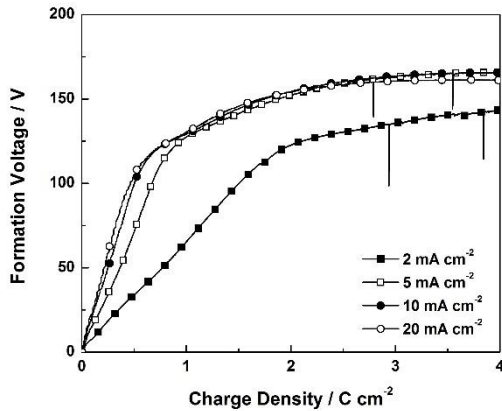


**Fig. 2.** Kinetic curves of antimony anodization in 0.01 M  $(\text{COOH})_2$  at different current densities

During galvanostatic anodization, the ionic current ( $J_i$ ) is known to depend on the intensity of the electric field ( $E$ ) in the oxide. This  $J_i(E)_T$ -dependence is described in a first approximation, known as the high field approximation, by Güntherschulze and Betz equation [15],

$$J_i = A_G \exp(B_G E)_T \quad (1)$$

At constant temperature, the constants  $A_G$  and  $B_G$  are independent of the field intensity. The current ( $J$ )

flowing through the system metal/oxide film/electrolyte is assumed to be completely ionic, i.e.  $J = J_i$ . It has been shown [12] that the high field approximation describes the anodization of antimony in a number of aqueous electrolytes as well. The validity of eqn. (1) has been further confirmed for the anodizing kinetics in a phosphate buffer [16], the anodic antimony oxide being determined as  $\text{Sb}_2\text{O}_3$ .

As a matter of fact, eqn. (1) describes well the anodizing kinetics of antimony even after the appearance of induction periods [13]. Unfortunately, there are differing opinions about the composition of the anodic antimony oxide and, moreover, no reliable methods for determining the film thickness. Hence, it seems impossible to calculate the electric field intensity ( $E$ ). Based on Faraday's law, this intensity can be expressed:

$$E = \frac{zF\rho}{M} \left( \frac{\partial U_f}{\partial Q} \right)_{J,T} \quad (2)$$

Here,  $F$  is the Faraday constant,  $M$  is the molecular mass and  $\rho$  is the density of the film,  $z$  is the number of electrons involved in the electrochemical process, and  $(\partial U_f / \partial Q)_{J,T}$  is the slope of the kinetic curve. The fact that the growth rate of formation voltage  $U_f$  with charge density ( $Q$ )<sub>J,T</sub> remains constant during the first anodizing stage, could be an indication that film growth dominates over film dissolution and a barrier type film is formed. In this case, the ionic current is controlled only by the film properties and  $(\partial U_f / \partial Q)_{J,T}$  should depend on the current density. The Güntherschulze and Betz equation can be used to describe the anodizing kinetics on replacing the field intensity ( $E$ ) by its proportional magnitude  $(\partial U_f / \partial Q)_{J,T}$ . An assessment of the validity of eqn. (1) was carried out by replacing the field intensity in eqn. (1) by the proportional magnitude  $(\partial U_f / \partial Q)_{J,T}$  from eqn. (2):

$$J_i = A_G \exp \left[ B_G^* (\partial U_f / \partial Q)_T \right], \quad (3)$$

The notation  $B_G^*$  marks here the expression  $B_G^* = B_G z F \rho / M$ .

Figure 3 presents the plot of  $(\partial U_f / \partial Q)_{J,T}$  vs.  $\ln J$ . The obtained linear dependence shows that eqn. (3) adequately describes the anodizing kinetics of antimony in 0.01 M  $(\text{COOH})_2$ .

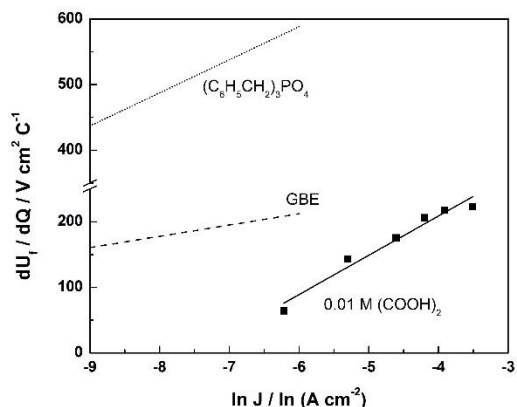


**Fig. 3.**  $(\partial U_f / \partial Q)_{J,T} / \ln J$  - dependence for galvanostatic anodization of antimony in 0.01 M  $(\text{COOH})_2$ . Similar relationships for two other electrolytes are presented for comparison.

Values for the constants  $A_G$  and  $B_G^*$  were determined from the data in Fig. 3. These values were then compared (Table 1) with those estimated for anodization of antimony in a glycol-borate electrolyte (GBE) [12] and in a phosphate ester  $(\text{C}_5\text{H}_5\text{CH}_2\text{O})_3\text{PO}_4$  [13].

**Table 1** Values of the constants  $A_G$  and  $B_G^*$  in equation (3)

Electrolyte	$A_G$ ( $\text{A cm}^{-2}$ )	$B_G^*$ ( $\text{C V}^{-1} \text{cm}^{-2}$ )
0.01 M $(\text{COOH})_2$	$0.56 \times 10^{-8}$	0.017
GBE [12]	$1.25 \times 10^{-8}$	0.058
$(\text{C}_5\text{H}_5\text{CH}_2\text{O})_3\text{PO}_4$ $B_G^*$ [13]	$2.30 \times 10^{-8}$	0.020

It is worth noting that the anodization in  $(\text{C}_5\text{H}_5\text{CH}_2\text{O})_3\text{PO}_4$ , which occurs with the appearance of a pronounced induction period, is also well described by eqn. (3) [13]. It was of interest to study the dependence of  $(\partial U_f / \partial Q)_{J,T}$  on the concentration of  $(\text{COOH})_2$  during anodization at a constant current density. An example of such dependence during anodizing with  $J = 10^{-2} \text{ A cm}^{-2}$  is presented in Figure 4. It turned out that the dependence was linear only at lower concentrations (under 0.02 M). A similar picture is observed [17] during anodization of antimony in sulfuric acid solutions.

#### Breakdown phenomena

The breakdown phenomena are important anodizing characteristics. It is well known that the increase in anodic film thickness, respectively the anodizing voltage, is limited by the occurrence of electrical breakdowns. The first evidence for a limiting voltage attained during anodization has been furnished in the pioneer work of Güntherschulze and Betz [15].

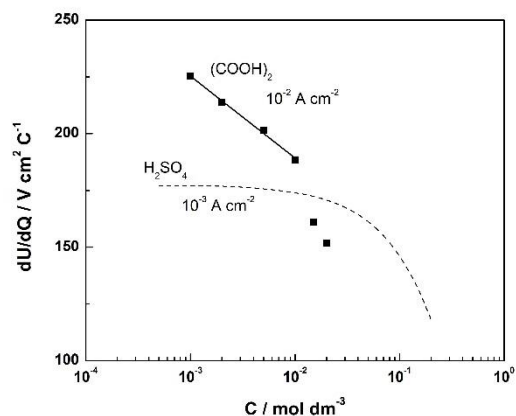


**Fig. 4.**  $(\partial U_f / \partial Q)_{J,T} / \log C$  - dependence for anodization of antimony in  $(\text{COOH})_2$  solutions. For comparison, a similar dependence in  $\text{H}_2\text{SO}_4$  solutions is presented [17].

Numerical values for breakdown voltages of antimony oxide in some acid, base and salt solutions have been calculated by Ammar and Saad [3, 9]. The dependence of the breakdown voltage ( $U_B$ ) on the electrolyte resistivity ( $\rho$ ) for anodic films on different valve metals is well described by the empirical equation of Burger and Wu [18]:

$$U_B = a_B + b_B \log \rho \quad (4)$$

The only question remaining controversial is whether the constants  $a_B$  and  $b_B$  depend on the electrolyte composition. To clarify this, the breakdown voltage of Sb was studied in oxalic acid solutions with different concentrations (or specific resistances  $\rho$ , respectively), as shown in Fig. 5. Current density and temperature were held constant.

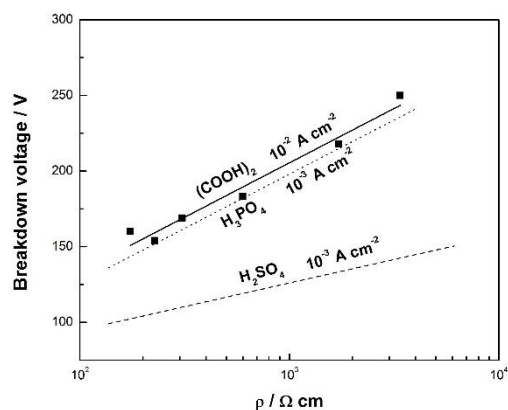


**Fig. 5.** Breakdown voltages are shown as a function of the specific resistance of the oxalic acid electrolyte. The results are compared with those obtained in two other solutions.

The anodizing process was conducted in galvanostatic regime with a current density of  $10^{-2} \text{ A cm}^{-2}$  at a constant temperature (293 K). In all cases, after reaching a specific value of  $U_f$ , voltage oscillations which are typical for the electric

breakdown could be observed (Fig.1). The oscillations began at different values of  $U_f$  depending on the type and concentration of the contact electrolyte. Next, the voltage increased slowly, with continuous oscillations and after a certain time (or charge density passed) remained practically constant. The value of  $U_f$  after a charge of  $3 \text{ C cm}^{-2}$  passed since the first appearance of oscillations [17], was adopted to be the breakdown voltage ( $U_B$ ). The data obtained for  $U_B$  (Fig. 6) allowed the calculation of the constants in eqn. (4). This equation proved to describe well the experimental data obtained during anodization of antimony in oxalic acid solutions. The values of the constants  $a_B$  and  $b_B$  are presented in Table 2. For comparison, values for the same constants obtained in solutions of other two acids,  $\text{H}_3\text{PO}_4$  [12] and  $\text{H}_2\text{SO}_4$  [17], are also presented.

**Table 2** Values of the constants in the Burger and Wu equation

Electrolyte	Current density	$a_B$ (V)	$b_B$ (V)
$(\text{COOH})_2$	$10^{-2} \text{ A cm}^{-2}$	$-10.4 \pm 1.8$	$72 \pm 5$
$\text{H}_3\text{PO}_4$ [12]	$10^{-3} \text{ A cm}^{-2}$	$-18.0 \pm 2.3$	$72 \pm 8$
$\text{H}_2\text{SO}_4$ [17]	$10^{-3} \text{ A cm}^{-2}$	$58.5 \pm 4.2$	$24 \pm 3$

The studies on breaking down during anodization of antimony in aqueous oxalic acid solutions showed that breakdowns obeyed the common regularities typical for valve metals. On the other hand, the constants  $a_B$  and  $b_B$  for antimony oxide in Burger and Wu equation [18] depended on the nature of the forming electrolyte as the other oxides on valve metals. The amplitude and frequency of the voltage oscillations during breaking down were analyzed. Fragments of the oscillations are presented in Fig. 6.

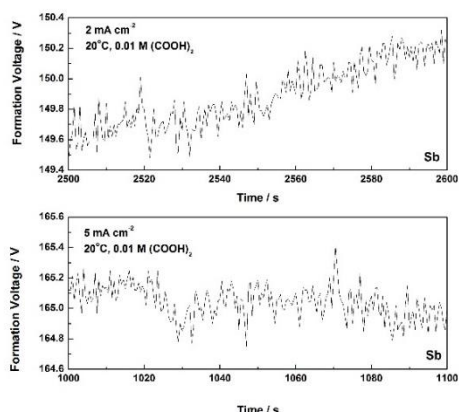


**Fig. 6.** Fragments of the kinetic curves during breaking down for anodization with two current densities

The results show that both the frequency and the amplitude of voltage oscillations during breaking down are insensitive to the applied current density. A similar result has been obtained with oxide films on other typical valve metals.

## CONCLUSIONS

Oxalic acid solutions are suitable for the formation of anodic oxide films on antimony. The common kinetics of linear increase of the formation voltage with time in galvanostatic conditions were observed only at current densities greater than  $2 \text{ mA cm}^{-2}$  and electrolytes with concentrations lower than  $0.01 \text{ M}$   $(\text{COOH})_2$ . The kinetics of formation is subject to known relationships between current density and field intensity (*Güntherschulze* and *Betz* equation). Breaking down is discussed on the base of *Burger* and *Wu* equation which describes well the experimental data. Furthermore, the amplitude and frequency of formation voltage oscillations during electric breakdowns is found to be practically independent of current density.

**Acknowledgement:** The authors are grateful for the financial support of The Human Resources Development Program of The European Social Fund for contract BG 051PO001-3.3.06-0014.

## REFERENCES

- O. E. Linarez Pérez, M. D. Sánchez, M. López Teijelo, *J. Electroanal. Chem.*, **645**, 143 (2010).
- A. Vijh, *Electrochemistry of Metals and Semicconductors*, Marcel Dekker, inc., New York (1973).
- A. Ammar, A. Saad., *J. Electroanal. Chem.*, **30**, 395 (1971).
- S. Ikonopisov, A. Girginov, V. Tsochev, *Compt. rend. Acad. bulg. Sci.*, **25**, 653 (1972).
- A. Гиргинов, С. Иконописов, *Электрохимия*, **10**, 638 (1974).
- M. El-Basiouny, M. Hefny, A. Mogoda, *Corrosion*, **41**, 611 (1985).
- M. Metikoš-Huković, B. Lovrecek, *Electrochim. Acta*, **25**, 717 (1980).
- A. Mogoda, *Thin Solid Films*, **349**, 174 (2001).
- A. Ammar, A. Saad., *J. Electroanal. Chem.*, **34**, 159 (1972).
- M. Bojinov, I. Kanazirski, A. Girginov, *Electroch. Acta*, **40**, 873 (1995).
- I. Ammar, A. Saad, *J. Electroanal. Chem.*, **34**, 159 (1972).
- A. Girginov, E. Lilov, H. Vodenicharov S. Ikonopisov, *Compt. rend. Acad. bulg. Sci.*, **42**, 57 (1989).
- A. Girginov, E. Klein, V. Kalfova, S. Ikonopisov, *B. Electrochem.*, **4**, 631 (1988).
- I. Angelov, Ch. Girginov, E. Klein, *Bul. chem. comm.*, **43**, 144 (2011).
- A. Güntherschulze, H. Betz, *Z. Electrochem.*, **37**, 730 (1931).
- O. E. Linarez Pérez, M. A. Pérez, M. López Teijelo, *J. Electroanal. Chem.*, **632**, 64 (2009).

17. А. Гиргинов, В. Калфова, И. Каназирски, С. Иконописов, *Електрохимия*, **26**, 110 (1990).  
18. F. Burger, J. Wu, *J. Electrochem. Soc.*, **118**, 2039 (1971).  
19. M. M. Hefny, W. A. Badawy, A. S. Mogoda, M. S. El-Basiouny, *Electrochim. Acta*, **30**, 1017 (1985).  
20. M. Metikoš-Huković, R. Babić, S. Brinić, *Journal of Power Sources*, **157**, 563 (2006).  
21. S. Mogoda, *Thin Solid Films*, **394**, 6 (2001).  
22. S. Mogoda, T. M. Abd El-Haleem, *Thin Solid Films*, **441**, 173 (2003).  
23. W.A. Badawy, S. Mogoda, M. M. Ibrahim, *Electrochim. Acta*, **33**, 1367 (1988).

## МЕХАНИЗЪМ НА АНОДНО ОКИСЛЕНИЕ НА АЛУМИНИЕВИ СПЛАВИ В СУЛФАТНО-ФЛУОРИДЕН ЕЛЕКТРОЛИТ

Е. Лилов, К. Гиргинов, Е. Клайн\*

*Химикотехнологичен и металургичен университет, 1756 София, България*

Постъпила на 28 февруари, 2013 г.; Коригирана на 13 април, 2013 г.

(Резюме)

Изследвана е кинетиката на образуване на анодни оксидни филми във водни разтвори на оксалова киселина. Процесът е изучен при широко вариране на концентрацията и плътността на тока. Установено е, че обичайната кинетика с линейно нарастване на формиращото напрежение с времето (в галваностатични условия) се наблюдава при анодиране с плътности на тока над  $2 \text{ mA cm}^{-2}$  в електролити с концентрация по-ниска от  $0.01 \text{ M (COOH)}_2$ . При тези условия е в сила уравнението на Гюнтершулце и Бец, което описва зависимостта на йонния ток от силата на приложеното електрично поле. Получените експериментални данни за пробивните напрежения по време на анодирането на антимона се описват добре с емпиричното уравнение на Бургер и Ву. Стойностите на константите в уравнението са съпоставени с тези, получени при анодирането на антимон във водни разтвори на други киселини. Установено е също така, че амплитудата и честотата на осцилациите на напрежението по време на пробивите не се повлияват значително от плътността на тока. При определени условия водните разтвори на оксаловата киселина са подходящи за формирането на анодни оксидни филми върху антимон.

## Pulse electrolysis of alkaline solutions as highly efficient method of production of hydrogen/oxygen gas mixtures

V. I. Karastoyanov<sup>1\*</sup>, Tzv. B. Tzvetkoff<sup>2</sup>

<sup>1</sup>University of Chemical Technology and Metallurgy, 1756 Sofia, Bulgaria

<sup>2</sup>Hydrogen Technology Centre, University of Chemical Technology and Metallurgy, 1756 Sofia, Bulgaria

Received March 1, 2013; revised March 21, 2013

Pulse electrolysis of water solutions is a highly efficient method of production of hydrogen and hydrogen/oxygen gas mixtures, sometimes called hydroxygen. When pulse current is applied during electrolysis, the amount of hydroxygen formed is increased in comparison to the dc current regime. The aim of the present paper is to investigate the effect of ultra-short current pulses on the rate of hydroxygen gas mixture production as related to efficiency enhancement of the process by means of the reducing power consumption during electrolysis. Pulse electrolysis was carried out in a laboratory electrolysis stack consisting of nine cells featuring electrodes of 316L stainless steel at a spacing of 10 mm. Typically the experiments were carried out for 1min with current amplitudes of 1 – 1.4 A, frequencies of the signal 1 kHz and pulse saturation (duty cycle) between 1 - 5%. The volume of the produced hydroxygen gas mixture by pulse electrolysis was measured by gas flow meters and compared to the produced gas volume in the same electrolysis cell under a constant current regime of 1-5 A. On the basis of the results obtained, preliminary conclusions regarding optimization of the pulse current regime are drawn and a discussion on a possible mechanism of rate enhancement is given

**Keywords:** pulse electrolysis, electrical parameters, hydrogen/oxygen gas mixture, process efficiency

### INTRODUCTION

The potential of hydrogen for playing an important role in future energy systems has lead researchers to investigate methods of reducing hydrogen production costs to levels that can compete with petroleum products [1-3]. Nowadays, only 4–5% [4] of total global production of this most abundant substance of the universe [5] is being done by water electrolysis. Water electrolysis is known to be one of the important assets for hydrogen production [6-11]. One of these methods is the application of pulsed current regime to a practical electrolysis system [1-5]. Electricity power demand expense constitutes the largest fraction [12] of hydrogen production costs by using electrolysis method.

At temperature of 298 K and at pressure of 1 atm, the reversible decomposition voltage for water is 1.23 V. The required voltage value of an electrolysis cell is higher than the decomposition voltage of a water molecule. No gas evolution is observed in practice until voltages of 1.65 - 1.7 V are applied [13-17]. Practical cells operate at voltages of 1.8- 2.6 V, as a result of overvoltage

and ohmic losses. Overvoltage has mainly two components: (i) activation overvoltage that results from the finite rate of the electrode reactions. It varies with metal used as the electrode and its surface condition. It is reduced by operating at elevated temperatures and pressures, and increases with the current density of the electrode reaction. (ii) The concentration overvoltage arises as a result of changes in the composition of layers of electrolyte close to the electrodes. Ions are at discharged the electrode surface and hydrogen and oxygen are formed. Research results show that temperature, pressure, electrode material, electrolyte formulation and concentration, physical setup of the cell and power supply output waveform have an influence on the value of the overvoltage. In particular, when ultra-short pulses with somewhat longer pause periods between them are applied (i.e. using high-frequency pulse currents with low duty cycles), the structure of the double layer remains perturbed, the process of adsorption of intermediate products remain in a transient state and thus the overall rate of the process is expected to increase.

In that respect, the main objective of the present study is to quantify the effects of the electrical parameters of the pulse on the performance of water electrolysis for hydrogen gas mixture

\* To whom all correspondence should be sent:  
E-mail: [vasko\\_kar@yahoo.com](mailto:vasko_kar@yahoo.com)

generation. First, the pulse electrolysis system employed is briefly described. Second, results of the effect of pulse electrolysis parameters on the efficiency of the process are presented and discussed. Finally, some thoughts on a possible mechanism of rate enhancement in the pulse regime are given and directions for further work are outlined.

### EXPERIMENTAL

To test the influence of electrochemical parameters on the efficiency of the generator pulse electrolysis process of water tests was used generator for HHO gas mixture consists of nine series connected cells with electrodes of stainless steel 316L and area of 20 cm<sup>2</sup> and electrode spacing of 10 mm. During the tests were used two electrolytes with different concentration of KOH (0.1 and 0.4M) to monitor the effects of different concentrations of electrolyte. The volume of the KOH solutions used was 2 l. A laboratory made pulse generator "Electra 06" type VSDC-09/VO, 60V / 15A was used for the pulse current experiments, see **Error! Reference source not found.** Typically the experiments were carried out for 1 min with current amplitudes of 1.0 – 1.4 A, frequencies of the pulse 1 kHz and pulse saturation (duty cycle) between 1 - 5%. The volume of the produced hydrogen/oxygen gas mixture by pulse electrolysis was measured by gas flow meters and compared to the produced gas volume of the constant current electrolysis in the same electrolyzer and applied current of 1 – 5 A, in order to achieve optimal efficiency, i.e. the highest amount of gas produced spend at a small amount of applied electrical energy.

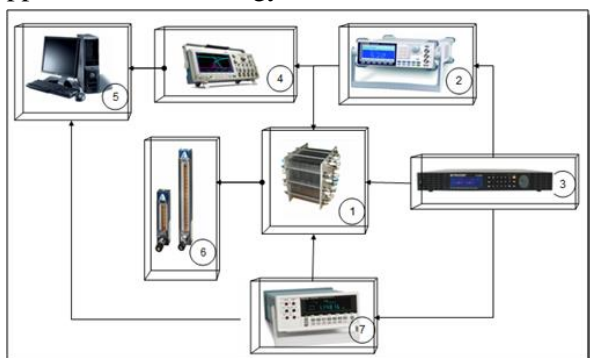


**Fig. 1.** Experimental setup: 1- electrolysis cell, 2- pulse generator, 60V/15 A, 3-dc power supply (100 V/15 A), 4 – digital oscilloscope, 5 - PC, 6 – flow meter (240 L/h), 7-digit multimeter.

### RESULTS AND DISCUSSION

During the test runs conducted to examine the influence of different process parameters, the

effects of electrolyte concentration, applied current and duty cycle are investigated. The constant current is varied from 1.0 A to 5 A, the applied current amplitude in pulsed current regime is from 1 to 1.4 A at a duty cycle from 1 to 5% for all of the experiments in 0.1 and 0.4 M KOH. The frequency of the pulse is kept constant at 1 kHz.

The electrolysis efficiency ( $P_0$ ) in constant current regime and the cell potential are shown in Fig. 2 as depending on the applied current in 0.4 M KOH electrolyte. The efficiency of the process increases with the applied current on the electrolysis cell. However, the cell potential increases together with the efficiency. For applied currents higher than  $I = 3$  A, the efficiency of the process becomes constant.

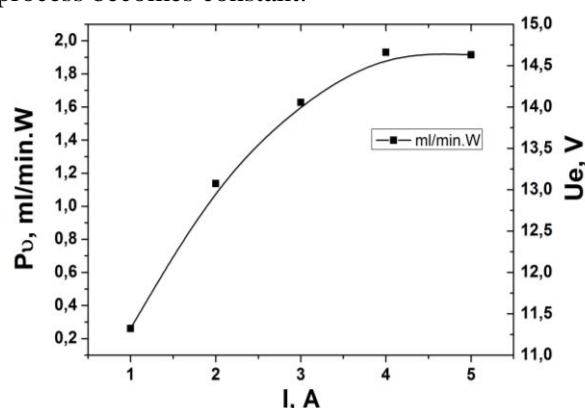


**Fig. 2.** Efficiency of water electrolysis in constant current regime. Electrolyte: 0.4 M KOH.

A typical test run in electrolyte of 0.1M KOH in constant current regime is show in Figure 3. The relatively high  $P_0$  efficiency for smaller currents drastically drops with increasing currents and reaches stabilization at 4 A.

The efficiency of water electrolysis in the pulse current regime in 0.4 M KOH as depending on the duty cycle  $D$  in the range 1 – 5 % at a frequency of 1 kHz is displayed in Fig.4. The examination of the figure reveals that at lower duty cycles (smaller than  $D = 2\%$ ) the efficiency increases with the current, whereas a reverse trend is observed above a duty cycle of 3%. During test run with  $I = 1$  A we obtain a maximum of  $P_0$  at  $D = 3\%$  and stabilization after this value. Test run with  $I = 1.4$  A efficiency is approximately constant which can be also observed in Figure 5 for experiments in 0.1 M KOH, the results being comparable. Comparable results we can observe also in bought curves of  $I = 1$  A applied current in the two different electrolytes we have used.

The efficiency of the electrolysis in pulsed current regime with duty cycle ( $D$ ) of 1 to 5 % and frequencies of 1 kHz in 0.1 M KOH and applied

current of 1 and 1.4 A is shown in Figure 4. In both cases the efficiency of the process increase with applied current. An interesting observation is that at a lower current ( $I = 1$  A)  $P_{O_2}$  increases in a monotonous fashion with duty cycle, whereas with applied current of 1.4A,  $P_{O_2}$  exhibits a maximum at a duty cycle of 3%, slowly decreasing at higher currents. Another observation is that the  $P_{O_2}$  have higher values when compared to the constant current regime at applied current of 1 A, which means that at only 5% of power consumption we have a higher efficiency of the water splitting process.

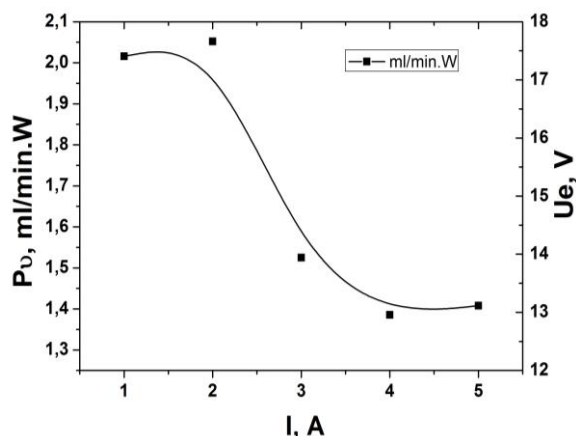


Fig. 3. Efficiency of water electrolysis in constant current regime. Electrolyte: 0.1M KOH.

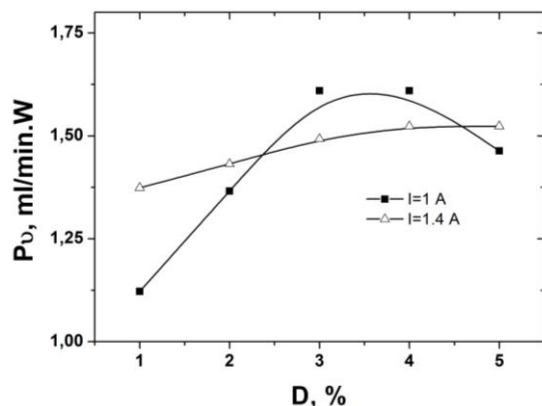


Fig. 4. Efficiency of water electrolysis in the pulsed current regime as a function of the duty cycle,  $f=1$  kHz, 0.4M KOH.

The interpretation of the phenomena associated with hydrogen/oxygen mixture (or hydroxygen) formation and its properties has been recently a cause of some controversy, invoking a range of explanations from the formation of new forms of matter [18-20] to that of charged water gas clusters [21]. The following mechanism of hydrogen evolution during electrolysis with inductive kickback pulses has been proposed: as no hydrogen adsorption/absorption peaks were detected for non-noble metal electrodes such as stainless steel,

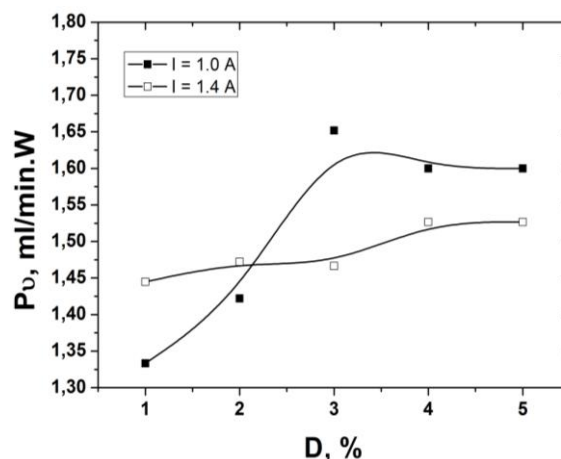


Fig. 5. Efficiency of water electrolysis in the pulsed current regime as a function of the duty cycle,  $f=1$  kHz, 0.1 M KOH.

during the very short pulse the electrons from the metal directly discharge hydrogen ions and  $H_2$  molecules are formed much more intensively than on Pt on which an adsorbed layer of atomic hydrogen forms [22-23]. In other words, our experiments are consistent with a picture in which the intermediate species of both the reduction and oxidation reactions of water are unstable and their rate of decomposition is much higher during pulse electrolysis when compared to conventional constant current process. Further investigations of the exact gas mixture composition are underway to try to elucidate the intimate mechanism of efficiency enhancement.

## CONCLUSIONS

In conditions of pulse electrolysis of water, the rate of the process significantly increases in comparison to the dc regime.

The largest efficiency is obtained using cycles of low duty (less than 5%) as well as **higher current amplitudes**.

Results in the two employed electrolytes are comparable to each other, i.e. the effect of electrolyte concentration in the studied range is small.

A concept of the process featuring much higher decomposition rates of intermediate species during both reduction and oxidation of water is advanced, based on previous ideas in the literature. Further work is needed to quantify this concept and propose a mechanism of the process in pulse electrolysis conditions.

**Acknowledgement.** This work is supported by the Bulgarian Science Fund, Ministry of Science, Youth and Education, under contract DDVU-02-99/2010 "Pulse electrolysis as a highly efficient method for generation of hydrogen gas mixtures".

#### REFERENCES

1. A.H. Shaaban, *J. Elchem. Sci.*, **140** 2863 (1993).
2. S. Wang, C. Ji, J. Zhang, B. Zhang, *Int J Hydrogen Energy*, **36**, 11164 (2011).
3. M. Vanags, J. Kleperis, G. Bajars, A. Lusis, *J. Phys.: Conference Ser.*, **93** 012025 (2007).
4. R.F. de Souza, *Journal of Power Sources*, **164**, 792 (2007).
5. M. Momirlan, T.N. Veziroglu, *Int. J. Hydrogen Energy*, **30**, 795 (2005).
6. S. Li, C. Wang, C. Chen, *Electrochim. Acta*, **54**, 3877 (2009).
7. C. Gabrielli, F. Huet, R. P. Nogueira, *Electrochim. Acta*, **50**, 3726 (2005).
8. S.A. Guelcher, Y.E. Solomentsev, P.J. Sides, J.L. Anderson, *J. Electrochem. Soc.*, **145**, 1848 (1998).
9. H. Matsushima, T. Nishida, Y. Konishi, Y. Fukunaka, Y. Ito, K. Kuribayashi, *Electrochim. Acta*, **48**, 4119 (2003).
10. G.F. Naterer, M. Fowler, J. Cotton, K. Gabriel, *Int. J. Hydrogen Energy*, **33**, 6849 (2008).
11. F. Gutiérrez-Martín, D. Confente, I. Guerra, *Int. J. Hydrogen Energy*, **35**, 7329 (2010).
12. J. Ivy, Summary of electrolytic hydrogen production: milestone completion report. NREL/MP-560-36734; September 2004.
13. K. Zeng, D. Zhang, *Prog. Energy Combust. Sci.*, **36**, 307 (2010).
14. M. Wang, Z. Wang, Z. Guo, *Int. J. Hydrogen Energy*, **35**, 3198 (2010).
15. M.E. Orazem, B. Tribollet, *Electrochemical Impedance Spectroscopy*. New Jersey: Wiley Online Library, 2008.
16. J.O. Bockris, T.N. Veziroglu, *Int. J. Hydrogen Energy*, **32**, 1605 (2007).
17. M. Philippe, H. Jérôme, B. Sebastien, P. Gérard, *Electrochim. Acta*, **51**, 1140 (2005).
18. R.M. Santilli, *Int. J. Hydrogen Energy*, **31**, 1113 (2006).
19. M. Calo, *Int. J. Hydrogen Energy*, **32**, 1309 (2007).
20. J.V. Kadeisvili, *Int. J. Hydrogen Energy*, **33**, 918 (2008).
21. M.B. King, *Physics Procedia*, **20**, 435 (2011).
22. M. Vanags, J. Kleperis, G. Bajars, *Int. J. Hydrogen Energy*, **36** (2011) 1316-1320.
23. M. Vanags, J. Kleperis, G. Bajars, *Latvian J. Phys. Tech. Sci.*, **48**, 34 (2011).

## ИМПУЛСНА ЕЛЕКТРОЛИЗА В АЛКАЛНИ ВОДНИ РАЗТВОРИ КАТО ВИСОКОЕФЕКТИВЕН МЕТОД ЗА ГЕНЕРИРАНЕ НА ОКСИВОДОРОДНИ ГАЗОВИ СМЕСИ

В. Карастоянов<sup>1</sup>, Цв. Цветков<sup>2</sup>

<sup>1</sup>Химикотехнологичен и Металургичен Университет, 1756 София, България

<sup>2</sup>Център по водородни технологии, Химикотехнологичен и Металургичен Университет, 1756 София, България

Постъпила на 1 март, 2013 г.; коригирана на 21 март, 2013 г.

(Резюме)

Импулсната електролиза във водни разтвори е високоефективен метод за производство на водород и водородно/кислородни газови смеси, понякога наричани оксигенород. Когато е приложен импулсен ток по време на електролизния процес, количеството получен оксигенород нараства в сравнение с електролиза при правотоков режим. Целта на тази работа е да изследва ефекта на приложени много къси пулсации на тока върху количеството на произведен газ, като се свърже с увеличаване на ефективността на процеса по отношение на намаляване консумацията на енергия по време на електролизата.

Импулсната електролиза е проведена в лабораторна електролизна клетка, съдържаща девет серии електроди от неръждаема стомана 316L с разстояние между електродите от 10 милиметра. Обемът на използвания алкален разтвор (0.5M KOH) е 2 л. Експериментите са проведени за една минута с амплитуда на тока от 0.7 до 1A, честота на сигнала от 0.4 до 1 kHz и наситеност на импулса от 2 до 95%. Обемът произведен газ/газова смес чрез импулсна електролиза е измерван чрез дебитомер и сравняван с произведеното количество газ от правотоковата електролиза, извършена в същия електролизатор при приложен ток от 5 до 10 A. На основата на получените резултати са представени предварителни изводи за оптимизация на импулсния режим и е дискутиран възможния механизъм за увеличаване на скоростта.

## Advances in synthesis, application and dependence of vaporization of micron sized particles in thermal plasma in SOFC technologies

K. D. Georgieva, G. Vissokov

*Institute of Catalysis, Bulgarian Academy of Sciences, Acad. G. Bonchev St., Bldg. 11, Sofia 1113, Bulgaria*

Received February 28, 2013; revised April 21, 2013

Different plasma-chemical methods have been used lately in SOFC technologies form creation of nano-layers by magnetron or laser plasma spaying methods to use of sintering nano sized powders. The use of nano-sized powders obtained by plasma-chemical reactors, as electric-arc plasmatron Vissokov and co-workers used or high frequency inductive thermal plasma reactors (HFI), proves to be efficient and ecologically friendly method. Optimizing the parameters of Fuel Cells using nano powders we achieve higher specific capacity, current density and lower degradation rates of the material, as it is proven by various novel approaches by using plasma-chemical methods for FC production. The process of powder vaporization is limiting for any PCR, so we are looking to optimize the characteristics of the plasma generator in order to obtain nano particles with high purity and the reaction taking place in gaseous phase should modeled to produce the right size uniform size nano powders. There have been considered schemes for vaporization of micron-sized particles in electric arc and high frequency inductive thermal plasma reactors (HFI). Making use of the set of equations (RCF-method), we also performed calculations for the following oxides:  $\text{Al}_2\text{O}_3$ ,  $\text{CaO}$ ,  $\text{CuO}$ ,  $\text{Fe}_2\text{O}_3$ ,  $\text{MnO}_2$ ,  $\text{MoO}_3$ ,  $\text{NiO}$ ,  $\text{SiO}_2$ ,  $\text{TiO}_2$ ,  $\text{ZrO}_2$ ,  $\text{MgO}$ . When modeling the process, one usually consider the most unfavorable case of vaporization taking in account the largest micron particle diameter. Changes in the diameter of micron-sized particles are calculated along the plasma-chemical reactor axis, using the set of equations constructed by the team searching for selection of the optimal parameters. A comparison is made between the calculated literature data and specific research results in thermal plasma.

**Keywords:** powder vaporization, plasma-chemical methods, (HFI), SOFC, nano powders

### INTRODUCTION

Different plasma techniques have been developed and adapted to the specific requirements of efficiency in SOFC fabrication. The nano-particles can be synthesized by a number of synthetic methods, such as co-precipitation method, assembly process, template method, sintering of nano-powders or cost-effective spray process as atmospheric plasma spray ("APS"), vacuum plasma spray ("VPS"), radio frequency plasma spray ("RF"PS), and high velocity oxy-fuel ("HVOF") spray. Solid oxide fuel cells ("SOFC"s) are capable of generating electric power through the chemical reaction between hydrocarbon fuels and oxygen with high efficiency. Their further mechanical reliability can be improved and manufacturing cost can be reduced by reducing cell operating temperature. Therefore, the development of intermediate temperature SOFC technology has attracted a lot of worldwide attention of future energy markets. As relates to SOFC technology,

lower operating temperature requires higher activity of electrodes, high ionic conductivity of electrolytes, low over potential of electrode/electrode, and lower overall internal resistance loss is a goal. It is how to fabricate the thin (<20  $\mu\text{m}$ ) electrolyte layer with the full density (>97%) that is required to provide satisfactory gas tightness and internal resistance loss. These requirements can be met by developing new electrode/electrolyte membrane materials, improving cell assembly concepts, and novel fabrication methods using plasma technologies. The theory and practice of heterogeneous catalysis have demonstrated that the activity of solid-phase catalysts is determined by their chemical and phase content, crystal structure and active specific surface. A correlation of slopes is usually observed between the catalysts' active and total specific surface dependencies. On the other hand, it is also known that one can use LTP [6,11] to produce condensed-phase compounds (metals, oxides, nitrides, spinel materials, etc.) that have highly developed specific surface with the size of their ultra-dispersed particles (UDP's) of the order of few tens of nanometers (nanopowders NP). These

---

\* To whom all correspondence should be sent:  
E-mail: dimovabas@gmail.com

compounds manifest high catalytic activity [1-3,14]. When the plasma-chemical synthesis (PCS) of UDP's is accompanied by chemical reactions, and when an effective quenching of the reaction products takes place at rate  $dT/d\tau = 105 - 106 \text{ K s}^{-1}$ , then conditions are created for condensation of UDP's with an unusual distribution of the additives [3,9], degenerated crystal structure [3,18,] and numerous defects in the crystal lattice; these also exhibit high catalytic activity in heterogeneous catalytic processes [1-3,9-18,] and low deteriorating rate in high temperature applications. All stated above makes the material obtained by plasma-chemical synthesis extremely suitable for SOFC applications. Plasma processes for sequential fabrication of the multiple layers in a SOFC unit by spraying or sintering are the best offer at present for the fabrication of nanostructured electrodes for high-performance primary and rechargeable lithium batteries are showing a great deal of promise when applied to SOFCs and stacks.

## 2. THERMAL PLASMA SYNTHESIS OF NANOSIZED METAL POWDERS -THEORY

Recently metal powders with relatively large sizes of 50 ~ 500 nm are increasingly in demand in various industries as the alternatives to conventional micron-sized ones. For example, Ni powders with sizes of 50 ~ 200 nm are very promising as the attractive electrode materials in high performance or SOFC. However practical applications for most kinds of metals with sizes of <50 nm exhibiting particular properties due to the size effect, are now limited because they are still expensive. The plasma-chemical technique (PCT) thus turns out to be efficient in synthesizing highly active catalysts [1-3, 9-103] Although at present the investigations on the preparation of highly active catalysts are still at the laboratory, pilot-plant, or patenting stage, reports on the item have been found in the specialized literature on the synthesis and activation of catalysts under low-temperature plasma conditions [1-3,6,9-17]. The way of catalyst preparation affects such important properties as its specific surface, porosity, density, mechanical strength, thermal stability, etc. This is why the preparation procedure is sometimes as important as the catalyst's chemical composition. According to Roginskiy's theory of over-saturation [17], catalysts obtained under the conditions of energy over-saturation must possess an increased activity.

The extent of energy over-saturation of a system increases with the increase in the rate of heat

transfer to the system, according to the following equation:

$$dQ/d\tau = \alpha(T_1 - T_2)dF_1 \quad (1)$$

where  $T_1$  is the temperature of heat carrier (plasma in the case considered here) and  $T_2$  is the temperature of the heated substance (micrometer-size particles),  $dF$  is the surface separating plasma and particles. If one assumes that the material treated is of spherical shape with radius  $R$ , then the specific surface of particles belonging to different fractions will be inversely proportional to their radii

$$F_1/F_2 = R_{12}/R_1 \quad (2)$$

or, the smaller the particles, the higher will be their specific surface. However, decreasing the particles size is only reasonable to a certain limit, defined by Biot's number

$$Bi = \alpha R/\lambda = (R/\lambda)/(1/\alpha) \quad (3)$$

where  $\lambda$  is the particle coefficient of heat conductivity and  $\alpha$  is the coefficient of the heat transfer from the heat carrier to the particle.

The numerator in Equation 3 characterizes the resistance to heat propagation from the surface to the centre of the particle, and the denominator, that to transfer of heat from the heat carrier to the particle surface. When  $R$  is large, the heat-transfer process is limited by the heat resistance of the particle, and inversely, for small  $R$ , by the heat resistance of the phase interface. There obviously exists a value of  $R$  for which the two quantities are equal ( $Bi = 1$ )

$$R = \lambda/\alpha \quad (4)$$

To create the maximal energy over-saturation, the raw material must be pre-dispersed to a particle size as close as possible to that defined by Equation 4. The calculations for the case of catalyst, e.g., elemental Fe or iron oxides yield a value of approximately 50  $\mu\text{m}$ . It is well known that industrial catalysts must comply with the following requirements:

- 1) Activity – the catalyst should provide sufficient reaction rate under the specific technological conditions;
- 2) Stability – the catalyst should not lost its activity over a lot period of time;
- 3) The catalyst should exhibit a lack of sensitivity to catalytic poisons, mostly chlorine and sulfur compounds;
- 4) Selectivity – the catalyst should accelerate the desired reaction only, and not side reactions;
- 5) It should have good mechanical strength;

6) Most of the catalysts are produced as oxides and have to be reduced before use the reduction period should be as short as possible in order to avoid a decrease in the production efficiency.

The assumption for the limiting role of the stage of condensed-phase vaporization in heterogeneous PCR has found wide acceptance. An important consequence of the assumption is that, besides ensuring suitable thermodynamic conditions (temperature, reagents ratio), one has to guarantee also sufficient time of residence of the particles in the PCR so that they are completely vaporized. The presence of these conditions will allow one to synthesize the product desired in gas phase. Following an appropriately fast cooling of the reacting mixture, i.e., at a given quenching rate  $dT/d\tau$ , the product can be obtained in the ND form needed. The above makes obvious the necessity of modeling the particles vaporization process. One could thus obtain sufficiently accurate data to determine the process' optimal parameters, such as, PCR dimensions, time of residence of the particles in it, temperature profile along the reactor's axis, temperature in the zone near the walls, temperature of the reactor wall, etc. Some researchers (Polack *et al.* [32]) have modelled the process up to the particles' melting point; others (Panfilov *et al.* [30,31]) have applied numerical methods to solve the set of differential equations describing the process - a procedure inconvenient for practical engineering calculations.

### 3. EXPERIMENTAL RESULTS

Primarily Vissokov and co-workers used to solve the set of equations for the case of an iron particle. Metal iron (radius 5  $\mu\text{m}$  and 30 $\mu\text{m}$ ) in electric-arc plasmatron LTP (cathode-anode distance of 10 mm and diameter of the anode-nozzle channel of 5 mm) is used as a raw material in the production of catalysts for ammonia synthesis. To perform the calculations, one needs to know the values of  $c_p$ ,  $c_p$ , J/kg.K;  $T_{p0}$ ,  $T_{g0}$ ,  $T_{pb}$ ,  $T_{pv}$ , K;  $L_{pb}$ ,  $L_{pv}$ , J/K;  $\rho_g$ ,  $\rho_p$ , kg/m<sup>3</sup>;  $M_g$ ,  $M_p$ ;  $G_{p0}$ ,  $G_{g0}$ , kg;  $g_g$ ,  $g_p$ , kg/s;  $V_{g0}$ ,  $V_{p0}$ , m/s, which can easily be found in the specialized reference literature; other parameters are set a-priori: plasma forming gas (argon) with consumption in the range 2.6.10<sup>-4</sup> kg/s (~0,5 m<sup>3</sup>/h Ar) - 9,93.10<sup>-4</sup> kg/s (~2 m<sup>3</sup>/h Ar); metal powder consumption (fraction 1 - 50  $\mu\text{m}$ ) (1,39 - 4,17).10<sup>-5</sup> kg/s (50 - 150 g/h); plasma temperature 8 000 K.

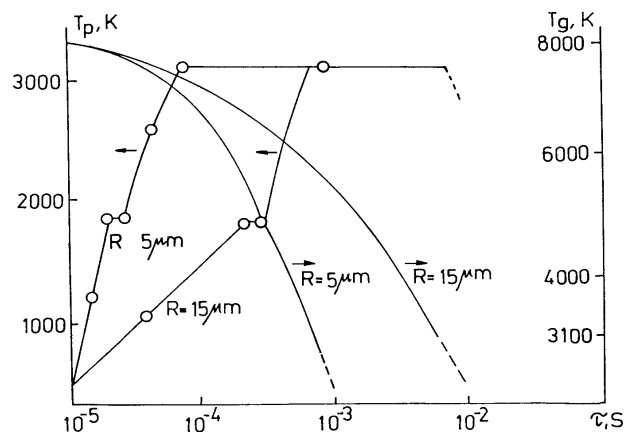


**Fig. 1** .Variation of the particles ( $T_p$ , K) and gas ( $T_g$ , K) temperature as functions of the time of contact ( $\tau$ , s) and particle radius ( $\tau$ , s).

As one can see in Fig.1 particles with diameter below 30  $\mu\text{m}$  are fully vaporized in the PCR, which is an important practical fact for the efficient quenching of the vapor-gas mixture in the production of nano-dispersed catalytic mass. The data obtained (Fig.1) concerning the temperature, time of particles melting and vaporization and the gas temperature as functions of the time of contact between the gas and the particles, and between the gas and the PCR walls, are in good agreement with the experimental data. the equations can also be employed to find preliminary values for the coefficients of heat-exchange between the gas and the particles and between the gas and the reactor walls.

The set of equations is solved by means of the RKF 45 program . The Runge-Kutta-Felberg technique is applied to solving sets of ordinary differential equations. When modeling the process, one usually considers the most unfavorable case of vaporization, namely, the largest particle diameter. In order to account more precisely for the influence of the vaporization kinetics on the product transformation degree, it is suitable [39] to introduce the quantity of relative (dimensionless) time of residence ( $\tau_r$ ) obtained by dividing the time of residence of the particle in the reactor ( $\tau_p$ ) to the time necessary for its total vaporization ( $\tau_v$ ) for the same average mass temperature in the reactor:

$$\tau_r = \frac{\tau_p}{\tau_v}, \quad (5)$$

To determine  $\tau_p$ , the set of equations (2.10 - 2.17) is solved for the following boundary conditions:  $d_p - d_{p0}$ , 0;  $S - 0$ ,  $S_0$ ;  $T_g = T_{g0}$ , where  $S_0$  is the length of the plasma chemical reactor, m;  $T_{g0}$  is the average mass temperature of the plasma-chemical reactor, determined by making use of its energy balance, K. To determine  $\tau_v$ , we apply the

following boundary conditions  $d_p - d_{p0}, 0; S - 0, S_0; T_g = T_{g0}$ . Besides the relative time of residence, let us now introduce with the same purpose the quantity of degree of vaporization ( $\beta$ ):

$$\beta = \frac{G_p^0 - G_p}{G_p^0} \cdot 100, \% \quad (6)$$

where  $G_p^0$  is the initial mass of the particle, kg; and  $G_p$  is the mass of the particle at the moment  $\tau_p$  at the reactor's exit, kg.

The set of equations constructed can be used in the selection of the optimal parameters (PCR dimensions, minimal necessary time of contact between the plasma jet and the particle, place of quenching agents' introduction, as a result of determining the temperature profile along the reactor axis, the temperature strength of the reactor material, etc.) of processes taking place in high-temperature jets with the participation of a vaporizing phase, including the preparation of NDP. Considering the least favorable case, namely, the radius reduction of an iron particle due to vaporization for initial radius of  $50 \mu\text{m}$  as a

function of the plasma-forming gas (argon) consumption and of the particle's location along the PCR axis (Fig. 2). As one can see, due to vaporization, the iron particle's radius at the PCR exit is reduced to approximately  $1 \mu\text{m}$ ; while an iron particle with initial diameter of  $20 \mu\text{m}$  is fully vaporized when the temperature of  $8000 \text{ K}$  is reached (Fig. 3). Of course, in the cases of PC preparation of complex compounds (e.g., catalysts, amorphous alloys, composite materials), one can also add in the system of ingredients compounds (oxides, salts, elements) with boiling temperature lower than  $3000 \text{ K}$ . For example, one can see in Fig. 4 that, for initial diameter of  $20 \mu\text{m}$ , the particles of all elements considered (Mg, Al, Si, Ca, Ti, Mn, Fe, Ni, Co, Cu, Zn, Zr, Mo) are fully vaporized in the PCR. Returning to the least favorable case (vaporization of particles with diameter of  $50 \mu\text{m}$ ), one sees that the Mg and Ca particles are fully vaporized, while the degree of vaporization of the other elements is negligible.

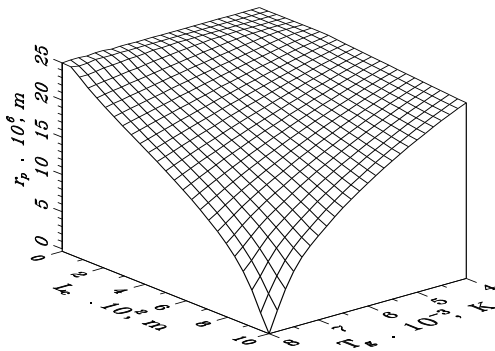


**Fig. 2.** Variation of the radius of an iron particle with initial diameter  $25 \mu\text{m}$  depending on the plasma jet temperature and on the particle location along the PCR axis.

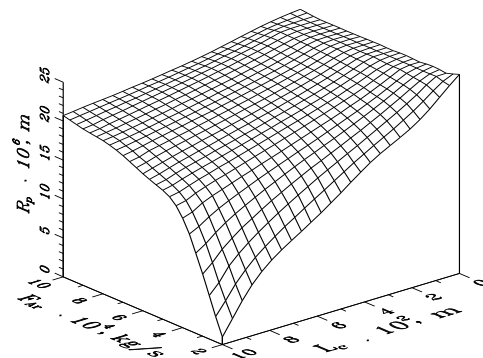


**Fig. 3** Variation of the radius of an iron particle with initial diameter  $20 \mu\text{m}$  depending on the plasma-forming gas (argon) consumption and on the particle location along the PCR axis.

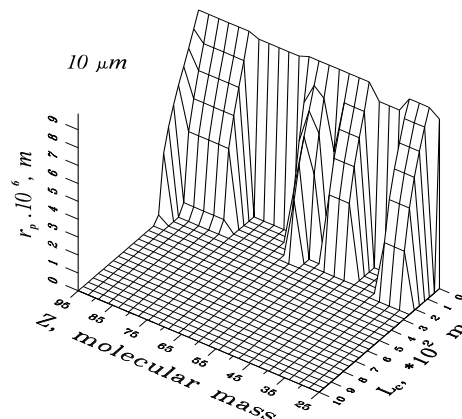
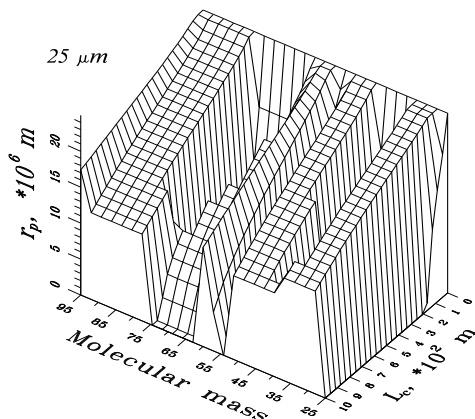


**Fig. 4** Variation of the radius of a particle with initial diameter  $50 \mu\text{m}$  and  $20 \mu\text{m}$  depending on the molecular mass of the respective element and the particle location along the PCR axis.

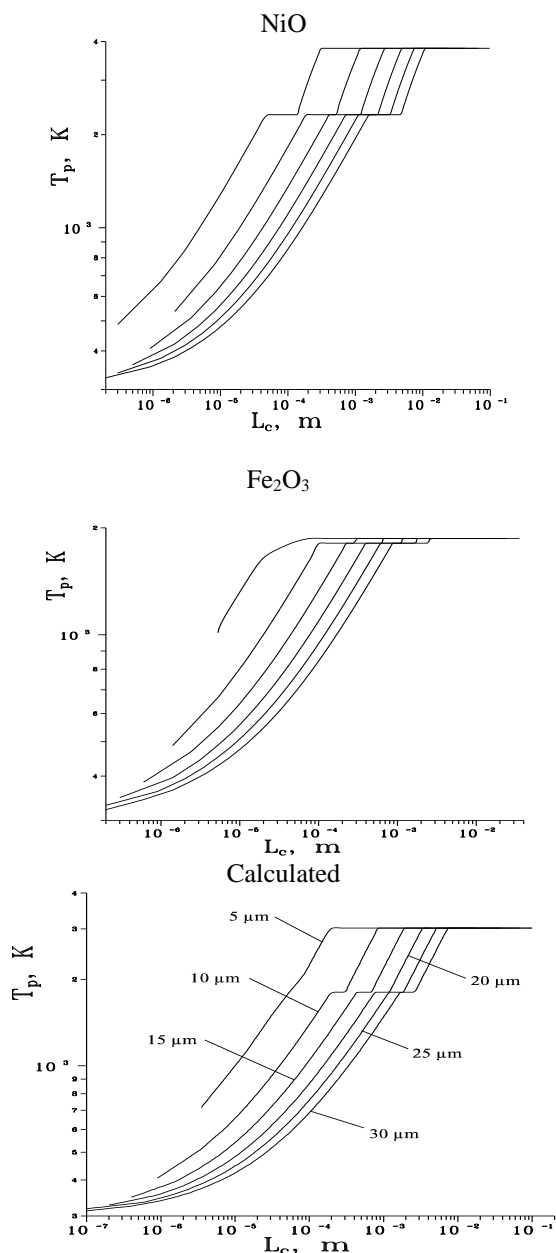


**Fig.5a.** Variation of oxide particles' temperature ( $T_p$ , K) as a function of their location along the PCR axis initial diameter from left to right :5, 10, 20, 25 and 30  $\mu\text{m}$ .

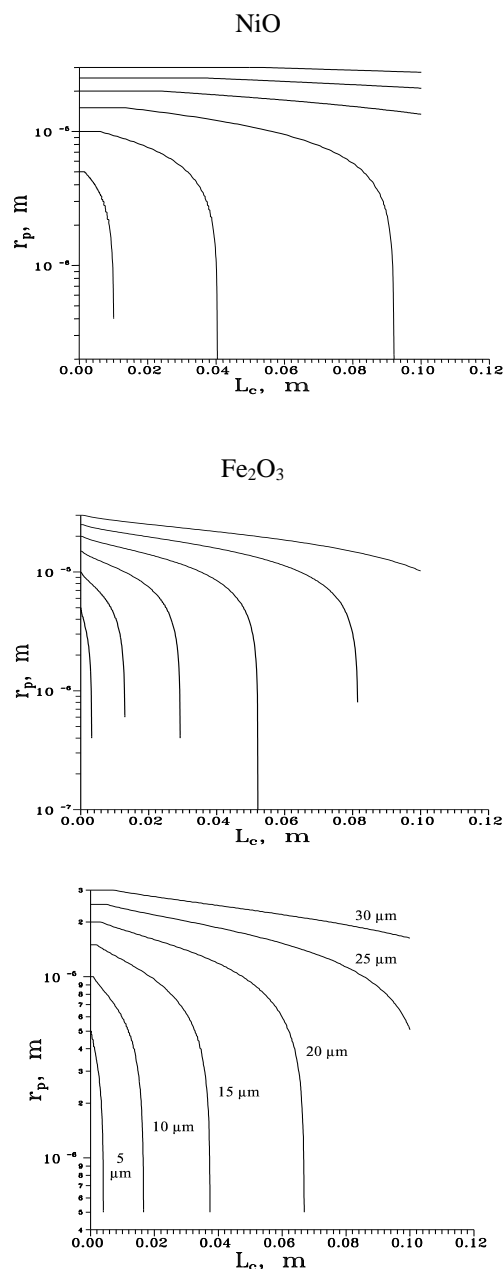


**Fig. 5b.** Oxide particles' radius ( $r_p$ , m) variation as a function of their location along the PCR axis ( $L_c$ ) initial diameter from left to right :5, 10, 20, 25 and 30  $\mu\text{m}$ .

The particles with  $d_p = 20 \mu\text{m}$  reach the boiling temperature within the first 1/3 - 1/5 of the PCR length while those with the largest diameter  $d_p = 50 \mu\text{m}$  are heated up to the boiling.

Making use of the set of equations, we performed calculations for the following oxides:  $\text{Al}_2\text{O}_3$ ,  $\text{CaO}$ ,  $\text{CuO}$ ,  $\text{Fe}_2\text{O}_3$ ,  $\text{MnO}_2$ ,  $\text{MoO}_3$ ,  $\text{NiO}$ ,  $\text{SiO}_2$ ,  $\text{TiO}_2$ ,  $\text{ZrO}_2$ ,  $\text{MgO}$ . These are used as raw materials for various types of syntheses of NDP. We plotted the variation of the particles' radius of the respective oxide as a function of their location

along the PCR axis and illustrated the variation of the temperature of the oxide particles depending on their location along the PCR axis giving example with  $\text{NiO}$  and  $\text{Fe}_2\text{O}_3$ . PCR parameters are set *a-priori*: plasma forming gas (argon) with consumption in the range  $2,6 \cdot 10^{-4} \text{ kg/s}$  ( $\sim 0,5 \text{ m}^3/\text{h Ar}$ ) -  $9,93 \cdot 10^{-4} \text{ kg/s}$  ( $\sim 2 \text{ m}^3/\text{h Ar}$ ); metal powder consumption (fraction 1 - 50  $\mu\text{m}$ )  $(1,39 - 4,17) \cdot 10^{-5} \text{ kg/s}$  (50 - 150 g/h); plasma temperature 8 000 K.

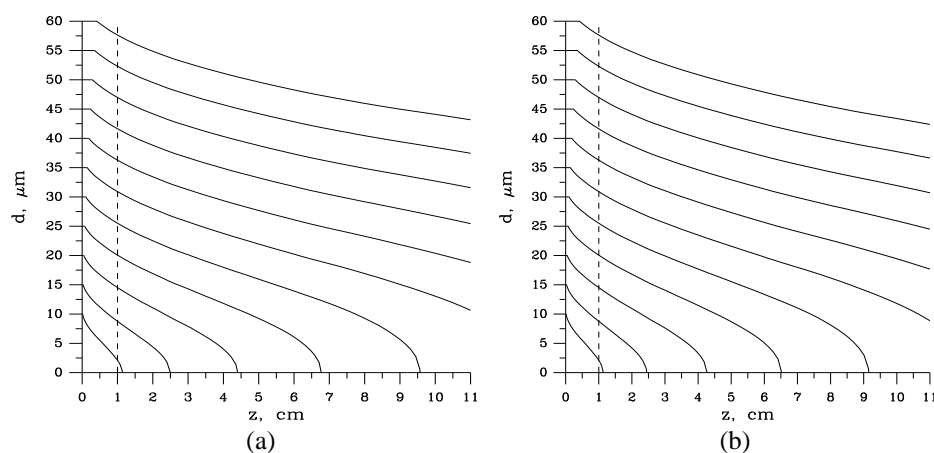


**Fig. 6.** Variation of  $\text{Fe}_2\text{O}_3$  particles diameter along the axis of a CW PCR (a) and WW PCR (b)

In order to select appropriate experimental conditions (PCR length and diameter, ingredients' granulometry) for PC preparation (activation of spent samples) of nano-dispersed catalysts for steam conversion of hairdo carbons (natural gas reforming), we calculated the motion, heating, melting and vaporization of micron-sized particles ( $d_{eq} = 10, 15, 20, 25, 30$  и  $35 \mu\text{m}$ ) of Ni, NiO, Al,  $\text{Al}_2\text{O}_3$ , CaO,  $\text{Fe}_2\text{O}_3$  Mg and MgO in CW and WW PCR.

### CONCLUSIONS

The results of the calculations performed agree well with the results of the synthesis and/or regeneration of catalysts for natural gas reforming (steam conversion of methane) and all experimental data received of nano powder obtained. Depending on the features of the target materials and employed plasma torches, various synthesis routes have been analyzed In order to select appropriate experimental conditions for PC preparation of nano-dispersed powders. In-flight treatment of solid precursors may be preferable in the preparation of nano-sized glass powders and single phase oxides, such as,  $\text{ZrO}_2$ , NiO,  $\text{SiO}_2$ ,  $\text{Al}_2\text{O}_3$  and  $\text{TiO}_2$ . Among them, single phase oxides can be prepared by reactive thermal plasmas synthesis. However, their reproducibility and stoichiometry problems should be solved for practical applications with the use of proper computational methods. Depending on the physical properties of ceramic materials, such as melting points, enthalpy, evaporating rate and quenching the treated products can become a metal core – ceramic shell structured particle or a metal catalyst dispersed on ceramic supports. For the ceramic powder of  $\text{BaTiO}_3$  with relatively low melting point, the mixed Ni metals can be buried into  $\text{BaTiO}_3$  droplets and reformed into Ni core -

$\text{BaTiO}_3$  shell structured nano-composite. We can conclude that the advantages of thermal plasmas, such as, high enthalpy flows combined with a rapid quenching rate, can be very promising in the synthesis of not only a single phase material but also binary or higher nano-materials useful for SOFC production. Nanosized powders in the range of 10–120 nm have been prepared by introduction and evaporation of coarse-grained commercially available powders of chemical elements, oxides or salts in radio-frequency nitrogen, oxygen or air plasma as well as electric arc plasmatron. The necessary conditions for preparation of nanosized powders include evaporation of precursors, control of particle growth and elimination of formation of precursor particles or extra phases and promotion of formation of product particles. Evaporation of mixture of raw powders in the inductively coupled plasma creates good conditions for preparation of multicomponent, highly homogeneous nanoparticulate composites Main advantages of plasma technique are relative high production rate, production ability of several composite powders with high definite specific surface area, phase and chemical composition. The main drawbacks of the plasma technique relate to high energy consumption and wide particle size distribution. Nanostructural materials from prepared powders are manufactured by using conventional pressureless sintering, hot pressing and spark plasma sintering.

The knowledge accumulated and production experience convinces that nano-sized powders produced by ICP plasma technique can be applied successfully for manufacturing advanced ceramic materials.

## REFERENCES

1. G. Vissokov, P. Pirgov, *Ultradispersed Powders (Plasma-chemical Preparation and Properties)*, Poliprint, Sofia, 1998: 395 (in Bulgarian)
2. G. Vissokov, *Plasma Nanotechnologies – nanopowders, preparation, properties and applications*, Publ. House “St. Iv. Rilski”, Sofia, 2005: 303
3. K. Klabunde, *Nanoscale Materials in Chemistry*, John Wiley and Sons Inc, 2001, p. 292
4. J. Nurmi, P. Tratnyek, V. Sarathy et al., *Environ. Sci. Technol.*, **39**, 1221 (2005).
5. R. Kalyanaraman, S. Yoo, M. Krupashankara et al. *Nanostructure Materials*, **10**, 1379 (1998).
6. Wan Julin, Gasch M, Mukherjee A. US Patent, No.2004179969, 2004.
7. X. Sun, H. Cong et al., *Nanostructure Materials*, **11**, 917 (1999).
8. M. Shigeta, T. Watanabe, N. Nishiyama, *Thin Solid Films*, **457**, 192 (2004).
9. G. Vissokov, *Applied Plasma-chemistry, Pt.1, Low Temperature Plasma Application in Inorganic Technologies*, Teknika, Sofia, 1984, p. 294 (in Bulgarian).
10. G. Vissokov, *Applied Plasma-chemistry, Pt.2, Low Temperature Plasma Application in Organic Technologies*, Teknika, Sofia, 1987, p. 333 (in Bulgarian).
11. G. Vissokov, N. Videnov, *Chemistry&Industry*, **50**, 389 (1978).
12. G. Vissokov, B. Stephanov., et al., *J. Materials Sci.*, **23**, 2415 (1988).
13. J. Grabis, *Interface Controlled Materials*, Euromat’99, 2000, 9, p. 267 - 272
14. I. Zalite, S. Ordanyan, G. Korb, *Powder Metall.*, 2003, 46 (2): 143 ~ 147
15. O. Kaidash, *Ceramics International*, **26**, 303 (2000).
16. V. Lavrenko, N. Boshitskaya in: NATO Advanced Research Workshop, *Nanostructure Materials and Coatings for Biomedical and Sensor Applications*, August 4-8 2002, Kiev, Ukraine.
17. T. Ishigaki, S.-M. Oh, J.-G. Li, D.-W. Park, *Science and Technology of Advanced Materials*, 2005, In Press
18. H. Itoh, S. Utampanya et al., *Chemical Materials*, **5**, 71 (1993).
19. C. Bossel, J. Dutta, R. Houriet et al., *Mat. Sci. Eng. A*, **204**, 107 (1995).
20. R. Philipp, K. Omata, A. Aoki et al., *J. Catal.*, **134**, 422 (1992).
21. T. Ito, J.-X. Wang, C.-H. Liu. et al., *J. Am. Chem. Soc.*, **107**, 5062 (1985).
22. D. Driscoll, W. Martir, J.-X. Wang et al., *J. Am. Chem. Soc.*, **107**, 107 (1985).
23. X. Peng, D. Richards, P. Stair et al., *J. Catal.*, **121**, 99 (1990).
24. A. Stakheev, E. Shapiro, J. Apijok, *J. Phys. Chem.*, **97**, 5668 (1993).
25. J. Stark, K. Klabunde, *Chemical Materials*, **8**, 1904 (1996).
26. K. Klabunde, A. Khalee, D. Park, *High Temperature Materials Science*, **33**, 99 (1995).
27. S. Decker, K. Klabunde, *J. Am. Chem. Soc.*, **118**, 124 (1996).
28. Y. Jiang, S. Decker et al., *J. Catal*, **180**, 24 (1998).
29. Li Y.-L, T. Ishigaki, *Thin Solid Films*, **407**, 79 (2002).
30. J. Grabis, I. Steins et al., *J. Eur. Ceram. Soc.* **17**, 1437 (1997).
31. A.G. Zverev, S.A. Shevchenko, S.I. Pavlov, in: *Proceedings of II All-union meeting on plasma – chemical technology and equipment*, Moscow, VDNH USSR, 1977, vol.2, p.60 (In Russian).
32. A. Popov, G. Vissokov et al., *Nanoscience and Nanotechnology Nanostructured materials Application and Innovation Transfer*, E. Balabanova (Editor), Sofia, Heron Press, vol.2, 2002, pp. 30-34.

## НАПРЕДЪК В СИНТЕЗА И ОПРЕДЕЛЯНЕ НА ЗАВИСИМОСТТА ОТ ИЗПАРИЕНИЕТО НА ЧАСТИЦИТЕ С МИКРОННИ РАЗМЕРИ В ТЕРМИЧНА ПЛАЗМА -ПРИЛОЖЕНИЕ ВЪВ ВИСОКОТЕМПЕРАТУРНИ ГОРИВНИ ЕЛЕМЕНТИ

К. Георгиева, Г. Високов

*Институт по Катализ, Българска Академия на Науките, ул. Академик Г. Бончев Бл. 11, София 1113, България*

Постъпила на 28 февруари 2013 г.; Коригирана на 21 април, 2013 г.

(Резюме)

Направена е обширната литературна справка ,проучване и оценка на съвременното ниво на развитие на проблематиката при приложение на плазмените технологии в производство- то на твърдо оксидни горивни елементи (SOFC). Направена е оценка на синтезираните нано дисперсни прахове от проф. Високов и колектив. Оценена е зависимостта на изпарение на тринадесет химични елемента е, а също на различни оксиди като циркониев оксид явяващ се основен материал при изработката на мембрани твърдо оксидните горивни елементи ,както и специфичните физикохимични характеристики на полученият материал. Вземайки под внимание екологичния импакт, можем да отнесем плазмените методи на синтез към щадящи екологията производства.

## Behaviour of gas-diffusion electrode in various non-aqueous electrolytes for the lithium-air system

I. Popov<sup>1\*</sup>, B. Velev<sup>1</sup>, J. Milusheva<sup>1</sup>, R. Boukoureshtlieva<sup>1</sup>, S. Hristov<sup>1</sup>, T. Stankulov<sup>1</sup>, B. Banov<sup>1</sup>, A. Trifonova<sup>2</sup>

<sup>1</sup>*Institute of Electrochemistry and Energy Systems, Bulgarian Academy of Sciences, Sofia, Bulgaria*

<sup>2</sup>*AIT Austrian Institute of Technology, Vienna, Austria*

Received March 5, 2013; accepted April 19, 2013

Lithium-air batteries have recently received attention due to their high theoretical specific capacity, which is much higher than that of existing lithium-ion batteries.

This work aims to study the gas-diffusion electrode behavior in various non-aqueous electrolytes, potential candidates for use in lithium-air battery, and also its work in a semi cell against lithium metal electrode.

Gas-diffusion electrode was prepared with two catalysts – pyrolyzed CoTMPP and Active Carbon Co/Ni tested in a standard 2032 button cell. The slow cycling voltammetry (CV) of CoTMPP electrode shows irreversible O<sub>2</sub> reaction instead of Co/Ni electrode where the capacity of oxygen evolution reaction is about 3 times less than of the oxygen reduction reaction. Nevertheless, the obtained reversibility at slow CV, the galvanostatic cycling tests at 1 mA shows irreversibility of the process most probably to the very high polarization at that current.

**Keywords:** lithium-air battery, non-aqueous aprotic electrolyte, catalysts for oxygen reduction reaction, gas-diffusion electrode, cobalt tetramethoxyphenil porphirine (CoTMPP).

### INTRODUCTION

The progress of humanity demands more and more energy resources, which in most cases are limited. The technological revolution led to invention of steam engine, in-exhausting engines, automobiles, fossil-fuel power plant etc., uses fossil materials as source of energy. These materials are both exhaustible and ecological polluters and lead to a global change of climate. Therefore the science community must seek new high effective electrochemical power sources, with bigger energy capacity for saving of the energy obtained by renewable resources as photovoltaic, wind power electricity, hydroelectricity etc.

Such battery could be based on the Lithium-Air electrochemical system, because of its high theoretical specific capacity (13000Wh/kg) [1] close to that of the petrol (13200 Wh/kg). This would allow applying this system in areas demanding high electricity power as electrical vehicles, mobile electronics, UPS etc.

The concept of Li-air battery was introduced by researchers at Lockheed in 70s years of 20th century. They proposed aqueous alkaline solution as electrolyte but the problems relating to low

efficiency and safety problem due to the parasitic chemical reaction of Li with the water generating hydrogen led to the abandonment of this concept in the 1980s [2-5].

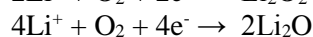
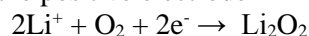
In 1996 Abraham and Jiang [6] devise a prototype of a working reverse system: Li-Air using non-aqueous aprotic electrolyte. The interest of this electrolyte is generated by its successful usage in lithium-ion batteries and will lead to the faster usage of the new system in real products.

The possible electrochemical reactions in the Lithium-Air system with non-aqueous aprotic electrolyte are done on the limit of gas-diffusion electrode (GDE) – electrolyte [3] and are as follow:

On the negative electrode



On the positive electrode



It becomes clear that the electrochemical mechanism of the reactions on the positive electrode is not totally defined and the ultimate results depend a lot from the used catalysts.

To the present moment the problems with the contemporary Lithium-Air batteries are the following:

1. Low practical energy density versus the theoretical

\* To whom all correspondence should be sent:

E-mail: ip1997alp@yahoo.com

2. High polarization of the air electrode during the charge-discharge cycles;
3. The oxidation of the electrolyte and the gas-diffusion electrode leads to side products ( $\text{CO}_2$ )
4. Low power density according to Li-ion
5. Battery capacity depends on the electrolyte quantity that is wetted the electrode. The low solubility and diffusion of the oxide in contemporary electrolytes also has resulted in low outcomes.
6. The metal lithium tends to transformation of dendrites leading to the necessity of using a protective layer between the metal and the electrolyte
7. Keeping of the reaction products ( $\text{Li}_2\text{O}$ ,  $\text{Li}_2\text{O}_2$ );

These problems are mainly a result of the inefficiency of gas-diffusion electrode including the difficult transportation of  $\text{O}_2$  through the pores and the more important depositing of the products of the reaction of oxygen reduction in the active layer of the electrode [7-9].

The usage of suitable catalysts could solve the biggest part of the existing problems, to improve the reaction dynamic which will lead to the diminishing of energy loss connected to polarization and also to the perspective of a reverse reaction to be done. The literature data [10, 11] pointed that the usage of bipolar catalysts can improve the oxygen reduction and the fragmentation of the ultimate products. The cobalt containing catalysts Co/Ni (Cobalt/Nickel) and CoTMPP (Co-tetramethoxyphenylporphyrin) we used in metal-air systems with water based electrolytes were checked in Li-air system in order to see the reaction kinetics and the polarization of charge/discharge cycles. Reason for this is given to us by the fact that these catalysts were explored in detail and successfully installed in the Zn-Air and Mg-Air batteries developed in IEES – BAS.

The aim of this research is to study the sustainability of the electrode gas-diffusion layer in several electrolyte solutions as well as the electrochemical behaviour of a couple different catalysts in lithium-air system with aprotic non-aqueous electrolyte.

## EXPERIMENTAL

The CoTMPP-700 catalyst was especially immobilized on VS-50 for SEM and EDS investigations. The CoTMPP solution was impregnated on dispersed  $\text{SiO}_2$  (VS50) and after drying was heated in Ar atmosphere at  $700\text{ }^\circ\text{C}$ . Pyrolysed CoTMPP catalyst was produced by impregnation of acetylene black with CoTMPP

solution, drying and subsequent treatment in Ar at  $800\text{ }^\circ\text{C}$ . During the heat treatment the CoTMPP molecule is decomposed and the pyrolysis residual products are formed in the porous structure of the carbon substrate and are responsible for the observed high electrochemical activity of the catalyst in Zn-Air system [12]. Active Carbon CoNi catalyst was prepared by impregnation of active carbon Norit NK with a solution of both Co- and Ni-acetates, drying and heat treatment in air at  $300\text{ }^\circ\text{C}$ . The electrodes were prepared via consecutive pressing of gas-diffusion layer and catalyst active layer.

We observe the behavior of a couple carbon materials in non-aqueous non-proton electrolytes and explore the behavior of cobalt containing catalysts Co/Ni and CoTMPP. That's why we did two types of experiments: wetting tests and basic electrochemical examinations.

Gas diffusion (GD) layer was prepared by a special technology described previously [13]. Teflonized acetylene black with PTFE content of 35% (XC-35) or 40% (XC-40) were used for preparing. The PTFE was used as binder and lyophobic agent. After the teflonizing, the material was palletized by pressing at  $200\text{ kg cm}^{-2}$ . Thus prepared gas-diffusion layer mainly contains mesopores with sizes 20nm and 50nm and it is successfully used in our Zn-Air and Mg-Air batteries [14]. The pores size significantly influences the electrode behavior in the Li-air system and the optimal size mentioned in the literature [15-17] is also between 20 to 60nm.

We check pellets of teflonized acetylene black, carbon paper TP 0,120mm thick and also polymeric material Nafion<sup>®</sup> of the company Alfa Aesar 0,180mm thick for wetting in Propylene carbonate (PC)/Ethylene carbonate (EC), Dimethoxyethane (DME) and PC/Dimethyl carbonate (DMC) solvents.

A simple weight method was used for checking the porosity of the GD layer. The pellets with previously checked weight and volume were wetted in acetone for few hours. After drying of the surface the weight of the pellets was checked again. The porosity was calculated on the collected data. Mercury porosimetry method was not used due to the flexibility of the pellet which will be smashed by the pressure.

The gas diffusion electrode (GDE) was prepared by adding the mixture of catalyst and teflonized acetylene black on the one side of the pellet and a nickel grid on the other as a current collector and

for mechanic stability. The components again were pressed with  $300 \text{ kg cm}^{-2}$ .

For the electrochemical tests of gas-diffusing electrode we did a semi-cell against metal lithium electrode. The cell assembling was done in an argon glove box with less than 50 ppm moisture. A standard button cell type 2032 with five 0,2 mm holes on the can was used for this purpose. The used electrolyte was  $\text{LiClO}_4$  solved in a solution of PC:EC – 1:1. The used separators were AGM type, the thickness of the lithium foils was 0,3mm. A layer of Parafilm® was putted on the holes of the assembled cell before taking out from the box and the cell was closed with the device for button cell 2032. Before the electrochemical research start the Parafilm® layer was removed and the open circuit voltage (OCV) was measured. Cycling voltammetry (CV) analysis was done on EcoChemie® Autolab® device and the charge-discharge cycling was carried out on a homemade galvanostatic cycling device in the voltage limits between 1,8 to 4,6 V at a constant current of 0,5 and 1 mA.

## RESULTS AND DISCUSSION

The SEM images of Co/Ni catalyst incorporated on Norit NK substrate are shown on Fig. 1 where the places of EDS analysis are numbered. The Co/Ni catalyst mainly covers the surface of Norit NK particles. The results of EDS analysis are illustrated in Fig. 2. Except the presence of carbon due to the Norit NK it is evident the catalyst of Co and Ni oxides (non-stoichiometric ones). The traces of magnesium registered by EDS (Fig. 2a, b) most probably are due to some impurities in Norit NK.

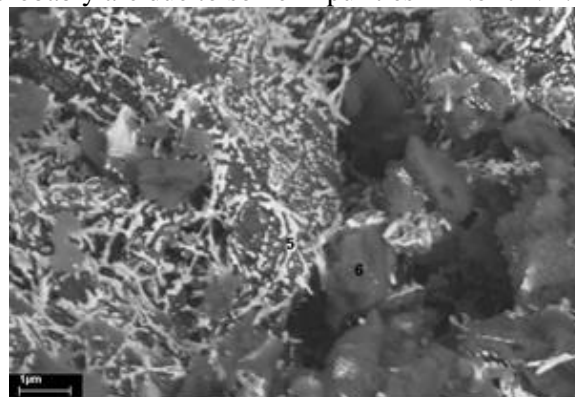
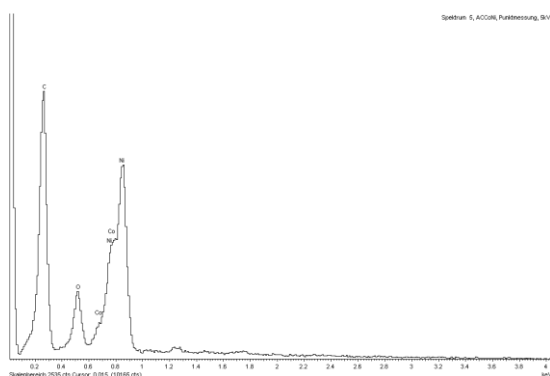
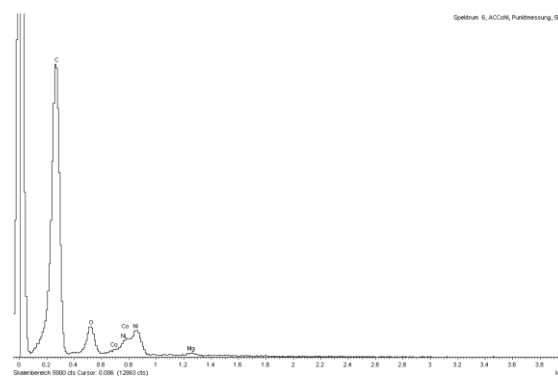


**Fig. 1.** SEM image of Norit NK immobilized with Co/Ni catalyst



(a)



(b)

**Figure 2.** EDS analysis results from points 5 (a) and 6 (b) on SEM picture (**Fig. 1**).

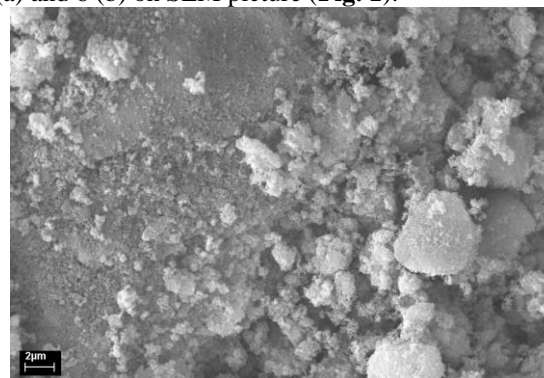
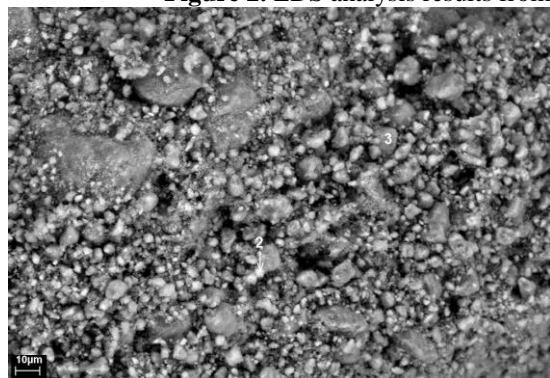


**Figure 3.** SEM image of CoTMPP-700 catalyst incorporated on VS-50.

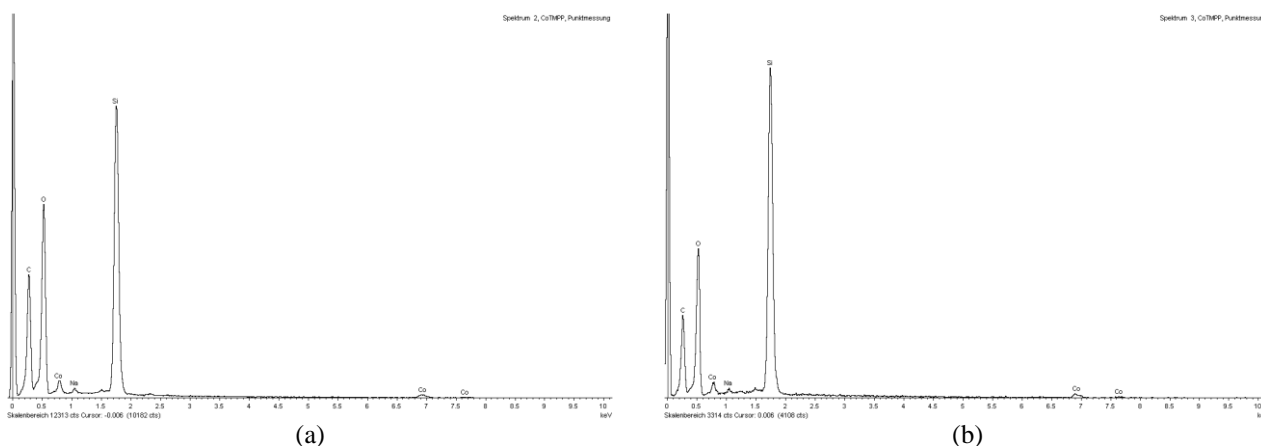


**Figure 4.** Results from EDS carried out in p. 2 and p. 3. (Fig.3a).

The same investigations were carried out for the other catalyst. SEM picture of CoTMPP-700 catalyst incorporated on VS-50 are shown on Fig.3. Different size of particles were obtained after the pyrolysis process which is probably due to the generation of carbon particles from CoTMPP pyrolysis and SiO<sub>2</sub> particles agglomeration initiated by the same process (Fig. 3a and Fig.3b).

Energy dispersion spectroscopy was applied in points 2 and 3 mentioned in Fig. 3a. The results are illustrated in Fig.4. VS-50 explained the presence of silicon while the carbon in the spectra is due to the CoTMPP pyrolysis. The choice of VS as a substrate allows us to demonstrate the carbon generation during the CoTMPP decomposition.

The registered small amount of Sodium most probably is due to the production of VS-50 which is dispersed SiO<sub>2</sub>.

The next stage of work was to explore the wetting ability of the carbon materials XC-35, XC-40, teflonized carbon paper and Nafion® in a solution of PC/EC, a mixture of PC/DMC and pure DME. The results are listed in Table1.

The results show that all carbon materials were wetted in PC/DMC and partially wetted in PC/EC after 40 days staying. DME solvent covers only the surface of the pellets and there is not wetting in the pellet volume. Based on these results for the initial electrochemical studies we worked with EC/PC solvent because it is a widely used solvent in the Li-Ion batteries. The Nafion® membrane was swelling after a prolonged contact with the tested solvents. Probably its usage as a protect layer for the metal lithium won't be proper.

The measured porosity of the teflonized carbon pellets (35% Teflon) by the method described above is in the range 76 – 79 %.

The second part of the work was the study of the electrochemical behaviour of the GDE with both catalysts. The assembled button cells 2032 were connected to the EcoChemie Autolab® device by a button cell holder (Fig.5) for a slow voltammetry cycling. The electrodes were tested in the potential range 1,8 – 4,8V with scan rate of 50 – 70 μV/s. The tests were started from the OCV potentials: OCV<sub>CoNi</sub> = 3,067V and OCV<sub>CoTMPP</sub> = 3,26V.

**Table1.** Wetting of teflonized carbons and Nafion® membrane in different aprotic electrolyte

Material	Solvent		
	EC/PC	PC/DMC	DME
XC35* 0,7 mm	Wetted	Wetted	Wetted surface
XC40* 0,7 mm	Wetted	Wetted	Wetted surface
NAFION* 0,18 mm	Material swelling and solvent color change	Solvent color change	Material swelling and solvent color change
Carbon Paper 0,12 mm	No wetting	No wetting	No wetting



**Fig. 5.** Li-Air button cell 2032 and holder

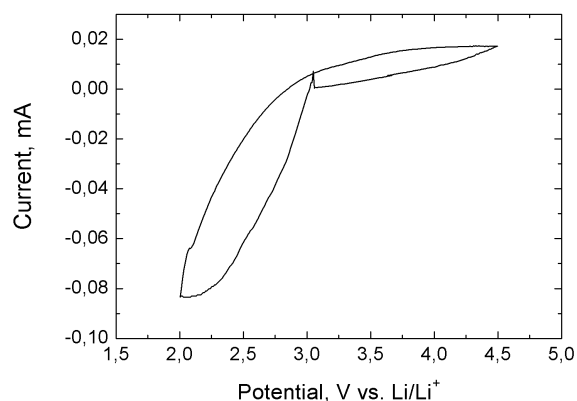


**Fig. 6.** Charge-discharge voltage curve for Co/Ni catalyst at 0,6mA current.

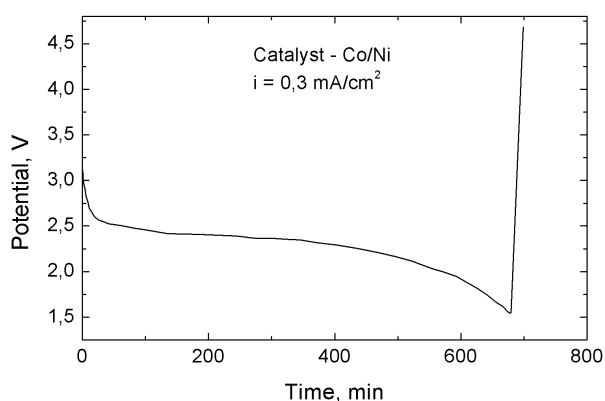


**Fig. 7.** Slow cycling voltage test of Co/Ni catalyst.

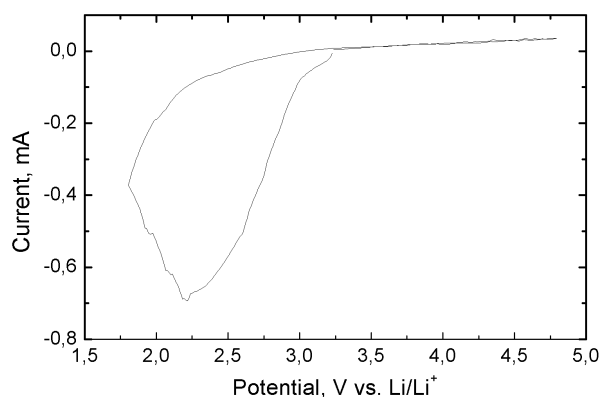


**Fig. 8.** Charge-discharge voltage curve for CoTMPP catalyst at 1mA current.

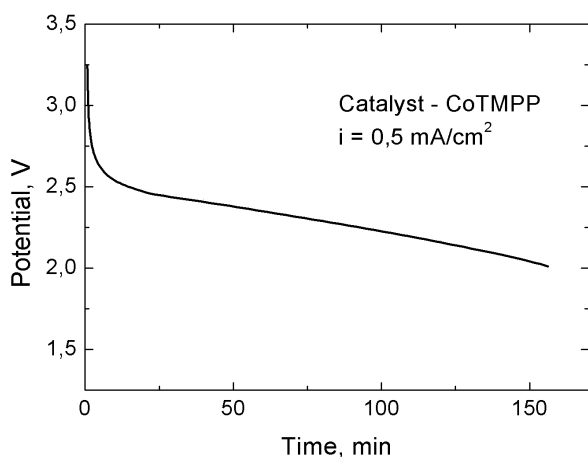


**Fig. 9.** Slow cycling voltage test of Co/Ni catalyst.

The obtained results from the slow CV of the electrodes with Co/Ni catalyst are shown on Fig.6. A sloping sharp voltage peak of the oxygen reduction reaction is evident. The average voltage value lies between 2.0 – 2.5 V. The obtained electrochemical capacity is 1.64 C. On the opposite side – oxygen evaluation reaction, a small broad peak between 3.1 – 3.6 V is evident. It can be concluded that this catalyst is not enough effective

for this reaction. This conclusion was confirmed from the galvanostatic tests.

The charge-discharge curve of cell with Co/Ni GDE is illustrated on Fig. 7. The electrode possesses specific capacity of 6 mAh at 0.6 mA current. A reverse reaction is not evident at this current rate.

The slow CV of the CoTMPP electrode is given on Fig. 8. A very large voltage peak was obtained for the oxygen reduction reaction with the average voltage value at 2.4 V. This means that the CoTMPP catalyst is very effective for this reaction but unfortunately this catalyst is not effective at all for the opposite oxygen evolution reaction. This is the reason to carry out only discharge galvanostatic test of the cell with CoTMPP GDE. The result is pointed out on Fig. 9. The obtained specific capacity from the electrode is 3 mAh at 1 mA current.

## CONCLUSIONS

The obtained discharge capacity is respectively 3 mAh for CoTMPP and 6 mAh for Co/Ni, but this value is obtained at twice less power charge (0,5 mA) from the case of CoTMPP electrode. These

results show that the two catalysts can be used as primary Li/O<sub>2</sub> batteries with non-aqueous electrolyte. The cell with catalyst Co/Ni shows reversibility at the slow cycling voltammetry test, but at a charge of 1mA it is very quickly polarized to the charge voltage limit.

#### REFERENCES

1. R. Padbury, X. Zhang, *J. Power Sources*, **196**, 4436, (2011).
2. D. Linden, T.B. Reddy, Handbook of Batteries, 3rd edition, McGraw-Hill, (2002).
3. D. Capsoni, M. Bini, S. Ferrari, E. Quartarone, P. Mustarelli, *J. Power Sources*, **220**, 253, (2012).
4. E.L. Littauer, K.C. Tsai, *J. Electrochem. Soc.*, **123**, 771 (1976).
5. I. Kowalczyk, J. Read, M. Salomon, *Pure Appl. Chem.*, **79**, 5, 851, (2007).
6. K.M. Abraham, Z. Jiang, *J. Electrochem. Soc.*, **143**, 1 (1996).
7. L. Zhanga, Z. Wang, D. Xua, X. Zhang and L. Wang, *Int. J. Smart Nano Materials*, **4**, 1 (2013).
8. A. Kraysberg, Y. Ein-Eli, *J. Power Sources*, **196**, 886 (2011).
9. S. S. Zhang, D. Foster, J. Read, *J. Power Sources*, **195**, 1235 (2010).
10. A. D'ebart, J. Bao, G. Armstrong, P. G. Bruce, *J. Power Sources*, **174**, 1177 (2007).
11. Y. Lu, Z. Xu, H. Gasteiger, S. Chen, K. Hamad-Schifferli, Y. Shao-Horn, *JACS*, **132**, 12170 (2010).
12. I. Iliev, A. Kaisheva, *US Patent*, 1392341.
13. R. Boukoureshlieva, S. Hristov, J. Milusheva, A. Kaisheva, *Bulg. Chem. Commun.*, **38**, 213 (2006).
14. S. R. Younesi, S. Urbonaite, F. Bjorefors, K. Edstrom, *J. Power Sources*, **196**, 9835 (2011).
15. C. Tran, X. Yang, D. Qu, *J. Power Sources*, **195**, 2057 (2010).
16. X. Yang, P. He, Y. Xia, *Electrochem. Commun.*, **11**, 1127 (2009).

### ПОВЕДЕНИЕ НА ГАЗОДИФУЗИОНЕН ЕЛЕКТРОД В НЕВОДНИ ЕЛЕКТРОЛИТИ ЗА СИСТЕМАТА ЛИТИЙ-ВЪЗДУХ

Ил. Попов<sup>1\*</sup>, Б. Велев<sup>1</sup>, Й. Милушева<sup>1</sup>, Р. Букурещлиева<sup>1</sup>, С. Христов<sup>1</sup>, Т. Станкулов<sup>1</sup>, Б. Банов<sup>1</sup>,  
А. Трифонова<sup>2</sup>

<sup>1</sup>Институт по електрохимия и енергийни системи, Българска академия на науките, София 1113

<sup>2</sup>АИТ Австрийски технологичен институт, Виена, Австрия

Постъпила на 5 март, 2013 г., приета на 19 април, 2013 г.

(Резюме)

Батериите литий-въздух са многообещаващи поради високият си теоретичен специфичен капацитет, който е много по-висок от съществуващите литиево-йонни батерии.

Целта на настоящата работа е да изследва поведението на газодифузионен електрод в неводни електролити за използване в системата литий-въздух, както и неговата работа в полуклетка срещу метален литиев електрод.

Газодифузионният електрод е приготвен с два вида катализатори: пиролизиран CoTMPP и активен въглен с Co/Ni и е изследван в стандартна клетка тип 2032. Цикличната волтаперометрия (CV) на електрода с катализатор CoTMPP показва необратима O<sub>2</sub> реакция, докато на електрода с Co/Ni катализатор беше установена обратимост на реакция – кислородна еволюция с капацитет 3 пъти по-малък от тази на кислородната редукция. Независимо от получената обратимост при бавна циклична волтаперометрия, на галваностатичните циклични тестове при 1 mA показват необратимост на процеса, който се дължи на много високата поляризация на обратната реакция в газодифузионния електрод при приложения тестов ток.

## Obtaining of electroless Ni-P/ZrO<sub>2</sub> composite coatings on flexible substrates of polyethylene terephthalate

M. Georgieva\*, M. Petrova, V. Chakarova

*Institute of Physical Chemistry, Bulgarian Academy of Sciences, Acad. G. Bonchev Str., Bl. 11, 1113 Sofia, Bulgaria,*

Received February 25, 2013; revised March 29, 2013

The incorporation of dispersed particles into metal matrices, achieved by the electroless codeposition process, has led to the obtaining of new generation of composite materials with definite chemical and physical properties.

The aim of these studies is to obtain Ni-P/ZrO<sub>2</sub> composite coatings by electroless plating process on flexible substrates from polyethylene terephthalate (PET). These coatings would ensure better mechanical properties in comparison with only electroless nickel plated samples.

In connection with the obtaining of these composite coatings, preliminary optimization of the electrolyte for electroless nickel plating is performed. For this purpose, the influence of its main parameters – i.e. NiSO<sub>4</sub>, NaH<sub>2</sub>PO<sub>2</sub>, surface active agents (SAA, known also as surfactants) and pH has been studied.

**Keywords:** Electroless Ni-P plating; Zirconium dioxide (ZrO<sub>2</sub>), Metal-matrix composites; Flexible materials; Metal dispersion coatings.

### 1. INTRODUCTION

The electroless nickel plating represents autocatalytic reduction of nickel ions on the interface of heterogeneous system. The most widely used electrolytes for electroless nickel plating contain two main components: nickel salt and reducing agent, such as sodium hypophosphite, borohydride, bor-nitrogen compounds, hydrazine, etc. Most widely used in the practice are the solutions with sodium hypophosphite as reducing agent. They also contain ligands of the nickel ion, buffer substances, stabilizers, accelerators, surface active substances (SAS), brighteners, etc.

The electroless nickel plating process with hypophosphite as reducing agent possesses the following characteristics:

- the reduction of the nickel ions is conducted only on several metals, which are capable of catalyzing the process, or on catalyzed dielectric surfaces;

- the obtained product does not represent pure nickel and always contain phosphorous, which is included in the coating in the form of intermetal compound. The quantity of phosphorous in the coating is changing depending on the conditions for the process implementation. The phosphorous content increases with the increase of the solution acidity; the process speed strongly depends on the temperature [1].

Stabilizers are added to increase the stability of the electroless nickel plating solutions. J. Cheong et al. in [2] have established that the adding of thiourea to the electroless nickel plating solution increases its stability. With the thiourea concentration increase the phosphorous content decreases. Upon the adding of 180 - 300 ml/l Maleic acid the coating becomes bright.

The optimization of the electroless nickel plating process of textile fabrics is very important for the industry. The process parameters such as - time, temperature, pH - are crucial for the obtained electroless coatings. They have been discussed by S.Q. Jiang et al. in [3].

S. Armyanov et al. in [4, 5] have studied in detail electroless deposition and some properties of Ni-Cu-P and Ni-Sn-P coatings. The introduction of Cu or Sn as a third component improves considerably the corrosion resistance of Ni-P alloys.

Most frequently metalized among the flexible polymer substrates is the polyethylene terephthalate (PET), since the textile industry needs material with average molecular mass of approx. 15 000. It is a linear homopolymer and a dominating composition of polyester fibres [6]. At room temperature they are acid-resistant. Long boiling in hydrochloric acid destroys the polyester, and the action of 96 % sulphuric acid causes destruction of the polymer.

C.W.M. Yuen et al. in [7, 8] have studied the properties of electroless nickel plated polyester after treatment with low-temperature plasma. It contains oxygen and argon and is used to obtain

---

\* To whom all correspondence should be sent:  
E-mail: [mgeorgieva@ipc.bas.bg](mailto:mgeorgieva@ipc.bas.bg)

hydrophilic properties of the polyester specimen and to facilitate the absorption of the palladium catalyst, which catalyzes the surface prior to the electroless nickel plating.

R.H. Guo, S.Q. Jiang et al. in [9] have also studied the properties of the electroless nickel plated polyester fabric, depending on the electrolyte composition and the metalizing conditions. It has been found out that with the increase of NiSO<sub>4</sub> concentration the deposition speed increases linearly, while the phosphorous contents decreases from 11 to 7 %. SEM-micrographs show nodular (knotty) type of coating structure, which is indicative of the presence of amorphous structure. The efficiency of the shielding of the nickel plated polyester fabric against the electromagnetic interferences depending on the concentration of Ni<sup>2+</sup> in the electrolyte is studied and it varies from 20 to 40 dB within a frequency interval from 10 to 18 GHz.

The preliminary processing of polymer (polypropylene and polycarbonate) substrates, aiming at increasing the adhesion of the chemically deposited metal coating is studied in [10]. M. Charbonnier and M. Romand replace the classical roughening of the polymers using a mixture of CrO<sub>3</sub> and H<sub>2</sub>SO<sub>4</sub> with preliminary treatment using plasma or UV laser in O<sub>2</sub>, H<sub>2</sub> / NH<sub>3</sub> atmosphere.

Obtaining chemical dispersion Ni-P/ZrO<sub>2</sub> coatings is poorly studied. Ye Yuzhong et al. in [11] have been shown that coating containing 5.6 % ZrO<sub>2</sub> possesses higher high temperature oxidation resistance than the nickel coating itself.

K. Zielińska et al. [12] and P.A. Gay et al. [13] describe the deposition of the composite Ni-P/ZrO<sub>2</sub> coatings by electroless process, and the characterization of their mechanical and tribological properties.

From the literature review it has been concluded that the electroless nickel plating of the polyester fabric is of high importance for the practice.

The aim of this work is the development of appropriate in terms of composition and operation mode electrolytes for obtaining of disperse nickel-phosphorous coating with ZrO<sub>2</sub> particles on polyethylene terephthalate, as well as study of the properties of the obtained coatings.

## 2. EXPERIMENTAL

The experiments have been made using substrates of flexible non-woven fabric from polyethylene terephthalate (PET), subject to reinforcement through additional compaction (pressing). The surface of the PET substrate is 8

cm<sup>2</sup>. The preliminary treatment of the substrates is accomplished according to the following technological scheme:

- Degreasing in alkaline solution at 60 °C for 15 min;
- Activation in PdCl<sub>2</sub> colloidal solution at room temperature for 5 min;
- Acceleration in alkaline solution at room temperature for 5 min;

The electroless nickel plating has been accomplished in a solution, containing the following components, described in Table 1.

**Table 1.** Chemical compositions and operating conditions of the plating bath.

<u>Electrolyte components:</u>	<u>Concentration:</u>
NiSO <sub>4</sub> .7H <sub>2</sub> O, g/l	25
NaH <sub>2</sub> PO <sub>2</sub> .H <sub>2</sub> O, g/l	22
CH <sub>3</sub> COONa, g/l	20
Lactic acid, g/l	20
Stabilizer 2, mg/l	1
(a commercial product of TU-Sofia)	
Sodium lauril sulphonate (NaLS), g/l	0.01
<u>Operating conditions:</u>	
pH	4.6 - 4.8
Temperature, (°C)	82
Time, (min)	30-60

ZrO<sub>2</sub> with different size of the particles: 30/60 nm, 1/3 μm and 7/10 μm has been added as dispersoid to this base electrolyte. Their concentration in the electrolyte has been varied within the limits 2.5 ÷ 5.0 g/l, while the particles have been preliminary wetted with SAA (NaLS = 0.01 g/l) and in this form added to the electrolyte.

The disperse coatings have been obtained under continuous air agitation using air flow – 100 ml/min/ 250 ml electrolyte (with open glass surface ~ 38 cm<sup>2</sup>).

The deposition speed of the disperse coatings has been determined gravimetrically through the conditional thickness of the obtained coatings δ (μm). At these investigations is used the term “confidential thickness”, as the surface of the samples is without determined geometry. The difference of mass of the deposited coating has been measured as a difference in the mass of the substrates after and before metallization.

$$\Delta m = M - M_0,$$

where Δm is the mass of the deposited coating [g], M<sub>0</sub> is the mass of the specimen prior to metallization [g], and M – after metallization [g].

The morphology of the composite coating has been determined with scanning electron microscopy (JSM 6390 apparatus, JEOL, Japan).

### 3. RESULTS AND DISCUSSION

#### Impact of the main nickel electrolyte components

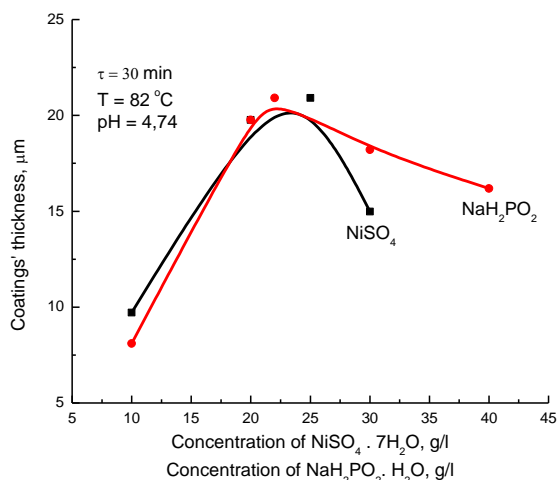


**Fig. 1.** Influence of  $\text{NiSO}_4$  and  $\text{NaH}_2\text{PO}_4$  concentration on the Ni-P coatings' thickness.

Usually acid solutions are used for electroless nickel plating of polymers. The concentration of the Sodium hypophosphite is of high importance for the deposition speed and the stability of the electrolytes [1]. In Fig. 1 the deposited Ni-P coatings' thickness upon a change in the  $\text{NaH}_2\text{PO}_2 \cdot \text{H}_2\text{O}$  and  $\text{NiSO}_4 \cdot 7\text{H}_2\text{O}$  content has been established. From the obtained data, shown on Fig.1, it is observed the appearance of the maximum at both components at concentrations 25 g/l for  $\text{NiSO}_4 \cdot 7\text{H}_2\text{O}$  and 22 g/l for  $\text{NaH}_2\text{PO}_2 \cdot \text{H}_2\text{O}$ . The ratio between  $\text{Ni}^{2+}$  and  $\text{H}_2\text{PO}_2^-$ , which should be within 0.25 – 0.6, is of high importance for the electrolytes' operation. For the following studies the used by us electrolyte included: 25 g/l  $\text{NiSO}_4 \cdot 7\text{H}_2\text{O}$ , 22 g/l  $\text{NaH}_2\text{PO}_2 \cdot \text{H}_2\text{O}$ , and the ratio between  $\text{Ni}^{2+}$  and  $\text{H}_2\text{PO}_2^-$  was 0.41. For concentrations above 30 g/l  $\text{NiSO}_4 \cdot 7\text{H}_2\text{O}$  and  $\text{NaH}_2\text{PO}_2 \cdot \text{H}_2\text{O}$  the solution becomes unstable and a spontaneous reduction of  $\text{Ni}^{2+}$  within the whole volume is possible. By this reason our studies were carried out with the above mentioned concentrations.

#### Influence of the organic additives

During reduction of the nickel ions with sodium hypophosphite the concentration of the hydrogen ions in the solution continuously increases – i.e. pH decreases. This leads to a change in the deposition speed. Therefore, organic acids and their salts are added to the electrolyte for nickel plating that exercises buffering effect and do not allow quick

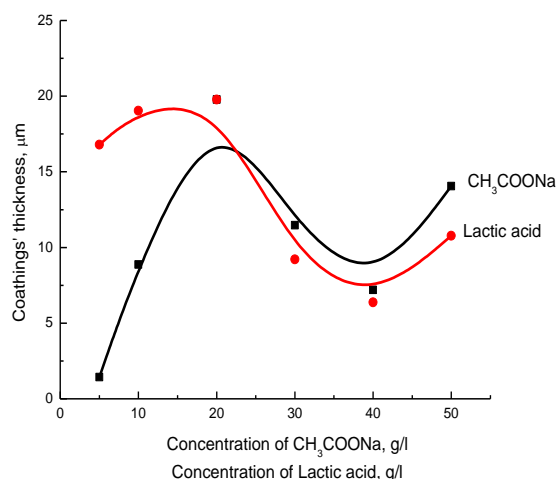


**Fig. 2.** Influence of the lactic acid and sodium acetate concentrations on the Ni-P coatings' thickness. Deposition time 30 min at 82 °C and  $\text{pH} = 4.8$ .

change of pH during operation. The anions of the organic acids, respectively of their salts, participate in the formation of different, sufficiently sustainable complex nickel ions and decrease the concentration of the free  $\text{Ni}^{2+}$  ions. Thus the electrolyte stability is increased.

Petrov [1], as well as Shalkayskas & Vashkialis [14] recommend as complexing agent in the acid solutions to use the following acids /or their salts/: lactic, aminoacetic (glycolic), citric, glycolic, etc. The complex formers can possess buffer properties as well. Such is the lactic acid, which at relatively low temperature possesses both properties. The organic additives exercise big influence on the speed of nickel reduction. For many of them the dependence of the nickel plating speed on the additive concentrations passes through a maximum.

The process acceleration is explained with the buffer action of the organic additives, and the speed reduction at high concentration of the additive is due to the blocking of the catalytic surface of the adsorbed organic substances.

According to Badet [15] the action of the accelerators can be explained with the loosening of the bond between the hydrogen and phosphorous in the sodium hypophosphite molecule. It should be noted that the majority of the accelerators are efficient buffers.

With aim of increasing the reduction speed of the nickel ions, we have studied the influence of the following buffering and complexing compounds: Sodium acetate and Lactic acid. From the obtained data, shown on Fig. 2, we had chosen 20 g/l as

optimal concentration for both organic additives used for the next investigations from us.

### Influence of pH

The change in the acidity of the nickel plating bath exercises big influence on its operation and stability, as well as on the phosphorous contents in the obtained coating.

For pH values below 4 the dissolution of the nickel coating in the acid medium is possible, which shows that uncovered sections are obtained.

**Table 2.** Influence of pH solution on the Ni-P coatings' thickness. Deposition time 30 min at 82 °C.

pH	3.8	4.0	4.8	5.0	5.5
δ, μm	13.63	20.52	38.57	37.85	37.31
(Δm, g)	(0.1067)	(0.1607)	(0.3021)	(0.2964)	(0.2922)
EDS, wt %					
C K	5.39		8.70		8.89
O K	0.78		1.03		2.79
P K	7.07		5.94		5.38
Ni K	86.76		84.33		82.94

Besides that during the reduction of the nickel ions high-soluble nickel phosphite is formed.

These studies were asked to establish the most appropriate pH - values for which the selected by us nickel electrolytes have the biggest deposition speed, stability and utilization. The dependence of the deposition speed on different pH values of the electrolyte is shown in Table 2.

From the obtained data it is seen that with pH increase the speed of reduction is increased, but during previous work at pH – value above 5.0 sediments of insoluble compounds are obtained and the probability for spontaneous reduction of the nickel ions within the whole electrolyte volume is increased. Due to this reason during our later studies we worked with pH within the range 4.6 ÷ 4.8. From the data in the table the change of the %

content of P in the coating is seen, which decreases with the pH increase of the solution [1].

### Influence of the surface active agents (SAA) and the stabilizers

According to the reference [1] SAA can also play the role of stabilizers of the electroless nickel plating.

The results from the dependence of the deposited nickel coating thickness on the different SAA (veranol H-10, sodium lauryl sulfonate(NaLS)

and PEG-4000) concentration on Fig. 3 were shown. The obtained results show that PEG-4000, which is non-ionogenic SAA, reveals constant values, but at high electrolyte concentrations. For anion-active surfactant such as NaLS, the deposition speed is the highest but at low concentrations in the electrolyte. The veranol, from one side, is environmentally danger and is forbidden from the EU because it contains polyphenol. From the other side, the obtained results from us show diminishing of the deposition speed. Therefore, we preferred to work with NaLS within the range 0.01÷0.1 g/l and by financial point of view also.

With the aim to optimize the electrolyte composition the influence of the coating thickness has been studied in relation of presence of preliminary selected by us optimal SAA (NaLS) concentrations and of the following stabilizers: Na<sub>2</sub>S<sub>2</sub>O<sub>3</sub>, Stabilizer 1 (a commercial product of TU-Sofia) and Stabilizer 2 (a commercial product of TU-Sofia).

**Table 3.** Influence of the Stabilizer type on Ni-P coatings' thickness in the presence of 0.01 g/l NaLS in electrolyte to electroless plating. Deposition time: 30 min.

Type of Stabilizer, 1 mg/l	δ, μm (Δm, g)
NaLS + Na <sub>2</sub> S <sub>2</sub> O <sub>3</sub>	22.08 (0.1729)
NaLS + Stabilizer 1	23.73 (0.1858)
NaLS + Stabilizer 2	26.04 (0.2039)

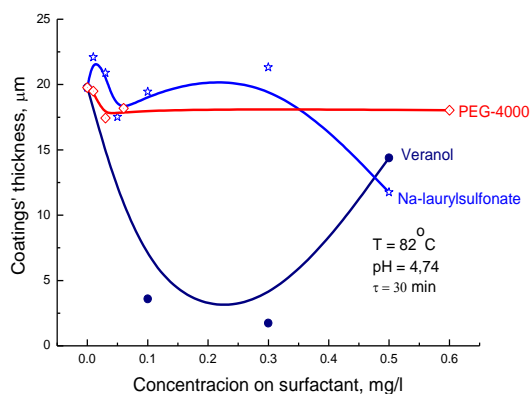


**Fig. 3.** Influence of the type and concentration of Surfactants on Ni-P coatings' thickness.

The obtained data in Table 3 has showed that in the presence of NaLS and Stabilizer 2, the deposition speed, respectively the thickness of the obtained coatings is the highest, due to which all further studies have been conducted using this combination.

#### Obtaining of composite Ni-P/ZrO<sub>2</sub> coatings

The data on Fig. 4 show the change in the thickness of the composite Ni-P coating in the presence of different size ZrO<sub>2</sub> particles. The studies have been conducted for two different

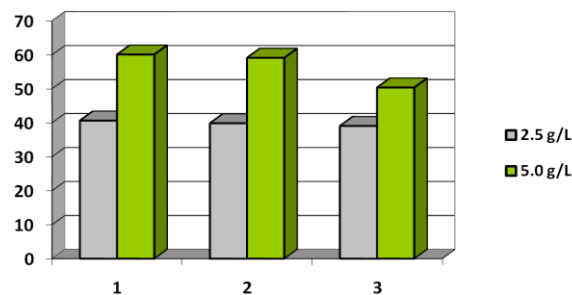


**Fig. 4.** Influence of ZrO<sub>2</sub> concentration and type on the conditional thickness of the composite coatings: 1 - ZrO<sub>2</sub> 30/60 nm; 2 - ZrO<sub>2</sub> 1/3 µm; 3 - ZrO<sub>2</sub> 7/10 µm.

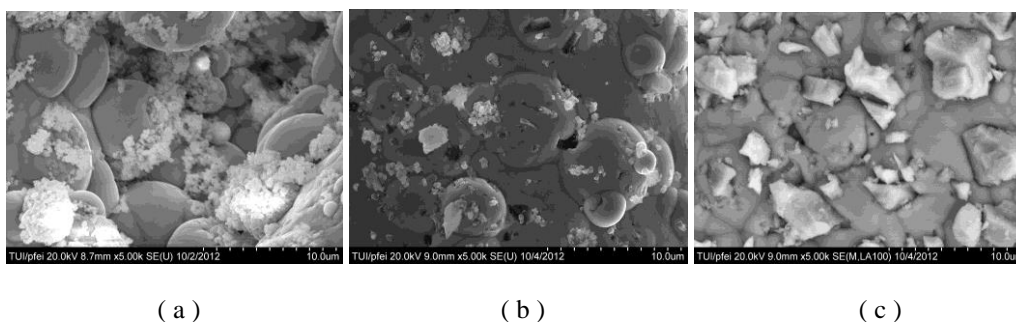


**Fig. 5.** SEM micrographs of the composite Ni-P/ZrO<sub>2</sub>: a) ZrO<sub>2</sub> 30/60 nm; b) ZrO<sub>2</sub> 1/3 µm; c) ZrO<sub>2</sub> 7/10 µm.

concentrations (2.5 g/l and 5.0 g/l) of the dispersoid in the electrolyte. No significant change in the thickness of the coatings depending on the particle sizes is observed. With the increase of the concentration of the dispersoid in the electrolyte the thickness of the composite coating is also increasing. With increasing of the particles' size in the electrolyte, their number in the composite coating diminishes.

The results for the increasing of ZrO<sub>2</sub> in the composite coating have been confirmed by the taken SEM-micrographs of the surface morphology of the three disperse coatings on Fig. 5 for equal concentration of the dispersoids in the electrolyte, and EDS-analysis, showing the contents of Zr incorporated in the coatings as follows: 1 (ZrO<sub>2</sub> 30/60 nm) – 30.60 wt. %, 2 (ZrO<sub>2</sub> 1/3 µm) - 20.30 wt. % and 3 (ZrO<sub>2</sub> 7/10 µm) - 18.44 wt. %.

#### CONCLUSIONS

In connection with the obtaining of electroless composite Ni-P/ZrO<sub>2</sub> coatings preliminary optimization of the electrolyte composition and of the electroless nickel plating has been conducted. For this purpose the influence of NiSO<sub>4</sub>, NaH<sub>2</sub>PO<sub>2</sub>, SAA, stabilizers and pH has been studied.

The inclusion of disperse ZrO<sub>2</sub> particles in metal Ni-P matrices, on flexible substrates has led to the obtaining of composite materials, characterized by

definite chemical and physical properties, which will be studied at our following investigations.

The obtained materials are implementable for raising the wear resistance of machine elements, as well as for restoration of worn working surfaces of rubbing parts.

#### ACKNOWLEDGEMENT:

The authors gratefully acknowledge the financial support of Project BG 051PO001-3.3.06-0038 and of National Foundation "Scientific Research" (Bulgaria) under Contract No. DID 02/28.

#### REFERENCES

1. H. Petrov, Galvanization of plastics, Technika Publ.H., Sofia, 1982.
2. J. Cheong, B.L. Luan, D.W. Shoosmith, *Appl. Surface Sci.*, **229**, 282 (2004).
3. S.Q. Jiang, C.W. Kan, C.W.M. Yuen, W.K. Wong, *J. Appl. Polymer Sci.*, **108**, 2630 (2008).
4. J. Georgieva, S. Armyanov, *J. Solid State Electrochem.*, **11**, 869 (2007).
5. S. Armyanov, J. Georgieva, D. Tachev, E. Valova, N. Nyagolova, S. Mehta, D. Leibman, A. Ruffini, *Electrochem. Solid State*, **2**, 323 (1999).
6. A. Bendak, S.M. El-Marsafli, *J. Islamic Acad. Sci.*, **4**, 275 (1991).
7. C.W.M. Yuen, S.Q. Jiang, C.W. Kan, W.S. Tung, *J. Appl. Polymer Sci.*, **105**, 2046 (2007).

8. C.W.M. Yuen, S.Q. Jiang, C.W. Kan, W.S. Tung, *App. Surface Sci.*, **253**, 5250 (2007).
9. R.H. Guo, S.Q. Jiang, C.W.M. Yuen, M.C.F. Ng, G.H. Zueng, *J. Coat. Technol. Res.*, Published Online: 01 December 2009.
10. M. Charbonnier, M. Romand, *Int. J. Adhesion Adhesives*, **23**, 277 (2003).
11. Y. Yuzhong, C.J. Zongde, W. Yinghua, *Diandu yu jingshi (Plat. and Finish)*, **15**, 9 (1993).
12. K. Zielińska, A. Stankiewicz, I. Szczygieł, *J. Colloid Interface Sci.* (2012); <http://dx.doi.org/10.1016/j.jcis.2012.03.049>
13. P.A. Gay, J.M. Limat, P.A. Steinmann, J. Pagetti, *Surface Coatings Technol.*, **202**, 1167 (2007).
14. M. Shalkayskas, A. Vashkialis, *Chemical Metallization of Plastics*, Chimia Publ. House, Leningrad, 1972
15. P. Badet, *Galvanoteknik*, **38**, 381(1968).

## ПОЛУЧАВАНЕ НА ХИМИЧНИ КОМПОЗИТНИ Ni-P/ZrO<sub>2</sub> ПОКРИТИЯ ВЪРХУ ГЪВКАВИ ПОДЛОЖКИ ОТ ПОЛИЕТИЛЕН ТЕРЕФТАЛАТ

М. Георгиева, М. Петрова, В. Чакърва

*Институт по физикохимия, Българска академия на науките, ул. „Акад. Г. Бончев“, Бл. 11, 1113 София, България,*

Постъпила на 25 февруари, 2013 г.; Коригирана на 29 март, 2013 г.

(Резюме)

Включването на дисперсни частици в метални матрици, постигнато чрез процеса на химично съотлагане, доведе до получаването на ново поколение композитни материали, характеризиращи се с определени химични и физични свойства.

Целта на тези изследвания е получаването на химични композитни Ni-P/ZrO<sub>2</sub> покрития върху гъвкави подложки от полиетилен терефталат (PET). С тези покрития се постигат по-добри механични характеристики, в сравнение с такива, в които няма включени частици.

Във връзка с получаването на тези композитни покрития предварително е проведено оптимизиране на електролита за химично никелиране. За тази цел е изследвано влиянието на основните му параметри, а именно NiSO<sub>4</sub>, NaH<sub>2</sub>PO<sub>2</sub>, ПАВ и рН.

## Glassy carbon (GC) electrode modified with electrodeposited $ZrO_2$ and $ZrO_2 + Ce_2O_3 + Y_2O_3$ nanostructures as a cathode in the obtaining of active chlorine

L.N. Petkov<sup>1\*</sup>, K.Sv. Yosifov<sup>1</sup>, A.S. Tsanev<sup>2</sup>, D. Stoychev<sup>2</sup>

<sup>1</sup>University of Chemical Technology and Metallurgy, bul. Kl. Ohridski 8, Sofia 1756

<sup>2</sup>Institute of Physical Chemistry, Bulgarian Academy of Sciences, ul. Akad. G. Bonchev 11, Sofia 1113

Received March 2, 2013; revised March 29, 2013

The experiments onto glassy carbon (GC), modified by electrodeposited oxide layers from zirconium, cerium and yttrium with sizes 30-100 nm are performed. The morphology and structure of deposits is characterised by SEM and elemental composition is investigated by XPS. Electrochemical activity of the modified glassy carbon is investigated by cyclic voltammetry as well by potentiodynamic method and tested with respect to the electrolysis of sodium chloride in order to obtain active chlorine. It is established, that the thin film of  $ZrO_2$  onto glassy carbon with intermediate layer of copper obtained in the regime of the reversible current increase the current efficiency of the process as a result of catalytic effect onto hydrogen evolution reaction.

**Keywords:** cyclic voltammetry, hypochlorite, modified cathode, nanostructures, oxides Ni-P plating; Zirconium dioxide ( $ZrO_2$ ), Metal-matrix composites; Flexible materials; Metal dispersion coatings.

### 1. INTRODUCTION

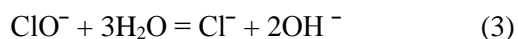
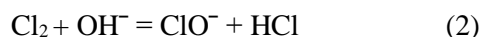
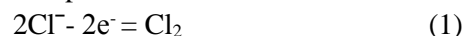
The modification of the electrode surface with deposits by organic and inorganic compounds, metals, metallic oxides, polymers, etc. favoured the widening of their application for the electrocatalytic and analytical properties, corrosion protection, improvement of magnetic and semiconducting properties and others. Especially the modification of the glassy carbon has important aspects. Some papers depict explanations of the obtaining of catalytic active thin films from the mixtures of  $RuCl_3 + K_4Ru(CN)_2$  [1] и  $OsO_4 + K_4Ru(CN)_6$  [2] onto glassy carbon. It has been proved, that rhuthenium film furthers the catalytic oxidation of  $As^{3+}$  [1] (also by mixed Os-Ru – thin film) methanol [3] and dythiocianat [4]. The coatings from  $Ag^{+1}$  and  $Mo(CN)_8^{-4}$  onto glassy carbon could also be used for the determination of the nonelectroactive ions [5].

In the last decade there has been a tendency in the modification of the surface of glassy carbon by films with the nuclei under 100 nm or shortly named nanostructures. The modification of the surface done this way gave the possibility for the wide application of the GS (mostly in the analytical chemistry) as an electrode with the increased sensitivity and selectivity for the determination of the different compounds as ascorbic acids [6], hydrazine [7], acetaminofenol [8], tyramine [9]

,  $Cr^{6+}$  [10], methylene blue [11], 2-4-6 trinitrotoluene [12], dopamine [13].

The method of obtaining electrochemically produced nanostructures is widely applied due to its advantages - ability to regulate the content of the coatings – the form and size of the particles, small expense, and easy control [14]. From this point of view the „template synthesis”, where the different materials – metals, oxides, semiconductors and other could be deposited onto porous substrate - polycarbonate „foams”, glassy carbon. By this way the process of the deposition ensures forming of nanotubes, nanorods and nanowires which dimensions could be easily controlled by changing the geometry of pores and the conditions of the electrodeposition [15-18].

It is well known that at by electrolysis of water solution of NaCl in the cell without diaphragm the follows processes proceed:



The reaction (3) occurs to be a secondary reaction which leads to a decrease of the yield of the active chlorine –  $ClO^-$ . In order to suppress this reaction some amount of  $Cr^{6+}$  is added which could be reduced onto the cathode to the  $Cr^{3+}$  and three valence chromium forms passive  $Cr(OH)_3$  film, which embarrass the access to the ions of  $ClO^-$  to the cathodic surface and thus, the rate of their reduction. This method is ineffective from an ecological point of view. Its alternative is a

\* To whom all correspondence should be sent:  
E-mail: Lubomir\_petkov@abv.bg

obtaining of suitable material with selective properties which allow the hydrogen evolution reaction and also embarrass the speed of cathodic reaction. Some appropriate material, investigated at the process of obtaining of active chlorine is  $ZrO_2$ , where the oxide is obtained by thermal and anodic oxidation of zirconium at the respected defined conditions [19].

The aim of the presented work is two-fold: modified glassy carbon electrode (500 pores  $inch^{-2}$ ) by nanosized layers of  $ZrO_2$  and  $ZrO_2 + Ce_2O_3 + Y_2O_3$  obtained electrochemically from organic (alcohol) solutions to be characterised by SEM, XPS, linear and cyclic voltammetry and moreover, by the method of cathodic efficiency the possibility to use this electrode as a cathodic material with mentioned selective properties to be proved.

## 2. EXPERIMENTAL

The experiments about modifying the electrode surface were performed onto samples from glassy carbon foam (500 pores  $inch^{-2}$ ) (with size 20x20 mm). Before electrolysis in the alcoholic solutions, containing Zr, Ce and Y onto carbon surface were deposited thin layer of copper (from sulfuric electrolyte) at different conditions (current density; time of deposition): sample 1 - 15  $mA\ cm^{-2}$ , 5 min; sample 2 - 1.5  $mA\ cm^{-2}$ , 2 - 5 min; sample 3 - reversive regime of deposition with cathodic period 240  $mA\ sec$  and anodic period - 15  $mA\ sec$  [20].

The samples has been deposited by  $ZrO_2$  in the solution of absolute ethyl alcohol, containing 60  $g\ dm^{-3}$  -  $ZrCl_3$  at the following conditions: for the sample 1 - at the temperature 15 °C, time of deposition - 1 hour, current density 250  $mA\ cm^{-2}$ , for the sample 2 - at the temperature 35 °C, time of deposition - 1 hour, current density 250  $mA\ cm^{-2}$ ; for the sample 3 - at the temperature 12 °C, time of deposition - 1 hour, current density 2000  $mA\ cm^{-2}$  [21].

The films of  $ZrO_2 + Ce_2O_3 + Y_2O_3$  was obtained onto glassy carbon with copper coatings, deposited during 50 sec - sample 4, 15 sec - for the sample 5 and the sample 6 was not deposited with sublayer of copper. The oxides were deposited in the solution of their respected salt in the absolute ethyl alcohol /  $ZrCl_3$  -3.2  $g\ dm^{-3}$ ,  $CeCl_3 \cdot 7H_2O$  -5.7  $g\ dm^{-3}$  и  $YCl_3 \cdot 6H_2O$  -3.5  $g\ dm^{-3}$  / at the potential 9 V, temperature 8-12 °C for 60 minutes/

The morphology, structure and the size of particles of the obtained  $ZrO_2$  and  $ZrO_2 + Ce_2O_3 + Y_2O_3$  thin films was studied by means of scanning electron microscopy (SEM) using a JEOL

200CX scanning microscope under conditions of secondary electron image (SEI).

The chemical states and composition of layers were investigated by XPS analysis. They were carried out by means of a VG Escalab Mk II spectrometer (England) using an Al  $K_{\alpha}$  excitation source (1486.6 eV) with a total instrumental resolution of ~1 eV, under a base pressure of  $1.10^{-8}$  Pa. The O 1s, Zr 3d, Ce 3d and Y 3d photoelectron lines were calibrated to the C 1s line. The surface composition of the mixed oxide layers was determined from the ratio of the corresponding peak areas, corrected with the photoionization cross sections [22].

Electrochemical characterisation was performed by cyclic voltammetry and potentiodynamic polarisation technique in the three electrode cell with volume 100  $cm^3$ . The counter electrode was platinum rode and reference electrode was Ag/AgCl with potential +0.197 V vs SHE. The experiments were performed onto potentiostat-galvanostat GAMRY FRAMEWORK PHE 200 with scan rate 25  $mV\ sec^{-1}$ . The concentration of the solutions was as follows: NaCl - 100  $g\ dm^{-3}$ ; NaOH - 40  $g\ dm^{-3}$ , NaCl 100  $g\ dm^{-3}$  + NaClO - 5.52  $g\ dm^{-3}$ .

Catalytic activities of the samples were investigated volumetric, by comparative analysis of the quantities of evolved from the cathode hydrogen. The experiments were performed at the cathodic current density -0.05  $A\ cm^{-2}$ , temperature -22° C and measuring time - 6 minutes. At this experiments the solutions of NaCl (100  $g\ dm^{-3}$ ), was used -100  $g\ dm^{-3}$  and NaCl - 100  $g\ dm^{-2}$ , containing NaClO - 5.52  $g\ dm^{-3}$  (obtained at the electrolysis of the solution of NaCl with ORTA) at the current density - 0.05  $A\ cm^{-2}$  and time - 4 hours.

## 3. RESULTS AND DISCUSSION

### *Morphology of the coatings*

The investigations of the structure and morphology of the modified glassy carbon with electrodeposited oxides of Zr, Ce and Y were performed by scanning electron microscopy. The systematic electron-microscopic investigation of the macro and microstructure of the porous carbon substrates, performed in the wide range of microscopic magnifications (from 50x to 100 000x) established that they are characterized with the size of macropores 50 to 300  $\mu m$  (Figure 1a). The elementary structural elements, that build the microstructure of the carbon material have a size about 10-20 nm, which firms the agglomerates with

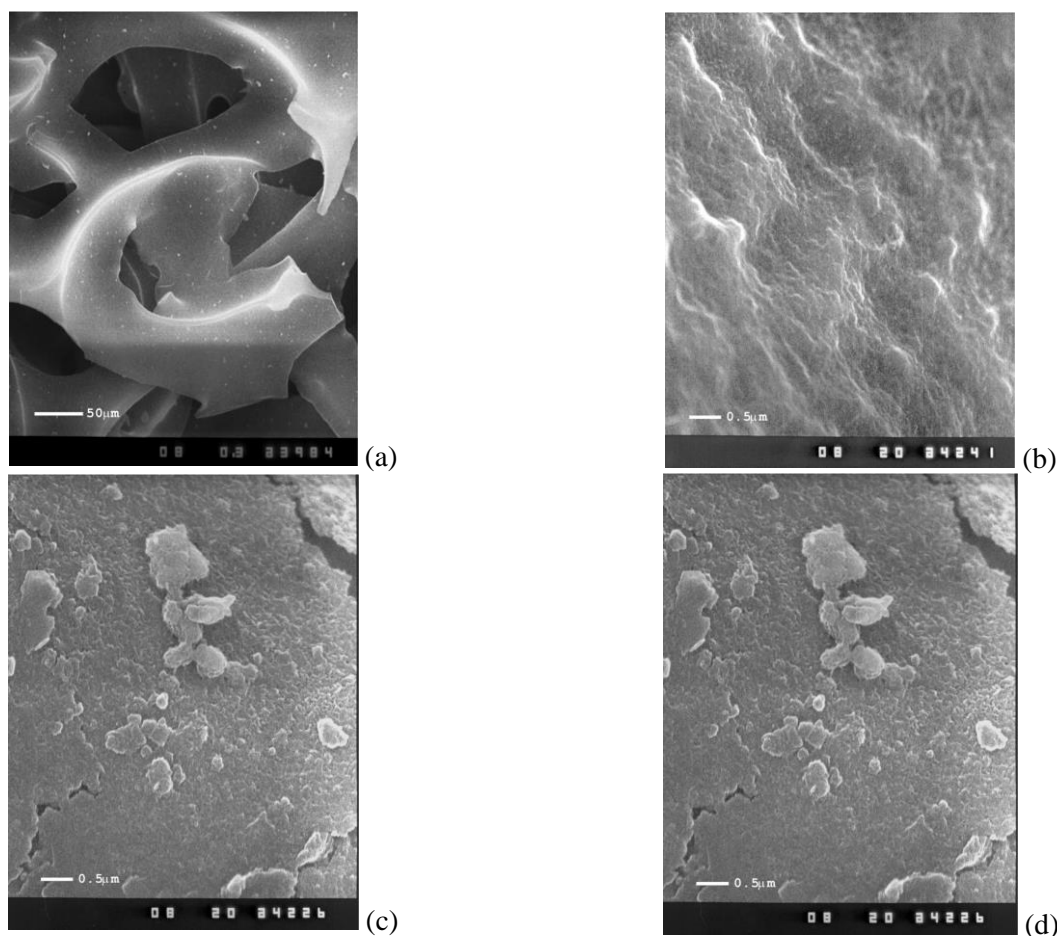


**Fig. 1.** Scanning electron images of glassy carbon: a) magnification 300x; b) modified with Cu (magnification 20 000x); c) modified with Cu and  $ZrO_2$  (20 000x) (sample 3) ; d) modified with c Cu и  $ZrO_2$ - $Ce_2O_3$ - $Y_2O_3$  (20 000x) (sample 5).

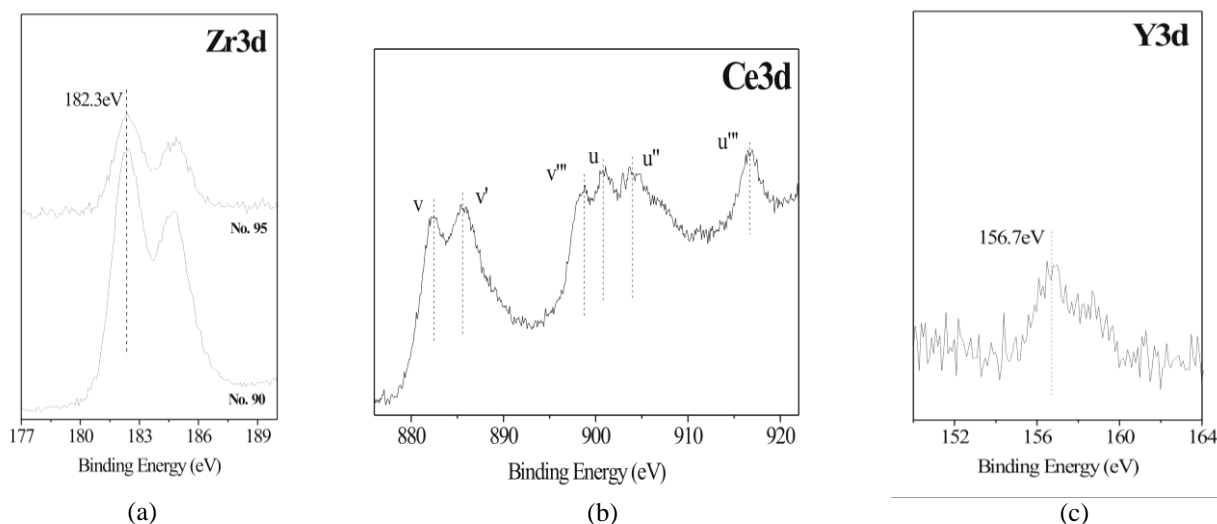


**Figure 2.** Photoelectron spectra of  $ZrO_2$  and  $ZrO_2$ - $Ce_2O_3$ - $Y_2O_3$  films, electrodeposited onto porous carbon surface (sample 3 and 5); a)  $Zr3d$  ; b)  $Ce3d$ ; c)  $Y3d$ .

size 25-50 nm. These agglomerates as well the existing much bigger „defects” (with size 0.5-4  $\mu m$ ) onto the smooth surface of the carbon material, which construct the macropores of the investigated „carbon foam”, most probably represent the

energetically favourable places for the growth/deposition (electrochemical or chemical) of the „carrier” from copper film (Figure 1 b) and „catalytic active phase” from oxides ( $ZrO_2$  or  $ZrO_2$ - $Ce_2O_3$ - $Y_2O_3$ ) layers (Figure 1c, d). The presence of

the carried copper layer with very high specific surface would guarantee the requisite adhesion of the coated afterward catalytic-active layers. Together, the high specific area of the copper sublayer with combination of extremely high specific (working) surface of the glassy carbon will work for the increasing of the catalytic activity of the complex system „foam carbon substrate- copper sulayer –  $ZrO_2$  or  $ZrO_2-Ce_2O_3- Y_2O_3$ .

Figure 1c and d shows that the electrodeposited layers of the real catalytic phases of  $ZrO_2$  or  $ZrO_2-Ce_2O_3-Y_2O_3$  (Figure 1 c, d) characterise with higher developed specific (working) surface, consisted from nanoparticles with sizes 30-100 nm.

#### XPS characterisation of the coatings

Figure 2 shows the parts of XPS spectra that were used for the characterisation of the chemical state of the elements in the electrodeposited oxide layers on the basis of Zr and Zr-Ce-Y onto deposited with a thin copper layer porous carbon substrates.

The binding energy of  $Zr3d_{5/2}$  peak in the spectrum of the electrodeposited thin film of  $ZrO_2$  at 182,3 eV (Fig.2a) for both samples (C/Cu/ $Zr_{Oxide}$  and C/Cu/ $Zr_{Oxide}-Ce_{Oxide}-Y_{Oxide}$ ) is characteristic for  $ZrO_2$  [23-26]. Also the obtained value of 2.4 eV for the peak separation between Zr  $3d_{3/2}$  and Zr  $3d_{5/2}$  is in accordance with other data for  $ZrO_2$ .

The Ce3d spectra (Figure 2b) are typical for Ce(III) and Ce (IV) oxidation state since the spectra contain two spin orbit doublets formed due to final state effects. Obviously,  $Ce_2O_3$  oxide is formed during the process of electrodeposition of ternary oxide system Zr –Ce –Y. The binding energy of the Y3d peak at 156.7 eV for electrodeposited mixed ternary system Zr –Ce –Y (Fig.3,c) corresponds to yttrium in  $Y_2O_3$  [27].

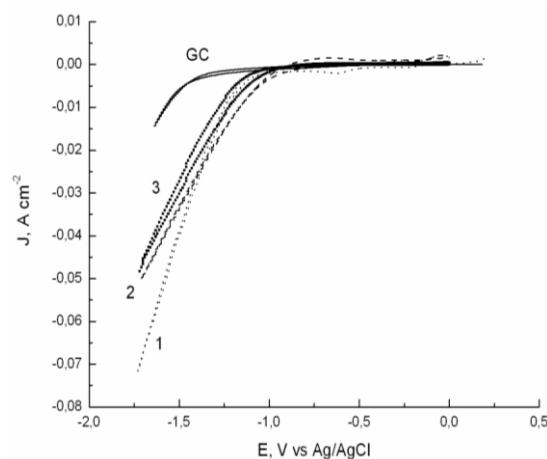
#### Cyclic voltammetry

Figure 3 presents the cyclic voltammetry curves, obtained onto glassy carbon with and without  $ZrO_2$  deposits - samples 1, 2 and 3 in the solution of NaCl . From the figures it can be seen that at the samples with oxide layer the depolarizing effect onto cathodic process - in this case, the hydrogen evolution reaction. The observed effect is about 400 mV and is not affected from the type of the sample.

The same effect of depolarisation of the cathodic process is observed at the relationships, recorded in 1M NaOH – Figure 4. In this case the depolarisation effect is smaller- about 200 mV. Moreover, the sharp increasing of the current density (second part of the polarisation curves) in

the samples 2 and 4 starts at the more positive, about 100 mV potentials.

The addition in the solution of  $NaClO /5.5 g dm^{-2}$  leads to the changes of the type of the investigation. The maximum of current onto sample 1 is observed at the potentials 0.6-0.8 V – Figure 5. The same correspond to the reduction of the  $NaClO$  and its height at the sample 1 is higher than those, observed



**Fig. 3.** Cyclic voltammetric curves in the solution of NaCl onto the glassy carbon, sample 1, 2 and 3.

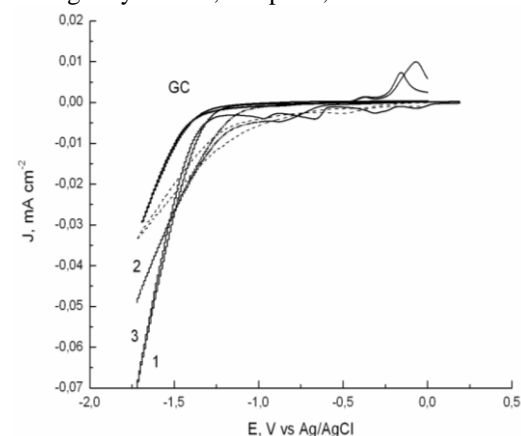


**Fig. 4.** Cyclic voltammetric curves in the solution of NaOH onto the glassy carbon, sample 2 and 3.

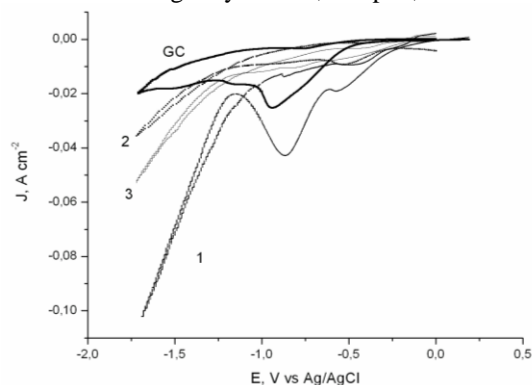


**Fig. 5 .** Cyclic voltammetric curves in the solution of NaCl+  $NaClO$  onto the glassy carbon, sample 1,2 and 3.

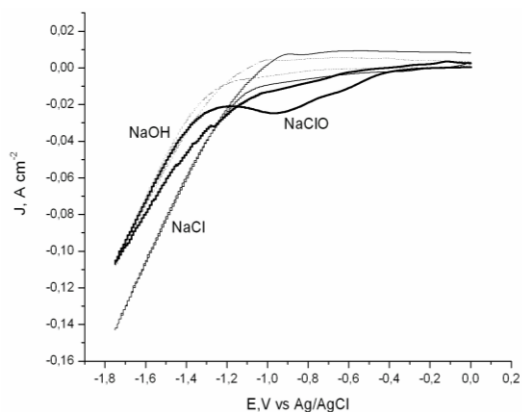


**Fig. 6.** Cyclic voltametric curves obtained onto sample 5 in three investigated solutions NaCl, NaOH and NaOH + NaClO.

onto the GC sample. As could be seen from the same figure onto the samples 2 and 3 the similar peak can not be observed (see Figure 5). Onto the samples from glassy carbon and the sample 1 the peak of current.

The maximum value of current density, respected to the reduction of NaClO also is observed at the samples from glassy carbon -  $ZrO_2 + Ce_2O_3 + Y_2O_3$  (samples 4, 5 and 6), but with smaller height in comparison with the sample 1 and the glassy carbon without oxide layer. Due to the similar behaviour of the run of the curves for all three above mentioned samples in Figure 6 the cyclic voltammetry curves for sample 5 are presented.

#### Potentiodynamic investigations

In Figures 7, 8 and 9 the potentiodynamic dependencies obtained in the solutions of NaCl, NaOH and NaCl + NaClO are depicted for samples 1, 2 and 3. From the obtained results it can be seen, that for all investigated solutions the dependencies have the same character. Some differences in the range of potentials for the cathodic parts of the sample 1 from one hand and samples 2 and 3 could be detected. Some conclusion about effect of depolarisation of the cathodic process which can be observed in sample 3 (and partially sample 2). Similar differences are not observed at the potentiodynamic dependencies for the samples with coatings from  $ZrO_2 + Ce_2O_3 + Y_2O_3$  - Figures 10 (due to the similarities the results for sample 5 only is given).

#### Volumetric determination of the catalytic activity

In order to determine the catalytic activity of the samples and their selectivity, experiments were conducted connected with the quantities of the evolved hydrogen from the solution of NaCl and

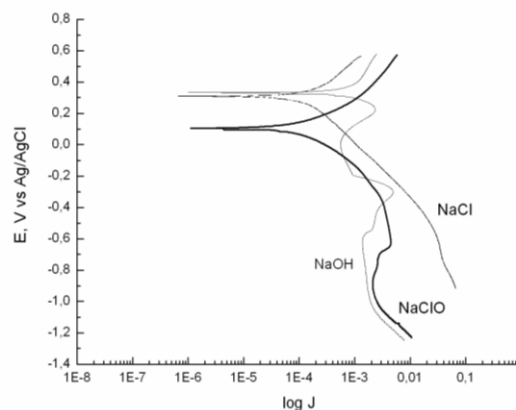


**Fig. 7.** Polarisation curves onto sample 1 – in the solutions NaCl, NaOH and NaCl + NaClO.

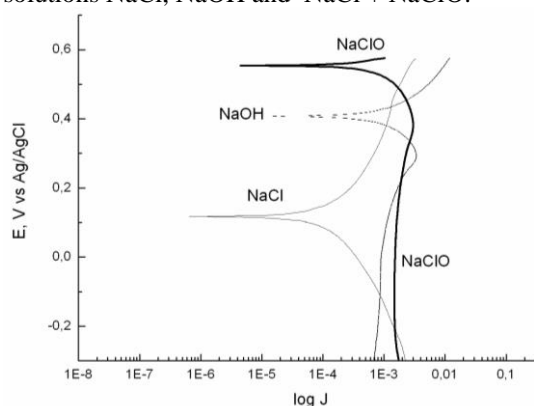


**Fig. 8.** Polarisation curves onto sample 2 – in the solutions NaCl, NaOH and NaCl + NaClO.

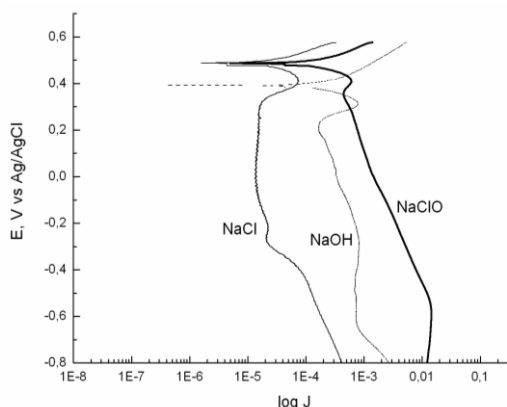


**Fig. 9.** Polarisation curves onto sample 3 – in the solutions NaCl, NaOH and NaCl + NaClO.

the solution of NaCl, containing NaClO ( $5.52 \text{ g} \cdot \text{dm}^{-3}$ ). The obtained results are presented in Table 1.

From the results, presented in Table 1 it can be seen, that the modifying of the surface of the glassy carbon with oxides of Zr and  $Zr+Ce + Y$  could lead to the increasing of the reaction rate of the hydrogen evolution reaction in comparison with the non-modified glassy carbon from the solution of NaCl.

The presence of NaClO leads to the decreasing of the quantity of the evolved hydrogen – results of the reduction onto the cathode. The slightest effect

is at probe 2 and just before probe 3 – at these samples the process of the reduction of the active chlorine  $Cl^+$  proceeds with smallest rate. The observed results correlate with the absence of the peak of current density onto the samples 2 and 3 onto the cyclic voltammetric curves, respected to the reduction of the

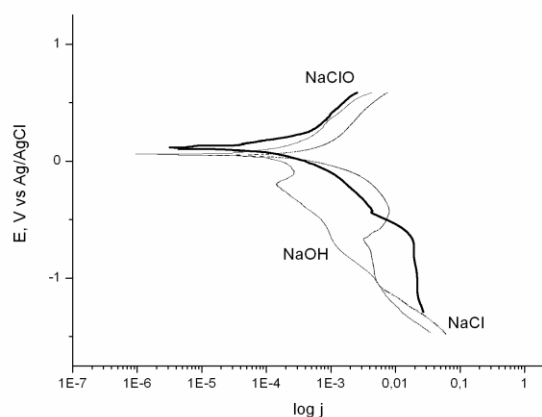


**Figure 10.** Polarisation curves onto sample 5 in the solution of NaCl, NaOH and NaCl +NaClO.

hypochlorite. It should be noted some depolarised effect of the process for sample 3, observed onto the potentiodynamic dependencies – Figure 8.

### CONCLUSIONS

1. The modification of the surface of the glassy carbon with nanosized  $ZrO_2$  и  $ZrO_2 + Ce_2O_3 + Y_2O_3$  leads to the increasing of deposition rate of the hydrogen evolution reaction in comparison with the cases of glassy carbon without coatings.

2. At the presence of the NaCl of the active chlorine /NaClO/ this effect is sliher due to the reduction of process of the reduction of active chlorine to chloride ions.

3. Deposition of sublayer onto the glassy carbon in the regime of reverse current effects positively onto the layer of  $ZrO_2$  in the relation of its selectivity of the hydrogen reaction and simultaneously the rate of reduction of  $Cl^+$  do not increase.

4. Modification of the surface of glassy carbon with a nanosized oxides of Zr and  $Zr + Ce + Y$  could be alternative to the compounds of  $Cr^{6+}$  related with suppressing of the process of reduction led to the decreasing of current efficiency of its electrochemical obtaining.

**Acknowledgments:** Financial support of the National Science Fund (Bulgaria) by project DVU-10-022-2012 and of the European project BG051PO001-3.3.06-003 is gratefully acknowledged.

**Table 1.** Quantity of evolved hydrogen in the solutions of NaCl and NaCl + NaClO.

Sample	$V_{H_2}/cm^{-3}$ NaCl, 100 g $dm^{-3}$	$V_{H_2}/cm^{-3}$ NaCl, 100 g $dm^{-3}$ + NaClO 5,52 g. $dm^{-3}$
Glassy carbon	6.4	3.0
1	8	3.6
2	8.4	5.0
3	7	6
4	7.8	4.4
5	7.8	4.6
6	8.2	4.4

As it was notes in the Experimentals the sample 3 presented the modified with  $ZrO_2$  glassy carbon, which should be coated with copper with the regime of reversive current. The obtained by these way coatings, characterized with high surface with comparison with copper coatings onto the other samples, obtained in the regime of direct current.

### REFERENCES

1. J.A. Cox, P.J. Kulesza, *Anal. Chem.*, **56**, 1021 (1984)
2. J.A. Cox, B.K. Das, *J. Electroanal. Chem.*, **223** 87 (1987)
3. P.J. Kulesza, *J. Electroanal. Chem.*, **220**, 295 (1987)
4. J.A. Cox, J. Gray, K.R. Kulkarni, *Anal. Chem.*, **60** 1710 (1988)
5. J.A. Cox, B.K. Das, *Anal. Chem.*, **57** 2739 (1985)
6. S. Kumar, V.V – Becket, Beilstein, *J. Nanotechnol.*, **3**, 388 (2012).
7. M. Coates, T. Nyokong, *Electrochim. Acta.*, **28**, 158 (2013).
8. J.B. Kaoof, R.Qjani, M. Baghayeri, M.A.– Aref, *Anal. Methods*, **6**, 1579 (2012).
9. B. Liu, L. Lu, M. Wang, Y Zi, *J. Chem. Soc.*, **5**, 493 (2008).
10. P. Arias, N.F. Ferrevra, G.S. Rivas, S. Bollo, *J. Electroanalyt. Chem.*, **634**, 123 (2009).
11. J. Wang, S.B. Hocevar, B. Ogorevc, *Electrochem. Comm.*, **6**, 2, 176 (2004)
12. S. Prakash, T. Chakrabarty, A.K. Singh, V.K. Shahi, *Electrochim. Acta*, **72**,157 (2012).
13. J. Nidhi, S. Alwarappan, S. Pillai, R. Shceekumar, S. Singh, R. Shree, M.K. Ram, A. Kumar, *Advanced Science Letters*, **5**, 131 (2012).
14. L.P. Bieceli, B. Bozzini, C. Mele, L.D. Urzo, *Int.J. Electrochem.Sci.*, **3**, 356 (2008)
15. R. Inguanta, S. Piazza, C. Sunsen, *Nanotechnology*, **18**, 561 (2007).

16. R. Inguanta, S. Piazza, C. Sunseri, *Electrochem. Soc.*, **205**, 115 (2009).
17. R. Inguanta, S. Piazza, C. Sunseri, *Electrochem. Solid*, **63**, 10 (2007).
18. R. Inguanta, M. Battera, C. Sunseri, S. Piazza, *Appl. Surf. Sci.*, **253**, 5447 (2007).
19. F. Herlitz, *J. Appl. Electrochem.*, **31**, 307 (2001).
20. D. Stoychev, I. Tomov, I. Vitanova, S. Rashkov, *Surf. Tech.*, **7**, 433 (1978).
21. A. Valov, D. Stoychev, Ts. Marinova, *Electrochem. Acta*, **47**, 4419 (2002).
22. J.H. Scofield, *J. Electron. Spectrosc. Rel. Fenom.*, **8**, 129 (1976).
23. T. L. Barr, *J. Phys. Chem.*, **82** (16), 1801 (1978).
24. P. Stefanov, G. Atanasova, D. Stoychev, Ts. Marinova, *Surf. Coat. Tech.*, **180-181**, 446 (2004).
25. B. V. CRIST, XPS Handbook of the Elements and Native Oxides, XPS International, Ames, IA, 1999
26. J. Moulder, W.F. Stickle, P.E. Sobol, K.D. Bomben, in: J. Chastain (Ed.), Handbook of X-ray Photoelectron Spectroscopy, second ed., Perkin-Elmer Corporation, Eden Prairie, MN, 1992
27. B.F. Dzhurinskii, D. Gati, N.P. Sergushin, V.I. Nefedov, YA. V. Salyn, *Rus. J. Inorganic Chem.*, **20**, 2307, (1975).

## СТЪКЛОВИДЕН ВЪГЛЕРОД (СВ) МОДИФИЦИРАН С ЕЛЕКТРООТЛОЖЕНИ НАНОСТРУКТУРИ НА $ZrO_2$ И $ZrO_2 + Ce_2O_3 + Y_2O_3$ КАТО КАТОД ПРИ ПОЛУЧАВАНЕТО НА АКТИВЕН ХЛОР

Л. Петков<sup>1</sup>, К. Йосифов<sup>1</sup>, А. Цанев<sup>2</sup>, Д. Стойчев<sup>2</sup>

<sup>1</sup>Химикотехнологичен и металургичен университет, 1756 София, България, бул. Кл. Охридски № 8

<sup>2</sup>Институт по физикохимия – БАН, 1113 София, България, ул. Акад. М. Бончев, бл.11, ет. IV

Постъпила на 2 март, 2013 г.; коригирана на 29 март, 2013 г.

(Резюме)

Проведени са експерименти със стъкловиден въглерод (СВ), модифициран с електроотложени оксиди на цирконий, церий и итрий с размери 30 – 100 nm. Морфологията и структурата на покритията е охарактеризирана чрез SEM, а елементният състав е изучен чрез XPS. Електрохимичната активност на модифицирания стъкловиден въглерод е изследвана, както чрез циклична волтаперометрия, така и чрез потенциодинамичен метод и е тествана по отношение на електролизата на натриев хлорид с цел получаването на активен хлор. Установено е, че тънък филм от  $ZrO_2$  върху стъкловиден въглерод с междинен меден слой, получен в режим на импулсен ток, повишава токовата ефективност на процеса в резултат на каталитичен ефект върху реакцията на отделяне на водород.

## Monitoring of the phenol biodegradation process with an electrochemical biosensor

R. Boukoureshtlieva<sup>1\*</sup>, S. Yankova<sup>2</sup>, V. Beschkov<sup>2</sup>, J. Milusheva<sup>1</sup>, G. Naydenova<sup>2</sup>, L. Popova<sup>2</sup>,  
G. Yotov<sup>2</sup>, S. Hristov<sup>1</sup>

<sup>1</sup>Institute of Electrochemistry and Energy Systems, Bulgarian Academy of Sciences, 1113 Sofia, Bulgaria

<sup>2</sup>Institute of Chemical Engineering, Bulgarian Academy of Sciences, 1113 Sofia, Bulgaria

Received March 1, 2013; revised May 05, 2013

Monitoring of the water (domestic and/or industrial) pollution continuously and on regular bases is a quite severe issue, which still demands proper solution. Here we report on development of an amperometric biosensor for detection of phenol degradation in water and we compare the analytical data with those obtained from the most common analytical method: HPLC (High Performance Liquid Chromatography).

The described biosensor consists of an enzyme electrode, comprising a porous hydrophobic carbon electrode with immobilized enzyme, namely: Tyrosinase from mushroom (EC 1.14.18.1). In accordance to study the efficiency of tyrosinase amperometric sensor for the determination of phenol concentration, experiments at constant potential of 0.0V vs. Ag/AgCl reference electrode in phosphate buffer solution (pH 7.0) are performed. The response time is not exceeding 3 min and the amperometric response increased linearly up to 2  $\mu\text{M}$  phenol concentration. The tyrosinase electrode exhibited a sensitivity of 330 nA  $\mu\text{M}^{-1}$  and the apparent Michaelis constant was calculated to be  $K^{\text{app}}_{\text{M}} = 12.6 \mu\text{M}$  with detection limit for phenol of 0.4  $\mu\text{M}$ . Moreover, the tyrosinase electrode exhibited a good reproducibility and stability during 35 days of periodical measurements.

The tyrosinase electrode investigated in our study is applied efficiently for the detection and determining of the phenol concentration in real water samples.

**Keywords:** biodegradation of phenol, tyrosinase, gas-diffusion electrode, *Klebsiella oxytoca* strain

### INTRODUCTION

Development of new, advanced technologies for removing wastewater contaminations is crucial issue regarding worldwide environmental pollution as result from human activities. Xenobiotics are one of the most toxic wastes from chemical, petrochemical, pharmaceutical, textile, and coke-chemical industry. Phenol and its derivatives are usually presented in higher than officially limited (restricted) concentrations in effluents from these industries [1].

The methods of wastewater treatment are various – physical [2, 3, 4], chemical [5, 6], physicochemical, thermal. The most advantageous among them are the biochemical methods, but phenol derivatives are among the most resistant compounds to biodegradation by microorganisms. However, here are known possibilities for degradation of phenol compounds by eukaryotic and prokaryotic organisms, despite their toxic effects in some cases. These organisms are capable of using such a phenolic compounds as a carbon and energy sources. This process involves a series of biochemical reactions, varying between different

strains of bacteria and yeast. Phenol degrading microorganisms belong to different taxonomic groups - bacteria, fungi, yeasts and algae and the very first example of biodegradation of phenols has been reported by Störmer (1908). Since then, over the decades of extensive research, were found many strains of microorganisms capable of degradation of phenol. Among them the most commonly used are: *Bacillus stearothermophilus* [7]; *Pseudomonas putida* [8]; *Agaricus bisporus*, [9], *Pseudomonas sp.* [10], *Fusarium sp.* [11], *Alcaligenes sp.* [12], *Klebsiella oxytoca* [13] and others. These microorganisms possess a multienzyme systems to break down organic compounds, converting them into harmless products. They are highly specific at very low energy consumption.

As we mentioned before, the most common methods for determination of phenolic compounds are colorimetric, gas or liquid chromatography and spectrophotometric analyses. However, some of these techniques are expensive, time consuming and they are unsuitable for on site or field based analyses [14, 15].

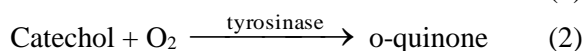
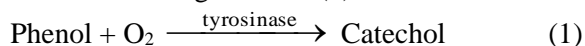
The use of electrochemical biosensors has been shown to be a suitable alternative with respect to conventional well established analytical techniques for the monitoring of phenolic compounds content

\* To whom all correspondence should be sent:  
E-mail: renirib@abv.bg

in local environment. Advantages of the presented analytical approach are its simplicity, relatively low cost and high selectivity [16].

The first report for polyphenoloxidases application in biosensors was published in 1977 by Macholan and Schanel [17]. Enzymes with wider substrate tolerance such as laccase, tyrosinase, peroxidase along with more specific enzymes, for e.g. phenolhydroxylase and catecholoxidase, could be used for enzyme electrode construction [18]. The phenoloxidizing enzymes mechanisms and some examples of their use in the construction of phenolselective biosensors are nicely reviewed by Peter and Wollenberger [19]. The biosensors based on the immobilization of tyrosinase on different electrode materials can be found in recent literature. Thus different materials [20-24] have been used to prepare tyrosinase electrochemical biosensors. In spite of the big amount of literature two general limitations need to be solved yet in order to improve their practical usefulness - the stability and high sensitivity of the biosensors [16].

The enzyme tyrosinase catalyzes phenols oxidation through hydroxylation with oxygen to catechols and subsequent dehydrogenation to the respective quinines compounds (1, 2). The electrochemical reduction of the product o-quinone is used as indicating reaction (3):



The catechol produced in the electrochemical reaction (3) is also taking place in the enzymatic reaction (2), so that an "enhancing effect" is observed [25].

The goals of this work is to study the feasibility of a biosensor for determining the phenol concentration during biodegradation of phenol using *Klebsiella oxytoca* VA 8391.

## EXPERIMENTAL

### *The experiment of phenol biodegradation*

*Klebsiella* is a genus of fixed, gram-negative, oxidase-negative, rod-shaped bacteria.

Inoculum of *Klebsiella oxytoca* strain is obtained on medium with a composition (Meat extract ("Fluka") - 10 g/l, Peptone ("Fluka") - 10 g/l, NaCl - 5 g/l and distilled water was added to 1 liter total volume, which is seeded from agar medium. Cultivation – on a shaker "WiseCube" at 30 °C, speed - 150 rpm, pH 7.0, duration of the process - 24 hours.

Experiments of phenol biodegradation were conducted in a thermostated glass reactor with a total volume of 200 ml with stirring (thermostat "MLW UH").

Medium used for biodegradation of phenol was MgSO<sub>4</sub>·7H<sub>2</sub>O - 0.2 g/l, CaCl<sub>2</sub>·2H<sub>2</sub>O - 0.2 g/l, NaCl - 5 g/l, phenol - 1 g/l and phosphate buffer (pH 7.0) with the following parameters: pH 7.0; revolution speed - 200 rpm; temperature 30 °C; inoculum aged 24 hours, pH ~ 7.0; volume of seed culture - 20 ml; volume of medium – 200 ml; temperature 30 °C; revolution speed = up to 100 rpm.

The biomass concentration was determined by measuring the absorbance of a sample at wavelength  $\lambda = 590$  nm on spectrophotometer Specol (CARL Zeiss, Jena, Germany). The biomass concentration of the bacterial strain *Klebsiella oxytoca* VA 8391 is calculated according to the equation (4):

$$C = (A - 0.0223) / 1.0019 \quad (4)$$

wherein C - biomass concentration g/l, A - absorption.

The concentration of phenol in the culture broth was determined by HPLC. The HPLC system was composed from a quaternary pump "Knauer S - 1000", UV - detector "Knauer", software for the collection and processing of data ("Eurochrom"), and C18 column "Discovery" (Shimadzu). As the mobile phase 10 % methanol in phosphate buffer pH 3.0 was used. The determination was carried out at a wavelength  $\lambda = 280$  nm at flow rate 1 ml/min.

Periodically, samples were taken to determine the biomass and the amount of the phenol in the culture medium.

### *Enzyme electrode preparation*

The investigated electrode comprises a porous carbon supporting layer placed in a conical plastic tube. Enzyme tyrosinase from mushroom (EC 1.14.18.1) is immobilized on the carbon electrode surface from the narrow end of the conic tube to form the enzyme electrode. For the enzyme immobilization the carbon electrode was treated with tyrosinase solution (4 mg/ml) and with neutralized Nafion 117 (Fluka) (5 weight %), solution. A porous carbon electrode made by pressing from a composite carbon material (acetylene black treated with polytetrafluorethylene (PTFE) by a special technology [26]) was used. This carbon electrode possesses a very high porosity (0.95 cm<sup>3</sup>/g) combined with a high hydrophobicity and electronic conductivity. The

collection of current is achieved by a Ni wire pressed into the porous carbon electrode.

The enzyme gas-diffusion electrode is mounted in the electrochemical cell in a way providing contact between its enzyme layer and the electrolyte. The opposite side of the working electrode is out of the cell and is in contact with the air.

The electrochemical measurements were performed in a two-electrode cell (5 cm<sup>3</sup>). A chlorinated silver wire was used both as reference Ag/AgCl and counter electrode respectively. Constant potential 0.00 V was maintained between the investigated and the reference electrodes.

Tyrosinase by "Sigma-Aldrich" – lyophilized powder,  $\geq 1000$  unit/mg solid was used in all experiments. The substrate, phenol, was purchased from "Sigma". 0.1 M phosphate buffer solution containing 0.1 M KCl with pH 7.0 was used as main background electrolyte.

The experimental set up for measurements includes a two-electrode cell with stirring, potentiostat connected with voltmeter and recording device for the plotting electrode signal vs. time.

## RESULTS AND DISCUSSION

### HPLC analysis

Batch process of phenol biodegradation by *Klebsiella oxytoca* strain at an initial concentration in the medium 0.200 g/l is presented on **Fig. 1**. The experiment was conducted using the methodology described in the experimental part above. Samples were taken every 30 minutes. They were analyzed chromatographically.

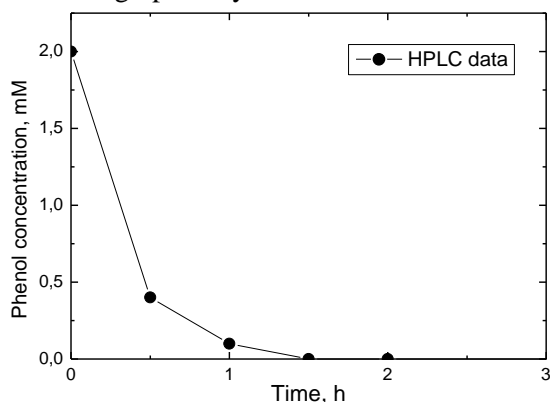


**Fig. 1.** HPLC analyses of the phenol biodegradation using *Klebsiella oxytoca*.

It is noteworthy that the time for biodegradation in these experiments is very short – 60-90 minutes.

### Enzyme electrode analysis

After a stable background current is obtained a definite amount of phenol was added to the

electrolyte in the cell and the amperometric response of the tyrosinase electrode was recorded. From our previous studies [25] the value of 0.00V versus Ag/AgCl reference electrode has been accepted for the working potential of the investigated tyrosinase electrode. The background current at this potential is practically zero. At this low potential interferences from easily oxidizable species are minimized. The amperometric signal of the investigated tyrosinase electrode (the steady-state current at a constant potential) is presented in **Fig. 2 (a)** as a function of the phenol concentration in the electrolyte. The experimental points are obtained by consecutive addition of aliquots of 0.1 mM phenol stock solution to the electrolyte in the cell with simultaneous registration of the current. The response time (defined as the time when 95% of the steady-state current is reached) was less than 3 min. It is seen that the amperometric signal increases linearly with the increase of the phenol concentration in the electrolyte up to 2  $\mu$ M. The detection limit for phenol was found to be 0.4  $\mu$ M calculated as being three times the signal-to-noise ratio ( $S/N = 3$ ). The values of the steady-state current are presented in the other part of the **Fig. 2 (b)** as a function of the sensitivity, expressed by the ratio between the steady-state current and the phenol concentration at which it is obtained (electrochemical Eadie-Hofstee plot). The biosensor sensitivity is calculated to be 330 nA  $\mu$ M<sup>-1</sup>. It is seen that the sensitivity of the investigated electrode is practically constant up to concentration of phenol at which a calibration curve is linear

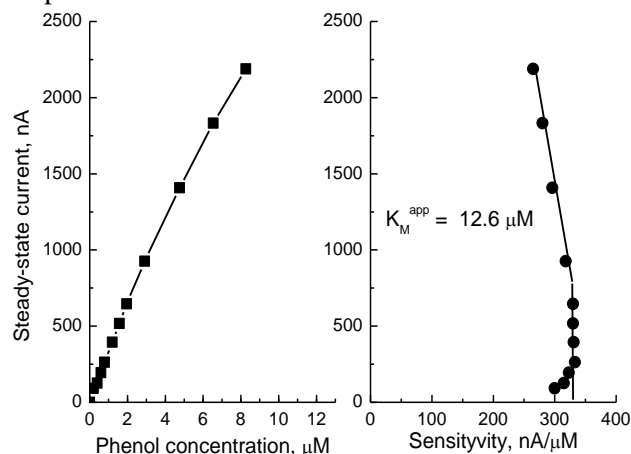


**Fig. 2. (a)** Steady-state current of the enzyme electrode as a function of the phenol concentration in the electrolyte. Experimental conditions: applied potential  $E = 0.00$  V vs. Ag/AgCl; 0.1 M phosphate buffer solution containing 0.1 M KCl (pH 7.0); phenol concentration 0.1 mM. **(b)** Corresponding electrochemical Eadie-Hofstee plot.

(vertical part of the curve). In this region of phenol concentration diffusion control of the processes on the electrode is predominate. At higher phenol concentration kinetic control predominates in the enzymatic reaction. From the curve in this region the value (slanted part of the curve) of the apparent Michaelis constant of the enzymatic reaction is estimated as  $K_M^{app} = 12.6 \mu\text{M}$ .

The calibration curve obtained with a stock solution of phenol is used as a foundation for calculating the unknown phenol concentrations in real samples taken at hour 0, hour 1 and hour 4 since the beginning of the process of biodegradation with *Klebsiella oxytoca* strain.

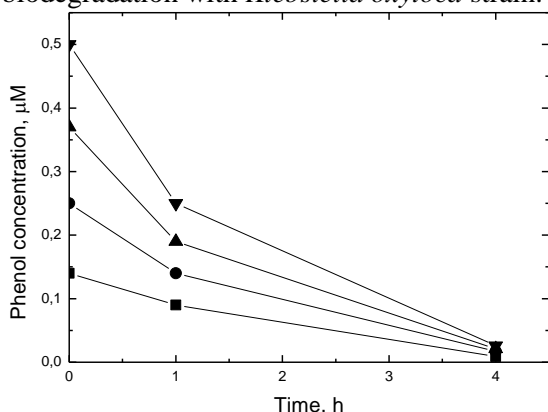


**Fig. 3.** Dependence of the phenol concentration in real samples on the biodegradation time. Experimental conditions: applied potential  $E = 0.00 \text{ V vs. Ag/AgCl}$ ; electrolyte – 0.1 M phosphate buffer solution containing 0.1 M KCl (pH 7.0); 150  $\mu\text{l}$  (■-), 250  $\mu\text{l}$  (●-), 350  $\mu\text{l}$  (▲-) and 450  $\mu\text{l}$  (▼-) diluted (1:9) solution of real samples.

The reducing of phenol concentration during the biodegradation process is illustrated on **Fig. 3**, which represents the dependence of phenol concentration from biodegradation time. Measurements are performed with the same electrode and the amperometric signals are obtained by addition of 150  $\mu\text{l}$ , 250  $\mu\text{l}$ , 350  $\mu\text{l}$  and 450  $\mu\text{l}$  of diluted (1:9) solution of real samples taken at hour 0, hour 1 and hour 4 since the onset of biodegradation. The unknown concentrations of phenol for real samples are obtained by recalculation based on the phenol calibration curve.

It is seen from the figure that over the first hour of phenol biodegradation, the phenol concentration decreases, compared with that, obtained from the 0 hours sample (i.e., immediately after “feeding” the microorganisms with phenol). Very low values of the steady-state current (and of the phenol concentration, respectively) are obtained with a sample taken on hour 4. This shows that the phenol concentration in the sample is drastically reduced of

the 4-th hour, i.e. the process of phenol biodegradation by then is completed.

A well-known fact is that enzyme immobilization is one of the crucial problems in the investigation and development of enzyme electrodes. Carbon electrode materials provide wide range for enzyme immobilization. A various ways for improving immobilization of the tyrosinase enzyme were tested and used [27 and reference therein]. It is possible to combine cross-linking with other immobilization techniques to produce very reliable tyrosinase sensors.

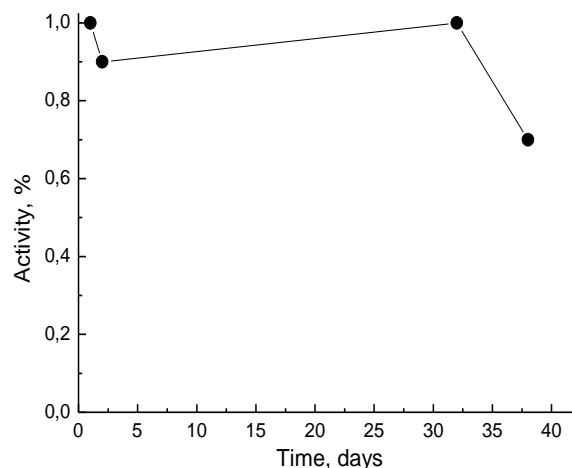


**Fig. 4.** Long-term stability of the tyrosinase electrode kept in buffer solution at 4 °C. The same experimental conditions as in Fig. 2.

To characterize the enzyme electrode stability, the response of the electrode to 0.8  $\mu\text{M}$  phenol solution at constant potential 0.00 V vs. Ag/AgCl was periodically registered. In between the measurements the electrode is kept in 0.1 M phosphate buffer solution at 4 °C for more than 40 days. The relative response (percentage of the electrode response to the initially measured one) for tyrosinase electrode as a function of the storage times is presented in **Fig. 4**. Between the fifth and the thirteenth day measurements have been carried out with real samples, so there is no information on the storage stability during this period. It should be noted that the measurements made with this electrode have commenced after forty days stay in buffer at 4 °C. **Fig. 4.** shows that tyrosinase electrode is still retained about 70 % of its original response after 35 days of storage. The investigations indicate that tyrosinase electrodes prepared by layering of pre-mixed mixed enzyme layer, containing carbon material, Nafion and tyrosinase shows relatively stable characteristics over long period.

## CONCLUSIONS

The possibilities of wastewater treatment via biodegradation, and particularly of phenol contaminations, using the microbial strain *Klebsiella oxytoca* in a batch process are explored. The biodegradation was monitored by HPLC analyses and compare with an electrochemical analysis with enzyme immobilized electrodes. Electrochemical biosensor for determination of concentration of phenol in water solution used is based on an enzyme gas-diffusion electrode with enzyme tyrosinase. This investigation indicates that tyrosinase electrodes display relatively stable and reproducible characteristics after 40 days of storage and during 35 days of periodically measurements. The unknown concentrations of phenol for real samples are obtained by recalculation based on the phenol calibration curve.

## REFERENCES

1. Instruction of the Ministry of Environment and Water of Bulgaria, State Gazette, **2002**, 8, 6.
2. M. Alam, S. Muyibi, M. Mansor, R. Wahid, *Environ. Sci. (China)*, **18**, 446 (2006).
3. S. Al-Asheh, F. Bant, L. Abu- Aitah, *Sep. Purif. Technol.*, **3**, 1 (2003).
4. R. Shawabkeh, O. Khashman, G. Bisharat, *Int. J. Chem.*, **2**, 2 (2010).
5. A. Fortuny, C. Ferrer, C. Bengoa, J. Font, A. Fabregat, *Catalysis Today*, **24**, 79 (1995).
6. G. Bayramoglu, M. Arica, *J. Hazard Materials*, **15**, 148 (2008).
7. G. Gurujeyalekshmi, P. Oreil, *Appl. Environ. Microbiol.*, **55**, 500 (1988).
8. A. Mordocco, K. Clern, J. Roger, *Enzyme Microbial Technol.*, **25**, 530 (1999).
9. S. Burton, R. John, Perry, T. Peter, *Biotechnol. Bioeng.*, **42**, 938 (1993).
10. P. Gotz, M. Reuss, *J. Biotechnol.*, **58**, 101 (1997).
11. D. Santos, M. David, M. Lopes, N. Peporine, G. Petto, *Biological&Pharmaceutical Bulletin*, **29**, 2236 (2006).
12. C. Nair, K. Jayachandran, S. Shashidhar, *J. Biotechnol.*, **7**, 4951 (2008).
13. R. Shawabkeh, O. Khashman, G. Bisharat, *Int. J. Chem.*, **2**, 2 (2010).
14. J. Perez, M. Lopez, E. Cabarcos, B. Lopez-Ruiz, *Biosensors & Bioelectronics*, **22**, 429 (2006).
15. D. Shan, J. Zhang, H. Guo Xue, Y. Zhang, S. Cosnier, S. Ding, *Biosensors&Bioelectronics*, **24**, 3671 (2009).
16. V.Carralero, M.Mena, A. Gonzalez-Cortes, P. Sedeno, J. Pingarron, *Biosensors&Bioelectronics*, **22**, 730 (2006).
17. L.Macholan, L.Schanel, *Coll. Czechoslovak Chem. Commun.*, **42**, 3667 (1977).
18. F. Scheller, F. Schubert, "Biosensors", Elsevier, Amsterdam, 1992.
19. M. Peter, U. Wollenberger, *Frontiers in Biosensorics*, 1997.
20. C. Mayorga-Martinez, M. Cadevall, M. Guix, J. Ros, A. Merkoçi, *Biosensors&Bioelectronics*, **40**, 57 (2013).
21. E. Han, D. Shan, H. Xue, S. Cosnier, *Biomacromolecules*, **8**, 971 (2007).
22. C. Apetrei, P. Alessio, C. Constantino, J. De Saja, M. Rodriguez-Mendez, F.J. Pavinatto, E. Fernandes, V. Zucolotto, O. Oliveira Jr., *Biosensors&Bioelectronics*, **26** 2513 (2011).
23. W. Song, D. Li, Y. Li, Y. Li, Y. Long, *Biosensors & Bioelectronics*, **26** 3181 (2011).
24. J. Pingarrón, P. Yáñez-Sedeño, A. González-Cortés, *Electrochimica Acta*, **53**, 5848 (2008).
25. A. Kaisheva, I. Iliev, R. Kazareva, S. Hristov, U. Wollenberger, F. Scheller, *Sensors&Actuators B*, **33**, 39 (1996).
26. I. Iliev, A. Kaisheva, US Patent No 4 031 033.
27. S. Cosnier, *Anal. Bioanal. Chem.*, **377**, 507 (2003).

The results obtained via both methods - HPLC analyses and electrochemical enzyme electrodes indicate that the phenol concentration in the sample is reduced over the 4-th hour, i.e. the process of phenol biodegradation by then is completed. For that reason biosensors for determining phenol concentration in biodegradation processes can find practical application. The future research will focus on extending the lifetime of the enzyme electrodes and on studies of other enzymes for the analysis of phenol in polluted waters.

**Acknowledgements:** The authors would like to thank the Bulgarian Science Fund - project № DO 02-185 for the financial support of this work. We thank Dr Christo D. Roussev for helpful discussion and editing of the manuscript.

## ПРОСЛЕДЯВАНЕ ПРОЦЕСА НА БИОДЕГРАДАЦИЯ НА ФЕНОЛ С ЕЛЕКТРОХИМИЧЕН БИОСЕНЗОР

Р. Букурещлиева<sup>1\*</sup>, С. Янкова<sup>2</sup>, В. Бешков<sup>2</sup>, Й. Милушева<sup>1</sup>, Г. Найденова<sup>2</sup>, Л. Попова<sup>2</sup>,  
Г. Йотов<sup>2</sup>, С. Христов<sup>1</sup>

<sup>1</sup>*Институт по Електрохимия и Енергийни Системи, БАН, 1113 София, България*

<sup>2</sup>*Институт по Инженерна Химия, БАН, 1113 София, България*

Постъпила на 1 март, 2013 г.; Коригирана на 5 май, 2013 г.

(Резюме)

Постоянният или периодичен контрол на степента на замърсеност на отпадъчни води (битови или индустриални) е доста сериозен въпрос, който все още не е решен. В тази статия докладваме за разработването на амперометричен биосензор за откриване на фенолна биодegradацията във вода и сравняваме аналитичните данни с тези, получени от най-често използвания аналитичен метод ВЕТХ (Високо Ефективна Течна Хроматография).

Описаният биосензор включва ензимен електрод, който се състои от порест хидрофобен въглероден електрод с имобилизиран върху него ензим Тирозиназа (ЕС 1.14.18.1). За изследване ефективността на тирозиназния амперометричен сензор за определяне на фенолна концентрация, бяха проведени експерименти при постоянен потенциал 0.0V спр. Ag/AgCl сравнителен електрод във фосфатен буфер с рН 7.0. Времето за отклик на сензора не надвишава 3 мин. и амперометричният сигнал нараства линейно до концентрация на фенол 2  $\mu\text{M}$ . Тирозиназният електрод показва чувствителност 330 nA  $\mu\text{M}^{-1}$ , изчислена е привидната Михаелисова константа  $K_M^{\text{app}} = 12.6 \mu\text{M}$  при откриваема граница за фенол 0.4  $\mu\text{M}$ . Освен това, тирозиназният електрод показва добра възпроизводимост и стабилност по време на 35 дневни периодични измервания.

Като заключение, описаният тирозиназен електрод би могъл да намери приложение за ефективно откриване и определяне на фенолни концентрации в реални водни проби в реално време.

## Impedance studies of porous electrolyte with mixed ion conductivity

M. Krapchanska<sup>1\*</sup>, D. Vladikova<sup>1</sup>, Z. Stoynov<sup>1</sup>, A. Chesnuad<sup>2</sup>, A. Thorel<sup>2</sup>, G. Raikova<sup>1</sup>, E. Mladenova<sup>1</sup>, I. Genov<sup>1</sup>

<sup>1</sup>*Institute of Electrochemistry and Energy Systems – Bulgarian Academy of Sciences, 10, Acad. G. Bonchev Str., Sofia 1113, Bulgaria*

<sup>2</sup>*Centre des Matériaux, Mines-ParisTech, BP 87, 91003 Evry Cedex, France*

Received March 05, 2013; revised May 03, 2013

In this study mixed ion conductivity of a composite material based on proton conducting  $\text{BaCe}_{0.85}\text{Y}_{0.15}\text{O}_{2.925}$  (BCY15) and oxide ion conducting  $\text{Ce}_{0.85}\text{Y}_{0.15}\text{O}_{1.925}$  (YDC15) electrolytes has been investigated by Electrochemical Impedance Spectroscopy in relation to its application as a membrane (named central membrane CM) in an innovative design of a high temperature Dual Membrane Fuel Cell (DMFC). One of the most important advantages of the new architecture is the separation of hydrogen, oxygen and exhaust water in three independent chambers. The key-point of the DMFC development is the design and fabrication of the porous CM, which has to combine high mixed ion (proton and oxide ion) conductivity with sufficient porosity necessary for the evacuation of the water produced in this layer. In order to understand and evaluate the processes taking place in the CM, impedance studies were carried out and presented in this work. The obtained results show that a composite central membrane with 50 v % BCY15 and 50 v % YDC15 and porosity about 35-40 % obtained by addition of pore former (graphite) could be used for the fabrication of the first (Proof of the Concept) generation Dual Membrane Fuel Cell.

**Keywords:** Impedance Studies, BCY15, YDC15, Composite Electrolyte, Central Membrane.

### INTRODUCTION

The classical solid oxide fuel cell (SOFC) is a high temperature device, that converts the chemical energy of fuel directly in electricity and heat. The oxide ions diffuse through the solid electrolyte toward the anode where they react with the hydrogen and produce water and electricity (Fig.1 a). The basic disadvantage of this concept is that water dilutes the fuel and inhibits the catalytic activity of the electrode.

The second existing concept is that of the proton conducting solid oxide fuel cell (PCFC). Here the reaction takes place on the cathode side (Fig.1 b) and thus the fuel dilutes the oxidizing gas. In addition the produced water is very aggressive and causes severe corrosion problems.

Recently a new concept named Dual Membrane Fuel Cell has been developed [1-4]. It combines the advantages and eliminates the disadvantages of both SOFC and PCFC in respect to the water formation. The main idea consists in joining the anode part of a PCFC with the cathode part of a SOFC by means of a central membrane where the

water is produced and evacuated (Fig. 1 c). Thus the cell consists of three independent chambers for hydrogen, oxygen and water which could be separately optimized.

The key factor for the performance of the new concept is the central membrane, which has to ensure high anionic and protonic conductivities in the presence of sufficient porosity. The proper connectivity among the different phases (proton conductor, oxide ion conductor, open porosity for water evacuation), should avoid tortuous and/or resistive paths. Moreover, both solid phases (BCY15 and YDC15) must percolate towards their respective electrolyte, and porosity must percolate towards the outside of the cell for water evacuation. Thus each triple phase boundary (TPB) segment should be connected to both electrolytes.

The aim of this study is impedance characterization and optimization of the CM which has to combine high proton and oxide ion conductivity, thermochemical and mechanical stability and porosity needed for the evacuation of the water.

\* To whom all correspondence should be sent:  
E-mail: milenazk@bas.bg

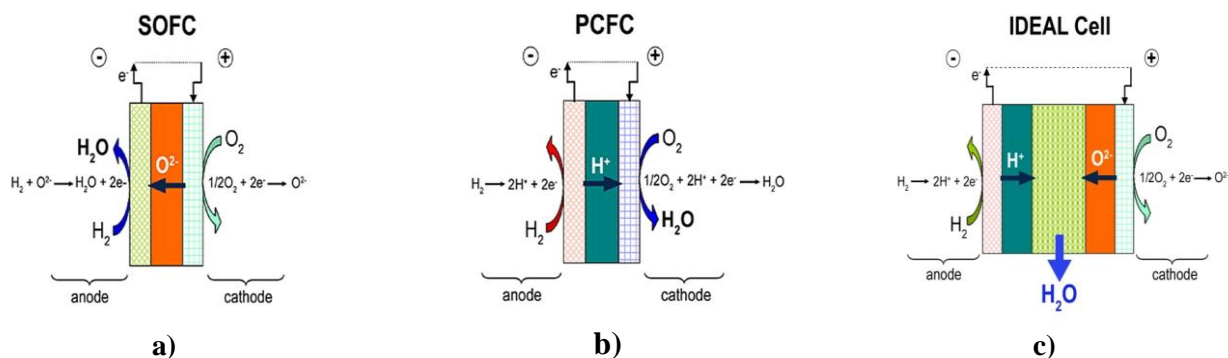


Fig. 1. Representation of: a) SOFC design, b) PCFC design and c) IDEAL-Cell concept.

### EXPERIMENTAL

The mixed conductivity of the CM has been ensured by the design of a composite based on proton conducting  $\text{BaCe}_{0,85}\text{Y}_{0,15}\text{O}_{2,925}$  and oxide ion conducting  $\text{Ce}_{0,85}\text{Y}_{0,15}\text{O}_{1,925}$ . Preliminary tests determined a composition of 50 % BCY15 and 50 % YDC15. For the performance of impedance studies a new type of electrolyte supported symmetrical half cell with metal electrodes:  $\text{Pt}/(\text{BCY15}+\text{YDC15})_{\text{porous}}/\text{Pt}$  and  $\text{Ag}/(\text{BCY15}+\text{YDC15})_{\text{porous}}/\text{Ag}$  was introduced. Graphite and starch (2 - 7 wt %) were used as pore former. The composite electrolytes were sintered at temperatures 1300-1350°C.

The impedance measurements were performed on Solartron 1260 Frequency Response Analyzer in temperature interval 100 - 800°C in a frequency range from 10 MHz down to 0,1 Hz and density of 5 points/decade. They were carried out in two modes: potentiostatic and galvanostatic. The change of mode and amplitude, which depends on the sample resistance, ensures higher quality of the measured data [4].

An original moment in this study is the performance of the measurements in  $\text{O}_2$  and in  $\text{H}_2$ . A correction of the parasitic inductance and resistance of the measurement rig has been also applied [5, 6]. As it can be seen in Fig. 2, at higher temperatures, the errors coming from the parasitic elements can reach 30 %.

### RESULTS AND DISCUSSION

For evaluation of the YDC15 and BCY15 conductivity, measurements of half cells with dense electrolyte support obtained in the absence of pore former and sintering temperatures respectively 1350 and 1450°C were performed. The comparison of the obtained results with data from the literature

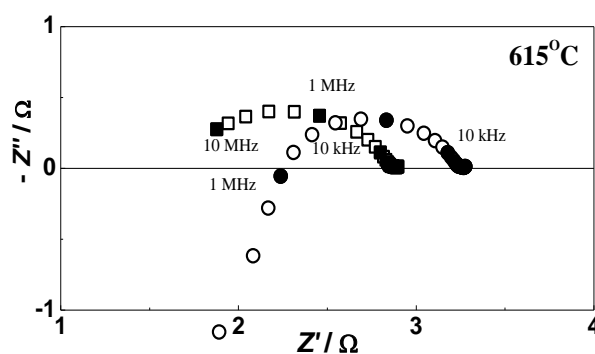
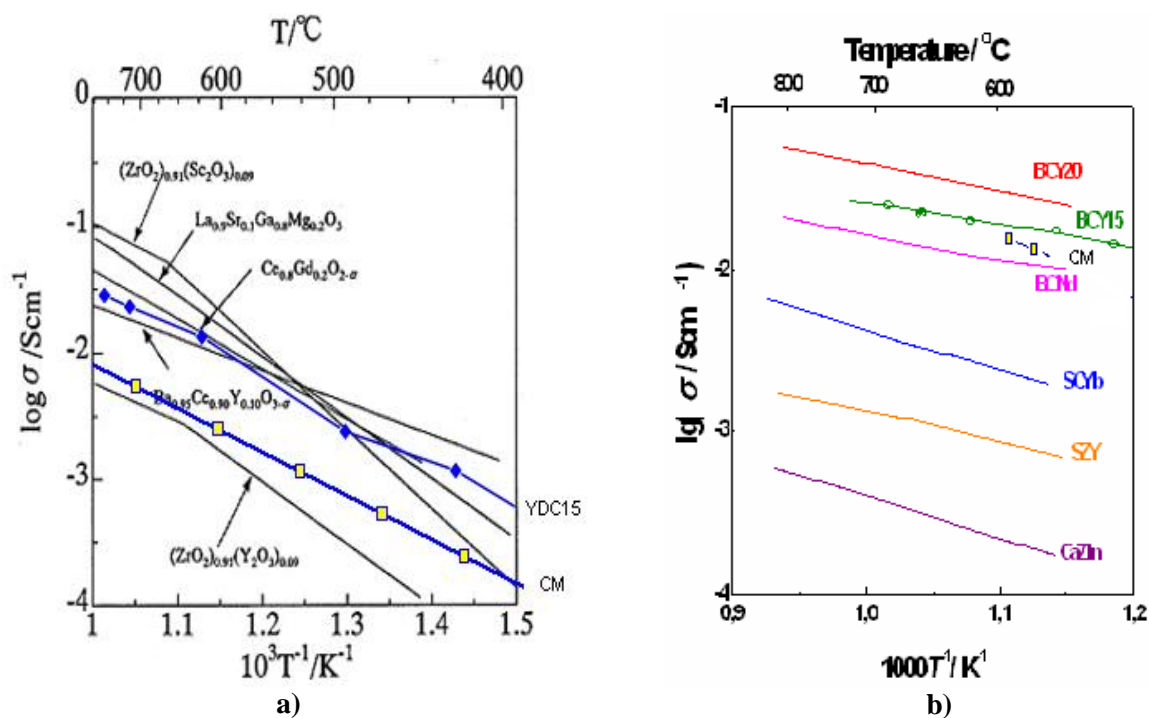


Fig. 2. Complex plane impedance diagrams of Pt/CM/Pt half cell before (●) and after (■) correction of parasitic resistance and inductance.

[7, 8] shows that the conductivity of YDC15 is similar to that of the commonly applied oxide ion conductors (Fig. 3 a). BCY15 enters in the group of the best proton conductors (Fig. 3 b).

The application of starch and graphite as pore formers influenced the microstructure of the composite CM. The results obtained by Scanning Electron Microscopy (SEM) showed that starch caused big cracks which made the samples mechanically fragile. The addition of 2 - 3 % graphite ensures mechanically stable structures with sufficient porosity (Fig. 4).

As already mentioned the impedance measurements of the CM were performed in  $\text{O}_2$  and  $\text{H}_2$ . The data obtained in oxygen ensure information about the conductivity of the YDC15 phase in the real structure, i.e. in the presence of the proton conducting phase and the pores. Measurements in hydrogen separate the conductivity of the proton conducting BCY15 phase. The Arrhenius plots of the CM with different porosity are presented in Fig. 5. Logically the results show that the increase of the porosity leads to decrease of the conductivity. This effect is more pronounced for the proton



**Fig. 3.** Comparison of the conductivity of: **a)** dense YDC15 and YDC15 in composite CM with 30% porosity ( $\square$ ) with data from the literature for oxide ion conducting electrolytes [7], **b)** dense BCY15 and BCY15 in composite CM with 30% porosity ( $\square$ ) with data from the literature for proton conducting electrolytes [8].

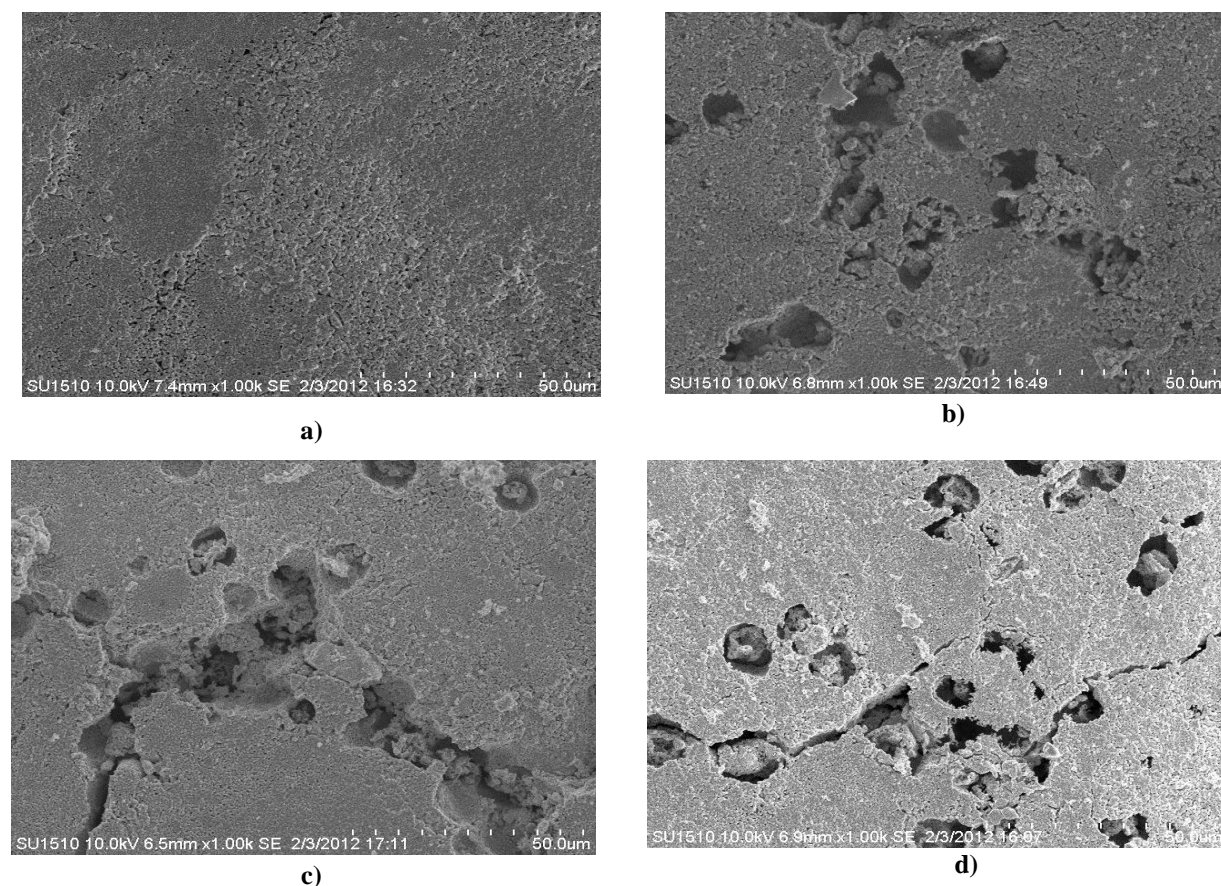


**Fig. 4.** SEM micrographs of central membrane with different microstructures: **a)** without pore former, grain size 1-2  $\mu\text{m}$ ; **b)** 2% graphite, grain size 1-5  $\mu\text{m}$ ; **c)** 5% starch, grain size 1-3  $\mu\text{m}$ ; **d)** 7% starch, grain size 1-3  $\mu\text{m}$ .

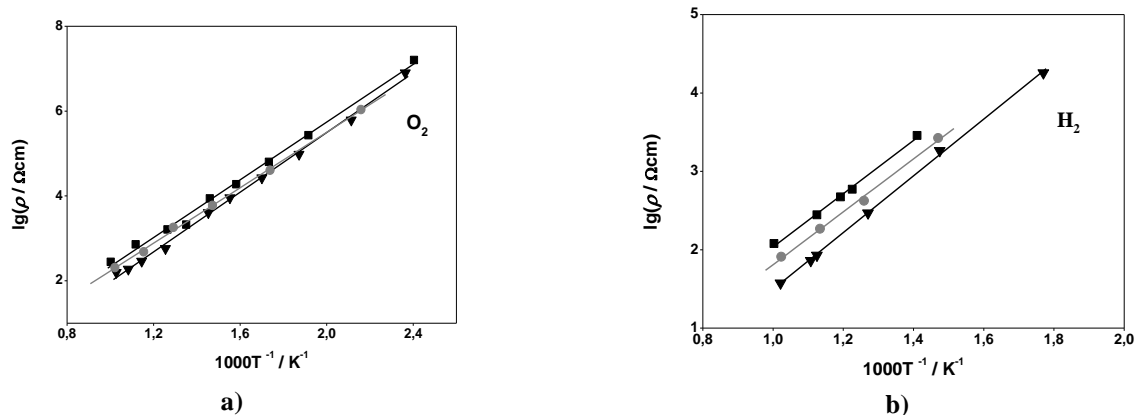


Fig. 5. Arrhenius plots for CM with different porosity: (■) 42 %, (●) 35 %, (▼) 28 %: a) in O<sub>2</sub>, b) in H<sub>2</sub>.

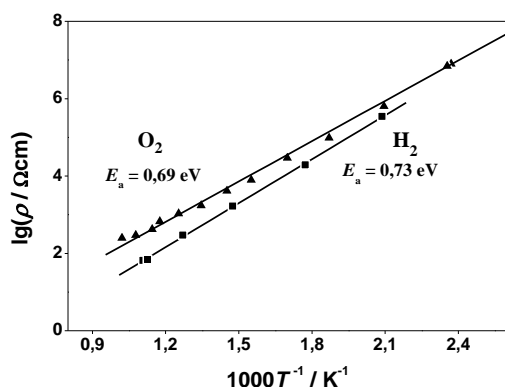


Fig. 6. Arrhenius plots for CM in O<sub>2</sub> and in H<sub>2</sub> atmosphere.

conducting phase which, however, has higher conductivity (Fig. 6), confirmed also by measurements of dense BCY15 and YDC15 samples (Fig. 3 a, b). The comparison of the conductivities for the two ceramic phases in the porous composite CM with data from the literature obtained for dense materials shows that the registered conductivities for samples with 30-40 % porosity are in the frames characteristic for the applied electrolyte materials (Fig. 3 a, b). Thus for composite central membranes with 50 v % BCY15 and 50 v % YDC15 and porosity 30-40 % obtained by graphite pore former good compromise between conductivity and porosity is obtained.

### CONCLUSIONS

The impedance studies of the new functional CM layer of the innovative DMFC concept ensured the design and fabrication of appropriate membrane combining sufficient mixed ion conductivity with optimal porosity and good mechanical and thermal stability. It was used for the construction of the first model cell with which the new concept was successfully proved [4, 9].

**Acknowledgements:** The research leading to these results has received funding from the European Community's Seventh Framework Programme (FP7/2007-2013) under grant agreement No 213389. The authors acknowledge also the project BG051PO001-3.3.05-0001 "Science and business" for the financial support that made possible the publication of this paper.

### REFERENCES

1. Patent No 0550696000, March 7th, 2005: CELLULE DE PILE A COMBUSTIBLE HAUTE TEMPERATURE A CONDUCTION MIXTE ANIONIQUE ET PROTONIQUE, International extension in 2006.
2. A. Thorel, A. Chesnaud, M. Viviani, A. Barbucci, S. Presto, P. Piccardo, Z. Ilhan, D. Vladikova and Z. Stoynov, in Solid Oxide Fuel Cells 11 (SOFCXI), edited by S.C. Singhal, and H. Yokokawa, The Electrochemical Society Proceedings Series 25, ECS Transactions, Pennington, NJ, 2009, p.753.
3. D. Vladikova, J. Kilner, S. Skinner, G. Raikova, Z. Stoynov, *Electrochim. Acta*, **51**, 1611 (2006).
4. D. Vladikova, Z. Stoynov, G. Raikova, A. Thorel, A. Chesnaud, J. Abreu, M. Viviani, A. Barbucci, S. Presto and P. Carpanese, *Electrochim. Acta*, **56**, 7955 (2011).
5. Z. Stoynov, D. Vladikova, Impedance Spectroscopy of Electrochemical Power Sources in: U. Garche (Ed.) Encyclopedia of Electrochemical Power Sources, Elsevier, 2009.
6. D. Vladikova, Z. Stoynov, Differential Impedance Analysis, Marin Drinov Academic Publishing House, Sofia, 2005.
7. S. Singhal, K. Kendal, Solid Oxide Fuel Cells: Fundamentals, Design and Applications, Elsevier, 2003.
8. H. Iwahara, *Solid State Ionics*, **86-88**, 9 (1996).
9. M. Viviani, G. Canu, M. Carpanese, A. Barbucci, A. Sanson, E. Mercadelli, C. Nicoletta, D. Vladikova, Z. Stoynov, A. Chesnaud, A. Thorel, Z. Ilhan, S. Ansar, "Dual Cells with Mixed Protonic-Anionic Conductivity for Reversible SOFC/SOEC Operation", Fuel Cells 2012 Science & Technology – A Grove Fuel Cell Event, *Energy Procedia*, **28**, 182 (2012).

## ИМПЕДАНСНО ИЗСЛЕДВАНЕ НА ПОРЕСТ ЕЛЕКТРОЛИТ СЪС СМЕСЕНА ПРОВОДИМОСТ

М. Кръпчанска<sup>1\*</sup>, Д. Владикова<sup>1</sup>, З. Стойнов<sup>1</sup>, А. Чесно<sup>2</sup>, А. Торел<sup>2</sup>, Г. Райкова<sup>1</sup>, Е. Младенова<sup>1</sup>, И. Генов<sup>1</sup>

<sup>1</sup>*Институт по електрохимия и енергийни системи "Акад. Е. Будевски" – БАН, ул. "Акад. Г. Бончев", бл. 10, 1113, София, България*

<sup>2</sup>*Център по материалознание, Миньо – Тех Париж, ВР 87, 91003, Еври, Франция*

Постъпила на 3 март, 2013 г.; Коригирана на 18 април, 2013 г.

(Резюме)

В настоящата статия с помощта на Електрохимична импедансна спектроскопия е изследвана смесената проводимост на композитен материал, състоящ се от протон проводящ  $\text{BaCe}_{0,85}\text{Y}_{0,15}\text{O}_{2,925}$  (BCY15) електролит и кислород проводящ  $\text{Ce}_{0,85}\text{Y}_{0,15}\text{O}_{1,925}$  (YDC15) електролит, с цел използването му като мембрана (т.н. централна мембрана - ЦМ) в нов дизайн на високотемпературна горивна клетка (ДМГК). Едно от най-важните предимства на новия дизайн е разделянето на водорода, кислорода и водата в три отделни, независими една от друга камери. Ключов момент в разработването на ДМГК е създаването на ЦМ, която трябва да комбинира висока смесена (протонна и кислородна) проводимост и оптимална пористост необходима за отвеждането на формираната в мембраната вода.

Представени тук импедансни измервания са извършени с цел да се разберат и оценят процесите които протичат в ЦМ. Получените резултати показват, че композитна ЦМ със състав 50 v % BCY15 и 50 v % YDC15 и пористост 35-40 % (получена с порообразовател графит) може да се използва за получаването на първа генерация ДМГК, което потвърждава валидността на новата концепция.

## Air gas-diffusion electrodes for operation in magnesium-air cells/NaCl – electrolyte

Y. D. Milusheva\*, R. I. Boukoureshtlieva, S. M. Hristov

<sup>1</sup>*Institute of Electrochemistry and Energy Systems – Bulgarian Academy of Sciences, 10, Acad. G. Bonchev Str., Sofia 1113, Bulgaria*

Received March 03, 2013; revised April 13, 2013

Metal-air batteries have attracted much attention for their future potential as clean mobile power sources. However, the study is mainly focused on alkaline electrolyte Zn-air batteries and Al-air batteries. A very few studies on neutral saline Mg-air battery were carried out so far.

Air gas-diffusion electrodes (GDE) for reduction of oxygen from the air are commonly used as cathodes in metal-air systems and fuel cell with alkaline electrolytes. They are also used in electrochemical cells operating with neutral electrolytes: Mg-air cells, Al-air batteries and microbial fuel cells. The electrodes, which are subject of this study, consisted of two layers: hydrophobic and an active one. One of the most important tasks in the development of air gas-diffusion electrodes is to find proper catalysts for the electrochemical reduction of oxygen, which ensures high electrochemical characteristics and long exploitation time. Various non-platinum catalysts, introduced into the active carbon, are studied: cobalt tetramethoxyphenylporphyrine (CoTMPP), VS50–CoTMPP–700 and active carbon with Co and Ni (ACCoNi). Transport hindrances that occur in the catalyst layers are evaluated with potential  $\Delta E$  vs. current density ( $i$ ) analysis. The optimal values of the parameters of the overall structure of the electrodes and the optimal composition of the catalyst are found.

Mg-air cells operating with saline electrolyte NaCl-solution are developed and investigated.

**Key-words:** air gas-diffusion electrodes, catalysts for the electrochemical reduction, CoTMPP, Mg-air cells

### INTRODUCTION

As efficient, clean, energy converters, fuel cells and metal-air batteries have attracted much attention in recent years due to the possible energy crisis induced by power demands and the increasing importance of protecting our environment. However at the current stage of technology, high cost is one of the big obstacles hindering the commercialization of fuel cells.

Bidault et al. [1] are given review of the state-of-the-art in gas diffusion cathode development. The overall cell performance and stability is dominated by the behavior of the cathode, leading to a focus of research effort on cathode development. Many publications have discussed the behavior of porous electrodes in alkaline fuel cells. Whereas some authors have focused on specific issues such as current distribution [2], or the degree of catalyst utilization [3, 4], the majority have tried to understand the overall mechanism of operation in the GDE related to the structure; considering factors such as gas diffusion and electrolyte

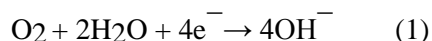
penetration. Several models have been used such as the simple pore model [5], the thin film model [6] or the dual scale of porosity model [7]. In the former, a range of porosities is considered, where macropores are gas filled and micropores are electrolyte filled [8, 9]. Giner [10] listed the limitations of this ‘flooded porous electrode’ model introducing the concept of ‘flooded agglomerates’. The operational mechanism of this structure consists of catalyst particles, which form porous agglomerates ‘flooded’ with electrolyte under working condition. It has been reported elsewhere that the concept of ‘flooded agglomerates’ gives a satisfactory explanation for the behavior of Polytetrafluoroethylene (PTFE) bonded gas diffusion electrodes, and is in good accordance with experimental findings [11–14].

Optimizing the cathode performance is essential because it governs the overall performance of the fuel cell. According to Bockris [15] at high current density, 80% of the polarization may be due to the oxygen reduction. The Oxygen Reduction Reaction (ORR) is a complex process involving four coupled proton and electron transfer steps. Several of the elementary steps involve reaction intermediates leading to a wide choice of reaction pathways. The

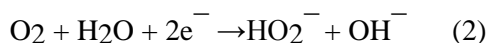
\* To whom all correspondence should be sent:  
E-mail: joschi@abv.bg

exact sequence of the reactions is still not known, and identification of all reaction steps and intermediates, and their kinetic parameters is required, which is clearly challenging. Appleby [16] has reviewed and discussed the issues relating to the ORR in acid and alkaline solution. In acid electrolyte, the ORR reaction is electrocatalytic, as pH values become alkaline, redox processes involving superoxide and peroxide ions start to play a role and dominate in strongly alkali media. The reaction in alkaline electrolytes may stop with the formation of the relatively stable  $\text{HO}_2^-$  solvated ion, which is easily disproportionated or oxidized to dioxygen. Although there is no consensus on the exact reaction sequence, two overall pathways take place in alkaline media [17]:

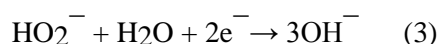
Direct 4-electron pathway:



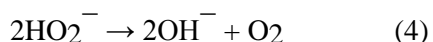
Peroxide pathway or '2 + 2-electron' pathway:



With:



The peroxide produced may also undergo catalytic decomposition with the formation of dioxygen and  $\text{OH}^-$ , given by:



Due to the inherently faster kinetics for the ORR in alkaline media, a wide range of catalysts have been studied including noble metals, non-noble metals, perovskites, spinels, *etc.* However, it is important to appreciate that the carbon support plays a role in the kinetics as well as the catalyst supported on its surface, so that in evaluating the performance, it is necessary to assess the loading of the catalyst and the type of carbon used where its hydrophobic properties as well as its surface groupings greatly affect the final hydrophobic structure of the electrode.

Developing non-noble catalysts to replace expensive platinum-based catalysts is one of the major approaches being explored to reduce the cost [18-20]. Among the non-noble catalysts that have been discovered, metalloporphyrin complexes have been investigated for several decades as promising candidates for a fuel cell ORR catalyst.

Oxygen electrocatalysis that J. Lee et al. [21] first defined is considered as the most important phenomenon in almost all electrochemical industries because it is the most sluggish reaction that governs the overall reaction rate in electrochemical cells. In this review, they covered

two main areas of oxygen–water electrocatalysis, oxygen reduction to water and oxygen evolution from water. This review will be of value to both electrochemists and other applied scientists interested in this field of electrocatalysis.

In the paper Liu H. et al. [22] described the mechanism and kinetics of oxygen and hydrogen peroxide electrochemical reduction that is catalyzed by an adsorbed CoTMPP on a graphite electrode was investigated using cyclic voltammetry and the rotating disk electrode technique. Carbon particle-based air cathodes catalyzed by CoTMPP were fabricated for metal-air fuel cell application. The obtained non-noble catalyst content cathodes show considerably improved performance and stability.

Catalysts containing mixed Ni-Co oxides prepared by impregnating active carbon with solution of Ni-acetate and Co-acetate and subsequent heat treatment are investigated [23].

Here we present a study on selection of hydrophobic material with optimal physical, chemical and electrochemical characteristics for the gas layer of the air gas-diffusion electrode and investigation and selection of suitable catalyst for the electrochemical reduction of oxygen that occurs on the air gas-diffusion electrode.

## EXPERIMENTAL

During the last few years in our laboratories research efforts in the field of Metal-air systems have been directed towards developing a Mg-air battery with neutral chloride electrolyte. The air gas-diffusion electrode is a porous, thin and light tablet, which serves as a wall of the metal-air cell and separates the electrolyte of the cell from the surrounding air. This configuration poses some conflicting requirements to the air electrode: it must be highly porous and permeable for gaseous oxygen and simultaneously the leakage of the electrolyte through the porous electrode must be completely avoided. The electrode must be electrically conductive and must possess enough mechanical strength to withstand the hydrostatic pressure of the electrolyte and the eventual hydrodynamic shocks. The air electrode must contain an active catalyst for electrochemical reduction of oxygen in contact with the electrolyte. Stable operation of the air electrode with time is also needed.

The air gas-diffusion electrode developed in our laboratory [24-30] is a double-layered tablet (thickness ca.1.5 mm), which separates the electrolyte of the cell from the surrounding air. The electrode comprises two layers: a porous, highly hydrophobic and electrically conductive gas layer

(from the side of the air) and a catalytic layer (from the side of the electrolyte). During operation oxygen from the atmospheric air diffuses in a gas phase through the free of electrolyte hydrophobic pores of the gas layer and through the catalytic layer's hydrophobic zones and reaches the partially flooded with electrolyte catalytic zones in the catalytic layer. Electrochemical reduction is taking place on the three-phase boundary oxygen/catalyst/electrolyte.

#### Porous hydrophobic material

The hydrophobic gas layer of the air electrode possesses high porosity ( $0.7\text{--}0.9\text{ cm}^3/\text{g}$ ) enabling effective oxygen transport through this layer. From the experimental programs measured by both mercury and KOH-porometry, the contact angle  $\theta_{\text{eff}}$  of the hydrophobic material with water electrolytes is obtained ( $\theta_{\text{eff}}=116^\circ - 118^\circ$ ). Because of this high hydrophobicity, the gas layer prevents completely the leakage of the electrolyte through the electrode. The hydrophobic material possesses relatively high electronic conductivity ( $1.0 - 2.0\ \Omega^{-1}\cdot\text{cm}^{-1}$ ), which allows the current collection to be achieved through a metal grid pressed on the gas layer of the electrode. In this way the current collector grid is not in contact with the electrolyte and thus corrosion is avoided. This is very important especially in the case when the electrode operates in NaCl-electrolyte.

#### Catalysts for the electrochemical reduction of $O_2$

Various carbon-based catalysts are tested in the investigated air gas-diffusion electrodes: active carbon promoted with mixed Co-Ni oxides and catalysts prepared by pyrolysis of active carbon impregnated with some N-4 chelate compounds.

ACCoNi catalyst was prepared as active carbon NORIT NK was impregnated with a solution containing both Co- and Ni-acetates, dried and heat treated at  $300^\circ\text{C}$  in open air. VS50-CoTMPP-700 type was prepared while dispersed  $\text{SiO}_2$  (VS) was impregnated with a solution of CoTMPP and after removing the solvent and drying, the material was treated at  $700^\circ\text{C}$  in argon. Pyrolyzed CoTMPP catalyst is produced by impregnation of a dispersed carbon material with a solution of CoTMPP, drying and subsequent heat treatment in Ar at  $800^\circ\text{C}$ .

Several types of experimental Mg-Air cells are tested, differing in their size (working area of the air electrodes used) [31].

## RESULTS AND DISCUSSION

Fig. 1 represents a comparison between the polarization curves of the air electrodes and the investigated types of catalysts: pyrolyzed CoTMPP, VS50-CoTMPP-700 and ACCoNi. The measurements were performed in 4M NaCl electrolyte operating both in air and in pure oxygen. The comparison with the polarization curve for the electrodes with CoTMPP catalyst shows that the chelate-promoted electrodes have also better current-voltage characteristic.

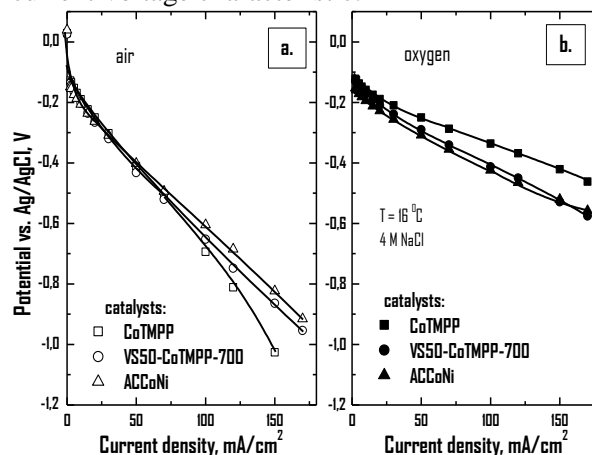


Fig. 1. Current-voltage characteristics of the electrodes with catalysts VS 50 CoTMPP 700, ACCoNi and pyrolyzed CoTMPP, operating in pure oxygen and in air in saline electrolyte.

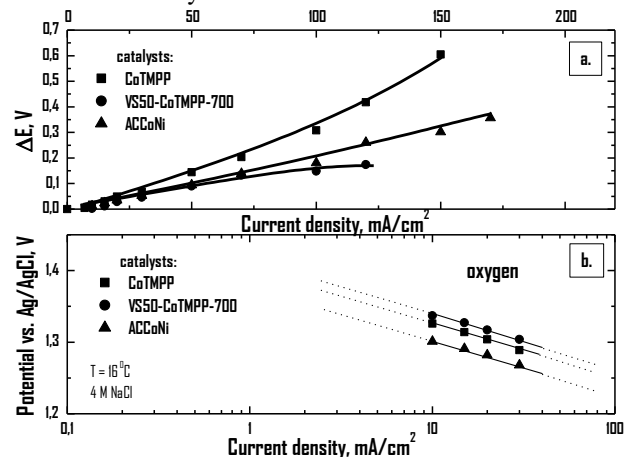
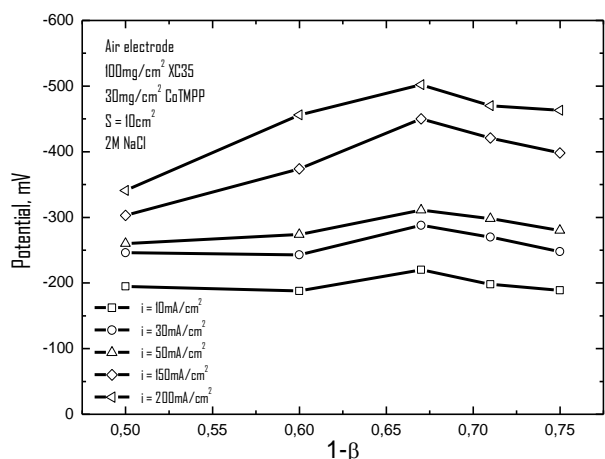


Fig. 2. Comparative methods for diagnostics of the transport hindrances (a) and activity (b) in the electrodes.

The differences in the behavior of the air electrodes with various catalysts is strongly influenced both by the activity of the catalyst used, and also by the hindrances in the transport of the reagent (oxygen) in the porous structure of the catalyst.

Comparative methods for diagnostics of the transport hindrances (Fig. 2a) and the activity (Fig. 2b) in the electrodes are used. The transport hindrances in the air electrodes with the



**Fig. 3.** Current of the air electrode as a function of the catalytic layer content at constant potential.

investigated catalysts are studied by the use of the difference  $\Delta E$  ( $\Delta E = E_{\text{oxygen}} - E_{\text{air}}$ ). It is theoretically shown that at low current densities, where the transport hindrances in the porous structure of the air electrode are negligible, the value of  $\Delta E$  remains constant. At higher current densities the value of  $\Delta E$  increases with the increase of the current density. This increase is much faster when the transport hindrances in the electrode are more pronounced. From the  $\Delta E$ - $i$  dependences of the air electrodes with the investigated catalysts, presented in Fig. 2a it can be seen that the transport hindrances in the electrode with catalyst VS50-CoTMPP-700 are comparatively low versus the electrodes with catalysts ACCoNi and pyrolyzed CoTMPP. The activity of the catalysts was compared based on the experimental Tafel plots (Fig. 2b). The more active catalysts are VS50-CoTMPP-700 and pyrolyzed CoTMPP.

One of the main advantages of the developed air electrode is the possibility to vary independently the parameters of its structure: thickness of the gas layer, thickness of the catalytic layer and the ratio catalyst/hydrophobic material in the catalytic layer. One of the important structural parameter of the air electrode is the ratio between the amounts of catalyst and hydrophobic material in the catalytic layer. This ratio is given by the value  $(1-\beta)$ , which expresses the amount of the catalyst per unit weight of the catalytic layer. In Fig. 3 the potential at constant current as a function of the ratio  $(1-\beta)$  is presented. At low value  $(1-\beta)$  the amount of the catalyst is low and the potential is also low. With the increases of  $(1-\beta)$  the current density increases and reaches a maximum value. Further increase of  $(1-\beta)$  value results in current density decrease. This is connected with the transport hindrances in the

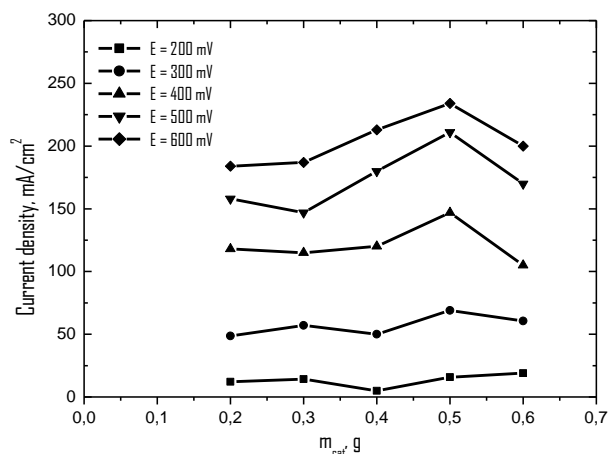


**Fig. 4.** Current generated from the air electrode at constant potential as a function of the ratio catalyst/hydrophobic material in the active layer.

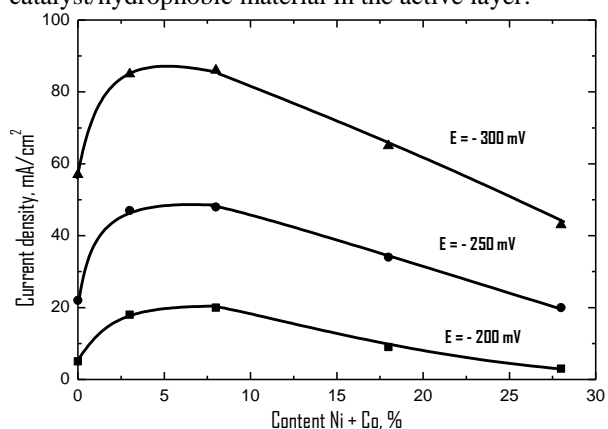


**Fig. 5.** Optimization of the oxides content in the catalyst ACCoNi.

catalytic layer. With the increase of  $(1-\beta)$  the dimensions of the hydrophobic zones in the catalytic layer decrease which results in an increase of the transport hindrances of the gaseous reactant towards the catalytic zones.

To investigate experimentally the influence of the active layer thickness, the polarization characteristics of a series of air supplying layers  $100 \text{ mg/cm}^2$  XC-35 and corresponding value of catalyst mixture (0,2 g (14%); 0,3 g (21%); 0,4 g (28%); 0,5 g (35%); 0,6 g (41%)) were measured. The dependence of the generated by the electrodes current at constant potential amount of catalyst mixture is studied. Measurements showed, that the optimal value is 0,5 g (35%) catalyst mixture (Fig. 4).

In Fig.5 are presented the current densities of air electrodes measured at constant potential as a function of the content of metal oxides (expressed as a sum of Co + Ni content) in the catalyst. From this figure the optimal content of the mixed Co-Ni oxides in the catalyst is found (ca. 5% Ni + Co).

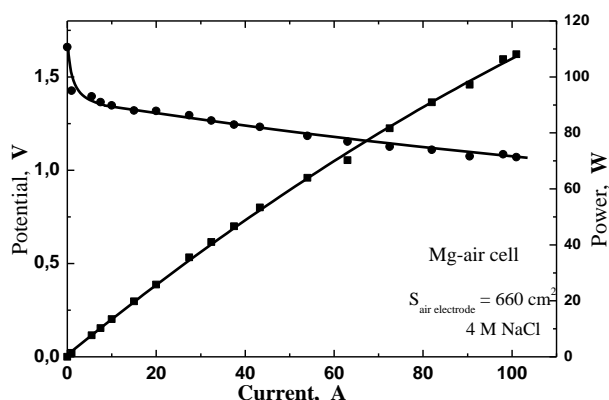


Fig. 6. Current-voltage and power characteristics of the Mg-air cell.

The experiments have shown that high power Mg-air cells can be constructed. In Fig.6 are presented the voltage and the power characteristics of an experimental Mg-air cell: air electrode with pyrolyzed CoTMPP catalyst (total area  $660\text{cm}^2$ ); Mg – electrode – Mg alloy type MA8M 06; electrolyte - 4M NaCl solution.

The described Mg-Air cells are designed as experimental "mechanically rechargeable cells". Once the magnesium anode has been discharged, it is removed out of the cell together with the electrolyte and new magnesium electrode and fresh saline electrolyte are introduced in it. After this "mechanically recharge" the magnesium-air cell is operational again. The essential feature in this case is that the air electrodes in the cell are used many times. The Mg-air cell can be stored for a long time without electrolyte and without Mg anode. When needed it can be put in operation only by introducing electrolyte and Mg-anode.

### CONCLUSIONS

Presented here is a study on selection of hydrophobic material with optimal physical, chemical and electrochemical characteristics for the gas layer of the air gas-diffusion electrode and investigation and selection of suitable catalyst for the electrochemical reduction of oxygen that occurs on the air gas-diffusion electrode. Accordingly, the air gas-diffusion electrodes suitable for operation in NaCl-solution are designed and tested under various conditions. Several carbon-based catalysts for the oxygen reduction reaction were developed.

The performance of the air gas-diffusion electrode is influenced not only by the activity of the catalyst but also by all transport processes taking place in its porous structure. At low current densities, where the transport hindrances in the electrode are negligible low, the value  $\Delta E$  is practically independent on the current density.

For the CoTMPP catalyst the ratio between catalyst and the amount of the hydrophobic material presented in the catalytic layer is experimentally investigated. The maximum reached value of the ratio is 0,68, which corresponds to catalyst contents of 68% at the active layer.

The investigation of the dependence of the generated by the electrodes current at constant potential amount of catalyst mixture showed optimal value when the amount of catalyst (CoTMPP)/hydrophobic material in the active layer is 35%.

For the ACCoNi catalyst the investigation of the current densities of air electrodes, measured at constant potential as function of the contents of metal oxides, showed that best mixture of Co-Ni oxides in the catalyst is ca. 5% Ni + Co.

The results shows that the Mg-air cells are with substantially increased power output. They could be used as primary and emergency power sources for the residential, commercial and industrial markets. A great advantage of the magnesium-air cells and batteries is the use of the non-toxic magnesium and a non-aggressive salt-water electrolyte and particularly see/ocean water.

### REFERENCES

1. F. Bidault, D.J.L. Brett, P.H. Middleton, N.P. Brandon, *Journal of Power Sources*, **187**, 39 (2009).
2. K.J. Euler *J. Appl. Electrochem.*, **2**, 105 (1972).
3. K. Mund, F.v. Sturm, *Electrochim. Acta*, **20**, 463 (1975).
4. N. Giordano, E. Passalacqua, V. Alderucci, P. Staiti, L. Pino, H. Mirzaian, E.J. Taylor, G. Wilemski *Electrochim. Acta*, **36**, 1049 (1991).
5. L.G. Austin, *Ind. Eng. Chem. Fundam.*, **4**, 321 (1965).
6. S. Srinivasan, H.D. Hurwitz, *Electrochim. Acta*, **12**, 495 (1967).
7. V.S. Markin, *Russian Chem. Bull.*, **12**, 1551 (1963).
8. E.A. Grens, *Electrochim. Acta*, **15**, 1047 (1970).
9. E.A. Grens, C.W. Tobias, *Electrochim. Acta*, **10**, 761 (1965).
10. J. Giner, *J. Electrochem. Soc.*, **116**, 1124 (1969).
11. W.M. Vogel, K.A. Klinedinst, *Electrochim. Acta*, **22**, 1385 (1977).
12. R.P. Iczkowski, *J. Electrochem. Soc.*, **127**, 1433 (1980).
13. W. Vogel, J. Lundquist, A. Bradford, *Electrochim. Acta*, **17**, 1735 (1972).
14. S.-C. Yang, P. Bjornbom, *Electrochim. Acta*, **37**, 1831 (1992).
15. J.O.M. Bockris, A.J. Appleby, *Energy*, **11**, 95 (1986).
16. A.J. Appleby, *J. Electroanal. Chem.*, **357**, 117 (1993).

17. E. Yeager, *Electrochim. Acta*, **29**, 1527 (1984).
18. W. Vielstich, A. Lamm, H. Gasteiger, Handbook of Fuel Cells – Fundamentals Technology and Applications, NJ, USA, Part 3, vol. 3–4, 2003.
19. B. Wang, *J. Power Sources*, **152**, 1(2005).
20. L. Zhang, J.J. Zhang, D.P. Wilkinson, H.J. Wang, *J. Power Sources*, **156**, 171 (2006).
21. J. Lee, B. Jeonga, J. D. Ocona, *Current Applied Physics*, **13**, 309 (2013).
22. H. Liu, L. Zhang, J. Zhang, D. Ghosh, J. Jung, B. W. Downing, *J. Power Sources*, **161**, 743 (2006).
23. A. Kaisheva, I. Iliev, NATO Science Series II Mathematics, Physics and Chemistry 229 (2006), p. 105
24. I. Iliev, S. Gamburgzev, A. Kaisheva, J.Mrha, *J. Appl. Electrochem.* **5**, 291 (1975).
25. I. Iliev, J.Mrha, A. Kaisheva, S. Gamburgzev, *J. Power Sources*, **1**, 35 (1976/1977).
26. A. Kaisheva, I. Iliev, S. Gamburgzev, *J. Appl. Electrochem.*, **9**, 511 (1979).
27. S. Gamburgzev, I. Iliev, A. Kaisheva, G. Steinberg, L. Makrousov, *Elektrokhimia* (in Russian) **16**, 1069 (1980).
28. I. Iliev, S. Gamburgzev, A. Kaisheva, A. Fuhrman, K.Wiesener, *J. Power Sources*, **13**, 217 (1984).
29. D. Ohms, S. Herzog, R. Franke, V. Neumann, K. Wiesener, S. Gamburgzev, A. Kaisheva, I. Iliev, *J. Power Sources*, **38**, 327 (1992).
30. J. Milusheva, R. Boukoureshtlieva, S. Hristov, *Bul. Chem. Commun.*, **43**, 42 (2011).
31. A.Kaisheva, I.Iliev, J.Milusheva, Mechanically rechargeable magnesium-air cell with non-aggressive electrolyte, Proc. International Congress for Battery Recycling, 2002, Vienna, Austria

## ВЪЗДУШНИ ГАЗОДИФУЗИОННИ ЕЛЕКТРОДИ ЗА ЕЛЕКТРОХИМИЧНИ КЛЕТКИ МАГНЕЗИЙ-ВЪЗДУХ, РАБОТЕЩИ С РАЗТВОР НА НАТРИЕВ ХЛОРИД

Й. Д. Милушева\*, Р. И. Букурещлиева, С. М. Христов

<sup>1</sup>Институт по електрохимия и енергийни системи “Акад. Е. Будевски” – Българска академия на науките, ул. Акад. Г. Бончев бл.10, София 1113, България

Постъпила на 03. 03. 2013; приета за печат на 13.04. 2013

(Резюме)

През последните години горивните клетки и метало-въздушните батерии привличат научно внимание като ефикасни преобразуватели на енергия. За катоди в метало-въздушните електрохимични клетки се използват предимно въздушни газодифузионни електроди (ВГДЕ), върху които протича електрохимична редукция на кислород и се осъществява контакт между електролитния разтвор и газообразния кислород. В литературата често се обсъжда поведението на порести електроди в алкални горивни клетки, но съществуват ограничен брой изследвания за работата на ВГДЕ в неутрален електролит. Цел на настоящото изследване е оптимизиране на ВГДЕ за работа в електрохимична клетка магнезий-въздух с електролит NaCl. Газовият слой е изработен от различни хидрофобирани сажди и е оптимизирана дебелината и количеството въглероден материал в газовия слой на електрода. Изготвени са катализатори за електрохимичната редукция на кислорода на базата на въглеродни материали и различни промотори и са определени електрохимичните характеристики на ВГДЕ с катализаторите: пиролизиран кобалт тетраметоксифенилпорфирин (CoTMPP), VS50 - CoTMPP - 700 и активен въглен с Co и Ni (ACCoNi). Изследвано е влиянието на дебелината на активния слой и съотношението на количествата на катализатора и хидрофобния материал в активния слой върху поляризационните характеристики и транспортните затруднения във въздушните електроди с различни катализатори. ВГДЕ е използван в първична електрохимична клетка магнезий-въздух, която показва добри електрохимични характеристики и работи с нетоксичен магнезиев електрод и неагресивен електролит NaCl.

## Direct ultrasonic synthesis of classical high temperature ceramic phases at ambient conditions by innovative method

P.V. Angelov<sup>1\*</sup>, S.S. Slavov<sup>2</sup>, Sv.R. Ganev<sup>2</sup>, Y.B. Dimitriev<sup>3</sup>, J.G. Katzarov<sup>4</sup>

<sup>1</sup>*Institute of Electrochemistry and Energy Systems, Bulgarian Academy of Sciences, Acad. G. Bonchev Str., Bldg. 10, 1113 Sofia, Bulgaria*

<sup>2</sup>*Department of Physics, University of Chemical Technology and Metallurgy, 8, Kl. Ohridski Blvd., 1756 Sofia, Bulgaria*

<sup>3</sup>*Department of Silicate Technology, University of Chemical Technology and Metallurgy, 8, Kl. Ohridski Blvd., 1756 Sofia, Bulgaria*

<sup>4</sup>*Magnetic and Ultrasound Technologies, Ltd., Sofia, Bulgaria*

Received March 05, 2013; Accepted May 18, 2013

It is well known that ultrasound waves accelerate chemical, physicochemical and electrochemical processes. In this respect, it deserves to investigate the applicability of this technique for synthesis of high tech materials with specific applications. Ferroelectric ceramics are used for production of various devices for electronic components like high-temperature capacitors, non-volatile memories (ROM), etc. The commonly used compounds for ferroelectric materials production are  $\text{Bi}_2\text{O}_3$ ,  $\text{TiO}_2$ ,  $\text{SiO}_2$  and  $\text{Nd}_2\text{O}_3$  and their different combinations. The classical route to obtain ferroelectric materials, particularly their high temperature specific phases, is to prepare a batch by weighing and mixing the precursors of the starting compounds in a hand mortar followed by high temperature melting usually over  $1300^\circ\text{C}$  which need higher class ovens and then tempering the molten compositions. This work presents a novel approach for synthesis of ferroelectric ceramic materials of the system  $\text{Bi}_2\text{O}_3\text{-TiO}_2\text{-SiO}_2\text{-Nd}_2\text{O}$  based on agitation of the precursors in powerful ultrasonic field generated by custom-made specialized device. The method is extremely simple and energy saving since it avoids using high temperature equipment. Applying this innovative approach the high-temperature phase  $\text{Bi}_{12}\text{TiO}_{20}$  having specific optical properties was synthesized at room temperature and verified by XRD analysis, optical microscopy and IR spectroscopy. The ultrasound agitation has pronounced effect on thermally treated samples too. Furthermore, studies are under way to establish the relationship between the mayor process parameters and the properties of the obtained ceramic materials (power of the applied ultrasonic field, temperature, duration, etc.). Our experiments show that this new useful method exhibits wide applicability in future hydrogen energy conversion systems, for optical, electro-optical and ferroelectric ceramic materials production. We suggest using it for production of other glass ceramics, superconductors, metal ceramics and composite materials, and also as an alternative or addition to the mechanochemical methods for both synthesis and activation.

**Keywords:** bismuth titanate ceramics, ultrasonic synthesis, electrical characteristics, microstructure, XRD

### INTRODUCTION

Aurivillius family oxides including  $\text{Bi}_4\text{Ti}_3\text{O}_{12}$  are of great interest in the last years due to their potential for electronic applications as transducers, capacitors, and acoustic piezo-sensors with high temperature piezoelectric properties, (high Curie temperature) [1, 2]. Many techniques have been employed for preparing a layered structure of bismuth titanate phases including powders and bulk ceramics: molten salt synthesis, co-precipitation, reactive calcinations, sol-gel synthesis, mechanochemical method and others. Between them the crystallization from melts or glasses [3-6] gives the possibility to control more easily the particle size distribution, morphology and

crystallographic orientation. As it is well known the phase formation and the properties of these materials are strongly influenced by the method of preparation. On the other hand co-doped  $\text{Bi}_4\text{Ti}_3\text{O}_{12}$  ceramics are very promising to direct commercialization. The introduction of  $\text{Nd}_2\text{O}_3$  as additive allows obtaining of materials with more effective electrical and dielectric properties, such as a higher remnant polarization and height resistance to fatigue [7-18]. The other challenge is the existence of solid solutions in the system  $\text{Bi}_2\text{O}_3\text{-TiO}_2\text{-Nd}_2\text{O}_3$ . By S. Kunej *et al.* [19] were described the solubility limits of three solid-solutions:  $\text{Bi}_{(1.6-1.08x)}\text{Nd}_x\text{Ti}_2\text{O}_{(6.4+0.3x)}$ , ( $0.25 < x < 0.96$ ),  $\text{Nd}_{2-x}\text{Bi}_x\text{Ti}_2\text{O}_7$ , ( $0 < x < 0.35$ ), and  $\text{Bi}_{4-x}\text{Nd}_x\text{Ti}_3\text{O}_{12}$ , ( $0 < x < 2.6$ ).

In the previous studies [20, 21] it has been shown that the introduction of 20 - 40 mol%  $\text{SiO}_2$  simulates the partial amorphization of the samples. The main established phases in super cooled melt

\* To whom all correspondence should be sent:  
E-mail: magnetics.ultrasonics@gmail.com

are either  $\text{Bi}_2\text{Ti}_2\text{O}_7$  and  $\text{Bi}_4\text{Ti}_3\text{O}_{12}$  or only  $\text{Bi}_4\text{Ti}_3\text{O}_{12}$ , in dependence of the cooling rate and composition. The other important result was that simultaneous introduction of  $\text{SiO}_2$  and  $\text{Nd}_2\text{O}_3$  as additives [21] in bismuth-titanate ceramics changes the glass-formation ability and electrical properties.

These results motivated us to continue our experiments in this field. The purpose of the present work is to prepare, by melt quenching method, polycrystalline or glass-crystalline materials in the system  $\text{Bi}_2\text{O}_3$ - $\text{TiO}_2$ - $\text{SiO}_2$ - $\text{Nd}_2\text{O}_3$  and to study their electrical properties depending on composition and temperature and to compare the results obtained after ultrasonication of precursors.

Beneficial effects at using ultrasound technology are described in [22, 23].

### EXPERIMENTAL

The melting is performed in alumina crucibles at  $500^\circ\text{C}$  to  $1450^\circ\text{C}$  according to way of preparation.

The samples are homogenized in two ways (Figure 1): 1) 15 minutes mixture; 2) 15 minutes mixture and then ultrasound homogenization (20 min).

The obtained samples with their batch compositions, visual observation and method of preparation are presented in Table 1 (obtained without ultrasound treatment) and Table 2 (obtained with ultrasound treatment).

Data for selected samples will be presented below. The samples, obtained by the first method, are heated in temperature range  $1260 - 1450^\circ\text{C}$ .

The samples, obtained by the second method, are heated in temperature range  $500 - 1200^\circ\text{C}$ .

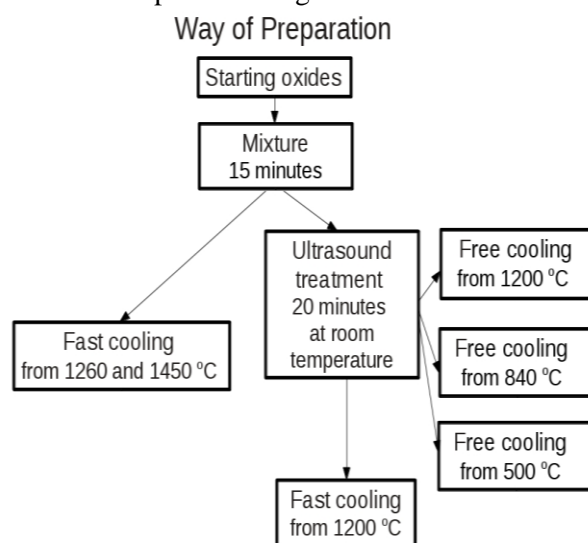


Fig. 1. Scheme of preparation of the samples.

### RESULTS AND DISCUSSION

In this method ferroelectric materials are melted in alumina crucibles at  $1450^\circ\text{C}$  and super cooled to room temperature by pouring between two cooper plates. The detected main phases are  $\text{Bi}_4\text{Ti}_3\text{O}_{12}$ ,  $\text{Bi}_{12}\text{TiO}_{20}$  and  $\delta\text{-Bi}_2\text{O}_3$ .

Samples were treated by ultrasound at room temperature which leads mainly to forming of phase  $\text{Bi}_{12}\text{TiO}_{20}$  (for samples J, L, 4D) and  $\text{Nd}_2\text{O}_3$  (for samples 6, 11). Subsequent thermal treatment shows the formation of the phase  $\text{Bi}_4\text{Ti}_3\text{O}_{12}$ , maintaining the phase  $\text{Bi}_{12}\text{TiO}_{20}$  (Figures 2- 4).

Table 1. The obtained without ultrasound treatment samples with their batch compositions, visual observation and method of preparation.

	Batch Composition	Phase formation according XRD	Method of Preparation
6	$40\text{Bi}_2\text{O}_3.40\text{TiO}_2.20\text{Nd}_2\text{O}_3$	$\text{Bi}_4\text{Ti}_3\text{O}_{12}$ , $\text{Bi}_{12}\text{TiO}_{20}$ , $\delta\text{-Bi}_2\text{O}_3$ .	$T_m=1450^\circ\text{C}$ Fast cooling $1450^\circ\text{C}$ , 15 min.
11	$50\text{Bi}_2\text{O}_3.40\text{TiO}_2.10\text{Nd}_2\text{O}_3$	$\text{Bi}_4\text{Ti}_3\text{O}_{12}$ , $\text{Bi}_{12}\text{TiO}_{20}$ , $\delta\text{-Bi}_2\text{O}_3$ .	$T_m=1450^\circ\text{C}$ Fast cooling $1450^\circ\text{C}$ , 10 min.
4D	$32\text{Bi}_2\text{O}_3.40\text{TiO}_2.20\text{SiO}_2.8\text{Nd}_2\text{O}_3$	$\text{Bi}_4\text{Ti}_3\text{O}_{12}$	$T_m=1450^\circ\text{C}$ Fast cooling $1450^\circ\text{C}$ , 10 min.
j	$40\text{Bi}_2\text{O}_3.40\text{TiO}_2.20\text{SiO}_2$	$\text{Bi}_4\text{Ti}_3\text{O}_{12}$	$T_m=1260^\circ\text{C}$ Fast cooling $1260^\circ\text{C}$ , 15 min.
1	$40\text{Bi}_2\text{O}_3.50\text{TiO}_2.10\text{SiO}_2$	$\text{Bi}_4\text{Ti}_3\text{O}_{12}$	$T_m=1260^\circ\text{C}$ Fast cooling $1260^\circ\text{C}$ , 15 min.



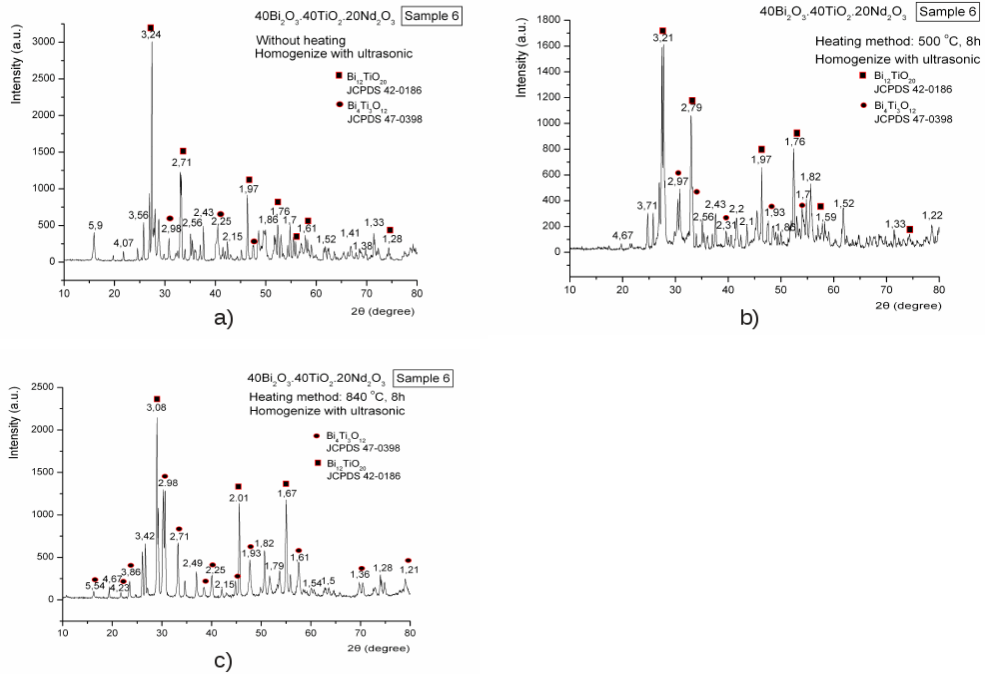


**Fig. 3.** XRD patterns of the external part of sample with composition: a) 40Bi<sub>2</sub>O<sub>3</sub>.40TiO<sub>2</sub>.20Nd<sub>2</sub>O<sub>3</sub> homogenized with ultrasound at room temperature; b) 40Bi<sub>2</sub>O<sub>3</sub>.40TiO<sub>2</sub>.20Nd<sub>2</sub>O<sub>3</sub> homogenized with ultrasound and heated at 500°C; c) 40Bi<sub>2</sub>O<sub>3</sub>.40TiO<sub>2</sub>.20Nd<sub>2</sub>O<sub>3</sub> homogenized with ultra sound and heated at 840°C.

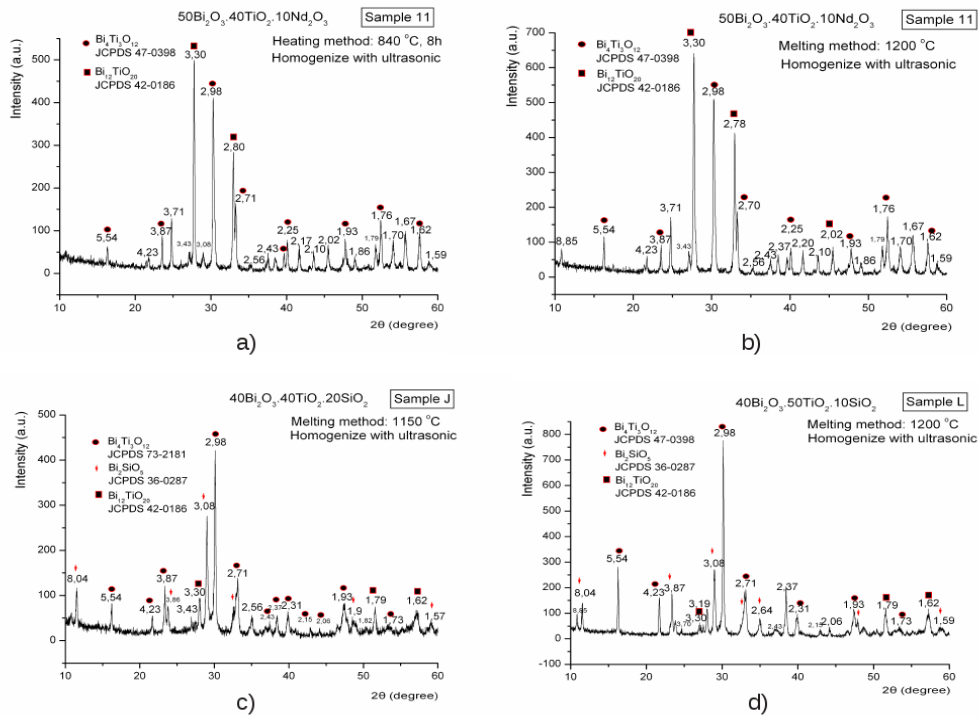


**Fig. 4.** XRD patterns of the external part of sample with composition: a) 50Bi<sub>2</sub>O<sub>3</sub>.40TiO<sub>2</sub>.10Nd<sub>2</sub>O<sub>3</sub> homogenized with ultra sound and heated at 840°C; b) 50Bi<sub>2</sub>O<sub>3</sub>.40TiO<sub>2</sub>.10Nd<sub>2</sub>O<sub>3</sub> homogenized with ultra sound and heated at 1200°C; c) 40Bi<sub>2</sub>O<sub>3</sub>.40TiO<sub>2</sub>.20SiO<sub>2</sub> homogenized with ultra sound and heated at 1150°C; d) 40Bi<sub>2</sub>O<sub>3</sub>.50TiO<sub>2</sub>.10SiO<sub>2</sub> homogenized with ultra sound and heated at 1200°C and fast cooled.

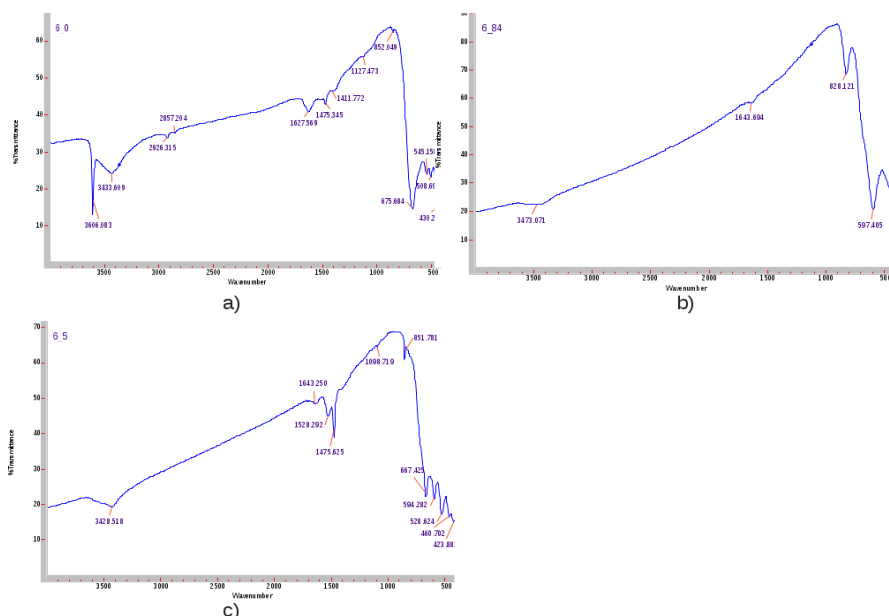


**Fig. 5.** IR spectrum of sample with composition: a)  $40\text{Bi}_2\text{O}_3.40\text{TiO}_2.20\text{Nd}_2\text{O}_3$ ; b)  $40\text{Bi}_2\text{O}_3.40\text{TiO}_2.20\text{Nd}_2\text{O}_3$ ; c)  $40\text{Bi}_2\text{O}_3.40\text{TiO}_2.20\text{Nd}_2\text{O}_3$ .

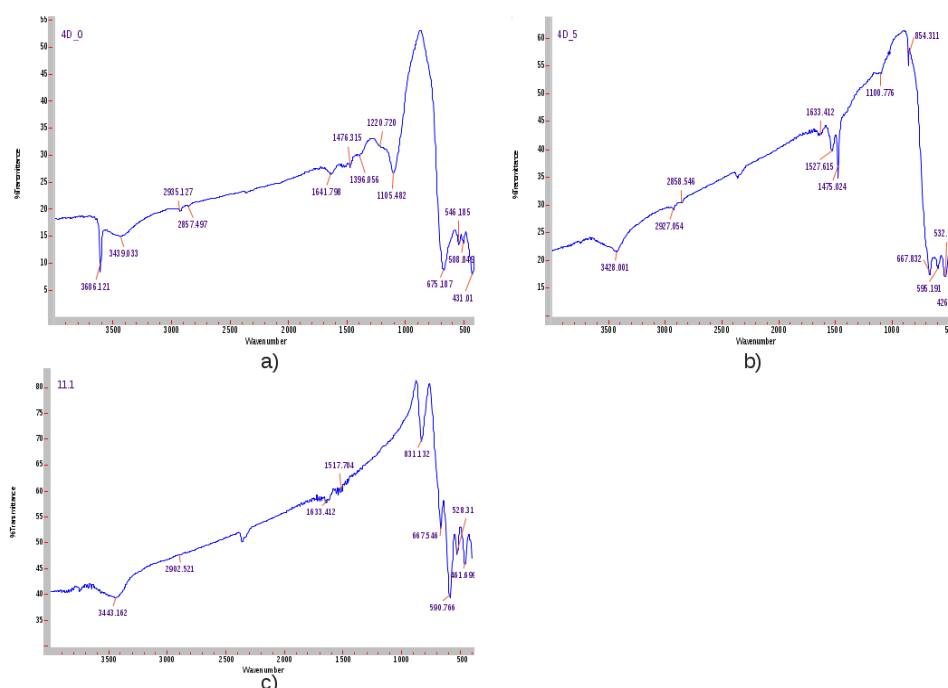


**Fig. 6.** IR spectrum of sample with composition: a)  $32\text{Bi}_2\text{O}_3.40\text{TiO}_2.20\text{SiO}_2.8\text{Nd}_2\text{O}_3$ ; b)  $32\text{Bi}_2\text{O}_3.40\text{TiO}_2.20\text{SiO}_2.8\text{Nd}_2\text{O}_3$ ; c)  $50\text{Bi}_2\text{O}_3.40\text{TiO}_2.10\text{Nd}_2\text{O}_3$ .

The infrared spectroscopy of the investigated material gives some additional information concerning especially the connectivity of the short range building units as well some characteristic bands corresponding to the obtained crystal phases. Several bands are observed in the spectrum. Bands near  $1000\text{ cm}^{-1}$ ,  $800\text{--}900\text{ cm}^{-1}$  as well as band near  $470\text{ cm}^{-1}$  are observed. This means that they may possess bridging bond Si-O-Si corresponding to the

band (above  $1000\text{ cm}^{-1}$ ) connected to partially polymerized  $\text{SiO}_4$  tetrahedra. At  $920\text{ cm}^{-1}$  bridging bond Ti-O-Si decrease, the band below  $920\text{ cm}^{-1}$  due to Bi-O vibration of  $\text{Bi}_2\text{O}_3$ . At decrease of  $\text{Bi}_2\text{O}_3$  content this band shifts to higher frequency. At frequency  $450\text{ cm}^{-1}$  replacement of silica by  $\text{Nd}_2\text{O}_3$  up to 10% is quite interesting because the spectrum will be as similar as for pure  $\text{Bi}_4\text{Ti}_3\text{O}_{12}$  for this compound. The typical band one is near  $820$

$\text{cm}^{-1}$ , the other band is near  $580 \text{ cm}^{-1}$  and the following one is near  $450 \text{ cm}^{-1}$ . Up to now there is no adequate explanation for the origin of this vibration (Figure 5, 6).

## CONCLUSIONS

The investigation carried out confirms that depending on the condition of the melting and additional heat treatment of the super-cooled melt different poly-phase ceramic materials with various microstructures could be obtained in the system  $\text{Bi}_2\text{O}_3\text{-TiO}_2\text{-SiO}_2\text{-Nd}_2\text{O}_3$ .

1. In the synthesized samples the presence of several phases including  $\text{Bi}_4\text{Ti}_3\text{O}_{12}$ ,  $\text{Bi}_2\text{O}_3$  polymorphs and  $\text{Bi}_{20}\text{TiO}_{20}$  are registered by melt quenching.

2. Samples treated by ultrasound without heating leads to formation mainly of the phase  $\text{Bi}_{12}\text{TiO}_{20}$  and of small amount of the phase  $\text{Bi}_4\text{Si}_3\text{O}_{12}$  (for samples with  $\text{SiO}_2$  presence in the batch composition) and  $\text{Nd}_2\text{O}_3$  (for samples with  $\text{Nd}_2\text{O}_3$  presence in the batch composition).

3. Subsequent heating of ultrasound treated samples (in temperature range  $500 - 1200^\circ\text{C}$ ) shows the formation of the phase  $\text{Bi}_4\text{Ti}_3\text{O}_{12}$ , and of the phase  $\text{Bi}_{12}\text{TiO}_{20}$ .

4. The IR spectra confirms the degree of the connectivity between different types of the polyhedral building the short range order in the structure of the materials:

a) The increased amount of  $\text{TiO}_2$  in glass ceramic material preserves the bridging bonds Si-O-Si and Si-O-Ti up to 40 %  $\text{TiO}_2$ .

b) The increased amount of  $\text{Bi}_2\text{O}_3$  instead of  $\text{SiO}_2$  leads to formation of isolated  $\text{SiO}_4$  units.

c) The introduction of  $\text{Nd}_2\text{O}_3$  does not change the IR spectra of the phase  $\text{Bi}_4\text{Ti}_3\text{O}_{12}$  up to 10 %  $\text{Nd}_2\text{O}_3$ .

5. Because of the proven efficiency of direct ultrasound synthesis (sonosynthesis) we can conclude it to be a very perspective technique for application in many cases like in glass, glass ceramics and ceramics pre-synthesis and preparation where evaporation or sublimation of volatile components occur in uncontrolled manner and in this way the final chemical and respectively, the phase composition is changed. In particular cases the composition is very different from the initial one and researchers try to use various analytical methods to determine the final composition. But all analytical methods have their respective natural limits, precision and reproducibility. These efforts, as well as, expenses and time wasted could be avoided by applying the proposed ultrasonication method. The best

analytical method appeared to be the analytical scales because 100% of the initial components are present in the final chemical and phase composition by using this method of preparation. One of the main problems in glass melting, as well as, in ceramics synthesis and sintering could be solved successfully by applying ultrasound treatment technique.

**Acknowledgements:** The presentation of the present research results has been supported by the Bulgarian Ministry of Youth, Education and Science, Project BG 051PO001-3.3.05/0001, cont. No. D002-170

## REFERENCES

1. B. Aurivillius, *Ark. Kemi*, **1**, 463-80 (1949).
2. B. Aurivillius, *Ark. Kemi*, **2**, 519 (1950).
3. Y. Shi, S. Feng, C. Cao, *Mater. Lett.*, **44**, 215(2000).
4. T. Rentschler, *Mater. Res. Bull.*, **32**, 351(1997).
5. R.E. Melgarejo, M.S. Tomar, P.S. Dopal, S.K. Flippov, R.S. Katiyar, K.A. Kuenhold, *Mater. Sci. Eng.*, **B83**, 89 (2001).
6. J. Maier, "Remarks on Application of Fast Ion Conductors," in NATO ASI Series, Vol. 199, Science and Technology of Fast Ion Conductors. pp. 299-301 (1989).
7. H.D. Megaw, *Crystal Structures: A Working Approach*; pp. 217-21. (1973).
8. S.T. Misture. "Oxygen Ion Conduction in Layered Aurivillius-Derived Ceramics", National Science Foundation Career Grant, Alfred University (1998).
9. J.B. Goodenough, J.E. Ruiz-Diaz, Y.S. Zhen, *Solid State Ionics*, **44**, 21 (1990).
10. W. Wong-Ng, J.A. Kaduk, Q. Huang, R.S. Roth, *Powder Diffr.* **15**, 227 (2000).
11. H. Bachhofer, H.v. Philipsborn, W. Hartner, C. Dehm, B. Jobst, A. Kiendl, H. Schroeder, R. Waser, *J. Mater. Res.*, **16**, 2966 (2001).
12. F. Krok, W. Bogusz, P. Kurek, M. Wasiucioneck, W. Jakubowski, J. Dygas, *Mater. Sci. Eng.*, **B21**, 70 (1993).
13. O. Schulz, M. Martin, *Solid State Ionics*, **135**, 549 (2000).
14. C. P. Udawatte, M. Kakihana, M. Yoshimura, *Solid State Ionics*, **128**,] 217 (2000).
15. K.R. Kendall, J.K. Thomas, H.-C. zur Loye, *Chem. Mater.*, **7**, 50 (1995).
16. L.M. Brekhovskikh, *Waves in Layered Media* 2nd Edition, Academic press, New York, 1980.
17. J.D. Achenbach, *Wave Propagation in Elastic Solids*, Elsevier Science Publisher, Amsterdam (1990).
18. B.A. Auld, *Acoustic Fields and Waves in Solids* (2nd Edition) Vol. 1&2, Krieger Publishing, Florida (1990).
19. J.L. Rose, *Ultrasonic Waves in Solid Media*, Cambridge University Press, Cambridge (1999).

20. K.F. Graff (1991) *Wave Motion in Elastic Solid*, Dover Publications, New York.
21. R. Wood, *Ultrasound Physics & Terminology*, Rev.1.0, 2009-11-13 15:40:34.168, UNIVERSITY OF ROCHESTER LIBRARIES. URL to cite or link to: <http://hdl.handle.net/1802/8508>
22. K.S. Suslick, In: *Kirk-Othmer Encyclopedia of Chemical Technology*; 4th Ed. J. Wiley & Sons: New York, 1998, vol. 26, 517-541.
23. K.S. Suslick, Y. Didenko, M.M. Fang, T. Hyeon, K.J. Kolbeck, W.B. McNamara, III; M.M. Mdleleni, M. Wong, *Phil. Trans. Roy. Soc. A*, **357**, 335-353 (1999).

## ДИРЕКТЕН УЛТРАЗВУКОВ СИНТЕЗ НА ВИСОКОТЕМПЕРАТУРНИ КЕРАМИЧНИ ФАЗИ ПРИ ОБИКНОВЕНИ УСЛОВИЯ ПО ИНОВАТИВЕН МЕТОД

П. В. Ангелов<sup>1</sup>, С. С. Славов<sup>2</sup>, Св. Р. Ганев<sup>2</sup>, Я. Б. Димитриев<sup>3</sup>, Ж. Г. Кацаров<sup>4</sup>

<sup>1</sup> *Институт по Електрохимия и Енергийни Системи, Българска академия на Науките, ул. Акад. Г. Бончев, Блок 10, 1113 София*

<sup>2</sup> *Катедра Физика, Университет по Химична Технология и Металургия, бул. Кл. Охридски 8, 1756 София*

<sup>3</sup> *Катедра Технология на Силикатите, Университет по Химична Технология и Металургия, бул. Кл. Охридски 8, 1756 София*

<sup>4</sup> *Магнитни и Ултразвукови Технологии ЕООД, София, България*

Получена на 5 март, 2013; приета на 18 май, 2013

(Резюме)

Добре известно е, че ултразвуковите вълни укоряват химичните, физикохимичните и електрохимичните процеси. Във връзка с това си заслужава да се изследва приложимостта на тази техника за синтез на високотехнологични материали със специфични приложения. Фероелектричните керамики се използват за производство на различни електронни компоненти като високотемпературни кондензатори, ROM памет за компютри и други. Широко използваните съединения за производство на фероелектрични материали са  $\text{Bi}_2\text{O}_3$ ,  $\text{TiO}_2$ ,  $\text{SiO}_2$  and  $\text{Nd}_2\text{O}_3$ , както и различни техни комбинации. Класическият начин на синтез за получаване на фероелектрични материали и особено високотемпературните им фази е да се приготви състав чрез претегляне и смесване на прекурсорите на изходните материали в ръчен хапан последвано от топене при висока температура обикновено до  $1300^\circ\text{C}$ . Това изисква по-висок клас пещи, след което следва темпериране на стопените композиции. Настоящата работа представлява нов подход за синтез на фероелектрични керамични материали от системата  $\text{Bi}_2\text{O}_3\text{-TiO}_2\text{-SiO}_2\text{-Nd}_2\text{O}$  основан на облъчване на прекурсорите с високо мощно ултразвуково поле, генерирано от специализирано устройство изработено по поръчка. Методът е много лесен и е енергоспестяващ, тъй като се избягва използването на високотемпературно оборудване. С прилагането на този иновативен подход високотемпературната фаза  $\text{Bi}_{12}\text{TiO}_{20}$ , която има специфични оптически свойства беше синтезирана при стайна температура, което беше потвърдено с ренгенов фазов анализ XRD, оптична микроскопия и инфрачервена спектроскопия. Облъчването с ултразвук има изявен ефект и върху термично третираните образци. В ход са изследвания, които целят да се установи връзката между основните технологични параметри и свойствата на получените керамични материали (мощността на приложеното ултразвуково поле, температурата, продължителността и др.). Нашите експерименти показват, че този нов полезен метод има широка приложимост в бъдещите водородни преобразуватели на енергия, както и за производство на оптични, електрооптични и фероелектрични керамични материали. Ние предлагаме използването на този метод и за други стъклокерамични материали, свръхпроводници, металокерамични и композитни материали, а също така и като алтернатива или допълнение на механохимичните методи с цел синтез и активиране на материали.

## Electrochemically deposited nanostructured ZnO layers on the front side of c-Si solar cell

K. Lovchinov<sup>1</sup>, M. Ganchev<sup>1</sup>, M. Petrov<sup>1</sup>, H. Nichev<sup>1</sup>, D. Dimova-Malinovska<sup>1</sup>,  
J. S. Graff<sup>2</sup>, Al. Ulyashin<sup>2</sup>

<sup>1</sup>Central Lab. of Solar Energy and New Energy Sources – Bulgarian Academy of Sciences, 72, Tzarigradsko Chaussee, 1784 Sofia, Bulgaria

<sup>2</sup>SINTEF, Forskningsveien 1, P.O. Box 124, Blindern, 0314, Oslo, Norway

Received March 13, 2013; revised April 03, 2013

ZnO nanostructures layers are deposited by electrochemical method on different c-Si solar cells structures. Acid aqueous solutions of ZnCl<sub>2</sub> (5 · 10<sup>-3</sup> M) and KCl (0.1 M) with pH 6.0 at temperature of 80°C is used as electrolyte using a three-electrode electrochemical cell and saturated calomel electrodes (SCE) as a reference electrode. ZnO layers deposition time varies between 20 and 90 min. An analysis of the surface morphology of such layers is performed by means of Scanning Electron Microscope (SEM). Measurements of the reflection and diffused reflection spectra of ZnO based nanostructures deposited on the front side of three different types of c-Si solar cells is performed, as well. The obtained structural and optical properties of the ZnO electrochemical thin films deposited on the top front surface of different c-Si solar cells for different deposition time are compared. The study demonstrates that the deposition of ZnO nanostructured films results in decreasing of the specular reflection and the diffused reflection better expressed in the case of un-textured Si surface. The obtained ZnO layers can be applied as antireflection coatings in c-Si solar cells to enhance their light harvesting properties.

**Key words:** ZnO, nanostructure, electrochemical deposition, c-Si solar cell.

### INTRODUCTION

ZnO is a unique material possessing variety of useful properties. It is among the most investigated II-VI group semiconductors with wide direct band gap of 3.4 eV and large free exciton binding energy of 60 meV [1]. ZnO possess hexagonal wurtzite structure with lattice parameters  $a = 3.25 \text{ \AA}$  and  $c = 5.12 \text{ \AA}$  [1].

Zinc oxide nanostructures are most promising one-dimensional (1D) materials received increased attention over last decade because of their exciting potential applications in optoelectronic devices, such as field effect transistors, nano-sensors, optical switches, solar cells and light emitting diodes [2-6]. Recently, J.Y Chen and K.W.Sun reported application of vertically aligned ZnO nanorod arrays as an antireflective coating on Si solar cells [7]. ZnO can be prepared with the large variety of nanostructure configurations as nano-rings, nano-springs, nano-belts, nano-combs, nano-rods, highly ordered nano-wires arrays or tower-like sticks [8] and can be synthesized by a diversity of chemical and physical methods [2-6, 9-10].

Among chemical methods are precipitation in non-aqueous solution [11], chemical-bath deposition [12, 13], hydro-thermal precipitation [13] and electrodeposition [6-8,15-17].

Electrodeposition has some advantages because it is a low cost industrially up-scalable process, relevant to different substrates for preparation of well defined nanostructures with reasonable physical parameters [2, 3, 15].

Design of novel functional configurations of the materials depends on depth understanding of connection between the electro-physical parameters of the material and particle size and morphology of nanostructure.

In this paper results from investigation of the optical and the structural properties of nanostructured ZnO thin films formed by electrochemical deposition on the top front side of c-Si solar cells are reported. The c-Si solar cell consists of ~0.4 μm n<sup>+</sup>- type emitter on p-type Si wafer with p<sup>+</sup>-type back surface field (BSF). Three different types of c-Si solar cells are used – type 1 – with deposited ITO film on the textures front side (ITO/(textured)n<sup>+</sup>-Si(~0.4μm, emitter)/p-Si-base,/p<sup>+</sup>-Si(~200μm, BSF)), type 2 - with deposited ITO film on the un-textures front side

\* To whom all correspondence should be sent:  
E-mail: lov4@abv.bg

(ITO/(un-textured) $n^+$ -Si( $\sim 0.4\mu\text{m}$ , emitter)/p-Si-base/p $^+$ -Si( $\sim 200\mu\text{m}$ , BSF)), and type 3 – without deposited ITO and un-textures front side ((un-textured) $n^+$ -Si( $\sim 0.4\mu\text{m}$ , emitter)/p-Si-base/p $^+$ -Si( $\sim 200\mu\text{m}$ , BSF)). The obtained ZnO layers are characterized by SEM, by spectra of specular reflectance, diffuse reflection and haze ratio in reflection.

## EXPERIMENTAL

ZnO nanostructured films were deposited by an electrochemical process from slightly acid aqueous solution of  $\text{ZnCl}_2$  ( $5 \cdot 10^{-3}$  M) and KCl (0.1 M) with pH 6.0 at  $80^\circ\text{C}$  and different deposition times (in the range of 20-90 min) using a three-electrode electrochemical cell and Saturated Calomel Electrodes (SCE) as a reference electrode. As a working electrode c-Si solar cell were used. Spectrally pure graphite rod electrode was used as anode. The electrolyte was agitated by magnetic stirrer. The oxygen is provided in the system by supplement of  $\text{H}_2\text{O}_2$ . The deposition was carried out controlling the redox potential of the high power potentiostat system WENKING HP 96. The deposition potential was kept at  $-700$  mV (vs. SCE). The oxygen content in solution was determined by Dissolved oxygen and temperature meter Hanna Instruments 9146. The surface morphology and the thickness of the deposited films were imaged under a Scanning Electron Microscope (SEM) Philips 515. The thickness of the deposited ZnO layers were between  $0.50$  and  $1.2 \mu\text{m}$ . The optical properties (specular reflectance, diffuse reflection and haze ratio in reflection) were measured by a spectrophotometer Shimadzu UV-3600 in the range of  $300 - 1200$  nm employing a  $60$  mm integrating sphere.

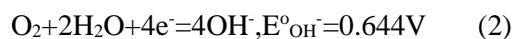
## RESULTS AND DISCUSSION

Despite the wide number of works, recipes and regimes for electrodeposition of ZnO, there is no adequate interpretation of the mechanism and reaction route. Deposition of thin film zinc oxide could be explained as a product of interaction of  $\text{OH}^-$  and  $\text{Zn}^{2+}$  in aqueous solution on the surface of the electrode.



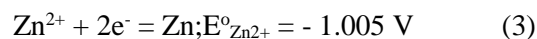
Since the zinc hydroxide is unstable, it does dehydrate into ZnO [18]. The standard free energy of formation of ZnO is  $G_{\text{ZnO}}^{298} = -361.08$  kJ/mol [18].

Hydroxide ions are produced by reduction of oxygen, dissolved in electrolyte:



Reaction (2) presents the reduction process on the oxygen electrode with standard electrode potential  $0.644$  V, against SCE [18].

Standard electrode potential of zinc according the reaction (3) is much more negative ( $-1.005$  V vs SCE) than that of  $\text{OH}^-$  by equilibrium (2):



The reaction of electrodeposition of ZnO depends on reduction of dissolved oxygen in the solution and can be described by four electron process according to the reaction:



The difference between standard electrode potentials of Zn and oxygen (according to the reaction (2)) is:

$$E_{\text{OH}^-}^0 - E_{\text{Zn}^{2+}}^0 = 1.163\text{V}, \quad (5)$$

while the factor  $G/nF$  for four electron process is:

$$G/4F = 0.936\text{V} \quad (6)$$

The comparison of the values in (5) and (6) shows that the difference between standard electrode potentials of zinc and  $\text{OH}^-$  (5) is bigger than the depolarization factor of the chemical reaction (6),  $(E_{\text{OH}^-}^0 - E_{\text{Zn}^{2+}}^0) > G^{298}/4F$ . This is the case of induced co-deposition mechanism by the rules described by Brener [19] and Kroger [20]. This means that at appropriate ratio of concentrations of  $\text{Zn}^{2+}$  and  $\text{OH}^-$  ( $[\text{Zn}^{2+}]/[\text{OH}^-] \geq 10^2 - 10^3$ ) a large interval of deposition potentials will exist, where the composition of the deposited material will be determined only by the thermodynamics of the process and will be close to the stoichiometric one.

Since the reduction of oxygen by Eq. (2) is a step determined by the potential [20], it is possible to control the overall electrodeposition process by measuring the Redox potential of the system. In the ideal case, in equilibrium the redox potential of the electrolyte determines the ability of deposition of ZnO.

In Figure 1 the dependences of both dissolved oxygen concentration (left) and Redox potential (right) on the time are shown. Initial time ( $T=0$ ) corresponds to the moment of the supplying of the hydrogen peroxide into deposition solution. The curves have similar behavior – a sharp rise until  $15$  min is observed and then the values decrease and go to equilibrium.

In order to provide electrical conductivity of the electrolyte, the process of electrodeposition of ZnO

in aqueous solutions is carried out in the electrolyte containing ZnCl and KCl. The KCl salt influences the solubility of the oxygen by Henry's Law. Another factor is the temperature of the electrolyte. In details this matter is treated in large extension by Cooper [21].

It has been reported that ZnO thin layers are obtaining at Redox potential in interval 300 ÷ 400 mV (vs SCE) [22]. At potentials below 300 mV there is no electrodeposition of ZnO because there is not enough dissolved oxygen in the solution. At potentials above 400 mV (vs SCE) the solution is over-saturated of oxygen and the deposition of zinc peroxide (ZnO<sub>2</sub>) takes a place. In this case the deposited layers have dendrit structure with very rough surface and are non-adherent to the substrate.

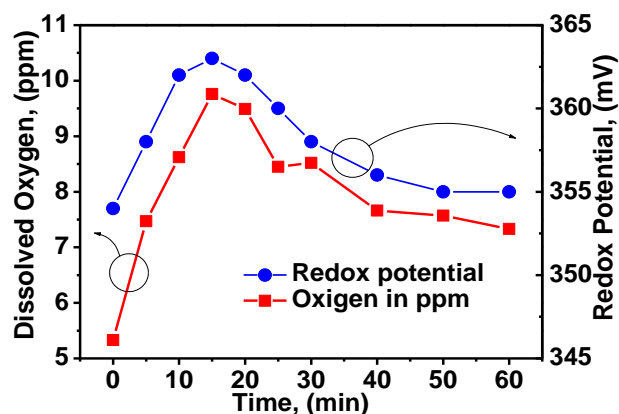


Fig. 1. Dependences of the concentration of the dissolved oxygen (left) and of the Redox potential (right) on time.

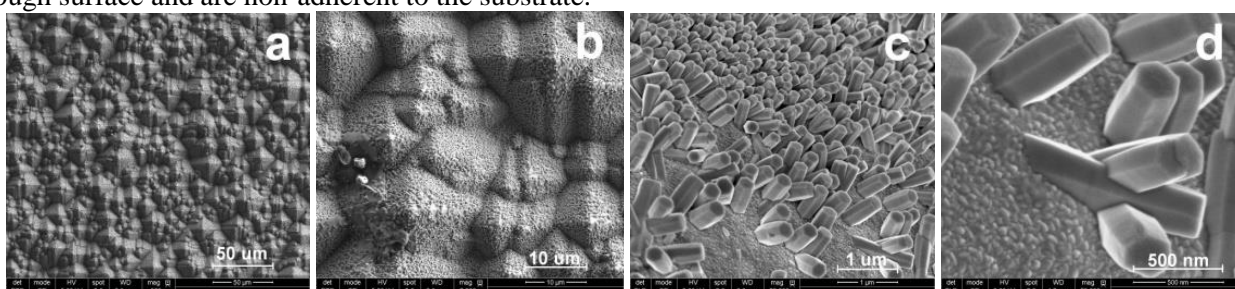


Fig. 2. SEM images (with different magnification) of ZnO electrochemical thin films deposited on textured Si-solar cells with ITO – type 1. The ZnO is deposited for 60 min.

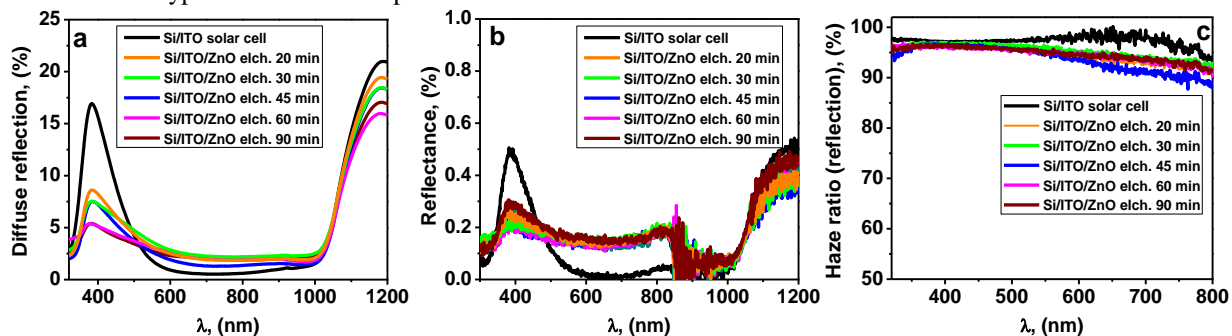


Fig. 3. Spectra of diffuse reflectance (a), specular reflection (b) and haze ratio in reflection (c) in visible region of ZnO electrochemical thin films deposited on textured Si-solar cells with ITO (type 1). The ZnO layers are deposited for different time.

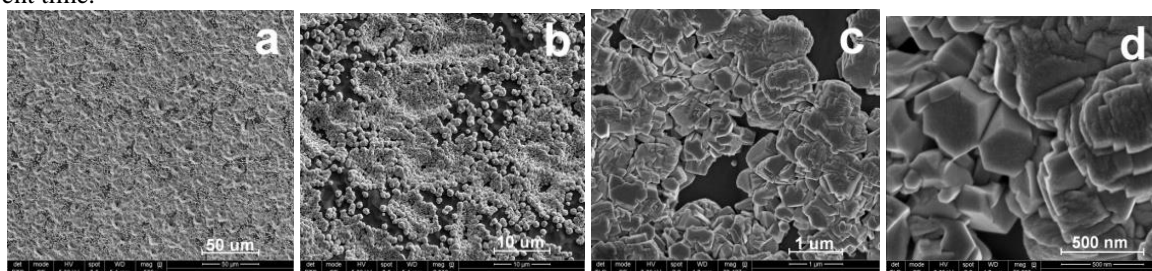


Fig. 4. SEM images (with different magnification) of ZnO electrochemical thin films deposited on untextured Si-solar cells with ITO - type 2. The ZnO layer is deposited for 40 min.

In this work the electrodeposition is carried out at cathode potential of -700 mV (vs SCE) where stoichiometric ZnO is produced. At potentials more positive than -700 mV the rate of the reaction (2), and respectively (4), is very low or does not run at all. At deep cathodic potentials, below -1050 mV,

the deposition potential of zinc is reached (reaction (3)) and the layers consist of ZnO with metallic zinc.

SEM images of the surface of electrochemically deposited ZnO on the top surface of the c-Si solar cell type 1 (with ITO and textured front surface) are

presented in Figure 2. It is seen that the ZnO nanowires with hexagonal shape have grown on the different side of the pyramidal etched surface of the solar cell. Similar hexagonal shape is reported in [23] and is typical for ZnO nanowires.

Figure 3 shows spectra of specular reflection, diffuse reflection and haze ratio in reflection of ZnO deposited on textured c-Si solar cell structures with ITO layers (type 1). ZnO layers are deposited for different time. The corresponding spectra of solar cells structures before deposition of ZnO are given for comparison as well.

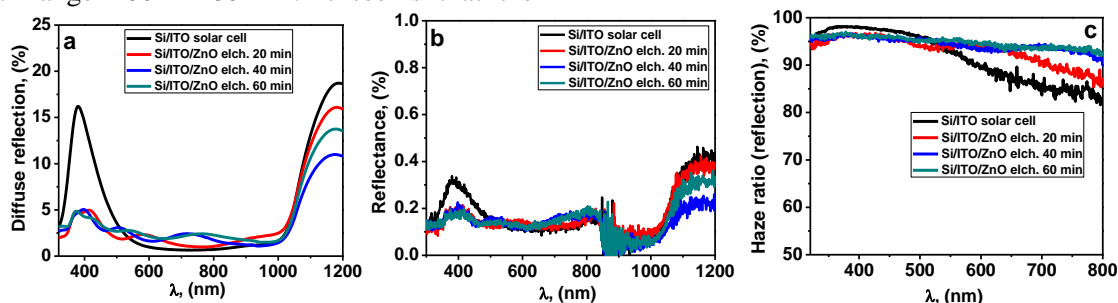
Electrochemical deposition of the ZnO results in decreasing of the intensity of the band of reflectance at about 400 nm by about 10% and slightly increase (about 0.2%) of the diffuse reflection in the range 550 - 1000 nm compared to the value of the based structure.

Applying ZnO nanorod areas on the surface of the solar cell could increase generation of the carriers and the value of the photocurrent in the spectral range 400 - 480 nm. It seems that the

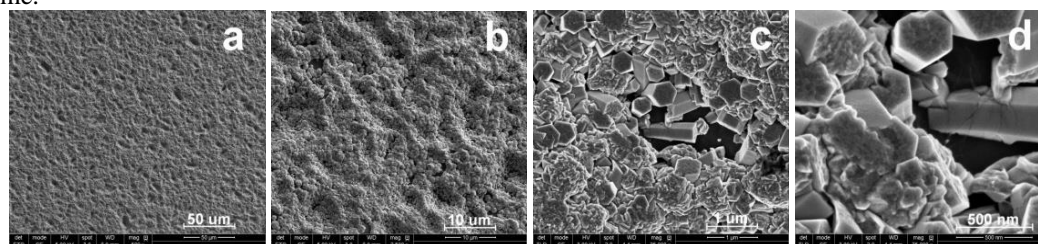
deposition time of 20 and 30 min for ZnO nanostructures could be more favorable.

Figure 4 shows the SEM of the surface of solar cell structure (type 2) with a flat front surface (untextured). ZnO nanostructured layer is electrochemically deposited for 40 min. The column structure of electrochemical layer deposited on untextured solar cell is recognizable and the hexagonal formations are seen.

The spectra of specular reflectance, diffused reflection and haze ratio in reflection from the surface of c-Si solar cell type 2 with ZnO deposited for different time are shown in Figure 5. As in the previous case, the values of reflectance and diffused reflection at in the range 350-500 nm decrease after ZnO grown, however in the range 550 - 1000 they increased slightly (for diffused reflection from 1 to 3 %) and the haze ratio (in the range 550-800 nm) is higher compared to the sample without deposited ZnO.



**Fig. 5.** Spectra of diffuse reflection (a), specular reflectance (b) and haze ratio in reflection (c) in visible region of ZnO electrochemical thin layers deposited on textured Si-solar cells with ITO (type 2). The ZnO layers are deposited for different time.



**Fig. 6.** SEM images (with different magnification) of ZnO thin films electrochemically deposited on untextured Si-solar cells without ITO - type 3. The ZnO was deposited for 60 min.

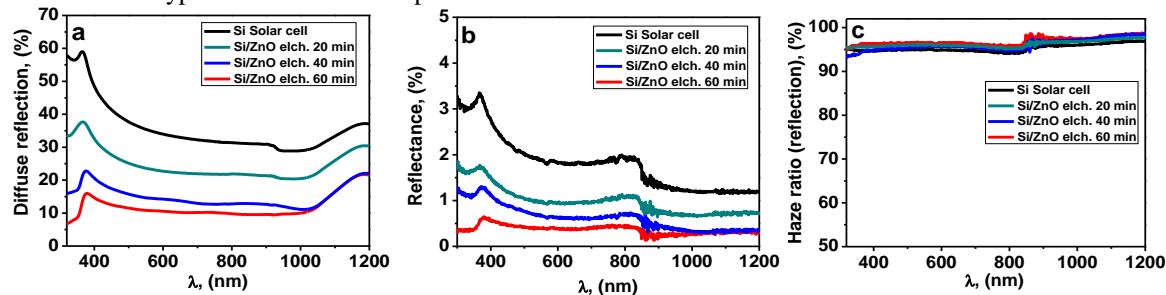


**Fig. 7.** Spectra of diffused reflection, specular reflectance and haze ratio in reflection of c-Si solar cells type-3 with ZnO electrochemically deposited for different time.

Similar experiments have been performed on the c-Si solar cell structure with untextured top however without front ITO layer – type 3. SEM pictures of the sample with ZnO electrochemically deposited for 60 min are shown in Figure 6. The hexagonal rods grown with different orientation to the substrate are seen.

The spectra of reflection, diffused reflection and haze ratio in reflection of the structure type 3 before and after deposition of ZnO nanowired layers are shown in Figure 7. Values of reflectance and diffused reflection decrease in the samples with deposited ZnO and with the time of deposition. The haze ratio in reflection is very high (~95%) and increases slightly after ZnO deposition.

The preliminary experiments for application of ZnO nanostructured films to solar cell demonstrate that the value of the diffused reflection and the specular reflectance can be decreased after deposition of ZnO nanostructured layers on the top side of the c-Si solar cells. Better antireflective properties are obtained when the ZnO nanorod arrays are deposited on the front surface the c-Si solar cells with un-textured front size.

## CONCLUSIONS

The study of the optical properties (diffuse reflection, reflectance and haze ratio in reflection) of nanostructured ZnO layers deposited by electrochemical methods on the front side of c-Si solar cell is performed. After deposition of ZnO layers the decrease of the reflectance is observed and this tendency increases with deposition time. Electrochemically deposited ZnO layers on c-Si solar cells with un-textured front surface results in significantly reduction of the reflectance and diffuse reflection and can be applied as antireflective coatings in c-Si solar cell.

**Acknowledgements** The work has been funded by the European FP7- project NanoPV № 246331.

## REFERENCES

1. V. A. Coleman, C. Jagadish, Zinc oxide bulk. Thin films and nanostructures, p. 1–5, UK, Elsevier, 2006.
2. O. Lupan, T. Pauporté, B. Viana, *Adv. Mater.*, **22**, 3298 (2010).
3. T. Pauporté, Design of solution-grown ZnO nanostructures (Ed. Z. M. Wang), Lecture Notes on Nanoscale Science and Technology, Toward Functional Nanomaterials, (vol. 5, p. 77–125, Springer Books), New York, 2009.
4. L. Luo, Y. Zhang, S.S. Mao, L. Lin, *Sens. Actuators A. Phys.*, **127**, 201 (2006).
5. O. Lupan, V.M. Guérin, I.M. Tiginyanu, V.V. Ursaki, L. Chow, H. Heinrich, T. Pauporté, J. Photochem, A. Photobiol, *Chem.*, **211**, 65 (2010).
6. T. Pauporté, D. Lincot, B. Viana, F. Pellé, *Appl. Phys. Lett.*, **89**, 233112 (2006).
7. J.Y. Chen, K.W. Sun, *Solar Energy Materials & Solar Cells*, **94**, 930 (2010).
8. Schmidt-Mende L, J. L. MacManus-Driscoll, *Mater Today*, **10**, 40 (2007).
9. C. Badre, T. Pauporté, M. Turmine, D. Lincot, *Nanotechnology*, **18**, 365705 (2007).
10. N. Wang, Y. Cai, R.Q. Zhang, *Mater. Sci. Eng. R.*, **60**, 1 (2008).
11. R. Jayakrishnan, G. Hodes, *Thin Solid Films*, **440**, 19 (2003).
12. Y. Lare, A. Godoy, L. Cattin, K. Jondo, T. Abachi, F. R. Diaz, *Appl. Surf. Sci.*, **255**, 6615 (2009).
13. M. M. Wang, S. H. Hahn, E. J. Kim, J. S. Kim, S. Kim, C. Park, *Thin Solid Films*, **516**, 8599 (2008).
14. B. Liu, H. C. Zeng, *J. Am. Chem. Soc.*, **125**, 4430 (2002).
15. T. Pauporté, D. Lincot, *Appl. Phys. Lett.*, **75**, 3817 (1999).
16. A. Goux, T. Pauporté, J. Chivot, D. Lincot, *Electrochim. Acta*, **50**, 2239 (2005).
17. T. Pauporté, D. Lincot, *J. Electroanal. Chem.*, **54**, 517 (2001).
18. D. R. Lide, H. P. R. Frederikse, in: Handbook of Chemistry and Physics, (77th ed., CRC Press, Boca Raton, FL), 1996.
19. A. Brenner, Electrodeposition of alloys, Academic press (1963).
20. F. A. Kroger, *J. Electrochem. Soc.*, **12**, 2028 (1978).
21. L.H.N. Cooper, *Journal of the Marine Biological Association of the United Kingdom*, **22**, 167 (1937).
22. D. Dimova-Malinovska, P. Andreev, M. Sendova-Vassileva, H. Nichev, V. Mikli, 24th European Photovoltaic Solar Energy Conference, Hamburg, Germany (2009),
23. D. Dimova-Malinovska, K. Lovchinov, M. Ganchev, O. Angelov, J. Graff, A. Ulyashin, *Physica Status Solidi A*, **1-6** pssa.201200565 (2012).

## НАНОСТРУКТУРИРАНИ ZnO СЛОЕВЕ, ОТЛОЖЕНИ ЧРЕЗ ЕЛЕКТРОХИМИЧЕН МЕТОД ВЪРХУ ФРОНТАЛНАТА СТРАНА НА ФОТОЕЛЕМЕНТИ ОТ c-Si.

К. Ловчинов<sup>1</sup>, М. Ганчев<sup>1</sup>, М. Петров<sup>1</sup>, Х. Ничев<sup>1</sup>, Д. Димова-Малиновска<sup>1</sup>,

Дж. С. Граф<sup>2</sup>, Ал. Уляшин<sup>2</sup>

<sup>1</sup> Централна лаборатория по слънчева енергия и нови енергийни източници – Българска академия на науките,  
72, Цариградско шосе, 1784 София, България

<sup>2</sup> СИНТЕФ, Изследователски път 1, П. кутия 124, Блиндерн, 0314, Осло, Норвегия

Постъпила на 13 март, 2013 г.; преработена на 3 април, 2013 г.

(Резюме)

Наноструктурирани слоеве от ZnO са отложени върху фронталната страна на фотоелементи от c-Si чрез електрохимичен процес в електролит от слабо кисел воден разтвор на ZnCl<sub>2</sub> (5 · 10<sup>-3</sup> M) и KCl (0.1 M) с pH=6.0 при 80°C, използвайки три електродна електрохимична клетка. Времето на отлагане на ZnO слоеве варира между 20 и 90 минути за отделните образци. Чрез метода на сканираща електронна микроскопия (SEM) е изследвана повърхностната морфология на отложените слоеве. Измерени са спектрите на отражение и дифузно отражение на ZnO наноструктурирани слоеве, отложени върху три различни вида фотоелементи с текстурирана и не-текстурирана повърхност от c-Si с ITO; и без ITO на не-текстурирана повърхност. Структурните и оптичните свойства на ZnO слоеве, отложени като горен слой в c-Si фотоелементи, са сравнени в зависимост от времето на отлагане. Резултатите от изследванията показват, че при отлагането на наноструктуриран ZnO се наблюдава намаляване на отражението и дифузното отражение, като това намаление е по-добре изразено при слоевете отложени върху не-текстурирани фотоелементи. Изследванията на свойствата на отложените ZnO слоеве могат да бъдат използвани като анти отразяващи покрития в c-Si фотоелементи за увеличаване на ефективността им.

## Investigations of glass-crystalline TiO<sub>2</sub>-V<sub>2</sub>O<sub>5</sub>-P<sub>2</sub>O<sub>5</sub> samples

D. V. Blaskova-Kochnitcharova<sup>1,2</sup>, T. Petkova<sup>2\*</sup>, L. Fachikov<sup>1</sup>, E. Lefterova<sup>2</sup>, I. Kanazirski<sup>3</sup>,  
P. Angelov<sup>2</sup>, S. Vassilev<sup>2</sup>

<sup>1</sup>University of Chemical Technology and Metallurgy, 8, Kl. Ohridski Blvd., 1756 Sofia, Bulgaria

<sup>2</sup>Institute of Electrochemistry and Energy Systems, Bulgarian Academy of Sciences, Acad. G. Bonchev Str., Bl. 10,  
1113 Sofia, Bulgaria

<sup>3</sup>University of Mining and Geology "St. Ivan Rilski", 1756 Sofia, Bulgaria

Received March 19, 2013; revised April 23, 2013

Bulk samples of the ternary system TiO<sub>2</sub>-V<sub>2</sub>O<sub>5</sub>-P<sub>2</sub>O<sub>5</sub> have been synthesized by standard melt quenching technique. The structure of the materials has been studied by X-ray diffraction. The obtained samples possess glassy-crystalline structure. Impedance investigations have been performed by using impedance spectroscopy at different temperatures. The spectra are analyzed by two phase concept: crystalline grains distributed in glassy matrix. The conductivity is obtained using fitting procedure. The conductivity is most likely caused by polaron hopping between aliovalent vanadium ions.

**Keywords:** oxides, X-ray diffraction, impedance analysis

### INTRODUCTION

The oxide semiconductors are large group of the semiconducting glassy alloys. The electrical properties of oxide glasses containing transition-metal ions such as V, Fe and W are of interest because of their switching properties. The semiconducting behaviors of the glasses are due to the presence of transition-metal ions in more than one valence state. Oxide glasses with high content of V<sub>2</sub>O<sub>5</sub> exhibit considerable electronic conductivity governed by cross-linking of the glass network supporting enhanced electron hopping along V<sup>4+</sup>-O-V<sup>5+</sup> bonds [1-2].

Pietrzak *et al.* [3] have shown that vanadate-phosphate glasses with a composition 90V<sub>2</sub>O<sub>5</sub>-10P<sub>2</sub>O<sub>5</sub> undergo thermal nanocrystallization, which leads to a significant increase in the electronic conductivity.

Hirashima *et al.* [4] have studied TiO<sub>2</sub>-V<sub>2</sub>O<sub>5</sub>-P<sub>2</sub>O<sub>5</sub> glasses containing up to 30 mol% TiO<sub>2</sub> at different temperatures and have established that the ternary glasses are semiconducting due to polaron hopping similarly to the V<sub>2</sub>O<sub>5</sub>-P<sub>2</sub>O<sub>5</sub> glasses. The d.c. conductivity has been established to decrease when V<sub>2</sub>O<sub>5</sub> is replaced by TiO<sub>2</sub> but increases when P<sub>2</sub>O<sub>5</sub> is replaced by TiO<sub>2</sub>. The variations of the conductivity values are mainly due to changes in

the activation energy.

The aim of the present work is to study electrical transport in the ternary TiO<sub>2</sub>-V<sub>2</sub>O<sub>5</sub>-P<sub>2</sub>O<sub>5</sub> glass-crystalline materials with a view to their further application in electrochemical systems.

### EXPERIMENTAL

Bulk samples with compositions (TiO<sub>2</sub>)<sub>20</sub>(V<sub>2</sub>O<sub>5</sub>)<sub>50</sub>(P<sub>2</sub>O<sub>5</sub>)<sub>30</sub> and (TiO<sub>2</sub>)<sub>10</sub>(V<sub>2</sub>O<sub>5</sub>)<sub>60</sub>(P<sub>2</sub>O<sub>5</sub>)<sub>30</sub> were synthesized by melt-quenching method. As raw materials were used powders of TiO<sub>2</sub> and V<sub>2</sub>O<sub>5</sub> and liquid H<sub>3</sub>PO<sub>4</sub>. The samples were thoroughly ground (homogenized) in agate mortar, melted in quartz crucibles at temperature 1000-1200 °C and fast cooled between ice cold copper plates. To obtain samples with a specific form required for impedance measurements, the melts were cooled in a copper matrix with 1 cm diameter, depth of 1 mm and pressed with copper plate.

The phase formation of the samples was studied by X-ray diffraction (XRD) method. XRD patterns were recorded by means of X-ray diffractometer Philips APD-15. The data were collected with a constant rate of 0.02 deg.s<sup>-1</sup> over an angle range 2θ = 20°÷70 deg using CuK<sub>α</sub> radiation (λ = 1.54178 Å). All X-ray investigations were performed at ambient temperature.

The preparation of the samples for impedance study included polishing and deposition of silver paste contacts on the surfaces. The impedance measurements were carried out by means of

\* To whom all correspondence should be sent:  
E-mail: [tpetkova@bas.bg](mailto:tpetkova@bas.bg)

Autolab PGSTAT 30 (Eco Chemie) frequency response analyzer, in the frequency range 0.05Hz - 1MHz. The study was performed at different temperatures in the temperature range from 20 to 120°C with a step of 20°C.

## RESULTS AND DISCUSSION

### • XRD

XRD spectra of the synthesized samples are presented in Fig. 1. The spectra show a combination of broad diffraction halos and crystalline peaks, which prove the glassy-crystalline structure. Peaks of rutile (TiO<sub>2</sub>) (JCPDS-PDF#89-4202) are obtained on the XRD-spectrum of the (TiO<sub>2</sub>)<sub>20</sub>(V<sub>2</sub>O<sub>5</sub>)<sub>50</sub>(P<sub>2</sub>O<sub>5</sub>)<sub>30</sub> sample. The peak positions on the (TiO<sub>2</sub>)<sub>10</sub>(V<sub>2</sub>O<sub>5</sub>)<sub>60</sub>(P<sub>2</sub>O<sub>5</sub>)<sub>30</sub> diffractogram are very close to those of the compounds Ti<sub>4</sub>P<sub>6</sub>O<sub>23</sub> (JCPDS-PDF#39-0004), NaTi<sub>2</sub>(PO<sub>4</sub>)<sub>3</sub> and NaVTi(PO<sub>4</sub>)<sub>3</sub> (JCPDS-PDF #49-1114, #84-2012). The crystalline structure of the last two corresponds to NASICON type structure (acronym of Na Super Ionic Conductor). This is mixed metal phosphates type structure with a general formula A<sub>x</sub>B<sub>2</sub>(PO<sub>4</sub>)<sub>3</sub>, where A is a monovalent ion and B is ion in three, tetra, or penta-valent state [5, 6]. The structure is described as a covalent skeleton [B<sub>2</sub>(PO<sub>4</sub>)<sub>3</sub>]<sup>-</sup> consisting of the PO<sub>4</sub> tetrahedral and the BO<sub>6</sub> octahedral units, forming 3D interconnected channels with two types of interstitial spaces M<sub>I</sub> and M<sub>II</sub>, where conducting A<sup>+</sup> cations are distributed. When cations are absent (x=0) the NASICON structure is termed empty. Since this structure is discovered in some binary and ternary metal phosphates like NbTi(PO<sub>4</sub>)<sub>3</sub>,

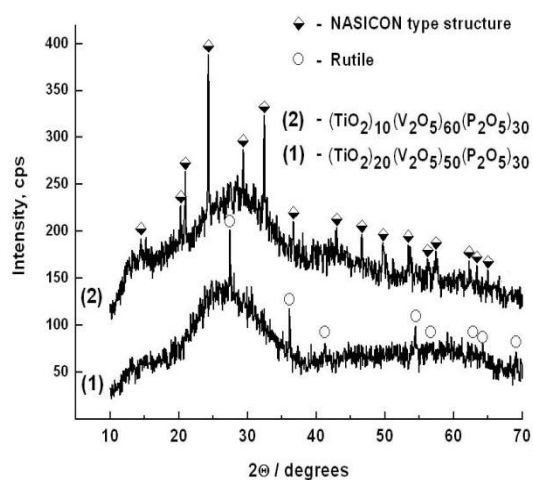


**Fig. 1.** X-ray diffraction patterns of (TiO<sub>2</sub>)<sub>20</sub>(V<sub>2</sub>O<sub>5</sub>)<sub>50</sub>(P<sub>2</sub>O<sub>5</sub>)<sub>30</sub> and (TiO<sub>2</sub>)<sub>10</sub>(V<sub>2</sub>O<sub>5</sub>)<sub>60</sub>(P<sub>2</sub>O<sub>5</sub>)<sub>30</sub> samples.

NbV<sub>0.5</sub>Ti<sub>0.5</sub>(PO<sub>4</sub>)<sub>3</sub> [6] our hypothesis is that titan-vanadium phosphate possesses empty NASICON structure. It is correlated with the investigation of S. Titlbach and co-workers, who has established the NASICON related structure in vanadyl (V) titanium(IV) phosphate with structural formula (V<sup>VO</sup>)Ti<sup>IV</sup><sub>6</sub>(PO<sub>4</sub>)<sub>9</sub> [7].

### • Impedance

Figure 2 represents the complex-plane impedance (Nyquist) plots of the samples under investigation. Two semicircles (arc) observed for the both samples are interpreted with two phase concept. The phases observed on the diffractograms: crystalline and amorphous correspond to the two arcs on the impedance plots. They define crystalline grains and the area between them (grain boundary) where the glassy phase is distributed. The simplest equivalent circuit describing two phase model consists of two Voigt elements in series, as presented in Fig. 2c. (Voigt element is R and Capacitor - R/C or R and Constant Phase Element-R/CPE in parallel) [8, 9]. The high-frequency semicircle is due to ac response of the grains R<sub>gr</sub>/CPE<sub>gr</sub> while the lower-frequency part expresses electrical properties of glass matrix R<sub>gl</sub>/CPE<sub>gl</sub>. The conductivity is obtained using fitting procedure and the activation energies are determined from slopes of the Arrhenius plots (lnσ versus 1/T) presented in fig.3. The calculated values of the conductivity at room temperature and activation energy are presented in Table 1.

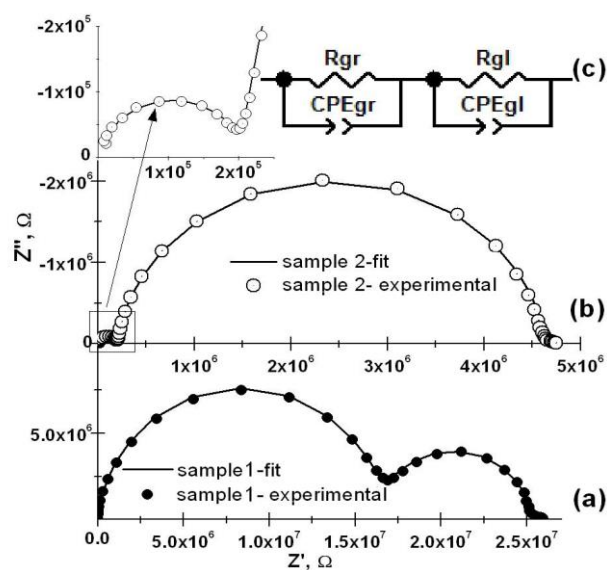


**Fig. 2.** Nyquist plots of (a) (TiO<sub>2</sub>)<sub>20</sub>(V<sub>2</sub>O<sub>5</sub>)<sub>50</sub>(P<sub>2</sub>O<sub>5</sub>)<sub>30</sub>; (b) (TiO<sub>2</sub>)<sub>10</sub>(V<sub>2</sub>O<sub>5</sub>)<sub>60</sub>(P<sub>2</sub>O<sub>5</sub>)<sub>30</sub> samples and (c) equivalent circuit.

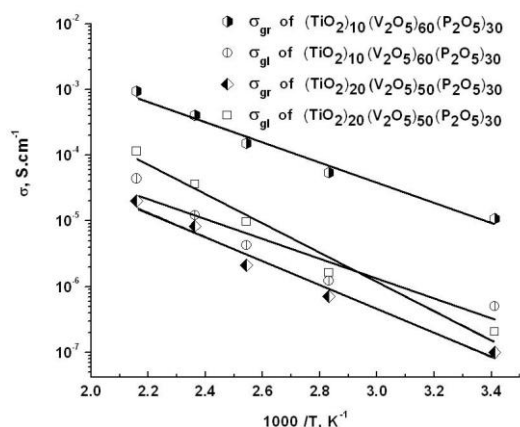


**Fig. 3** Arrhenius plots of the conductivities of (TiO<sub>2</sub>)<sub>20</sub>(V<sub>2</sub>O<sub>5</sub>)<sub>50</sub>(P<sub>2</sub>O<sub>5</sub>)<sub>30</sub> and (TiO<sub>2</sub>)<sub>10</sub>(V<sub>2</sub>O<sub>5</sub>)<sub>60</sub>(P<sub>2</sub>O<sub>5</sub>)<sub>30</sub> glass-crystalline samples.

**Table 1.** Conductivities and activation energies of the (TiO<sub>2</sub>)<sub>20</sub>(V<sub>2</sub>O<sub>5</sub>)<sub>50</sub>(P<sub>2</sub>O<sub>5</sub>)<sub>30</sub> and (TiO<sub>2</sub>)<sub>10</sub>(V<sub>2</sub>O<sub>5</sub>)<sub>60</sub>(P<sub>2</sub>O<sub>5</sub>)<sub>30</sub> glass-crystalline samples.

Sample	$\sigma_{gr}$ S.cm <sup>-1</sup>	$E_{agr}$ eV	$\sigma_{gl}$ S.cm <sup>-1</sup>	$E_{agl}$ eV
(TiO <sub>2</sub> ) <sub>20</sub> (V <sub>2</sub> O <sub>5</sub> ) <sub>50</sub> (P <sub>2</sub> O <sub>5</sub> ) <sub>30</sub>	$9.9 \times 10^{-8}$	0.37	$2.1 \times 10^{-7}$	0.44
(TiO <sub>2</sub> ) <sub>10</sub> (V <sub>2</sub> O <sub>5</sub> ) <sub>60</sub> (P <sub>2</sub> O <sub>5</sub> ) <sub>30</sub>	$1.1 \times 10^{-5}$	0.31	$5.0 \times 10^{-7}$	0.30

and this suggests that higher conductivity of the samples with higher TiO<sub>2</sub> content is due most probably to inclusion of vanadium into the rutile structure.

The increase of the V<sub>2</sub>O<sub>5</sub> content (sample (TiO<sub>2</sub>)<sub>10</sub>(V<sub>2</sub>O<sub>5</sub>)<sub>60</sub>(P<sub>2</sub>O<sub>5</sub>)<sub>30</sub>) leads to an increase in the  $\sigma_{gr-nasicon}$  conductivity in two orders in respect to  $\sigma_{gr-rutile}$ . The conductivity values of the glassy components caused by electron hopping between V<sup>4+</sup> and V<sup>5+</sup> centers (polaron conductivity) are very alike in the both samples. The results propose that vanadium is incorporated into NASICON type crystal structure which correlates with XRD results.

### CONCLUSIONS

The conclusions drawn from the results obtained in this study can be summarized as follows:

- the investigated oxide system reveal two phase glassy-crystalline structure;
- the XRD results demonstrate that the crystalline phase in the sample with lower titanium content is mixed titan-vanadium phosphate with NASICON type crystal structure while the diffraction peaks in the sample with higher titanium concentration belong to rutile phase;
- The conductivity of the glass crystalline samples is most likely caused by polaron hopping between polyvalent vanadium ions.

**Acknowledgments:** D. Blaskova-Kochnitcharova acknowledges the financial support of project BG 051PO001-3.3.06-0038.

The first arc of the (TiO<sub>2</sub>)<sub>20</sub>(V<sub>2</sub>O<sub>5</sub>)<sub>50</sub>(P<sub>2</sub>O<sub>5</sub>)<sub>30</sub> sample is connected with ac response of the rutile phase, however the obtained conductivity is ( $\sigma_{gr-rutile} = 9.9 \times 10^{-8}$  S.cm<sup>-1</sup>) much higher compared with the pure TiO<sub>2</sub>-rutile ( $\sigma_{rutile} \leq 10^{-12}$  S.cm<sup>-1</sup>). It is well known that the electrical conductivity of undoped rutile is very dependent on sample preparation conditions like temperature, atmosphere during sintering and cooling rate. The samples become increasingly semiconducting when quenched from temperatures above ~700°C in ambient atmosphere [10]. On the other side the solid solution of rutile with vanadium exhibits also semiconducting properties [11]. The values of conductivity ( $\sigma_{gr-rutile}$ ) and activation energy of the samples under this study are close to those of the Ti<sub>0.91</sub>V<sub>0.09</sub>O<sub>2</sub>

### REFERENCES

1. P. Jozwiak, J. E. Garbarczyk, M. Wasiucione, *Mater. Sci. -Poland*, **24**, 147 (2006).
2. M-C. Ungureanu, M. Levym, J-L Souquet, *Ceram. Silik.*, **44**, 81 (2000).
3. T. K. Pietrzak, J. E. Garbarczyk, M. Wasiucione, I. Gorzkowska, J. L. Nowinski, S. Gierlotka, *Solid State Ionics*, **192**, 210 (2011).
4. H. Hirashima, K. Nishi, T. Yoshida, *J. Am. Ceram. Soc.*, **66**, 704 (1983).
5. S. Benmokhtar, A. El Jazouli, A. Aatiq, J.P. Chaminade, P. Gravereau, A. Wattiaux, L. Fournes, J.C. Grenier, *J. Solid State Chem.*, **180**, 2004 (2007).
6. P.A. Agaskar, R.K.Grasselli, D.J.Butterey and B. White, in Third World Congress on Oxidation Catalysis, by S.T. Oyama, A.M. Gaffney, J.E. Lyons, R.K. Grasselli (eds), Elsevier Science B.V, 1997, p. 219.
7. S. Titlbach, W. Hoffbauer, R. Glaum, *J. Solid State Chem.*, **196**, 565 (2012).
8. Z. Stoynov, D.Vladikova, Differential Impedance Analysis, Marin Drinov Publishing House, 2005.
9. N. Bonanos, B.C.H. Steele, E.P. Bulter, Application of Impedance Spectroscopy, in Impedance Spectroscopy, Theory, Experiment, and Applications, E. Barsoukov, J. Ross Macdonalds (eds), John Wiley & Sons, Inc., Hoboken, New Jersey, 2005, p. 205.
10. Y. Liu, A.R. West, *J. Am. Ceram. Soc.*, **96**, 218 (2013).
11. M.A. Tena, M. Llusar, J.A. Badenes, J. Calbo, G. Mondros, *J. Mater. Sci. & Mater. Electronics*, **15**, 265, (2004).

## ИЗСЛЕДВАНЕ НА TiO<sub>2</sub>-V<sub>2</sub>O<sub>5</sub>-P<sub>2</sub>O<sub>5</sub> СЪБКЛО-КРИСТАЛНИ МАТЕРИАЛИ

Д. В. Блъскова-Кошничарова<sup>1,2</sup>, Т. Петкова<sup>2\*</sup>, Л. Фачиков<sup>1</sup>, Е. Лефтерова<sup>2</sup>, И. Каназирски<sup>3</sup>,  
П. Ангелов<sup>2</sup>, С. Василев<sup>2</sup>

<sup>1</sup>*Химикотехнологичен и Металургичен Университет, бул. "Кл. Охридски" 8, 1756, София, България*

<sup>2</sup>*Институт по Електрохимия и Енергийни системи, Българска Академия на Науките, ул. „Акад. Г. Бончев”  
бл.10, 1113, София, България*

<sup>3</sup>*Минно-Геоложки Университет ул. "Св. Иван Рилски", София, 1700 България*

Постъпила на 19 март 2013 г.; Преработена на 23 април 2013 г.

(Резюме)

Синтезирани са образци от системата TiO<sub>2</sub>-V<sub>2</sub>O<sub>5</sub>-P<sub>2</sub>O<sub>5</sub> по метода на бързото охлаждане. Структурата на материалите е изследвана с рентгенова дифракция. Установено е, че образците имат стъкло-кристална структура. Импедансните изследвания са проведени при различни температури. За определяне на проводимостта, получените спектри са анализирани и апроксимирани с двуфазен модел (кристални частици, разпределени в стъклообразна матрица). Проводимостта се обяснява с поларонни прескачания между алиовалентните ванадиеви йони.

## Chemical and phase content of alloyed tin-cobalt plating deposited in direct-current or impulse modes

D. S. Lilova\*, Il. H. Gadjov, D. Dimitrov

University of Chemical Technology and Metallurgy, 1756 Sofia, Bulgaria, 8 Kl. Ohridsky bld.

Received March 22, 2013; accepted April 10, 2013

The subject of the recent study is the impact of various factors on the chemical and phase content of alloyed tin-cobalt plating that deposit out of electrolyte containing original, patented three-component additive by means of direct and pulse current. Through application of AAA and RFA it is found that depending on the combination of the three components, the Sn-Co plating that deposit are low-alloyed (up to 0.01 wt.% Co), and middle-alloyed (up to 6 wt.% Co), and high-alloyed (up to 13 wt.% Co) in the case of constant-current electrolysis. The application of pulse current of appropriate characteristics, i.e. frequency and fill factor, in the same electrolyte results in deposition of only high-alloyed alloys with twice as high content of cobalt 20 – 22 wt. %. The experimentally obtained dependencies about the impact of chemical content are duly described through derived mathematical equations. Using HRD analysis, the phase content of the deposited low-, middle- and high-alloyed Sn-Co plating is characterized as fully as possible. It is found out that the first are mechanical mixture of  $\beta$ Sn,  $\beta$ Co and  $\alpha$ Co, and the latter except  $\beta$ Sn contain chemical compounds of the type  $\text{Co}_3\text{Sn}_2$  and  $\text{CoSnO}_3$ . A high-alloyed Sn-Co alloy of typical amorphous structure is obtained for the first time in both deposition modes, i.e. stationary and non-stationary. The textures of the registered phases are identified with their typical crystal lattices.

**Key words:** tin-cobalt plating, fluoride-sulfate and fluoride-chloride electrolytes, direct and pulse current, chemical content, phase content, AAA, RFA, HRD

### INTRODUCTION

According to RoHs (Restriction of Hazardous Substances) Directive 2002/95/EU, stringent restrictions are introduced on the use of the classical tin-lead resist (70/30) in manufacture of PCBs and for industrial electronics and electrical engineering beginning 27.01.2003, as well as for use of hexavalent chromium compounds for the process of chroming. There are various options suggested for replacing this type of plating [1-3]. The use of tin-cobalt alloys [4-5] is a very resourceful solution of the problem.

The reason is that those alloys can be obtained with various contents of cobalt. According to this indicator, it is appropriate to classify the plating as low- (below 0.1 wt. %), middle- (up to 5÷6 wt. %) and high-alloyed - (above 6 wt. %) [6 – 9]. The first are applicable mainly as a metal resist in manufacture of PSBs, and the second are applicable for replacement of silver plating of the contact elements, and the third are applicable as alternative to shining chromium finishes. In recent years another strategic areas for their application are also outlined: as active anode material in manufacturing of lithium elements, as high-efficient catalyzer in relation to evolution of hydrogen, as well as in

elaboration of solar collectors [10 – 12]

The recent investigations prove the possibility to obtain low-, middle- and high-alloyed Sn-Co plating out of fluoride electrolyte containing an original additive that enables to obtain the three types of alloys solely through various combinations of the components and without alteration of the basic composition and the operation mode.

There are few references available for the structure and the phase content, and they mainly concern the plating obtained from pyrophosphate, citrate and gluconate electrolytes [13 – 15]

The impact of various factors on the chemical and phase content of Sn-Co plating deposited from fluoride electrolytes that contain an original patented additive at constant and pulse current modes is studied.

### EXPERIMENTAL CONDITIONS AND METHODS OF INVESTIGATION

The basic composition of the investigated electrolyte is:

SnSO <sub>4</sub> :	60 g/l
CoSO <sub>4</sub> · 7H <sub>2</sub> O:	80 g/l
NH <sub>4</sub> F:	70 g/l
KD – 2:	1 ml/l
Sodium hypophosphite:	5 g/l
pH = 4; room temperature; $i_k = 1.5 \text{ A/dm}^2$	

\* To whom all correspondence should be sent:  
E-mail: dani709@abv.bg

When adding KSCN of concentration 30 g/l to the electrolyte in question, there are high-alloyed plating formed in the range of cathode current densities from 1 A/dm<sup>2</sup> to 4 A/dm<sup>2</sup>.

The phase content is studied using X-Ray diffraction (XRD). All samples are X-rayed in angular range from 15 to 58 degrees. For identification of the different phases and textures, the data are compared with the JCPDS cards with extent of compliance at least three reflexes. The thickness of the plating is 12 μm.

The chemical content is determined using Atomic Absorption Analysis (AAA) and X-ray Fluorescence Analysis (RFA). The studies on the influence of various factors on the percentage of cobalt in the plating were carried out with varying each parameter while the basic values of the others remain constant, as follows: T = 25 °C; i = 1 A/dm<sup>2</sup>; pH = 4.5; C<sub>CoSO<sub>4</sub>·7H<sub>2</sub>O</sub> = 80 g/l. The content of SnSO<sub>4</sub> is constant (60 g/l), the concentration of NH<sub>4</sub>F is 70 g/l.

The weight percentage content of the two metals in the alloy is estimated from the data from AAA.

The study for the impact of different factors on the percentage content of cobalt in the plating in impulse mode are carried out applying fractional factorial experiment of the type 2<sup>n-1</sup> for four variables: X<sub>1</sub> (Θ), X<sub>2</sub> (i<sub>m</sub>), X<sub>3</sub>(T), X<sub>4</sub> (C<sub>Sn/Co</sub>). The fill factor Θ is changed through τ<sub>r</sub> at constant value τ<sub>p</sub> = 50 μsec, and the average pulse density i<sub>m</sub> Θ was changed through the amplitude density of current i<sub>p</sub>. The basic concentration of CoSO<sub>4</sub>·7H<sub>2</sub>O for obtaining both low- and high-alloyed plating was the assumed value 80 g/l. Therefore, when planning the experiment the ratio of the two metals

in the solution C<sub>Sn/Co</sub> was varied by lowering C<sub>SnSO<sub>4</sub></sub> in the electrolyte at constant value of C<sub>CoSO<sub>4</sub>·7H<sub>2</sub>O</sub> = 80 g/l.

## EXPERIMENTAL RESULTS AND DISCUSSION

### Chemical content

First of all, using AAA the impact of different factors (i<sub>k</sub>, T, C<sub>CoSO<sub>4</sub></sub>, pH) on the percentage of cobalt in the low-alloyed plating was studied.

It is seen from the experimental results presented in Fig. 1 that the percentage of cobalt at the above values of basic parameters is about 0.01%. Except pH, the increase of i<sub>k</sub>, C<sub>CoSO<sub>4</sub>·7H<sub>2</sub>O</sub> and T results in increased content of cobalt in the alloy. It is worth noting, however, that the temperature is the most influential characteristic since with increase from 25 °C to 55 °C the percentage of cobalt increases ten times. The influence of the rest two characteristics (i<sub>k</sub>, C<sub>CoSO<sub>4</sub>·7H<sub>2</sub>O</sub>) is equal and less significant, i.e. for times increase.

Despite the too low concentration of cobalt, we believe that it is included in the plating by electrochemical way. The observed dependencies can be explained considering the regularities of electrolytic alloying and the fact that the deposition potential of cobalt E<sub>i</sub> (Co) in this particular case is more negative than that of tin E<sub>i</sub> (Sn), although the opposite is valid for their corrosion potentials: E<sub>C</sub>, (Co) = - 500 mV; E<sub>C</sub>, (Sn) = - 670 mV. Based on the experimental results we can assume that the increase of temperature has stronger depolarization impact on kinetics of deposition of cobalt than on kinetics of deposition of tin.

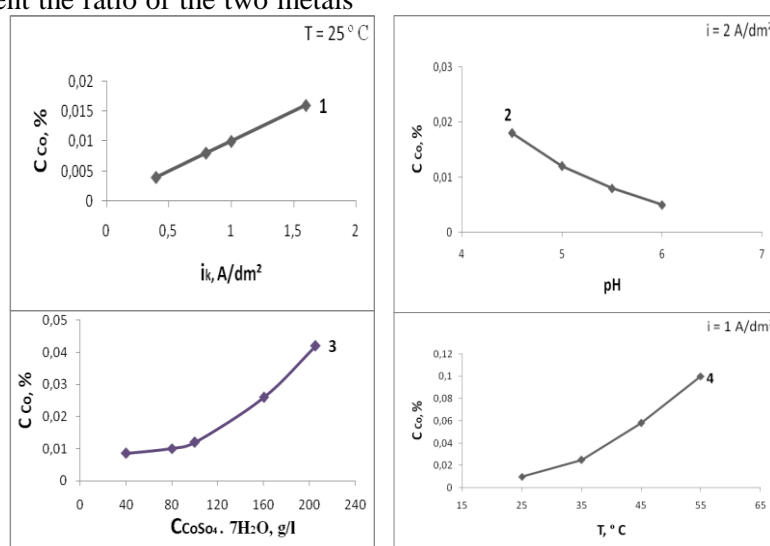
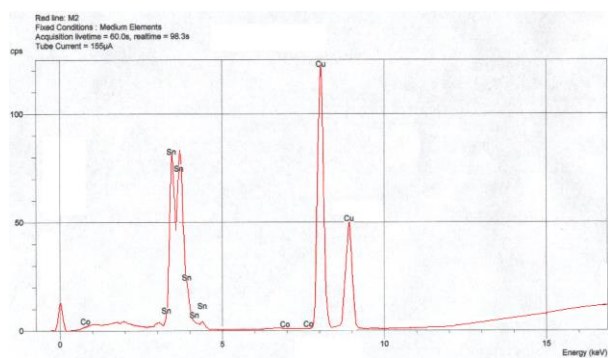


**Fig. 1.** Impact of cathode density of current (1), pH of the medium (2), concentration of CoSO<sub>4</sub>·7H<sub>2</sub>O in the electrolyte (3) and temperature (4) on the percentage of tin plating low-alloyed with cobalt in presence of KD- 2 with concentration 1ml/l.

Similar but less pronounced is the effect of increasing the concentration of cobalt, regardless of its deposition control, as in the range of current densities studied from 0.4 A/dm<sup>2</sup> to 1.6 A/dm<sup>2</sup> the needed condition for alloying is achieved, i.e.  $E_i(\text{Sn}) = E_i(\text{Co})$

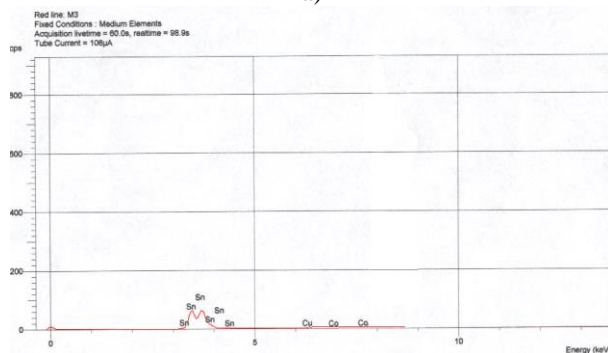
The most probable and most logical explanation of dependence 2, Fig. 1, is the variation of the constant of resistance of the complex tin compounds that is known to be largely dependant on pH, as the most stable tin compounds are formed in the range pH = 4 to 4.5.

The data from AAA were fully confirmed after applying RFA (Fig. 2).



Analyte	Concentration	Intensity
Co	54 ppm	0,8
Sn	99.99 Wt %	3655.7

a)



Analyte	Concentration	Intensity
Co	188 ppm	2.2
Sn	99.98 Wt %	2808.1

b)

**Fig. 2.** RFA of low-alloyed tin-cobalt plating deposited in presence of KD- 2 at direct (a) and pulse (b) current:  $i_k = i_m = 1 \text{ A/dm}^2$ ;  $\Theta = 0,01$ ,  $\tau_p = 50 \mu\text{s}$ ;  $\delta = 5\mu\text{m}$

When applying the impulse mode (Fig. 2b) in the same electrolyte, a significant increase of cobalt in the alloy (2 times) is achieved without changing the other conditions. Likewise in DC electrolysis, that can be explained with the kinetics of processes but necessarily taking the specifics of non-stationary electrolysis into account.

Similar studies have been performed for the high-alloyed plating too, where KSCN of basic concentration 30 g/l is added to the basic electrolyte composition with pH = 4.5 containing KD – 2. Comparison of the dependences in Fig. 3 with those of Fig. 1 shows that the regularities of the process of electrolysis alloying are also observed in obtaining high-alloyed plating: the content of metal with more negative electric deposition potential, i.e. Co, increases with the increase of cathode density of current, the temperature and the concentration of  $\text{CoSO}_4 \cdot 7\text{H}_2\text{O}$  in the electrolyte.

The main differences are in the degree of involvement of the individual factors. While the deposition of low-alloyed compounds is mostly dependent on the temperature, in the other case this parameter has the most insignificant impact, i.e. the content of Co increases from 12 % to 15 % while T varies from 25 °C to 50 °C. As seen in 1, the linear dependence is maintained until cathode density 2 A/dm<sup>2</sup>. An important advantage is the fact that in the intensive mode  $i_k = 2\div3 \text{ A/dm}^2$  recommended for using in practice, the percentage of cobalt remains constant, which is a prerequisite for formation of alloy plating on profile cathodes that are uniform in composition and properties.

Until 1 A/dm<sup>2</sup> middle-alloyed Sn-Co plating are obtained with Co content up to 60 %.

In Table 1 the levels and the ranges of variation of the individual factors in impulse deposition of Sn-Co plating are presented.

**Table 1.** Plan of the experiment for studying the impact of various factors on the percentage of cobalt in Sn-Co plating at pulse mode.

	X <sub>1</sub>	X <sub>2</sub>	X <sub>3</sub>	X <sub>4</sub>			
	( $\Theta$ )	$i_m, \text{ A/dm}^2$	T, °C	$C_{\text{Sn}}/C_{\text{Co}}$ g/l			
-1	0.01	-1	0.5	-1	25	-1	0.5
+1	0.02	-1	0.5	-1	25	+1	2
-1	0.01	+1	3	-1	25	+1	2
+1	0.02	+1	3	-1	25	-1	0.5
-1	0.01	-1	0.5	+1	60	+1	2
+1	0.02	-1	0,5	+1	60	-1	0.5
-1	0.01	+1	3	+1	60	-1	0.5
+1	0.02	+1	3	+1	60	+1	2

After processing the results, the following regression equation was obtained:

$$Y = 17.5 + 0.53 \cdot X_1 + 0.73 \cdot X_2 + 0.15 \cdot X_3 - 0.89 \cdot X_4 \quad (1)$$

Using equation (1), graphical dependencies (Fig. 4) were built representing the impact of each of the four factors on the percentage of Co in the plating, while the rest factors were assumed constant at basic levels  $\Theta = 0,01$ ;  $i_m = 2 \text{ A/dm}^2$ ; T = 30 °C;  $C_{\text{Sn}}/C_{\text{Co}} = 2$ .

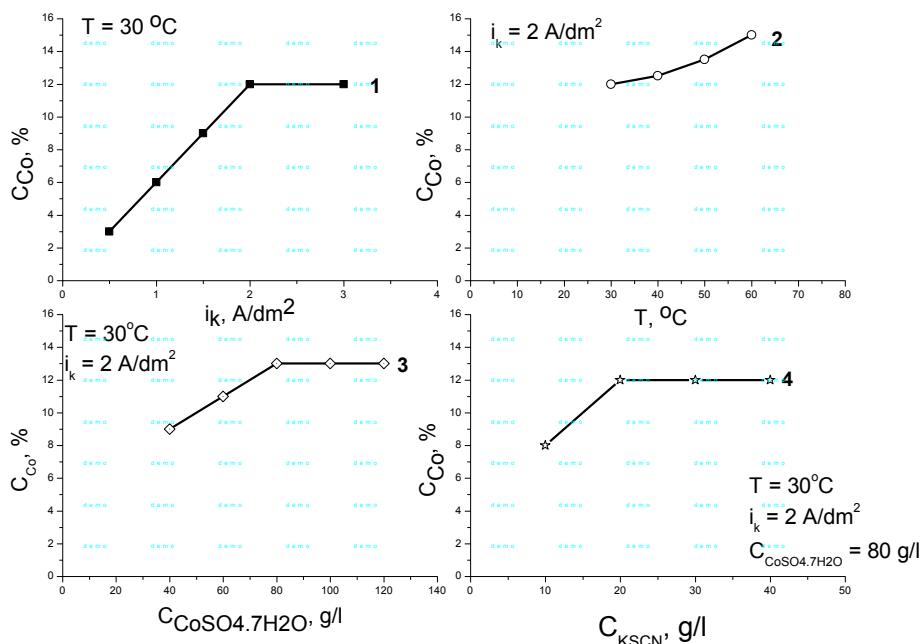


**Fig. 3.** Impact of cathode density of current (1), temperature (2), concentration of  $CoSO_4 \cdot 7H_2O$  in the electrolyte (3) and concentration of KSCN (4) on the percentage of cobalt in high-alloyed Sn-Co plating.

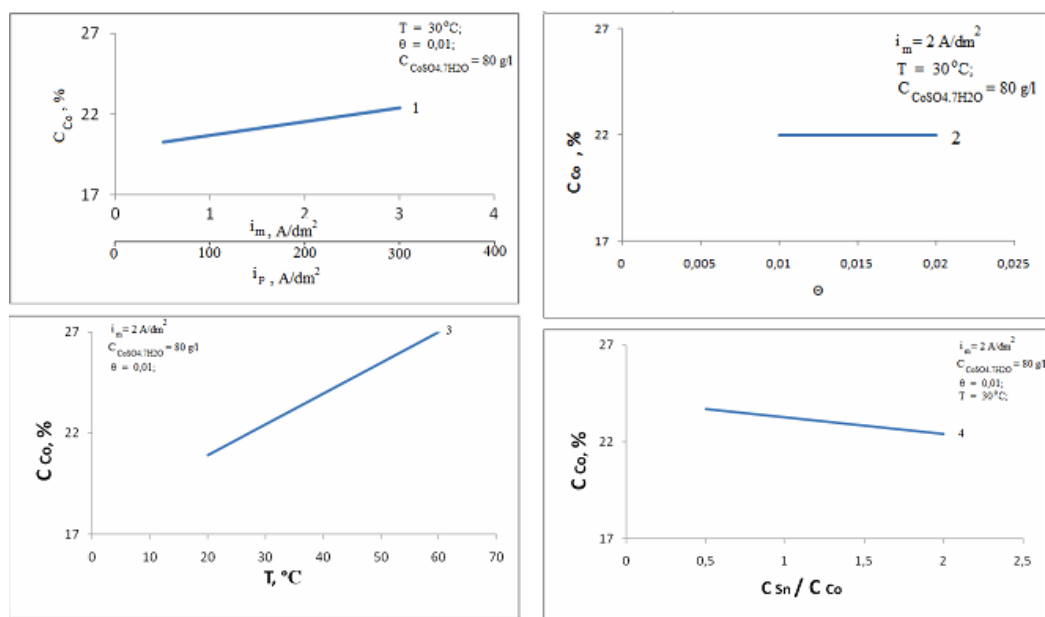


**Fig. 4.** Impact of average current density during pulse deposition (1), fill factor (2), temperature (3), and ratio between  $C_{Sn}/C_{Co}$  in the electrolyte (4) upon the percentage of cobalt in high-alloyed Sn-Co plating at pulse mode of electrolysis.

It turned out that the change of  $\theta$  through variation of  $\tau z$  practically has no effect. For both modes of deposition the change of  $Y$  depending on  $C_{Sn}/C_{Co}$  is negligibly small (Fig. 36, dependence 3 and Fig. 37, dependence. 4), regardless of the fact that the ratio  $C_{Sn}/C_{Co}$  is varied in two ways: either through decrease of concentration of  $SnSO_4$  (in impulse mode), or through increase that of  $CoSO_4 \cdot 7H_2O$  (in direct current mode).

The main differences are associated with the density of current. While in DC deposition its

variation in the range from 0.5 A/dm<sup>2</sup> to 2 A/dm<sup>2</sup> results in threefold increase of  $Y$  (from 4 to 12 %), in pulse mode this parameter's effect is less significant, i.e. 1.07 times (from 20.3 to 21.7 %).

The impact of temperature in the range from 30 °C to 60 °C is commensurate in both modes:  $Y$  increases 1.2 times from 12 % to 15 % at direct current, and from 22.4 % to 27 % at pulse current.

The application of pulse current results in almost double increase of the concentration of cobalt in the plating that changes insignificantly at normal

temperature from 20.53 % to 22.4 % at  $i_m = 0,5 \div 3$  A/dm<sup>2</sup>.

The results from RFA of high-alloyed plating deposited at two different densities of pulse current are presented in Fig. 5. It is seen that the concentration of Co determined mathematically completely coincides with the one read from dependencies a and b, Fig. 4, which confirms the adequacy of the derived mathematic equation /1/ again. The observed effect indirectly suggests the conclusion that the kinetics of processes is radically changed in the case of pulse deposition. It can be also assumed that the polarization phenomena would also affect the kinetics of other parallel processes, e.g. release of hydrogen, which in turn leads to a change of pH in the cathode area.

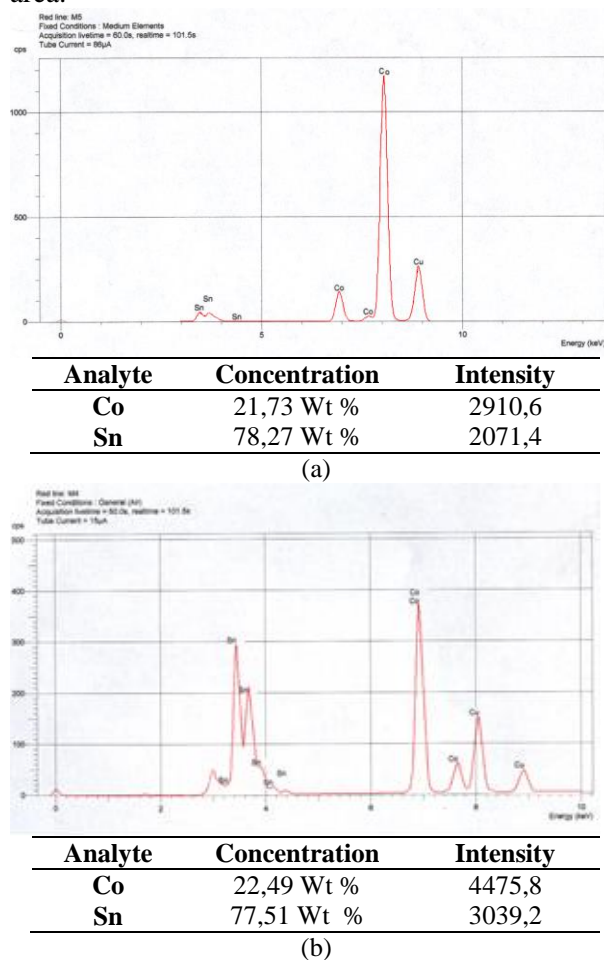


**Fig. 5.** RFA of high-alloyed Sn-Co plating obtained applying pulse current of parameters  $i_m = 2$  A/dm<sup>2</sup>, (a); and  $i_m = 3$  A/dm<sup>2</sup>, (b).

#### Phase content

The X-Ray image of low-alloyed Sn-Co alloy deposited at DC density 1 A/dm<sup>2</sup> is presented in Fig. 6.

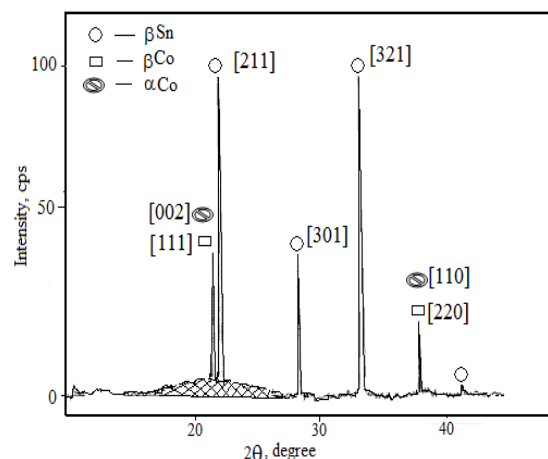


**Fig. 6.** X-ray analysis of low-alloyed Sn-Co plating deposited in presence of KD-2;  $i = 1$  A/dm<sup>2</sup>

The clearly formed five diffraction peaks give grounds to characterize the plating as such of marked crystal structure although the insignificant increase of background in the range from 20.5 to 26 degrees suggests certain amorphousness too. The three most intensive reflections  $\Theta = 22.5$ , 27.5, and 32.45 correspond to distances between surfaces equal to 2.01, 1.66 and 1.44 accordingly. These distances are typical for the  $\beta$ - crystallographic modification of tin with its typical tetragonal lattice. There is a pronounced texture effect observed along [211] and [321], and a less significant one along [301].

At  $\Theta = 37.7$  and 22.15 degree, another two reflection peaks are registered that correspond to the presence of both phases, as the  $\beta$ -phase being predominant with its characteristic cubic crystal lattice. Its orientation is along [111] and [220], while the  $\alpha$ -modification (hexagonal crystal lattice) is orientated along [002] and [110].

Analogical studies were also carried out for middle- and high-alloyed plating deposited in the presence of KD-2 and potassium rodanide composition.

The first essential difference compared to electro-deposition of low-alloyed alloys is that there the variation of direct current density strongly affects the crystal structure and the phase content. While up to  $i = 1$  A/dm<sup>2</sup> where middle-alloyed plating are formed, the alloy has a marked crystal structure, especially that at  $i = 1$  A/dm<sup>2</sup> (Fig. 7, positions a and b), than the alloy is typically amorphous in a wide range of current densities from 2 A/dm<sup>2</sup> to 4 A/dm<sup>2</sup> (position c).

Existence of the following three phases is established:  $\beta$ Sn (above 80%) and the chemical compounds  $\text{Co}_3\text{Sn}_2$  and  $\text{CoSnO}_3$ . The orientations of  $\beta$ Sn at  $i = 1$  A/dm<sup>2</sup> are along [101] and [211], but

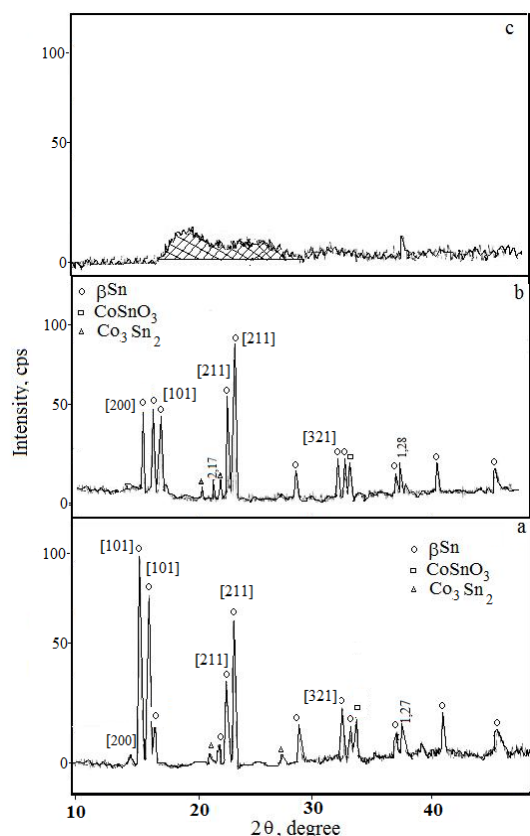


**Fig. 7.** X-ray analysis of middle- (a, b) and high-alloyed (c) with cobalt tin plating at various densities of direct current: a - 0,5; b - 1; c - 2, 3, 4 A/dm<sup>2</sup>.

at  $i = 0,5 \text{ A/dm}^2$  a clear diffraction reflection is registered along [200] too. The impact of the parameters of pulse current on the phase content of high-alloyed plating was studied in more details.

It is clearly seen from the X-ray images presented in Fig. 8 that at a constant average pulse density  $i_m = 0,5 \text{ A/dm}^2$ , the change of fill factor  $\Theta$  (through variation of  $\tau_z$ ) does not affect the type of diffractograms and they are completely identical. The alloy plating have the same crystal structure as in deposition with direct current although a certain amorphousness is observed, most probably due to amorphous tin. In the pulse mode mainly three phases are registered:  $\beta \text{ Sn}$ ,  $\text{Co}_3\text{Sn}_2$  and  $\text{CoSnO}_3$  that are analogical to those in direct current deposition. In our understanding, the similarity in the phase contents of the two modes observed can be explained with the high frequencies selected initially (from 0.40 kHz up to 6.67 kHz) that correspond to those during examination of the chemical content. As was found during studying the impact of various factors upon the chemical content of the Sn-Co plating in pulse mode, the variation of  $\Theta$  through  $\tau_z$  does not affect the percentage of tin, but it increases significantly from 12÷14 % to nearly 22÷23 % compared to the direct current deposition.

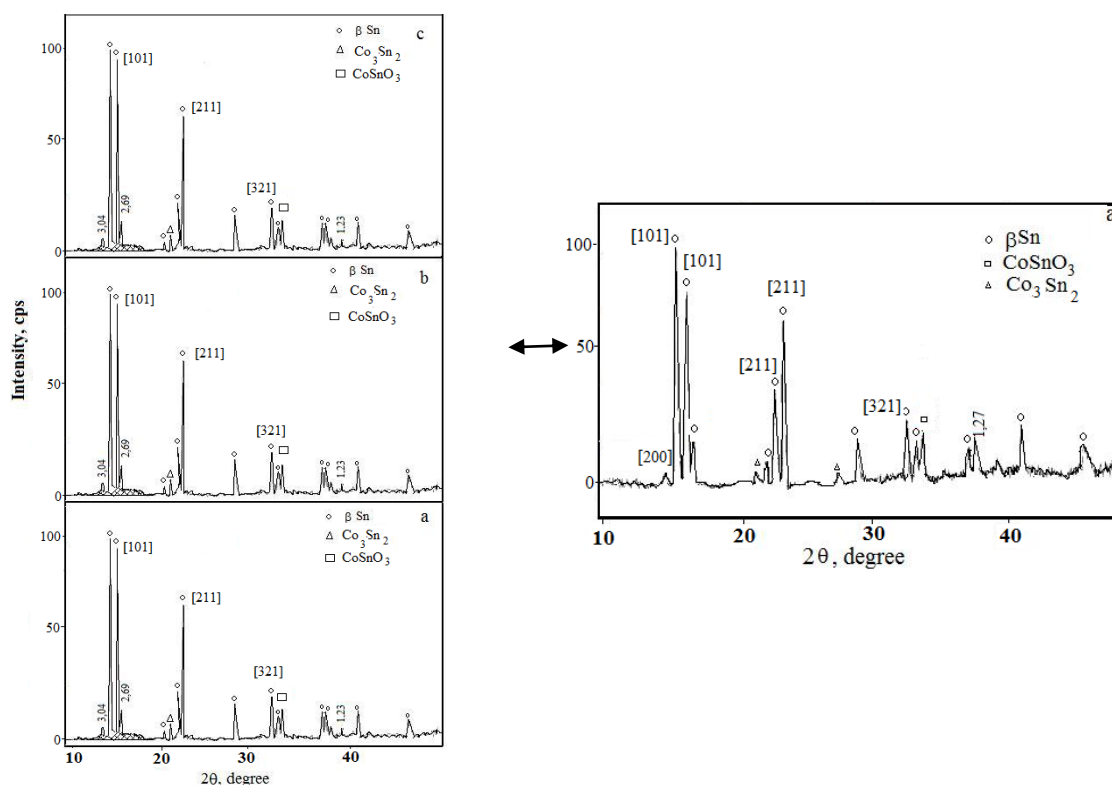


**Fig. 8.** X-ray analysis of high alloyed tin-cobalt plating obtained at pulse current of various fill factors  $\Theta$ : a -  $\Theta = 0,5$ ; b -  $\Theta = 0,25$ ; c -  $\Theta = 0,01$ ;  $\tau_p = 50 \text{ μsec}$ ;  $i_m = 0,5 \text{ A/dm}^2$ ; d - middle-alloyed Sn-Co plating obtained at direct current of density  $i = 0,5 \text{ A/dm}^2$ .

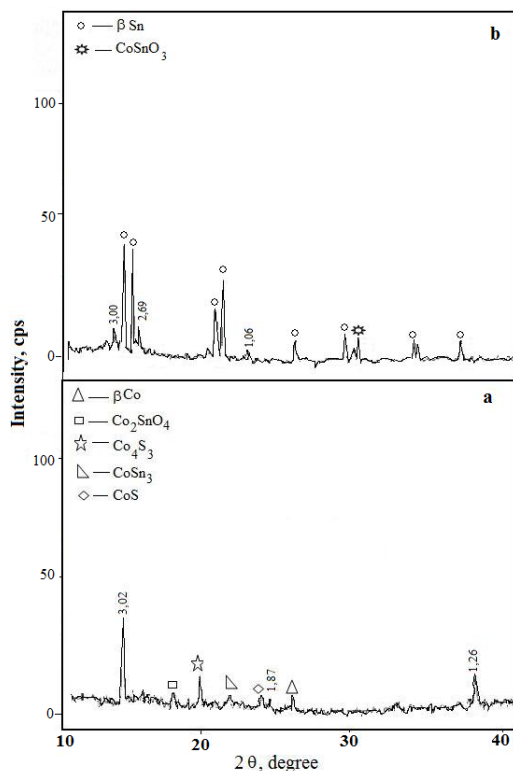


**Fig. 9.** X-ray analysis of high alloyed tin-cobalt plating obtained at pulse current of different fill factors  $\Theta$ : **a** -  $\Theta = 0,01$ ; **b** -  $\Theta = 0,5$ ;  $\tau_p = 500 \mu\text{sec}$ ;  $i_m = 0,5 \text{ A/dm}^2$ .

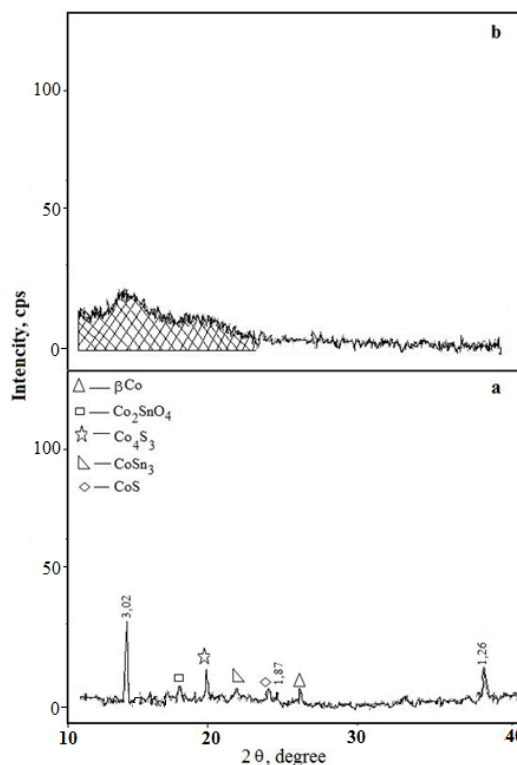


**Fig. 10.** X-ray analysis of high-alloyed tin-cobalt plating obtained at pulse current of different densities: **a** -  $i_m = 0,5 \text{ A/dm}^2$ ; **b** -  $i_m = 0,8 \text{ A/dm}^2$ ;  $\tau_p = 500 \mu\text{sec}$ ;  $\Theta = 0,01$ .

Therefore, the chemical content is not a determinant for the phase content in the electrochemical system studied.

At analogical fill factors  $\Theta$ , however realized at ten time lower frequencies (from 40 Hz to 670 Hz), the diffractograms change significantly (Fig. 9), which means that the impact of  $\Theta$  is substantial in this case.

The comparison between the diffractograms indicates that at lower frequencies and equal fill factors, the plating have less pronounced crystal structure (having about 3 times higher density), as the phase content is also changed. Except the three abovementioned phases, in this case the alloy contains another compounds between the two metals, i.e.  $\text{CoSn}_3$  and  $\text{Co}_2\text{SnO}_4$ , as reflexes corresponding to cobalt sulfides  $\text{CoS}$  and  $\text{Co}_4\text{S}_3$  are also registered. We found out that at frequency 40 Hz and low fill factor  $\Theta = 0,01$ , after insignificant increase of  $i_m$  through  $i_p$  (from 0.5 to 0.8  $\text{A/dm}^2$ ), the alloyed plating obtained have typical amorphous structure (Fig. 10), while at direct current this effect is achieved at density about 2 times higher.

## CONCLUSION

The impact of various factors on the chemical and phase contents of alloyed tin-cobalt plating deposited from fluoride electrolytes containing an original patented three-component addition in direct-current and pulse modes is studied. It is proved that in presence of KD - 2 only, the content of cobalt in the low-alloyed plating is about 0.01% at normal temperature and density of direct current  $i = 1 \text{ A/dm}^2$ , and in the case of pulse deposition it increases two times at appropriate parameters of the pulse current. Through adding KCNS with concentration 20÷30 g/l, low- (up to 6 %) and high-alloyed (up to 13 %) tin-cobalt plating are obtained only through variation of cathode density of direct current. The application of pulse current of appropriate frequency and fill factor ( $\nu = 200 \text{ Hz}$ ,  $\Theta = 0,01$ ) allows deposition of only high-alloyed plating with twice higher content of cobalt (from 20 to 22 %), in a wide range of densities of current from 0.5  $\text{A/dm}^2$  to 3  $\text{A/dm}^2$ .

The phase content of the deposited low-, middle- and high alloyed tin-cobalt plating obtained from fluoride electrolytes is characterized as fully as possible. It is indicated that the first are mechanical composition of  $\beta\text{Sn}$ ,  $\beta\text{Co}$ ,  $\alpha\text{Co}$ , as their

contents decrease in the same order; and the second, except  $\beta\text{Sn}$ , also contain compounds of the type  $\text{Co}_3\text{Sn}_2$  and  $\text{CoSnO}_3$ . The high-alloyed tin-cobalt plating obtained has typical amorphous structure, while the low- and middle alloyed ones have marked crystal structure. The texture of the phases registered with their typical crystal lattices is identified.

#### REFERENCES

1. E.W. Brooman, *Metal Finish*, **102**, 75 (2004).
2. „Alternative fur die dekorative sechswertige Verchromung“, *Galvanotechnik*, **100**, 2781 (2009).
3. Lauper Bernard, *Galvano-organo-trait. Surface*, **69**, 675 (2001).
4. Wei Zidong, Dong Haiwen, *Diandu yu jingshi (Plat. and Finish.)*, **18**, 26(1996).
5. B.P. Penchev, Inventor's certificate 50907A from 15.12.92
6. Tyutin K., L. Lukyanov G. Selivanov, V. Koloncov, R. Voronov, Inventor's certificate 922186, , 1980.
7. Bobrovskiy L., V. Kreizberg, N. Kukushkina, G. bereznikov, M. Slepcev, Y. Cofin, A. Petrov, Inventor's certificate 954528, 1982.
8. E.G. Vinokurov, A. Kvartalnyi, V.V. Bondar, Patent 2377344 Russia, 2009.
9. St. Vitkova, V. Ivanova, GALVANO 91: Proc. Int. Symp. "GALVANO 91", Varna, 30 Sept. - 2 Oct., 1991. Sofia. 1992, c. 164-170.
10. Li Jun-Tao, Chen Shu-Ru, Ke Fu-Sheng, Wei Guo-Zhen, Huang Ling, Sun Shi-Gang, *J. Electroanal. Chem.*, **649**, 171 (2010).
11. Xiao-Yong Fan, Fu-Sheng Ke, Guo-Zhen Wei, Ling Huang, Shi-Gang Sun, *J. Alloys Compnds*, **476**, 70 (2009).
12. Huang Tao, Yao Yu, Wei Zhen, Liu Zheng, Yu Aishui, *Electrochim. Acta*, **56**, 476 (2010).
13. I. Vina, V. Rubene, V. Belmane, A. Krumina, *Latv. kim. zh.*, **3**, 227 (2007).
14. E. Gomez, E. Guaus, I. Torrent, X. Alcobe, E. Valles, *J. Appl. Electrochem.*, **31**, 349 (2001).
15. A. Survila, Z. Mockus, S. Kanapeckaitė, Joint International Meeting: The 200th Meeting of the Electrochemical Society and the 52 Meeting of the International Society of Electrochemistry, San Francisco, Calif., 2-7 Sept, 2001, *Electrochem. Soc.*, 2001, p. 683.

## ХИМИЧЕН И ФАЗОВ СЪСТАВ НА СПЛАВНИ КАЛАЙ-КОБАЛТОВИ ПОКРИТИЯ ОТЛОЖЕНИ ПРИ ПОСТОЯННОТОКОВ И ИМПУЛСЕН РЕЖИМ

Д. С. Лилова, Ил. Х. Гаджов, Д. Димитров

*Химикотехнологичен и Металургичен Университет – София, България, бул. Кл. Охридски 8*

Получена на 22 март, 2013; приета на 10 април, 2013

(Резюме)

Изследвано е влиянието на различни фактори върху химичния и фазов състав на сплавни калай-кобалтови покрития, отлагани с постоянен и импулсен ток от флуориден електролит, съдържащ оригинална, патентно защитена трикомпонентна добавка. Чрез прилагане на ААА и РФА е установено, че в зависимост от комбинацията на трите компонента на добавката при постоянно-токова електролиза могат да се отлагат, както нисколегирани (до 0,01 т. % Co), така и средно (до 6 т. % Co) и високолегирани (до 13 т. % Co) Sn-Co покрития. Прилагането на импулсен ток с подходящи параметри (честота и коефициент на запълване) в същия електролит води до отлагането само на високолегирани сплави с двойно по-високо съдържание на кобалт 20 – 22 т. %. Експериментално получените зависимости за влиянието на различни фактори върху химични състав са адекватно описани, с изведени математични уравнения. Чрез HRD анализ възможно най-пълно е охарактеризиран фазовия състав на отлаганите ниско, средно и високолегирани калай-кобалтови покрития. Намерено е, че първите представляват механична смес от  $\beta\text{Sn}$ ,  $\beta\text{Co}$ ,  $\alpha\text{Co}$ , а вторите, освен  $\beta\text{Sn}$  съдържат и химични съединения от вида –  $\text{Co}_3\text{Sn}_2$  и  $\text{CoSnO}_3$ . За пръв път е получена високолегирана калай-кобалтова сплав с типична аморфна структура и при двата режима на отлагане – стационарен и нестационарен. Идентифицирана е текстурата на регистрираните фази с характерните за тях кристални решетки.

## Electrochemical characteristics and structural specifics of carbonaceous electrodes, modified with micro- and nanodeposits of platinum metals

T. M. Dodevska<sup>1</sup>, E. G. Horozova<sup>2\*</sup>, N. D. Dimcheva<sup>2</sup>

<sup>1</sup> *University of Food Technologies, Department of Inorganic Chemistry and Physical Chemistry, 26 Maritsa Blvd., Plovdiv 4002, Bulgaria*

<sup>2</sup> *P. Hilendarski University of Plovdiv, Department of Physical Chemistry 24 Tsar Asen St., Plovdiv 4000, Bulgaria*

Received March 22, 2013; revised May 13, 2013

For a series of graphite and glassy carbon electrodes, modified with micro- and nanodeposits of (Pd+Pt) and (Pd+Au) mixtures in varied proportions of the catalytically active components, surface topography of the modified electrodes has been studied with atomic force microscopy (AFM). It has been established that, catalytic activity of the modified electrodes in the reduction of H<sub>2</sub>O<sub>2</sub> depends on the specific nature and structure of the metal phase, electrochemically deposited on the carbonaceous carrier. Moreover, the specifics of the structure, morphology of the metal deposits as well as their surface coverage has been shown to dramatically depend on the type of catalytically active components (nature and ratio of the two metals in the modifying mixture) and the nature of the carbonaceous matrix (type, porosity and surface condition).

**Key words:** modified electrodes, nanoparticles, electrocatalysis, electroreduction of hydrogen peroxide, AFM studies

### INTRODUCTION

The reaction of electroreduction of hydrogen peroxide is of current significance to modern electrochemical science and technology [1-5]. The rate and selectivity of this reaction to a great extent determine the working basic characteristics of a series of amperometric biosensors of the first generation, applied in the selective quantitative analysis of various analytes in medicine, food industry, ecology and other spheres.

The rate of the reaction electroreduction of hydrogen peroxide, as well as its selectivity, depends on the used electrocatalysts, the best of which are platinum metals. Due to their high price, limited availability and insufficient specific activity, the modern trends in developing electrocatalysts are connected with reducing their use to the minimum and, at the same time, achieving a significant catalytic effect. In connection with this, these studies are aimed at developing electrocatalysts on the basis of micro- and nanosized multi-component systems (binary and trimetal catalytic phases) [6-21].

Fundamental and applied research in the field of

platinum electrocatalysts shows that their catalytic activity depends on their nature, on the nature of their surface layer, on their structure and specific surface. All these factors can be utilized by optimizing the conditions and methods for obtaining them. By choosing a suitable type of carrier, composition and proportion of the components in the modifying mixture and the method of obtaining, new electrocatalysts with an enhanced catalytic activity and stability can be obtained. Such a research method aimed at obtaining new, inexpensive modified carbon electrodes for selective reduction of hydrogen peroxide was applied by us. Based on the advantages of carbon materials (chemical inertness, wide working range of potentials, low cost, etc.), our research in recent years has shown that porous graphite (porosity of 20 – 25%) and glassy carbon, electrochemically modified with nano- and microquantities of mixtures in different proportions of (Pd + Pt) and (Pd + Au), are effective electrocatalysts for the reduction of H<sub>2</sub>O<sub>2</sub> at low working potentials – 0 and -50 mV (vs. Ag/AgCl) [14-21]. The modification of the carbonaceous materials in the above-mentioned studies was conducted while modeling the conditions for obtaining – deposit time of the catalytically active

---

\* To whom all correspondence should be sent:  
E-mail: horozova@uni-plovdiv.bg

phase 10 s and deposit potential of -50 mV (in relation to a reversible hydrogen electrode). An inexpensive method, not requiring costly equipment, was used to obtain nanosized metal coating, namely electrodeposition. In all these publications the prospective application of the developed peroxide electrodes as a basis for creating first-generation amperometric biosensors has been demonstrated, as well. The carbon materials, thus modified, show the following positive characteristics: presence of high electrocatalytic activity in the reduction of H<sub>2</sub>O<sub>2</sub> in a wide range of potentials – from 250 to -250 mV (vs. Ag/AgCl); simplified procedure of obtaining; high working stability in a wide pH range; sufficient electrocatalytic activity for a long period of time – for over a year, etc.

It is evident from the stated above that the main way of influencing the electrocatalytic activity of the electrodes is the choice of suitable conditions, procedure and method of obtaining. The improvement of the methods of obtaining electrocatalysts with the specified properties and the understanding of the nature of their catalytic activity require not only electrochemical tests but also investigation of the structure of their surface layer.

With reference to this, the aim of this study, which is a follow-up of our previous studies referred to above [14-21], is to investigate the surface morphology of the modified carbon electrodes and to compare the structural data with the results from their electrocatalytic activity in the target reaction – the reduction of H<sub>2</sub>O<sub>2</sub>. On this basis, the main factors ensuring the increase of the electrochemical activity and stability of the obtained modified carbonaceous electrodes are to be identified.

## EXPERIMENTAL

### *Materials*

Two types of inert carbon matrices were used as carriers:

1. Graphite of the GMZ type with  $S_{\text{geom}} = 1.7 \text{ cm}^2$  and with the following structural characteristics: specific surface of  $0.8 \text{ cm}^2 \cdot \text{g}^{-1}$ ; density of  $1.6 - 1.7 \text{ g} \cdot \text{cm}^{-3}$ ; porosity of 20 – 25 %.
2. Glassy carbon with  $S_{\text{geom}} = 1.35 \text{ cm}^2$ .

### *Modification of the electrode surface*

The electrochemical modification of the carbon matrixes with nano- and microquantities of mixtures of (Pd + Pt) and (Pd + Au) was performed as follows: the catalytically active components are

deposited in a potentiostatic mode  $E_r = 0.05 \text{ V}$  (in relation to a reversible hydrogen electrode) via a brief electrolysis (10 s) from the following electrolytes: mixture (Pd + Pt) of 2% PdCl<sub>2</sub> + 2% H<sub>2</sub>PtCl<sub>6</sub> + 0.1 M HCl (in the following proportions Pd:Pt 50:50; Pd:Pt 70:30; Pd:Pt 90:10, volumetric parts); mixture (Pd + Au) of 2% PdCl<sub>2</sub> + 2% HAuCl<sub>4</sub> + 0.1 M HCl (in the following proportions Pd:Au 50:50; Pd:Au 70:30; Pd:Au 90:10, volumetric parts).

### *Apparatuses and determining polarization dependencies*

A standard three-electrode glass cell with separate electrode spaces and a working volume of 11 – 15 cm<sup>3</sup>, reference electrode – Ag/AgCl (1M KCl) and a counter electrode – a platinum wire, was used for the electrochemical tests. The electrode sensitivity was determined as the relation of the stationary current ( $I_s$ ) to the substrate concentration (C).

For the purpose, the concentration polarization dependencies of the stationary current are established: the working electrode – modified graphite or glassy carbon is placed in the working space of the electrochemical cell containing 11 cm<sup>3</sup> 0.1M phosphate-citrate buffer with a pH = 7.0 at 25°C. It is connected to the electrochemical system comprising the following apparatus modules: bipotentiostat Bi-PAD (TACUSSEL, France), generator EG 20 (Elpan, Lubawa, Poland) and a recording device of the XY type (VEB, Messapparatewerk; Scholtheim, Germany).

The methods of determining the concentration polarization dependencies of the stationary current is described in studies [14-21].

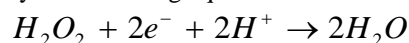
### *Surface structure of the modified electrodes*

Detailed information about the topography of the modified electrode surface was obtained by applying the method of atomic-force microscopy (AFM). The surface structure of the modified carbonaceous electrodes was investigated using an atomic-force microscope AFM (Anfatec Instruments, Germany).

## RESULTS AND DISCUSSION

### *Electrochemical characteristics of the modified carbonaceous electrodes in the reaction of electroreduction of H<sub>2</sub>O<sub>2</sub>*

The electrochemical reduction of hydrogen peroxide on the modified carbonaceous electrodes proceeds by the following equation:



The dependence of the current of electroreduction from the concentration of  $\text{H}_2\text{O}_2$  is linear, allowing its quantitative determination. The ratio of the current to the concentration of  $\text{H}_2\text{O}_2$ , which is determined from the linear portion of the concentration polarization curve, gives the sensitivity of the electrode.

The ratio between the components (in volumetric and molar %) of the electrolyte mixtures of (Pd + Pt) and of (Pd + Au), used for modifying the matrixes of graphite and glassy carbon is shown in Table 1. This table also presents the electrochemical characteristics (electrode sensitivity and linearity of the signal) of the investigated electrodes in the reaction of hydrogen peroxide electroreduction.

The investigated catalytic systems (Table 1) are based on the element Pd. Pd is relatively inexpensive (approximately 2.5 times cheaper than Pt) and therefore it is a very promising electrocatalyst. The graphite and glassy carbon modified with nano- and microquantities of pure Pd are characterized by the following electrochemical properties in the electroreduction of  $\text{H}_2\text{O}_2$ : for Pd/C – electrode sensitivity of  $0.56 \mu\text{A} \cdot \mu\text{M}^{-1}$  and linearity of the signal of up to  $500 \mu\text{M}$ , and for Pd/GC –  $0.26 \mu\text{A} \cdot \mu\text{M}^{-1}$  sensitivity and up to  $500 \mu\text{M}$  linearity of the signal [21].

The increase of the electrocatalytic activity of Pd was achieved by introducing microquantities of Pt and of Au in the modifying mixture (Table 1). The microadditions of 13 molar % of Pt and 18 molar % of Au to the main element in the mixture (Pd) result in a 1.5 increase of the electrode sensitivity of graphite modified with a mixture of (Pd + Pt) (electrode №2) and with a mixture of (Pd + Au) (electrode №5). The addition of 25 molar % of Pt to Pd doubles the electrode sensitivity of the graphite modified with a mixture of (Pd + Pt) (electrode №3). The glassy carbon matrix modified by 6 and 34 molar % of microquantities of Au to Pd exhibits electrocatalytic activity which is approximately 1.4 times as high as that of electrode Pd/GC. In the three investigated series of modified graphite, the microadditions of Pt and Au to Pd in all molar percentages shown in Table 1 result in an improvement of the linear range of concentration dependence of the signal, as compared with electrodes Pd/C and Pd/GC.

The data provided in Table 1 shows that modified glassy carbon electrodes (series III) exhibit a lower electrode sensitivity in the quantitative determination of  $\text{H}_2\text{O}_2$  as compared to modified graphite. This fact is probably due to the structural peculiarities of glassy carbon, which is

known to be characterized by an exceptionally uniform, homogeneous, almost flawless outer surface. The reasons for the lower activity of this series of catalysts can be summed up as follows: 1/ substantial reduction of  $S_{\text{real}}$  of modified glassy carbon during the specific processes of recrystallization, occurring after the deposition of the metal phase; 2/ mechanical loss of part of the deposition; 3/ resistance of the glassy carbon material.

In conclusion, the modified graphite electrode of the type Pd:Au (82 molar % : 18 molar %) exhibits the best electrochemical characteristics among all the investigated electrodes – it has the highest sensitivity ( $0.86 \mu\text{A} \cdot \mu\text{M}^{-1}$ ) and the longest linearity range of the calibration graph (up to  $1270 \mu\text{M}$ ).

#### *AFM (atomic-force microscopy) of the surface of modified carbonaceous electrodes*

The surface structure of modified carbonaceous electrodes was examined by applying the method of AFM. Fig. 1 shows AFM-images of the surface of graphite modified with mixtures of (Pd + Pt). It can be seen that there is a substantial difference in the relief of the electrode surface depending on the content of the microaddition of Pt to Pd in the modifying mixture. When a metal phase (Pd + Pt), in which the Pt content is at least 4 molar per cent, is deposited on the graphite, an electrode (№1) with the lowest sensitivity ( $0.22 \mu\text{A} \cdot \mu\text{M}^{-1}$ ) is obtained. The AFM – image of the surface of this catalyst (Fig. 1a) clearly shows different in size dendrites (60 – 400 nm), densely populated with unclearly shaped fine-grained formations.

When the Pt content in the modifying mixture is increased to 13 molar per cent, the metal phase of (Pd + Pt) is deposited on the graphite (electrode №2) mainly in the form of metal islands (Fig. 1b). Fine, parallel plates, forming compact plateau-like, sharp-edged structures, can clearly be seen in the said image. In the periphery of these plateaus, there are fine formations, under 50 nm in size. This type of metal deposition exhibits the highest electrode sensitivity –  $0.82 \mu\text{A} \cdot \mu\text{M}^{-1}$  of all the electrodes in series I. When a metal phase (Pd + Pt) with an even higher Pt content – 25 molar per cent, is deposited, the surface of the electrocatalyst (electrode №3) is densely strewn with a multitude of different in size oval formations (20 – 120 nm). The metal deposition with this structure also shows a relatively high electrode sensitivity in the electroreduction of  $\text{H}_2\text{O}_2$  –  $0.62 \mu\text{A} \cdot \mu\text{M}^{-1}$ .

**Table 1.** Composition of the electrochemical bath (in volume and molar %), electrode sensitivity ( $I_s/C$ ) and linearity range of the electrocatalytic electrodes response at the reduction of  $H_2O_2$ ; temperature 25 °C; 0.1M phosphate-citrate buffer pH = 7.0; E = - 0.05 V(vs.Ag/AgCl, 1M KCl).

Electrode №	Type of matrix	Bath composition			Electrode sensitivity $\mu A \cdot \mu M^{-1}$ at E=-0.05V	Linearity range, $\mu M$
		modifying components	volume %	molar %		
1	graphite	Pd:Pt (series I)	90:10	96:4	0.22	up to 400
2			70:30	87:13	0.82	up to 600
3			50:50	75:25	0.62	up to 500
4	graphite	Pd:Au (series II)	90:10	94:6	0.30	up to 750
5			70:30	82:18	0.86	up to 1270
6			50:50	66:34	0.34	up to 840
7	glassy carbon	Pd:Au (series III)	90:10	94:6	0.35	up to 980
8			70:30	82:18	0.19	up to 1020
9			50:50	66:34	0.36	up to 760

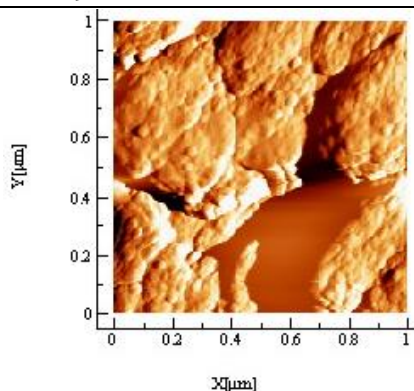


Fig. 1a

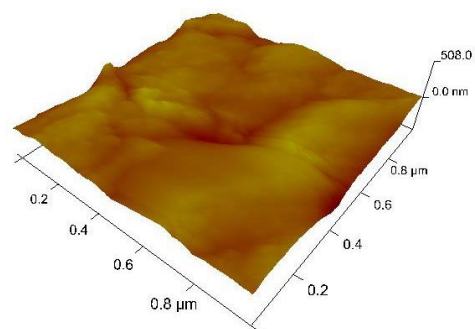


Fig. 1a, 3D

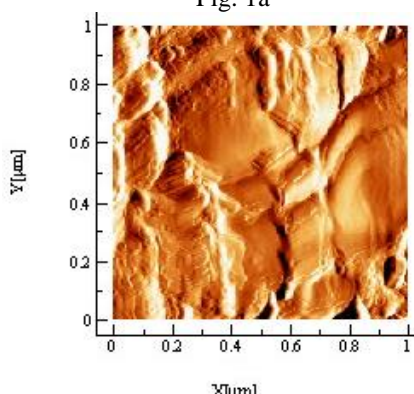


Fig. 1b

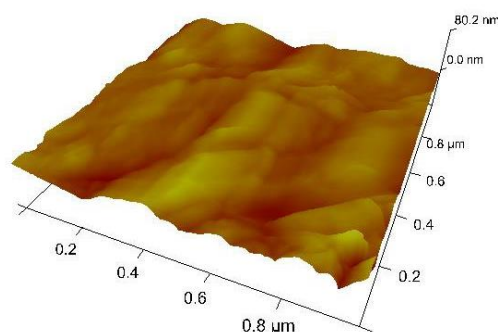


Fig. 1b, 3D

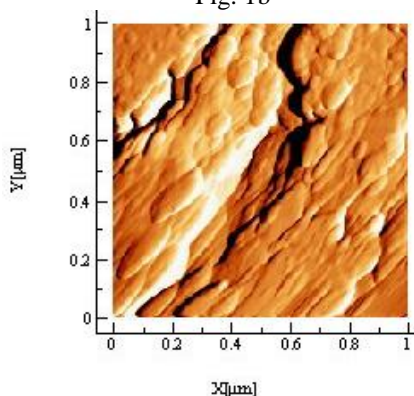


Fig. 1c

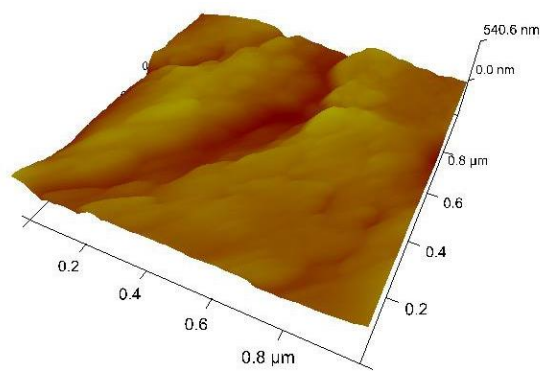


Fig. 1c, 3D

Fig. 1. AFM images of the surface morphology of modified graphites: a) 96%Pd:4%Pt/C; b) 87%Pd:13%Pt/C; c) 75%Pd:25%Pt/C (ratio of the modifying components in molar %).

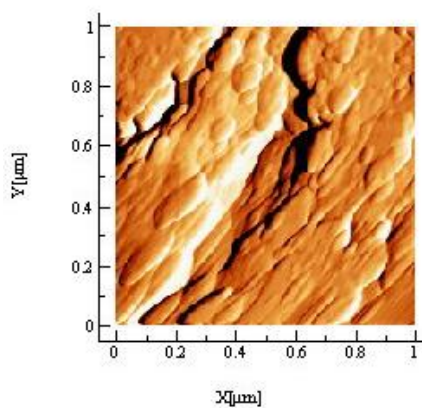


Fig. 2a

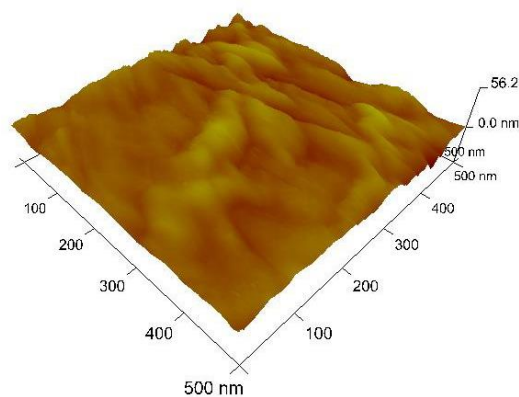


Fig. 2a, 3D

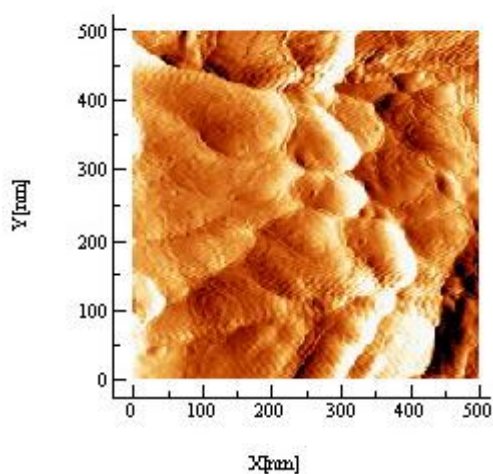


Fig. 2b

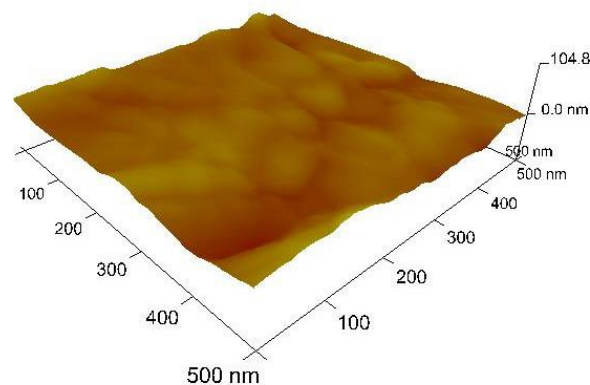


Fig. 2b, 3D

**Fig. 2.** AFM images of the surface morphology of modified graphites: a) 82%Pd:18%Au/C; b) 66%Pd:34%Au/C (ratio of the modifying components in molar %).

The AFM – images presented in Fig. 1b and Fig. 1c differ in the size and shape of the insular formations of the deposited metal phase. On electrode №2 (Fig.1b) they are smaller in size and have sharper building components – a structure which probably contributes to the higher activity of this electrode, as compared to that of electrode №3 (Fig.1c).

The microadditions of Au to Pd in the modifying mixture radically change the surface morphology of the depositions of (Pd + Au) on the same graphite carrier (Fig. 2). The topography of the surface of the graphite thus modified significantly differs from that of the ones discussed so far (Fig. 1).

With electrode №5, where 18 molar per cent of Au were added to Pd (Fig. 2a) and electrode №6, where 34 molar per cent of Au were added to Pd (Fig. 2b), different in size formations are observed on the surface. These formations are ribbed,

probably as a result of the gradual overlaying of the metal phase. With electrode №5 (Fig. 2a) the deposition (Pd + Au) is visibly with clusters which are smaller in size and sharper in shape, both in the periphery of the islands and in their inner part, as compared to electrode №6 (Fig. 2b). On the basis of the observations of the structure of electrode №5 it can be concluded that the smaller content of the Au microaddition (18 molar per cent) to Pd results in the formation of a structure with the highest electrocatalytic activity in the quantitative determination of  $H_2O_2$  (electrode №5 of series II is the most active one – Table 1).

Fig. 3 shows the AFM images of the surface of depositions of the same modifying mixture (Pd + Au), but on another carbonaceous matrix – glassy carbon. With electrode №7, in which the Au addition to Pd is only 6 molar per cent, the image of the surface is specific and does not resemble any of the ones discussed so far. Two forms of deposition

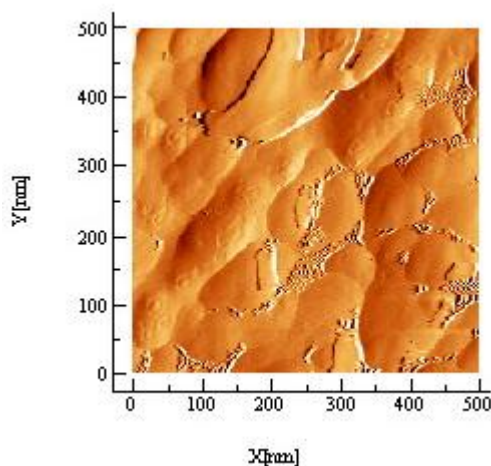


Fig. 3a

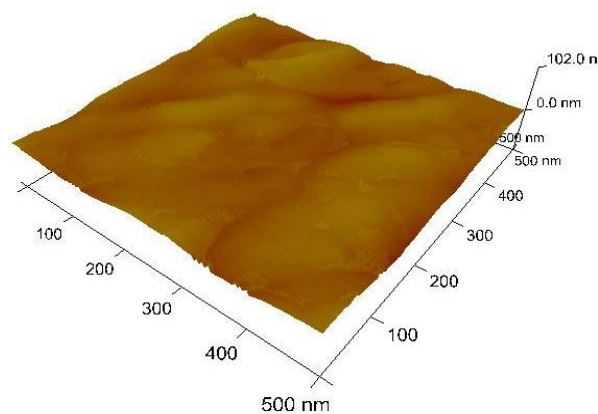


Fig. 3a, 3D

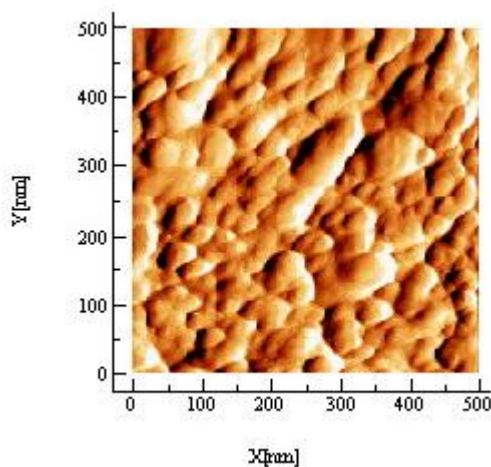


Fig. 3b

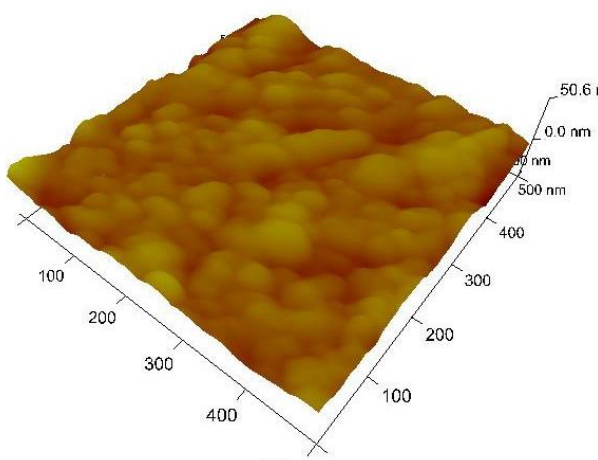


Fig. 3b, 3D

**Fig. 3.** AFM images of the surface morphology of modified glassy carbon electrodes: a) 94%Pd:6%Au/GC; b) 66%Pd:34%Au/GC (ratio of the modifying components in molar %).

are clearly identifiable (Fig. 3a): light plates tightly covering the protruding areas of the matrix, and a multitude of well-shaped grains, approximately and less than 10 nm in size. Most of these fine grains are grouped in structures resembling chains, situated in the grooves of the relief, with an insignificant number of them clearly separated.

In the deposition of a metal phase (Pd + Au), in which the Au content is much higher – 34 molar per cent (electrode №9), the surface of the electrocatalyst (Fig. 3b) is very different from that in Fig. 2b, which shows the deposition of the same modifying mixture but on a different carrier – graphite. With electrode №9 the metal phase is deposited evenly on the glassy carbon, forming grains of the same type (Fig. 3b). The grains in this metal formation are less than 50 nm in size, and vary within relatively narrow range (from 10 to 50 nm).

The comparative examination of Fig. 2b and Fig. 3b, showing AFM images of metal depositions

of the same modifying component (Pd + Au) (66 molar %: 34 molar %), but on different carbon matrixes, proves that the nature of the carbon material also has a significant effect on the structure of the deposited active phase. While the structures observed on the graphite matrix (Fig. 2b) are ribbed, most probably following the morphology of the carrier itself, with the glassy carbon matrix (Fig. 3b) the granular formations are distinctly shaped and distributed across the whole visible surface.

## CONCLUSION

The presented AFM images of the surface of the modified carbonaceous electrodes provide sufficient grounds to conclude that the catalytic activity of the electrocatalysts upon the electrochemical reduction of  $H_2O_2$  depends both on the type of the catalytically active modifying component (nature and ratio between the two

platinum metals) and on the nature of the carbon matrix, with the following being established:

- the optimal catalytic activity in the target reaction shows the deposits on graphite of the catalytically active phase, in which the content of the main element Pd is approximately 85 molar per cent, regardless of the nature of the second modification component (Pt or Au), and forms structures with similar in size and shape;
- the substitution of Au microaddition for Pt in the modification electrolytic solution (while preserving the percentage of the principal component Pd) results in deposits on graphite distinguished for their ribbed formations; the graphites modified by (Pd + Au) deposits are characterized by about twice as long linear range of concentration dependence of the amperometric signal;
- the modification by the same mixture (Pd + Au) (66 molar % : 34 molar %) of various carbonaceous materials (glassy carbon and graphite) produces electrocatalysts with practically the same catalytic activity, despite the notable differences in the structure of the deposited catalytic phase.

**Acknowledgments:** Financial support from the Bulgarian National Science Fund (grant DDVU – 02/38) and University of Food Technologies Research Fund (grant 5/12–N) is gratefully acknowledged.

#### REFERENCES

1. R. Cretu, D. Gligor, L. Muresan, I. Popescu, L. M. Muresan, *J. Appl. Electrochem.*, **36**, 1327 (2006).
2. A. Eftekhari, *Microchim. Acta*, **141**, 15 (2003).
3. J. Li, R. Yuan, Y. Chai, T. Zhang, X. Che, *Microchim. Acta*, **171**, 125 (2010).
4. R. Pauliukaite, S.B. Hočevár, E. A. Hutton, B. Ogorevc, *Electroanalysis*, **20**, 47 (2008).
5. P. A. Fiorito, V. R. Gonçalves, E. A. Ponzio, S. I. de Torresi, *Chem. Commun. (Camb.)*, **3**, 366 (2005).
6. X. Luo, A. Morrin, A. Killard, M. Smith, *Electroanalysis*, **18**, 319 (2006).
7. O. Niwa, *Bull. Chem. Soc. Jpn.*, **78**, 555 (2005).
8. P. Yang, W. Wei, C. Tao, B. Xie, X. Chen, *Microchim. Acta*, **162**, 51 (2008).
9. S. Hrapovic, Y. Liu, K. B. Male, J. H. Luong, *Anal. Chem.*, **76**, 1083 (2004).
10. M. Yang, Y. Yang, Y. Liu, G. Shen, R. Yu, *Biosens. Bioelectron.*, **21**, 1125 (2006).
11. I. Gurrappa, L. Binder, *Sci. Technol. Adv. Mater.*, **9**, 043001-12 (2008).
12. A.E. Alvarez, D. R. Salinas, 2<sup>nd</sup> Mercosur Congress on Chemical Engineering – Brasil, report 808, (2005).
13. J. Hrbac, V. Halouzka, R. Zboril, K. Papadopoulos, T. Triantis, *Electroanalysis*, **19**, 1850 (2007).
14. N. Dimcheva, E. Horozova, Z. Jordanova, *Z. Naturforsch., C*, **57**, 883 (2002).
15. N. Dimcheva, E. Horozova, Z. Jordanova, *Z. Naturforsch., C*, **57**, 705 (2002).
16. T. Dodevska, E. Horozova, N. Dimcheva, *Anal. Bioanal. Chem.*, **386**, 1413 (2006).
17. E. Horozova, T. Dodevska, N. Dimcheva, *Journal of the University of Chemical Technology and Metallurgy*, **43**, 59 (2008).
18. E. Horozova, T. Dodevska, N. Dimcheva, *Bioelectrochemistry*, **74**, 260 (2009).
19. T. Dodevska, E. Horozova, N. Dimcheva, *Central European Journal of Chemistry*, **8**, 19 (2010).
20. E. Horozova, T. Dodevska, N. Dimcheva, *International Journal of Electrochemistry*, Article ID 697698, 8 pages ; doi: 10.4061/2011/697698 (2011).
21. T. Dodevska, PhD Thesis, UFT, Plovdiv, 2011.

## ЕЛЕКТРОХИМИЧНИ ХАРАКТЕРИСТИКИ И СТРУКТУРНИ ОСОБЕНОСТИ НА ВЪГЛЕРОДНИ ЕЛЕКТРОДИ, МОДИФИЦИРАНИ С МИКРО- И НАНООТЛОЖЕНИЯ ОТ ПЛАТИНОВИ МЕТАЛИ

Т. М. Додевска<sup>1</sup>, Е. Г. Хорозова<sup>2</sup>, Н. Д. Димчева<sup>2</sup>

<sup>1</sup>Университет по хранителни технологии, катедра „Неорганична химия и физикохимия“, Пловдив 4002

<sup>2</sup>Пловдивски университет „Паисий Хилендарски“, катедра „Физикохимия“, Пловдив 4000

Постъпила на 22 март, 2013 г.; Коригирана на 13 май, 2013 г.

(Резюме)

Повърхностната топография на серия от графитови и стъкловъглеродни електроди, модифицирани с микро- и нанootложения от смеси (Pd + Pt) и (Pd + Au) в различни съотношения на каталитично-активните компоненти, беше изследвана с атомна силова микроскопия (AFM). Установи се, че каталитичната активност на модифицираните електродите в реакцията на редукция на H<sub>2</sub>O<sub>2</sub> зависи от спецификите в природата и структурата на металната фаза, електрохимично отложена върху въглеродния носител. Особеностите в структурата и морфологията на металните отложения, както и степента на заселеност на електродната повърхност, се определят от вида на каталитично-активните компоненти (природа и съотношение на двата метала в модифициращата смес) и природата на въглеродната матрица (тип, порьозност и състояние на повърхността).

## Catalytic activity of co-sputtered PtIr thin films toward oxygen reduction

I. Radev<sup>1,3</sup>, G. Topalov<sup>1</sup>, G. Ganske<sup>2</sup>, E. Lefterova<sup>1</sup>, G. Tsotridis<sup>3</sup>, U. Schnakenberg<sup>2</sup>, E. Slavcheva<sup>1,2</sup>

<sup>1</sup>Acad. Evgeni Budevski Institute of Electrochemistry and Energy Systems, Bulgarian Academy of Sciences, 1113 Sofia, Bulgaria

<sup>2</sup>Institute of Materials in Electrical Engineering I, RWTH, Aachen University, 52074 Aachen, Germany

<sup>3</sup>European Commission, Directorate-General Joint Research Centre, Institute for Energy and Transport, PO Box 2, 1755 ZG Petten, The Netherlands

Received January 14, 2013; revised March 23, 2013

The work presents a research on the preparation, physical characterisation, and electrochemical activity of bimetallic platinum-iridium (Pt-Ir) thin films with varying metal ratio as oxygen reduction reaction (ORR) catalysts. The films are deposited upon gas permeable hydrophobic carbon paper substrates by co-sputtering from Pt and Ir pure metal targets. To achieve different metal ratios, the sputtering power applied on the iridium target is varied in the range 0 - 100 W at constant power of the Pt target. The ORR catalytic activity is investigated in 0.5M H<sub>2</sub>SO<sub>4</sub> and proton conductive polymer electrolyte Nafion. The study reveals that the efficiency of the co-sputtered Pt-Ir catalysts is superior compared to pure Pt and depends on the sputter regime and alloy composition.

**Keywords:** oxygen reduction, magnetron sputtering, platinum iridium electrocatalysts, PEM fuel cell

### INTRODUCTION

The oxygen reduction reaction (ORR) is the main source of energy dissipation in the polymer electrolyte membrane fuel cells (PEFC) [1]. The best ORR catalyst among the pure metals is Pt but its performance even at comparatively high loadings (0.4 mg.cm<sup>-2</sup>) is not fully satisfactory for PEFC mass production. To improve the ORR efficiency, catalysts with enhanced activity and better utilisation at decreased catalytic loadings are required [2,3]. The stability and durability are also a serious challenge for the successful PEMFC commercialisation. Various Pt alloys have shown improved catalytic activity compared to pure Pt. Typical examples are the alloys of Pt with transition metals (Cr, Fe, Co, Ni, Cu, etc.) which have been studied intensively over the last decades [4-6]. However, these metals are not stable in acidic media and can be easily leached out from the alloy, causing degradation of the catalyst, poisoning of the polymer electrolyte, and gradual decay in the fuel cell performance.

The platinum group metals (Au, Pd, Ir, Os, Ru, Rh) on the other hand, have excellent chemical stability and are attractive alloying elements capable to enhance the activity of Pt, at the same

time improving the catalyst durability [7-9]. Among these metals, iridium is of particular interest since it shows extremely high stability. The existing literature data on the catalytic performance of Pt-Ir alloys are still scarce and refer mainly to Pt-Ir nanoparticles prepared by wet chemical reduction or thermal decomposition of metal salts. Ioroi and Yasuda investigated unsupported Pt-Ir alloys with varying Ir-content as oxygen reduction catalysts [8]. In acidic solutions they observed increase in the kinetic current density by a factor of about 1.5 for Pt-Ir samples containing 5-20 wt. % Ir. Similarly, under PEMFC working conditions, the dependence between Ir content and the specific current density showed an enhanced ORR activity at Ir concentration in the range 5-20 wt.%. Popov et al. studied mixtures of unsupported Pt- and Ir-black as catalysts for unitized regenerative fuel cells [9]. They reported that the Pt-Ir mixed catalyst with 15 wt. % Ir and electrochemical active surface area comparable to that of Pt-black, showed the highest round-trip efficiency at various current densities. At the same time, the fuel cell performance of this catalytic mixture was very similar to the efficiency of the Pt-black, despite the fact that Ir is known to possess lower ORR activity than Pt. In the last decade there is an increased interest to the method of magnetron sputtering as an alternative catalysts preparation technique [10-15]. It can be easily

\* To whom all correspondence should be sent:  
E-mail: ivan.radev@gmail.com

adopted for direct incorporation of variety of catalytic materials into the active PEMFC element – the membrane electrode assembly (MEA) [12,13]. The method offers advantages related both to the optimisation of the catalytic properties and the assembling of the MEA [14,16]. The surface structure and morphology of the catalytic film can be strictly controlled by simple variation of the process parameters [10,17,18]. Other advantageous feature of the method is its excellent reproducibility as well as the possibility to deposit not only pure metals but also alloys (co-sputtering) and compounds (reactive sputtering). In a more recent work an optimal regime for sputtering of low Pt loaded catalytic films directly on gas diffusion substrates was found [14]. This paper is focused on the fabrication of thin bimetallic Pt-Ir films by co-sputtering from Pt and Ir pure metal targets. The aim is by varying the power of the applied electrical field to optimise the composition and morphology in order to obtain catalysts with high ORR efficiency at low overall metal loading. Intra-atomic electronic interactions between both metals, resulting in increased ORR efficiency are also expected.

## EXPERIMENTAL

The co-sputtered Pt-Ir films were deposited on commercial gas diffusion electrodes (hydrophobic carbon paper E-TEK 120/30 WP) over a thin Ti-adhesion layer [18]. The pressure of the argon plasma ( $p_{Ar}$ ), the working distance between the metal target and the substrate ( $WD$ ), and the dc power applied to the Pt target ( $P_{Pt}$ ) were held constant for each sample (9 Pa, 78 mm, and 100 W, respectfully). To provide thin Pt-Ir films with various metal ratio the power of the Ir target ( $P_{Ir}$ ) was varied in the range between 20 and 100 W. Further in the text the samples are referred in accordance to the power of the Ir target (Pt-Ir20 stays for the sample sputtered at  $P_{Pt} = 100$  W and  $P_{Ir} = 20$  W).

The films were characterised by energy dispersive X-ray spectroscopy (EDX), X-Ray diffraction (XRD), scanning electron microscopy (SEM), and X-ray photoelectron spectroscopy (XPS) [19]. The influence of the Pt-Ir ratio on the catalytic activity toward oxygen reduction in 0.5 M  $H_2SO_4$  electrolyte was studied at room temperature by cyclic voltametry (CV) and linear sweep voltametry (LSV) on rotating disc electrode (EG&G PARC, Model 616). The experiments were performed in a three electrode electrochemical cell

with Pt wire counter electrode and saturated Ag/AgCl reference electrode. In the text all potentials are referred to reference hydrogen electrode (RHE). The Pt and Pt-Ir catalytic films deposited on commercial gas diffusion layers (carbon Toray paper, 30% water proofed, 300  $\mu m$  thick) were attached mechanically to a glassy carbon disk electrode, leaving working area of 0.5  $cm^2$  exposed to the electrolyte. The CV measurements were carried out in Ar-saturated electrolyte. The electrochemical active surface area ( $S_A$ ) was calculated via integration of the area under the hydrogen adsorption/desorption peaks according a common electrochemical procedure [2]. The polarisation curves were obtained in oxygen saturated electrolyte. The activity of the catalysts was assessed comparing the current density in the kinetic range of the curves ( $j$  at 0.9 V vs. RHE). Selected samples were integrated in membrane electrode assemblies using a commercial Nafion 117 membrane (Alfa Aesar) and tested as cathodes in a single cell hardware supplied with Pt hydrogen reference electrode (Fuel Cell Technologies Inc.). The testing conditions were: 80  $^{\circ}C$ , total pressure of 2.5 atm abs., fully humidified hydrogen and air. The electrochemical experiments were performed using Solartron Analytical 1287 Electrochemical Interface potentiostat and CorrWare<sup>TM</sup> software.

## RESULTS AND DISCUSSION

### Structural and morphological characterisation

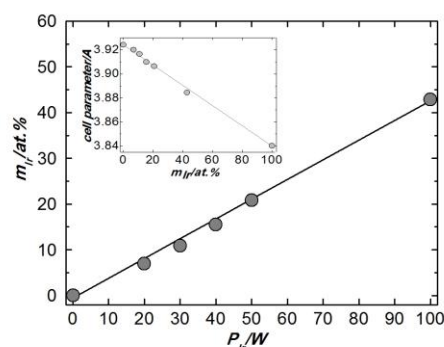


**Fig. 1.** Influence of sputtering power on the content of Ir in the co-sputtered Pt-Ir films; Cell parameter of Pt-Ir films as function of Ir content (inset figure).

The iridium content ( $m_{Ir}$ , at.%) determined via EDX is given in Table 1. In the same table are included the measured catalytic loadings and some

**Table 1.** Structural characteristics of Pt-Ir films co-sputtered at various power of Ir target ( $P_{Ir}$ ) on carbon paper;  $WD = 78$  mm;  $p_{Ar} = 9$  Pa;  $P_{Pt} = 100$  W.

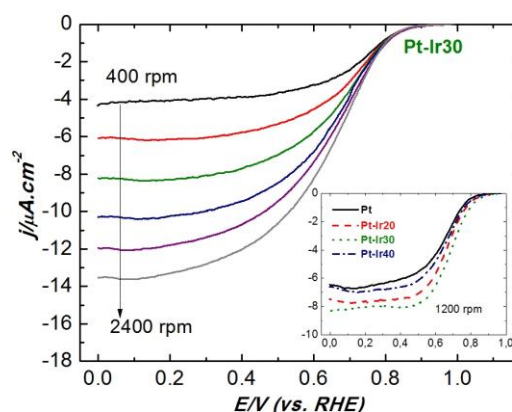
Sample	PtIr [W]	$l_{cat}$ [mg.cm <sup>-2</sup> ]	$m_{Ir}$ [at.%]	$D_{111}$ [nm]	$D_{200}$ [nm]	a [Å]
Pt	0	0.143	0	11.8	7.7	3.9244
PtIr20	20	0.108	6.8	11.7	8.7	3.9202
PtIr30	30	0.107	10.7	11.0	8.2	3.9167
PtIr40	40	0.118	15.3	10.4	11.5	3.9100
PtIr50	50	0.110	20.5	9.7	10.7	3.9065
PtIr100	100	0.078	42.5	7.6	7.9	3.8846
Pure Ir	100	0.067	100	6.0	5.0	3.8403

structural data extracted by the XRD analysis. The established linear dependence between  $m_{Ir}$  and  $P_{Ir}$  (Fig. 1) allows an easy control of the catalyst composition and loading by simple variation of the sputtering power and duration of the process. The results show that although the sputtering time was kept constant for all samples, their catalytic loadings ( $l_{cat}$ ) are not identical. A general trend of decrease in  $l_{cat}$  with the increasing  $P_{Ir}$  is observed. This is related to the lower deposition rate of Ir which grows in a more disordered columnar structure with smaller crystallites compared to Pt [20]. For this reason the increase in  $m_{Ir}$  leads to formation of layers with higher porosity, more open structure and lower density.

The effect of  $P_{Ir}$  on the surface morphology and film structure the Pt-Ir samples was investigated using SEM and XRD analysis and these results have been presented in details elsewhere [17,19]. Briefly, the size of the particles decreases with the increasing  $P_{Ir}$ , varying varies in the range 20-10 nm, while the increase in Ir content leads to changes in the crystallites shape and formation of elongated structures, more clearly seen on the samples obtained at  $P_{Ir} \geq 30$  W. The observed changes in the morphology are related to the increasing amount of Ir atoms taking part in the film growth that compete with the sputtered Pt for the most favourable surface sites, leading to change in the preferential plains of the crystal growth and formation of smaller crystallites with different crystal habitus. The XRD analysis revealed displacement of the diffraction peaks with the increasing  $m_{Ir}$  to higher angles in respect to pure Pt, indicating a lattice contraction due to the inclusion of Ir atoms. The increase in  $m_{Ir}$  leads also to decrease in the cell parameter following a linear trend (the inset in fig. 1) and in accordance with the empirical Vegard's law proves a substitution of a solid solution type [21]. The estimated structural characteristics of the catalysts are summarized in Table 1.

The positions of Pt 4f<sub>7/2</sub> and Ir 4f<sub>7/2</sub> peaks (at bonding energies of 71.2–71.6 eV and 60.6–61 eV, respectively) derived from XPS spectra [19] indicated that both components are in metallic form. With the increase of Ir content a shift of about 0.3 – 0.4 eV to higher binding energies was registered for the Pt4f<sub>7/2</sub> line. At the same time the Ir 4f<sub>7/2</sub> peak was equally shifted to lower binding. The observed displacements in the binding energy of the core-level orbital are related to changes in the electron density, indicating an intra-atomic charge transfer [8].

#### Electrochemical tests

**Fig. 2.** RDE polarisation curves of Pt-Ir30 at different rotation rates; RDE polarisation curves of pure Pt and selected Pt-Ir films obtained at 1200 rpm (inset figure)

The electrochemical activity of the co-sputtered Pt-Ir films was investigated using linear sweep voltammetry (LSV) on rotating disk electrode (RDE). Figure 2 shows the polarisation curves of the Pt-Ir30 sample obtained at varying rotation rate ( $\omega$ ). The typical regions of kinetic, mixed and diffusion control of the reaction are well distinguished. The inset in fig. 2 presents the current-potential curves of the Pt-Ir films having an enhanced ORR efficiency compared to the pure Pt at rotation rate of 1200 rpm. The oxygen reduction is most intensive on the Pt-Ir30 catalyst. In order to

evaluate the catalytic efficiency of each sample, it is necessary to determine the kinetic current density ( $j_k$ ), to construct the Tafel plots, and using the equation  $\eta = a + b \log j_k$ , to calculate the exchange current density ( $j_o$ ), which is a measure for the intrinsic catalytic activity.

According to the Levich RDE theory, the overall disk current ( $j$ ) is related to the diffusion limited current ( $j_{lim}$ ), the kinetic current ( $j_k$ ), and the reaction order ( $m$ ) according to eq. (1):

$$\log j = m \log(1 - j/j_{lim}) + \log j_k \quad (1)$$

while, the limiting current density is represented by eq. (2):

$$j_{lim} = 0.62nFC_oD_o^{2/3} \nu^{1/6} \omega^{1/2} \quad (2),$$

where  $n$  is the number of electrons transferred per molecule of  $O_2$ ,  $F$  - the Faraday constant,  $C_o$  - the bulk concentration of oxygen,  $D$  - its diffusion coefficient,  $\nu$  - the kinematic viscosity, and  $\omega$  - the electrode rotation rate.

The equation (2) is an ideal response of a fast electron transfer processes. For reactions proceeding under mixed transport-kinetic control, the electrode current is described by the modified Koutecky-Levich equation (3):

$$1/j = 1/j_{lim} + 1/j_k \quad (3)$$

According the RDE theory, for fixed overpotentials the plots  $1/j$  vs.  $1/\omega^{1/2}$  should generate straight lines with intercepts proportional to  $j_k$  and slopes independent on the potential and proportional to  $n$ . The Koutecky-Levich analysis is broadly used to estimate the kinetic current density

However, it should be noted that Eq. (3) is valid only for first order reactions [6,22-24]. In order to verify its validity for the catalysts under study the plots of  $\lg j$  vs.  $\lg(1 - j/j_{lim})$  for the sputtered Pt (Fig.

3 a) and Pt-Ir30 (Fig. 3 b) catalytic films were built at different rotation rates and electrode potentials. The obtained slopes of the straight lines were higher than 1 (in the range 1.32-1.45), showing a deviation of the ORR from the first order kinetics. The observed deviations in the hydrodynamics of the studied systems most probably are related to the highly porous structure of the electrodes. In this case the Koutecky-Levich analysis is not valid and the catalytic activity can be compared using the current density at low overvoltages normalized by the real surface area of the electrode,  $S_A$ . [14, 23]. The values of  $S_A$  for the Pt-Ir samples (Table 2) were determined by cyclic voltammetry (Fig. 4) following the well established experimental procedure [2]. The  $S_A$  of the Pt-Ir sample under study does not differ significantly as Pt-Ir20 and Pt-Ir30 have slightly higher active surfaces than pure Pt.

**Table 2.** Electrochemical data obtained from the cyclic voltammetry curves and the Tafel plots.

Sample	$j_{0.9V}$ mA.cm <sup>-2</sup>	$S_A$ cm <sup>2</sup> <sub>real</sub> .cm <sup>-2</sup>	Tafel slope $b$ mV.dec <sup>-1</sup>
Pt	$4.7 \times 10^{-5}$	22.5	110
Pt-Ir20	$7.22 \times 10^{-5}$	23.9	102
Pt-Ir30	$10.2 \times 10^{-5}$	25.5	98
Pt-Ir40	$5.4 \times 10^{-5}$	25.4	108

The data in Table 2 show that the oxygen reduction is most intensive on the Pt-Ir30 catalyst. Fig. 5 presents the current density  $j_s$  normalised to the  $S_A$  vs. potential in the kinetic range where the mass transport effects are negligible (0.9V vs. RHE). The values of the Tafel slope  $b$  determined from these plots are included in Table 2. The lowest is the slope for the Pt-Ir30 sample but in general, the values for all samples are very close (101-111).

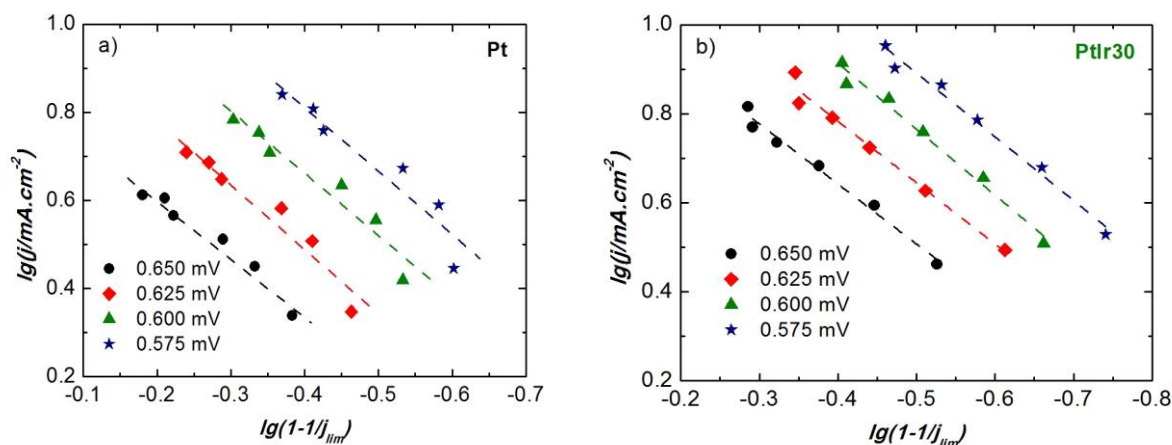


**Fig. 3.** Reaction order plots for Pt (a) and Pt-Ir30 (b) catalytic films in 0.5M H2SO4 at various electrode potentials

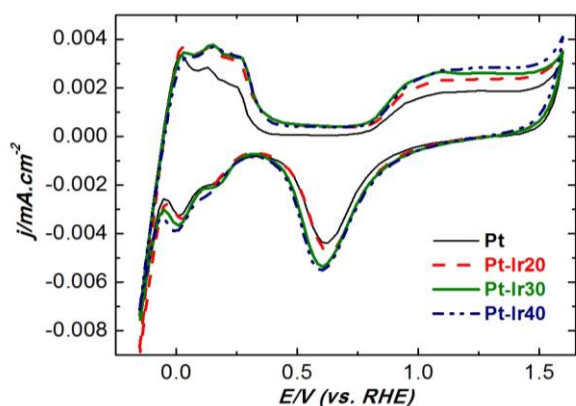


**Fig. 4.** Cyclic voltammetry curves of selected sputtered Pt-Ir films recorded at  $100 \text{ mV}\cdot\text{s}^{-1}$  scan rate in  $0.5\text{M H}_2\text{SO}_4$ .

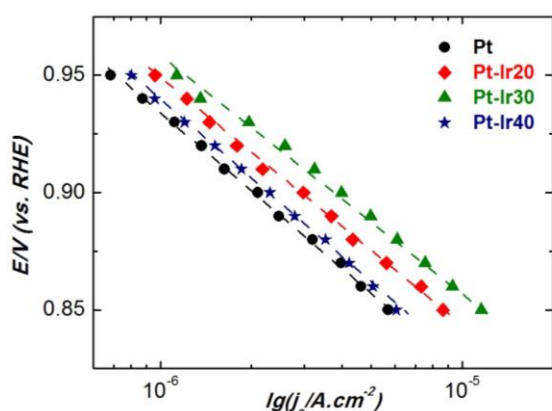


**Fig. 5.** Tafel kinetic plots for selected sputtered Pt-Ir films in  $0.5\text{M H}_2\text{SO}_4$

$\text{mV}\cdot\text{dec}^{-1}$ ), suggesting that the rate determining step is the transfer of the first electron to the oxygen molecule ( $b = 120 \text{ mV}\cdot\text{dec}^{-1}$ ). The comparison of all the results obtained indicates that the bimetallic Pt-Ir films are more efficient ORR catalysts than the pure Pt film. With the increase of  $m_{\text{Ir}}$ , the rate of the reaction increases, goes through maximum at concentrations around 11 at.% Ir (for Pt-Ir30 the increase is by factor of 2.2 compared to Pt), and at higher  $m_{\text{Ir}}$  decreases again.

While Pt is known to possess the highest ORR activity among the pure metals, including those from the Pt group (Pt > Pd > Ir > Rh), numerous theoretical calculations and experimental data have shown that various Pt alloys (if properly designed) demonstrate an improved catalytic behavior compared to pure Pt [24–26]. The enhanced ORR activity is related to geometry factors such as particle size effect and the Pt-Pt nearest neighbour bond distance and/or electronic factors such as intra atomic interactions resulting in modification of Pt electronic structure [27]. The results obtained in

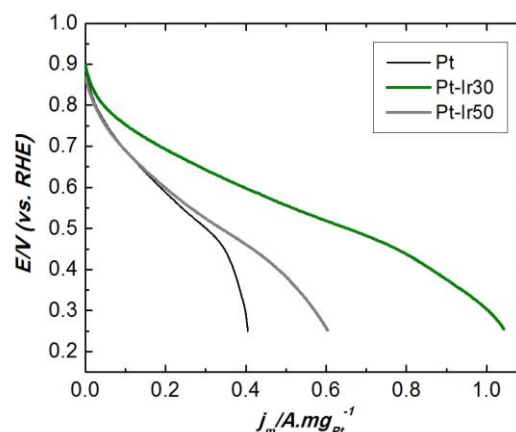


**Fig. 6.** ORR polarisation curves in PEMFC presented as mass activity

this study show that the concentration of Ir influences strongly the catalytic efficiency of the sputtered Pt-Ir alloy as both groups of the afore mentioned factors are involved. The performed XRD and SEM analysis registered systematic change in the morphology, particle size, and lattice parameter with the change of the sputtering power, respectively with the content of Ir in the sputtered film. The alloying leads to shrinkage of the metal lattice and decrease of the Pt-Pt nearest neighbour distance thus, inducing low energy Pt surface sites for enhanced oxygen adsorption. At the same time due to the stronger affinity of Ir to OH adsorption, the formation of Ir-OH<sub>ads</sub> starts at less positive potentials than the Pt-OH<sub>ads</sub> surface coverage (Fig. 4). The earlier formation of Ir-OH coverage and the steric hindrance between the already adsorbed OH-groups leave more free active Pt sites for the adsorption of oxygen. It should be noticed that both the decrease in the lattice parameter and the increase of Ir concentration follow a linear trend with the increasing sputtering power  $P_{\text{Ir}}$ , while the electrochemical measurements proved a superior catalytic activity for the Pt-Ir30. This most active catalyst has moderate lattice parameter and Ir content of  $\sim 11$  at.%. Obviously, at higher Ir concentration ( $m_{\text{Ir}} > 15$  at.%) the discussed positive effects induced by Ir diminish due to the accompanying decrease of the Pt active surface sites which in turn, hinders the adsorption of oxygen and results in lower ORR intensity. The observed enhanced activity of the Pt-Ir films can be related also to the electronic interactions between both metals registered by the XPS analysis [19]. The displacement in the binding energies of Pt  $4f_{7/2}$  and Ir  $4f_{7/2}$  is a result of changes in the electron density, indicating an intra-atomic charge transfer between both metals. In general, the partial electron transfer in an alloy occurs from the less

electronegative to the more electronegative component. The electronegativity values of Pt and Ir are 2.18 and 2.22 respectively. Therefore, in Pt-Ir alloy the partial electron transfer should be from Pt to Ir. This assumption is in agreement with the XPS analysis where a positive shift in the binding energy of the core level electrons of Pt atom is observed.

Since the sputtered PtIr films are envisaged for fuel cell applications PtIr30, PtIr50 and the pure Pt were integrated in membrane electrode assemblies and investigated in laboratory PEMFC. The obtained polarisation curves are shown in fig. 6 where the current density is normalized to the catalytic loading and presented as mass activity,  $j_m$ . In accordance with the results obtained in sulfuric acid solution, the performance of MEA with PtIr30 cathode (mass activity per overvoltage) in the potentials range 0.75 – 0.5 V vs. RHE exceeds by a factor of 2 that of MEA with a pure Pt cathode.

### CONCLUSIONS

The influence of Ir sputtering power on the film composition, structure and morphology, and the ORR electrocatalytic activity were studied in details. It was found that the increasing power results in gradual Ir enrichment of the film, leading to formation of catalysts with higher porosity, decrease in the particles size, and shrinkage of the metal lattice. Electronic interactions and intra-atomic charge transfer between both metals were also registered. It was shown that these effects reflect on the catalytic activity of the co-sputtered films that goes through maximum at Ir concentrations in the range 10-15 at.%. The results obtained give credence to consider the co-sputtered PtIr films as promising durable cathodes for PEFC applications capable to offer enhanced ORR efficiency at relatively low metal loading.

*Acknowledgements: The presentation of the research results has been supported by Bulgarian Ministry of Youth, Education and Science, project BG 051PO001-3.3.05/0001, cont № DO2 –551*

### REFERENCES

1. U.A. Paulus, T. J. Schmidt, H.A. Gasteiger, R.J. Behm, *J. Electroanal. Chem.*, **495** 134 (2001).
2. H.A. Gasteiger, S.S. Kocha, B. Sompalli, F.T. Wagner, *Appl. Catal. B: Environmental*, **56**, 9 (2005).
3. Lj. M. Vračar, N.V. Krstajić, V.R. Radmilović, M.M. Jakšić, *J. Electroanal. Chem.*, **587**, 99 (2006).
4. A. U. Nilekar, Y. Xu, J. Zhang, M. B. Vukmirovic, K. Sasaki, R. R. Adzic, M. Mavrikakis, *Top Catal.*, **46**, 276 (2007).
5. J. Greeley, I.E.L. Stephens, A.S. Bondarenko, T.P. Johansson, H.A. Hansen, T.F. Jaramillo, J. Rossmeisl, I. Chorkendorff, J.K. Nørskov, *Nature Chemistry*, **1**, 552 (2009).
6. J.S. Cooper, P.J. McGinn, *Appl. Surface Sci.*, **254**, 662 (2007).
7. H.R. Colon-Mercado, B.N. Popov, *J. Power Sources*, **155**, 253 (2006).
8. T. Ioroi, K. Yasuda, *J. Electrochem. Soc.*, **152**, A1917- (2005).
9. Ho-Young Jung, Sehkyu Park, B.N. Popov, *J. Power Sources*, **191**, 357 (2009).
10. E. Slavcheva, G. Ganske, G. Topalov, W. Mokwa, U. Schnakenberg, *Appl. Surface Sci.*, **255**, 6479 (2009).
11. A.T. Haug, R.E. White, J.W. Weidner, W. Huang, S. Shi, T. Stoner, N. Rana, *J. Electrochem. Soc.*, **149**, A280 (2002).
12. E. Slavcheva, I. Radev, G. Topalov, E. Budevski, *Electrochimica Acta*, **53**, 362 (2007).
13. S. Mukerjee, S. Srinivasan, A.J. Appleby, *Electrochimica Acta*, **38/12**, 1661 (1993).
14. E. Slavcheva, G. Topalov, G. Ganske, I. Radev, E. Lefterova, U. Schnakenberg, *Electrochimica Acta*, **55/ 28**. 8992 (2010).
15. O'Hayre R, Lee S.J., Cha S.W. and Prinz F.B., *J. Power Sources*, **109**, 483 (2002).
16. T. Nakakubo, M. Shibata, K. Yasuda, *J. Electrochem. Soc.*, **152/12**, A2316 (2005).
17. G. Topalov, G. Ganske, E. Lefterova, U. Schnakenberg, E. Slavcheva, *Int.J. Hydrogen Energy*, **36**, 15437 (2011).
18. C.-H. Wan, M.-T. Lin, Q.-H. Zhuang, C.-H. Lin, *Surface & Coatings Technol.*, **201**, 214 (2006).
19. I. Radev, G. Topalov, E. Lefterova, G. Ganske, U. Schnakenberg, G. Tsotridis, E. Slavcheva, *Int. J. Hydrogen Energy*, **37**, 7730 (2012).
20. G. Ganske, E. Slavcheva, A. van Ooyen, W. Mokwa, U. Schnakenberg, *Thin Solid Films*, **519**, 3965 (2011).
21. L. Vegard, *Z. Physic*, **5** (1921) 17, *Z. Krystallogr.* **67** (1928) 239, K.T. Jacob, S. Raj, L. Rannesh, *Int. J. Materials Res.*, **98**, 776 (2007).
22. A.J. Bard, L.R. Faulkner, *Electrochemical methods: Fundamentals and applications*, Wiley, NY, 2001.
23. S. Treimer, A. Tanga, D.C. Johnson, *Electroanalysis*, **14**, 165 (2002).
24. K.J.J. Mayrhofer, D. Strmcnik, B.B. Blizanac, V. Stamenkovic, M. Arenz, N.M. Markovic, *Electrochimica Acta*, **53**, 3181 (2008).
25. J. Nørskov, J. Rossmeisl, A. Logadotir, L. Lindqvist, J. Kitchin, T. Bligaard, et al., *J. Phys. Chem. B*, **108**, 86 (2004).
26. O. Savadogo, K. Lee, K. Oishi, S. Mitsushima, N. Kamiya, K.-I. Ota, *Electrochem. Commun.*, **6**, 105 (2004).
27. T. Toda, H. Igarashi, M. Watanabe, *J. Electrochem. Soc.*, **145** 4185 (1998).
28. R. R. Adzic, J. Zhang, K. Sasaki, M. B. Vukmirovic, M. Shao, J. X. Wang, A. U. Nilekar, M. Mavrikakis, J. A. Valerio, F. Uribe, *Top Catal.*, **46**, 249 (2007).

## КАТАЛИТИЧНА АКТИВНОСТ НА СЪ-РАЗПРАШЕНИ ФИЛМИ ОТ Pt-Ir СПРЯМО РЕДУКЦИЯ НА КИСЛОРОД

И. Радев<sup>1,3</sup>, Г. Топалов<sup>1</sup>, Г. Ганске<sup>2</sup>, Е. Лефтерова<sup>1</sup>, Г. Цотридис<sup>3</sup>, У. Шнакенбург<sup>2</sup>, Е. Славчева<sup>1,2</sup>

<sup>1</sup> *Институт по електрохимия и енергийни системи "Акад. Евгени Будевски", Българска академия на науките, ул. „Акад. Г. Бончев“ бл.10, 1113, София, България*

<sup>2</sup> *Институт на материалите по електротехника I, RWTH, Университет в Аахен, 52074 Аахен, Германия*

<sup>3</sup> *Европейска комисия, Генерална дирекция Съвместен изследователски център, Институт по енергетика и транспорт, PO Box 2, 1755 ZG Петен, Холандия*

Постъпила на 14 януари, 2013 г.; преработена на 23 март, 2013 г.

(Резюме)

Настоящата статия е посветена на приготвяне, физико-химично характеризиране и оценка на електрохимичната активност на биметални платина-иридий (Pt-Ir) тънки филми с различно съотношение между двата метала като катализатори спрямо редукция на кислород. Филмите са отложени върху газо-пропусклива хидрофобизирана въглеродна хартия посредством съ-разпрашване на Pt и Ir метални мишени. За да се постигнат различни Pt-Ir съотношения, мощността на разпрашване, приложена върху иридийевата мишена е променяна в диапазона 0 - 100 W при постоянна мощност на платиновата мишена. Електро-каталитичната активност спрямо редукция на кислород е изследвана в 0,5 M H<sub>2</sub>SO<sub>4</sub> и протон проводящ полимерен електролит Nafion. Резултатите показват, че електро-каталитичната активност на съ-разпрашените Pt-Ir катализатори е по-висока в сравнение с тази на Pt и силно се повлиява от режима на разпрашване и състава на сплавта.

## A novel non-carbon gas diffusion layer for PEM water electrolysis anodes

G. R. Borisov\*, A. E. Stoyanova, E. D. Lefterova, E. P. Slavcheva

*Institute of Electrochemistry and Energy Systems,  
Bulgarian Academy of Sciences, G. Bonchev Str. 10, 1113 Sofia, Bulgaria*

Received: January 11, 2013; revised: June 30, 2013

The work presents a research on the development of novel gas diffusion layer (GDL) suitable for application in PEM water electrolysis. The traditionally used carbon-based GDL is replaced by GDL containing sub-stoichiometry Magneli phase titanium oxide. The newly developed GDL is integrated in a membrane electrode assembly (MEA) containing highly active Pt catalyst and proton conductive polymer electrolyte membrane. The MEA performance is characterized in a laboratory PEM electrolyser at standard operative conditions by cyclic voltammetry and steady state polarization techniques. It is found that the new layer ensures excellent electrical conductivity and has very good stability at high anodic potentials. The determined morphology factors of the platinum catalyst however, show that further optimization of the porosity is required in order to improve the water transport to the reactive zone and the catalyst utilization.

**Keywords:** gas diffusion layer, PEM water electrolysis, Ebonex, membrane electrode assembly

### INTRODUCTION

PEM water electrolysis (PEMWE) is an innovative technology for production of hydrogen, offering several advantages overall the traditional methods such as high efficiency, low current losses, and excellent (more than 99.99%) purity of the produced gasses. The usage of polymer proton conductive membrane as an electrolyte is also very favorable since it allows the size of the electrolyzer to be dramatically reduced and avoids hazardous leakages in the environment. All these advantages make PEM water electrolysis a very attractive and highly efficiency technology. The main energy converting component in the PEMWE is the membrane electrode assembly (MEA) which consists of two gas diffusion electrodes separated by the polymer electrolyte membrane. The gas diffusion layer (GDL) is an important part of the gas diffusion electrode, providing the water flow to the reactant zone where the electrochemical reactions take place, the removal of the produced gases ( $H_2$  and  $O_2$ ), and serving as a current collector. Therefore, the performance of PEMWE strongly depends on the properties of GDL. It has to possess a low resistant micro porous structure and optimal hydrophobicity. The traditional GDLs broadly used in PEM fuel cells are based on carbon

materials - carbon blacks (mainly XC72), carbon fibers, nanotubes etc. [1]. In order to provide the required hydrophobicity, different agents such as polytetrafluoroethylene (PTFE) [2-4], polyvinylidene fluoride (PVDF) [5], fluorinated ethylene propylene (FEP) are used [6-7]. The GDL preparation includes mixing of carbon with the hydrophobic agent at optimized ratio, spreading of the obtained emulsion on an electrically conductive carrier, drying, and thermal treatment at elevated temperature to form a homogeneous porous layer. The commercially available GDLs based on carbon black XC72 provide excellent electrical conductivity and highly developed surface area but are not stable at the operative potentials of PEM water electrolysis (generally above 1.8 V). At such high anodic potentials the carbon is easily oxidized to  $CO_2$  leading to lose of electrical conductivity, decrease of the catalyst active surface area, gradual decomposition of the anode, and degradation of the whole MEA.

The aim of this work was to develop a new gas diffusion layer, stable at the high anodic potentials typical for the oxygen evolution reaction in PEM water electrolysis. The chosen material for the replacement of carbon is a nonstoichiometric titanium oxide known under the commercial name Ebonex® (Atraverda, UK) having excellent electrical conductivity and high stability to oxidation.

---

\* To whom all correspondence should be sent:  
E-mail: gal.rusev@gmail.com

## EXPERIMENTAL

*Catalyst*

The novel gas diffusion electrode was prepared using a commercial product Ebonex® (Atraverda, UK), which is a mixture of Magneli phase titanium oxides with common formula  $Ti_nO_{2n-1}$ . This material has unique properties among which an electrical conductivity closes to that of the metals ( $\approx 1.103 \text{ S.cm}^{-1}$ ) and corrosion resistance approaching that of ceramics both in acid and in alkaline media [8]. A disadvantage of Ebonex in view of its application as a GDL is the large size of the particles ( $5\mu\text{m}$ ) resulting in a low surface area ( $4 \text{ m}^2.\text{g}^{-1}$ ). To reduce the particles size, the commercial product was treated mechanically in a planetary ball mill for 40 h. The obtained much finer powder (particle size in the range 40-60 nm) was mixed with isopropanol and stirred with a magnetic stirrer at temperature of  $60^\circ\text{C}$  until a homogeneous suspension was formed. After that a polytetrafluoroethylene emulsion (Teflon®, DuPont,  $0.95\text{g.ml}^{-1}$ ) was added drop wise to achieve Ebonex/PTEF ratio 70/30 wt. %. The obtained paste was spread over a carbon cloth (DeNORA), dried at  $80^\circ\text{C}$  for 30 min and weighted. The procedure was repeated to obtain a loading of  $10 \text{ mg.cm}^{-2}$ . The next step was sintering at  $360^\circ\text{C}$  for 30 minutes to create the required porous structure of the layer. To prepare a MEA for PEM water electrolysis, thus obtained GDL was loaded with  $5 \text{ mg.cm}^{-2}$  Ebonex-supported Pt catalyst forming the oxygen evolution electrode (anode) which is the working electrode under study. The cathode (hydrogen evolution electrode) was a commercial electrode with a carbon-based GDL and Pt/C catalyst (E-TEK, 40 wt. % Pt) with the same loading. Both electrodes were hot pressed on a proton conductive polymer electrolyte membrane Nafion® 117 (DuPont, USA) applying the laboratory procedure described elsewhere [9]. The evaluation of the newly developed GDL was performed by cyclic voltammetry and steady state polarization techniques in a self made laboratory cell, consisting of two gas compartments where the reactions of hydrogen and oxygen evolution take place, separated by the MEA and a reference electrode (E-TEK 40 wt. % Pt) situated in the  $\text{H}_2$  compartment. The electrochemical tests were performed at  $20^\circ\text{C}$  (room temperature) and  $80^\circ\text{C}$  (typical operative temperature for PEMWE).

All electrochemical measurements were carried out with a commercial Galvanostat/ Potentiostat POS 2 Bank Elektronik, Germany.

## RESULTS AND DISCUSSION

In the last years Ebonex has been intensively studied as an alternative catalyst support [9]. In addition to the already mentioned unique properties, namely the high electrical conductivity and corrosion resistance, this material due to its hypo-d-electron character is capable to interact with hyper-d-electron metals such as Pt, Ni, Co etc. which results in well defined synergetic catalytic effects [9, 10]. Since the commercial product has low surface area, usually a mechanical treatment is necessary in order to reduce the size of the particles. The exact parameters of this treatment (gaseous atmosphere, temperature, duration, etc.) have been optimized to achieve a reliable process leading to essential decrease in the size of the particles and a tenfold increase in the surface area, measured by BET method (from 4 to  $40 \text{ m}^2.\text{g}^{-1}$ ). These effects, highly desirable when Ebonex is used as catalytic support, are also required for its application as a replacement of the commonly used carbon materials in GDLs.

Fig.1 and fig. 2 present the XRD spectra and the SEM images of the as-obtained and the mechanically treated Ebonex, respectively. The results show that the crystallinity of the material after 40 hours of mechanical activation sustains, while the size of the particles is visibly reduced.

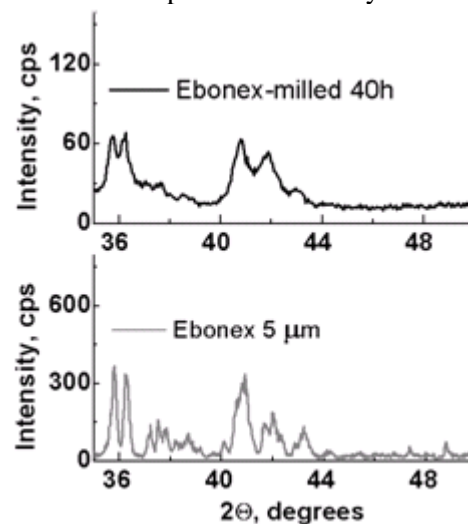


**Fig. 1.** XRD spectra of Ebonex before and after 40 hours mechanical treatment

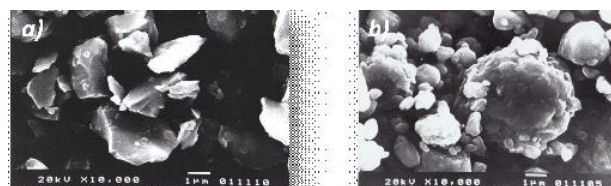


**Fig. 2.** SEM images of Ebonex a). before and b). after 40 hours mechanical treatment

The Ebonex-based gas diffusion layer was prepared using the mechanically treated material mixed with PTFE in accordance with the already described procedure. A membrane electrode assembly with an anode (as working electrode), containing this novel GDL and a cathode (a counter electrode) with a standard carbon-based GDL, both having catalytic loading of  $0.5 \text{ mgPt.cm}^{-2}$  was tested in the laboratory PEM electrolysis cell presented schematically in fig. 3.

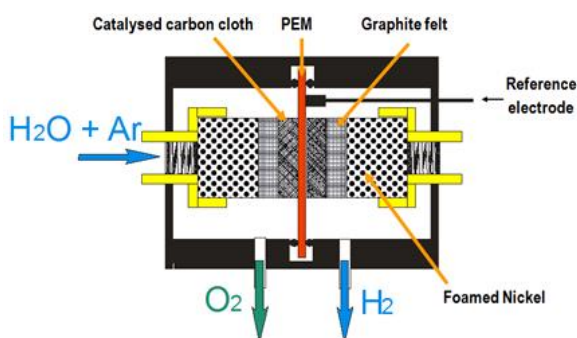


**Fig. 3.** Principle scheme of the laboratory PEM water electrolyser

Fig. 4 presents the cyclic voltammetry curves recorded in the potential range of water electrolysis (-0.1 to 1.8V) after different numbers of potential cycles. All current peaks typical for Pt are well depicted at the corresponding potentials in the hydrogen and oxygen ranges. The shape of the curve is characteristic for an electrode with comparatively low porosity and a crystalline Pt catalyst with a prevailing (111) orientation. The latter has been proven previously by XRD and SEM analysis [11], while the former can be explained by the high density and comparatively low specific surface area of Ebonex ( $3600 \text{ kg.cm}^{-3}$  and  $1\text{-}3 \text{ m}^2.\text{g}^{-1}$  compared to  $264 \text{ kg.cm}^{-3}$  and  $254 \text{ m}^2.\text{g}^{-1}$  for carbon black XC72) [8]. The area under the CV curve and its shape do not change with the potential cycling (the curves of the 10<sup>th</sup> and 100<sup>th</sup> cycles are identical). At the same time, the anodic current peak at about 0.7-0.8V related to oxidation of carbon, that is characteristic for electrodes with carbon-based GDLs, is not seen on the CV.

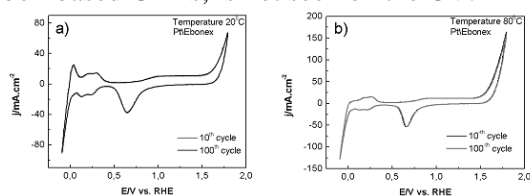


**Fig. 4.** CV curves of Pt/Ebonex anode with Ebonex-based GDL after different number of potential cycles in the range -0,1 to 1,8V, scan rate  $100 \text{ mV.s}^{-1}$  and working temperature a)  $20^\circ\text{C}$  and b)  $80^\circ\text{C}$

The experimental data demonstrate stable performance of the anode under study at the applied aggressive operative conditions – oxygen in presence of moisture and high temperature.

To investigate the electrode stability at close to real operative conditions and to verify the protective properties of the new GDL (expected and demonstrated by the cyclic voltammetry results), potentiostatic tests at high anodic potentials of intensive oxygen evolution were performed. In fig. 5 are compared the anodic polarisation curves obtained at 1,8 V at room and elevated temperatures. The current reaches quickly a stable value and does not change further during the test duration. The electrode performance at  $80^\circ\text{C}$  is superior due to the lower activation energy of the process. The inset graph presents the performance of the electrode for a period of 24 hours at this typical PEMWE temperature. No changes in the curve and degradation phenomena both of the catalyst and GDL are registered, confirming the stability of thus prepared MEA. On the other hand, the obtained values of the current density are lower in comparison to those obtained previously for the same catalyst deposited on a carbon-supported GDL [9].

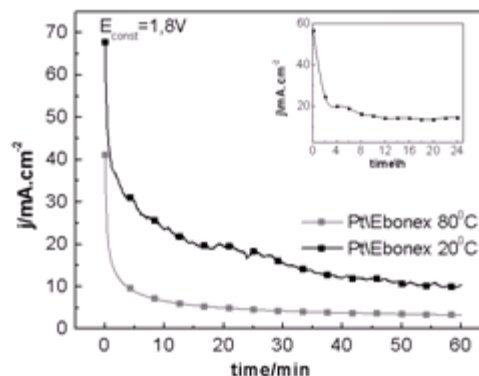


**Fig. 5.** Potentiostatic polarization curves of the electrode under study at different temperatures and test duration

In order to estimate the real active surface available for the electrochemical reaction of interest, the morphological factor ( $f$ ) serving as a measure for the unusable part of the catalyst was calculated. The approach firstly suggested by da Silva [12, 13] is based on a repetitive potential cycling in the water window potential range (-0.1 to 1,8 V) at varying scan rate ( $5 - 300 \text{ mV.s}^{-1}$ ) followed by determination of the anodic current density ( $j_a$ ) at fixed potential, just before the beginning of intensive oxygen evolution. The morphology factor is determined from the dependence of the current density on the scan rate ( $v$ ). The slope of the linear section of the curve at

low scan rates is a measure for the capacity of the total active electrode surface ( $C_t$ ), while the slope at high cycling rates represents the easily accessible electrode surface ( $C_{ext}$ ). The difference between both values gives the capacity of “internal”, hardly accessible part of the catalytic film ( $C_{int}$ ) and the ratio  $C_{int}/C_t$  determines the morphology factor  $f$ .

The obtained experimental data of  $j_a$  (at potential of 1,6V) as function of scan rate are illustrated in fig. 6. There are two well distinguished linear regions of the curve, suggesting that at high scan rates part of the electrode surface is not accessible for the reaction. The calculated value of the morphology factor is about 0,7. This means that only about 30% of the Pt in the catalytic layer is used efficiently. For comparison, the typical catalyst utilization in MEA with a carbon-based GDL is more than 60% [14].

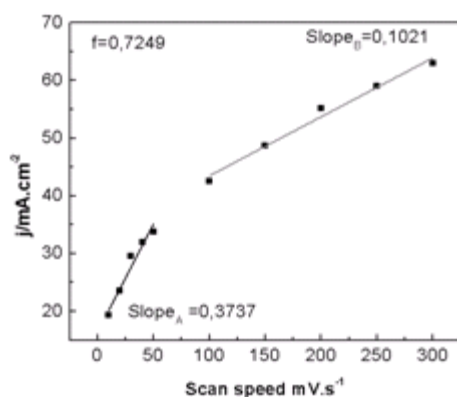


**Fig. 6.** Dependence of current density  $j_a$  at 1.6 V on the scan rate  $v$

The results obtained prove the stability of the developed Ebonex-based GDL to oxidation at the conditions of PEM water electrolysis. The low current density and the calculated values of the morphology factor however, support the CV data implying insufficient porosity. To improve further the properties of this novel GDL, it is necessary to optimize the process of sintering during which the porous structure is formed.

## CONCLUSION

A new GDL based on Ebonex, suitable for application in PEMWE was developed. The research performed proved a stable electrochemical behavior at high anodic potentials. The new gas diffusion layer prevents degradation of the anode, ensuring a reliable work of MEA and long term

service of the electrolyser. The obtained results established insufficient porosity of the electrode which requires further optimisation of GDL preparation procedure in order to improve the utilization of catalyst and thus, the efficiency and cost of electrolysis.

**Acknowledgements:** The presentation of the research results has been supported by Bulgarian Ministry of Youth, Education and Science, project BG 051PO001-3.3.05/0001, cont № D002-170

## REFERENCES

- 1 Guo-Bin Jung, Wei-Jen Tzeng, Ting-Chu Jao, Yu-Hsu Liu, Chia-Chen Yeh, Applied Energy (Available online 1 October 2012).
- 2 J. Ahn, R. Holze, J. Appl. Electrochem., 22, 11167 (1992).
- 3 D. Brever, R. Rogers, M. Bradke, J. Power Sources, 63, 193 (1996).
- 4 G. G. Park, Y. J. Sohn, T. H. Yang, Y. G. Yoon, W. Y. Lee, C. S. Kim, J. Power Sources, 131, 182 (2004).
- 5 I. Cabass, Y. Yuan, X. Xu, US patent No 5783, 325 (1998).
- 6 C. Lim, C. Y. Wang, Electrochim. Acta, 49, 4149 (2004).
- 7 R. Borup, D. Wood, J. Davey, P. Welch, F. Garzon, DOE hydrogen program review (2006)
- 8 E. Antolini, E. R. Gonzalez, Solid State Ionics, 180, 746 (2009).
- 9 A. Stoyanova, G. Borisov, E. Lefterova, E. Slavcheva, Int. J. Hydrogen Energy, 37, 16515 (2012).
- 10 A. Stoyanova, E. Lefterova, V. Nikolova, P. Iliev, I. Dragieva, E. Slavcheva, Bulg. Chem. Commun., 42, 167 (2010).
- 11 E. Lefterova, A. Stoyanova, G. Topalov, D. Radev, E. Slavcheva, in: “Nanoscience & Nanotechnology“ - Nanostructured Materials Applications and Innovation Transfer, Vol. 10, E. Balabanova, I. Dragieva (Eds.), “BPS” Ltd., Sofia, Bulgaria, 2010, p. 105
- 12 M. D. De Silva, L. A. De Faria, J.F.C. Boodts, Electrochim. Acta, 47, 395 (2001).
- 13 E. Slavcheva, V. Nikolova, T. Petkova, E. Lefterova, I. Dragieva, T. Vitanov, E. Budevski, Electrochim. Acta, 50, 5444 (2005).
- 14 G. Borisov, A. Stoyanova, E. Slavcheva, E. Lefterova, C. R. Acad. Bulg. Sci., 65, 919 (2012).

## НОВ НЕСЪДЪРЖАЩ ВЪГЛЕРОД ГАЗОДИФУЗИОНЕН СЛОЙ ЗА АНОДИ В ПЕМ ВОДНА ЕЛЕКТРОЛИЗА

Г. Р. Борисов\*, А. Е. Стоянова, Е. Д. Лефтерова, Е. П. Славчева

*Институт за Електрохимия и Енергийни Системи - БАН,*

*ул. Г. Бончев бл. 10, 1113 София, България*

Постъпила на 11 януари, 2013 г.; преработена на 30 юни, 2013 г.

(Резюме)

Настоящата работа е базирана на разработването на иновативен газодифузионен слой, приложим във водните електролизатори с полимерна протонпроводяща мембрана. Традиционно използваните въглеродни газодифузионни слоеве са заменени със слоеве, базирани на нестехеометричен титаниев оксид Magneli фаза. Новият газодифузионен слой (ГДС) е интегриран в мембранен електроден пакет (МЕП), който съдържа високо активен платинов катализатор и полимерна протонпроводяща мембрана. МЕП е охарактеризиран лабораторно в ПЕМ електролизна клетка посредством методите на цикличната волтаметрия и различни поляризационни техники. Установено е, че новият ГДС има добра електрическа проводимост и стабилно поведение при високи анодни потенциали. Стойността за морфологичния фактор на платиновия катализатор обаче показва, че е необходима по-нататъшна оптимизация на структурата на ГДС, с цел увеличаване на порьозността му и съответно подобряването на доставката на реагент до катализатора и неговото по-пълно оползотворяване.

## MEA with carbon free Pt-Fe catalysts and gas diffusion layers for application in PEM water electrolysis

A.E. Stoyanova\*, G.R. Borisov, E.D. Lefterova, E.P. Slavcheva

*Institute of Electrochemistry and Energy Systems, Bulgarian Academy of Sciences, Acad. G. Bontchev Str., Bl. 10, 1113 Sofia, Bulgaria*

Received September 10, 2012; revised November 15, 2012

Mono and bimetallic compositions containing Pt and Pt-Fe supported on Magneli phase titania (Ebonex®) are integrated in membrane electrode assemblies with novel carbon-free gas diffusion layers and investigated in relation to their electrocatalytic activity and stability toward the oxygen evolution reaction in PEM water electrolysis. The investigated Pt-Fe/Ebonex exhibits enhanced efficiency compared to pure Pt with the same catalytic loading due to formation of surface oxides and electronic hypo hyper-d-electron interactions between the hypo-d metallic components (Fe and Ti), on one hand and the hyper-d Pt, on the other hand. The utilization of the catalysts is assessed applying a repetitive potential cycling at varying scan rate to determine the morphology factor  $f$ , serving as a measure for the unusable part of the catalyst. The results obtained show that the part of the Pt-Fe/Ebonex not accessible for the electrochemical reaction, is less than that for the pure platinum catalyst. The Ebonex-based GDL has a good electrical conductivity and is more resistant to oxidation than a commercial carbon black GDL which has a positive impact on the stability of the catalyst, the oxygen electrode, and the MEA.

**Keywords:** PEM water electrolysis, oxygen evolution reaction, Pt, Fe, Ebonex, GDL

### INTRODUCTION

The electrocatalysts play an important role in the electrochemical energy systems such as hydrogen generators based on electrolysis of water in polymer electrolyte membrane (PEM) cells. In this regard, the development of highly active and durable catalysts, particularly for the oxygen evolution reaction (OER) is one of the most important issues with great impact both on the efficiency and the cost of PEM water electrolysis (PEMWE). To date, Pt-based materials are the most successful PEMWE catalysts employed in the practice. However, even these expensive and highly active materials are not capable to accelerate significantly the naturally sluggish OER kinetics. There are intensive research efforts to reduce or replace Pt with less expensive metal alloys in form of nanoparticles [1-5]. One of the main approaches is the development of composite catalysts with increased activity through realization of synergetic effects between the metallic components of the catalyst and the catalytic substrate. In this way, partial or total replacement of Pt with cheaper metals can be achieved without sacrifice of OER efficiency.

Another successful approach to reduce the cost of catalysis is the dispersion of the catalytic nanoparticles on proper supports, ensuring highly developed active surface and thus, better utilization of Pt. It is commonly recognized that the supporting material plays a critical role in both the activity and durability of the catalyst. Carbon and graphite are the most widely used catalyst supports, offering excellent electrical conductivity and large active surface (up to 200-300 m<sup>2</sup>.g<sup>-1</sup>). However, the majority of the C-based supporting materials are not stable at the aggressive operating conditions of PEMWE anode (high anodic potentials, moisture, oxygen, enhanced temperature) which in turn often leads to gradual degradation of the anode and severe performance losses [6]. Therefore, in order to improve durability of PEM water electrolysis cells, it is necessary to explore novel more stable alternatives.

The gas diffusion layer (GDL) is another essential component of the polymer electrolyte membrane assembly. It distributes the reactant over the catalyst layer and conducts the electrons from the reaction sites to the outer electric circuit. Therefore, the structure of GDL is also essential for MEA performance.

It has been shown recently that nonstoichiometry Magneli phase titania is a good candidate as catalyst support. Our previous results

---

\* To whom all correspondence should be sent:  
E-mail: antonia.stoyanova@gmail.com

have demonstrated that the partial substitution of Ebonex-supported Pt catalyst with Fe increases the mass activity toward oxygen evolution reaction (OER) in PEM water electrolysis. The supporting material of choice is known for its stable behaviour and good corrosion resistance at the high anodic potentials of intensive oxygen evolution and its ability to contribute to the catalytic efficiency via electronic interactions with the metallic components (the so called strong metal support interaction, SMSI) [7]. However, since these composite Ebonex-supported catalysts were spread onto carbon GDL, gradual degradation of the anode in the course of electrolysis was observed [8]. The objective of this work is to investigate the efficiency and reliability of Pt-Fe/Ebonex as anode catalyst integrated in MEA with a novel carbon-free GDL, prepared by mixing Ebonex powder with a hydrophobic agent polytetrafluoroethylene (PTFE, Teflon®).

## EXPERIMENTAL

The synthesis of the chosen composite catalysts consisted in direct selective grafting of the metals from acetylacetonate precursors ( $M((C_5H_7O_2)_n)_m$  or M-acac (M = Pt, Fe). The substrate used was a commercial Ebonex powder (non-stoichiometric titanium oxide with common formula  $Ti_nO_{2n-1}$ ) with average particle size 5  $\mu m$ . Before synthesis it was subjected to mechanical treatment in a planetary ball mill for 40h, resulting in reduced particle size and increased surface. The metallic part in each of the catalysts was 20 wt. % while the Pt:Fe weight ratio in the precursors was 1:1. The preparation procedure included two steps. The first one was the pretreatment of the support and the precursors using magnetic stirrer and ultrasonic bath, their mixing and heating at temperature 60°C until a fine gel was obtained. In the second step of the synthesis, the mixture was heated in inert atmosphere at temperature at 200 °C (for Pt/Ebonex) and 250°C (for Pt-Fe/Ebonex. The reduction atmosphere was 100% H<sub>2</sub> and 95% Ar + 5% H<sub>2</sub>, respectively.

The composition, morphology and surface structure of the prepared materials were studied by bulk and surface analysis, such as EDX, XRD, and SEM. The catalysts composition was examined by energy-dispersive X-ray spectroscopy (EDX) as a part of scanning electron microscope appliance. XRD spectra were recorded by X-ray diffractometer Philips APD15. The diffraction data were collected at a constant rate of 0.02 °.s<sup>-1</sup> over an angle range of  $2\theta = 10 - 90$  degrees. The size of Pt

crystallites was determined by Scherrer equation [9]. The morphology and surface structure were studied by scanning electron microscopy (SEM) using a ZEISS GEMINI 982 microscope with an acceleration voltage 10 kV.

The electrochemical tests were performed on membrane electrode assemblies (MEAs) with a commercial polymer membrane Nafion 117 (Alfa Aesar), as an electrolyte. MEA was prepared by hot pressing of the electrodes for hydrogen and oxygen evolution on both sides of the membrane using a 5% Nafion solution as a binder. The electrodes with geometric area of 0.5 cm<sup>2</sup> had a double layered structure, consisting of a hydrophobic backing layer (GDL) and an active catalytic one. The synthesized Ebonex-supported catalysts were used to prepare the electrode for the oxygen evolution reaction (OER). A commercial E-TEK catalyst containing 20% Pt on carbon support was used for the reference (RE) and the hydrogen (HE) electrodes.

The catalytic layers were spread upon the backing one as an ink (catalyst particles mixed with diluted Nafion ionomer) at several steps as after each one the electrode was dried for 30 min at 80°C. The procedure was repeated until a metal loading of 0.5 mg.cm<sup>-1</sup> was reached. The gas diffusion layer for the anode was prepared mixing Ebonex with 30 wt.% Teflon emulsion as described elsewhere [10].

The performance characteristics of the prepared MEA were investigated in a self made laboratory PEM electrolytic cell, consisting of two gas compartments where hydrogen and oxygen evolution take place, separated by the membrane electrode assembly under study. A reference electrode was situated in the hydrogen evolution compartment. The catalytic activity of the prepared catalysts was studied using the techniques of cyclic voltammetry and steady state polarization at temperatures of 20°C and 80°C. All electrochemical measurements were carried out with a commercial Galvanostat/Potentiostat POS 2 Bank Elektronik, Germany.

## RESULTS AND DISCUSSION

The XRD spectra of the synthesized Pt/Ebonex and Pt-Fe/Ebonex catalysts are presented in Figure 1. For easier phase identification the spectrum of the Ebonex support is also included. In all spectra the characteristic peaks of the Magneli phase titanium oxide are registered. The typical fcc Pt peaks that appear on the spectrum of the pure Pt/Ebonex shift significantly to higher diffraction angles with Fe addition. The new positions are closer to the PtM<sub>3</sub>

crystal phases than to PtM (M=Fe) [11]. The cell parameter decreases from 3.916 Å for Pt/Ebonex to 3.769 Å for Pt-Fe/Ebonex (Table 1).

**Table 1.** Calculated Pt crystallite size and cell parameters

Sample	Pt/Ebonex	Pt-Fe/Ebonex
Crystallite size $D_{111}$ , nm	14	6
Pt cell parameter, Å	3.916	3.769

The results indicate that most of Fe atoms are incorporated in the Pt crystal cell. Additionally,  $Fe_3O_4$  phase is also identified.

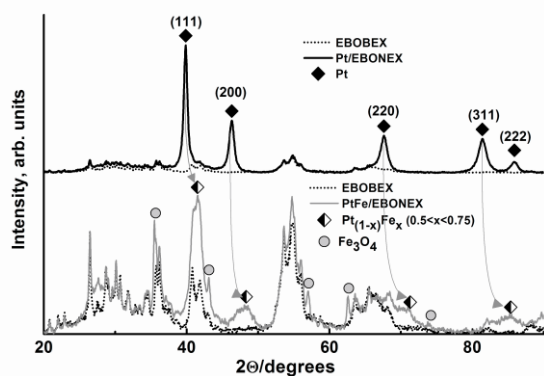


**Fig. 1.** XPD spectra of the composite catalysts

SEM images of the investigated catalysts are presented in Figure 2. It can be seen that the catalytic particles are uniformly distributed on the Ebonex- surface. There is a correlation between the results of the XRD spectra and SEM images. For Pt/Ebonex (Fig. 2a) the size of Pt- particles is larger than this of Pt-Fe (Fig. 2b). Moreover Pt-Fe particles are less contrast due to the presence of  $Fe_3O_4$  phase of the surface.

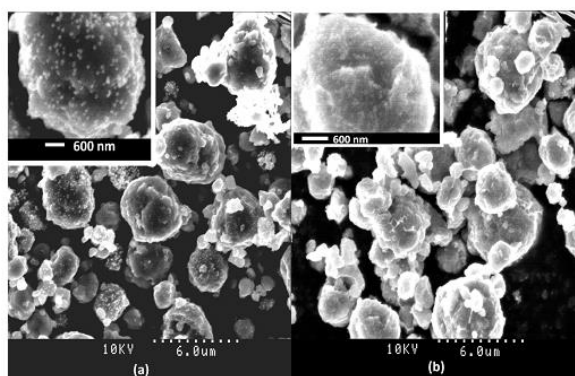


**Fig. 2.** SEM images of the composite catalysts: (a) Pt/Ebonex; (b) Pt-Fe/Ebonex

The composition of the synthesized materials was determined by EDX analysis and is presented in Table 2.

**Table 2.** EDX data for Pt/Ebonex and Pt-Fe/Ebonex

Catalyst	Pt/Ebonex		Pt-Fe/Ebonex	
	Weight %	Atomic %	Weight %	Atomic %
Ti	76.8	94.6	81.7	88.3
Pt	23.2	5.3	8.0	2.2
Fe	-	-	10.3	9.5

The determined Pt:Ti ratio in Pt/Ebonex is 0.23:0.77. The metallic part in Pt-Fe/Ebonex (Pt and Fe) is around 18 wt. % and the ratio between both metals is Pt:Fe $\approx$ 0.8:1, i.e. almost identical to the ratio of both metals in the precursors. The cyclovoltammetry tests at temperature of 20°C were performed to obtain a qualitative information about the nature of the processes occurring on the catalyst surface (Fig.3).

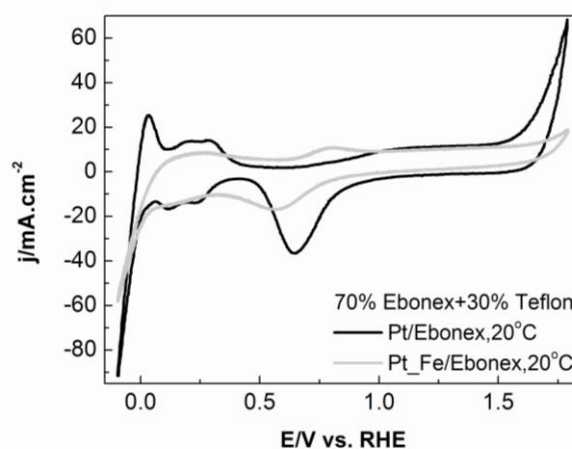
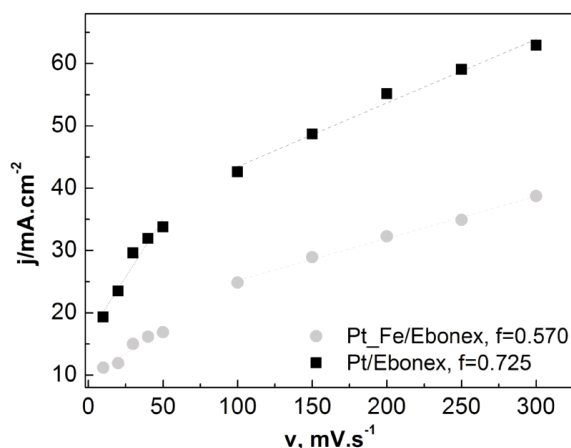


**Fig. 3.** CV curves of Pt/Ebonex and Pt-Fe/Ebonex at 20°C and 100  $mV \cdot s^{-1}$

On the CV curve of Pt/Ebonex all current peaks typical for Pt are well represented at the corresponding potentials in the hydrogen and oxygen regions. The shape of the curve is characteristic for an electrode with comparatively low porosity and a crystalline Pt catalyst with a prevailing (111) orientation [10]. At the same time, the characteristic anodic current peak at about 0.7-0.8V which almost always presents on CVs of electrodes with carbon-based GDLs does not appear in this case. The CV of the Pt-Fe/Ebonex shows two nearly reversible anodic and cathodic peaks situated in the potential range 0.75 – 0.80 V. These peaks are prescribed to the redox  $Fe^{3+}/Fe^{2+}$  transition. Their existence corresponds well with the results from XRD and the previously published XPS analysis [8], indicating an existence of  $Fe_3O_4$  phase.

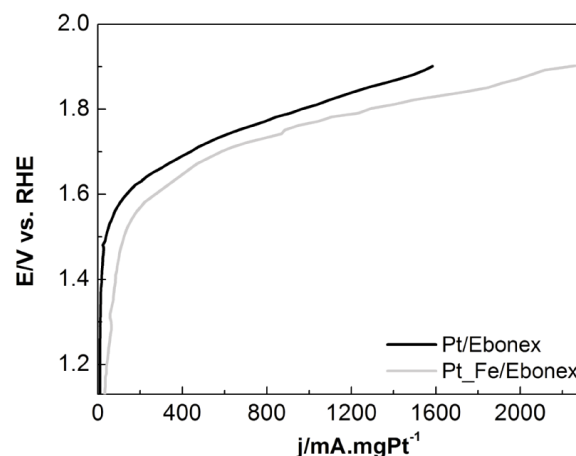
One of the goals in this study was to estimate the real active surface area of the anode when the conventional carbon based GDL in the MEA is replaced by GDL consisting of Magnelli phase

titanium. This was done determining the value of morphological factor ( $f$ ) which is a measure for the unusable part of the catalyst. The approach, firstly suggested by de Silva is based on a repetitive potential cycling in the water window potential range (0 - 1.8 V) at varying scanning rate (5 – 300  $\text{mV}\cdot\text{s}^{-1}$ ), followed by determination of the anodic current density ( $j_a$ ) at fixed potential, just before the beginning of intensive oxygen evolution [12]. Fig 4 presents the  $j_a/v$  plot of both catalysts. As seen, there are two linear sections with different slopes at low and high potential scan rates. This is an indication that at high rates, respectively at the high operative overvoltages, part of the catalytic loading is not used for the electrochemical reaction of interest. The determined morphological factors are 0.725 for Pt/Ebonex and 0.570 for Pt-Fe/Ebonex. These values are significantly higher than those for Pt/Ebonex catalyst integrated in MEA with GDL containing carbon black Vulcan XC72 [13]. The corresponding utilization of platinum in Pt/Ebonex is only about 30%, while the morphological factor for the bi-metallic catalyst indicates a slightly better utilization. The results can be explained with the low surface area of the catalysts, spread on GDL with insufficient porosity.



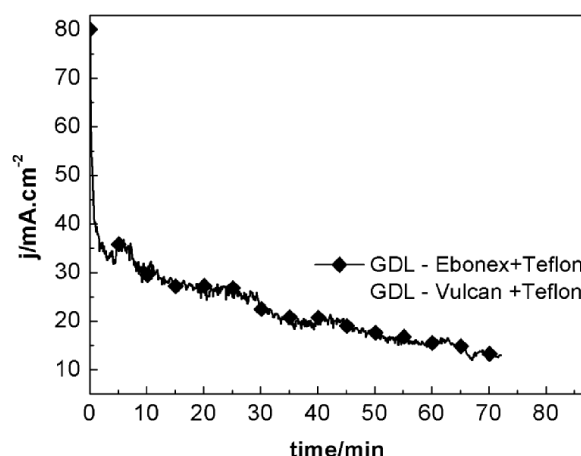
**Fig. 4.** Dependence of current density  $j_a$  at 1.6 V on the potential scan rate  $v$

Figure 5 shows the results obtained from polarization experiments carried out at the typical PEMWE working temperature of 80°C. It should be noted that the content of Pt in the bimetallic Pt-Fe/Ebonex is essentially reduced compared to pure Pt/Ebonex, leading to much lower noble metal loading. That is way, for better comparison the anodic current of the oxygen evolution reaction was normalised relative to the Pt content and presented as mass activity,  $j_m / \text{mA}\cdot\text{mgPt}^{-1}$ .



**Fig. 5.** Polarization curves of Pt/Ebonex and Pt-Fe/Ebonex at 80°C and scan rate  $1 \text{ mV}\cdot\text{s}^{-1}$

The polarization curves demonstrate an enhanced efficiency of the binary Pt-Fe/Ebonex. It can be seen that the OER on the bimetallic Ebonex-supported catalyst starts at lower potentials compared to pure Pt. Similarly, an improved efficiency of OER in presence of Pt-Fe/Ebonex was found previously when these catalysts were integrated in MEA with carbon-based GDL. The effect was prescribed to occurrence of hypo-hyperd-electron interaction between Pt and Fe, leading to changes in the electron density of Pt d-orbital [8]. The data in Table 1 show that in the recent case, structural effects and geometry factors (smaller particle size, respectively the higher active surface area available for the electrochemical reaction) also contribute to the increased efficiency of Pt-Fe/Ebonex. An additional positive effect of the second metallic component, related to the cost of catalysis, is the nearly double reduction of Pt-loading.



**Fig. 6.** Potentiostatic polarization curves obtained at 1.8V and 80°C

Having in mind the stable behaviour and good corrosion resistance of Ebonex at the high anodic

potentials of intensive oxygen evolution it was to be expected that the replacement of carbon in the GDL with Ebonex should increase additionally the anode stability and thus, the MEA durability. In the research presented herein, this effect was verified. It is illustrated in Fig. 6, presenting durability tests of anodes with identical catalytic layers spread on different (carbon- and Ebonex-based) GDLs.

The results confirm the suitability of Ebonex as a reliable electrode material at aggressive operative conditions of intensive oxygen evolution, moisture, and high temperature. This conductive oxide is not only an attractive alternative of carbon as catalytic support but can be also considered as a promising material for fabrication of gas diffusion layers with specific application in PEMWE.

### CONCLUSIONS

The bimetallic Pt-Fe catalyst dispersed on mechanically treated Ebonex support and integrated in anode with a carbon-free GDL possess higher mass activity toward oxygen evolution in PEM water electrolysis than pure Pt, resulting from realization of electronic interactions between the components of the catalyst and geometry factors related to the size of the catalyst crystallites, the increased active surface, and the improved catalyst utilization. A realization of synergetic effect as a result of hypo-hyper-d-electronic interactions between the catalyst and the support, which further increases the OER efficiency, is also assumed. The used newly developed Ebonex-based GDL is resistant to oxidation and degradation phenomena which has an additional positive impact on the stability of the anode and durability of the MEA

**Acknowledgment:** The authors would like to acknowledge the financial support of Bulgarian Ministry of Youth, Education and Science, project BG 051PO001-3.3.05/0001, contract № DO2 –552 for dissemination of the research results.

### REFERENCES

1. P.J.S. Jikovskiy, I. Panas, A. Alberg, S. Romani, D. J. Schiffrin, *J. Am. Chem. Soc.*, **133**, 19432 (2011)
2. L. Profeti, E. Ticianelli, E. Assaf, *Fuel*, **87**, 2076 (2008).
3. N.R. Elezovic, B.M. Babic, V.R. Radmilovic, Lj.M. Vracar, N.V. Krstijajic, *Electrochim. Acta*, **54**, 2402 (2009).
4. P. Millet, N. Dragoie, S. Grigoriev, V. Fateev, C. Etievant, *Int. J. Hydrogen Energy*, **34**, 4974 (2009).
5. E. Slavcheva, V. Nikolova, T. Petkova, E. Lefterova, I. Dragieva, T. Vitinov, E. Budevski, *Electrochim. Acta*, **50**, 5444 (2005)
6. M. Mathias, M. Makharia, H. Gasteiger, J. Conley, T. Fuller, C. Gittelmann, S. Kocha, D. Miller *et al.*, *Interface*, **14**, 24 (2005).
7. E. Antolini, E.R. Gonzalez, *Solid State Ionics*, **180**, 746 (2009).
8. A. Stoyanova, G. Borisov, E. Lefterova, E. Slavcheva, *Int. J. Hydrogen Energy*, **37**, 16515 (2012).
9. H.P. Klug, L. Alexander (Eds.), *X-Ray Procedures for Polycrystalline and Amorphous Materials*, Wiley/Interscience, New York, 1980.
10. G. Borisov, A. Stoyanova, E. Lefterova, E. Slavcheva, *Bulg. Chem. Comm.* (in press)
11. K. Kim, S. Lee, T. Wiener and D. Lynch, *J. Appl. Phys.*, **89**, 244 (2001).
12. M.D. de Silva, L.A. De Faria, J.F.C. Boodts, *Electrochim. Acta*, **47**, 395 (2001).
13. G. Borisov, A. Stoyanova, E. Slavcheva, E. Lefterova, *C. R. Acad. Bulg. Sci.*, **65**, 919 (2012).

## МЕП С НЕСЪДЪРЖАЩИ ВЪГЛЕРОД Pt-Fe КАТАЛИЗАТОР И ГАЗОДИФУЗИОНЕН СЛОЙ ЗА ПЕМ ВОДНА ЕЛЕКТРОЛИЗА

А. Е. Стоянова\*, Г. Р. Борисов, Е. Д. Лефтерова, Е.П. Славчева

*Институт за електрохимия и енергийни системи - БАН, ул. Акад. Г. Бончев бл. 10, 1113 София, България*

Постъпила на 10 септември 2012 г.; Коригирана на 15 ноември, 2012 г.

(Резюме)

Моно- и биметални композиции, съдържащи Pt и Pt-Fe върху носител Ебонекс са интегрирани в мембранни електродни пакети (МЕП) с нов, несъдържащ въглерод газодифузионен слой. Изследвани са тяхната електрокаталитична активност и стабилност по отношение на реакцията на отделяне на кислород в ПЕМ водна електролиза. Синтезираните Pt-Fe/Ebonex катализатори показват увеличена ефективност в сравнение с чистата Pt при едно и също каталитично натоварване, дължащи се на формиране на повърхностни оксиди и hupo hyper-d-електронни взаимодействия между hupo-d металните компоненти (Fe и Ti) от една страна и hyper-d Pt от друга. За оценка на използваемостта на катализатора е изчислен морфологичния му фактор (f) чрез снемане на циклични криви в една и съща потенциална област при различни скорости на сканиране на потенциала. Резултатите показват, че недостъпната за електродната реакция повърхност за Pt-Fe/Ebonex е по-малка от тази за катализатора, съдържащ чиста платина. Газодифузионният слой, базиран на Ебонекс, има добра електропроводимост и е по-устойчив към окисление спрямо комерсиалния, съдържащ въглен, което влияе положително върху стабилността на катализатора, кислородния електрод и МЕП.

# Electropolymerization of poly(3,4-ethylenedioxythiophene) layers in the presence of different dopants and their effect on the polymer electrocatalytic properties. Oxidation of ascorbic acid and dopamine

D. G. Filjova, G. P. Ilieva, V. Ts. Tsakova\*

*Institute of Physical Chemistry, Bulgarian Academy of Sciences, Acad. G. Bontchev Str., Bl. 11, 1113 Sofia, Bulgaria*

Received June 12, 2013; revised June 25, 2013

Electrochemical synthesis of poly(3,4-ethylenedioxythiophene) (PEDOT) is carried out in four different polymerization solutions. Three sulfonate-based dopants, i.e. dodecylsulfonate (SDS), polystyrenesulfonate (PSS) and poly(acrilamidopropane-sulfonate) (PAMPS), as well as the non-ionic surfactant polyoxyethylene-10-laurylether (PLE) in combination with LiClO<sub>4</sub> are used to obtain the polymer layers. The electrocatalytic performance of the four types of PEDOT-coated electrodes is investigated with respect to ascorbic acid (AA) and dopamine (DA) oxidation in phosphate buffer solution. It is found that the PEDOT/PLE layers are most suitable for the oxidation of ascorbate anions whereas the PEDOT/PSS-coated electrodes are most appropriate for the oxidation of the positively charged dopamine species. These results are commented in terms of possible hydrophobic/hydrophilic and/or electrostatic interactions occurring between the analyte molecules and the anion-doped PEDOT surface.

**Keywords:** PEDOT, ascorbic acid, dopamine, polyanions

## INTRODUCTION

Conducting polymers are often studied for electrocatalytic applications due to their intrinsic redox activity that supports the catalytic reactions. In the recent years a great number of studies were devoted to the involvement of conducting polymers in electroanalytical measurements for the detection of a variety of bioactive molecules that take part in the human metabolism, e.g. ascorbic and uric acids, glucose, neurotransmitters, drugs [1-4].

Poly(3,4-ethylenedioxythiophene) (PEDOT) is a conducting polymer with high electrochemical stability in aqueous solutions preserving its electrochemical redox activity in a large pH range [5,6]. For that reason it is most suitable for electroanalytical applications under physiological conditions and more specifically for the oxidation of bioactive compounds, e.g. dopamine (DA), ascorbic acid (AA), nicotinamide adenine dinucleotide, paracetamol, morphine etc. [3,4].

In general, the electrochemical and morphological properties of conducting polymer-coated electrodes depend on the electrochemical procedure for polymerization and the composition of the polymerization solutions [5,6]. The anions available in the electrolyte play a specific role and act as doping agents compensating the positive

electrical charge arising along the polymer chains in the course of their formation. They become incorporated and eventually immobilized in the polymer layer and specify to a great extent the morphology of the layer and the ionic exchange in the course of electrochemical redox transition. There are several papers exploring these effects in the case of PEDOT [7-12].

Most of the papers on the electrocatalytic activity and electroanalytical properties of PEDOT do not address the role of the dopant used during synthesis. The PEDOT layers are synthesized in a given environment (most frequently in the presence of polystyrenesulfonate, PSS) and no comparison is drawn between polymer layers obtained in the presence of various dopants.

In our former investigations we have demonstrated that PEDOT layers modified with copper crystalline species present sensitive electrode materials for the determination of DA (in the nanomolar concentration range) in the presence of excess (millimolar concentration) of AA [13,14]. The PEDOT layers were synthesized in the presence of inorganic perchlorate anions and the non-ionic surfactant PLE that is necessary to increase the solubility of the EDOT monomers in the polymerization solution [15, 16]. In the present study the synthesis of PEDOT is carried out in the presence of four different dopants – perchlorate anions combined with bulky anions, i.e. PSS, sodium dodecylsulfate (SDS) or poly(acrylamido-

\* To whom all correspondence should be sent:  
E-mail: tsakova@ipc.bas.bg

propane-sulfonate) (PAMPS) and the non-ionic surfactant polyoxyethylene-10-laurylether (PLE) in the presence of perchlorate anions.

The aim of the present investigation is to reveal the role of the doping agent and the thickness of the PEDOT layers for their electrocatalytic properties with respect to the electrooxidation of AA and DA. These two compounds are chosen not only for their practical importance in the electroanalysis of blood and urine but also due to the opposite charge of the corresponding species when dissolved in aqueous solution. It is expected that the surface of the PEDOT layers obtained in the presence of various dopants will have a different amount and type of surface charging. Thus charge selective interaction between the two oppositely charged analyte species and the charge-carrying surface of the PEDOT layers is expected to take place [17].

### EXPERIMENTAL

All electrochemical measurements were performed in a three-electrode set-up consisting of a glassy carbon electrode with surface area  $S = 0.08 \text{ cm}^2$ , a platinum plate counter electrode and a mercury/mercury sulfate ( $\text{Hg}/\text{Hg}_2\text{SO}_4/0.5 \text{ M K}_2\text{SO}_4$ ) reference electrode. All potentials in the text are referred to the saturated mercury sulfate electrode (MSE) ( $E_{\text{MSE}} = 0.66 \text{ V}$  vs. standard hydrogen electrode). All solutions were de-aerated with argon before the onset of the electrochemical measurements. The electrochemical measurements were carried out by means of a computer driven potentiostat/galvanostat (Autolab PGSTAT 12, Ecochemie, The Netherlands).

Each experiment consisted of several steps occurring consecutively in four electrochemical cells:

1. Electrochemical polymerization of EDOT was carried out in four different aqueous solutions consisting of 10 mM EDOT, 0.5 M  $\text{LiClO}_4$  and 34 mM anionic dopant (PSS, PAMPSA or SDS) or non-ionic surfactant (PLE). Polymerization of EDOT occurred at constant anodic potential,  $E_a = 0.37 \text{ V}$ , for different times. PEDOT layers with four different polymerization charges (1, 2, 4 and 8 mC) were used in this study. The polymerization charge is expected to be proportional to the polymer layer thickness with a  $240 \text{ mC cm}^{-2}$  per  $1 \text{ }\mu\text{m}$  ratio commonly used to estimate roughly the PEDOT thickness.

2. After synthesis the polymer coated electrodes were transferred in supporting electrolyte (0.5 M  $\text{LiClO}_4$ ) to measure their voltammetric behaviour.

3. Voltammetric measurements in phosphate buffer solution (PBS), consisting of 0.1 M  $\text{K}_2\text{HPO}_4$  and 0.1 M  $\text{KH}_2\text{PO}_4$ , ( $\text{pH} = 7.0$ ), were carried out for all PEDOT-coated electrodes in the absence of analytes in the buffer solution. These reference measurements were necessary for assessing the contribution of the current due to the intrinsic electroactivity of the PEDOT in the buffer solution. The scan rate used in these experiments was  $20 \text{ mV s}^{-1}$ .

4. Voltammetry in the presence of 1 mM DA or 1 mM AA was carried out in PBS for all synthesized PEDOT layers. The scan rate used for the voltammetric measurements was  $20 \text{ mV s}^{-1}$ .

### RESULTS AND DISCUSSION

#### Formation of PEDOT layers in the different polymerization solutions

PEDOT layers with four different polymerization charges were synthesized in each polymerization solution containing one of the four different dopants (PSS, SDS, PAMPS or PLE). Although the concentration of the EDOT monomers in all solutions was one and the same the polymerization rate was found to depend significantly on the type of the available dopants (Fig.1).

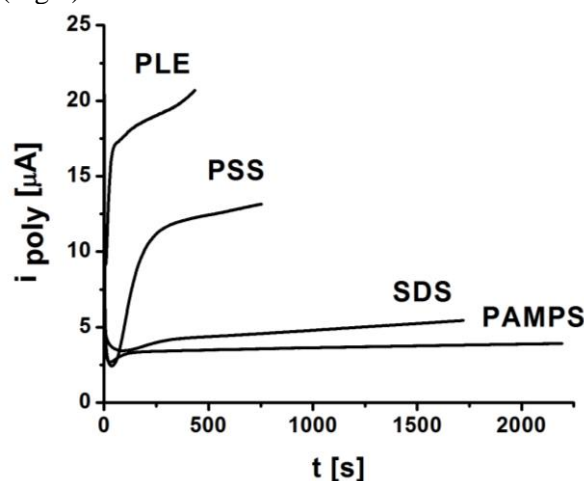


Fig. 1. Current transients obtained in the course of potentiostatic polymerization of EDOT at  $E=0.34 \text{ V}$  in the presence of different dopants.

The time necessary to obtain layers with one and the same polymerization charge (e.g. 8 mC) varied between 440 s (for the PLE solution) and 2200 s (for the PAMPS solution). Intermediate times were found for polymerization in the two remaining solutions – 750 s and 1730 s for PSS and SDS, respectively. Various factors, e.g. hydrophobic/hydrophilic interactions, extent of deprotonation (for PSS and PAMPS) and

competitive doping due to the available large excess of perchlorate ions in all four polymerization solutions may affect the rate of polymer formation. In fact the anions available in the polymerization solution provide the necessary negative charge compensation of the positively charged PEDOT chains arising in the course of polymer synthesis. It is obvious that the non-ionic surfactant PLE does not take place in the charge compensation process and thus the perchlorate ions that are small and mobile (in comparison to the remaining anions used in this study) are the only source for charge compensation in the PLE containing solution. It was suggested that at the concentrations of PLE used in the polymerization solution the surfactant builds micelles that play the role of reservoirs for the EDOT molecules and deliver the monomer at the electrode surface without interfering with the growth of the polymer chains [16]. The presence of bulky anions with hydrophobic tails (e.g. SDS) or polyanions (e.g. PAMPS and PSS) together with a large excess of perchlorate anions in the course of polymer synthesis provides a more complicated situation. Bearing in mind that the general trend of the polymerization curves (Fig. 1) remains one and the same for PLE and PSS solutions it could be argued that PSS does not significantly affect the polymerization process in comparison to SDS and PAMPS. The delayed polymerization observed in SDS and PAMPS solutions shows a marked influence of these two dopants on the polymer layer formation. It could be expected that partial doping with these bulky anions occurs but the bulky hydrophobic parts of the anionic species present at the polymer surface impede the growth of the already existing polymer chains.

#### Oxidation of ascorbic acid

In neutral solutions ascorbic acid exists as a monodeprotonated ascorbate anion. The oxidation of these species proceeds in two consecutive steps through the following reactions [3]:

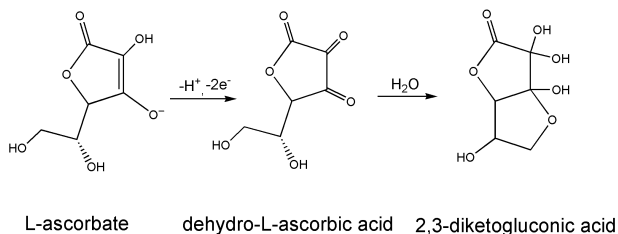
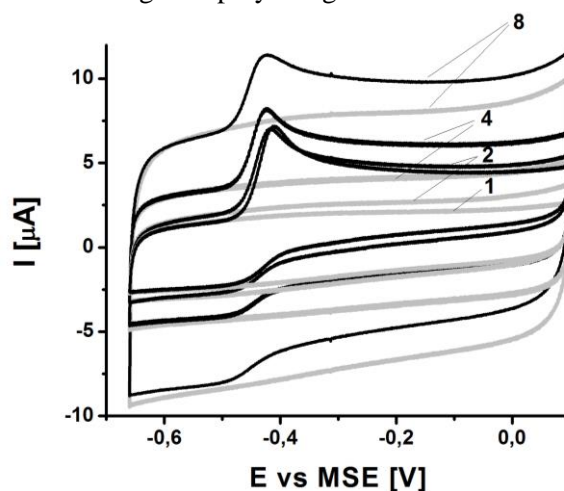


Figure 2 shows voltammetric curves measured in PBS with and without ascorbic acid by using four PEDOT-coated electrodes. The PEDOT layers are obtained in the SDS-containing solution for

different times and have different polymerization charges. The grey lines denote the intrinsic pseudocapacitive currents of the polymer layers that are due to the charging of the individual polymer chains within the layers and increase with increasing the amount of deposited polymer. A small difference in the intrinsic capacitive currents (grey lines in Fig.2) is observed for the layers with 1 and 2 mC polymerization charge indicating very probably the packing of the initially formed polymer structure. A further increase in the polymerization charge (from 2 to 4 and to 8 mC) results in a proportional increase of the intrinsic pseudocapacitive currents pointing to an increase of the internal polymer surface proportional to the amount of deposited PEDOT. Thus a preservation of the polymer structure should be assumed at the advanced stages of polymer growth.



**Fig. 2.** Voltammetric curves measured in the presence (full lines) and the absence (grey lines) of 1 mM AA in PBS using PEDOT/SDS layers with different polymerization charges: 1, 2, 4 and 8 mC.

The measurement carried out in the presence of ascorbic acid (full lines in Fig.2) show the appearance of an oxidation peak at about -0.42 V. The peak is irreversible as the electrochemical step of ascorbate oxidation is followed by a fast chemical step resulting in the formation of electrochemically inactive species. It is obvious that the intrinsic currents of the PEDOT layers have a significant contribution to the measured oxidation peaks. In order to obtain the peak currents due to AA oxidation alone the voltammetric curve of each PEDOT layer, measured in PBS (without AA), is subtracted from the corresponding curve obtained in the presence of the analyte. The resulting voltammetric curves (Fig. 3) show that with increasing amount of deposited polymer the AA oxidation peak decreases.

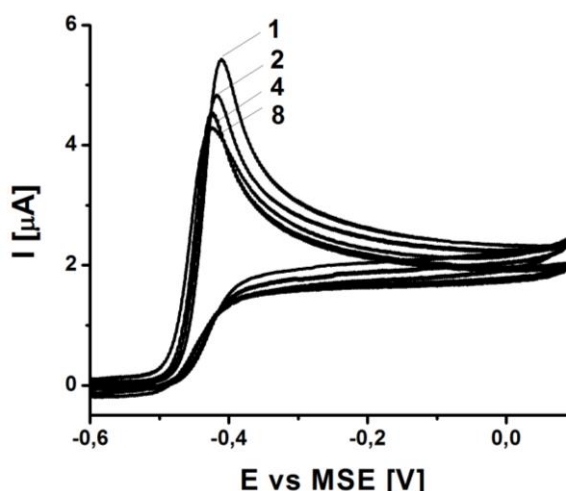


**Fig. 3.** Voltammetric curves of AA oxidation obtained after subtraction of the curves measured in PBS alone at PEDOT/SDS layers with different polymerization charges: 1, 2, 4 and 8 mC.

Similar measurements were carried out with PEDOT layers synthesized in the three remaining polymerization solutions containing PLE, PSS or PAMPS. The results for the AA oxidation currents, after subtraction of the corresponding PEDOT-related capacitive components, are represented in Fig. 4.

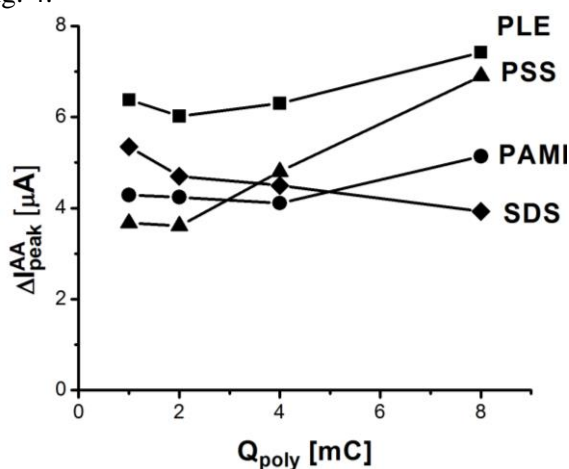


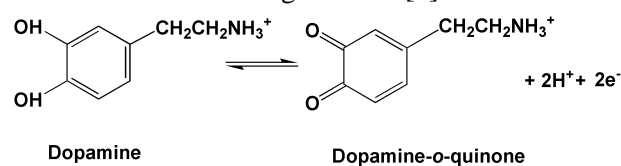
**Fig. 4.** Data for the AA oxidation currents obtained with PEDOT layers synthesized in different polymerization solutions at various amounts of the deposited polymer.

The polymer layers synthesized in the presence of PLE which is nonionic and can not be involved in the doping of PEDOT are the highest. Lower AA oxidation currents are observed for all bulky sulfonate-based anionic dopants used in the course of the synthesis due very probably to electrostatic repulsion between the ascorbate ions and the immobilized dopants. It is interesting to note that the dependences on the amount of deposited polymer (i.e. on the polymerization charge used to obtain the PEDOT layer) have different trends for the various dopants. For all four type of layers the

data for the lowest amounts (polymerization charges 1 and 2 mC) show a slight decrease in the electrocatalytic activity. This effect may relate to the already discussed effect of compressing the layers occurring in the initial stages of growth. A further decrease in the AA oxidation currents with increasing amount of deposited PEDOT is observed only for layers obtained in the presence of SDS. In all remaining cases thickening of the layers (beyond polymerization charge of 2 mC) results in increase of the AA oxidation currents which becomes significant for the PEDOT/PSS layers. In this respect the difference in the behavior of the SDS-doped layers, on the one hand, and the PSS and PAMPS-doped layers, on the other hand, should relate either to strong hydrophobic interactions in the case of SDS or to a different surface morphology of the layers. Scanning electron micrographs (not shown here) give evidence for a more compact surface morphology of the PEDOT/SDS layers in comparison to PEDOT/PSS and PEDOT/PAMPS layers.

#### Oxidation of dopamine

The electrochemical oxidation of dopamine occurs via the following reaction [3]:



The experiments on the oxidation of DA were carried out with PEDOT layers synthesized in the four different polymerization solutions and with four polymerization charges for each solution. Fig. 5 shows a series of voltammetric curves obtained in the dopamine containing solution at PEDOT/SDS layers.

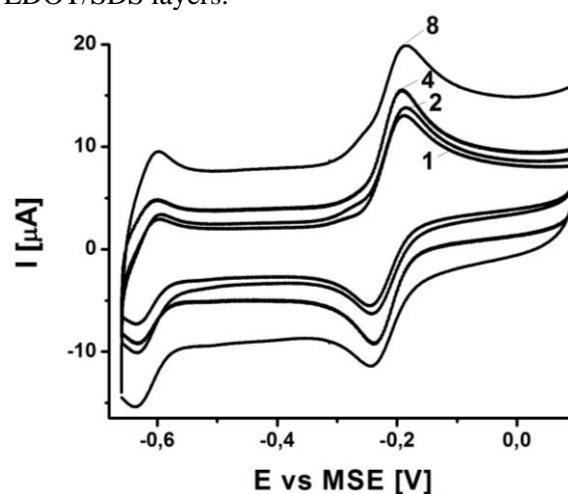


**Fig. 5.** Voltammetric curves measured in the presence 1 mM DA in PBS using PEDOT/SDS layers with different polymerization charges.

The redox pair observed at about -0.2 V relates to the dopamine oxidation/reduction according to the reaction depicted above. The more negative voltammetric peak pair should be ascribed to the dopaminechrome/leucodopaminechrome redox transition as commented by Li *et al* [18] and Luczak [19]. In order to compare the electrocatalytic activity of the various layers for the dopamine reaction the corresponding voltammetric curves measured in buffer (without DA) were subtracted from the curves obtained in the presence of DA. The data for the DA oxidation currents (Fig. 6) taken at -0.2 V, after subtraction, show generally one and the same trend for all solutions.

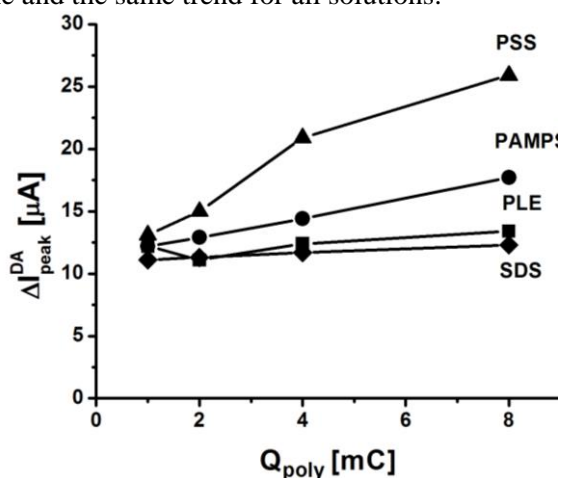


**Fig. 6.** Data for the DA oxidation currents obtained with PEDOT layers synthesized in different polymerization solutions at various amounts of the deposited polymer.

Nevertheless, also in this case the PEDOT/SDS layers are the least suitable for DA oxidation thus confirming the suggested role of hydrophobic interactions impeding the access of the dopamine species to the polymer surface. Obviously, the PEDOT/PSS and PEDOT/PAMPS layers that are expected to have immobilized polyanions are advantageous for the oxidation of the positively charged dopamine moieties. The PEDOT/PLE layers that show the highest oxidation currents for AA are however not suitable for the DA electrocatalytic reaction due most probably to the fact that there are no immobilized anionic species and the general charge distribution over the polymer surface favors the access of negative rather than positively charged moieties such as DA.

### CONCLUSIONS

The investigations presented in this study demonstrate the role of the dopants for the electrocatalytic properties of PEDOT layers with respect to the oxidation of organic species. It is found that even at low analyte concentrations (i.e. 1 mM) the rate of both AA and DA oxidation

reactions is not controlled only by diffusion but depends also on the surface properties of the polymer layer. The charge state and hydrophilicity of the dopants used in the course of the PEDOT synthesis affect the final state of the PEDOT polymer surface and provoke marked differences in the sensitivity for the oxidation of positively or negatively charged species. Thus the most hydrophobic surface that is least suitable for both oxidation reactions is obtained in the case of PEDOT/SDS. The synthesis in the presence of the non-ionic surfactant PLE and perchlorate anions results in a polymer surface suitable for oxidation of negatively charged species. An exchange of the mobile perchlorate anions with ascorbate anions is assumed to occur in this case and favor the oxidation reaction. On the other hand the synthesis of PEDOT in the presence of bulky polyanions (i.e. PAMPS and PSS) that results in immobilization of these species in the polymer structure is advantageous for the oxidation of positively charged species, e.g. dopamine.

Another aspect of this study is to reveal the role of the “thickness” of the various polymer layers for their electrocatalytic activity for AA and DA oxidation. Apart from the very thin layers where an effect of packing of the initial structure is assumed to occur [20] the general trend is increase in the electrocatalytic currents with increasing the amount of polymerized material. This could be ascribed to the involvement of a larger external and occasionally internal polymer surface in the oxidation reactions. The only exception present the PEDOT/SDS layers in the case of AA oxidation where the hydrophobic interactions together with electrostatic repulsion between immobilized anionic species and analyte moieties seem to play a determining role.

Finally, the investigations presented so far show that the involvement of conducting polymers in electrocatalytic and electroanalytic applications requires a fine tuning of their properties which may be achieved by varying both the type of the dopant (and/or surfactants) used in the course of electrochemical synthesis and the amount of deposited polymer. These effects may become of major importance when selectivity and high sensitivity with respect of one of several coexisting analyte species present in the same solution should be achieved.

**Acknowledgment:** Financial support of the Bulgarian Ministry of Education and Science under contract DTK 02-25/2009 of the Bulgarian Science Fund is gratefully acknowledged.

## REFERENCES

1. J. Bobacka and A. Ivaska, in: Electropolymerization, Concepts, Materials and Applications, S. Cosnier and A. Karyakin (eds.), Wiley-VCH Verlag & Co. KGaA, Weinheim, 2010, p. 173.
2. V. Tsakova in: Nanostructured Conductive Polymers, A. Eftekhari (ed.), John Wiley & Sons, 2010, p. 289.
3. V. Tsakova, in: Applications of Electrochemistry in Medicine, Modern Aspects of Electrochemistry, M. Schlesinger (ed.), Volume 56, Springer Science+Business Media New York 2013, p. 283.
4. K. Jackowska, P. Kryszewski, *Anal. Bioanal. Chem.*, **405**, 3753 (2013).
5. A. Elschner, St. Kirchmeyer, W. Lövenich, U. Merker, K. Reuter, PEDOT, Principles and Applications of an Intrinsically Conductive Polymer, CRC Press, Taylor & Francis Group, 2011.
6. G. Inzelt, Conducting Polymers: A New Era in Electrochemistry, Springer Verlag, 2012.
7. W. Plieth, A. Bund, U. Rammelt, S. Neudeck, LeMinhDuc, *Electrochim. Acta*, **51**, 2366 (2006).
8. A. Bund, R. Peipmann, *Electrochim. Acta*, **53**, 3772 (2008).
9. A. I. Melato, A. S. Viana<sup>1</sup>, L. M. Abrantes, *Electrochim. Acta*, **54**, 590 (2008).
10. A. R. Hillman, S. J. Daisley, S. Bruckenstein, *Electrochim. Acta*, **53**, 3763 (2008).
11. E. Tamburria, S. Orlanducci, F. Toschia, M. L. Terranova, D. Passeri, *Synth. Met.*, **159**, 406 (2009).
12. T. F. Otero, J. G. Martinez, K. Hosaka, H. Okuzaki, *J. Electroanal. Chem.*, **657**, 23 (2011).
13. A. Stoyanova and V. Tsakova, *J. Solid State Electrochem.*, **14**, 1947 (2010).
14. A. Stoyanova and V. Tsakova, *J. Solid State Electrochem.*, **14**, 1957 (2010).
15. S. Winkels, V. Tsakova, J. W. Schultze, *Proceedings Electrochem. Soc.*, **98-26**, 97 (1998).
16. V. Tsakova, S. Winkels and J. W. Schultze, *Electrochim. Acta*, **46**, 759 (2000).
17. S. Senthil Kumar, J. Mathiyarasu, K. L. Phani, *J. Electroanal. Chem.*, **578**, 95 (2005).
18. Y. Li, M. Liu, C. Xiang, Q. Xie, S. Yao, *Thin Solid Films*, **497**, 270 (2006).
19. T. Łuczak, *Electrochim. Acta*, **53**, 5725 (2008).
20. K. Bade, V. Tsakova, J. W. Schultze, *Electrochim. Acta*, **37**, 2255 (1992).

## ЕЛЕКТРОПОЛИМЕРИЗАЦИЯ НА ПОЛИ (3,4- ЕТИЛЕНЕДИОКСИТИОФЕН) СЛОЕВЕ В ПРИСЪСТВИЕТО НА РАЗЛИЧНИ ДОПАНТИ И ЕФЕКТА ИМ ВЪРХУ ЕЛЕКТРОКАТАЛИТИЧНИТЕ СВОЙСТВА НА ПОЛИМЕРИТЕ. ОКИСЛЯВАНЕ НА АСКОРБИНОВА КИСЕЛИНА И ДОПАМИН

Д. Г. Фильова, Г. П. Илиева, В. Ц. Цакова

*Институт по физикохимия, Българска академия на науките, ул. „Акад. Г. Бончев“, бл. 11, 1113 София, България*

Получена на 12 юни, 2013; коригирана на 25 юни, 2013

(Резюме)

Електрохимичния синтез на поли (3,4-етиленетиленедиокситиофен) (PEDOT) е проведен в четири различни полимеризационни разтвори. Три сулфонат-базирани допанти, а именно додецил сулфонат (SDS), полистирен сулфонат (PSS) и поли(акриламидопропан сулфонат) (PAMPS), както и нейонно повърхностно активно вещество полиоксиетилен-10-лаурилетер (PLE) в комбинация с LiClO<sub>4</sub> се използват за получаване на полимерните слоеве. Електрокаталитичните характеристики на четирите вида покрити с PEDOT електроди са изследвани по отношение на окисление с аскорбинова киселина (AA) и допамин (DA) във фосфатен буферен разтвор. Установено е, че слоевете PEDOT/PLE са най-подходящи за окисление на аскобинови аниони, докато електроди покрити с PEDOT/PSS са най-подходящи за окисление на положително заредени допаминови видове. Тези резултати са обсъдени по отношение на възможни хидрофобни/хидрофилни и/или електростатични взаимодействия възникващи между анализиранияте молекули и анион-дотираната повърхност на PEDOT.





**Hydrogen economy cooperation network for research – public awareness – business opportunities across Greek – Bulgarian borders**

Dear Reader,

This section of the special issue collects selected papers, presented during the International Scientific Workshop “HYDROGEN ECONOMY – A ROADMAP TO THE FUTURE”, which held on 30th November 2012 in Blagoevgrad, Bulgaria. The workshop was organized by the Bulgarian partners from South-West University “Neofit Rilski” – Blagoevgrad and Eco Energy Foundation within the framework of the project “Hydrogen economy cooperation network for research - public awareness - business opportunities across Greek-Bulgarian borders” (HYDECON), funded by European Territorial Cooperation Programme “Greece-Bulgaria 2007-2013” through a Contract B1.33.01/2011.

The scope of the workshop was focused on the state-of-the art of research and development activities in the field of hydrogen technologies in Greece and Bulgaria and the perspectives for their application in the both neighbour countries in the context of Hydrogen Economy concept. Greek and Bulgarian scientists and students from Chemical Process & Energy Resources Institute, Center for Research and Technology - Hellas (CPERI / CERTH), Thessaloniki; Aristotle University, Thessaloniki; Plovdiv University “Paisii Hilendarski”; Institute of Electrochemistry and Energy Systems - Bulgarian Academy of Sciences, Sofia; Institute of Chemical Engineering - Bulgarian Academy of Sciences, Sofia; University of Chemical Technology and Metallurgy, Sofia; and South-West University “Neofit Rilski”, Blagoevgrad, presented 14 scientific reports and 8 posters, divided into three thematic sessions - Novel Materials for Energy Conversion; Hydrogen Production and Storage; Fuel Cell Technologies. Students from universities as well as high schools participated in a Round table discussion “Possibilities for Hydrogen Applications”. A special demonstration of “Off-grid system for power generation based on hydrogen technologies” was made for all participants in the

## *Scientific Workshop* **Hydrogen Economy – a Roadmap to the Future**

newly developed "INNOVATIVE CENTER FOR ECO ENERGY TECHNOLOGIES".

The organizers of the workshop and all participants in the successfully completed project HYDECON truly believe that the established network between researchers from both countries will assist the further promotion of hydrogen technologies among the society and decision-makers. We gratefully use the chance to disseminate a part of our achievements among the audience of this journal.

*Professor Mario Mitov,  
Chairman of the Organizing Committee*



## Optimization of conditions for formation of electrochemically active biofilm on carbon felt anodes during operation of yeast-based biofuel cells

E.Y. Chorbadzhiyska<sup>1\*</sup>, M.Y. Mitov<sup>1</sup>, Y.V. Hubenova<sup>2</sup>

<sup>1</sup>Department of Chemistry, South-West University, Blagoevgrad, Bulgaria

<sup>2</sup>Department of Biochemistry and Microbiology, Plovdiv University, Plovdiv, Bulgaria

Received May 27, 2013; Revised July 18, 2013

In this study, yeast-based biofuel cells using *Saccharomyces cerevisiae* as a biocatalyst were investigated under different operation conditions. The biofuel cells were operated under permanent load in a semi-batch regime. The increase of the anode mass as well as the improvement of the MFC outputs during operation indicates a formation of electrochemically active biofilm on the anode. The most active biofilm, resp. highest generated power, was obtained with the lowest load (100  $\Omega$ ) applied. Besides the complexity of the system, a good reproducibility of the results was observed under controlled experimental conditions.

**Key words:** yeast-based biofuel cell, *Saccharomyces cerevisiae*, electrochemically active biofilm

### INTRODUCTION

Microbial fuel cells (MFCs) are devices that convert the chemical energy of natural available organic substrates directly into electricity by using different microorganisms as bio-microreactors [1, 2]. In a typical MFC, electron donors, such as organic materials in wastewater, are oxidized by the electrochemically active bacteria mostly growing as a biofilm on the anode surface [3, 4]. The power generation is still insufficient for the practical applications. In order to improve the MFC performance, efforts have been made to enrich more electrochemically active bacteria [5, 6], to improve reactor configuration [7], to identify better electrode materials [7, 8, 9], as well as to optimize process parameters [7,10]. Many factors, such as nutrient supply, flow rate, pH, temperature [4, 7, 11, 12, 13], have been found to strongly affect the MFC performance and start-up time. Optimizing the growth conditions for the electrochemically active bacteria on the anode is also an important consideration for improving the performance of MFCs.

One of the most important and most investigated factors is the anode potential at which the MFC is operated, as it controls the theoretical energy gain for microorganisms [14]. Finkelstein et al. [15] reported that a larger and earlier maximum current was obtained at a more positive applied potential due to the increased energy yield for microbial colonization. Besides the anode potential,

the effect of external resistance applied to the electrical circuit also received wild attention since controlling the growth condition for the electrochemically active bacteria by changing the external resistance is more feasible than poisoning the anode potential in MFC applications. In general, MFC performance improves with decreasing the applied external resistance. Liu et al. [16] demonstrated that the lower external resistance was applied, the higher maximum power output was obtained.

Bacteria such as *Escherichia coli* [17, 18] *Geobacter sulfurreducens*, *Pseudomonas aeruginosa* [17, 18, 19], *Rhodospirillum rubrum*, *Shewanella oneidensis*, *Shewanella putrefaciens* [17, 18], *Enterobacter cloacae* [2, 18], etc., have been most frequently studied for application in MFCs. Eukaryotes, e.g. yeasts, are still rarely investigated for this purpose.

In this study, the influence of the experimental conditions (load resistance value, temperature, purging with nitrogen) on the formation of yeast anodic biofilm on carbon felt electrodes and its impact on the performance of yeast-based biofuel cell were investigated.

### MATERIALS AND METHODS

Baker's yeast *Saccharomyces cerevisiae* was applied as a biocatalyst in double-chamber MFC. 1g dry yeast biomass was suspended in 80 ml of a modified minimal M9 salts nutrient medium [20], prepared as follows:

\* To whom all correspondence should be sent:  
E-mail: elli\_e1@abv.bg

M9 salts solution consisted of 64 g/l  $\text{Na}_2\text{HPO}_4 \cdot \text{H}_2\text{O}$ , 15 g/l  $\text{KH}_2\text{PO}_4$ , 2.5 g/l  $\text{NaCl}$  and 5.0 g/l  $\text{NH}_4\text{Cl}$  was prepared and sterilized by autoclaving. 0.489 g/l  $\text{MgSO}_4$ , 0.011 g/l  $\text{CaCl}_2$  and 4 g/l glucose as a carbohydrate source were added to 200 ml of M9 solution, and the volume was adjusted to 1 l with distilled water. The final nutrient solution was sterilized again by autoclaving.

The prepared yeast suspension was used as an anolyte in the MFCs. 1 ml (0.1%) methylene blue was added to the anolyte suspension as an exogenous mediator. 100 mM  $\text{K}_3[\text{Fe}(\text{CN})_6]$  dissolved in 67 mM phosphate buffer (pH 7.0) was applied as a catholyte and terminal electron acceptor. Rectangular carbon felt samples (5 cm height, 3 cm width; SPC-7011, 30  $\text{g}/\text{m}^2$ , Weibgerber GmbH & Co. KG) were used for both anodes and cathodes. Prior to use the electrodes were sonicated in ethanol-acetone mixture (1:1) for 15 min. Samples with equal specific resistance were applied as electrodes. The anode and cathode chambers of the MFCs were connected with a salt bridge – Fig.1.

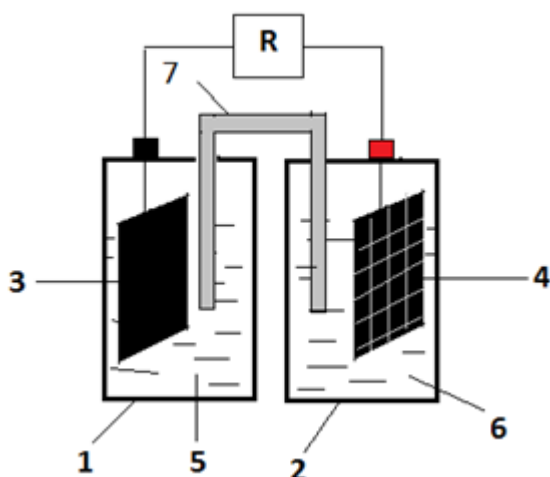


**Fig. 1.** Scheme of double-chamber MFC: 1-anode chamber (volume 100 cm<sup>3</sup>); 2-cathode chamber volume 100 cm<sup>3</sup>); 3-anode; 4-cathode; 5-anolyte; 6-catholyte; 7-salt bridge.

The fuel cells were operated at a load of 100, 500, 1000 or 5000  $\Omega$  for at least one week. During these experiments, the terminal voltage as well as the anode and cathode potential, measured against  $\text{Ag}/\text{AgCl}$  reference electrode, were monitored with time. After the 3<sup>rd</sup> day from the beginning of experiments every day the anolyte was replaced with a fresh cultivation medium. Before each medium replacement, polarization measurements under a variable resistor load were carried out using resistor box. The voltage was measured by digital multimeter and the current was calculated by using the Ohm's law. At each load the voltage was

allowed to stabilize for at least 2 minutes before a reading was taken. The results were plotted as polarization curves  $U=f(I)$ . The generated power at each load was estimated by equation  $P = U \cdot I$  and plotted as power curves  $P = f(I)$ .

In a series of experiments the yeast biofuel cells were operated at the same conditions, but part of them were incubated in a thermostat at a constant temperature ( $22 \pm 1$  °C) and the rest were cultivated at a temperature varying between 15 and 25 °C. In another series of experiments part of the MFCs were operated with purging of nitrogen in the anode chamber to create strict anaerobic conditions, and the rest - under normal conditions (without purging with nitrogen).

During the MFC-experiments the optical density of the anolyte suspension was measured at the wavelength 600 nm (OD600). The spectrophotometric studies were performed by using Agilent Hewlett-Packard 8453A UV-VIS-NIR Spectrophotometer.

After the end of MFC operation, the anodes were dried overnight and weighted by using Mettler AE 100 analytical balance. The mass of the anodic biofilm was calculated as a difference of the masses of used anodes before and after the polarization tests in yeast-biofuel cell.

Each MFC-experiment at identical conditions was carried out in triplicate.

## RESULTS AND DISCUSSION

Relatively high values of the open circuit voltage (above 500 mV) were recorded few hours after the start-up of the investigated MFCs. After 3 days operation the OCV grew up to values exceeding 800 mV, but after the first replacement of the anolyte with a fresh medium a drop of about 100 mV was observed (Fig. 2).

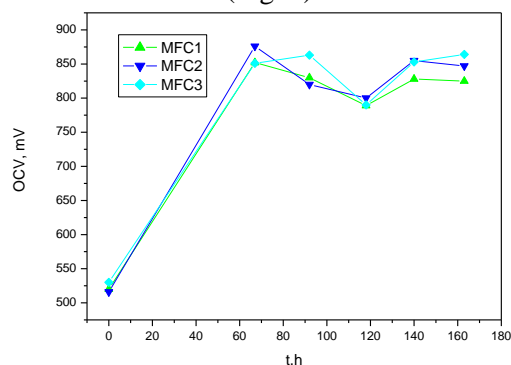


**Fig. 2.** Variation of open circuit voltage (OCV) of the studied yeast biofuel cells with time

Possible explanation of this decrease is that electrochemically active compounds, produced under polarization by yeast, are removed from the

system with the exhausted medium. Stabilization of the OCV at higher values was achieved after six days operation of the MFCs at constant load.

In parallel, a shift of the anode potentials from  $160 \pm 30$  mV to  $-530 \pm 20$  mV was observed in a contrary to the cathode potentials, which values remain relatively constant (Fig. 3).

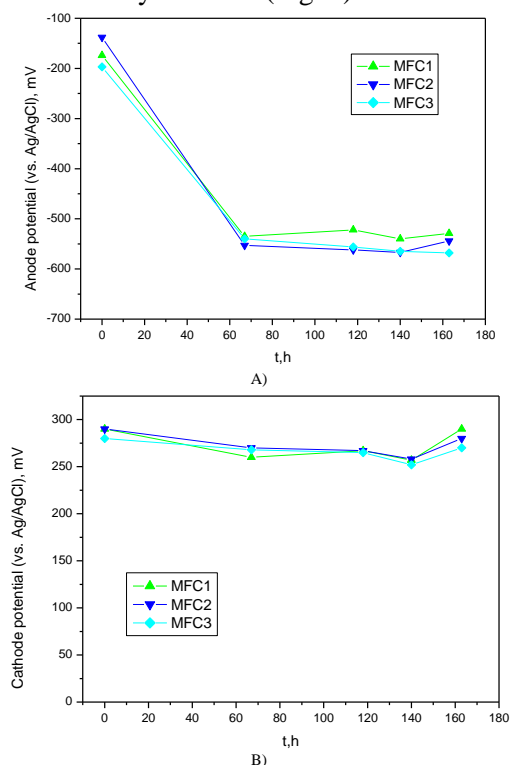


**Fig. 3.** Variation of anodic (A) and cathodic (B) potential of the yeast - biofuel cells with time

These results show that the processes taking place on the bioanode have predominant role for the performance of the examined yeast biofuel cells. Such abrupt changes of the anode potential in a negative direction by more than 300 mV is often associated with the formation of an active anodic biofilm [21]. The change in the optical density OD600 of the anolyte suspension, presented in Fig. 4, is in accordance with such suggestion. Three days after the start-up of the MFCs the measured optical density of the cell suspension drastically decreased in comparison to the initial one and the subsequent refreshments of the nutrient medium practically did not change its values. The observed decrease of the optical density of the anolyte can be connected with a lack of yeast cells in suspension due to formation of anodic biofilm.

After stabilization of the anode potential referred to a biofilm formation the achieved terminal voltage values under a load also showed relatively constant and high values - Fig. 5.

Very close electrical outputs (open circuit voltage, short circuit current, maximum power) can

be derived from the polarization (Fig. 6A) and power curves (Fig. 6B) of MFCs operated under the same load and other conditions.

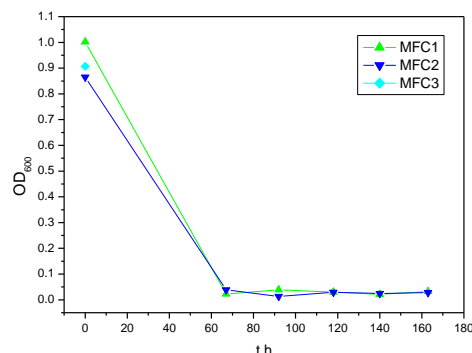


**Fig. 4.** Variation of the optical density OD600 of the anolyte cell suspension with time

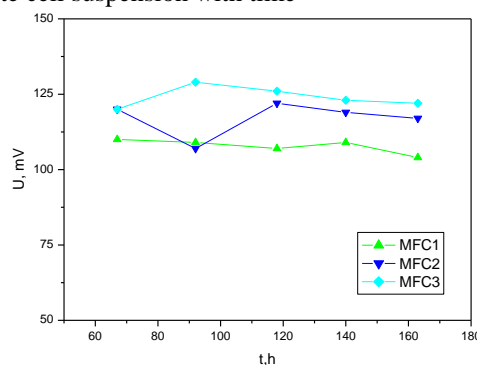


**Fig. 5.** Variation of the terminal voltage of studied MFCs under a load of 1000  $\Omega$

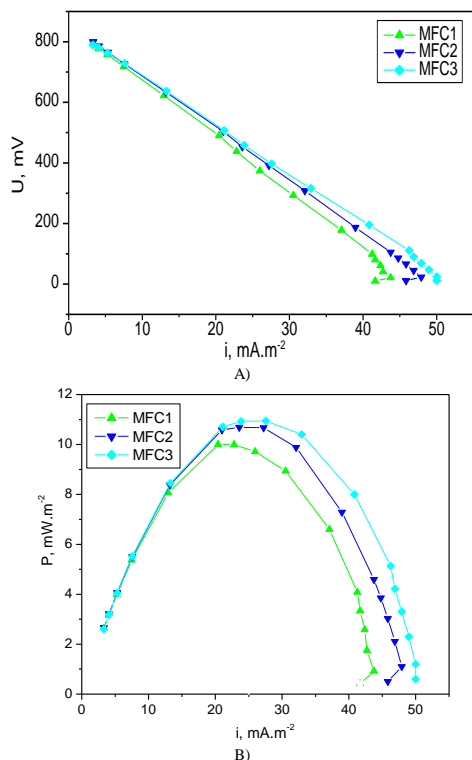


**Fig. 6.** (A) Polarization curves and (B) power curves obtained at the 3<sup>rd</sup> day after the start-up of the yeast biofuel cell

This indicates that reproducible characteristics could be obtained at controlled conditions besides the complexity of the system.

The maximum power, obtained from different MFC operated under the same conditions, also shows same tendencies of variation with time and close values (Fig. 7). Connecting these results with those received for open circuit voltage (Fig. 2), anode potential (Fig. 3) and optical density (Fig. 4), it can be concluded that six days are optimal for the formation of an active anode biofilm, and the periodic replacement of the medium contributes to its stability and activity for a longer period of time.

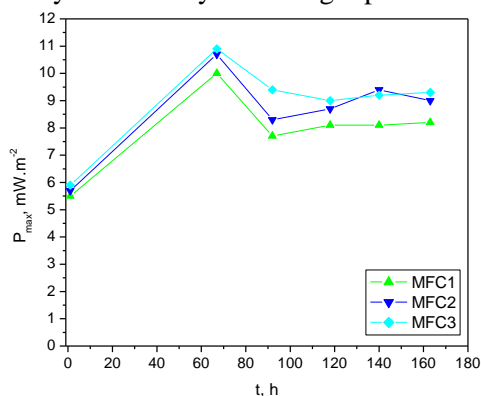


Fig. 7. Variation of generated maximum power from yeast biofuel cells with time

Table 1 presents the results from the weight analysis of the formed biofilm. It is obvious that the mass of the formed biofilm on the anodes of three MFCs, operated under the same conditions, is quite close and the observed deviations of the values are insignificant. These results explain the similar electrochemical behaviour of the studied yeast biofuel cells and confirmed the suggestion that the behaviour of the MFC strongly depends on the formed anodic biofilm.

Table 1. The mass of biofilm, formed on the anode of three yeast biofuel cells, operated for one week (load resistance 1000 Ω)

No MFC	Mass of the biofilm, g
1	0.0325
2	0.0346
3	0.0362

Set of experiments aiming to clarify the factors that contribute for the optimum of the operating characteristics were performed. The results presented on Fig. 8 show that maintaining a strict constant temperature is not essential for the electric outputs of the studied yeast biofuel cells.

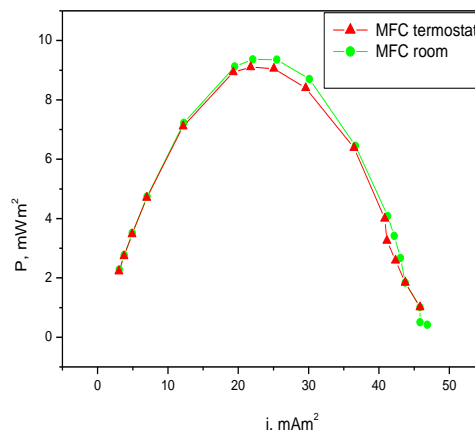


Fig. 8. Power curves obtained with the yeast biofuel cells operating in a thermostat and at ambient temperature

In contrary, the maintenance of strict anaerobic conditions results in significantly lower operating characteristics than those obtained under normal conditions (without purging with nitrogen) - Fig. 9. This is associated with the fact that in aerobic conditions yeast catabolizes the substrate (glucose) through the processes of cellular respiration, in which the total number of generated electrons is much bigger than those of anaerobic fermentation. Such results have been also reported for other types of yeasts [22].

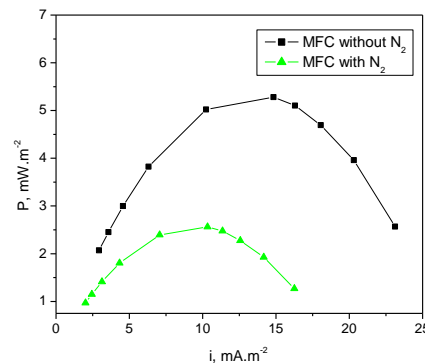


Fig. 9. Power curves obtained with the yeast biofuel cells operating with and without purging of nitrogen

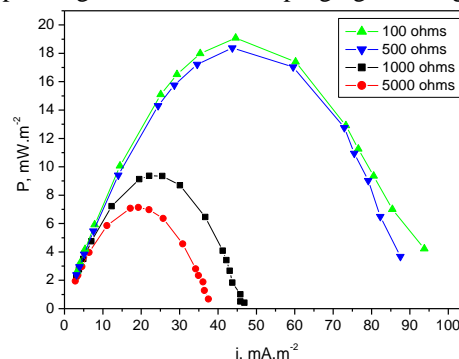


Fig. 10. Power curves obtained with the yeast biofuel cells polarized with different load resistances one day after the first change of the medium

The role of the load resistance on the activity of the formed anode biofilm, resp. MFC outputs, was also examined. The highest maximum power of  $19 \pm 3$  mW/m<sup>2</sup> was achieved with MFCs operated under the lowest load of 100  $\Omega$  and the generated power decreased with an increase of applied external resistance – Fig.10. The same tendency for formation of more active biofilms at lower loads was also reported by other researchers [23, 24].

### CONCLUSION

A long-term operation of yeast-based biofuel cells using *Saccharomyces cerevisiae* as a biocatalyst can be accomplished by periodical replacement of the anolyte with a fresh nutrient medium. The formation of electrochemically active biofilm on the anode has a predominant role for the MFC-performance. From all studied factors, the major impact on the activity of the formed anode biofilm has the load resistance, by which the MFC is polarized. The lower resistance is applied, the more active biofilm is formed. The maintenance of strictly anaerobic conditions diminishes the MFC-outputs due to the fact that at such conditions the facultative yeasts catabolize the substrate through fermentation, which generates quite less electrons in comparison with the processes of respiration.

**Acknowledgements:** *The present study was funded by the program "Hydrogen Economy Cooperation Network for Research - Public Awareness - Business Opportunities across Greek-Bulgarian borders – HYDECON". The Project is co-funded by the European Regional Development Fund and by national funds of the countries participating in the ETCP "Greece-Bulgaria 2007-2013" through contract B1.33.01.*

### REFERENCES

1. K. Rabaey, W. Verstraete, *Trends Biotechnol.*, **23**, 292 (2005).
2. Y. Mohan, S. Kumar, D. Das, *Int. J. Hydrogen Energy*, **33**, 423 (2007).
3. B.E. Logan, B. Hamelers, R. Rozendal, U. Schröder, J. Keller, S. Freguia, P. Aelterman, W. Verstraete, K. Rabaey, *Environ. Sci. Technol.*, **40**, 5181 (2006).
4. K. Rabaey, W. Verstraete, *Trends Biotechnol.*, **23**, 291 (2005).
5. S. Freguia, K. Rabaey, Z. Yuan, J. Keller, *Environ. Sci. Technol.*, **41**, 2915 (2007).
6. X. Cao, N. Huang, P. Boon, M. Fan Liang, *Electrochem. Commun.*, **10**, 1392 (2008).
7. H. Liu, R. Ramnarayanan, B.E. Logan, *Environ. Sci. Technol.*, **38**, 2281 (2004).
8. Q. Deng, X. Li, J. Zuo, A. Ling, B.E. Logan, *J. Power Sources*, **195**, 1130 (2010).
9. P. Aelterman, M. Versichele, M. Marzorati, N. Boon, W. Verstraete, *Bioresour. Technol.*, **99**, 8895 (2008).
10. G.C. Gil, I.S. Chang, B.H. Kim, M. Kim, J.K. Jang, H.S. Park, H.J. Kim, *Biosens. Bioelectron.*, **18**, 327 (2003).
11. G.S. Jadhav, M.M. Ghangrekar, *Bioresour. Technol.*, **100**, 717 (2009).
12. T. Catal, P. Kavanagh, V. O'Flaherty, D. Leech, *J. Power Sources*, **196**, 2676 (2011).
13. S. You, Q. Zhao, J. Zhang, J. Jiang, C. Wan, M. Du, S. Zhao, *J. Power Sources*, **173**, 172 (2007).
14. R.C. Wagner, D.F. Call, B.E. Logan, *Environ. Sci. Technol.*, **44**, 6036 (2010).
15. D.A. Finkelstein, L.M. Tender, J.G. Zeikus, *Environ. Sci. Technol.*, **40**, 6990 (2006).
16. H. Liu, S. Cheng, B.E. Logan, *Environ. Sci. Technol.*, **39**, 658 (2005).
17. A. Rinaldi, B. Mecheri, V. Garavaglia, S. Licoccia, P. Nardo, E. Traversa, *Energy Environ. Sci.*, **1**, 417 (2008).
18. O. Schaetzle, K. Baronian, *Energy Environ. Sci.*, **1**, 1 (2008).
19. D.R. Lovley, *Curr. Opin. Biotechnol.*, **17**, 327 (2006).
20. R. Ganguli, V. Mehrotra, *US Patent* 20 110 097 605 A1 (2011).
21. Y. Hubenova, R. Rashkov, V. Buchvarov, M. Arnaudova, S. Babanova, M. Mitov, *Ind. Eng. Chem. Res.*, **50**, 557 (2011).
22. S. Babanova, Y. Hubenova, M. Mitov, *J. Biosci. Bioeng.*, **112**, 379 (2011).
23. S. Jung, J.M. Regan, *Appl. Environ. Microbiol.*, **77**, 564 (2011).
24. K.P. Katuri, K. Scott, I.M. Head, C. Picioreanu, T.P. Curtis, *Bioresour. Technol.*, **102**, 2758 (2011).

ОПТИМИЗИРАНЕ НА УСЛОВИЯТА ЗА ПОЛУЧАВАНЕ НА ЕЛЕКТРОХИМИЧНО-АКТИВЕН  
БИОФИЛМ ВЪРХУ ВЪГЛЕРОДНИ АНОДИ В ДРОЖДЕН БИОГОРИВЕН ЕЛЕМЕНТ

Е. Й. Чорбаджийска<sup>1\*</sup>, М. Й. Митов<sup>1</sup>, Й. В. Хубенова<sup>2</sup>

<sup>1</sup>Катедра „Химия“, Югозападен университет „Неофит Рилски“, Благоевград, България

<sup>2</sup>Катедра „Биохимия и Микробиология“, Пловдивски Университет „Паусий Хилендарски“, България

Получена на Май 27, 2013; Ревизирана на Юли 18, 2013

(Резюме)

В настоящата разработка са изследвани дрождени биогоривни елементи, използващи дрожди *Saccharomyces cerevisiae* като биокатализатор, при различни условия. Биогоривните елементи бяха тествани в полунепрекъснат режим при постоянно приложено товарно съпротивление. Увеличаването на масата на анода, както и подобряването стойностите на операционните характеристики на микробиологичните горивни елементи свидетелства за образуването на електрохимично-активен аноден биофилм. Най-активен биофилм, съответно най-голяма електрическа мощност, бяха получени с най-малкото приложено товарно съпротивление (100 Ω). Въпреки сложността на системата, поддържането на постоянни експериментални условия води до получаването на добре възпроизводими резултати.

## Novel materials as oxygen carriers for energy applications

A. Evdou<sup>1,2</sup>, V. Zaspalis<sup>1,2</sup>, L. Nalbandian<sup>1\*</sup>

<sup>1</sup>Laboratory of Inorganic Materials (LIM), Chemical Process & Energy Resources Institute, Center for Research and Technology - Hellas (CPERI / CErTH), P.O. Box 60361, 57001, Thessaloniki, Greece,

<sup>2</sup>Department of Chemical Engineering, Aristotle University, P.O. Box 1517, 54006, Thessaloniki, Greece

Received May 27, 2013; Revised August 18, 2013

Perovskites have the ability to accommodate large concentrations of vacancies in their structure and to reversibly pick up and deliver oxygen at high temperatures, thus they are ideal candidates for use as oxygen carrier materials. The performance of perovskites with the general formula  $\text{La}_{1-x}\text{Me}_x\text{M}_y\text{Fe}_{1-y}\text{O}_3$  (Me = Sr, Ca, M = Ni, Co, Cr, Cu) as both oxygen carriers for syngas generation from methane in the Chemical Looping Reforming (CLR) concept and as dense membrane materials in the Dense Membrane Reactor (DMR) concept is explored in the present work. Oxygen is withdrawn from the crystal lattice of the perovskites by oxidation of a fuel. Water, oxygen or carbon dioxide, are then added to the solid which provide the necessary oxygen atoms to fill-in the lattice vacancies. The performance of the mixed perovskitic materials doped with 5% M in the B-site (M=Ni, Co, Cr or Cu), is compared. Also, substitution of Sr with Ca in the A-site of the perovskite is explored. Dense, disc shaped membranes of the materials were utilized in a membrane reactor. Experiments at 1000°C revealed the possibility of performing the reduction and oxidation steps simultaneously and isothermally on each side of the membrane reactor. The system is able to operate on partial pressure based desorption without the need of a carbon containing reductant, so that a process towards hydrogen production, based only on renewable hydrogen source such as water, can be established.

**Key words:** Hydrogen, Perovskites, Chemical-looping reforming, Dense membrane reactor

### INTRODUCTION

It has been established that CO<sub>2</sub> emissions resulting from human activity have led to an increase in the atmospheric CO<sub>2</sub> concentration, from a pre-industrial level of 280 to 450ppm [1]. This results in a mean annual temperature increase at the earth's surface which is commonly known as global warming.

The optimum approach to minimize CO<sub>2</sub> emissions is to enhance the use of renewable energy resources, such as biomass, solar and wind energies. However, in the medium-term, other ways to reduce CO<sub>2</sub> emissions are receiving increasing interest.

A possible solution is CO<sub>2</sub> sequestration which consists of capturing CO<sub>2</sub> in an emission source and storing it where it is prevented from reaching the atmosphere. [2]. There are currently a number of available processes for CO<sub>2</sub> capture. Increasing interest among them is being gained in the recent years by the Chemical Looping Combustion (CLC) technology [3]. CLC involves the use of a metal oxide as an oxygen carrier. This process is configured with two interconnected fluidized bed reactors: an air reactor and a fuel reactor. The solid oxygen carrier is circulated between the air and fuel

reactors. In CLC, the gaseous fuel is fed into the fuel reactor where it is completely oxidized by the lattice oxygen of the metal oxide to CO<sub>2</sub> and water vapor. By condensing water vapour the free-of-water CO<sub>2</sub> can be sequestered or/and used for other applications. The technology has recently been successfully demonstrated for more than 1000 h and at scales up to 140 kW [4-6].

An alternative promising option to reduce the CO<sub>2</sub> emissions is the use of H<sub>2</sub> as fuel. Presently, hydrogen is produced mostly by reforming of natural gas (i.e. methane), partial oxidation of heavy oils and naphtha and gasification of coal [7-8]. However, in the conventional process, air is used for the oxidation of methane, thus the generation of NO<sub>x</sub> is inevitable. Furthermore, the N<sub>2</sub> in the product dilutes the produced syngas and brings about severe purification demands. A promising new procedure for H<sub>2</sub> production from natural gas is the "Chemical Looping Reforming (CLR)" process [9]. In CLR a suitable oxide catalyst is circulated between two reactors as in CLC. In the first reactor methane is oxidized to synthesis gas by the lattice oxygen of the oxide, and in the second reactor, the reduced oxide is re-oxidized by air. This way the products are not diluted with N<sub>2</sub>. A schematic diagram of the CLR and/or the CLC process is presented in Figure 1a.

\* To whom all correspondence should be sent:  
E-mail: nalbanti@cpери.certh.gr

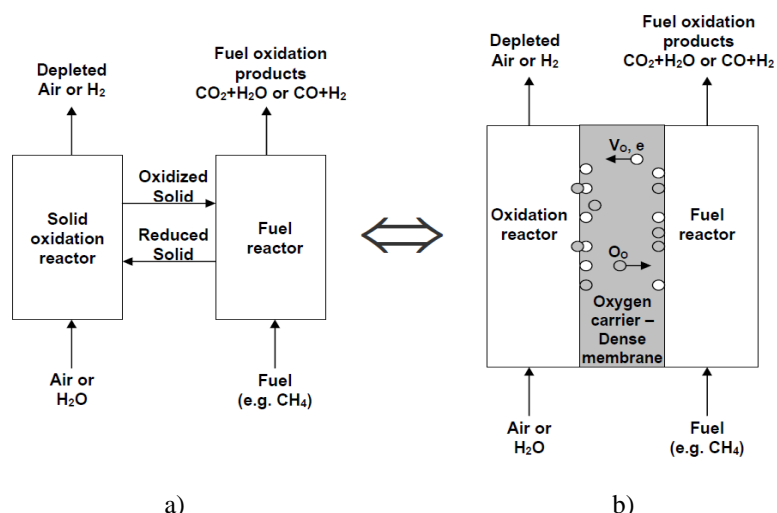


**Fig. 1.** (a) Schematic diagram of the Chemical Looping Combustion (CLC) and/or the Chemical Looping Reforming (CLR) process (b) Dense Membrane Reactor-Chemical Looping Combustion (DMR-CLC) and/or Dense Membrane Reactor-Chemical Looping Reforming (DMR-CLR).

### *Chemical Looping -Dense Membrane Reactor Concept*

One of the biggest concerns in Chemical Looping processes generally and of the CLR specifically is the recirculation of the solid materials between the two reactors. Many materials with good oxygen transfer capacity are not suitable due to their high attrition indices. Furthermore all this movement of solids requires a lot of energy.

In order to overcome these problems the dense membrane reactor concept (Figure 1b) is proposed in this work. It is based on the use of a dense mixed conducting membrane reactor to perform the reduction and oxidation steps simultaneously at either membrane side. It is composed of two compartments gas tightly separated by the dense membrane. A hydrocarbon (e.g. natural gas) is oxidized in the “Fuel” compartment in the absence of gaseous oxygen, by pulling oxygen atoms from the solid. Due to chemical potential difference, oxygen is transferred through the membrane from the opposite “oxidation” side. If air is added in the “oxidation” compartment, gaseous oxygen molecules decompose on the membrane surface and the oxygen atoms fill the oxygen vacancies of the membrane. Alternatively, water can be added in this compartment, which decomposes on the membrane surface into oxygen atoms that fill the oxygen vacancies and pure gaseous hydrogen, ready to use in fuel cell applications.

In either case, a net oxygen flow is formed in the dense membrane from the “oxidation” side to the “fuel” side, which renews continuously the oxygen content of the oxygen carrier, thus permitting the uninterrupted oxidation of the fuel. At the same

time, a counter flow of oxygen vacancies ( $V_o$ ) is formed from the “fuel” side to the “oxidation” side of the membrane, thus permitting the uninterrupted consumption of oxygen.

The dense membrane reactor (Figure 1b) is compared to the general scheme of the chemical looping processes (Figure 1a). The general scheme of the 2 processes is very much alike. They both have a “fuel reactor” in which the fuel is oxidized in the absence of gaseous oxygen, by utilizing the lattice oxygen of a solid “oxygen carrier (OC)”. They also both have an “oxidation reactor” where the solid OC is refilled with oxygen, by either air or  $H_2O$ . In the Chemical Looping the OC is a powdered solid while in the dense membrane reactor the OC is the membrane itself. Thus the two processes are equivalent and readily interchangeable. The advantage of the dense membrane reactor process is that it ensures continuous and isothermal operation of the Chemical Looping Processes, while there is no need for energy demanding solid recirculation.

One key issue with the Dense Membrane Reactor - Chemical Looping Reforming (DMR-CLR) process that needs to be further studied is the development of the proper materials that can serve as both oxygen carriers and oxygen ion conducting membranes. The ideal candidate materials should:

- be able to accommodate large concentrations of vacancies in their structure
- be able to reversibly pick up and deliver oxygen at high temperatures
- have high catalytic activity in methane partial oxidation

- have good thermal stability and suitable mechanical properties
- exhibit mixed type conductivity for the necessary transfer of anions, vacancies and electrons

Perovskite-type mixed conducting materials are ideal candidates for use in Dense Membrane Reactor - Chemical Looping Reforming, since they fulfil most of the above characteristics.

The performance of the candidate materials is ranked by taking into account the H<sub>2</sub> and CO yields during the fuel oxidation step as well as the amount of oxygen per mole solid ( $\delta$ ) that can be delivered reversibly to the fuel.

## EXPERIMENTAL

### *Powder material synthesis and membrane preparation*

The metal precursors used were: La(NO<sub>3</sub>)<sub>2</sub>·6H<sub>2</sub>O (Fluka Analytical), Sr(NO<sub>3</sub>)<sub>2</sub> (Sigma Aldrich), Fe(NO<sub>3</sub>)<sub>3</sub>·9H<sub>2</sub>O (Merck), Ni(NO<sub>3</sub>)<sub>2</sub>·6H<sub>2</sub>O (Merck), Co(NO<sub>3</sub>)<sub>2</sub>·6H<sub>2</sub>O (Sigma Aldrich), Cr(NO<sub>3</sub>)<sub>3</sub>·9H<sub>2</sub>O (Merck) and Cu(NO<sub>3</sub>)<sub>2</sub>·3H<sub>2</sub>O (Merck). High purity Black Nickel Oxide (NiO) (Ni content 76.6-77.9%) was purchased from Inco Special Products. Anhydrous citric acid (purity >99.5%) was purchased from Sigma Aldrich.

Materials are synthesized by the citrate method [10]. Stoichiometric amounts of the precursors of the corresponding metals are dissolved in deionised water. After the addition of an aqueous citric acid solution, 10% in excess, the solution is stirred, evaporated at 70°C and the obtained solid is dried at 250°C, overnight. Finally the solids are calcined at 1000°C, in air, for 6 h.

The dried powdered sample was initially ball-milled, dried, roll-granulated and uniaxially pressed in the form of cylindrical pellets with a diameter of 10mm and height 15mm. The compacted specimens were sintered in air and cut in thin slices, thickness 1–5mm, with a diamond micro wheel (Struers, Accutom-5).

### *Material characterization*

The basic physicochemical characterization of the prepared samples includes crystalline phase identification, surface area determination and morphology observation by Scanning Electron Microscopy. The crystalline phases formed in the prepared samples are examined by X-ray diffraction. Powder XRD patterns are recorded with a Siemens D500 X-ray diffractometer, with auto divergent slit and graphite monochromator using CuK $\alpha$  radiation, having a scanning speed of 2° min<sup>-1</sup>.

<sup>1</sup>. The characteristic reflection peaks (d-values) are matched with JCPDS data files and the crystalline phases are identified. Specific surface area, pore volume and pore size distribution are determined by Nitrogen adsorption – desorption isotherms at the boiling point of liquid nitrogen (77 K) under atmospheric pressure using a Micromeritics, Tristar instrument. Prior to N<sub>2</sub> sorption measurements, the samples are degassed at 523 K, under vacuum, for at least 16 hours. A JEOL 6300 instrument equipped with Oxford – ISIS EDS was used for the morphology observation of the samples.

### *Pulse reaction experiments*

The capability of the prepared powders to deliver oxygen at high temperatures and to convert CH<sub>4</sub> to synthesis gas during the fuel oxidation step, as well as their ability to reversibly pick up oxygen during the solid oxidation step are evaluated by pulse reaction experiments in a fixed bed pulse reactor. Reaction experiments with the materials in powder form are performed in a reaction unit (Altamira AMI-1) using a U-type quartz reactor into which 100±3 mg catalyst is inserted (Figure 2). A detailed description of the experimental unit is provided elsewhere [11-12]. During the fuel oxidation step, methane is fed to the reactor as constant volume pulses, through a special closed loop valve, in pulses of volume 100µl. During the catalyst oxidation step, either oxygen or water is injected to the reactor, also as constant volume pulses, at its entrance before the catalyst. The reactor outlet stream is directed to a quadrupole mass spectrometer (Baltzers – Omnistar) where all the reaction products are continuously monitored and quantitatively analyzed, based on calibration curves for all reactants and products of the process.

### *Membrane reactor experiments*

The membrane reactor consists of two co-axial tubes as shown in Figure 3. The membrane specimen is fixed on top of the inner  $\alpha$ -Al<sub>2</sub>O<sub>3</sub> tube and divides the membrane reactor into two compartments. An inlet and an outlet stream exist in each compartment, all connected individually to a mass spectrometer (Balzers-Omnistar) for chemical analysis. The membrane specimen is gas tightly sealed at the end of the inner tube with specially developed ceramic sealing mixtures based on commercially available ceramic kits. To control leakage free operation during the entire duration of the experiment, different inert carrier gases are used; helium is used in compartment 1 and argon in compartment 2.

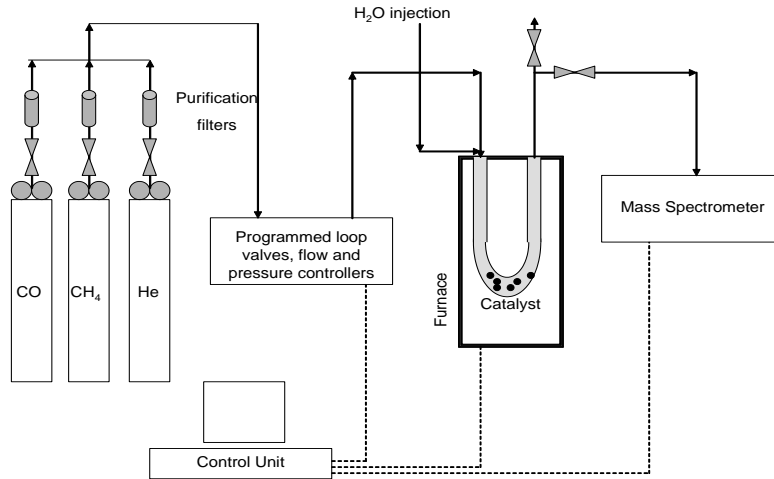


Fig. 2. Schematic flow diagram of the experimental setup used for the reaction experiments

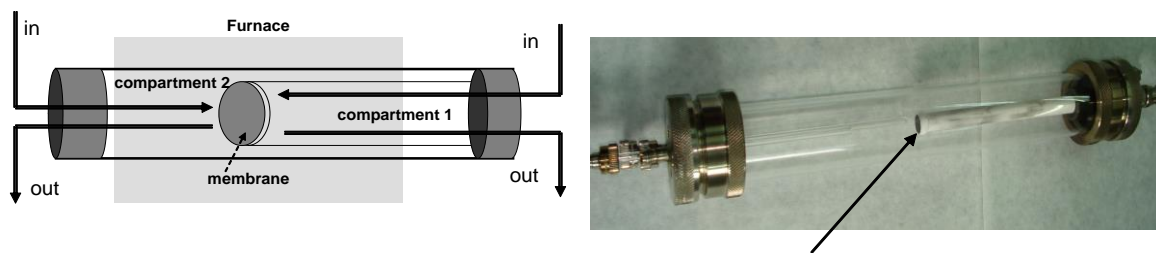


Fig. 3. Schematic diagram (left) and image (right) of the laboratory constructed membrane reactor

## RESULTS AND DISCUSSION

### Physicochemical characterization

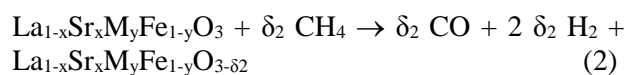
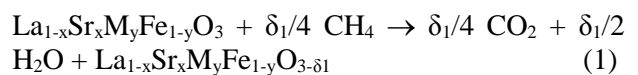
The prepared  $\text{La}_{0.7}\text{Sr}_{0.3}\text{M}_{0.05}\text{Fe}_{0.95}\text{O}_3$ , samples for  $\text{M}=\text{Ni}, \text{Co}, \text{Cr}$  and  $\text{Cu}$ , are examined by X-ray diffraction in order to identify the crystalline phases formed. All the samples are crystallized in mixed perovskitic structures similar to the mixed compound  $\text{La}_{1-x}\text{Sr}_x\text{FeO}_3$  (JCPDS card 35-1480) which is the major phase identified in the  $\text{La}_{0.7}\text{Sr}_{0.3}\text{FeO}_3$  sample. No impurities or unreacted species are identified in the XRD patterns of the prepared powders with 5% substitution of Fe, indicating that the second metal (M) is in all cases incorporated in the perovskitic structure.

The surface area of all the synthesized powders is relatively small ( $< 5 \text{ m}^2/\text{g}$ ), as they are prepared by calcination at high temperatures ( $1000^\circ\text{C}$ ).

### Pulse reaction experiments

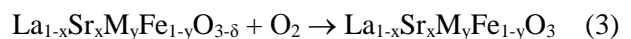
**Experimental procedure:** The capability of all the prepared powders to reversibly deliver and pick up oxygen was evaluated by successive reduction – oxidation steps in the fixed bed reactor. During the reduction – fuel oxidation step,  $\text{CH}_4$  was used as the reductant, in all experiments. During the solid oxidation step air, water or carbon dioxide injections were used.

A typical plot of the amount of oxygen exchanged by the perovskite sample during three different experiments is shown in Figure 4a. Both experiments start with 25 constant volume ( $100 \mu\text{l}$ ) injections of  $\text{CH}_4$ . During the  $\text{CH}_4$  injections step, the solid is delivering its lattice oxygen to the fuel, according to the reactions (1) and (2):



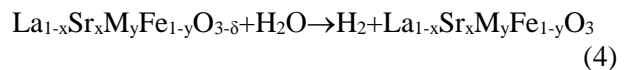
thus becoming oxygen deficient.

In the first experiment air, as constant volume pulses, is injected to the reactor, in order to oxidize the solid. During the oxidation step, the solid is recovering its oxygen stoichiometry, according to the reaction (3):

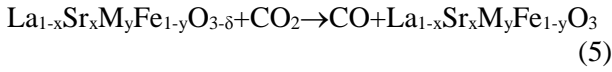


reaching its initial, fully oxidised state.

In the second experiment, the 25 methane pulses are followed by water injections. The solid in this case splits water in order to replenish its lattice oxygen, while producing  $\text{H}_2$ .



In the third experiment carbon dioxide is injected to the reactor, in order to oxidize the solid. In this case carbon monoxide is produced, according to reaction (5).



As shown in Figure 4a, the final state reached by the solid in the 2 later cases is not the fully oxidised state, as with the O<sub>2</sub> injections. This is due to the different Gibbs free energies of the 2 oxidation reactions of the B-cation (Fe<sup>2+</sup> → Fe<sup>3+</sup> and Fe<sup>3+</sup> → Fe<sup>4+</sup>), required in order the perovskite to reach its initial oxidation state, as has been discussed elsewhere [13].

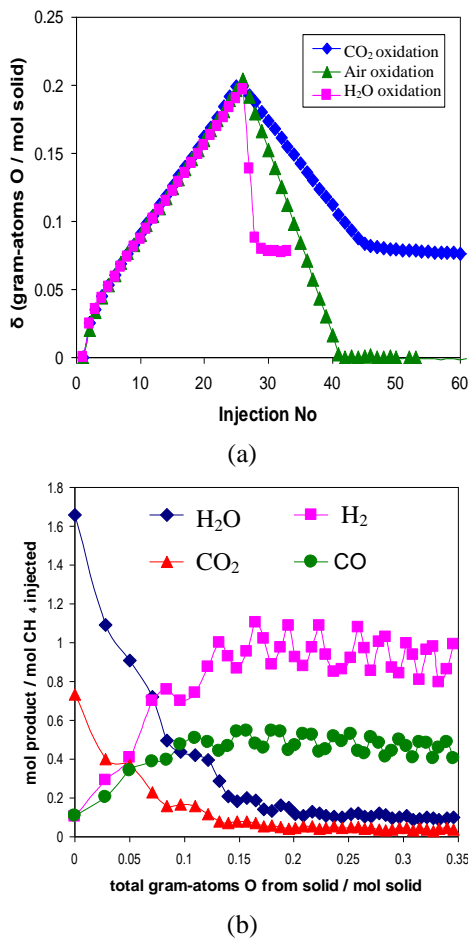


**Fig. 4.** Sample La<sub>0.7</sub>Sr<sub>0.3</sub>FeO<sub>3</sub> (a) Oxygen loss and uptake (b) product distribution during the fuel oxidation step

A typical product distribution during the fuel oxidation step is shown in Figure 4b. Initially, at low  $\delta$ , only H<sub>2</sub>O and CO<sub>2</sub> are produced. At higher oxygen deficiency of the solid, the yields of water and carbon dioxide decrease and finally only H<sub>2</sub> and CO are produced. As shown in Figure 4b, the product yields are almost stable in a wide range of  $\delta$  values.

Effect of a second metal addition in the B-position: The performance in the fuel oxidation and the solid oxidation reactions was studied initially for the “reference case” sample La<sub>0.7</sub>Sr<sub>0.3</sub>FeO<sub>3</sub> with no substitution in the B-position ( $y=0$ ).

The mixed perovskites with the general formula La<sub>0.7</sub>Sr<sub>0.3</sub>M<sub>y</sub>Fe<sub>1-y</sub>O<sub>3</sub> (M=Ni, Co, Cu and Cr) are tested at the pulse reactor. Their capability to reversibly exchange oxygen, the product yields during the fuel oxidation step as well as hydrogen production during oxidation with water are compared to each other and to the “reference case” La<sub>0.7</sub>Sr<sub>0.3</sub>FeO<sub>3</sub> ( $y=0$ ) material.

In Figure 5 the performance of the mixed perovskite materials doped with 5% M (M=Ni, Co, Cr or Cu), are compared.

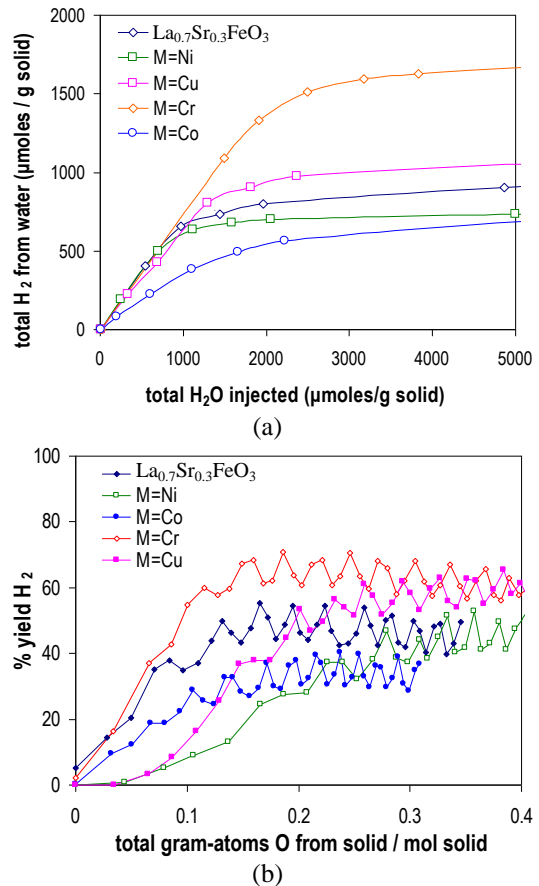


**Fig. 5.** Effect of B-site doping of the La<sub>0.7</sub>Sr<sub>0.3</sub>FeO<sub>3</sub> perovskite with 5% Ni, Co, Cr and Cu

The H<sub>2</sub> yields obtained with the above samples are compared to the reference sample La<sub>0.7</sub>Sr<sub>0.3</sub>FeO<sub>3</sub> in Figure 5b. The fully oxidized samples ( $\delta$  close to 0) present negligible H<sub>2</sub> production. The measured H<sub>2</sub> yields increase with increasing oxygen deficiency of the solid, for all tested samples, until they reach an almost equilibrium value when the oxygen deficiency of the solid exceeds a minimum  $\delta$  value. Cr and Cu doping increase the obtained H<sub>2</sub>

yields compared to the reference case, Ni doping has almost no effect and Co doping has a negative effect, decreasing the obtained  $H_2$  yields during the fuel oxidation step.

In Figure 5a the hydrogen production capability of the prepared 5% doped perovskites, when water is injected instead of air during the solid oxidation step, is compared to the corresponding  $H_2$  production capability of the “reference case”  $La_{0.7}Sr_{0.3}FeO_3$  perovskite.

In Figure 5a, the total quantity of produced  $H_2$  is shown as a function of the quantity of injected  $H_2O$ . The total quantity of produced hydrogen with the Cu and Cr doped perovskites is higher than the “reference case”, while total  $H_2$  with the Ni and Co doped samples is lower. Doping with Cr gives the best hydrogen production capability, among the perovskites prepared in this study.

By combining the results shown in Figure 5 it can be concluded that the Cr doped sample gives the best performance, both in the fuel oxidation step where it has the highest  $H_2$  yield and in water splitting during the oxidation step where it produces the highest  $H_2$  quantities.

**Effect of a second metal addition in the A-position:** In order to study the effect of replacing the metal at the A site of the perovskite, Sr was replaced by Ca. The performance of the perovskites with the general formula  $La_{1-x}Ca_xFeO_3$  ( $x=0.3, 0.5, 0.7$ ) is compared to the “reference case”  $La_{0.7}Sr_{0.3}FeO_3$  in Figure 6.

From Figure 6a, where the  $H_2$  yield during the fuel oxidation step is shown, it can be observed that for all the Ca containing perovskites the maximum  $H_2$  yields are identical to the “reference case” sample. However, the production of the desired products,  $H_2$  and CO in the presence of all  $La_{1-x}Ca_xFeO_3$  samples, reaches its maximum at significantly lower oxygen non-stoichiometry values ( $\delta$ ). In Figure 6b the water splitting capability of the  $La_{1-x}Ca_xFeO_3$  materials, during the solid oxidation step, as percent  $H_2O$  conversion, is compared to that of the “reference case” perovskite. It can be observed that for all the Ca containing samples, oxidation with water proceeds until much lower O-nonstoichiometry ( $\delta$ ) values, compared to the reference case perovskite. Furthermore, the final  $\delta$  value becomes lower as the Ca/La ratio of the perovskite decreases.

#### Membrane reactor experiments

In the membrane reactor the two steps of the water splitting reaction, lattice oxygen removal-activation and hydrogen production-deactivation,

are performed simultaneously at the different compartments of the reactor.

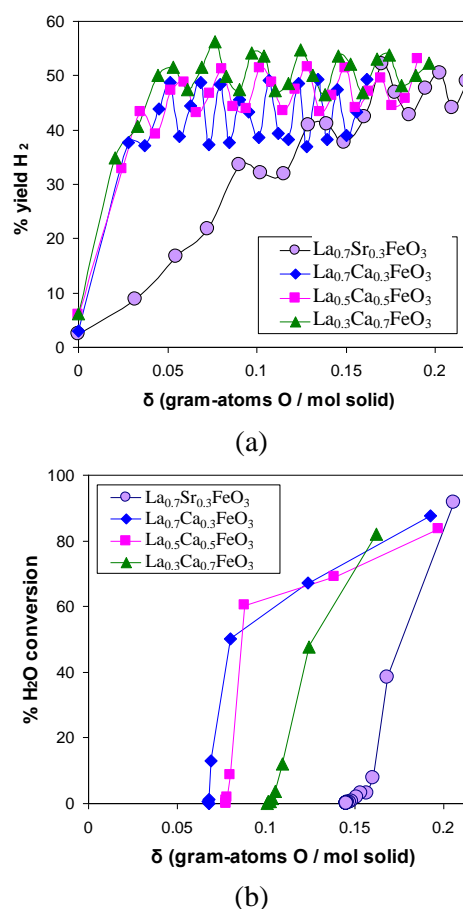


**Fig. 6.** Effect of A-site doping of the  $La_{1-x}Me_xFeO_3$  perovskite with Sr or Ca

Membrane specimens of the composition  $La_{0.7}Sr_{0.3}FeO_3$  are mounted in and tested at the membrane reactor. Because of technical reasons related with the complexity of mass spectrometry analysis, the experiments towards demonstrating the membrane reactor principle are performed with carbon monoxide as the reductant at the activation step, instead of methane which was used during the batch reactor experiments.

During a typical experiment, the membrane reactor is heated to  $860^\circ C$ , initially with inert gas flow in both compartments, while the signals of water and hydrogen in compartment 1 are continuously monitored. The injection of water in compartment 1 does not involve any changes in the signal of hydrogen in compartment 1, which maintains its background value, since the membrane is initially inactive.

The injection of CO in compartment 2, results in the reduction of the membrane surface in side 2, creating oxygen vacancies. Due to the ionic conductivity of the perovskitic material the oxygen

vacancies are transported through the crystal lattice to the surface of the membrane in compartment 1 and activate it. The water that is injected in compartment 1 is thus split, hydrogen is produced, while simultaneously oxygen is delivered to the solid which fills its anion vacancies. The lattice oxygen is transported once again via the material to the surface of membrane in compartment 2, where it is continuously consumed oxidising CO. Globally a clean flow of oxygen ions, originating from water, is created, from side 2 to side 1 of the membrane, while simultaneously oxygen vacancies flow from side 1 to side 2 of the membrane. Thus a steady state is reached where the surface of the membrane in compartment 2 is rich in oxygen, continuously oxidising CO, while the membrane surface in compartment 1 is rich in oxygen vacancies, continuously splitting water at the highest initial conversion. By optimising the process parameters e.g. gas flows, temperature, membrane thickness, it is possible to keep the membrane material at its highest activation state, during the steady state operation of the reactor.

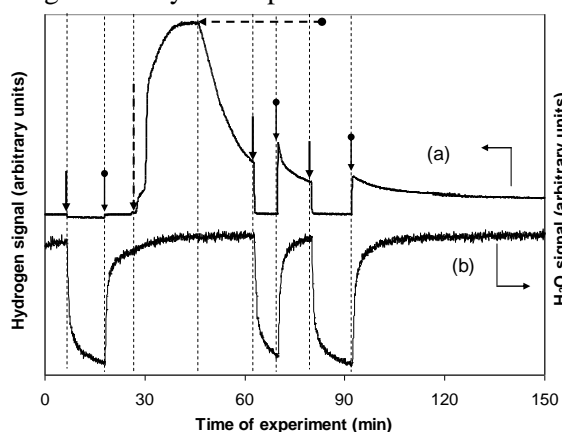


**Fig. 7.** Hydrogen and water MS signals in compartment 1 during a typical experiment with  $\text{La}_{0.3}\text{Sr}_{0.7}\text{FeO}_{3\pm\delta}$  (a) produced  $\text{H}_2$  (b) injected  $\text{H}_2\text{O}$ ,

—▶: water off, ●▶: water on, - -▶: CO on,; ● -▶: CO off

The interruption of CO injection in compartment 2 results in decreased hydrogen production rate in compartment 1. However, hydrogen yield does not become zero, instead it reaches a new steady value, which is of course lower than before (Figure 7). In this case the oxygen ions are desorbed from the membrane surface in side 2 as molecular  $\text{O}_2$ , only under the effect of oxygen partial pressure difference between the two sides of the membrane. The flow of oxygen ions is in this case smaller, however it is not insignificant. The water continues to be split, producing hydrogen which originates only from renewable water.

Periodical water feed shut downs in compartment 1, were performed during this steady state, in order to exclude the possibility of baseline shifting and quantify the obtained results. As shown in Figure 7, interruption of  $\text{H}_2\text{O}$  injection results in a significant drop of the  $\text{H}_2$  signal, down to its background value, which proves that the observed hydrogen signal is due to real hydrogen produced from the decomposition of the injected water.

Similar experiments with inactive membrane materials ( $\alpha\text{-Al}_2\text{O}_3$  and fused silica) did not show any significant change in the hydrogen signal during water feed shut downs, either before or after CO injection in compartment 2.

## CONCLUSION

Perovskite materials are suitable for use as oxygen carriers in Chemical Looping Reforming. Upon reduction with methane, powdered  $\text{La}_{1-x}\text{Sr}_x\text{M}_y\text{Fe}_{1-y}\text{O}_3$  ( $\text{M} = \text{Ni}, \text{Co}, \text{Cr}, \text{Cu}$ ) materials are found to lose oxygen. Subsequent oxidation of the solid is performed either with gaseous oxygen or water or with carbon dioxide. When oxidation takes place with air, heat is generated because the reaction is exothermic. When  $\text{H}_2\text{O}$  is used to oxidize the material, simultaneously is produced very pure  $\text{H}_2$ , ready to use in fuel cell applications, but the oxidation reaction is endothermic. After oxidation with  $\text{CO}_2$ , CO is produced but again the oxidation reaction is endothermic. The additional heat required during the oxidation with  $\text{H}_2\text{O}$  or  $\text{CO}_2$ , is the energy penalty for the additional production of  $\text{H}_2$  or CO. The best, thus far, performance was obtained with the  $\text{La}_{0.7}\text{Sr}_{0.3}\text{Cr}_{0.05}\text{Fe}_{0.95}\text{O}_3$  sample, with  $\text{H}_2$  yield up to 70% and very good stability in repetitive

**Acknowledgements:** The present study was funded by the program "Hydrogen Economy Cooperation Network for Research - Public Awareness - Business Opportunities across Greek-Bulgarian borders – HYDECON". The Project is co-funded by the European Regional Development Fund and by national funds of the countries participating in the ETCP "Greece-Bulgaria 2007-2013" through contract B1.33.01.

## REFERENCES

1. Blesl M, Kober T, Bruchof D, Kuder R. *Energy Policy*; **38**, 6278 (2010)
2. ADEME, BRGM, IFP.  $\text{CO}_2$  capture and storage in the subsurface. Geoscience Issues, France, 2007.
3. Hossain MM, Lasa HI. *Chem. Eng. Sci.*, **63**, 4433 (2008)

4. Pröll T, Bolhår-Nordenkamp J, Kolbitsch P, Hofbauer H. *Fuel*, **89**,1249 (2010)
5. Linderholm C, Mattisson T, Lyngfelt A., *Fuel*, **88**, 2083 (2009)
6. Adánez J, Dueso C, Diego LF, García-Labiano F, Gayán P, Abad A. *Energy & Fuels*; **23**, 130 (2009)
7. Balat M., *Energy Sources Part A*, **31**, 39 (2009)
8. Chen WH, Chiu TW, Hung HL., *Int J Hydrogen Energy*, **35**, 12808 (2010).
9. Diego LF, Ortiz M, Adánez J, García –Labiano F, Abad A, Gayán P., *Chem. Eng. J.*, **144**, 289 (2008)
10. Pecchi G, Reyes P, Zamora R, Campos C, Cadus LE, Barbero BP. *Catal. Today*, **133–135**, 420 (2008)
11. Evdou A, Zaspalis V, Nalbandian L., *Int J Hydrogen Energy*; **33**, 5554 (2008)
12. Evdou A, Nalbandian L, Zaspalis VT., *J Membr Sci.*, **325**, 704 (2008)
13. Nalbandian L, Evdou A, Zaspalis V., *Int J Hydrogen Energy*, **34**, 7162 (2009)

## НОВИ МАТЕРИАЛИ КАТО ПРЕНОСИТЕЛИ НА КИСЛОРОД ЗА ЕНЕРГИЙНИ ПРИЛОЖЕНИЯ

А. Евдоу<sup>1,2</sup>, В. Заспалис<sup>1,2</sup>, Л. Налбандиан<sup>1\*</sup>

<sup>1</sup>Лаборатория по неорганични материали, Институт по химични процеси и енергийни ресурси,

Научно-изследователски и технологичен център – Хелас, Терми-Солун, Гърция

<sup>2</sup>Катедра по химическо инженерство, Аристотелов университет, Солун, Гърция

Получена на Май 27, 2013; Ревизирана на Август 18, 2013

(Резюме)

Перовскитите имат способността да формират голямо количество ваканции в своите структури и да приемат и отдават обратимо кислород при високи температури, което ги прави идеални кандидати за преносители на кислород. В настоящата разработка е изследвано поведението на перовскити с обща формула  $\text{La}_{1-x}\text{Me}_x\text{M}_y\text{Fe}_{1-y}\text{O}_3$  ( $\text{Me} = \text{Sr}, \text{Ca}, \text{M} = \text{Ni}, \text{Co}, \text{Cr}, \text{Cu}$ ) като преносители на кислород за генериране на сингаз от метан, както и като плътни мембранни материали. Кислородът се изтегля от кристалната решетка на перовскитите чрез окисление на гориво. След това към твърдата фаза се добавя вода, кислород или въглероден диоксид, което осигурява запълване на ваканциите с необходимите кислородни атоми. Сравнено е поведението на смесени перовскитни материали, заместени с 5% М на В-място ( $\text{M}=\text{Ni}, \text{Co}, \text{Cr}$  и  $\text{Cu}$ ). Изследвано е също така и заместването на Sr с Ca на А-място в перовскитите. Плътни мембрани от материалите с формата на диск са използвани в мембранен реактор. Проведените експерименти при 1000°C разкриват възможността за едновременно и изотермично провеждане на етапите на редукция и окисление от двете страни на мембранный реактор. Системата може да функционира без добавянето на въглерод-съдържащ редуктор, така че е възможно реализирането на процес за производство на водород, основаващ се на възобновяем водороден източник, напр. вода.

## Comparison investigation of Co-based catalysts for the catalytic hydrolysis of sodium borohydride

G. Y. Hristov<sup>1\*</sup>, E. Y. Chorbadzhiyska<sup>1</sup>, R. S. Rashkov<sup>2</sup>, Y. V. Hubenova<sup>3</sup>, M. Y. Mitov<sup>1</sup>

<sup>1</sup>Department of Chemistry, South-West University "Neofit Rilski" - Blagoevgrad, Bulgaria

<sup>2</sup>Institute of Physical Chemistry „Acad. Tostislav Kaishev”, Bulgarian Academy of Sciences, Bulgaria

<sup>3</sup>Department of Biochemistry and Microbiology, Plovdiv University "Paisii Hilendarski", Bulgaria

Received May 27, 2013; Revised June 28, 2013

Catalyzed borohydride hydrolysis is a perspective method for hydrogen-on demand production. The produced hydrogen is with high purity, the process requires no energy and its kinetics can be easily controlled by proper catalysts. In this study, three Co-based nanocomposites (CoMnB, CoNiMnB and CoNiMoW) electrodeposited on nickel foam were investigated as catalysts for borohydride hydrolysis. Kinetics of the catalyzed reaction was investigated by water-displacement method at different temperatures from 16 °C to 40 °C. The highest hydrogen generation rates of 0,9 ml/min at 16 °C and 2,1 ml/min at 40 °C was obtained with CoNiMnB catalyst. At the same time, the process takes place with the lowest activation energy of 36,9 kJ/mol with this catalyst. The obtained results show that CoNiMnB-electrodeposits possess the highest catalytic activity among studied materials and can be used as a catalyst in hydrogen-on-demand generators for portable applications.

**Key words:** Hydrogen, borohydride, hydrolysis, hydrogen generator.

### INTRODUCTION

Among all alternative power sources, hydrogen is claimed as the cleanest fuel of the future. Both in combustion engines and fuel cells its reaction with oxygen produces only water. In 1970's John Bockris first coined the term "hydrogen economy" as a concept for delivering energy using hydrogen. Nowadays, both the depletion of the fossil fuels and the environmental pollution drive to intensification of the R&D of the hydrogen technologies as an alternative to the current energy system.

Except the cost, hydrogen seems as a perfect fuel. The by-products of hydrogen combustion are electricity, water and heat. Although its low density makes efficient storage difficult, hydrogen has the highest energy of combustion per unit of mass. Energy conversion devices using hydrogen are highly efficient and produce very little or no harmful emissions. As an energy carrier, hydrogen can be produced safely and abundantly from diverse renewable resources such as hydroelectricity, solar and wind power. Since many of these are domestic sources, it can help decrease the dependence of nations on others for fuels eliminating the political polarizations that arise from cartel pricing, conflicting ideological and economic policies and hostilities among nations.

For the same reasons, hydrogen is anticipated to join electricity as the foundation of a globally sustainable energy system using renewable energy [1, 2].

A wide range of technologies for hydrogen production has been developed. However, the steam methane reforming accounts for about 95 percent of the hydrogen produced today in the United States [3]. Another method, called partial oxidation, produces hydrogen by burning methane in air. Both processes produce a "synthesis gas", which is reacted with water to produce more hydrogen. Another attractive method is the renewable electrolysis, which uses an electric current to split water into hydrogen and oxygen. The electricity required can be generated using renewable energy technologies, such as wind, solar, geothermal, and hydroelectric power.

The wide use of hydrogen has several disadvantages. The production of hydrogen gas currently relies on fossil fuels, mainly natural gas, which results in huge CO<sub>2</sub> emissions and environmental pollution. The storage is tough, because hydrogen is a low-density gas. The distribution and infrastructure need to be refurbished to cope with hydrogen [4].

One of the promising methods for production of hydrogen-on-demand is the hydrolysis of alkaline borohydrides. Using sodium borohydride as a hydrogen carrier has several advantages. The

\* To whom all correspondence should be sent:

E-mail: george\_ggg@abv.bg

produced hydrogen is quite pure. In some cases it is extremely important, because any waste may damage the proton-exchange membrane (PEM) in the fuel cells, for example. The borohydride hydrolysis reaction can be highly controllable – it stops if the catalyst is removed from the reactor. The reaction needs no energy and can operate at ambient temperature and pressure. According to the application, the amount of the released gas can be controlled by using proper catalyst. Among all catalysts studied, ruthenium catalysts possess the highest activity [5].

Low cost and effective transition metal catalysts are of interest for the development of on-board hydrogen generation systems for the fuel cell vehicles. With the aim of designing an efficient low-cost hydrogen generator for portable fuel cell applications, nickel–cobalt materials were reported to be promising catalysts [6-7]. The main method for their preparation is by a chemical reduction method [8].

In the present study, three types of Co-based composites were electrodeposited on Ni foam and investigated as catalysts for borohydride hydrolysis. The kinetics of the process was monitored through the volume of the evolved hydrogen at different temperatures. For each catalyst, the hydrogen evolution rate as well as the activation energy were estimated and compared.

## EXPERIMENTAL

### Catalyst preparation

CoMnB, CoNiMnB and CoNiMoW coatings were produced by electrodeposition from on Ni-foam. Complex electrolytes consisted of 5 g/l  $\text{Co}^{2+}$ , 5 g/l  $\text{Mn}^{2+}$ , 0.5 g/l  $\text{Ni}^{2+}$  and 35 g/l  $\text{H}_3\text{BO}_3$  were used to produce CoMnB- and CoNiMnB-electrodeposits. The electrolysis was carried out at 40 °C for 30 min. Cobalt was used as an anode and the supported material (Ni-foam) was connected as a cathode. The electrolyte for CoNiMoW preparation consisted of sodium citrate – 72 g/l,  $\text{Na}_2\text{WO}_4 \cdot 2\text{H}_2\text{O}$  – 24 g/l,  $\text{Na}_2\text{MoO}_4$  – 6g/l,  $\text{Ni}(\text{SO}_3\text{NH}_2)_2$  – 16 g/l,  $\text{Co}(\text{SO}_3\text{NH}_2)_2$  – 16 g/l. The pH of the obtained solution was adjusted to pH = 10 with  $\text{NH}_4\text{OH}$ . The morphology of the developed materials was analyzed by scanning electron microscopy (SEM) using Leo 1455VP microscope.

### Experimental setup

The experimental setup used in this investigation is presented on Fig. 1. 10,0 ml alkaline solution of sodium borohydride (5%  $\text{NaBH}_4/6\text{M KOH}$ ) was placed in the reactor (2).

The temperature of the reactor was controlled by a thermostat (1). The investigated catalyst (5) was placed in the borohydride solution and the reactor was closed hermetically with rubber stopper with a gas outlet (3). The produced hydrogen was measured by water displacement method. The hydrogen generation rate was estimated as a volume of the produced hydrogen per unit of time. Series experiments were carried out for each catalyst at different temperatures in the range from 16 °C to 45 °C. Using the obtained kinetic data, the activation energy was calculated.

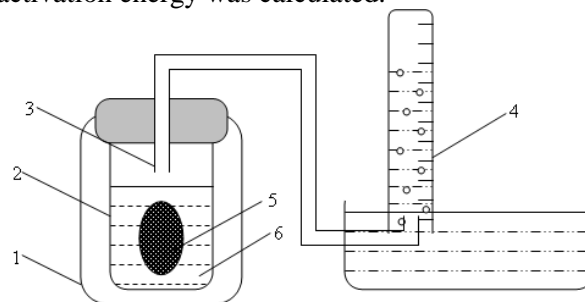


**Fig. 1.** Experimental setup: 1 – Thermostat; 2 – Reactor; 3 – Outlet for the generated gases; 4 – Cylinder; 5 – Catalyst; 6 – 5 %  $\text{NaBH}_4/6\text{M KOH}$  solution.

## RESULTS AND DISCUSSION

All produced electrodeposits have similar dendrite structure. The coatings cover almost the whole surface of the supported material (Ni-foam), following its porous structure - Fig. 2.

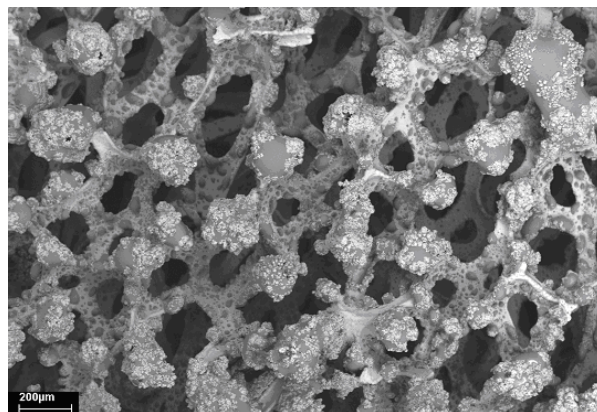


**Fig. 2.** SEM image of CoMnB electrodeposit on Ni-foam.

The kinetics of the borohydride hydrolysis by using studied catalysts is presented on Fig. 3. As seen from the graphs, the hydrogen evolution begins right after the catalyst contacts with the borohydride solution and linear dependences of the quantity of generated hydrogen with time are observed for all investigated materials. The values of the reaction rate obtained with the electrodeposited catalysts, however, are higher than that with the bare Ni-foam.

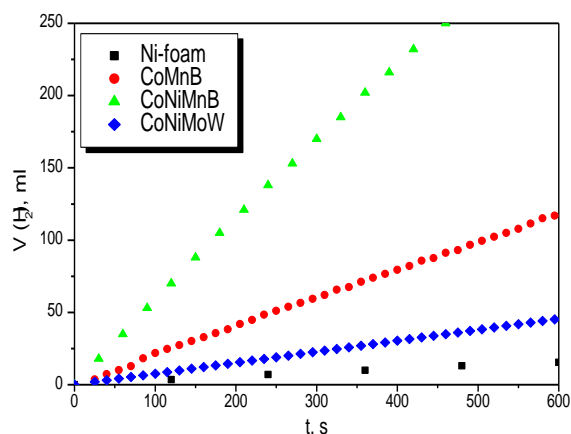


Fig. 3. Hydrogen generation during sodium borohydride hydrolysis process, catalyzed by Ni-foam, CoMnB, CoNiMnB and CoNiMoW at 25 °C.

The values of the hydrogen generation rate obtained with the catalysts at different temperatures as well as the activation energy, estimated from the Arrhenius plots, are summarized in Table 1. The highest rate values, exceeding with an order of magnitude those with the other materials, were achieved with the CoNiMnB catalyst. The lowest activation energy of 36,9 kJ/mol, which is even lower than the values reported for the ruthenium catalyst ( $E_a = 56$  kJ/mol) [9], was also obtained with this catalyst. Besides the similar composition and close activation energy with that of CoNiMnB, the lowest reaction rates were achieved with CoNiMoW catalysts, which reveals their potentials as anodic electrocatalysts for direct borohydride electrooxidation.

**Table 1.** Hydrogen generation rate (ml/s) and activation energy (kJ/mol) of the sodium borohydride hydrolysis, catalyzed by the investigated materials.

Material	Hydrogen generation rate (ml/s)				$E_a$ (kJ/mol)
	16 °C	25 °C	30 °C	40 °C	
CoMnB	0,061	0,162	0,277	0,501	54,9
CoNiMnB	0,901	1,300	1,402	2,101	36,9
CoNiMoW	0,063	0,076	0,115	0,252	37,8

### CONCLUSION

The results from the present study show that the CoNiMnB electrodeposits possess the highest catalytic activity towards borohydride hydrolysis

among investigated materials. Although the achieved hydrogen generation rates are lower than those with other reported catalysts, these materials can be used in hydrogen-on-demand generators for portable applications. The low catalytic activity of the other two catalysts (CoMnB and CoNiMoW) makes them proper candidates as anode electrocatalysts for Direct Borohydride Fuel Cells, where the hydrolysis is a competitive process to the direct borohydride electrooxidation.

**Acknowledgements:** The present study was funded by the program "Hydrogen Economy Cooperation Network for Research - Public Awareness - Business Opportunities across Greek-Bulgarian borders – HYDECOR". The Project is co-funded by the European Regional Development Fund and by national funds of the countries participating in the ETCP "Greece-Bulgaria 2007-2013" through contract B1.33.01.

### REFERENCES

- 1.S. Bilgen, K. Kaygusuz, *Energ. Source.*, **26**, 1119 (2004).
2. A. Rodes, J. M. Penez, A. Aldaz, in: Handbook of fuel cells: advances in electrocatalysis, materials, diagnostics and durability, W. Vielstich, H. A. Gasteiger, A. Lamm (eds) **6**, Hoboken: Wiley, (2009).
- 3.H. Schlesinger, H. Brown, A. Finholt, J. Gilbreath, H. Hoekstra, E. Hyde *J. Am. Chem. Soc.*, **75**, 215 (1953).
- 4.D. Ross, *Vacuum*, **80**, 1084 (2006).
- 5.S. Amendola, S. Sharp-Goldman, M. Janjua, N. Spencer, M. Kelly, P. Petillo, M. Binder, *Int. J. Hydr. Energy*, **25**, 969 (2000).
- 6.B. H. Liu, Z. P. Li, S. Suda, *J. Alloys Compd.*, 415 (1-2), 288 (2006).
- 7.H. Dai, Y. Liang, P. Wang, H. Cheng, *J. Power Sources*, **177**, 17 (2008).
- 8.J. Ingersoll, N. Mani, J. C. Thenmozhival, A. Muthaiah, *J. Power Sources*, **173** (1), 450 (2007).
- 9.S. Jeong, R. Kim, E. Cho, H. Kim, S. Nam, I. Oh, S. Hong, S. Kim, *J. Power Sources*, **144**, 129 (2005).

## СРАВНИТЕЛНО ИЗСЛЕДВАНЕ НА СО-СЪДЪРЖАЩИ КАТАЛИЗАТОРИ ЗА ХИДРОЛИЗА НА НАТРИЕВ БОРХИДРИД

Г. Христов<sup>1\*</sup>, Е. Чорбаджийска<sup>1</sup>, Р. Рашков<sup>2</sup>, Й. Хубенова<sup>3</sup>, М. Митов<sup>1</sup>

<sup>1</sup>Катедра „Химия“, Югозападен университет „Неофит Рилски“ – Благоевград, България

<sup>2</sup>Институт по Физикохимия „Акад. Ростислав Каисhev“, Българска Академия на Науките, България

<sup>3</sup>Катедра „Биохимия и микробиология“, Пловдивски университет „Паисий Хилендарски“, България

Получена на Май 27, 2013; Ревизирана на Юни 28, 2013

(Резюме)

Каталитичната хидролиза на борхидриди е перспективен метод за производство на водород. Получаваният водород е с висока чистота, процесът не изисква внасяне на енергия и кинетиката му може лесно да се контролира чрез подходящи катализатори. В настоящата разработка, три Со-съдържащи нанокмозита (СоMnВ, СоNiMnВ и СоNiMoW), електроотложени върху пенообразен никел, са изследвани като катализатори на хидролизата на натриев борхидрид. Скоростта на процеса бе определяна чрез измерване на обема вода, изместен от генерирания водород за единица време. Кинетиката на реакцията бе проследявана при различни температури в интервала от 16 °С до 40 °С. Най-големи скорости на получаване на водород от 0,9 ml/min при 16 °С и 2,1 ml/min при 40 °С бе получена с СоNiMnВ катализатор. В същото време, с този катализатор реакцията протича и с най-ниска активираща енергия от 36,9 kJ/mol. Получените резултати показват, че електроотложените СоNiMnВ нанокмозити притежават най-висока каталитична активност от изследваните материали и може да бъдат използвани като катализатори в генератори на водород за портативни мобилни приложения.

## Sediment microbial fuel cell utilizing river sediments and soil

I. Bardarov<sup>1</sup>, Y. Hubenova<sup>2</sup>, M. Mitov<sup>1\*</sup>

<sup>1</sup> Department of Chemistry, South-West University, 66 Ivan Mihajlov str., 2700 Blagoevgrad, Bulgaria

<sup>2</sup> Department of Biochemistry and Microbiology, Plovdiv University, 24 Tsar Asen str., 4000 Plovdiv, Bulgaria

Received May 27, 2013; Revised July 11, 2013

In this study, results obtained during eighteen months operation of column-type Sediment Microbial Fuel Cells (SMFCs) using river sediments and soil collected near Blagoevgrad, Bulgaria, are presented and discussed. The SMFCs were operated without any supplying of nutrients except periodic addition of water for compensation of the losses from evaporation. Polarization measurements under constant as well as variable load resistances were carried out during SMFCs operation. Higher electric characteristics and efficiency as well as more stable performance were obtained with the SMFC using river sediments. Power supply, constructed of two SMFCs connected in series, is able to supply low-power consumers, which demonstrate the perspectives for further development and application of the technology.

**Key words:** sediment microbial fuel cells, fresh water sediments, electrogenic bacteria, electricity generation, power supply.

### INTRODUCTION

Sediment Microbial Fuel Cells (SMFCs), in which bacteria-assisted conversion of the organic matter in aquatic sediments into electricity takes place, are considered as one of the most perspective representatives of the innovative Microbial Fuel Cell (MFC) technology for power supplying electronics in remote areas or for monitoring of different aquatoria. SMFCs offer a unique opportunity to investigate the efficiency of harvesting electricity from natural systems and the potentials for their real application in power generation or bioremediation in natural environments.

SMFCs are adaptation of reactor-type microbial fuel cells (MFCs), where anode and cathode are contained in one or two closed compartments. The anode is embedded into the sediment placed at the bottom of the reactor and the cathode is immersed in the aerobic water column above the phase boundary with the sediment and the device operates on the potential gradient at a sediment-water interface (Fig. 1). Unlike other MFCs, where proton-exchange membrane (PEM) and mediators are used to create the needed conditions for the bacteria to generate current, SMFCs are very cost-effective since the expensive PEM is not necessary. Sediments themselves act as a nutrient-rich anodic media, inoculum and proton-exchange membrane. This fact allows cheap and easy to build SMFC, which can be used successfully on the field.

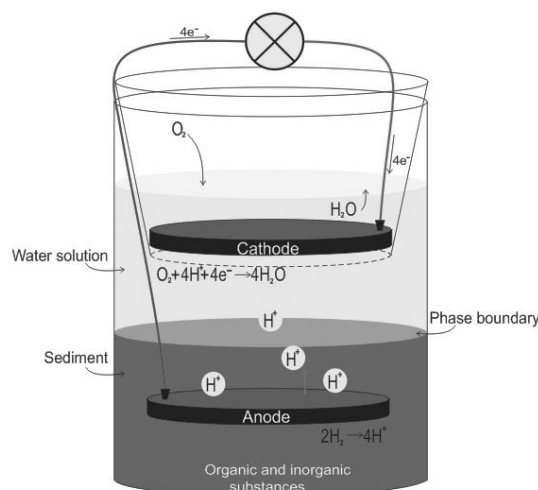


**Fig.1.** Scheme of SMFC.

The first practical devices to be powered by SMFC technology were reported in 2008 [1]. Meteorological buoys capable of measuring variety of parameters and transferring data via real-time line were powered by benthic SMFCs. Until now, most of the research in the field has been performed with marine sediments [1-3] and very few reports reveal the potential application of freshwater sediments [4, 5] or soil [6, 7] for electricity generation.

In this paper, we report the results from over eighteen months operation of SMFCs using river sediments and soil collected near the town of Blagoevgrad, Bulgaria. The collected data verify the possibility for electricity generation by utilization of these widely spread natural materials and the potential of SMFC technology for power supply application.

\* To whom all correspondence should be sent:  
E-mail: mitovmario@mail.bg

## EXPERIMENTAL

River sediments and water were collected from the basin of river Struma (GPS coordinates: 41.990354, 23.067501). Soil samples were taken near Blagoevgrad (GPS coordinates: 42.051209, 23.076744).

Cylindrical plastic vessels were used for construction of single-chamber fuel cells. Half of the vessel volume was fulfilled with the collected sediments/soil. Graphite disk (6 cm diameter, 1 cm thickness; GES Co., apparent density 1.68 g/cm<sup>3</sup>, porosity 24%, electrical resistance 6.0 μΩ.m) served as anode was buried into the sediment 3 cm above the vessel bottom. Water from the place of the sample collection was poured above the sediment layer. Graphite cathode with the same dimensions as the anode was placed few millimeters beneath the water surface.

The constructed SMFCs were operated for over 18 months without any supplying of nutrients except periodic addition of water for compensation of the losses from evaporation. Polarization measurements under constant or variable load resistances were carried out periodically using resistor box. The cell voltage was measured with a digital voltmeter MAS- 345 and the current was estimated by using Ohm's law.

## RESULTS AND DISCUSSION

Few hours after the start up the open circuit voltage (OCV) of both types of MFCs stabilized and began to rise slowly. This increase continued till the 15<sup>th</sup> day for the river sediment MFC and the 20<sup>th</sup> day for the soil MFC, respectively, after which a slow drop began – Fig.2. When the drop of voltage was significant some measures, such as replacing the water layer, cleaning and shifting the cathode, were taken in order to restore it.

Two months after the start up, the SMFCs were polarized for 20 days using a 510 Ω load resistor. After switching the external resistance, the voltage dropped initially and stabilized at relatively constant values. The estimated mean current values were 0.30 mA for the sediment MFC and 0.15 mA for the soil MFC, respectively, which shows that the electrochemical processes in the sediment MFC take place twice faster.

Right after disconnecting the loads, the OCV of the both MFC rose sharply to 450 mV for the sediment MFC and 300 mV for the soil MFC. After the initial sharp increase, the voltage continued to rise slowly and in the following days, values up to 350 mV for the soil MFC and 770 mV for the sediment MFC were recorded. Such high values

had not been achieved to that moment. This fact indicates that the operation of the SMFCs under an electric load stimulates the metabolism and growth of the electrogenic bacteria.

At the end of the fourth month of the MFCs operation an electrical air ozonator was placed near them. Its purpose was to enrich the air around the cells with the highly reactive ozone. This led to an increase in the voltage of both MFCs. The OCV of the Soil MFC reached a record value of 590 mV.

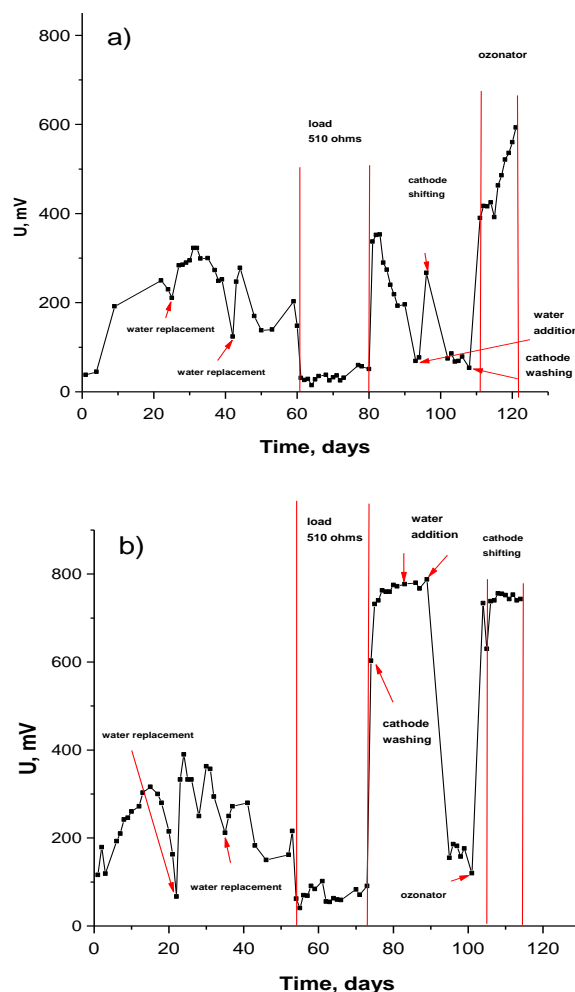


**Fig.2.** Variation of the measured voltage with time during operation of : a) Soil MFC; b) Sediment MFC.

Along with the voltage measurements at open and closed circuit conditions under constant load, polarization measurements of the studied SMFCs under variable resistances were also carried out. The obtained data were plotted as polarization ( $U$ - $I$ ) and power ( $P$ - $I$ ) curves – Figs. 3 and 4. As seen from the graphs, the sediment MFC generates higher current and power and at the same time the data fluctuations are smaller.

From the linear slopes of the polarization curves, the values of the MFCs internal resistance were calculated. Despite some fluctuations, the

estimated values of the internal resistance maintain near constant throughout the whole long-term experiment and they are close to the resistance of the load, at which the maximum power is achieved. This is in accordance with the theory, which claims that the internal resistance of a galvanic element is equal to the external resistance at which the element generates maximum power.

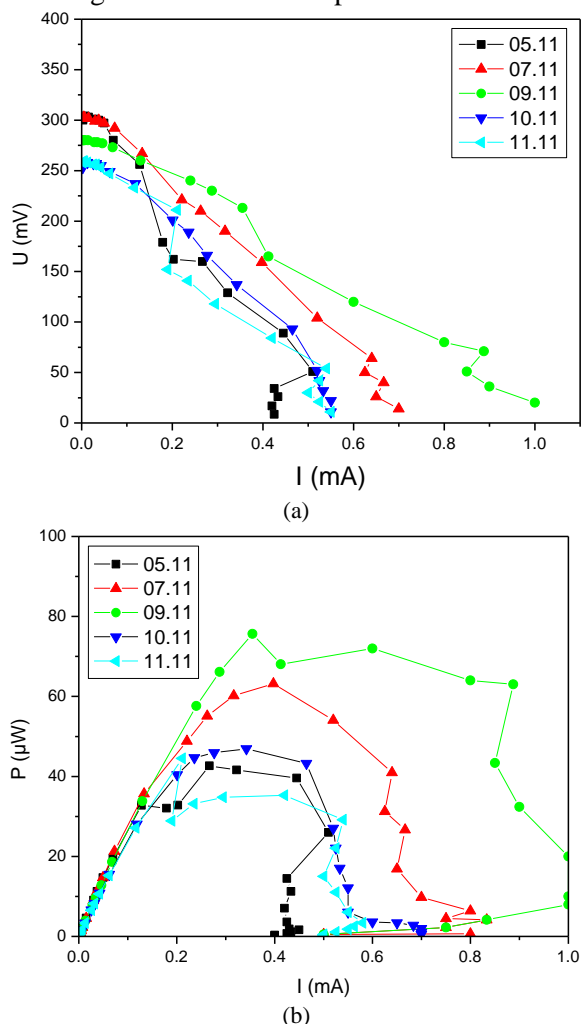


**Fig. 3.** a) Polarization curves; b) power curves obtained with Soil MFC at several subsequent days (shown as dates in the legend) starting from the 50th day after the beginning of experiment.

It is worth noticing that the polarization characteristics obtained with Sediment MFC few days after the continuous work under load were much higher than those achieved before. The maximum power reached 410  $\mu$ W, which is over five times higher than the maximum power measured in the previous period. In contrary, the Soil MFC showed worse polarization characteristics, which indicated that the system was exhausted from the continuous work under a load.

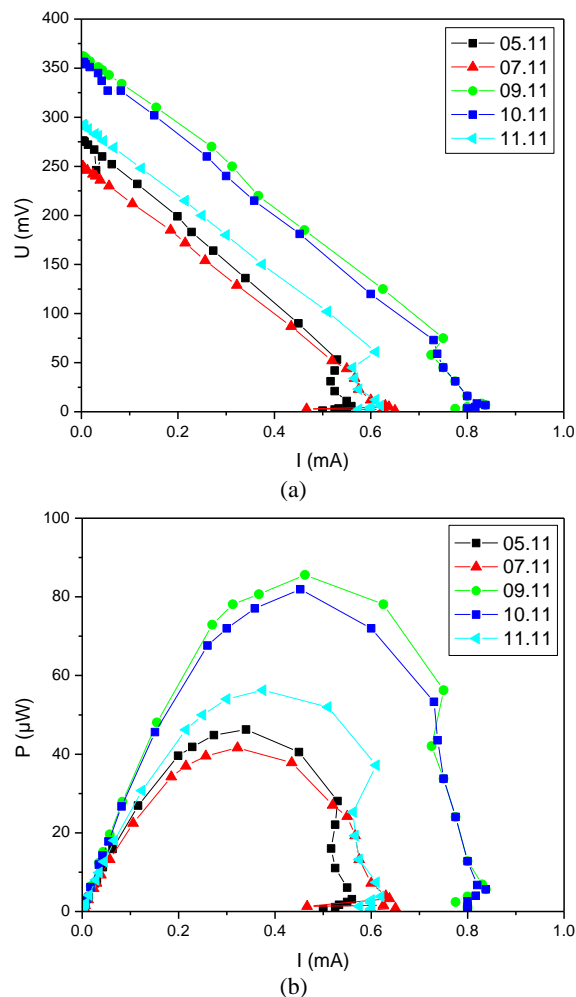


**Fig. 4.** a) Polarization curves; b) power curves obtained with Sediment MFC at several subsequent days (shown as dates in the legend) starting from the 50th day after the beginning of experiment.

After 18 months operation, the SMFCs' outputs have continued to be stable and even grown up. The OCV values 900 mV and 650 mV have been achieved with the Sediment MFC and Soil MFC, respectively [9]. Connected in series, both SMFCs are able to supply low-power consumers – Fig. 5.



**Fig. 5.** Connected in series SMFCs supplying digital watch

## CONCLUSION

Based on the results obtained in this study, it can be concluded that Sediment microbial fuel cells using river sediments and soil are able to generate current during long term operation. The better performance of the SMFC utilizing river sediments is probably due to the higher content of organic matter as well as to specific electrogenic properties of the bacteria in this type of sediments. The low cost and easy maintenance make sense the further research and development of this promising power supply devices.

**Acknowledgements:** *The present study was funded by the program "Hydrogen Economy Cooperation Network for Research - Public Awareness - Business Opportunities across Greek-Bulgarian borders – HYDECON". The Project is co-funded by the European Regional Development Fund and by national funds of the countries participating in the ETCP "Greece-Bulgaria 2007-2013" through contract B1.33.01.*

## REFERENCES

1. L. Tender, S. Gray, E. Groveman, D. Lowry, P. Kauffman, *J. Power Sources*, **179**, 571 (2008).
2. C.E. Reimers, L.M. Tender, S. Fertig, W. Wang, *Environ. Sci. Technol.*, **35**, 192 (2001).
3. D.R. Bond, D.E. Holmes, L.M. Tender, D.R. Lovley, *Science*, **295**, 483 (2002).
4. K. Scott, I. Cotlarciuc, I. Head, K.P. Katuri, D. Hall, J.B. Lakeman, D. Browning, *J. Chem. Technol. Biotechnol.*, **83**, 1244 (2008).
5. Z. He, H. Shao, L.T. Angenent, *Biosens. Bioelectron.*, **22**, 3252 (2007).
6. S.W. Hong, Y.S. Choi, T.H. Chung, J.H. Song, H.S. Kim, *World Academy of Science, Engineering and Technology*, **54**, 683 (2009).
7. S. Parot, M.-L. Délia, A. Bergel, *Bioresource Technol.*, **99**, 4809 (2008).
8. S. Dulon, S. Parot, M.-L. Délia, A. Bergel, *J. Appl. Electrochem.*, **37**, 173 (2007).
9. I. Bardarov, Y. Hubenova, M. Mitov, A. Popov, in: Proc. 5<sup>th</sup> International Scientific Conference – FMNS2013, Blagoevgrad, 2013, Vol. 4: Chemistry, p.109.

## СЕДИМЕНТНИ МИКРОБИАЛНИ ГОРИВНИ ЕЛЕМЕНТИ ИЗПОЛЗВАЩИ РЕЧНИ СЕДИМЕНТИ И ПОЧВИ

И. Бърдаров<sup>1</sup>, Й. Хубенова<sup>2</sup>, М. Митов<sup>1\*</sup>

<sup>1</sup>Катедра „Химия“, Югозападен университет „Неофит Рилски“ – Благоевград, България  
<sup>2</sup>Катедра „Биохимия и микробиология“, Пловдивски университет „Паисий Хилендарски“, България

Получена на Май 27, 2013; Ревизирана на Юни 28, 2013

(Резюме)

В настоящата работа са представени и дискутирани резултати от 18-месечни изпитания на Седиментни Микробиални Горивни Елементи (СМГЕ) от колонен тип, използващи речни седименти и почви, събрани от покрайнините на Благоевград. През целия период на изследване горивните елементи работеха без подаване на хранителни вещества, освен периодично добавяне на вода за компенсация на загубите от изпарение. Работата на изследваните СМГЕ бе оценена чрез провеждане на поляризационни измервания както при постоянни, така и при променливи товарни съпротивления. По-добри електрически характеристики, по-висока ефективност, както и по-стабилен режим на работа бяха постигнати със СМГЕ с речни седименти. Захранващ блок, конструиран от два последователно свързани СМГЕ, бе успешно използван за захранване на електрически устройства с малка консумация, което демонстрира перспективите за понататъшно развитие и приложение на технологията.

## Synthesis and characterization of Si-coated superparamagnetic nanoparticles for bioelectrochemical applications

E. Patrikiadou<sup>1</sup>, V. Zaspalis<sup>1,2</sup>, L. Nalbandian<sup>1\*</sup>, E. Chorbadzhiyska<sup>3</sup>, M. Mitov<sup>3</sup>, Y. Hubenova<sup>4</sup>

<sup>1</sup>Laboratory of Inorganic Materials (LIM), Chemical Process & Energy Resources Institute, Centre for Research and Technology - Hellas (CPERI / CErTH), Thessaloniki, Greece

<sup>2</sup>Department of Chemical Engineering, Aristotle University, Thessaloniki, Greece

<sup>3</sup>Department of Chemistry, South-West University, Blagoevgrad, Bulgaria

<sup>4</sup>Department of Biochemistry and Microbiology, Plovdiv University, Bulgaria

Received May 27, 2013; Revised August 1, 2013

In this study, silica coated iron oxide nanoparticles were loaded on carbon felt by means of two different techniques - impregnation of carbon felt samples in suspension of silica coated Fe<sub>3</sub>O<sub>4</sub> nanoparticles (Method 1) and attachment of silica coated Fe<sub>3</sub>O<sub>4</sub> nanoparticles to carbon felts samples with covalent bonding through amine functional groups (Method 2). The surface morphology of the newly prepared nanomodified carbon materials was studied by scanning electron microscopy (SEM). The Si-coating efficiency was monitored by High-resolution transmission electron microscopy (HR-TEM) in combination with X-ray EDS Microanalysis. The performed physicochemical characterization analysis showed that Method 2 is superior for the deposition of the magnetite nanoparticles than Method 1. Based on this, the electrochemical performance of the samples prepared by Method 2 in neutral phosphate buffer solution was investigated in respect to their potential application as electrodes in microbial fuel cells (MFCs) and/or microbial electrolysis cells (MECs).

**Key words:** silica coated iron oxide nanoparticles; nanomodified carbon felt; modified electrode materials; microbial fuel cells; microbial electrolysis cells.

### INTRODUCTION

Bioelectrochemical systems (BESs) based on utilization of whole microorganisms as biocatalysts such as Microbial Fuel Cells (MFCs) and Microbial Electrolysis Cells (MECs) are intensively studied during the last decade as promising technologies for simultaneous wastewater purification and electricity generation or bio-hydrogen production [1-6]. Mimicking the ability of some microorganisms, known as exoelectrogens, to use an exogenous final electron acceptor, both technologies are based on an extracellular electron transfer from the living cells to a solid conductor serving as a BES anode. The most studied are the so-called “metal respiring” bacteria from *Geobacter* and *Shewanella* families, which naturally use iron or manganese (hydr)oxides as final electron acceptors for their respiration processes [7].

Carbon-based materials such as graphite, carbon cloth, carbon felt, etc., are most commonly used as electrodes in BESs due to their biocompatibility, good conductivity, corrosion stability and low price.

In previous studies [8, 9], it has been found that modified with nickel and iron carbon felt materials used as anodes improve significantly the electric outputs of mediatorless yeast-biofuel cell. In another study [10], it has been demonstrated that the same materials possess high corrosion resistance and electrocatalytic activity towards hydrogen evolution reaction (HER) in neutral and weak acidic solutions, which makes them proper cathodes for MECs in respect to bio-hydrogen production.

The aim of this study was to develop methods for loading silica coated iron oxide nanoparticles on carbon felt and examine the electrochemical performance of the prepared nanomodified materials in neutral electrolyte in respect to their potential applications as electrodes in MFCs and/or MECs.

### MATERIALS AND METHODS

#### Materials

Chemicals used in experiments were of analytical grade and used without any further purification. Ferric chloride (FeCl<sub>3</sub>·6H<sub>2</sub>O), ferrous chloride (FeCl<sub>2</sub>·4H<sub>2</sub>O), sodium hydroxide (NaOH),

\* To whom all correspondence should be sent:  
E-mail: nalbanti@cpери.certh.gr

ammonia (NH<sub>4</sub>OH), tetraethylorthosilicate (TEOS) and ethanol were purchased from Merck. Aminosilane coupling agent 3-aminopropyltriethoxysilane (APTES) was obtained from Sigma Aldrich. In this study, only deionized water (18 MΩ) was used. Carbon felt (SPC-7011, 30 g/m<sup>2</sup>) was purchased from Weißgerber GmbH & Co. KG.

#### *Preparation and silica coating of the magnetic nanoparticles*

Magnetic nanoparticles (NP's) of Fe<sub>3</sub>O<sub>4</sub> were synthesized by a conventional chemical co-precipitation method [13-14]. Aqueous solutions of Fe<sup>2+</sup> and Fe<sup>3+</sup> chlorides in a molar ratio of Fe<sup>2+</sup>/Fe<sup>3+</sup> = 0.5 were precipitated by NaOH, under N<sub>2</sub> flow in order to prevent oxidation. The precipitate was aged for 10min and ultrasonicated for another 10min. The resulting magnetic nanoparticles underwent washing with water.

In order to coat the surface of the nanoparticles with thin silica (SiO<sub>2</sub>) layer, 40mg of the synthesized Fe<sub>3</sub>O<sub>4</sub> nanoparticles were dispersed in a solution of ethanol/water (4:1) and the pH of the solution was adjusted to 9 by addition of NH<sub>4</sub>OH. Finally the Si-source, TetraEthylOrthoSilicate (TEOS) was added dropwise and the solution was stirred mechanically for 10 hrs [15-16]. The precipitate was washed several times with water. Subsequently, water was added to redisperse ultrafine magnetic particles. The obtained magnetite dispersion will be called in the next paragraphs magnetic fluid (MF).

Two types of NP's were prepared, with different TEOS concentration, which resulted in different silica layer thickness (S0.008 has thinner silica layer than S0.016).

#### *Loading of silica coated Fe<sub>3</sub>O<sub>4</sub> nanoparticles to carbon felt samples*

Circular pieces of carbon felt with diameter 1cm are used. Prior to the deposition of the nanoparticles the carbon felt samples are rinsed with ethanol, unless otherwise mentioned. Two different methods were used for attaching the magnetic nanoparticles, either by simple physical adherence or through the formation of covalent bonds.

Impregnation of carbon felt samples in suspension of silica coated Fe<sub>3</sub>O<sub>4</sub> nanoparticles (Method No1): The magnetic fluid is ultrasonicated for 15 minutes in order to achieve the best dispersion of the NP's and to become homogeneous. Then a piece of carbon felt is added in the dispersion and stirred at room temperature

for 2 hrs. The carbon felt is removed, washed with water and dried at room temperature.

Attachment of silica coated Fe<sub>3</sub>O<sub>4</sub> nanoparticles to carbon felts samples with covalent bonding through amine functional groups (Method No2): 3-aminopropyl triethoxysilane (APTES), as a source of amine groups, is added to the suspension of silica coated iron oxide nanoparticles. After stirring for 2 min, a circular piece of carbon felt with diameter 1cm, previously washed with ethanol (unless mentioned otherwise), is inserted in the solution and stirred for 5 hrs. In the end the carbon felt specimen is removed, washed with water, ultrasonicated in water for 30 min and dried at room temperature.

#### *Physicochemical Characterization*

The crystalline phases present in the prepared nanoparticles are identified by X-ray diffraction (XRD). Powder XRD patterns are recorded with a Siemens D 500 X-ray diffractometer, with an autodivergent slit and graphite monochromator using CuKα radiation, with a scanning speed of 2°min<sup>-1</sup>. The characteristic reflection peaks (d-values) are matched with JCPDS data files and the crystalline phases are identified.

Scanning electron microscopy (SEM) is used for inspecting the morphology of the prepared samples. The instrument used is a JEOL JSM 6300 scanning electron microscope equipped with an Oxford ISIS 2000 energy dispersive analysis system (EDS).

High-resolution transmission electron microscopy (HRTEM) images are obtained in a JEOL JEM 2010 microscope operating at 200 kV and equipped with an Oxford Instruments INCA EDS detector. In order to prevent eventual agglomeration, the sample was mixed with pure ethanol in an ultrasonic apparatus and superimposed on a lacey carbon film supported on a 3 mm Cu grid.

#### *Electrochemical characterization*

The electrochemical performance of the newly produced nanomodified carbon felt materials in phosphate buffer (PBS, pH 7.0) solutions was investigated by means of Linear Sweep Voltammetry (LSV). The studied samples with a geometric area 1 cm<sup>2</sup> were connected as a working electrode in a three electrode arrangement. A platinum-titanium mesh (10 cm<sup>2</sup>) was used as a counter electrode. All potentials were measured against Ag/AgCl reference electrode.

To examine the corrosion behaviour of the materials, the potential was swept with a scan rate 2

mV/s in a positive direction in the range from -400 mV to 600 mV (vs. Ag/AgCl). To evaluate the electrocatalytic activity of the studied materials towards hydrogen evolution reaction (HER), LSV measurements with the same scan rate were performed in a negative direction from 0 to -1200 mV (vs. Ag/AgCl).

The electrochemical studies were performed by using potentiostat - galvanostat PJT 35-2 (Radiometer-Tacussel) with IMT 101 interface and VoltaMaster 2 data acquisition system. LSV tests were carried out in triplicate and the third scan was used for analysis of the performance.

## RESULTS AND DISCUSSION

Two types of nanoparticles were used in these experiments, nanoparticles with thin silica layer (samples 1,5) and nanoparticles with a relatively thick silica layer (samples 2,3).

### *Physicochemical properties of the Si-coated magnetic nanoparticles*

Only stable magnetic fluids were used in the further steps of the study. Optical inspection gave a first indication whether the prepared samples had properly dispersed nanoparticles. The prepared nanoparticles were examined by X-ray diffraction in order to identify the crystalline phases formed. The experimental peaks were perfectly matched with the theoretical data of the JCPDS card No 19-629, thus indicating the presence of pure magnetite. The crystallite size, determined from the line broadening by the Scherrer formula, was in the range 9-12 nm.

The Si-coating efficiency was monitored by HR-TEM, in combination with X-ray EDS Microanalysis. Figure 1 presents a characteristic image of crystalline magnetite nanoparticles, coated with a surface silica layer. The nanoparticles are visible as agglomerates of small nanoparticles of 10-20nm, coated with a thin layer of silica.

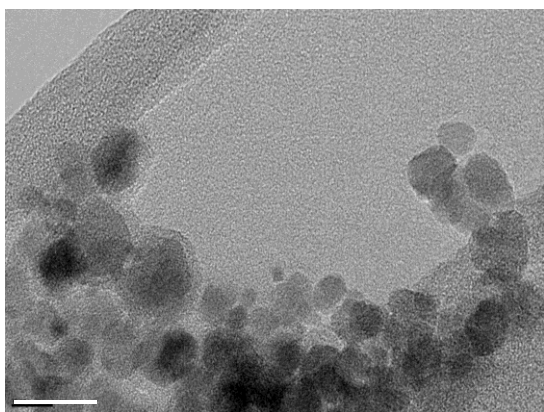


Fig. 1. TEM image of silica coated Fe<sub>3</sub>O<sub>4</sub> nanoparticles

### *Physicochemical Characterization of NP-loaded Carbon Felt Samples*

Samples prepared by Method No1: Magnetite nanoparticles after different treatment were used for the preparation of each of the following samples:

Sample P0: Pure Fe<sub>3</sub>O<sub>4</sub> nanoparticles, without further modification were loaded on the carbon felt sample. In Figure 2, SEM images of the prepared sample show that only few big aggregates have been attached to the carbon felt fibers.

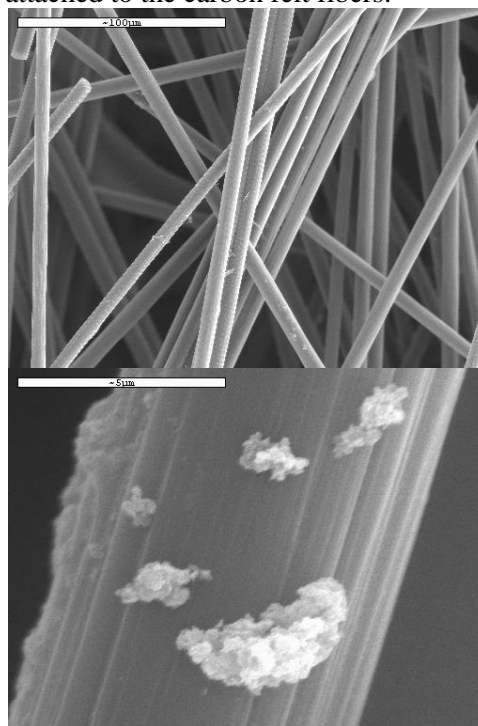
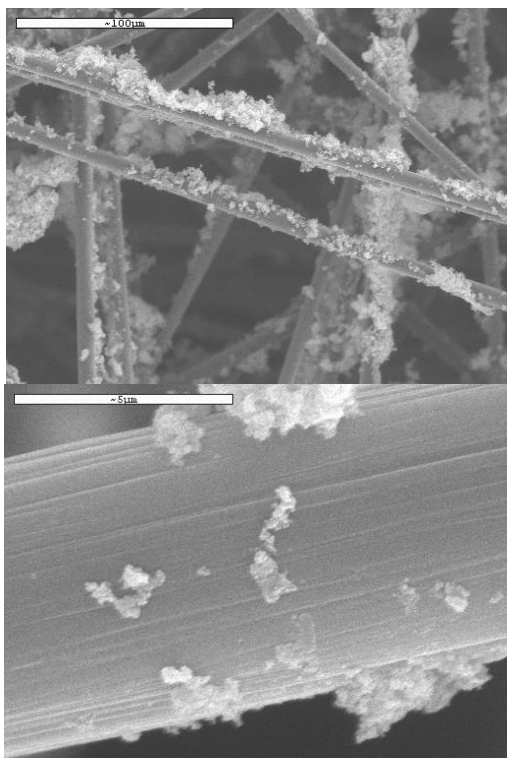


Fig. 2. SEM images of sample P0

Sample P1: Magnetite (Fe<sub>3</sub>O<sub>4</sub>) nanoparticles, treated with TEOS in order to obtain a silica layer (S0.016) were loaded on this sample. SEM images reveal that the silica coating increases the number of attached NP's and also reduces the size of the aggregates, however the results are still not acceptable.

Sample P2: The carbon felt sample was immersed in an aqueous suspension of silica coated (S0.016) magnetite (Fe<sub>3</sub>O<sub>4</sub>) nanoparticles, functionalized with surface amine groups, after treatment with 3-AminoPropyl-ThriEthoxySilane (APTES). As shown in Figure 3, the presence of amine groups of the surface of the nanoparticles has greatly enhanced their affinity to the carbon felt fibers. However, the NP's are still loosely attached as aggregates, not forming a homogeneous layer of the surface of the fibers.



**Fig. 3.** SEM morphology of sample P2

**Sample P3:** Finally the effect of reducing the thickness of the silica layer has been examined. Sample P3 was prepared by using an aqueous suspension of amine functionalized magnetite ( $\text{Fe}_3\text{O}_4$ ) nanoparticles coated with a thinner silica layer (S0.008). By observing the morphology of the prepared carbon felt sample, no major difference from sample P2 can be seen, thus it is concluded that the thickness of the silica layer does not have a significant effect on the adhesion behavior of the NP's on the carbon felt fibers.

**Samples prepared by Method No2:** The reaction of the surface hydroxyl groups of silica with the amine

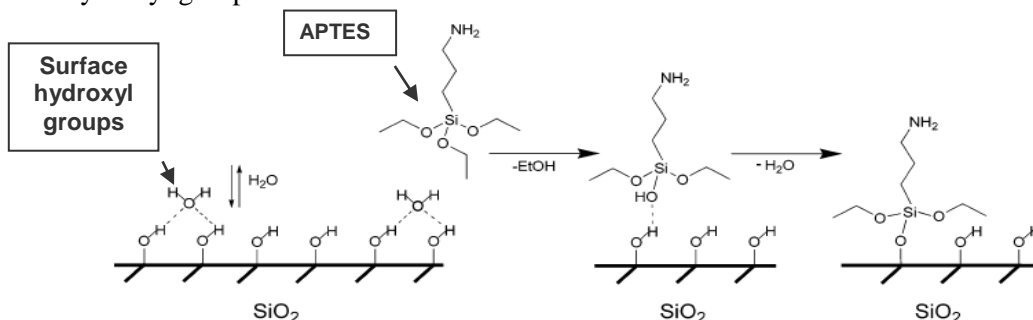


**Fig. 4.** Reaction scheme for the formation of surface amine groups.

source, which leads to the formation of functional surface amine groups, is shown schematically in Figure 4.

The parameters studied for the samples loaded through the formation of covalent bonding between the nanoparticles and the carbon felt fibers were:

- the pretreatment of the carbon felt samples with ethanol
- the thickness of the surface silica layer of the nanoparticles
- the quantity of nanoparticles available to be attached to a carbon felt specimen

**Sample C1:** The carbon felt sample used for preparing sample C1 was pretreated with ethanol for 120 minutes before the nanoparticles loading procedure. Magnetite ( $\text{Fe}_3\text{O}_4$ ) nanoparticles, treated with TEOS in order to obtain a silica layer (S0.016) were loaded on the sample, the same NP's as those used in Sample P1. In Figure 5 the SEM images obtained from sample C1 are shown. It is clear that the affinity of the nanoparticles to the carbon felt fibers has been greatly enhanced. The NP's have been attached almost uniformly around the fibers, forming a continuous magnetite layer. Local elemental analysis with X-ray EDS (Figure 6) clearly reveals the presence of iron and silica, thus confirming that the deposited layer is composed from the magnetic NP's.

At this point it should be emphasized that prior to the SEM morphology observation, the samples have been placed in the ultrasonic bath for 30 minutes, nevertheless the adherence of the nanoparticles remained strong, showing that Method 2 for the deposition of the NP's is superior than Method 1.

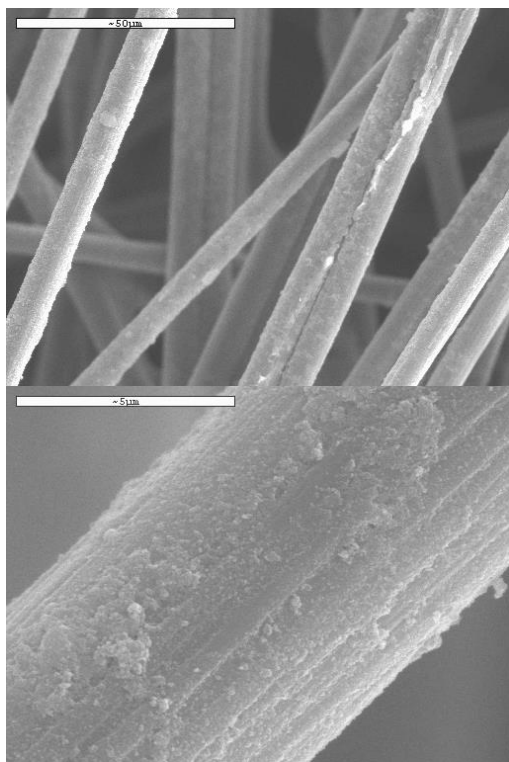


Fig. 5. SEM morphology of sample C1

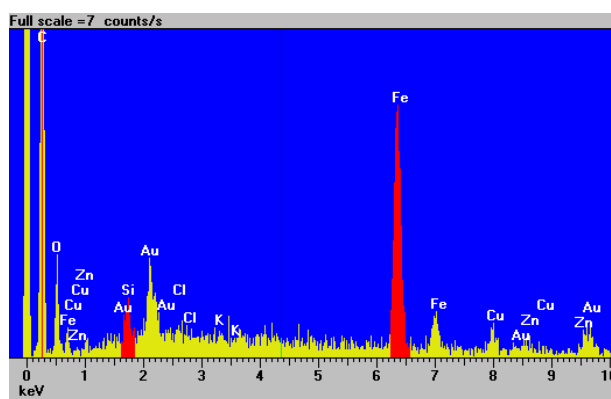


Fig. 6. Elemental analysis (X-ray EDS) of sample C1.

**Sample C2:** Sample C2 was prepared to investigate the effect of the pretreatment of the carbon felt with ethanol. Thus the preparation of sample C2 was exactly the same as sample C1, but without pretreatment with ethanol. The results, presented in Figure 7a, indicate that there is not a significant difference in the morphology of the fibers, from sample C1.

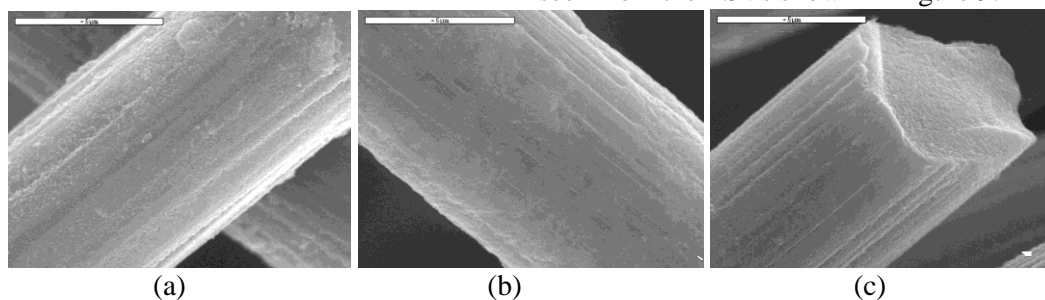


Fig. 7. SEM morphology of (a) sample C2, (b) sample C3 and (c) sample C4

**Sample C3** Sample C3 was prepared in order to study the effect of reducing the thickness of the silica layer. Magnetite ( $\text{Fe}_3\text{O}_4$ ) nanoparticles, treated with TEOS in order to obtain a thinner silica layer (S0.008) were used, the same NP's as in sample P3. By comparing the SEM images of the prepared carbon felt specimens, shown in Figure 7b, to the images of samples C1 and C2, it is concluded that the effect of the silica layer thickness on the fibers morphology is not significant.

**Sample C4** Finally, the quantity of nanoparticles available to be attached to the carbon felt specimen was investigated by preparing sample C4. Magnetite ( $\text{Fe}_3\text{O}_4$ ) nanoparticles, treated with TEOS in order to obtain a thinner silica layer (S0.008) were used, the same NP's as in sample C3. However, 30% less nanoparticles were used for the deposition. The morphology of the obtained sample C4 is shown in Figure 7c. The number of attached nanoparticles on the fiber surface is significantly smaller than in the previous samples, eventually there were not enough NP's to form a continuous layer as in the previous samples C1-C3. However, the NP's are still not aggregated and very firmly attached to the fibers.

#### Electrochemical performance

The LSV studies performed in a positive (anodic) direction indicate a good corrosion stability of all studied materials in neutral PBS solution. As a measure of the corrosion rate, the exchange current density values estimated from the Tafel plots, presented in Figure 8, varies in the range  $10^{-8} \div 10^{-7} \text{ mA/cm}^2$ . These low corrosion rates reveal the potential possibility to use the modified materials, produced by covalent bonding of  $\text{Fe}_3\text{O}_4$  nanoparticles to carbon felt, as electrodes in MFCs or MECs, in which neutral PBS solution is commonly used as an electrolyte. The performed potentiodynamic measurements with modified materials at negative potentials from 0 to -1200 mV (vs. Ag/AgCl), however, show an absence of reduction process in a broad range of potentials, as seen from the LSVs shown in Figure 9.

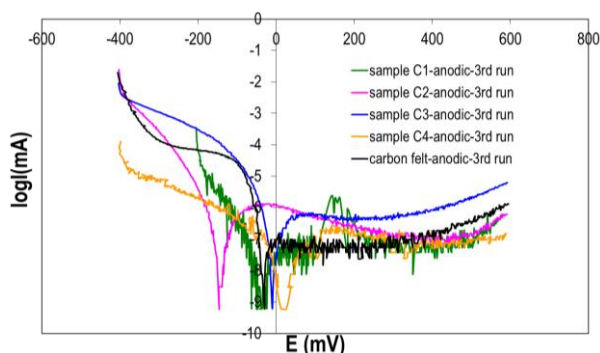


**Fig. 8.** Tafel plots of modified and non-modified carbon felt samples obtained by LSV with a scan rate 2 mV/s in PBS (pH 7)

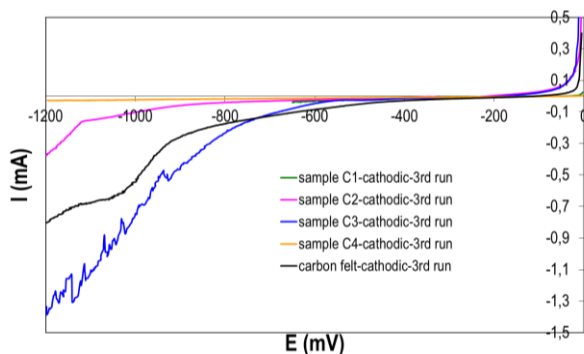


**Fig. 9.** Linear voltammograms of modified and non-modified carbon felt samples obtained with a scan rate 2 mV/s in PBS (pH 7)

The highest electrochemical activity at potentials more negative than -700 mV (vs. Ag/AgCl), corresponding to a noticeable hydrogen evolution, is observed with sample C3. Although the rate of HER, estimated from the slope of the linear region in voltammogram is twice higher for sample C3 than that for the non-modified carbon felt, it is rather small in comparison with the hydrogen production rates of electrode materials with a practical impact [10-12]. The rest of the studied modified materials exhibit even less than the carbon felt or negligible electrocatalytic activity towards HER. This excludes these materials as potential cathodes for bio-hydrogen production in MECs.

### CONCLUSION

Two different methods were used for attaching magnetic Fe<sub>3</sub>O<sub>4</sub> nanoparticles on carbon felt in order to obtain modified electrode materials for BESs application. The direct immersion of carbon felt samples in an aqueous suspension of silica coated magnetite nanoparticles results in loose attachment of NPs aggregates. In the contrary, the attachment of silica coated Fe<sub>3</sub>O<sub>4</sub> nanoparticles through covalent bonding with amine functional groups leads to the formation of a uniform

magnetite layer around the carbon fibers, showing that the second method for deposition of the NPs is superior.,

All the carbon felt samples modified by covalent bonding of the magnetite nanoparticles possess high corrosion resistance in neutral PBS solution, commonly used as an electrolyte in bioelectrochemical systems. However the prepared samples are not suitable for use as cathodes for bio-hydrogen production in MECs.

The newly synthesized Fe<sub>3</sub>O<sub>4</sub>/carbon felt materials need to be further examined as anodes in MFCs using metal respiring bacteria (e.g. *G. metallorodens*, *S. oneidensis*) as biocatalysts, since they combine high corrosion stability in neutral medium and specific properties due to the attached NPs.

**Acknowledgements:** The present study was funded by the program "Hydrogen Economy Cooperation Network for Research - Public Awareness - Business Opportunities across Greek-Bulgarian borders – HYDECOR". The Project is co-funded by the European Regional Development Fund and by national funds of the countries participating in the ETCP "Greece-Bulgaria 2007-2013" through contract B1.33.01.

### REFERENCES

1. A.E. Franks, K.P. Nevin, *Energies*, **3**, 899 (2010).
2. I.S. Kim, K.J. Chae, M.J. Choi, W. Verstraete, *Environ. Eng. Res.*, **13**, 51 (2008).
3. Z. Du, H. Li, T. Gu, *Biotechnol. Adv.*, **25** 464 (2007)
4. D.R. Lovley, *Curr. Opin. Biotechnol.*, **19**, 1 (2008).
5. B.E. Logan, D. Call, S. Cheng, H.V.M. Hamelers, T.H.J.A. Sleutels, A.W. Jeremiasse, R.E.A. Rozendal, *Environ. Sci. Technol.*, **42**, 8630 (2008)
6. H. Liu, H. Hu, J. Chignell, Y. Fan, *Biofuels* **1**, 129 (2010)
7. L. Shi, T.C. Squier, J.M. Zachara, J.K. Fredrickson, *Mol. Microbiol.* **65**, 12 (2007)
8. Y. Hubenova, R. Rashkov, V. Buchvarov, M. Arnaudova, S. Babanova, M. Mitov, *Ind. Eng. Chem. Res.*, **50**, 557 (2011)
9. Y. Hubenova, R. Rashkov, V. Buchvarov, S. Babanova, M. Mitov, *J. Mater. Sci.*, **46**, 7074 (2011)
10. M. Mitov, E. Chorbadzhiska, R. Rashkov, Y. Hubenova, *Int. J. Hydrogen Energy*, **37**, 16522, (2012)
11. H. Hu, Y. Fan, H. Liu, *Int. J. Hydrogen Energy*, **34**, 8535 (2009)
12. Y. Zhang, M.D. Merrill, B.E. Logan, *Int. J. Hydrogen Energy*, **35**, 12020 (2010)
13. A. Kumar Gupta, M. Gupta, *Biomaterials*, **26** 3995 (2005)
14. P. Tartaj, M. Morales, S. Veintemillas, T. Gonzalez, C. Serna, *J Phys. D: Appl Phys*, **36**, R182 (2003)

15. H. Shen, W. Chen, J. Li, X. Li, H. Yang, *Microchim Acta*, **157**, 49 (2007)

16. X. Liu, Z. Ma, J. Xing, H. Liu, *J. Magn. Magn. Mater.*, **270**, 1 (2004)

## СИНТЕЗ И ОХАРАКТЕРИЗИРАНЕ НА ПОКРИТИ СЪС СИЛИКАГЕЛ СУПЕРПАРАМАГНИТНИ НАНОЧАСТИЦИ ЗА БИОЕЛЕКТРОХИМИЧНИ ПРИЛОЖЕНИЯ

Е. Патрикиаду<sup>1</sup>, В. Заспалис<sup>1,2</sup>, Л. Налбандиан<sup>1\*</sup>, Е. Чорбаджийска<sup>3</sup>, М. Митов<sup>3</sup>, Й. Хубенова<sup>4</sup>

<sup>1</sup>Лаборатория по неорганични материали, Институт по химични процеси и енергийни ресурси, Научно-изследователски и технологичен център – Хелас, Терми-Солун, Гърция

<sup>2</sup>Катедра по химическо инженерство, Аристотелов университет, Солун, Гърция

<sup>3</sup>Катедра „Химия“, Югозападен университет „Неофит Рилски“, Благоевград, България

<sup>4</sup>Катедра „Биохимия и Микробиология“, Пловдивски Университет „Паисий Хилендарски“, България

Получена на Май 27, 2013; Ревизирана на Август 1, 2013

(Резюме)

В настоящата разработка, наночастици от магнетит, покрити със силикагел, бяха нанесени върху въглеродно кече чрез две различни техники – импрегниране на образци от въглеродно кече в суспензия от  $\text{Fe}_3\text{O}_4$  наночастици, покрити със силикагел (Метод 1) и ковалентно свързване на покритите със силикагел  $\text{Fe}_3\text{O}_4$  наночастици с въглеродното кече чрез функционални аминок-групи (Метод 2). Повърхностната морфология на новосъздадените наномодифицирани въглеродни материали бе охарактеризирана чрез сканираща електронна микроскопия (СЕМ). Ефективността на Si-покрытие бе оценена чрез високо-разделителна трансмисионна електронна микроскопия (ВР-ТЕМ) в комбинация с енерго-дисперсионна рентгенова спектроскопия. Проведените физикохимични анализи показаха, че Метод 2 е по-добър за отлагане на наночастиците от магнетит. Въз основа на това, бе изследвано електрохимичното поведение на образци, изготвени по Метод 2, в неутрален фосфатен буфер с оглед на потенциалното им използване като електроди в микробиални горивни елементи (МГЕ) и/или микробиални електролизни клетки (МЕК).



## BULGARIAN CHEMICAL COMMUNICATIONS

### Instructions about Preparation of Manuscripts

**General remarks:** Manuscripts are submitted in English by e-mail or by mail (in duplicate). The text must be typed double-spaced, on A4 format paper using Times New Roman font size 12, normal character spacing. The manuscript should not exceed 15 pages (about 3500 words), including photographs, tables, drawings, formulae, etc. Authors are requested to use margins of 3 cm on all sides. For mail submission hard copies, made by a clearly legible duplication process, are requested. Manuscripts should be subdivided into labelled sections, e.g. **Introduction, Experimental, Results and Discussion, etc.**

**The title page** comprises headline, author's names and affiliations, abstract and key words.

Attention is drawn to the following:

a) **The title** of the manuscript should reflect concisely the purpose and findings of the work. Abbreviations, symbols, chemical formulas, references and footnotes should be avoided. If indispensable, abbreviations and formulas should be given in parentheses immediately after the respective full form.

b) **The author's** first and middle name initials, and family name in full should be given, followed by the address (or addresses) of the contributing laboratory (laboratories). **The affiliation** of the author(s) should be listed in detail (no abbreviations!). The author to whom correspondence and/or inquiries should be sent should be indicated by asterisk (\*).

**The abstract** should be self-explanatory and intelligible without any references to the text and containing not more than 250 words. It should be followed by key words (not more than six).

**References** should be numbered sequentially in the order, in which they are cited in the text. The numbers in the text should be enclosed in brackets [2], [5, 6], [9–12], etc., set on the text line. References, typed with double spacing, are to be listed in numerical order on a separate sheet. All references are to be given in Latin letters. The names of the authors are given without inversion. Titles of journals must be abbreviated according to Chemical Abstracts and given in italics, the volume is typed in bold, the initial page is given and the year in parentheses. Attention is drawn to the following conventions:

a) The names of all authors of a certain publications should be given. The use of “*et al.*” in

the list of references is not acceptable.

b) Only the initials of the first and middle names should be given.

In the manuscripts, the reference to author(s) of cited works should be made without giving initials, e.g. “Bush and Smith [7] pioneered...”. If the reference carries the names of three or more authors it should be quoted as “Bush *et al.* [7]”, if Bush is the first author, or as “Bush and co-workers [7]”, if Bush is the senior author.

**Footnotes** should be reduced to a minimum. Each footnote should be typed double-spaced at the bottom of the page, on which its subject is first mentioned.

**Tables** are numbered with Arabic numerals on the left-hand top. Each table should be referred to in the text. Column headings should be as short as possible but they must define units unambiguously. The units are to be separated from the preceding symbols by a comma or brackets.

Note: The following format should be used when figures, equations, *etc.* are referred to the text (followed by the respective numbers): Fig., Eqns., Table, Scheme.

**Schemes and figures.** Each manuscript (hard copy) should contain or be accompanied by the respective illustrative material as well as by the respective figure captions in a separate file (sheet). As far as presentation of units is concerned, SI units are to be used. However, some non-SI units are also acceptable, such as °C, ml, l, etc.

The author(s) name(s), the title of the manuscript, the number of drawings, photographs, diagrams, etc., should be written in black pencil on the back of the illustrative material (hard copies) in accordance with the list enclosed. Avoid using more than 6 (12 for reviews, respectively) figures in the manuscript. Since most of the illustrative materials are to be presented as 8-cm wide pictures, attention should be paid that all axis titles, numerals, legend(s) and texts are legible.

The authors are asked to submit **the final text** (after the manuscript has been accepted for publication) in electronic form either by e-mail or mail on a 3.5” diskette (CD) using a PC Word-processor. The main text, list of references, tables and figure captions should be saved in separate files (as \*.rtf or \*.doc) with clearly identifiable file names. It is essential that the name and version of

the word-processing program and the format of the text files is clearly indicated. It is recommended that the pictures are presented in \*.tif, \*.jpg, \*.cdr or \*.bmp format, the equations are written using "Equation Editor" and chemical reaction schemes are written using ISIS Draw or ChemDraw programme.

The authors are required to submit the final text with a list of three individuals and their e-mail addresses that can be considered by the Editors as potential reviewers. Please, note that the reviewers should be outside the authors' own institution or organization. The Editorial Board of the journal is not obliged to accept these proposals.

## EXAMPLES FOR PRESENTATION OF REFERENCES

### REFERENCES

1. D. S. Newsome, *Catal. Rev.–Sci. Eng.*, **21**, 275 (1980).
2. C.-H. Lin, C.-Y. Hsu, *J. Chem. Soc. Chem. Commun.*, 1479 (1992).
3. R. G. Parr, W. Yang, *Density Functional Theory of Atoms and Molecules*, Oxford Univ. Press, New York, 1989.
4. V. Ponec, G. C. Bond, *Catalysis by Metals and Alloys* (Stud. Surf. Sci. Catal., vol. 95), Elsevier, Amsterdam, 1995.
5. G. Kadinov, S. Todorova, A. Palazov, in: *New Frontiers in Catalysis* (Proc. 10th Int. Congr. Catal., Budapest, 1992), L. Guzzi, F. Solymosi, P. Tetenyi (eds.), Akademiai Kiado, Budapest, 1993, Part C, p. 2817.
6. G. L. C. Maire, F. Garin, in: *Catalysis. Science and Technology*, J. R. Anderson, M. Boudart (eds), vol. 6, Springer-Verlag, Berlin, 1984, p. 161.
7. D. Pocknell, *GB Patent 2 207 355* (1949).
8. G. Angelov, PhD Thesis, UCTM, Sofia, 2001.
9. JCPDS International Center for Diffraction Data, Power Diffraction File, Swarthmore, PA, 1991.
10. *CA* **127**, 184 762q (1998).
11. P. Hou, H. Wise, *J. Catal.*, in press.
12. M. Sinev, private communication.
13. <http://www.chemweb.com/alchem/articles/1051611477211.html>.

## CONTENTS

<i>Preface</i> .....	5
<i>Z.P.Nenova, S.V.Kozhukharov, T.G.Nenov, N.D.Nedev, M.S.Machkova</i> , Characterization of humidity sensors with Ce-modified silica films prepared via sol-gel method.....	11
<i>V. Bozhilov, S. Kozhukharov, E. Bubev, M. Machkova, V. Kozhukharov</i> , Classification and functional characterization of the basic types of photovoltaic elements .....	17
<i>D. S. Rodriguez, S. Kozhukharov, M. Machkova, V. Kozhukharov</i> , Influence of the deposition conditions on the properties of D16 AM clad alloy, dip-coated in Ce-containing baths .....	24
<i>J. A. P. Ayuso, S. Kozhukharov, M. Machkova, V. Kozhukharov</i> , Electrodeposition of cerium conversion coatings for corrosion protection of D16 AM clad alloy .....	33
<i>G. A. Hodjaoglu, I. S. Ivanov</i> , Influence of hydroxyethylated-2-butyne-1,4-diol on copper electrodeposition from sulphate electrolytes containing large amounts of zinc .....	41
<i>P. L. Stefchev, R. P. Kirilov, Ch. A. Girginov, E. H. Klein</i> , AC-anodized and Ni-pigmented aluminum for selective solar absorption .....	47
<i>Ch. A. Girginov, I. A. Kanazirski, V. G. Ilcheva</i> , Electrolytic coloring of porous aluminum oxide films in CoSO <sub>4</sub> solution .....	52
<i>K. N. Ignatova, Y. S. Marcheva</i> , Electrodeposition and structure of Co coatings (CoCu, NiCo and CoNiCu) in potentiostatic and pulse potential modes .....	57
<i>S. V. Mentus, I. A. Pašti, N. M. Gavrilov</i> , Thermogravimetric way to test the oxidation resistance of Pt/C catalysts for fuel cells .....	64
<i>R. Harizanova, C. Bocker, G. Avdeev, C. Rüssel, I. Gugov</i> , Crystallization and dielectric properties of BaTiO <sub>3</sub> -containing invert aluminoborosilicate glass-ceramics.....	69
<i>D. Hristova, I. G. Betova, Tzv. B. Tzvetkoff</i> , Ionic and electronic conductivity of the surface film on titanium during pulse electrolysis of water .....	74
<i>K. Draganova, Vl. Stefanova, P. Iliev</i> , Analytical study of the process of sulphuric acid dissolution of Waelz-clinker with Eh - pH diagrams .....	82
<i>Ch.A. Girginov, M.S. Bojinov</i> : Anodic oxidation mechanism of aluminum alloys in a sulfate-fluoride electrolyte .....	88
<i>E. Lilov, Ch. Girginov, E. Klein</i> , Anodic oxide films on antimony formed in oxalic acid solutions .....	94
<i>V. I. Karastoyanov, Tzv. B. Tzvetkoff</i> , Pulse electrolysis of alkaline solutions as highly efficient method of production of hydrogen/oxygen gas mixtures .....	99
<i>K. D. Georgieva, G. Vissokov</i> , Advances in synthesis, application and dependence of vaporization of micron sized particles in thermal plasma in SOFC technologies .....	103
<i>I. Popov, B. Velev, J. Milusheva, R. Boukoureshlieva, S. Hristov, T. Stankulov, B. Banov, A. Trifonova</i> , Behaviour of gas-diffusion electrode in various non-aqueous electrolytes for the lithium-air system .....	110
<i>M. Georgieva, M. Petrova, V. Chakarova</i> , Obtaining of electroless Ni-P/ZrO <sub>2</sub> composite coatings on flexible substrates of polyethylene terephthalate .....	116
<i>L. N. Petkov, K. Sv.Yosifov, A. S. Tsanev, D. Stoychev</i> , Glassy carbon (GC) electrode modified with electrodeposited ZrO <sub>2</sub> and ZrO <sub>2</sub> + Ce <sub>2</sub> O <sub>3</sub> + Y <sub>2</sub> O <sub>3</sub> nanostructures as a cathode in the obtaining of active chlorine .....	122
<i>R. Boukoureshlieva, S. Yankova, V. Beschkov, J. Milusheva, G. Naydenova, L. Popova, G. Yotov, S. Hristov</i> , Monitoring of the phenol biodegradation process with an electrochemical biosensor ..	129
<i>M. Krapchanska, D. Vladikova, Z. Stoynov, A. Chesnuad, A. Thorel, G. Raikova, E. Mladenova, I. Genov</i> , Impedance studies of porous electrolyte with mixed ion conductivity .....	135
<i>Y. D. Milusheva, R. I. Boukoureshlieva, S. M. Hristov</i> , Air gas-diffusion electrodes for operation in magnesium-air cells/NaCl – electrolyte .....	140
<i>P. V. Angelov, S. S. Slavov, Sv. R. Ganev, Y. B. Dimitriev, J. G. Katarov</i> , Direct ultrasonic synthesis of classical high temperature ceramic phases at ambient conditions by innovative method .....	146
<i>K. Lovchinov, M. Ganchev, M. Petrov, H. Nichev, D. Dimova-Malinovska, J. S. Graff, Al. Ulyashin</i> , Electrochemically deposited nanostructured ZnO layers on the front side of c-Si solar cell .....	153
<i>V. Blaskova-Kochnitcharova, T. Petkova, L. Fachikov, E. Lefterova, I. Kanazirski, P. Angelov, S. Vassilev</i> , Investigations of glass-crystalline TiO <sub>2</sub> -V <sub>2</sub> O <sub>5</sub> -P <sub>2</sub> O <sub>5</sub> samples .....	159

<i>D. S. Lilova, Il. H. Gadjov, D. Dimitrov</i> , Chemical and phase content of alloyed tin-cobalt plating deposited in direct-current or impulse modes .....	163
<i>T. M. Dodevska, E. G. Horozova, N. D. Dimcheva</i> , Electrochemical characteristics and structural specifics of carbonaceous electrodes, modified with micro- and nanodeposits of platinum metals .....	171
<i>I. Radev, G. Topalov, G. Ganske E. Lefterova, G. Tsotridis, U. Schnakenberg, E. Slavcheva</i> , Catalytic activity of co-sputtered PtIr thin films toward oxygen reduction .....	179
<i>G. R. Borisov, A. E. Stoyanova, E. D. Lefterova, E. P. Slavcheva</i> , A novel non-carbon gas diffusion layer for PEM water electrolysis anodes .....	186
<i>A. E. Stoyanova, G. R. Borisov, E. D. Lefterova, E. P. Slavcheva</i> , MEA with carbon free Pt-Fe catalysts and gas diffusion layers for application in PEM water electrolysis .....	191
<i>D. G. Filjova, G. P. Ilieva, V. Ts. Tsakova</i> , Electropolymerization of poly(3,4-ethylenedioxythiophene) layers in the presence of different dopants and their effect on the polymer electrocatalytic properties. Oxidation of ascorbic acid and dopamine .....	196
<i>Scientific Workshop Hydrogen Economy – a Roadmap to the Future</i> .....	203
<i>E.Y. Chorbazhiyska, M.Y. Mitov, Y.V. Hubenova</i> , Optimization of conditions for formation of electrochemically active biofilm on carbon felt anodes during operation of yeast-based biofuel cells .....	205
<i>A. Evdou, V. Zaspalis, L. Nalbandian</i> , Novel materials as oxygen carriers for energy applications .....	211
<i>G. Y. Hristov, E. Y. Chorbazhiyska, R. S. Rashkov, Y. V. Hubenova, M. Y. Mitov</i> , Comparison investigation of Co-based catalysts for the catalytic hydrolysis of sodium borohydride .....	219
<i>I. Bardarov, Y. Hubenova, M. Mitov</i> , Sediment microbial fuel cell utilizing river sediments and soil ...	223
<i>E. Patrikiadou, V. Zaspalis, L. Nalbandian, E. Chorbazhiyska, M. Mitov, Y. Hubenova</i> , Synthesis and characterization of Si-coated superparamagnetic nanoparticles for bioelectrochemical applications. ....	227
INSTRUCTIONS TO THE AUTHORS .....	235

## СЪДЪРЖАНИЕ

Предговор .....	5
З. П. Ненова, С. В. Кожухаров, Т. Г. Ненов, Н. Д. Недев, М. С. Мачкова, Охарактеризиране на сензори за влажност с Се-легирани силициево-диоксидни слоеве, изготвени по зол-гел метод.....	16
В. Божилков, С. Кожухаров, Е. Бубев, М. Мачкова, В. Кожухаров, Класификация и функционална характеристика на основните видове фотоволтаични елементи .....	23
Д. С. Родригез, С. Кожухаров, М. Мачкова, В. Кожухаров, Влияние на условията на отлагане на покрития от Се-конверсионни бани върху свойствата на плакирана сплав Д16 АМ ...	32
Х. А. П. Айосо, С. Кожухаров, М. Мачкова, В. Кожухаров, Електрохимично отлагане на цериеви конверсионни покрития за корозионна защита на плакирана сплав Д16 АМ .....	40
Г. А. Ходжаоглу, Ив. С. Иванов, Влияние на хидоксиетилирания-2-бутин-1,4-диол върху електроотлагането на мед от сулфатни електролити съдържащи големи количества цинк	46
П. Л. Стефчев, Р. П. Кирилов, К. А. Гиргинов, Е. Х. Клайн, Селективни покрития на основа на променливотоково анодиран и оцветен с Ni алуминий .....	51
К. А. Гиргинов, И. А. Каназирски, В. Г. Илчева, Електрохимично оцветяване на порести оксидни филми върху алуминий в разтвори на CoSO <sub>4</sub> .....	56
К. Н. Игнатова, И. С. Марчева Електроотлагане и структура на Co покрития (CoCu, NiCo AND CoNiCu) в потенциостатичен и импулсен режим .....	63
С. В. Ментус, И. А. Папшти, Н. М. Гаврилов, Термогравиметричен метод за тестване на устойчивостта на окисление на Pt/C катализатори за горивни клетки .....	68
Р. Харизанова, Хр. Бокър, Г. Авдеев, Хр. Рюсел, Ив. Гугов, Кристализация и диелектрични свойства на инвертни алумо-боросиликатни стъклокерамики, съдържащи бариев титанат .....	73
Д. Ст. Христова, И. Г. Бетова, Цв. Б. Цветков, Йонна и електронна проводимост на повърхностни филми върху титан по време на импулсна електролиза във вода .....	81
К. Драганова, Вл. Стефанова, П. Илиев, Аналитично изледване на процеса на разтваряне на велц-клинкер в сярна киселина с помощта на Eh – рН диаграми .....	87
К. А. Гиргинов, М. С. Божинов, Механизъм на анодно окисление на алуминиеви сплави в сулфатно-флуориден електролит .....	93
Е. Лилов, К. Гиргинов, Е. Клайн, Механизъм на анодно окисление на алуминиеви сплави в сулфатно-флуориден електролит .....	98
В. Карастоянов, Цв. Цветков, Импулсна електролиза в алкални водни разтвори като високоефективен метод за генериране на оксигенородни газови смеси .....	102
К. Георгиева, Г. Високов, Напредък в синтеза и определяне на зависимостта от изпарението на частиците с микронни размери в термична плазма – приложение във високотемпературни горивни елементи .....	109
Ил. Попов, Б. Велев, Й. Милушева, Р. Букурещлиева, С. Христов, Т. Станкулов, Б. Банов, А. Трифонова, Поведение на газодифузионен електрод в неводни електролити за системата литий-въздух.....	115
М. Георгиева, М. Петрова, В. Чакърва, Получаване на химични композитни Ni-P/ZrO <sub>2</sub> покрития върху гъвкави подложки от полиетилен терефталат .....	121
Л. Петков, К. Йосифов, А. Цанев, Д. Стойчев, Стъкловиден въглерод (СВ) модифициран с електроотложени наноструктури на ZrO <sub>2</sub> и ZrO <sub>2</sub> +Ce <sub>2</sub> O <sub>3</sub> +Y <sub>2</sub> O <sub>3</sub> като катод при получаването на активен хлор .....	128
Р. Букурещлиева, С. Янкова, В. Бешиков, Й. Милушева, Г. Найденова, Л. Попова, Г. Йотов, С. Христов, Проследяване процеса на биодеградация на фенол с електрохимичен биосензор, .....	134
М. Кръпчанска, Д. Владикова, З. Стойнов, А. Чесно, А. Торел, Г. Райкова, Е. Младенова, И. Генов, Импедансно изследване на порест електролит със смесена проводимост .....	139
Й. Д. Милушева, Р. И. Букурещлиева, С. М. Христов, Въздушни газодифузионни електроди за електрохимични клетки магнезий-въздух, работещи с разтвор на натриев хлорид .....	145

П. В. Ангелов, С. С. Славов, Св. Р. Ганев, Я. Б. Димитриев, Ж. Г. Кацаров, Директен ултразвуков синтез на високотемпературни керамични фази при обикновени условия по иновативен метод .....	152
К. Ловчинов, М. Ганчев, М. Петров, Х. Ничев, Д. Димова-Малиновска, Дж. С. Граф, Ал. Уляшин Наноструктурирани ZnO слоеве, отложени чрез електрохимичен метод върху фронталната страна на фотоелементи от c-Si .....	158
Д. В. Блъскова-Кошничарова, Т. Петкова, Л. Фачиков, Е. Лефтерова, И. Каназирски, П. Ангелов, С. Василев, Изследване на TiO <sub>2</sub> -V <sub>2</sub> O <sub>5</sub> -P <sub>2</sub> O <sub>5</sub> стъкло-кристални материали .....	162
Д. С. Лилова, Ил. Х. Гаджов, Д. Димитров, Химичен и фазов състав на сплавни калай-кобалтови покрития отложени при постояннотоков и импулсен режим .....	170
Т. М. Додевска, Е. Г. Хорозова, Н. Д. Димчева, Електрохимични характеристики и структурни особености на въглеродни електроди, модифицирани с микро- и нанотложения от платинови метали .....	178
И. Радев, Г. Топалов, Г. Ганске, Е. Лефтерова, Г. Цотридис, У. Шнакенбург, Е. Славчева, Каталитична активност на съ-разпраснени филми от Pt-Ir спрямо редукция на кислород .	185
Г. Р. Борисов, А. Е. Стоянова, Е. Д. Лефтерова, Е. П. Славчева, Нов несъдържащ въглерод газодифузионен слой за аноди в ПЕМ водна електролиза .....	190
А. Е. Стоянова, Г. Р. Борисов, Е. Д. Лефтерова, Е. П. Славчева, МЕМ с несъдържащи въглерод Pt-Fe катализатор и газодифузионен слой за ПЕМ водна електролиза .....	195
Д. Г. Фильова, Г. П. Илиева, В. Ц. Цакова, Електрополимеризация на поли (3,4-етилениленидиокситиофен) слоеве в присъствието на различни допанти и ефекта им върху електрокаталитичните свойства на полимерите. Окисляване на аскорбинова киселина и допамин .....	201
Научен симпозиум „Водородната икономика - пътна карта за бъдещето“ .....	203
Е. Й. Чорбаджийска, М. Й. Митов, Й. В. Хубенова, Оптимизиране на условията за получаване на електрохимично-активен биофилм върху въглеродни аноди в дрожден биогоривен елемент .....	210
А. Евдоу, В. Заспалис, Л. Налбандиан, Нови материали като преносители на кислород за енергийни приложения .....	218
Г. Христов, Е. Чорбаджийска, Р. Рашков, Й. Хубенова, М. Митов, Сравнително изследване на Со-съдържащи катализатори за хидролиза на натриева борхидрид .....	222
И. Бърдаров, Й. Хубенова, М. Митов, Седиментни микробиални горивни елементи използващи речни седименти и почви .....	226
Е. Патрикиаду, В. Заспалис, 2, Л. Налбандиан, Е. Чорбаджийска, М. Митов, Й. Хубенова, Синтез и охарактеризиране на покрити със силикагел суперпарамагнитни наночастици за биоелектрохимични приложения .....	233
ИНСТРУКЦИЯ ЗА АВТОРИТЕ .....	235